

# Expanded

by MicroVention



*Advanced*

*HyperSoft 3D*  
complex coil  
*Advanced*

## A NEW DIMENSION IN COMPLEX SOFTNESS

MicroVention has expanded the scope of use for the popular HyperSoft® Coil by creating a complex form. This all-in-one hybrid design lets you Frame, Fill and Finish with the softness you need.

- A V-Trak® Advanced Coil for enhanced control
- Used with



For more information or a product demonstration,  
contact your local MicroVention representative:



**MicroVention, Inc.**

**Worldwide Headquarters**

1311 Valencia Avenue

Tustin, CA 92780 USA

MicroVention UK Limited

MicroVention Europe, S.A.R.L.

MicroVention Deutschland GmbH

PH +1.714.247.8000

PH +44 (0) 191 258 6777

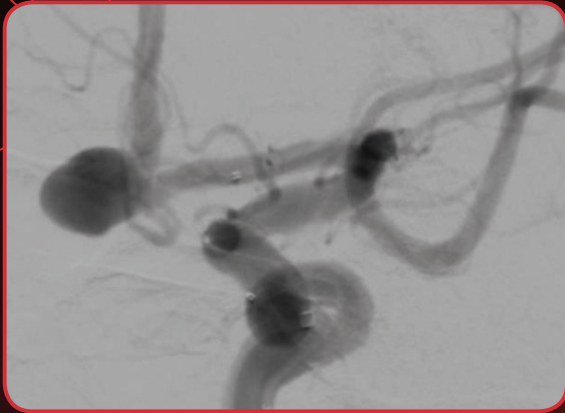
PH +33 (1) 39 21 77 46

PH +49 211 210 798-0

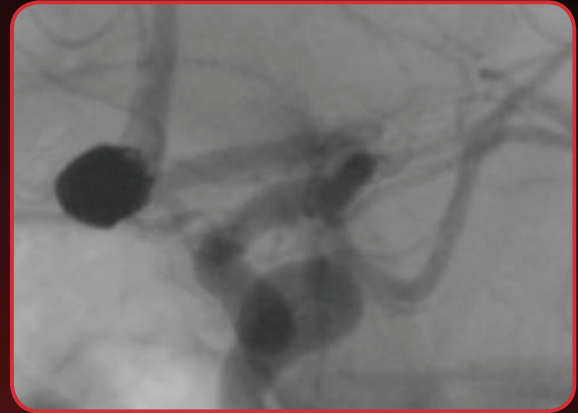
# BARRICADE™ COIL SYSTEM

## COILS THAT PERFORM

STENT ASSISTED COILING OF LEFT ACA ANEURYSM WITH THE BARRICADE COIL SYSTEM



PRE-TREATMENT



POST TREATMENT

“In this tortuous system, the Barricade coils were stable and conforming without issues of catheter kickback, even when working close to the neck, and they filled in the margins of neck very well.”

-Gary R. Duckwiler, M.D.

## COILS THAT SAVE \$

BARRICADE  
COILS  
SAVED  
**\$17,900\***

Images courtesy of Gary R. Duckwiler, M.D.

\* Estimated savings in this case, data on file.

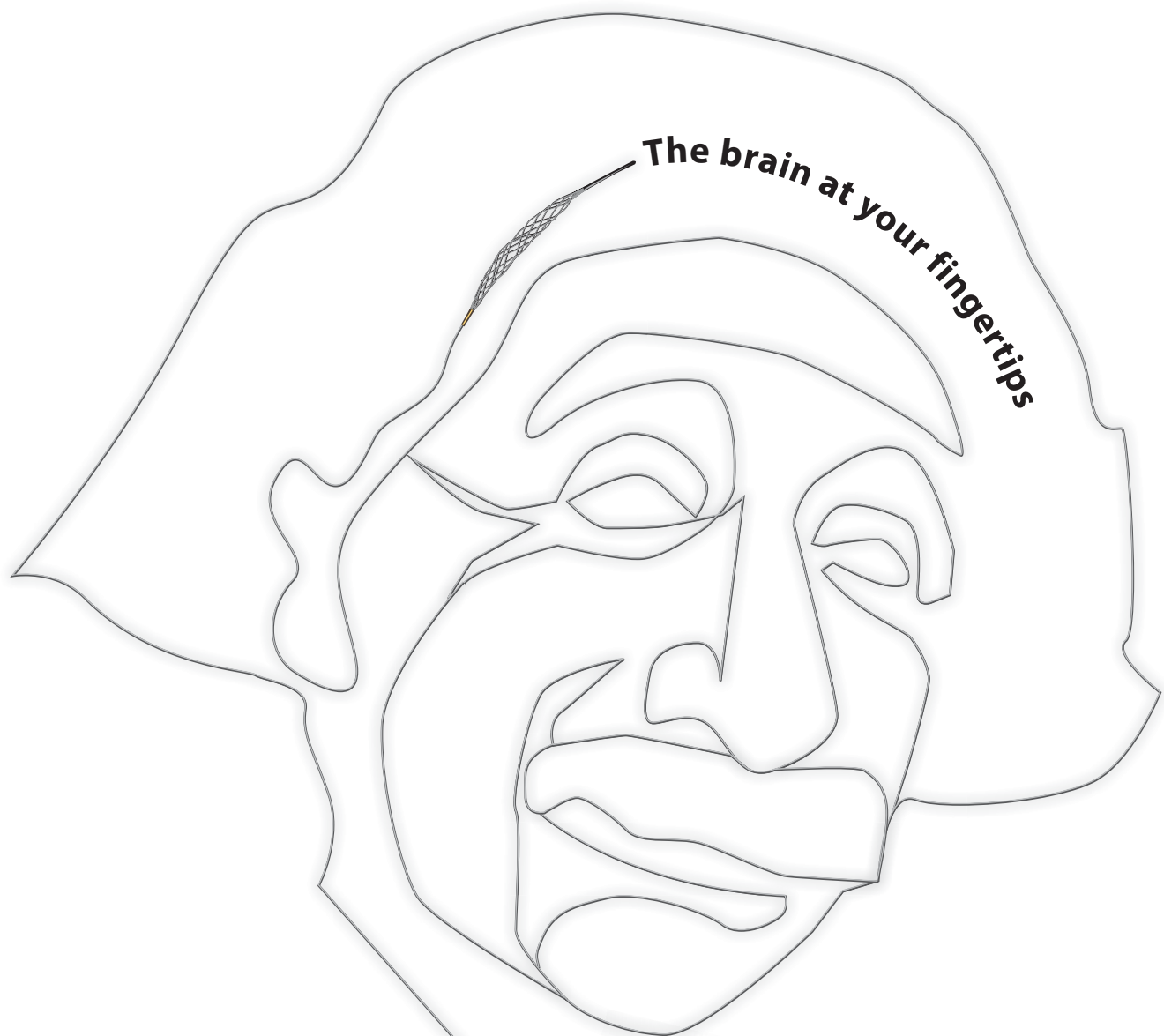
The Barricade Coil System is intended for the endovascular embolization of intracranial aneurysms and other neurovascular abnormalities such as arteriovenous malformations and arteriovenous fistulae. The System is also intended for vascular occlusion of blood vessels within the neurovascular system to permanently obstruct blood flow to an aneurysm or other vascular malformation and for arterial and venous embolizations in the peripheral vasculature. Refer to the instructions for use for complete product information.

18 TECHNOLOGY DRIVE #169, IRVINE CA 92618 | p: 949.788.1443 | f: 949.788.1444  
[WWW.BLOCKADEMEDICAL.COM](http://WWW.BLOCKADEMEDICAL.COM)

MKTG-045 Rev. A



**BLOCKADE**  
M E D I C A L



The brain at your fingertips

 **Rapid Medical**

[www.rapid-medical.com](http://www.rapid-medical.com) > [comaneci](#)





## Smooth and stable.

Target Detachable Coils deliver consistently smooth deployment and exceptional microcatheter stability. Designed to work seamlessly together for framing, filling and finishing. Target Coils deliver the high performance you demand.

For more information, please visit [www.strykerneurovascular.com/Target](http://www.strykerneurovascular.com/Target) or contact your local Stryker Neurovascular sales representative.



**Target®**  
DETACHABLE COILS

**The Foundation of the  
ASNR Symposium 2017:  
Discovery and Didactics  
April 22-23, 2017**

**ASNR 55<sup>th</sup> Annual Meeting:  
Diagnosis and Delivery  
April 24-27, 2017**



Long Beach Convention & Entertainment Center © Long Beach Convention & Visitors Bureau

**Jacqueline A. Bello, MD, FACR**  
**ASNR 2017 Program Chair/President-Elect**

*Programming developed in cooperation with and appreciation of the...*

**American Society of Functional Neuroradiology (ASFNR)**  
Kirk M. Welker, MD

**American Society of Head and Neck Radiology (ASHNR)**  
Rebecca S. Cornelius, MD, FACR

**American Society of Pediatric Neuroradiology (ASPNR)**  
Susan Palasis, MD

**American Society of Spine Radiology (ASSR)**  
Joshua A. Hirsch, MD, FACR, FSIR

**Society of NeuroInterventional Surgery (SNIS)**  
Blaise W. Baxter, MD

**American Society of Neuroradiology (ASNR)  
Health Policy Committee**  
Robert M. Barr, MD, FACR

**Computer Sciences & Informatics (CSI) Committee**  
John L. Go, MD, FACR

**Research Scientist Committee**  
Dikoma C. Shungu, PhD and Timothy, P.L. Roberts, PhD

**The International Hydrocephalus Imaging Working Group (IHIWG)/CSF Flow Group**  
William G. Bradley, Jr., MD, PhD, Harold L. Rekate, MD and Bryn A. Martin, PhD



**ASNR 55<sup>th</sup> Annual Meeting**  
c/o American Society of Neuroradiology  
800 Enterprise Drive, Suite 205 • Oak Brook, Illinois 60523-4216  
Phone: 630-574-0220 • Fax: 630 574-0661 • [www.asnr.org/2017](http://www.asnr.org/2017)



**ASFNR ASHNR ASPNR ASSR SNIS**

THE FOUNDATION OF THE ASNR



**Come to the beach!** Please join us in Long Beach, California, April 22-27, 2017, for the 55<sup>th</sup> Annual Meeting of the ASNR. Known for its 5.5 miles of Pacific Ocean waterfront, this southern California beach resort boasts a blend of city sophistication and seaside serenity. ASNR is delighted to provide a “4D” focus for this meeting, as depicted by our meeting logo: **Discovery and Didactics** for The Foundation of the ASNR Symposium 2017: **Diagnosis and Delivery** for the ensuing Annual Meeting Program.

Centered on Discovery and Didactics, the symposium will feature sessions on “What’s New?” in the role neuroimaging plays defining CNS disease mechanisms and how to best prepare for “What’s Next?” for our subspecialty in terms of training, teaching, and leading the process of lifelong learning. The annual meeting programming will address best practices in Diagnosis and Delivery, as we strive to provide value, promote quality in better health and care and consider cost. Our discussions will consider how to navigate the changing landscape of healthcare reform and reimbursement as subspecialists in a field that is changing at an equally “fast forward” pace!



Hyatt Regency Long Beach  
© Hyatt Regency Long Beach



Westin Long Beach  
© The Westin Long Beach



AMA Preferred Provider Offers and Services



**AMA Preferred Provider Offers and Services**

*Special offers that fit you and your practice's needs.*

Which savings would benefit you the most? Discounts on pharmaceuticals, medical supplies and equipment? Or on travel, practice financing, and financial and insurance services? Now physicians can save in all of these professional and personal categories and more through the AMA Preferred Provider Offers and Services program.

Please activate your 2016 AMA membership by calling **(800) 262-3211** or visit **[ama-assn.org/go/join](http://ama-assn.org/go/join)**.



\* Subsidiary of the American Medical Association.

# MODERN IMAGING AND RADIATION THERAPY:

APPROPRIATE, COLLABORATIVE AND TARGETED

67th ANNUAL SCIENTIFIC MEETING | GOLD COAST, AUSTRALIA



RANZCR 2016  
ranzcr2016.com

## KEYNOTE SPEAKERS

### Radiology

#### Dr Russell Fritz

National Orthopedic Imaging Associates  
San Francisco, USA

#### Professor Fiona Gilbert

Cambridge University Hospitals  
Cambridge, UK

#### Professor Meng Law

University of Southern California  
Los Angeles, USA

#### Dr Claude Sirlin

University of California  
San Diego, USA

### Radiation Oncology

#### Dr Silvia Formenti

New York Presbyterian Hospital  
New York, USA

#### Professor William Mendenhall

University of Florida  
Florida, USA

#### Dr Colleen Lawton

Medical College of Wisconsin  
Wisconsin, USA

## KEY DATES

### Registrations Open

April 2016

### Early Bird

### Registrations Close

July 2016

### Standard

### Registrations Close

August 2016

Details published are correct at the time of design and are subject to change without notice.  
For up to date information please visit [ranzcr2016.com](http://ranzcr2016.com)

## INTERESTED IN SPONSORING AND/OR EXHIBITING?

Contact Helen McGowan at [Helen@wsm.com.au](mailto:Helen@wsm.com.au) or +61 3 9645 6311



13 – 16 OCTOBER 2016

GOLD COAST CONVENTION & EXHIBITION CENTRE

[ranzcr2016.com](http://ranzcr2016.com)



## Simplify the MOC Process



## Manage your CME Credits Online



## CMEgateway.org

### It's Easy and Free!

Log on to CME Gateway to:

- View or print reports of your CME credits from multiple societies from a single access point.
- Print an aggregated report or certificate from each participating organization.
- Link to SAMs and other tools to help with maintenance of certification.

### American Board of Radiology (ABR) participation!

By activating ABR in your organizational profile, your MOC-fulfilling CME and SAM credits can be transferred to your own personalized database on the ABR Web site.

### Sign Up Today!

go to [CMEgateway.org](http://CMEgateway.org)

### Available to Members of Participating Societies

American Board of Radiology (ABR)

American College of Radiology (ACR)

American Roentgen Ray Society (ARRS)

American Society of Neuroradiology (ASNR)

Commission on Accreditation of Medical

Physics Educational Programs, Inc. (CAMPEP)

Radiological Society of North America (RSNA)

Society of Interventional Radiology (SIR)

SNM

The Society for Pediatric Radiology (SPR)

## Target® Detachable Coil

See package insert for complete indications, contraindications, warnings and instructions for use.

### INTENDED USE/ INDICATIONS FOR USE

Target Detachable Coils are intended to endovascularly obstruct or occlude blood flow in vascular abnormalities of the neurovascular and peripheral vessels.

Target Detachable Coils are indicated for endovascular embolization of:

- Intracranial aneurysms
- Other neurovascular abnormalities such as arteriovenous malformations and arteriovenous fistulae
- Arterial and venous embolizations in the peripheral vasculature

### CONTRAINDICATIONS

None known.

### POTENTIAL ADVERSE EVENTS

Potential complications include, but are not limited to: allergic reaction, aneurysm perforation and rupture, arrhythmia, death, edema, embolus, headache, hemorrhage, infection, ischemia, neurological/intracranial sequelae, post-embolization syndrome (fever, increased white blood cell count, discomfort), TIA/stroke, vasospasm, vessel occlusion or closure, vessel perforation, dissection, trauma or damage, vessel rupture, vessel thrombosis. Other procedural complications including but not limited to: anesthetic and contrast media risks, hypotension, hypertension, access site complications.

### WARNINGS

- Contents supplied STERILE using an ethylene oxide (EO) process. Do not use if sterile barrier is damaged. If damage is found, call your Stryker Neurovascular representative.
- For single use only. Do not reuse, reprocess or resterilize. Reuse, reprocessing or resterilization may compromise the structural integrity of the device and/or lead to device failure which, in turn, may result in patient injury, illness or death. Reuse, reprocessing or resterilization may also create a risk of contamination of the device and/or cause patient infection or cross-infection, including, but not limited to, the transmission of infectious disease(s) from one patient to another. Contamination of the device may lead to injury, illness or death of the patient.

- After use, dispose of product and packaging in accordance with hospital, administrative and/or local government policy.
- **This device should only be used by physicians who have received appropriate training in interventional neuroradiology or interventional radiology and preclinical training on the use of this device as established by Stryker Neurovascular.**
- Patients with hypersensitivity to 316LVM stainless steel may suffer an allergic reaction to this implant.
- MR temperature testing was not conducted in peripheral vasculature, arteriovenous malformations or fistulae models.
- The safety and performance characteristics of the Target Detachable Coil System (Target Detachable Coils, InZone Detachment Systems, delivery systems and accessories) have not been demonstrated with other manufacturer's devices (whether coils, coil delivery devices, coil detachment systems, catheters, guidewires, and/or other accessories). Due to the potential incompatibility of non Stryker Neurovascular devices with the Target Detachable Coil System, the use of other manufacturer's device(s) with the Target Detachable Coil System is not recommended.
- To reduce risk of coil migration, the diameter of the first and second coil should never be less than the width of the ostium.
- In order to achieve optimal performance of the Target Detachable Coil System and to reduce the risk of thromboembolic complications, it is critical that a continuous infusion of appropriate flush solution be maintained between a) the femoral sheath and guiding catheter, b) the 2-tip microcatheter and guiding catheters, and c) the 2-tip microcatheter and Stryker Neurovascular guidewire and delivery wire. Continuous flush also reduces the potential for thrombus formation on, and crystallization of infusate around, the detachment zone of the Target Detachable Coil.
- Do not use the product after the "Use By" date specified on the package.
- Reuse of the flush port/dispenser coil or use with any coil other than the original coil may result in contamination of, or damage to, the coil.
- Utilization of damaged coils may affect coil delivery to, and stability inside, the vessel or aneurysm, possibly resulting in coil migration and/or stretching.

- The fluoro-saver marker is designed for use with a Rotating Hemostatic Valve (RHV). If used without an RHV, the distal end of the coil may be beyond the alignment marker when the fluoro-saver marker reaches the microcatheter hub.
  - If the fluoro-saver marker is not visible, do not advance the coil without fluoroscopy.
  - Do not rotate delivery wire during or after delivery of the coil. Rotating the Target Detachable Coil delivery wire may result in a stretched coil or premature detachment of the coil from the delivery wire, which could result in coil migration.
  - Verify there is no coil loop protrusion into the parent vessel after coil placement and prior to coil detachment. Coil loop protrusion after coil placement may result in thromboembolic events if the coil is detached.
  - Verify there is no movement of the coil after coil placement and prior to coil detachment. Movement of the coil after coil placement may indicate that the coil could migrate once it is detached.
  - Failure to properly close the RHV compression fitting over the delivery wire before attaching the InZone® Detachment System could result in coil movement, aneurysm rupture or vessel perforation.
  - Verify repeatedly that the distal shaft of the catheter is not under stress before detaching the Target Detachable Coil. Axial compression or tension forces could be stored in the 2-tip microcatheter causing the tip to move during coil delivery. Microcatheter tip movement could cause the aneurysm or vessel to rupture.
  - Advancing the delivery wire beyond the microcatheter tip once the coil has been detached involves risk of aneurysm or vessel perforation.
  - The long term effect of this product on extravascular tissues has not been established so care should be taken to retain this device in the intravascular space.
- Damaged delivery wires may cause detachment failures, vessel injury or unpredictable distal tip response during coil deployment. If a delivery wire is damaged at any point during the procedure, do not attempt to straighten or otherwise repair it. Do not proceed with deployment or detachment. Remove the entire coil and replace with undamaged product.
- After use, dispose of product and packaging in accordance with hospital, administrative and/or local government policy.

### CAUTIONS / PRECAUTIONS

- Federal Law (USA) restricts this device to sale by or on the order of a physician.
- Besides the number of InZone Detachment System units needed to complete the case, there must be an extra InZone Detachment System unit as back up.
- Removing the delivery wire without grasping the introducer sheath and delivery wire together may result in the detachable coil sliding out of the introducer sheath.
- Failure to remove the introducer sheath after inserting the delivery wire into the RHV of the microcatheter will interrupt normal infusion of flush solution and allow back flow of blood into the microcatheter.
- Some low level overhead light near or adjacent to the patient is required to visualize the fluoro-saver marker; monitor light alone will not allow sufficient visualization of the fluoro-saver marker.
- Advance and retract the Target Detachable Coil carefully and smoothly without excessive force. If unusual friction is noticed, slowly withdraw the Target Detachable Coil and examine for damage. If damage is present, remove and use a new Target Detachable Coil. If friction or resistance is still noted, carefully remove the Target Detachable Coil and microcatheter and examine the microcatheter for damage.
- If it is necessary to reposition the Target Detachable Coil, verify under fluoroscopy that the coil moves with a one-to-one motion. If the coil does not move with a one-to-one motion or movement is difficult, the coil may have stretched and could possibly migrate or break. Gently remove both the coil and microcatheter and replace with new devices.
- Increased detachment times may occur when:
  - Other embolic agents are present.
  - Delivery wire and microcatheter markers are not properly aligned.
  - Thrombus is present on the coil detachment zone.
- Do not use detachment systems other than the InZone Detachment System.
- Increased detachment times may occur when delivery wire and microcatheter markers are not properly aligned.
- Do not use detachment systems other than the InZone Detachment System.



**Stryker Neurovascular**  
47900 Bayside Parkway  
Fremont, CA 94538

[strykerneurovascular.com](http://strykerneurovascular.com)

Date of Release: MAR/2016

EX\_UN\_US

Copyright © 2016 Stryker  
NV00018669.AA

## AXS Catalyst™ 6 Distal Access Catheter

See package insert for complete indications, complications, warnings, and instructions for use.

### INTENDED USE/INDICATIONS FOR USE

The AXS Catalyst Distal Access Catheter is indicated for use in facilitating the insertion and guidance of appropriately sized interventional devices into a selected blood vessel in the peripheral and neurovascular systems. The AXS Catalyst Distal Access Catheter is also indicated for use as a conduit for retrieval devices.

### CONTRAINDICATIONS

None known.

### ADVERSE EVENTS

Potential adverse events associated with the use of catheters or with the endovascular procedures include, but are not limited to: access site complications, allergic reaction, aneurysm perforation, aneurysm rupture, death, embolism (air, foreign body, plaque, thrombus), hematoma, hemorrhage, infection, ischemia, neurological deficits, pseudoaneurysm, stroke, transient ischemic attack, vasospasm, vessel dissection, vessel occlusion, vessel perforation, vessel rupture, and vessel thrombosis.

### WARNING

Contents supplied sterile using an ethylene oxide (EO) process. Do not use if sterile barrier is damaged. If damage is found, call your Stryker Neurovascular representative. For single use only. Do not reuse, reprocess or resterilize. Reuse, reprocessing or resterilization may compromise the structural integrity of the device and/or lead to device failure which, in turn, may result in patient injury, illness or death. Reuse, reprocessing or resterilization may also create a risk of contamination of the device and/or cause patient infection or cross-infection, including, but not limited to, the transmission of infectious disease(s) from one patient to another.

Contamination of the device may lead to injury, illness or death of the patient. After use, dispose of product and packaging in accordance with hospital, administrative and/or local government policy.

- Limited testing has been performed with solutions such as contrast media, and saline. The use of these catheters for delivery of solutions other than the types that have been tested for compatibility is not recommended.
- Not intended for use with power injectors.
- If flow through catheter becomes restricted, do not attempt to clear catheter lumen by infusion. Doing so may cause catheter damage or patient injury. Remove and replace catheter.

- Never advance or withdraw an intravascular device against resistance until the cause of the resistance is determined by fluoroscopy. Movement of the device against resistance could dislodge a clot, perforate a vessel wall, or damage the device.

### PRECAUTIONS

- Carefully inspect all devices prior to use. Verify size, length, and condition are suitable for the specific procedure. Do not use a device that has been damaged in any way. Damaged device may cause complications.
- To control the proper introduction, movement, positioning and removal of the catheter within the vascular system, users should employ standard clinical angiographic and fluoroscopic practices and techniques throughout the interventional procedure.
- Use the product prior to the "Use By" date printed on the label.
- To prevent thrombus formation and contrast media crystal formation, maintain a constant infusion of appropriate flush solution through catheter lumen.
- Torquing the catheter may cause damage which could result in kinking or separation of the catheter shaft.

Copyright © 2016 Stryker  
NV00018756.AA



**Stryker Neurovascular**  
47900 Bayside Parkway  
Fremont, CA 94538

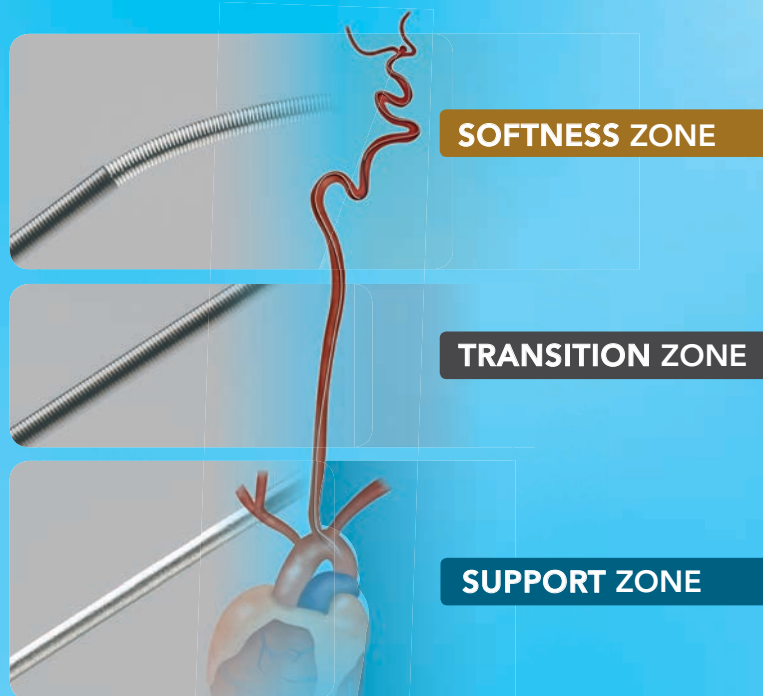
[strykerneurovascular.com](http://strykerneurovascular.com)

Date of Release: MAR/2016

EX\_UN\_US

# Advanced

by MicroVention



## ENHANCED CONTROL TO MAXIMIZE COIL PERFORMANCE

The V-Trak® Advanced Coil System, the next generation to power the performance of our most technically advanced line of coils. Offering the optimal combination of support and flexibility.

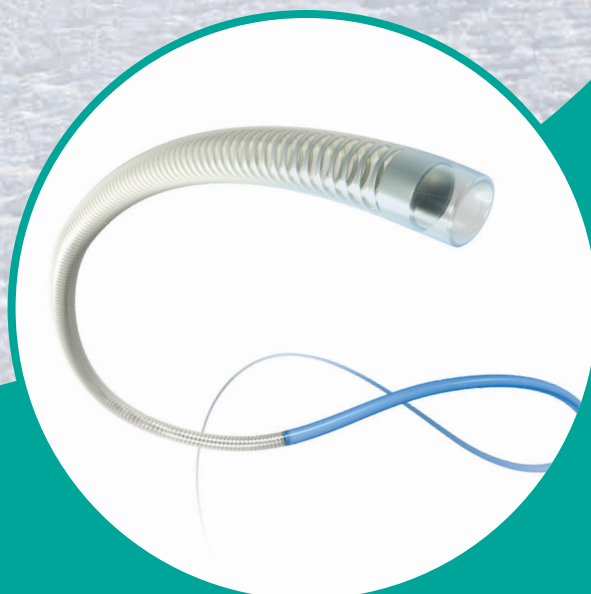
[microvention.com](http://microvention.com)

MICROVENTION, V-Trak, HyperSoft and Headway are registered trademarks of MicroVention, Inc. Scientific and clinical data related to this document are on file at MicroVention, Inc. Refer to Instructions for Use for additional information. Federal (USA) law restricts this device for sale by or on the order of a physician.  
© 2014 MicroVention, Inc. 8/14

## Success accelerated.

With superior trackability, resilient design and strong aspiration force, the AXS Catalyst™ 6 Distal Access Catheter is designed for fast access and rapid revascularization with Trevo® XP Retrievers.\*†

\*To facilitate revascularization with Trevo XP ProVue Retrievers.  
†Bench test results. n=3 trackability, aspiration. n=1 kink resistance.  
Bench test results may not necessarily be indicative of clinical performance.

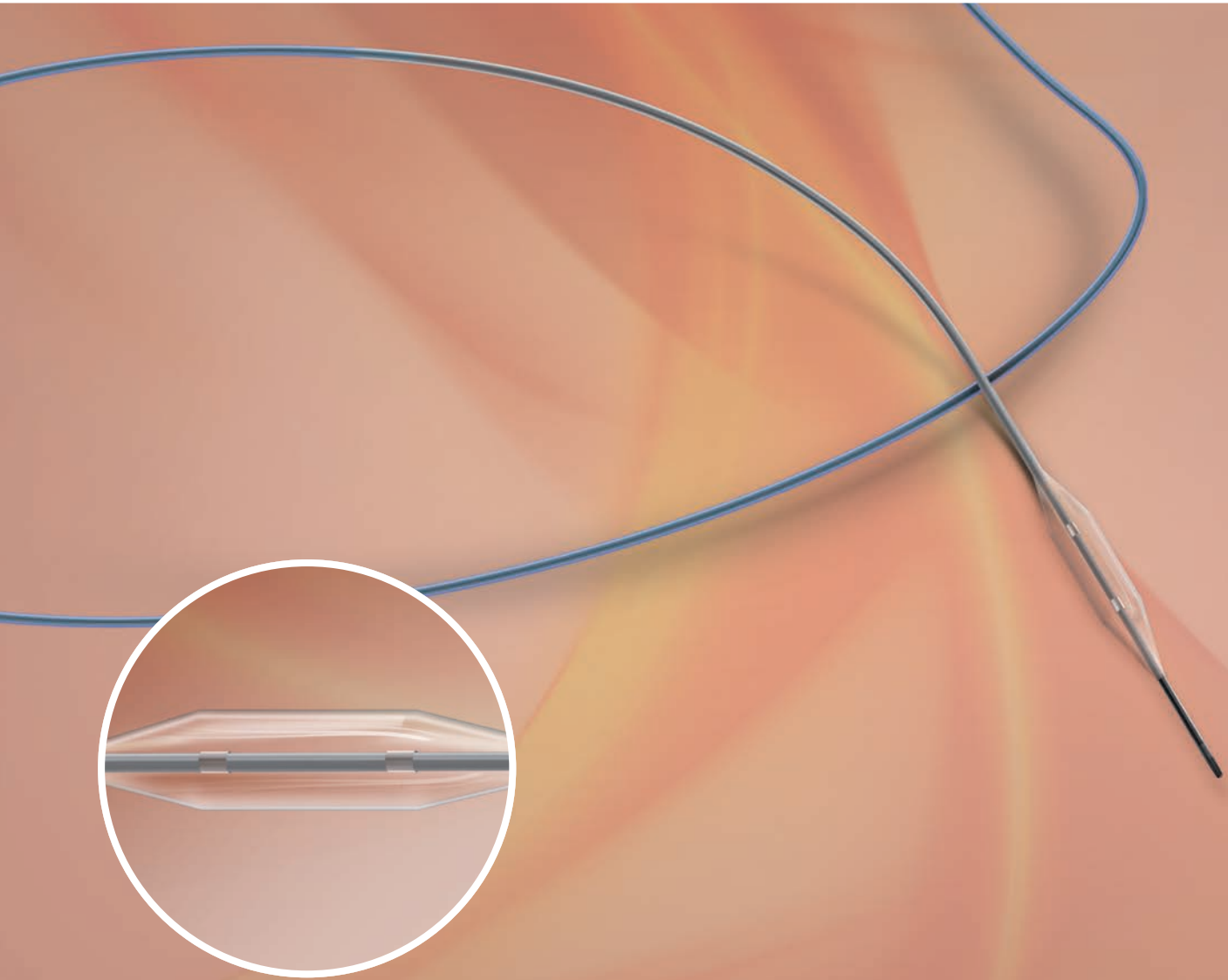


**AXS Catalyst™ 6**  
DISTAL ACCESS CATHETER



ENGINEERING STROKE SOLUTIONS

## NeuroSpeed® PTA Balloon Catheter



Not for sale within the territory of the United States

### UNIQUE BALLOON COMPLIANCE

- Broad range of diameters (1.5 mm to 4.0 mm)
- Access to very distal lesions

# AJNR

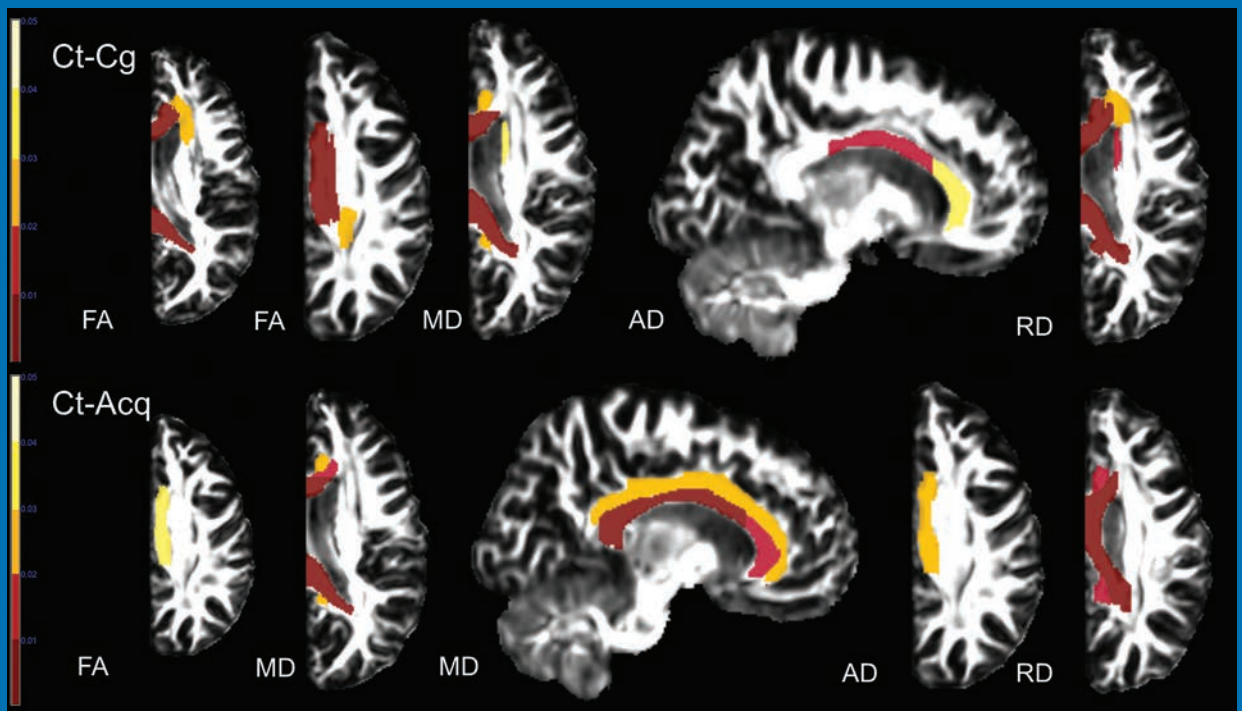
## AMERICAN JOURNAL OF NEURORADIOLOGY

MAY 2016  
VOLUME 37  
NUMBER 5  
WWW.AJNR.ORG

THE JOURNAL OF DIAGNOSTIC AND  
INTERVENTIONAL NEURORADIOLOGY

Hypercapnia BOLD fMRI in symptomatic carotid artery occlusion  
Quantitative susceptibility mapping in Parkinson disease  
Pipeline embolization in treatment of previously stented aneurysms

Official Journal ASNR • ASFNR • ASHNR • ASPNR • ASSR



# AJNR

## AMERICAN JOURNAL OF NEURORADIOLOGY

MAY 2016  
VOLUME 37  
NUMBER 5  
WWW.AJNR.ORG

Publication Preview at [www.ajnr.org](http://www.ajnr.org) features articles released in advance of print. Visit [www.ajnrblog.org](http://www.ajnrblog.org) to comment on AJNR content and chat with colleagues and AJNR's News Digest at <http://ajnrdigest.org> to read the stories behind the latest research in neuroimaging.

773 **PERSPECTIVES** *S. Yamada*

### REVIEW ARTICLE

-   774 **Distinguishing Neuroimaging Features in Patients Presenting with Visual Hallucinations** *T.T. Winton-Brown, et al.* **ADULT BRAIN**

### GENERAL CONTENTS

-   782 **Lateral Asymmetry and Spatial Difference of Iron Deposition in the Substantia Nigra of Patients with Parkinson Disease Measured with Quantitative Susceptibility Mapping** *M. Azuma, et al.* **ADULT BRAIN**
-   789 **Quantitative Susceptibility Mapping Suggests Altered Brain Iron in Premanifest Huntington Disease** *J.M.G. van Bergen, et al.* **ADULT BRAIN FUNCTIONAL**
- 797 **Quantitative MRI for Rapid and User-Independent Monitoring of Intracranial CSF Volume in Hydrocephalus** *J. Virhammar, et al.* **ADULT BRAIN**
-   802 **Quantitative Intracranial Atherosclerotic Plaque Characterization at 7T MRI: An Ex Vivo Study with Histologic Validation** *A.A. Hartevelde, et al.* **ADULT BRAIN**
-    811 **Mitotic Activity in Glioblastoma Correlates with Estimated Extravascular Extracellular Space Derived from Dynamic Contrast-Enhanced MR Imaging** *S.J. Mills, et al.* **ADULT BRAIN**
-   818 **Identifying Significant Changes in Cerebrovascular Reactivity to Carbon Dioxide** *O. Sobczyk, et al.* **ADULT BRAIN FUNCTIONAL**
-   825 **Cough-Associated Changes in CSF Flow in Chiari I Malformation Evaluated by Real-Time MRI** *R.A. Bhadelia, et al.* **ADULT BRAIN SPINE**
- 831 **Imaging Findings Associated with Space-Occupying Edema in Patients with Large Middle Cerebral Artery Infarcts** *A.D. Horsch, et al.* **ADULT BRAIN INTERVENTIONAL**
- 838 **TICI and Age: What's the Score?** *L.A. Slater, et al.* **INTERVENTIONAL**
- 844 **Validity of the Meyer Scale for Assessment of Coiled Aneurysms and Aneurysm Recurrence** *A. Rouchaud, et al.* **INTERVENTIONAL**
-  849 **Pipeline Embolization Device in the Treatment of Recurrent Previously Stented Cerebral Aneurysms** *B. Daou, et al.* **INTERVENTIONAL ADULT BRAIN**

AJNR (Am J Neuroradiol ISSN 0195-6108) is a journal published monthly, owned and published by the American Society of Neuroradiology (ASNR), 800 Enterprise Drive, Suite 205, Oak Brook, IL 60523. Annual dues for the ASNR include \$170.00 for journal subscription. The journal is printed by Cadmus Journal Services, 5457 Twin Knolls Road, Suite 200, Columbia, MD 21045; Periodicals postage paid at Oak Brook, IL and additional mailing offices. Printed in the U.S.A. POSTMASTER: Please send address changes to American Journal of Neuroradiology, P.O. Box 3000, Denville, NJ 07834, U.S.A. Subscription rates: nonmember \$380 (\$450 foreign) print and online, \$305 online only; institutions \$440 (\$510 foreign) print and basic online, \$875 (\$940 foreign) print and extended online, \$365 online only (basic), extended online \$790; single copies are \$35 each (\$40 foreign). Indexed by PubMed/Medline, BIOSIS Previews, Current Contents (Clinical Medicine and Life Sciences), EMBASE, Google Scholar, HighWire Press, Q-Sensei, RefSeek, Science Citation Index, and SCI Expanded. Copyright © American Society of Neuroradiology.

-  856 **A Systematic Review and Meta-Analysis of Treatment and Outcome of Blister-Like Aneurysms** *S. Peschillo, et al.* **INTERVENTIONAL ADULT BRAIN**
- 862 **Endovascular Treatment of Very Small Intracranial Aneurysms: Meta-Analysis** *V.N. Yamaki, et al.* **INTERVENTIONAL**
-  868 **Endovascular Treatment of Intracranial Aneurysms with the WEB Device: A Systematic Review of Clinical Outcomes** *X. Armoiry, et al.* **INTERVENTIONAL ADULT BRAIN**
-  873 **Endovascular Coiling versus Surgical Clipping for Poor-Grade Ruptured Intracranial Aneurysms: Postoperative Complications and Clinical Outcome in a Multicenter Poor-Grade Aneurysm Study** *B. Zhao, et al.* **INTERVENTIONAL ADULT BRAIN**
-  879 **Inter- and Intrarater Agreement on the Outcome of Endovascular Treatment of Aneurysms Using MRA** *S. Jamali, et al.* **INTERVENTIONAL ADULT BRAIN**
-  885 **Endovascular Cooling Catheter for Selective Brain Hypothermia: An Animal Feasibility Study of Cooling Performance** *G. Cattaneo, et al.* **INTERVENTIONAL**
-  892 **WEB in Partially Thrombosed Intracranial Aneurysms: A Word of Caution** *G. Anil, et al.* **INTERVENTIONAL**
-   897 **Different Functional and Microstructural Changes Depending on Duration of Mild Cognitive Impairment in Parkinson Disease** *N.-Y. Shin, et al.* **FUNCTIONAL ADULT BRAIN**
- 904 **Impaired Cerebrovascular Reactivity Predicts Recurrent Symptoms in Patients with Carotid Artery Occlusion: A Hypercapnia BOLD fMRI Study** *S.D. Goode, et al.* **FUNCTIONAL ADULT BRAIN**
- 910 **Imaging Features of Juvenile Xanthogranuloma of the Pediatric Head and Neck** *D.T. Ginat, et al.* **HEAD & NECK PEDIATRICS**
-   917 **Diffusion Tractography Biomarkers of Pediatric Cerebellar Hypoplasia/Atrophy: Preliminary Results Using Constrained Spherical Deconvolution** *S. Fiori, et al.* **PEDIATRICS FUNCTIONAL**
-    924 **Cerebral Reorganization after Hemispherectomy: A DTI Study** *A. Meoded, et al.* **PEDIATRICS FUNCTIONAL**
- 932 **Quantitative Assessment of Neovascularization after Indirect Bypass Surgery: Color-Coded Digital Subtraction Angiography in Pediatric Moyamoya Disease** *H.-H. Cho, et al.* **PEDIATRICS INTERVENTIONAL**
-    939 **Brain Structural and Vascular Anatomy Is Altered in Offspring of Pre-Eclamptic Pregnancies: A Pilot Study** *M.T. Rätsep, et al.* **PEDIATRICS HEAD & NECK**
-    946 **Diagnostic Value of Prenatal MR Imaging in the Detection of Brain Malformations in Fetuses before the 26th Week of Gestational Age** *G. Conte, et al.* **PEDIATRICS**
- 952 **Normal Development and Measurements of the Occipital Condyle-C1 Interval in Children and Young Adults** *P. Smith, et al.* **PEDIATRICS SPINE**
-  958 **Application of Normative Occipital Condyle-C1 Interval Measurements to Detect Atlanto-Occipital Injury in Children** *B. Corcoran, et al.* **PEDIATRICS SPINE**
-   963 **Improved Lesion Detection by Using Axial T2-Weighted MRI with Full Spinal Cord Coverage in Multiple Sclerosis** *S. Galler, et al.* **SPINE**
-  970 **Comparison of Sagittal FSE T2, STIR, and T1-Weighted Phase-Sensitive Inversion Recovery in the Detection of Spinal Cord Lesions in MS at 3T** *P. Alcaide-Leon, et al.* **SPINE**
- 976 **35 YEARS AGO IN AJNR**

## ONLINE FEATURES

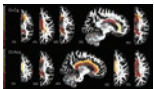
### LETTERS

- E41** **Macrocyclic Gadolinium-Based Contrast Agents Do Not Cause Hyperintensity in the Dentate Nucleus** *T. Kanda, et al.*
- E42** **Reply** *J. Ramalho, et al.*
- E43** **Cortical Superficial Siderosis Presumed due to Cerebral Amyloid Angiopathy: Minimum Standards for Rating and Reporting** *A. Charidimou*
- E45** **Cooling Catheters for Selective Brain Hypothermia** *T.K. Mattingly, et al.*
- E46** **Reply** *G. Cattaneo, et al.*
- E48** **Hypothalamic Adhesions: Asymptomatic, Incidental, or Not?**  
*A. Vossough, et al.*

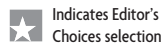
### BOOK REVIEWS

*R.M. Quencer, Section Editor*

Please visit [www.ajnrblog.org](http://www.ajnrblog.org) to read and comment on Book Reviews.



Compared with controls (Ct), patients with anatomic hemispherectomy because of a congenital (Cg) and acquired (Acq) underlying etiology showed a decrease in FA and AD and an increase in MD and RD in multiple white matter tracts.



Indicates Editor's Choices selection



Indicates Fellows' Journal Club selection



Indicates open access to non-subscribers at [www.ajnr.org](http://www.ajnr.org)



Indicates article with supplemental on-line table



Indicates article with supplemental on-line photo



Indicates article with supplemental on-line video



Evidence-Based Medicine Level 1



Evidence-Based Medicine Level 2

### Official Journal:

American Society of Neuroradiology  
American Society of Functional Neuroradiology  
American Society of Head and Neck Radiology  
American Society of Pediatric Neuroradiology  
American Society of Spine Radiology

### EDITOR-IN-CHIEF

#### Jeffrey S. Ross, MD

Professor of Radiology, Department of Radiology,  
Mayo Clinic College of Medicine, Phoenix, Arizona

### SENIOR EDITORS

#### Harry J. Cloft, MD, PhD

Professor of Radiology and Neurosurgery,  
Department of Radiology, Mayo Clinic College of  
Medicine, Rochester, Minnesota

#### Thierry A.G.M. Huisman, MD

Professor of Radiology, Pediatrics, Neurology, and  
Neurosurgery, Chairman, Department of Imaging  
and Imaging Science, Johns Hopkins Bayview,  
Director, Pediatric Radiology and Pediatric  
Neuroradiology, Johns Hopkins Hospital,  
Baltimore, Maryland

#### C.D. Phillips, MD, FACR

Professor of Radiology, Weill Cornell Medical  
College, Director of Head and Neck Imaging,  
New York-Presbyterian Hospital, New York,  
New York

#### Pamela W. Schaefer, MD

Clinical Director of MRI and Associate Director of  
Neuroradiology, Massachusetts General Hospital,  
Boston, Massachusetts, Associate Professor,  
Radiology, Harvard Medical School, Cambridge,  
Massachusetts

#### Charles M. Strother, MD

Professor of Radiology, Emeritus, University of  
Wisconsin, Madison, Wisconsin

#### Jody Tanabe, MD

Professor of Radiology and Psychiatry,  
Chief of Neuroradiology,  
University of Colorado, Denver, Colorado

### STATISTICAL SENIOR EDITOR

#### Bryan A. Comstock, MS

Senior Biostatistician,  
Department of Biostatistics,  
University of Washington, Seattle, Washington

### EDITORIAL BOARD

Ashley H. Aiken, *Atlanta, Georgia*  
A. James Barkovich, *San Francisco, California*  
Walter S. Bartynski, *Charleston, South Carolina*  
Barton F. Branstetter IV, *Pittsburgh, Pennsylvania*  
Jonathan L. Brisman, *Lake Success, New York*  
Julie Bykowski, *San Diego, California*  
Donald W. Chakeres, *Columbus, Ohio*  
Asim F. Choudhri, *Memphis, Tennessee*  
Alessandro Cianfoni, *Lugano, Switzerland*  
Colin Derdeyn, *St. Louis, Missouri*  
Rahul S. Desikan, *San Francisco, California*  
Richard du Mesnil de Rochemont, *Frankfurt,  
Germany*  
Clifford J. Eskey, *Hanover, New Hampshire*  
Massimo Filippi, *Milan, Italy*  
David Fiorella, *Cleveland, Ohio*  
Allan J. Fox, *Toronto, Ontario, Canada*  
Christine M. Glastonbury, *San Francisco,  
California*

John L. Go, *Los Angeles, California*  
Wan-Yuo Guo, *Taipei, Taiwan*  
Rakesh K. Gupta, *Lucknow, India*  
Lotfi Hachein-Bey, *Sacramento, California*  
David B. Hackney, *Boston, Massachusetts*  
Christopher P. Hess, *San Francisco, California*  
Andrei Holodny, *New York, New York*  
Benjamin Huang, *Chapel Hill, North Carolina*  
George J. Hunter, *Boston, Massachusetts*  
Mahesh V. Jayaraman, *Providence, Rhode Island*  
Valerie Jewells, *Chapel Hill, North Carolina*  
Timothy J. Kaufmann, *Rochester, Minnesota*  
Kenneth F. Layton, *Dallas, Texas*  
Ting-Yim Lee, *London, Ontario, Canada*  
Michael M. Lell, *Erlangen, Germany*  
Michael Lev, *Boston, Massachusetts*  
Karl-Olof Lovblad, *Geneva, Switzerland*  
Franklin A. Marden, *Chicago, Illinois*  
M. Gisele Matheus, *Charleston, South Carolina*  
Joseph C. McGowan, *Merion Station,  
Pennsylvania*

Kevin R. Moore, *Salt Lake City, Utah*  
Christopher J. Moran, *St. Louis, Missouri*  
Takahisa Mori, *Kamakura City, Japan*  
Suresh Mukherji, *Ann Arbor, Michigan*  
Amanda Murphy, *Toronto, Ontario, Canada*  
Alexander J. Nemeth, *Chicago, Illinois*  
Laurent Pierot, *Reims, France*  
Jay J. Pillai, *Baltimore, Maryland*  
Whitney B. Pope, *Los Angeles, California*  
M. Judith Donovan Post, *Miami, Florida*  
Tina Young Poussaint, *Boston, Massachusetts*  
Joana Ramalho, *Lisbon, Portugal*

Otto Rapalino, *Boston, Massachusetts*  
Álex Rovira-Cañellas, *Barcelona, Spain*  
Paul M. Ruggieri, *Cleveland, Ohio*  
Zoran Rumboldt, *Rijeka, Croatia*  
Amit M. Saindane, *Atlanta, Georgia*  
Erin Simon Schwartz, *Philadelphia, Pennsylvania*  
Aseem Sharma, *St. Louis, Missouri*  
J. Keith Smith, *Chapel Hill, North Carolina*  
Maria Vittoria Spampinato, *Charleston, South  
Carolina*  
Gordon K. Sze, *New Haven, Connecticut*  
Krishnamoorthy Thamburaj, *Hershey, Pennsylvania*  
Kent R. Thielen, *Rochester, Minnesota*  
Cheng Hong Toh, *Taipei, Taiwan*  
Thomas A. Tomsick, *Cincinnati, Ohio*  
Aquila S. Turk, *Charleston, South Carolina*  
Willem Jan van Rooij, *Tilburg, Netherlands*  
Arastoo Vossough, *Philadelphia, Pennsylvania*  
Elysa Widjaja, *Toronto, Ontario, Canada*  
Max Wintermark, *Charlottesville, Virginia*  
Ronald L. Wolf, *Philadelphia, Pennsylvania*  
Kei Yamada, *Kyoto, Japan*

### EDITORIAL FELLOW

Hillary R. Kelly, *Boston, Massachusetts*

### SPECIAL CONSULTANTS TO THE EDITOR

#### AJNR Blog Editor

Neil Lall, *Denver, Colorado*

#### Case of the Month Editor

Nicholas Stence, *Aurora, Colorado*

#### Case of the Week Editors

Juan Pablo Cruz, *Santiago, Chile*  
Sapna Rawal, *Toronto, Ontario, Canada*

#### Classic Case Editor

Sandy Cheng-Yu Chen, *Taipei, Taiwan*

#### Facebook Editor

Peter Yi Shen, *Sacramento, California*

#### Health Care and Socioeconomics Editor

Pina C. Sanelli, *New York, New York*

#### Physics Editor

Greg Zaharchuk, *Stanford, California*

#### Podcast Editor

Yvonne Lui, *New York, New York*

#### Twitter Editor

Ryan Fitzgerald, *Little Rock, Arkansas*

### YOUNG PROFESSIONALS

#### ADVISORY COMMITTEE

Asim K. Bag, *Birmingham, Alabama*  
Anna E. Nidecker, *Sacramento, California*  
Peter Yi Shen, *Sacramento, California*

Founding Editor

Juan M. Taveras

Editors Emeriti

Mauricio Castillo, Robert I. Grossman,  
Michael S. Huckman, Robert M. Quencer

Managing Editor

Karen Halm

Electronic Publications Manager

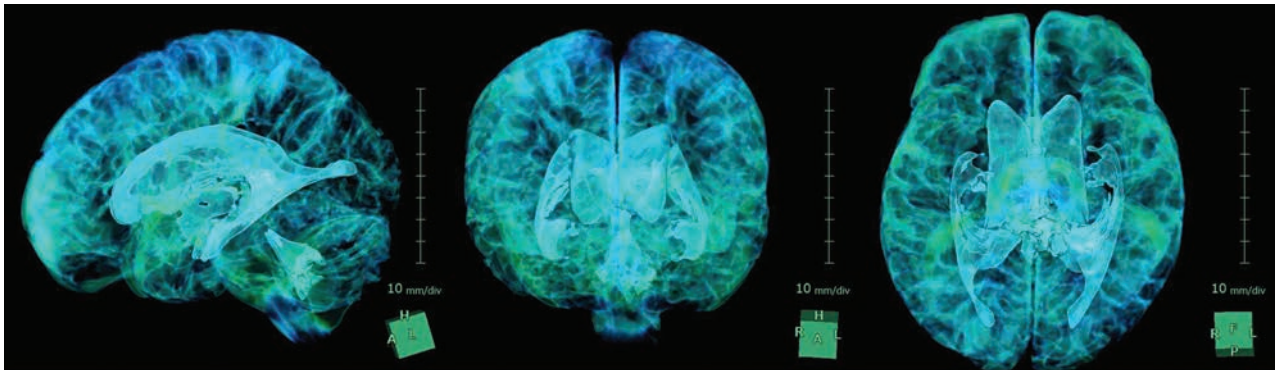
Jason Gantenberg

Executive Director, ASNR

James B. Gantenberg

Director of Communications, ASNR

Angelo Artemakis



Title: 3D View of the Intracranial CSF Space in the Normal Brain. Explanation: It is a splendid visualization created by using an independent 3D volume analyzer workstation. A 73-year-old man had no medical history including dementia. CSF spaces were automatically extracted from brain parenchyma by using a simple threshold algorithm on the T2-weighted 3D-SPACE sequence with a 64-channel 3-Tesla MRI system. His total CSF volume was automatically calculated as 509 mL which was constructed total ventricular volume (97 mL) and total cisternal volume (412 mL). His brain parenchymal volume was calculated as 1221 mL.

*Shigeki Yamada, MD, PhD, Department of Neurosurgery, Stroke Center, NPH Center, Rakuwakai Otowa Hospital, Kyoto, Japan*

# Distinguishing Neuroimaging Features in Patients Presenting with Visual Hallucinations

 T.T. Winton-Brown,  A. Ting,  R. Mocellin,  D. Velakoulis, and  F. Gaillard



## ABSTRACT

**SUMMARY:** Visual hallucinations are relatively uncommon presentations in medical and psychiatric clinics, where they are generally regarded as a marker of possible underlying “organic” brain disease. Thus, patients with visual hallucinations are often referred for imaging of the brain. This article presents a pragmatic approach for the radiologist reviewing such imaging. Because conditions that can present with visual hallucinations are legion, a familiarity with the features of the hallucinations themselves, which can serve as clues to the underlying cause, can be helpful in interpreting such cases. We consider the nature of visual hallucinations and the mechanisms underlying their formation. We then provide a framework to guide the search for their cause, first in terms of focal lesions along the visual pathway and then global conditions affecting >1 region.

**ABBREVIATIONS:** CJD = Creutzfeldt-Jakob disease; VH = visual hallucination

The presentation of visual hallucinations (VHs) to general medical and psychiatric clinics often triggers a search for underlying “organic” brain disease and a referral for imaging of the brain, first with CT and then MR imaging. If the findings are interpreted as normal, patients who in actuality have underlying organic disease can have delays in diagnosis and prolonged inappropriate management. Therefore, it behooves the reporting radiologist to be familiar with visual hallucinations and the possible causes thereof.

The organic causes of VHs represent a veritable Augean stable of pathologies, ranging widely in etiology and location within the brain (Table 1). Although in some instances, a focal defined lesion can lead to VHs (eg, an occipital lobe cavernoma), pathology can also affect large or multiple areas simultaneously (eg, posterior cortical atrophy or Creutzfeldt-Jakob disease [CJD]). When one reviews scans of patients with VHs, it is important to assess not only each part of the visual system but also more diffuse, global, or multiregional pathologies. We have pragmatically divided this article into focal and global causes based simply on localization

rather than on a clear understanding of the pathophysiology of VHs. We briefly consider the nature of hallucinations and clues in the clinical context on the request form. We then consider mechanisms underlying the formation of VHs to guide the search for their cause. We suggest looking first at focal lesions along the visual pathway and then conditions affecting >1 region. Only when no lesion is found and in the absence of other organic clinical features should functional causes then be considered.

## Types of Visual Hallucinations

A hallucination is a “percept without object,”<sup>1</sup> “a sensory perception that has the compelling sense of reality but that occurs without stimulation of the relevant sensory organ.”<sup>2</sup> Hallucinations are distinguished from the following: 1) distortions, in which the real objects are perceived as changed in some way; 2) illusions, in which the perception of real objects is transformed in size (micropsia or macropsia), shape (metamorphopsia), or color (dyschromasia) or into other objects; or 3) pseudohallucinations, which arise from vivid inner mental experience and can often be recognized as such. Although hallucinations are experienced as real, patients experiencing them have varying degrees of insight into the nature of their experiences, which engender varying responses, from indifference to marked distress. Hallucinations vary in content and complexity and occur in every sensory technique: Visual hallucinations are commonly linked to underlying organic etiology but also occur frequently in psychotic states, though half as commonly as auditory hallucinations. Olfactory, tactile, and gustatory hallucinations occur

From the Departments of Neuropsychiatry (T.T.W.-B., R.M., D.V.) and Radiology (A.T., F.G.), Royal Melbourne Hospital, Parkville, Victoria, Australia; and Melbourne Neuropsychiatry Centre (D.V.), National Neuroscience Facility, Carlton, Victoria, Australia.

Please address correspondence to Frank Gaillard, Royal Melbourne Hospital, Grattan St, Parkville, 3050 Victoria, Australia; e-mail: Frank.gaillard@gmail.com

 Indicates open access to non-subscribers at [www.ajnr.org](http://www.ajnr.org)

 Indicates article with supplemental on-line table.

 Indicates article with supplemental on-line photo.

<http://dx.doi.org/10.3174/ajnr.A4636>

less often and are seen in a variety of both psychiatric and organic conditions. The use of the term “organic” here is by convention and should not be taken to imply an absence of brain dysfunction in psychiatric illness.<sup>3</sup>

The content of visual hallucinations can offer some clue as to their origin (Table 1) and may relate to the mechanism of production.

**Table 1: Type of hallucination**

Feature	Possible Cause
Monocular	Eye disease or optic nerve proximal to optic chiasm
Limited visual field	Focal lesion in visual pathway
Simple, brief, unformed	Eye disease, migraine, seizure, calcarine lesions
Visual distortion	Seizures, CJD
Lilliputian	Delirium, intoxication, withdrawal
Frightening	Delirium, hallucinogens, psychosis
Unconcerned/preserved insight	Charles Bonnet syndrome, peduncular hallucinosis

**Table 2: Associated symptoms**

Feature	Possible Cause
Vision loss	Charles Bonnet syndrome
Headache, nausea/vomiting	Migraine
Impaired/fluctuating level of consciousness	Delirium, epilepsy
Confusion/disorientation	Delirium, intoxication, encephalopathy, dementia
Focal neurologic signs	Space-occupying lesion
Agitation, depression, mania, anxiety, disordered/unusual thought content	Delirium, intoxication, psychiatric disorders (psychosis, severe mood disorders)

**Simple Visual Hallucinations.** Brief, stereotyped unformed flashes of light and color or indistinct forms may reflect stimulation or irritation of primary visual areas, for example by tumor, migraine, or focal epileptogenic lesions.

**Complex Visual Hallucinations.** In contrast, complex visual hallucinations suggest disruption to the wider visual system<sup>4</sup> and include branching or tessellated patterns, individuals or crowds of people, animals, and complex scenes often associated with sensory distortions. Lilliputian hallucinations, classically seen in alcohol withdrawal and delirium, are complex VHs consisting of miniature people in lines or groups performing strange actions and eliciting curiosity or wonder. Complex VHs due to psychiatric disturbance, delirium, or intoxication/withdrawal are often perceived as real and frightening, while those seen in peduncular hallucinosis or the Charles Bonnet syndrome may provoke indifference, and insight into the nature of the experience as unreal may be preserved. Associated symptoms such as headaches or focal seizures may help point toward a specific

etiology, as may the presence of associated deteriorating cognitive function, focal neurologic symptoms, or psychiatric symptoms (Table 2).

**Visual Pathway and Mechanisms of Disruption**

The anatomy of the primary visual pathway is well-described: Information from the retina passes along the optic nerve, chiasm, and tract to the lateral genic-

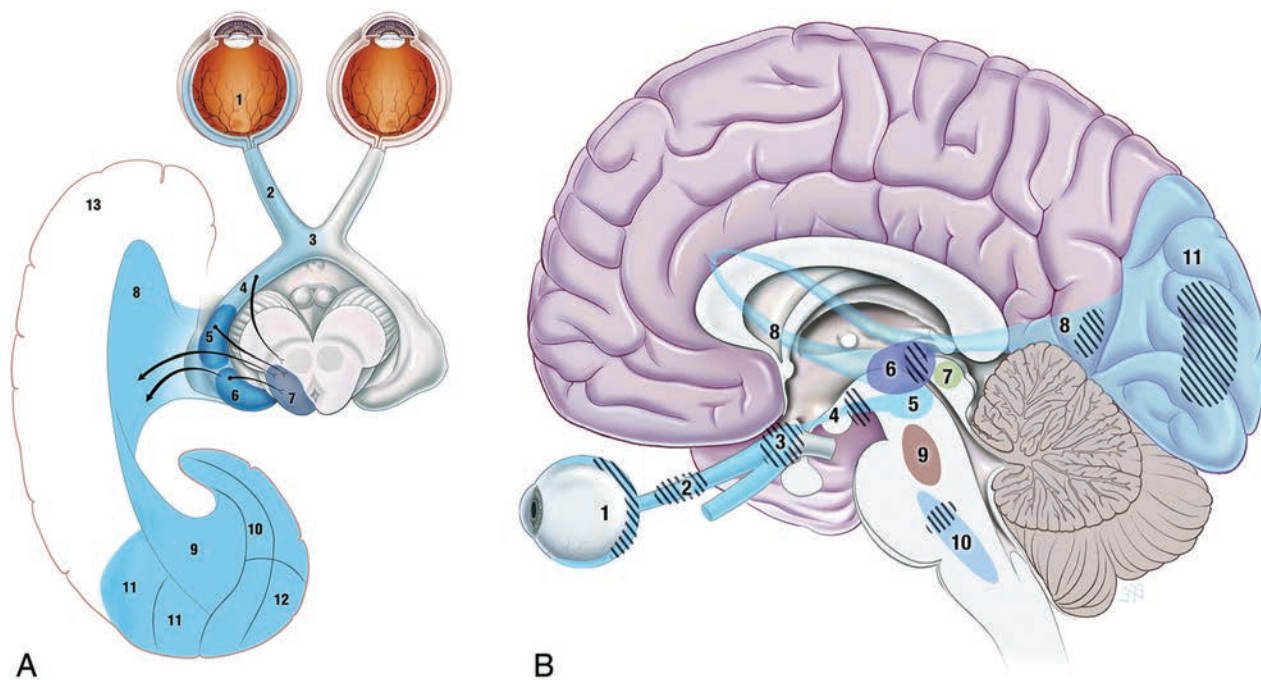


**FIG 1.** Visual pathways. *A*, Retino-geniculo-calcarine tract. Optical information from the retina (1) passes along the optic nerve (2) through the optic chiasm (3) and optic tract (4) into the lateral geniculate nucleus of the thalamus (5), where it receives input from the superior colliculus (7) via the pulvinar (6) and then traverses the optic radiation (8 and 9) through the temporal lobe (13) into the visual cortex (10–12). *B*, Intersection of ascending pathways. Optical information in the retino-geniculo-calcarine tract (1–8 and 11) is modulated by ascending input from the pedunculopontine and parabrachial nuclei (9) and raphe nuclei (10) via the superior colliculus (7). *Hashed areas* show regions where interruptions are known to produce visual hallucinations: in the retino-geniculo-calcarine tract via deafferentation, in the thalamus through reducing signal-to-noise ratio, and in the ascending pathways via removal of inhibitory control. Reproduced with permission from Dr. Ramon Moccellini.

late nucleus in the thalamus and then to the optic radiation through the temporal lobe to the primary and secondary visual cortices (Fig 1). The flow of visual information is modulated by ascending input from the pedunculo-pontine and parabrachial nuclei and raphe nuclei via the superior colliculi (Fig 2) and involves the cholinergic, GABAergic, and glutamateric systems (Fig 2).

Interruptions to this system at any point, either in the primary direct pathway or in its ascending modulatory projections, may lead to visual hallucinations. One series by Braun et al<sup>5</sup> suggested that the occipital and occipitotemporal regions were the most commonly implicated cortical regions, and the midbrain, cerebral

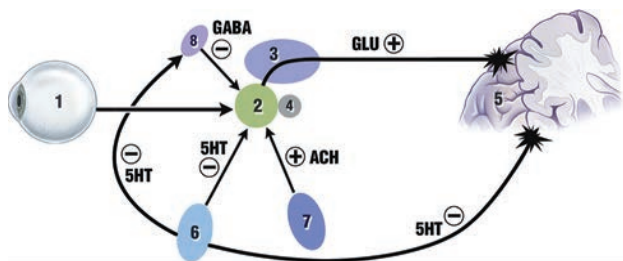


**FIG 2.** Neurochemistry of vision. Input from the retina (1) reaches the lateral geniculate nucleus of the thalamus (2). This structure and the adjacent pulvinar of the thalamus (3), an accessory visual structure that may act to filter out eye-movement “noise,” act as a junction between retino-geniculo-calcarine and ascending brain stem circuits, receiving inhibitory serotonergic input from the raphe nuclei (6) and excitatory cholinergic input from the pedunculo-pontine and parabrachial nuclei (7). The reticular nucleus of the thalamus (8) also provides inhibitory GABAergic innervation to the geniculate, which is itself modulated by the same ascending cholinergic and serotonergic input. The glutamatergic excitatory circuits from the geniculate to the occipital cortex (5) are also modulated by the superior colliculus (4). Reproduced with permission from Dr. Ramon Moccasin.

peduncles, pons, and thalamus, the usual subcortical regions. A search for focal lesions on MR imaging should progress with this pathway in mind.

The exact mechanisms underlying these hallucinations remain unclear but may involve cortical release or deafferentation phenomena (Fig 3A)<sup>6</sup> and/or the disinhibition of projections from ascending pathways or the intact nearby visual cortex. Disruption of ascending input, for example at the lateral geniculate nucleus, may lead to aberrant projections forward to the visual cortex (Fig 3B) or a loss of central sensory filtering function and degradation of signal to noise (Fig 3C).

### Focal Causes of Visual Hallucinations

**Retinal Pathology.** Traction, irritation, injury, or disease of the retina can stimulate retinal photoreceptors, causing brief simple hallucinations in the form of flashes, sparks, or streaks of light. Often both the condition and hallucinations are monocular, and insight is invariably preserved.

**Charles Bonnet Syndrome.** In 1769, Charles Bonnet described complex VHs of people, birds, and buildings in his cataract-affected grandfather and later experienced similar phenomena himself.<sup>7</sup> The Charles Bonnet syndrome describes a wide variety of VHs associated with visual impairment of any cause—in clear sensorium, with retained insight and without other psychopathology. Typically the visions are colorful images of people, animals, and inanimate objects, occurring especially later in the day, in poor light, or in isolation. Charles Bonnet syndrome has been reported in 12%–65% of visually impaired individuals, particularly in women and with increasing age (mean onset at 74.5 years) and reduced cognitive reserve, with white matter lesions on MR imaging, and with polypharmacy.<sup>8,9</sup> Although Charles Bonnet

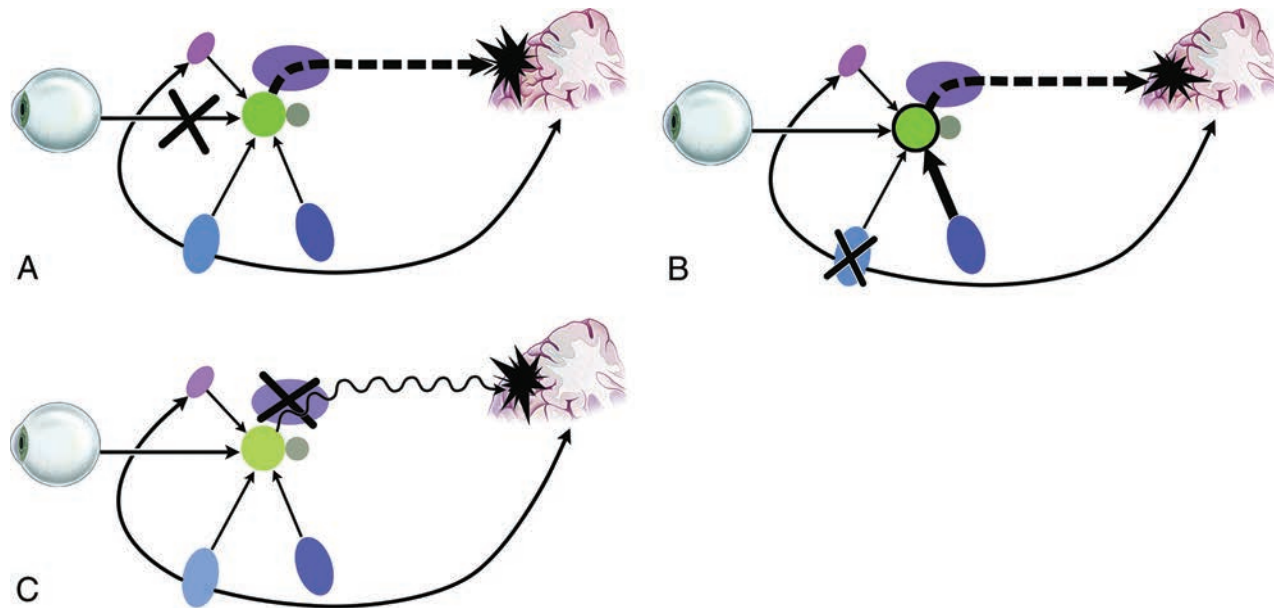


**FIG 3.** Possible mechanisms of visual hallucinations. *A*, Deafferentation: lesions responsible for pathway complex visual hallucination in which deafferentation from ocular input results in “release” activity in the cortex. *B*, Disinhibition: lesions responsible for ascending complex visual hallucinations in which a loss of ascending inhibition to the geniculate results in a hyperexcited geniculate and excess glutamatergic activity in the optic radiation, with resultant poor-quality signal to the cortex. *C*, Central: lesions producing central complex visual hallucinations in which damage to the geniculate may again “deafferent” the striate cortex and lesions to the pulvinar of the thalamus may reduce the signal-to-noise ratio of cortical input due to a loss of the visual filter function of the pulvinar. Reproduced with permission from Dr. Ramon Moccasin.

syndrome was initially described in ocular causes of reduced visual input, more recently the term is increasingly used as a catchall denoting complex VHs arising from lesions affecting vision anywhere along the primary visual pathway from the retina onward. The frequency of underlying causes reflects the most prevalent conditions affecting vision, particularly in the elderly: age-related macular degeneration, glaucoma, diabetic retinopathy, and cerebral infarction.<sup>8,9</sup>

**Imaging Features.** A discussion of all causes of Charles Bonnet syndrome is clearly beyond the scope of this article, and many cases will be obvious. A careful review of the globes, usually not the focus of attention in patients undergoing brain imaging, is however useful in potentially alerting the clinician to causes of visual loss as an etiology of complex visual hallucinations. Calcified optic nerve drusen (hyaline calcific deposits) are usually incidental findings; however, they may sometimes be associated with visual field loss or macular degeneration and appear on CT as punctate calcifications at the optic nerve insertion.<sup>10</sup> Phthisis bulbi, from prior trauma or infection, may be evident as a small hyperattenuated globe, with a thickened and calcified sclera. Chronic retinal detachment typically appears as subretinal fluid of variable attenuation on CT and signal intensity on MR imaging. Evidence of a prior ocular operation may be evident in the form of scleral buckling or intraocular lens replacement.

**Space-Occupying and Vascular Lesions.** Structural disruptions to the visual pathway, for example from neoplastic or vascular lesions, may also lead to complex VHs. In some cases, these are the result of reduced visual input (Charles Bonnet syndrome), whereas in many other instances, the lesions result in VHs without significant loss of vision, supporting the concept of a cortical release of activity from the intact neighboring visual cortex. In historical case series, approximately one-fourth of patients with temporal lobe tumors<sup>11</sup> and 15% with occipital tumors<sup>12</sup> had VHs, the latter usually simpler in content. Posterior cerebral artery infarction leading to lesions in the occipital cortex or visual thalamus may also lead to VHs, usually restricted to the abnormal visual field.<sup>13</sup> In most cases, the hallucinations came days to weeks after the initial infarct and resolved during a period of weeks.

**Peduncular Hallucinosis.** These complex and vivid hallucinations arise in the context of lesions in the midbrain pons or thalamus, not just the cerebral peduncles. They can be due to a wide range of pathologic states, including vascular, infectious, neoplastic, and compressive lesions.<sup>14,15</sup> These lead to visual hallucinations via disruptions to ascending inputs to the visual pathway, such as inhibitory afferents to the dorsal lateral geniculate nucleus, which then project aberrantly to the visual cortex (Fig 3B).

**Imaging Features.** Attention should be paid to the brain stem, in particular the cerebral peduncles, pons, and midbrain, for intrinsic or compressive pathology. Peduncular hallucinosis has been reported following infarcts affecting the cerebral peduncle, as well as compression from lesions such as medulloblastoma and meningioma.<sup>15</sup>

**Posterior Cortical Seizures.** Aberrant electrical activity arising anywhere along the primary or ascending visual pathways leading to focal seizures may result in VHs. Occipital seizures, occurring

in approximately 5% of patients with epilepsy,<sup>16</sup> are frequently associated with visual manifestations. These are often experienced as simple brief fragmentary stereotyped flashing lights, patterns, or blobs of color or distortions and illusions. Seizures associated with complex VHs suggest involvement of the secondary visual cortex or may arise in association with other symptoms of a perictal psychosis.<sup>15</sup>

**Migraine.** Between 15% and 30% of people with migraines experience auras; of these, 90% are visual.<sup>17-19</sup> As with seizures, visual hallucinations and distortions associated with migraine aura are usually simple: The classic aura is of a flickering central zigzag line or crescent progressing peripherally, leaving a central scotoma. Colored patterns and more complex hallucinations may also occur, particularly in rarer causes of migraine, such as familial hemiplegic migraine and migraine coma. Spreading depression of cortical activity may be important in the generation of an aura, with pathologic excitation in visual areas responsible for complex VHs in migraine.<sup>15</sup> Notable neuroimaging findings in migraine are well described.<sup>20,21</sup>

**Posterior Reversible Encephalopathy Syndrome.** Posterior reversible encephalopathy syndrome is a radiologic and clinical neurotoxic state secondary to failure of cerebral autoregulation in response to acute changes in blood pressure in patients with eclampsia and posttransplantation states and in a range of other conditions.<sup>22</sup> While visual symptoms (including cortical blindness, homonymous hemianopia, blurred vision, and neglect) are relatively common,<sup>23</sup> hallucinations are less common, though several cases including complex VHs have been reported.<sup>24</sup> Diagnosis relies on strong clinical suspicion and characteristic MR imaging/CT features. Patients may present with severe headache, confusion, visual disturbance, nausea, vomiting, and seizures; recovery occurs relatively quickly following treatment, with resolution of both clinical and radiologic deficits.<sup>23</sup> Key neuroimaging features in posterior reversible encephalopathy syndrome are well known (On-line Fig 1).<sup>25</sup>

**Reversible Cerebral Vasoconstriction Syndromes.** Reversible cerebral vasoconstriction syndromes encompass Call-Fleming syndrome (reversible cerebral arterial segmental vasoconstriction), migrainous vasospasm, benign angiopathy of the central nervous system, postpartum angiopathy, and drug-induced arteritis.<sup>26,27</sup> These conditions share underlying reversible segmental or multifocal cerebral vasoconstriction and carry the risk of ischemic deficits because of vasoconstriction. Patients may present with sudden-onset posterior thunderclap headache (with or without associated neurologic symptoms) and/or recurrent headaches associated with nausea, vomiting, photophobia, and phonophobia.<sup>27,28</sup> Visual hallucinations are a rare manifestation, though again cases have been reported.<sup>29</sup> Important neuroimaging features of reversible cerebral vasoconstriction syndromes are widely known.<sup>30</sup>

### **Global Causes of Visual Hallucinations**

Visual hallucinations arise in a wide range of other neurologic and systemic disorders, due to localized structural disruption from neurofibrillary tangles or synuclein deposition or to widespread

neurochemical derangement in neurometabolic disorders, intoxication/withdrawal states, and delirium.

**Synucleinopathies with Lewy Body Formation.** Synucleinopathies are a diverse group of related neurodegenerative diseases with a high incidence of VHs characterized by abnormal  $\alpha$ -synuclein metabolism, which, in some instances, results in the formation of intracellular inclusions known as Lewy bodies.<sup>31,32</sup> The number and distribution of Lewy bodies, particularly in mesial temporal structures, are associated with the frequency of VHs.<sup>33</sup> VHs may also relate to synuclein deposition in visual areas, altered ascending input from loss of serotonergic and cholinergic brain stem nuclei, and the use of dopaminergic medications.<sup>34</sup> In contrast, synucleinopathies without Lewy bodies, such as multisystem atrophy, have a low incidence of visual hallucinations.<sup>35</sup>

**Lewy Body Dementia.** Lewy body dementia is the second most common form of dementia after Alzheimer disease. Visual hallucinations form part of the core clinical diagnostic criteria for Lewy body dementia and are typically seen early in the course of the disease, before the development of Parkinsonian motor symptoms.<sup>36</sup> The incidence of VHs in Lewy body dementia varies between 20% and 75%,<sup>31,33,35</sup> and the presence of VH provides an 83% positive predictive value for distinguishing Lewy body dementia from Alzheimer disease.<sup>37</sup> VHs in Lewy body dementia typically manifest as prolonged well-formed complex scenes of figures and objects and provoke varied reactions from fear through to indifference.

**Imaging Features.** A lack of mesial temporal atrophy in Lewy body dementia is perhaps the most useful finding in distinguishing Lewy body dementia from Alzheimer disease.<sup>38-40</sup> A pattern of relatively focused atrophy of the midbrain, hypothalamus, and substantia innominata, with a relative sparing of the hippocampus and temporoparietal cortex, may be seen (On-line Fig 2).

**Parkinson Disease/Parkinson Disease Dementia.** Parkinson disease is one of the most common neurodegenerative diseases, seen in 1% of patients older than 60 years of age.<sup>41</sup> Patients may present with the classic motor triad of tremor at rest, rigidity, and hypokinesia, as well as a range of nonmotor symptoms. VHs are common and occur in 25%–50% of patients with Parkinson disease<sup>42</sup> and are similar in content to those of Lewy body dementia, ranging from people or animals to complex, formed, and animated scenes.

**Imaging Features.** In most instances, imaging plays a supportive role in the diagnosis of Parkinson disease,<sup>39</sup> which is usually established clinically. Loss of normal susceptibility-induced signal drop-out in the substantia nigra pars compacta on T2\*-weighted images is potentially the most useful feature, but this has been difficult to demonstrate reliably.<sup>43</sup> Other features include mild T1 signal hyperintensity of the reticular parts of the substantia nigra and red nuclei and dotlike areas of hyperintensity in the compact part of the substantia nigra; however, the clinical utility of such findings is limited because they are subtle and are only reported late in the disease.<sup>44,45</sup>

**Alzheimer Disease/Posterior Cortical Atrophy.** VHs may also be seen in Alzheimer disease, particularly in patients with advanced

disease and when combined with confusion and loss of visual acuity.<sup>37,46</sup> VHs in Alzheimer disease may result from Alzheimer plaques and tangles in the visual-association cortices and have been associated with periventricular white matter lesions and occipital atrophy.<sup>47,48</sup>

VHs are seen in approximately 25% of patients diagnosed with the posterior cortical atrophy variant of Alzheimer disease, in which cortical loss is localized, particularly to the occipital and parietal lobes, leading to visual agnosia and apraxia.<sup>49</sup> Those patients with posterior cortical atrophy and complex VHs have disproportionate involvement of the midbrain, thalamus, and primary visual cortex, and interplay between these regions may be responsible.<sup>49</sup>

**Imaging Features.** Cortical atrophy tends to occur within the mesial temporal structures, with widening of the parahippocampal fissures. SPECT and FDG-PET examinations demonstrate reduced bitemporoparietal uptake, reflecting reduced cerebral blood flow. The presence of parietal-predominant volume loss is suggestive of the posterior cortical atrophy variant.<sup>50</sup> MR imaging demonstrates gray matter atrophy involving the occipital, parietal, and posterior temporal lobes, often more pronounced on the right side (On-line Fig 3).<sup>51</sup> In patients with visual hallucinations, additional regions involved include the primary visual cortex, thalamus, basal nuclei, midbrain, basal forebrain, and posterior frontal and medial temporal lobes.<sup>49</sup>

**Frontotemporal Lobar Degeneration.** Frontotemporal lobar degeneration covers a spectrum of genetically and neuropathologically heterogeneous disorders, including behavioral variant frontotemporal dementia, semantic dementia, and progressive nonfluent aphasia.<sup>52</sup> Frontotemporal lobar degeneration leads primarily to personality and behavioral changes and language disturbance but also to psychotic symptoms in 10%–30% of cases<sup>53,54</sup> and visual hallucinations in up to 14%.<sup>54</sup> Psychotic symptoms are more prevalent in carriers of the *C9orf72* mutation, whose thalamus and cerebellum are more frequently affected.<sup>55</sup> VHs are more common in the right than in the left temporal variant frontotemporal lobar degeneration,<sup>56</sup> often associated with delusions.<sup>57</sup>

**Imaging Features.** While atrophy in the anterior temporal and medial frontal lobes is characteristic of frontotemporal lobar degeneration (On-line Fig 4),<sup>58</sup> specific imaging findings can reflect underlying subtypes. Bilaterally symmetric or right frontal atrophy is seen in the behavioral subtype. In the semantic dementia subtype, there is anterior temporal–predominant atrophy. Left dominant atrophy is seen if speech apraxia predominates, with right dominant atrophy if prosopagnosia predominates.<sup>40</sup> Frontostriatal dysfunction also varies among these different subtypes, with the behavioral variant having the greatest involvement: Caudate heads are relatively reduced in size in these patients compared with those with the language variant of frontotemporal lobar degeneration.<sup>59</sup>

**Creutzfeldt-Jakob Disease.** In Creutzfeldt-Jakob disease, a rare, rapidly progressive neurodegenerative condition caused by prion infection, VHs may accompany the typical rapid cognitive decline, anxiety, personality change, myoclonic jerks, and ataxia.<sup>60</sup> Visual effects may include color changes, field defects, visual ag-

nosia, and distortions progressing to frank hallucinations,<sup>61</sup> seen particularly in the Heidenhain variant of CJD and associated with periodic electroencephalography complexes over the occipital region.<sup>62</sup>

**Imaging Features.** Sporadic CJD classically results in cortical diffusion restriction as the earliest imaging manifestation (Online Fig 5), which may be bilateral or unilateral, symmetric or asymmetric. Bilateral areas of increased signal intensity predominantly affecting the caudate nuclei and the putamina should also suggest the diagnosis of CJD.<sup>63</sup> In variant CJD, FLAIR/T2 hyperintensity may be demonstrated in the pulvinar nuclei bilaterally (pulvinar sign) and both the dorsomedial thalamus and pulvinar (hockey stick sign).<sup>64,65</sup>

**Intoxication, Withdrawal, and Delirium.** Delirium tremens, seen in severe alcohol withdrawal, is associated with frightening VHS, tremor, autonomic disturbance, and agitation.<sup>15</sup> Similar withdrawal states may follow the sudden cessation of benzodiazepines or barbiturates, suggesting a shared role of altered  $\gamma$ -aminobutyric acid signaling.<sup>66</sup> Drugs such as lysergic acid diethylamide and mescaline have hallucinogenic properties correlated with their serotonergic activity and lead to colored patterns, distortions, and illusions that progress to include complex scenes of animals and people. These are often vivid and associated with heightened sensory arousal, with preserved insight and without paranoia or delusional interpretation. Cocaine and amphetamines in contrast, which act to increase synaptic dopamine transmission, tend to produce VHS with heightened paranoia and agitation.<sup>66</sup>

Delirium is a syndrome of disturbed consciousness and impaired attention associated with a raft of metabolic, infectious, toxic, and intracranial causes.<sup>67</sup> Hallucinations are often a prominent part of this syndrome and are typically visual, with vivid, complex, and often frightening scenes of people and animals that may be accompanied by paranoia and fleeting delusions.<sup>66</sup>

**Imaging Features.** In most cases of intoxication, withdrawal, and delirium, imaging is performed to rule out underlying structural pathology. MR imaging in Wernicke-Korsakoff syndrome, induced by thiamine deficiency in starvation and alcoholism, demonstrates T2 hyperintensity in the mammillary bodies, thalami, periaqueductal gray tectal plate, and dorsal medulla, with possible associated contrast enhancement.<sup>68</sup>

### Psychiatric and Other Causes of Visual Hallucinations

Once focal and global brain pathology has been excluded with MR imaging and other investigations, psychiatric causes including major affective and psychotic disorders should be considered. Brain MR imaging findings are usually normal.<sup>69</sup> In schizophrenia, VHS are around half as common as auditory hallucinations; when experienced by people with schizophrenia, VHS are also usually accompanied by auditory hallucinations.<sup>70,71</sup> In one sample, visual hallucinations were present in 16% of subjects and were related to the severity of illness.<sup>72</sup> Visual hallucinations are also common in states of reduced consciousness, such as entering and awakening from sleep, particularly in the presence of sleep disor-

**Table 3: Reported incidence of visual hallucinations in various conditions**

Condition	Incidence of VH
Lewy body dementia	20%–75% <sup>31,33,35</sup>
Parkinson disease	15%–75% <sup>35</sup>
PCA/AD	25% <sup>49</sup>
FTD	10%–14% <sup>54</sup>
Occipital seizures	≤100% <sup>16</sup>
Migraine	90% with visual aura <sup>17–19</sup> , CVH rarer
PRES	Case reports only <sup>23,24</sup>
RVCS	Case reports only <sup>24</sup>

**Note:**—PCA indicates posterior cortical atrophy; AD, Alzheimer disease; FTD, frontotemporal dementia; CVH, complex visual hallucination; PRES, posterior reversible encephalopathy syndrome; RVCS, reversible cerebral vasoconstriction syndrome.

ders,<sup>73</sup> and may be induced by prolonged visual deprivation, a syndrome akin to that described in Charles Bonnet syndrome.

### Conclusions and Imaging Recommendations

Considering the range of focal and global pathology that can result in VHS, a sensible approach to imaging is needed (Online Table). Often the type or features of VHS being experienced are not indicated on imaging requests, so highly targeted protocols are unreliable. Instead, we recommend a relatively generic approach able to adequately image the entire optic pathway and identify, if not necessarily fully characterize, all likely pathologies. The key sequences are high-resolution T1 and T2/FLAIR, preferably isotropic volumetric imaging, susceptibility-weighted imaging, and diffusion-weighted imaging. Time permitting, additional catchall sequences may be added (eg, MR perfusion, double inversion recovery, MRA).

A systematic approach to the review of these sequences with regard to direct and ascending visual pathways looking first for focal and patterns of global pathologies outlined above will ensure detection of the most important pathology underlying the presentation of visual hallucinations (Table 3).

Disclosures: Toby T. Winton-Brown—UNRELATED: Grants/Grants Pending: Wellcome Trust, UK (Research Training Fellowship, WT08779MA), Dennis Velakoulis—UNRELATED: Royalties: Neuropsychiatry Unit Cognitive Assessment Tool; Stock/Stock Options: Prana Biotechnology Ltd, a company with research into neurodegenerative disorders. Frank Gaillard—UNRELATED: Employment: Radiopaedia.org (Founder, Editor, and CEO).

### REFERENCES

- Esquirol E. *Des Maladies Mentales Considérées sous les Rapports Médical, Hygiénique et Médico-Légal*. Paris: JB Baillière; 1838
- American Psychiatric Association; American Psychiatric Association. Task Force on DSM-IV. *Diagnostic and Statistical Manual of Mental Disorders*. Washington: American Psychiatric Association; 2000
- Sachdev P. A critique of 'organic' and its proposed alternatives. *Aust N Z J Psychiatry* 1996;30:165–70 Medline
- Santhouse AM, Howard RJ, ffytche DH. Visual hallucinatory syndromes and the anatomy of the visual brain. *Brain* 2000;123(pt 10): 2055–64 CrossRef Medline
- Braun CM, Dumont M, Duval J, et al. Brain modules of hallucination: an analysis of multiple patients with brain lesions. *J Psychiatry Neurosci* 2003;28:432–49 Medline
- West LJ. A general theory of hallucinations and dreams. In: West LJ, ed. *Hallucinations*. Oxford: Grune & Stratton; 1962: 275–90
- Bonnet C. *Essai Analytique sur les Facultés de L'Âme*. Copenhagen: Philibert; 1760:426–28
- Tennisse RJ, Cruysberg JR, Hoefnagels WH, et al. Visual hallucina-

- tions in psychologically normal people: Charles Bonnet's syndrome. *Lancet* 1996;347:794–97 Medline
9. Menon GJ. **Complex visual hallucinations in the visually impaired: a structured history-taking approach.** *Arch Ophthalmol* 2005;123:349–55 CrossRef Medline
  10. LeBedis CA, Sakai O. **Nontraumatic orbital conditions: diagnosis with CT and MR imaging in the emergent setting.** *Radiographics* 2008;28:1741–53 CrossRef Medline
  11. Cushing H. **Distortions of the visual field in cases of brain tumour (6th paper): the field defects produced by temporal lobe lesions.** *Brain* 1922;44:341–96 CrossRef
  12. Parkinson D, Rucker CW, Craig WM. **Visual hallucinations associated with tumors of the occipital lobe.** *AMA Arch Neurol Psychiatry* 1952;68:66–68 CrossRef Medline
  13. Vaphiades MS, Celesia GG, Brigell MG. **Positive spontaneous visual phenomena limited to the hemianopic field in lesions of central visual pathways.** *Neurology* 1996;47:408–17 CrossRef Medline
  14. Mocellin R, Walterfang M, Velakoulis D. **Neuropsychiatry of complex visual hallucinations.** *Aust N Z J Psychiatry* 2006;40:742–51 CrossRef Medline
  15. Manford M, Andermann F. **Complex visual hallucinations: clinical and neurobiological insights.** *Brain* 1998;121(pt 10):1819–40 CrossRef Medline
  16. Panayiotopoulos CP. **Elementary visual hallucinations, blindness, and headache in idiopathic occipital epilepsy: differentiation from migraine.** *J Neurol Neurosurg Psychiatry* 1999;66:536–40 CrossRef Medline
  17. Rasmussen BK, Olesen J. **Symptomatic and nonsymptomatic headaches in a general population.** *Neurology* 1992;42:1225–31 CrossRef Medline
  18. Goadsby PJ, Lipton RB, Ferrari MD. **Migraine: current understanding and treatment.** *N Engl J Med* 2002;346:257–70 CrossRef Medline
  19. Kelman L. **The aura: a tertiary care study of 952 migraine patients.** *Cephalalgia* 2004;24:9728–34 Medline
  20. Rocca MA, Ceccarelli A, Falini A, et al. **Brain gray matter changes in migraine patients with T2-visible lesions: a 3-T MRI study.** *Stroke* 2006;37:1765–70 CrossRef Medline
  21. Kruijt MC, Launer LJ, Ferrari MD, et al. **Infarcts in the posterior circulation territory in migraine: the population-based MRI CAMERA study.** *Brain* 2005;128(pt 9):2068–77 CrossRef Medline
  22. Bartynski WS. **Posterior reversible encephalopathy syndrome, part 1: fundamental imaging and clinical features.** *AJNR Am J Neuroradiol* 2008;29:1036–42 CrossRef Medline
  23. Hinchey J, Chaves C, Appignani B, et al. **A reversible posterior leukoencephalopathy syndrome.** *N Engl J Med* 1996;334:494–500 CrossRef Medline
  24. Tallaksen C, Kerty E, Bakke S. **Visual hallucinations in a case of reversible hypertension-induced brain oedema.** *Eur J Neurol* 1998;5:615–18 CrossRef Medline
  25. Hugonnet E, Da Ines D, Bobby H, et al. **Posterior reversible encephalopathy syndrome (PRES): features on CT and MR imaging.** *Diagn Interv Imaging* 2013;94:45–52 CrossRef Medline
  26. Calabrese LH, Gragg LA, Furlan AJ. **Benign angiopathy: a distinct subset of angiographically defined primary angiitis of the central nervous system.** *J Rheumatol* 1993;20:2046–50 Medline
  27. Ducros A. **Reversible cerebral vasoconstriction syndrome.** *Lancet Neurol* 2012;11:906–17 CrossRef Medline
  28. Singhal AB, Hajj-Ali RA, Topcuoglu MA, et al. **Reversible cerebral vasoconstriction syndromes: analysis of 139 cases.** *Arch Neurol* 2011;68:1005–12 CrossRef Medline
  29. Yagi Y, Watanabe Y, Yokote H, et al. **Transient Charles Bonnet syndrome in a patient with reversible cerebral vasoconstriction syndrome.** *Neurol Sci* 2013;34:1023–25 CrossRef Medline
  30. Ducros A, Fiedler U, Porcher R, et al. **Hemorrhagic manifestations of reversible cerebral vasoconstriction syndrome: frequency, features, and risk factors.** *Stroke* 2010;41:2505–11 CrossRef Medline
  31. Jellinger KA. **Neuropathological spectrum of synucleinopathies.** *Mov Disord* 2003;18(suppl 6):S2–12 Medline
  32. Martí MJ, Tolosa E, Campdelacreu J. **Clinical overview of the synucleinopathies.** *Mov Disord* 2003;18(suppl 6):S212 Medline
  33. Harding AJ, Broe GA, Halliday GM. **Visual hallucinations in Lewy body disease relate to Lewy bodies in the temporal lobe.** *Brain* 2002;125(pt 2):391–403 CrossRef Medline
  34. Zahodne LB, Fernandez DHH. **Pathophysiology and treatment of psychosis in Parkinson's disease: a review.** *Drugs Aging* 2008;25:665–82 CrossRef Medline
  35. Bertram K, Williams DR. **Visual hallucinations in the differential diagnosis of parkinsonism.** *J Neurol Neurosurg Psychiatry* 2012;83:448–52 CrossRef Medline
  36. McKeith I, Mintzer J, Aarsland D, et al; International Psychogeriatric Association Expert Meeting on DLB. **Dementia with Lewy bodies.** *Lancet Neurol* 2004;3:19–28 CrossRef Medline
  37. Tiraboschi P, Salmon DP, Hansen LA, et al. **What best differentiates Lewy body from Alzheimer's disease in early-stage dementia? Brain** 2006;129(pt 3):729–35 CrossRef Medline
  38. Taylor JP, O'Brien J. **Neuroimaging of dementia with Lewy bodies.** *Neuroimaging Clin N Am* 2012;22:67–81, viii CrossRef Medline
  39. Broski SM, Hunt CH, Johnson GB, et al. **Structural and functional imaging in parkinsonian syndromes.** *Radiographics* 2014;34:1273–92 CrossRef Medline
  40. Atlas SW. *Magnetic Resonance Imaging of the Brain and Spine.* Philadelphia: Wolters Kluwer Health/Lippincott Williams & Wilkins; 2009
  41. Connolly BS, Lang AE. **Pharmacological treatment of Parkinson disease: a review.** *JAMA* 2014;311:1670–83 CrossRef Medline
  42. Williams DR, Lees AJ. **Visual hallucinations in the diagnosis of idiopathic Parkinson's disease: a retrospective autopsy study.** *Lancet Neurol* 2005;4:605–10 CrossRef Medline
  43. Minati L, Grisoli M, Carella F, et al. **Imaging degeneration of the substantia nigra in Parkinson disease with inversion-recovery MR imaging.** *AJNR Am J Neuroradiol* 2007;28:309–13 Medline
  44. Adachi M, Hosoya T, Haku T, et al. **Evaluation of the substantia nigra in patients with Parkinsonian syndrome accomplished using multishot diffusion-weighted MR imaging.** *AJNR Am J Neuroradiol* 1999;20:1500–06 Medline
  45. Schwarz ST, Rittman T, Gontu V, et al. **T1-weighted MRI shows stage-dependent substantia nigra signal loss in Parkinson's disease.** *Mov Disord* 2011;26:1633–38 CrossRef Medline
  46. Chapman FM, Dickinson J, McKeith I, et al. **Association among visual hallucinations, visual acuity, and specific eye pathologies in Alzheimer's disease: treatment implications.** *Am J Psychiatry* 1999;156:1983–85 Medline
  47. Lin SH, Yu CY, Pai MC. **The occipital white matter lesions in Alzheimer's disease patients with visual hallucinations.** *Clin Imaging* 2006;30:388–93 CrossRef Medline
  48. Holroyd S, Shepherd ML, Downs JH. **Occipital atrophy is associated with visual hallucinations in Alzheimer's disease.** *J Neuropsychiatry Clin Neurosci* 2000;12:25–28 CrossRef Medline
  49. Josephs KA, Whitwell JL, Boeve BF, et al. **Visual hallucinations in posterior cortical atrophy.** *Arch Neurol* 2006;63:1427–32 CrossRef Medline
  50. Crutch SJ, Lehmann M, Schott JM, et al. **Posterior cortical atrophy.** *Lancet Neurol* 2012;12:170–78 CrossRef Medline
  51. Whitwell JL, Jack CR Jr, Kantarci K, et al. **Imaging correlates of posterior cortical atrophy.** *Neurobiol Aging* 2007;28:1051–61 CrossRef Medline
  52. Neary D, Snowden JS, Gustafson L, et al. **Frontotemporal lobar degeneration: a consensus on clinical diagnostic criteria.** *Neurology* 1998;51:1546–54 CrossRef Medline
  53. Shinagawa S, Nakajima S, Plitman E, et al. **Psychosis in frontotemporal dementia.** *J Alzheimers Dis* 2014;42:485–99 CrossRef Medline
  54. Landqvist Waldö M, Gustafson L, Passant U, et al. **Psychotic symptoms in frontotemporal dementia: a diagnostic dilemma? Int Psychogeriatr** 2014;27:531–39 CrossRef Medline
  55. Mahoney CJ, Beck J, Rohrer JD, et al. **Frontotemporal dementia with the C9ORF72 hexanucleotide repeat expansion: clinical, neuroana-**

- tomical and neuropathological features. *Brain* 2012;135(pt 3):736–50 CrossRef Medline
56. Chan D, Anderson V, Pijnenburg Y, et al. **The clinical profile of right temporal lobe atrophy.** *Brain* 2009;132(pt 5):1287–98 CrossRef Medline
  57. Omar R, Sampson EL, Loy CT, et al. **Delusions in frontotemporal lobar degeneration.** *J Neurol* 2009;256:600–07 CrossRef Medline
  58. Kitagaki H, Mori E, Yamaji S, et al. **Frontotemporal dementia and Alzheimer disease: evaluation of cortical atrophy with automated hemispheric surface display generated with MR images.** *Radiology* 1998;208:431–39 CrossRef Medline
  59. Looi JCL, Lindberg O, Zandbelt BB, et al. **Caudate nucleus volumes in frontotemporal lobar degeneration: differential atrophy in subtypes.** *AJNR Am J Neuroradiol* 2008;29:1537–43 CrossRef Medline
  60. Johnson RT, Gibbs CJ. **Creutzfeldt-Jakob disease and related transmissible spongiform encephalopathies.** *N Engl J Med* 1998;339:1994–2004 CrossRef Medline
  61. Armstrong RA. **Creutzfeldt-Jakob disease and vision.** *Clin Exp Optom* 2006;89:3–9 CrossRef Medline
  62. Nozaki I, Hamaguchi T, Noguchi-Shinohara M, et al. **The MM2-cortical form of sporadic Creutzfeldt-Jakob disease presenting with visual disturbance.** *Neurology* 2006;67:531–33 CrossRef Medline
  63. Finkenstaedt M, Szudra A, Zerr I, et al. **MR imaging of Creutzfeldt-Jakob disease.** *Radiology* 1996;199:793–98 CrossRef Medline
  64. Kallenberg K, Schulz-Schaeffer WJ, Jastrow U, et al. **Creutzfeldt-Jakob disease: comparative analysis of MR imaging sequences.** *AJNR Am J Neuroradiol* 2006;27:1459–62 Medline
  65. Collie DA, Summers DM, Sellar RJ, et al. **Diagnosing variant Creutzfeldt-Jakob disease with the pulvinar sign: MR imaging findings in 86 neuropathologically confirmed cases.** *AJNR Am J Neuroradiol* 2003;24:1560–69 Medline
  66. Walterfang M, Mocellin R, Velakoulis D. **Visual hallucinations in consultation-liaison neuropsychiatry.** *Acta Neuropsychiatrica* 2007;19:330–37 CrossRef
  67. Burns A, Gallagley A, Byrne J. **Delirium.** *J Neurol Neurosurg Psychiatry* 2004;75:362–67 CrossRef Medline
  68. Zuccoli G, Gallucci M, Capellades J, et al. **Wernicke encephalopathy: MR findings at clinical presentation in twenty-six alcoholic and nonalcoholic patients.** *AJNR Am J Neuroradiol* 2007;28:1328–31 Medline
  69. Velakoulis D, Wood SJ, Wong MT, et al. **Hippocampal and amygdala volumes according to psychosis stage and diagnosis: a magnetic resonance imaging study of chronic schizophrenia, first-episode psychosis, and ultra-high-risk individuals.** *Arch Gen Psychiatry* 2006;63:139–49 CrossRef Medline
  70. Black DW, Nasrallah A. **Hallucinations and delusions in 1,715 patients with unipolar and bipolar affective disorders.** *Psychopathology* 1989;22:28–34 CrossRef Medline
  71. Goodwin DW, Alderson P, Rosenthal R. **Clinical significance of hallucinations in psychiatric disorders: a study of 116 hallucinatory patients.** *Arch Gen Psychiatry* 1971;24:76–80 CrossRef Medline
  72. Mueser KT, Bellack AS, Brady EU. **Hallucinations in schizophrenia.** *Acta Psychiatr Scand* 1990;82:26–29 CrossRef Medline
  73. Dauvilliers Y, Billiard M, Montplaisir J. **Clinical aspects and pathophysiology of narcolepsy.** *Clin Neurophysiol* 2003;114:2000–17 CrossRef Medline

# Lateral Asymmetry and Spatial Difference of Iron Deposition in the Substantia Nigra of Patients with Parkinson Disease Measured with Quantitative Susceptibility Mapping

M. Azuma, T. Hirai, K. Yamada, S. Yamashita, Y. Ando, M. Tateishi, Y. Iryo, T. Yoneda, M. Kitajima, Y. Wang, and Y. Yamashita



## ABSTRACT

**BACKGROUND AND PURPOSE:** Quantitative susceptibility mapping is useful for assessing iron deposition in the substantia nigra of patients with Parkinson disease. We aimed to determine whether quantitative susceptibility mapping is useful for assessing the lateral asymmetry and spatial difference in iron deposits in the substantia nigra of patients with Parkinson disease.

**MATERIALS AND METHODS:** Our study population comprised 24 patients with Parkinson disease and 24 age- and sex-matched healthy controls. They underwent 3T MR imaging by using a 3D multiecho gradient-echo sequence. On reconstructed quantitative susceptibility mapping, we measured the susceptibility values in the anterior, middle, and posterior parts of the substantia nigra, the whole substantia nigra, and other deep gray matter structures in both hemibrains. To identify the more and less affected hemibrains in patients with Parkinson disease, we assessed the severity of movement symptoms for each hemibrain by using the Unified Parkinson's Disease Rating Scale.

**RESULTS:** In the posterior substantia nigra of patients with Parkinson disease, the mean susceptibility value was significantly higher in the more than the less affected hemibrain substantia nigra ( $P < .05$ ). This value was significantly higher in both the more and less affected hemibrains of patients with Parkinson disease than in controls ( $P < .05$ ). Asymmetry of the mean susceptibility values was significantly greater for patients than controls ( $P < .05$ ). Receiver operating characteristic analysis showed that quantitative susceptibility mapping of the posterior substantia nigra in the more affected hemibrain provided the highest power for discriminating patients with Parkinson disease from the controls.

**CONCLUSIONS:** Quantitative susceptibility mapping is useful for assessing the lateral asymmetry and spatial difference of iron deposition in the substantia nigra of patients with Parkinson disease.

**ABBREVIATIONS:** aSN = anterior part of the substantia nigra; CN = caudate nucleus; GP = globus pallidus; mSN = middle part of the substantia nigra; PD = Parkinson disease; pSN = posterior part of the substantia nigra; PT = putamen; QSM = quantitative susceptibility mapping; RN = red nucleus; S = susceptibility; SN = substantia nigra; UPDRS = Unified Parkinson's Disease Rating Scale

Parkinson disease (PD) is characterized by the progressive loss of dopaminergic neurons in the substantia nigra (SN).<sup>1</sup> Histologic studies showed that the vulnerability of dopaminergic neurons varies spatially within the SN of patients with PD. This

loss is more severe in the SN pars compacta, particularly in the ventrolateral tier.<sup>1-4</sup> The increased iron in the SN pars compacta of patients with PD may promote oxidative stress harmful to dopaminergic neurons.<sup>5-9</sup> Devos et al,<sup>10</sup> who measured the level of SN iron on MR imaging in their clinical outcome assessment, reported a disease-modifying PD therapy by using deferiprone iron chelation.

Devos et al<sup>10</sup> used R2\* maps derived from gradient-echo data that are sensitive to nigral iron in patients with PD.<sup>11-20</sup> However, R2\* depends not only on the iron distribution in an object but also on the object orientation, the surrounding iron distribution (blooming artifacts), and the imaging parameters, including the TE, voxel size, and field strength.<sup>21,22</sup> This dependence renders the use of R2\* problematic for performing multicenter, cross-scanner longitudinal studies.

Quantitative susceptibility mapping (QSM) is a novel tech-

Received July 22, 2015; accepted after revision October 3.

From the Departments of Diagnostic Radiology (M.A., M.T., Y.I., M.K., Y.Y.), Neurosurgery (K.Y.), and Neurology (S.Y., Y.A.), Graduate School of Medical Sciences, and Department of Medical Physics in Advanced Biomedical Sciences (T.Y.), Faculty of Life Sciences, Kumamoto University, Kumamoto, Japan; Department of Radiology (T.H.), Faculty of Medicine, University of Miyazaki, Miyazaki, Japan; and Department of Radiology (Y.W.), Weill Cornell Medical College, New York, New York.

This work was supported in part by the National Institutes of Health (R01 EB013443).

Please address correspondence to Minako Azuma, MD, Department of Diagnostic Radiology, Graduate School of Medical Sciences, Kumamoto University, 1-1-1 Honjo, Kumamoto 860-8556, Japan; e-mail: coralcommunity@yahoo.co.jp

Indicates open access to non-subscribers at www.ajnr.org

<http://dx.doi.org/10.3174/ajnr.A4645>

**Table 1: Demographics and clinical status of the study participants**

	No. (Female, Male)	Age (Mean) (yr)	Disease Duration (mo) (Mean)	UPDRS Motor Score <sup>a</sup> (Mean)	More Affected Hemibrain
Patients with PD	24 (16, 8)	63.3 ± 11.0	77.1 ± 43.7	20.8 ± 11.6	Right 15, left 9
Healthy controls	24 (15, 9)	64.1 ± 10.0		More affected body side (8.5 ± 4.8), less affected body side (5.1 ± 3.9)	

<sup>a</sup> There was a significant difference in the UPDRS III motor scores between more and less affected body sides in patients with PD ( $P < .001$ ).

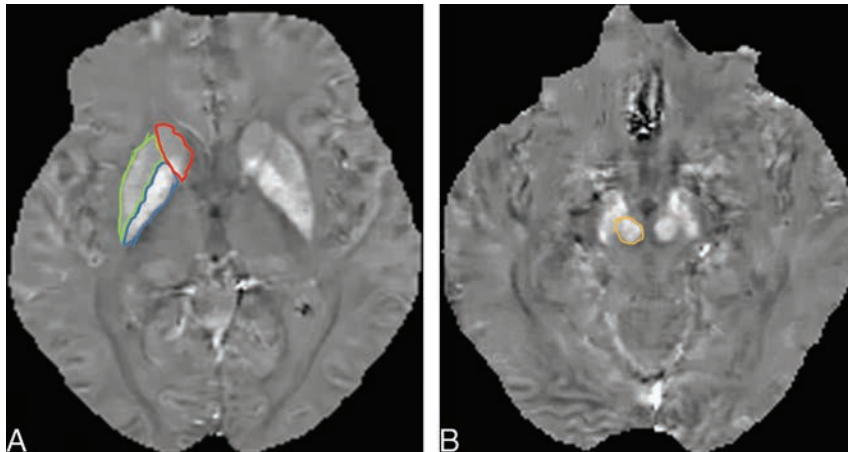


**FIG 1.** A 59-year-old woman with Parkinson disease. *A*, QSM, axial section at the level of the basal ganglia. ROIs as large as possible were placed. Areas encircled in red, green, and blue are the caudate nucleus, putamen, and globus pallidus. *B*, QSM, axial section at the level of the midbrain. The encircled area identifies the red nucleus medial to the substantia nigra.

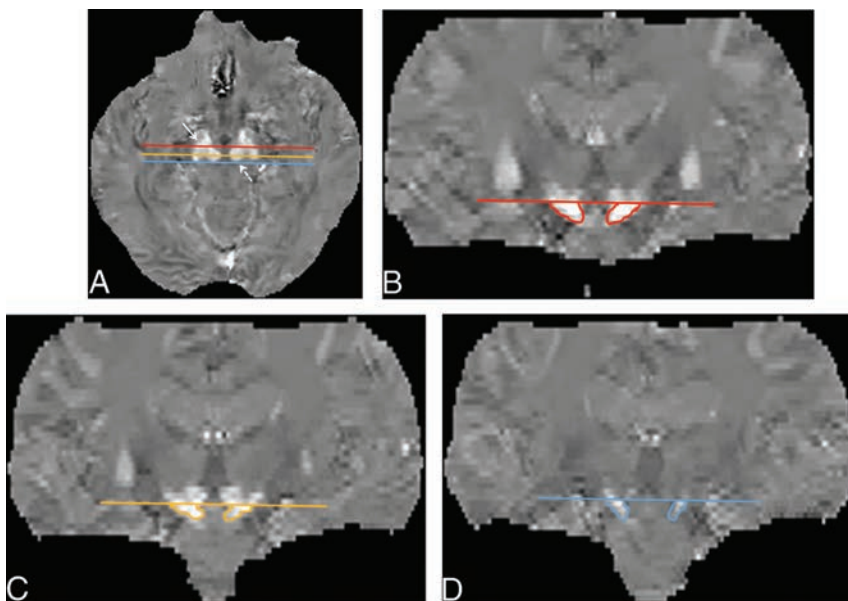


**FIG 2.** ROIs on the substantia nigra on QSM images. Multiplanar reconstruction coronal images were selected at the 3 planes, that is, the anterior (red line), middle (light orange line), and posterior (blue line) edges of the red nucleus on axial QSM images (A), to measure spatial susceptibility differences in the anterior, middle, and posterior parts of the SN. To avoid contamination by the subthalamic nuclei, we placed an ROI on the aSN (B), mSN (C), and pSN (D) below the caudal edge of the RN on coronal QSM images. The averaged value of the aSN, mSN, and pSN was defined as the value of the whole SN. Solid arrow indicates the SN; dotted arrow, the RN.

nique that calculates tissue magnetic susceptibility in vivo. It eliminates the blooming artifacts by deconvolving the susceptibility-generated magnetic field.<sup>23-30</sup> Postmortem studies revealed a strong correlation between the iron concentration and

QSM-measured susceptibility in the deep gray matter,<sup>31</sup> and QSM can be used to measure nigral iron accumulation in PD.<sup>32-34</sup> However, it can be difficult to identify the SN pars compacta on MR imaging scans,<sup>13,35</sup> and nigral iron measurements are easily contaminated by the adjacent subthalamic nucleus.<sup>35-38</sup> Consequently, the asymmetry and spatial difference in the accumulation of iron in the SN of patients with PD have not been fully evaluated with QSM, to our knowledge.

We describe a practical method to evaluate the subdivision of the SN. Our study aimed at determining whether QSM is useful for detecting asymmetry and spatial differences in the accumulation of iron in the SN of patients with PD.

## MATERIALS AND METHODS

### Subjects

The local ethics committee of Kumamoto University approved this study, and all subjects provided prior written informed consent. The patients were 16 women and 8 men ranging in age from 35 to 77 years (mean, 63.3 years). They were seen between April 2013 and November 2014 in Kumamoto University Hospital. Their clinical characteristics are summarized in Table 1. Ten patients underwent deep brain stimulation after MR imaging studies. The clinical diagnosis of PD was based on the UK Parkinson's Disease Society Brain Bank criteria.<sup>39</sup> Clinical disease severity of movement symptoms was assessed by using the motor section of the Unified Parkinson's Disease Rating Scale (UPDRS III) in the "on" state. According to a previous article,<sup>40</sup> the total daily levodopa-equivalent dose of patients with PD in our study ranged from 200 to 1016 mg (mean, 456.2 ± 265.5 mg). For

the more and less affected body sides, the lateralized UPDRS III motor score on each side was calculated (sum of items, 20-26). The contralateral hemibrain of the more affected body side was defined as the more affected, and the other, as the less affected hemibrain.<sup>19</sup>

The controls were 24 age- and sex-matched healthy volunteers (15 women, 9 men), ranging in age from 39 to 81 years (mean, 64.1 years); they were recruited from Kumamoto University Hospital staff and the local community. Volunteers with a history of cardiovascular, metabolic, neurologic, and psychiatric disorders or brain abnormalities on MR imaging were excluded from this study.

### MR Imaging

Brain MR imaging scans were acquired on a 3T MR imaging system (Magnetom Trio; Siemens, Erlangen, Germany) by using 12-channel head coils. All scans were in the axial plane parallel to the anterior/posterior commissure line. A 3D multiecho gradient-echo sequence was acquired; the parameters were TE = 6.2/12.4/18.6/24.8/31.0/37.2/43.4/49.6 ms; FOV = 24 cm; matrix = 256 × 256 mm<sup>2</sup>; flip angle = 15°; voxel size = 0.9 × 0.9 × 2.0 mm<sup>3</sup>; scan time = 5 minutes 35 seconds. The MR imaging protocol also included fluid-attenuated inversion recovery, turbo spin-echo T2-weighted, diffusion-weighted, and 3D T1-weighted magnetization-prepared rapid acquisition of gradient echo acquisitions.

The 3D multiecho gradient-echo data were used for generating QSM images; QSM was generated by using a morphology-enabled dipole inversion method and the complex data.<sup>25,41,42</sup>

### Image Analysis

The susceptibility (S) of the deep gray matter structures was determined by using ImageJ software (National Institutes of Health, Bethesda, Maryland). For the major deep gray matter structures, excluding the SN, the mean S value of the bilateral globus pallidus (GP), red nucleus (RN), putamen (PT), and caudate nucleus (CN) were measured on axial QSM by 2 neuroradiologists (M.A. and Y.I., with 5 and 9 years of MR imaging experience, respectively). They were blinded to clinical and neurologic findings and independently placed ROIs on the structures (Fig 1). The unit of S measured on QSM was expressed as parts per billion.

To measure the S value of the SN, we used coronal multiplanar reconstruction images to place an ROI in the SN with reference to the Schaltenbrand and Wahren atlas.<sup>36,37</sup> We selected 3 coronal multiplanar reconstruction images at the level of the anterior, middle, and posterior edges of the RN on axial images to measure the spatial susceptibility differences in the anterior, middle, and posterior parts of the SN (aSN, mSN, and pSN) (Fig 2). To avoid contamination by the subthalamic nuclei,<sup>36,37</sup> we placed ROIs on the aSN, mSN, and pSN inferior to the caudal edge of the RN (Fig 2). The averaged value of the aSN, mSN, and pSN was defined as the value of the whole SN.

### Statistical Analysis

We used the paired *t* test to assess the difference in the UPDRS III motor score between more and less affected body sides.

The 2 observers' measurements were averaged for each structure. Interobserver agreement for the 2 observers' measurements was assessed by using the intraclass correlation coefficient, in which an intraclass correlation coefficient of <0.40 = poor, 0.40–0.59 = fair, 0.60–0.74 = good, and >0.74 = excellent.<sup>43</sup> The paired *t* test was used to assess differences in the S value of the

**Table 2: Interobserver agreement for the ROI measurements: healthy controls, right and left hemibrain**

Structure	Right Hemibrain ICC (95% CI)	Left Hemibrain ICC (95% CI)
GP	0.9392 (0.8594–0.9737)	0.9644 (0.9187–0.9845)
RN	0.9419 (0.8669–0.9747)	0.9314 (0.8414–0.9703)
PT	0.9096 (0.7928–0.9607)	0.8607 (0.6763–0.9399)
CN	0.8953 (0.7599–0.9546)	0.9104 (0.7919–0.9613)
aSN	0.9177 (0.8089–0.9645)	0.8978 (0.7627–0.9559)
mSN	0.8893 (0.7428–0.9522)	0.8840 (0.7295–0.9500)
pSN	0.8757 (0.7130–0.9462)	0.9010 (0.7722–0.9571)

Note:—ICC indicates intraclass correlation coefficient.

**Table 3: Interobserver agreement for the ROI measurements: patients with PD, more and less affected hemibrain**

Structure	More Affected Hemibrain ICC (95% CI)	Less Affected Hemibrain ICC (95% CI)
GP	0.9146 (0.8050–0.9628)	0.8962 (0.7614–0.9550)
RN	0.9362 (0.8542–0.9722)	0.9136 (0.7993–0.9627)
PT	0.9046 (0.7818–0.9585)	0.9194 (0.8138–0.9651)
CN	0.9306 (0.8411–0.9699)	0.8625 (0.6856–0.9402)
aSN	0.8814 (0.7299–0.9484)	0.8926 (0.7531–0.9534)
mSN	0.8359 (0.6177–0.9293)	0.8659 (0.6948–0.9416)
pSN	0.8291 (0.6087–0.9257)	0.8907 (0.7511–0.9524)

Note:—ICC indicates intraclass correlation coefficient.

**Table 4: Hemispheric differences in mean susceptibility (parts per billion) in each structure of healthy controls<sup>a</sup>**

Structure	Mean Susceptibility Value		P Value
	Right	Left	
GP	184.6 ± 57.0	178.8 ± 50.1	.1077
RN	110.0 ± 20.1	112.4 ± 23.3	.4956
PT	92.7 ± 15.7	90.3 ± 17.3	.3243
CN	66.5 ± 13.5	70.0 ± 15.3	.0781
Whole SN	107.6 ± 30.8	104.8 ± 34.3	.4564
aSN	145.6 ± 44.3	140.2 ± 44.5	.2690
mSN	108.6 ± 30.0	103.5 ± 33.4	.3435
pSN	68.6 ± 27.8	70.6 ± 32.9	.5407

<sup>a</sup> Data are the means.

hemibrains of healthy controls. Differences between the healthy controls and the patients with PD were determined with the Bonferroni correction. *P* < .05 was considered to indicate a statistically significant difference. To assess the sensitivity and specificity of QSM for discriminating patients with PD from healthy subjects, we performed receiver operating characteristic analysis. The cutoff value for S was determined by using the maximum value of the Youden index.

## RESULTS

There was a significant difference in the UPDRS III motor scores between more and less affected body sides in patients with PD (*P* < .001) (Table 1). The more affected hemibrain was right in 19 and left in 5 patients. The intraclass correlation coefficient values for 2 observers' measurements ranged from 0.8291 to 0.9644 for the S values, and all values showed excellent agreement (Tables 2 and 3).

The mean S value for the GP, RN, PT, CN, whole SN, aSN, mSN, and pSN in healthy controls is shown in Table 4. The highest S value was found in the GP, followed by the RN, whole SN, PT, and CN. Between the right and left hemibrains, there was no significant difference in the S values of any of the structures. The

**Table 5: Comparison of the mean susceptibility values between healthy controls and the more and less affected hemibrains of patients with PD<sup>a</sup>**

Structure	Mean Susceptibility Value			P Value		
	More Affected	Less Affected	Healthy Controls <sup>a</sup>	More Affected vs Less Affected	Less Affected vs Healthy Controls <sup>b</sup>	More Affected vs Healthy Controls <sup>b</sup>
GP	165.6 ± 34.7	168.4 ± 37.4	181.8 ± 53.0	1.0000	.8353	.5735
RN	113.8 ± 43.1	114.2 ± 52.3	111.2 ± 20.1	1.0000	1.0000	1.0000
PT	83.9 ± 34.5	82.6 ± 33.1	91.5 ± 15.5	1.0000	.8768	1.0000
CN	66.8 ± 27.3	69.6 ± 31.8	68.2 ± 13.6	1.0000	1.0000	1.0000
Whole SN	158.0 ± 47.6	138.3 ± 43.9	104.7 ± 31.0	.3080	.0190 <sup>c</sup>	.0001
aSN	186.6 ± 57.5	178.6 ± 54.0	142.9 ± 43.7	1.0000	.0583	.0001 <sup>c</sup>
mSN	166.6 ± 53.2	141.4 ± 51.1	104.6 ± 28.7	.1811	.0200 <sup>c</sup>	<.0001 <sup>c</sup>
pSN	120.8 ± 38.7	94.7 ± 38.0	66.5 ± 25.6	.0362 <sup>c</sup>	.0189 <sup>c</sup>	<.0001 <sup>c</sup>

<sup>a</sup> Data are the means.

<sup>b</sup> Mean value of bilateral hemibrains in healthy controls.

<sup>c</sup> Significant.

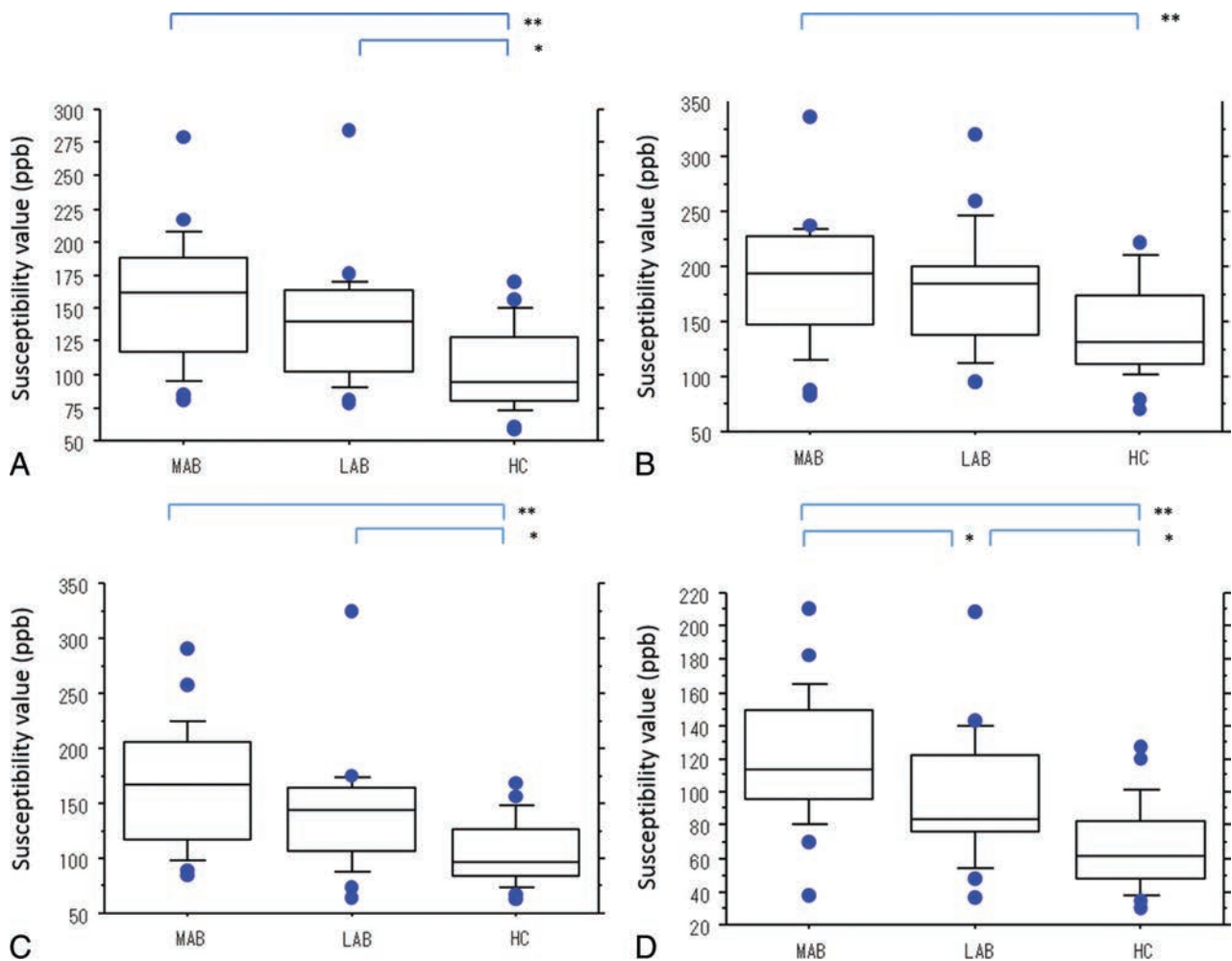


**FIG 3.** Boxplots of the mean susceptibility value (in parts per billion) of the more and the less affected hemibrains in patients with PD and healthy controls. Mean susceptibility values of the whole (A), anterior (B), middle (C), and posterior (D) parts of the substantia nigra. Lines in boxes indicate the median; lower and upper limits of boxes, the 25th and 75th percentiles, respectively; and whiskers, the 10th and 90th percentiles. Outliers are shown as individual points. One asterisk indicates  $P < .05$ ; double asterisks,  $P < .001$ . ppb indicates parts per billion; MAB, more affected hemibrain; LAB, less affected hemibrain; HC, healthy controls.

highest S value was observed in the aSN, followed by the mSN and pSN.

In Table 5 and Fig 3, we compare the mean S value of each structure in the controls and in the more and the less affected hemibrains of patients with PD. In the patients, the order of the mean S values, from high to low, was the following: GP, whole

SN, RN, PT, and CN. The mean S value of the mSN, pSN, and whole SN in the more and the less affected hemibrains was significantly higher in patients than in controls ( $P < .05$ ). In the pSN, the mean S value was significantly higher for the more affected hemibrain than for the less affected hemibrain ( $P < .05$ ).

In the patients with PD, there was no significant difference in the mean S value of the GP, RN, PT, and CN between the more and the less affected hemibrains. The mean S value of the GP and PT tended to be lower in the patients with PD than in the controls.

Receiver operating characteristic analysis showed that the area under the curve was highest (0.887) for the mean S value of the pSN in the more affected hemibrain (Table 6 and Fig 4); at a cutoff value of 68 parts per billion, sensitivity and specificity were 95.8% and 70.8%.

## DISCUSSION

Susceptibility in the mSN, pSN, and the whole SN was significantly higher in the more and the less affected hemibrains of patients with PD than in the healthy controls. Our findings agree with those of Barbosa et al<sup>33</sup> and Murakami et al,<sup>34</sup> who also used QSM. However, the latter did not address iron variation within

the SN, and the former used QSM generated by truncated *k*-space division, which is known to be poorer than QSM generated by morphology-enabled dipole inversion.<sup>24</sup> Their area under the curve was 0.77 for discriminating patients with PD from healthy controls; our area under the curve was 0.887.

We also found lateral asymmetry of iron deposition in the SN of patients with PD. Compared with the less affected hemibrain, susceptibility was significantly higher in the pSN of the more affected hemibrain. This lateral asymmetry was compatible with the manifestation of asymmetric signs and symptoms in PD. Earlier studies by using QSM<sup>33,34</sup> did not detect susceptibility asymmetry in the SN of patients with PD. Unlike those investigations, our study avoided contamination by subthalamic nuclei because our evaluation was based on 3 coronal planes. All patients included in our study presented with asymmetric signs and symptoms. We posit that this and application of our new evaluation method affected the findings.

Although the highest susceptibility value was observed in the aSN, followed by the mSN and the pSN in healthy controls, the highest area under the curve in patients with PD was obtained for the susceptibility value of the pSN in the more affected hemibrain. This suggests that QSM can measure spatial differences in susceptibility within the SN of patients with PD. This spatial difference may be explicable by earlier neuropathologic and 7T MR imaging findings. Degeneration of dopaminergic neurons is greatest in the ventrolateral tier of the SN pars compacta and least in the dorsomedial tier.<sup>1-8,18</sup> The ventrolateral tier is located mostly lateral and posterolateral to the RN<sup>2,3,18</sup> and corresponds to the mSN and pSN. On the other hand, the dorsomedial tier is located mostly anterolateral to the RN<sup>2,3</sup> and corresponds to the aSN.

In PD, iron increases within degenerated dopaminergic neurons in the SN.<sup>8,18</sup> We did not subdivide the SN into pars compacta and pars reticulata layers. Although some MR imaging stud-

**Table 6: Area under the curve and sensitivity and specificity of QSM for discriminating patients with PD from healthy subjects**

	Mean Susceptibility Value			
	AUC	Cutoff Value	Sensitivity	Specificity
			(%)	(%)
More affected brain vs healthy controls				
Whole SN	0.833	133.9	70.8	83.3
aSN	0.745	130.0	87.5	50.0
mSN	0.856	155.8	66.7	95.8
pSN	0.887	68.0	95.8	70.8
Less affected brain vs healthy controls				
Whole SN	0.750	118.1	70.83	70.83
aSN	0.695	131.5	83.33	54.17
mSN	0.755	124.0	70.8	75.0
pSN	0.731	68.0	79.2	70.8

**Note:**—Whole SN indicates averaged value of the anterior, middle, and posterior substantia nigra; AUC, area under the curve.

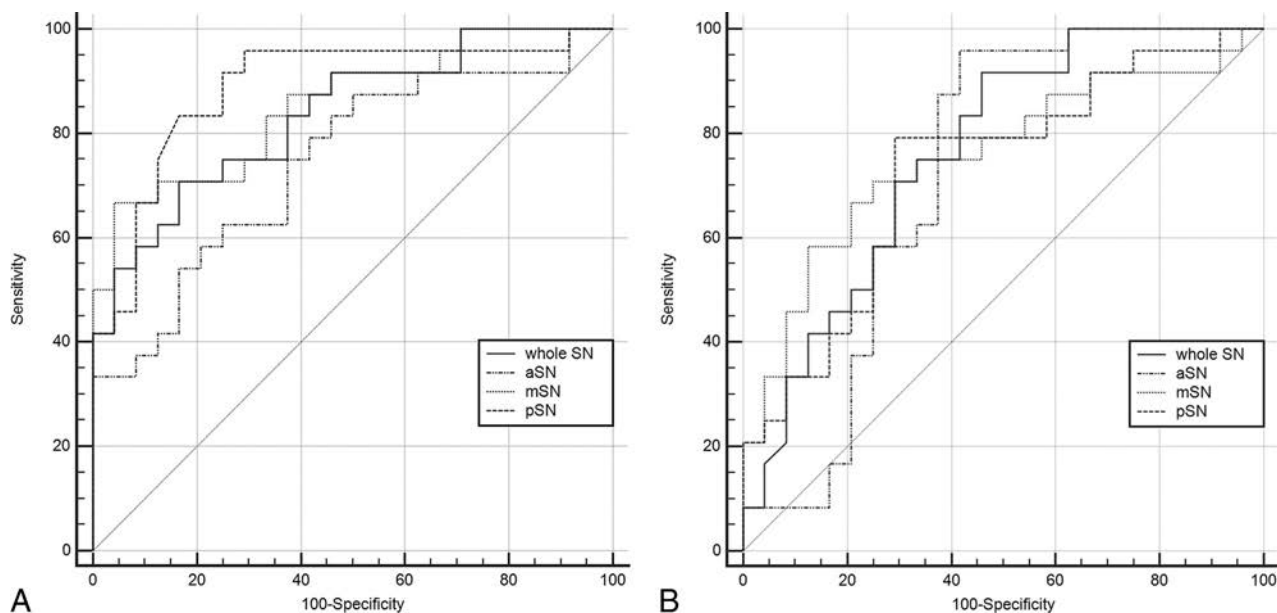


**FIG 4.** Diagnostic performance of QSM of the substantia nigra for discriminating patients with PD from healthy subjects. A, More affected hemibrain versus healthy controls. B, Less affected hemibrain versus healthy controls for the whole SN, and the anterior, middle, and posterior parts of the SN, respectively.

ies have shown the subdivision of the SN pars compacta and the SN pars reticulata, the definition of the 2 areas on MR images is not clear.<sup>13,14,35</sup> Studies of the 3D structure of the SN pars compacta in humans indicated a complex organization with clusters of tyrosine hydroxylase-positive neurons extending into the SN pars reticulata.<sup>44</sup> Consequently, the histologic determination of a boundary between the 2 areas in humans may be difficult, and it is even more difficult to resolve this issue at an MR imaging in-plane resolution of 0.9 mm. Instead, we chose to evaluate the spatial heterogeneity of the SN along its anteroposterior line, which approximates the rostral-caudal axis used in pathology studies, without a subdivision into the pars compacta and the pars reticulata.

According to histochemical studies, gray matter structures with a decreasing order of iron content are the GP, RN, SN, PT, and CN.<sup>41</sup> This order agrees with the order of susceptibility values in our healthy controls, suggesting that they are correlated with the accumulation of iron in the deep gray matter. In addition, in postmortem studies, the chemically determined iron concentration was strongly correlated with the QSM-determined susceptibility in the deep gray matter,<sup>31</sup> indicating that QSM measures iron in brain tissues.

The mean susceptibility value of the GP and PT in our patients with PD tended to be lower than that in the controls (Table 4). This finding is consistent with pathologic studies showing that iron in the GP and PT of patients with PD is lower than that in healthy controls.<sup>5,6</sup> Earlier MR imaging studies also demonstrated a decrease in the iron content of the GP and PT in patients with PD compared with healthy controls.<sup>42</sup> On the basis of the model of functional neuroanatomy of the basal ganglia, the activity of the GABAergic pathway from the PT to the GP is increased in patients with PD.<sup>45</sup> Evidence indicates that the use of gamma-aminobutyric acid leads to a reduction in the iron concentration.<sup>46</sup> Therefore, the iron decrease in the PT and GP of the PD brain may be explained by the altered metabolism of gamma-aminobutyric acid.<sup>42</sup>

Our study has some limitations. First, we did not mention the relationship between S value and progression of PD. As PD progresses, there are longitudinal changes in the R2\* values in the SN.<sup>19,20</sup> Others<sup>33,34</sup> reported that QSM is superior to R2\* mapping for the diagnosis of PD. Further QSM studies are needed to clarify the longitudinal changes for the spatial susceptibility difference in the SN in patients with PD. Second, the number of subjects in this study was relatively small. While we observed a susceptibility increase in the SN, we noted only a trend for a decrease in the PT and GP. Our findings warrant further studies with larger populations. Third, we did not evaluate differences in the susceptibility values between PD and other parkinsonian syndromes.

## CONCLUSIONS

Our study demonstrated a practical method to assess nigral iron accumulation using QSM. Our observations showed that QSM is useful for assessing the lateral asymmetry and spatial difference of iron deposition in the SN of patients with PD.

Disclosures: Satoshi Yamashita—UNRELATED: Grants/Grants Pending: Grants-in-Aid for Science Research from the Ministry of Education, Culture, Sports, Science and Technology of Japan.\* Yi Wang—RELATED: Grant: National Institutes of Health (R01 EB013443)\*; UNRELATED: Grants/Grants Pending: National Institutes of Health; Patents (planned, pending or issued): Cornell University.\* Comments: one of the inventors of QSM technology. \*Money paid to the institution.

## REFERENCES

- Fearnley JM, Lees AJ. **Ageing and Parkinson's disease: substantia nigra regional selectivity.** *Brain* 1991;114:2283–301 CrossRef Medline
- Damier P, Hirsch EC, Agid Y, et al. **The substantia nigra of the human brain, II: patterns of loss of dopamine-containing neurons in Parkinson's disease.** *Brain* 1999;122:1437–48 CrossRef Medline
- Gibb WR, Lees AJ. **Anatomy, pigmentation, ventral and dorsal subpopulations of the substantia nigra, and differential cell death in Parkinson's disease.** *J Neurol Neurosurg Psychiatry* 1991;54:388–96 CrossRef Medline
- Double KL, Reyes S, Werry EL, et al. **Selective cell death in neurodegeneration: why are some neurons spared in vulnerable regions?** *Prog Neurobiol* 2010;92:316–29 CrossRef Medline
- Dexter DT, Wells FR, Lees AJ, et al. **Increased nigral iron content and alterations in other metal ions occurring in brain in Parkinson's disease.** *J Neurochem* 1989;52:1830–36 CrossRef Medline
- Dexter DT, Carayon A, Javoy-Agid F, et al. **Alterations in the levels of iron, ferritin and other trace metals in Parkinson's disease and other neurodegenerative diseases affecting the basal ganglia.** *Brain* 1991;114:1953–75 CrossRef Medline
- Sofic E, Riederer P, Heinsen H, et al. **Increased iron (III) and total iron content in post mortem substantia nigra of parkinsonian brain.** *J Neural Transm* 1988;74:199–205 CrossRef Medline
- Oakley AE, Collingwood JF, Dobson J, et al. **Individual dopaminergic neurons show raised iron levels in Parkinson disease.** *Neurology* 2007;68:1820–25 CrossRef Medline
- Kaur D, Andersen J. **Does cellular iron dysregulation play a causative role in Parkinson's disease?** *Ageing Res Rev* 2004;3:327–43 CrossRef Medline
- Devos D, Moreau C, Devedjian JC, et al. **Targeting chelatable iron as a therapeutic modality in Parkinson's disease.** *Antioxid Redox Signal* 2014;21:195–210 CrossRef Medline
- Haacke EM, Cheng NY, House MJ, et al. **Imaging iron stores in the brain using magnetic resonance imaging.** *Magn Reson Imaging* 2005;23:1–25 CrossRef Medline
- Du G, Lewis MM, Styner M, et al. **Combined R2\* and diffusion tensor imaging changes in the substantia nigra in Parkinson's disease.** *Mov Disord* 2011;26:1627–32 CrossRef Medline
- Martin WR, Wieler M, Gee M. **Midbrain iron content in early Parkinson disease: a potential biomarker of disease status.** *Neurology* 2008;70:1411–17 CrossRef Medline
- Martin WR. **Quantitative estimation of regional brain iron with magnetic resonance imaging.** *Parkinsonism Relat Disord* 2009;15(suppl 3):S215–18 CrossRef Medline
- Zhang J, Zhang Y, Wang J, et al. **Characterizing iron deposition in Parkinson's disease using susceptibility-weighted imaging: an in vivo MR study.** *Brain Res* 2010;1330:124–30 CrossRef Medline
- Rossi ME, Ruottinen H, Saunamäki T, et al. **Imaging brain iron and diffusion patterns: a follow-up study of Parkinson's disease in the initial stages.** *Acad Radiol* 2014;21:64–71 CrossRef Medline
- Cosottini M, Frosini D, Pesaresi I, et al. **MR imaging of the substantia nigra at 7 T enables diagnosis of Parkinson disease.** *Radiology* 2014;271:831–38 CrossRef Medline
- Schwarz ST, Afzal M, Morgan PS, et al. **The 'swallow tail' appearance of the healthy nigrosome: a new accurate test of Parkinson's disease—a case-control and retrospective cross-sectional MRI study at 3T.** *PLoS One* 2014;9:e93814 CrossRef Medline
- Ulla M, Bonny JM, Ouchchane L, et al. **Is R2\* a new MRI biomarker for the progression of Parkinson's disease? A longitudinal follow-up.** *PLoS One* 2013;8:e57904 CrossRef Medline

20. Wieler M, Gee M, Martin WR. **Longitudinal midbrain changes in early Parkinson's disease: iron content estimated from R2\*/MRI.** *Parkinsonism Relat Disord* 2015;21:179–83 CrossRef Medline
21. Yablonskiy DA, Haacke EM. **Theory of NMR signal behavior in magnetically inhomogeneous tissues: the static dephasing regime.** *Magn Reson Med* 1994;32:749–63 CrossRef Medline
22. Li J, Chang S, Liu T, et al. **Reducing the object orientation dependence of susceptibility effects in gradient echo MRI through quantitative susceptibility mapping.** *Magn Reson Med* 2012;68:1563–69 CrossRef Medline
23. Wang Y, Liu T. **Quantitative susceptibility mapping (QSM): decoding MRI data for a tissue magnetic biomarker.** *Magn Reson Med* 2015;73:82–101 CrossRef Medline
24. de Rochefort L, Liu T, Kressler B, et al. **Quantitative susceptibility map reconstruction from MR phase data using Bayesian regularization: validation and application to brain imaging.** *Magn Reson Med* 2010;63:194–206 CrossRef Medline
25. Schweser F, Sommer K, Deistung A, et al. **Quantitative susceptibility mapping for investigating subtle susceptibility variations in the human brain.** *Neuroimage* 2012;62:2083–100 CrossRef Medline
26. Wharton S, Schäfer A, Bowtell R. **Susceptibility mapping in the human brain using threshold-based k-space division.** *Magn Reson Med* 2010;63:1292–304 CrossRef Medline
27. Shmueli KI, de Zwart JA, van Gelderen P, et al. **Magnetic susceptibility mapping of brain tissue in vivo using MRI phase data.** *Magn Reson Med* 2009;62:1510–22 CrossRef Medline
28. Liu T, Spincemaille P, de Rochefort L, et al. **Calculation of susceptibility through multiple orientation sampling (COSMOS): a method for conditioning the inverse problem from measured magnetic field map to susceptibility source image in MRI.** *Magn Reson Med* 2009;61:196–204 CrossRef Medline
29. de Rochefort L, Brown R, Prince MR, et al. **Quantitative MR susceptibility mapping using piece-wise constant regularized inversion of the magnetic field.** *Magn Reson Med* 2008;60:1003–09 CrossRef Medline
30. Zheng W, Nichol H, Liu S, et al. **Measuring iron in the brain using quantitative susceptibility mapping and X-ray fluorescence imaging.** *Neuroimage* 2013;78:68–74 CrossRef Medline
31. Langkammer C, Schweser F, Krebs N, et al. **Quantitative susceptibility mapping (QSM) as a means to measure brain iron? A post mortem validation study.** *Neuroimage* 2012;62:1593–99 CrossRef Medline
32. Lotfipour AK, Wharton S, Schwarz ST, et al. **High resolution magnetic susceptibility mapping of the substantia nigra in Parkinson's disease.** *J Magn Reson Imaging* 2012;35:48–55 CrossRef Medline
33. Barbosa JH, Santos AC, Tumas V, et al. **Quantifying brain iron deposition in patients with Parkinson's disease using quantitative susceptibility mapping, R2 and R2.** *Magn Reson Imaging* 2015;33:559–65 CrossRef Medline
34. Murakami Y, Kakeda S, Watanabe K, et al. **Usefulness of quantitative susceptibility mapping for the diagnosis of Parkinson disease.** *AJNR Am J Neuroradiol* 2015;36:1102–08 CrossRef Medline
35. Oikawa H, Sasaki M, Tamakawa Y, et al. **The substantia nigra in Parkinson disease: proton density-weighted spin-echo and fast short inversion time inversion-recovery MR findings.** *AJNR Am J Neuroradiol* 2002;23:1747–56 Medline
36. Liu T, Eskreis-Winkler S, Schweitzer AD, et al. **Improved subthalamic nucleus depiction with quantitative susceptibility mapping.** *Radiology* 2013;269:216–23 CrossRef Medline
37. Dormont D, Ricciardi KG, Tandé D, et al. **Is the subthalamic nucleus hypointense on T2-weighted images? A correlation study using MR imaging and stereotactic atlas data.** *AJNR Am J Neuroradiol* 2004;25:1516–23 Medline
38. Massey LA, Yousry TA. **Anatomy of the substantia nigra and subthalamic nucleus on MR imaging.** *Neuroimaging Clin N Am* 2010;20:7–27 CrossRef Medline
39. Fahn S, Marsden CD, Goldstein M, et al, eds. *Recent Developments in Parkinson's Disease.* Vol 2. Florham Park, New Jersey: Macmillan Healthcare; 1987:153–63
40. Tomlinson CL, Stowe R, Patel S, et al. **Systematic review of levodopa dose equivalency reporting in Parkinson's disease.** *Mov Disord* 2010;25:2649–53 CrossRef Medline
41. Hallgren B, Sourander P. **The effect of age on the non-haemin iron in the human brain.** *J Neurochem* 1958;3:41–51 CrossRef Medline
42. Graham JM, Paley MN, Grünewald RA, et al. **Brain iron deposition in Parkinson's disease imaged using the PRIME magnetic resonance sequence.** *Brain* 2000;123(pt 12):2423–31 CrossRef Medline
43. Oppo K, Leen E, Angerson WJ, et al. **Doppler perfusion index: an interobserver and intraobserver reproducibility study.** *Radiology* 1998;208:453–57 CrossRef Medline
44. Damier P, Hirsch EC, Agid Y, et al. **The substantia nigra of the human brain, I: nigrosomes and the nigral matrix, a compartmental organization based on calbindin D(28K) immunohistochemistry.** *Brain* 1999;122:1421–36 CrossRef Medline
45. Hill JM. **Iron concentration reduced in ventral pallidum, globus pallidus, and substantia nigra by GABA-transaminase inhibitor, gamma-vinyl GABA.** *Brain Res* 1985;342:18–25 CrossRef Medline
46. Christine CW, Aminoff MJ. **Clinical differentiation of parkinsonian syndromes: prognostic and therapeutic relevance.** *Am J Med* 2004;117:412–19 CrossRef Medline

# Quantitative Susceptibility Mapping Suggests Altered Brain Iron in Premanifest Huntington Disease

J.M.G. van Bergen, J. Hua, P.G. Unschuld, I.A.L. Lim, C.K. Jones, R.L. Margolis, C.A. Ross, P.C.M. van Zijl, and X. Li



## ABSTRACT

**BACKGROUND AND PURPOSE:** In patients with premanifest (nonsymptomatic) and advanced Huntington disease, changes in brain iron levels in the basal ganglia have been previously reported, especially in the striatum. Quantitative susceptibility mapping by using MR phase imaging allows in vivo measurements of tissue magnetic susceptibility, which has been shown to correlate well with iron levels in brain gray matter and is believed to be more specific than other imaging-based iron measures. The purpose of this study was to investigate the use of magnetic susceptibility as a biomarker of disease progression.

**MATERIALS AND METHODS:** Fifteen subjects with premanifest Huntington disease and 16 age-matched healthy controls were scanned at 7T. Magnetic susceptibility, effective relaxation, and tissue volume in deep gray matter structures were quantified and compared with genetic and clinical measures.

**RESULTS:** Subjects with premanifest Huntington disease showed significantly higher susceptibility values in the caudate nucleus, putamen, and globus pallidus, indicating increased iron levels in these structures. Significant decreases in magnetic susceptibility were found in the substantia nigra and hippocampus. In addition, significant volume loss (atrophy) and an increase effective relaxation were observed in the caudate nucleus and putamen. Susceptibility values in the caudate nucleus and putamen were found to be inversely correlated with structure volumes and directly correlated with the genetic burdens, represented by cytosine-adenine-guanine repeat age-product-scaled scores.

**CONCLUSIONS:** The significant magnetic susceptibility differences between subjects with premanifest Huntington disease and controls and their correlation with genetic burden scores indicate the potential use of magnetic susceptibility as a biomarker of disease progression in premanifest Huntington disease.

**ABBREVIATIONS:** CAG = cytosine-adenine-guanine; CAPs = CAG-age product scaled; CN = caudate nucleus; GP = globus pallidus; GRE = gradient recalled-echo; HD = Huntington disease; QSM = quantitative susceptibility mapping; PT = putamen; R2\*, R2 = transverse relaxation rates

Huntington disease (HD) is known to be caused by a cytosine-adenine-guanine (CAG)-repeat expansion in the *HTT* gene,<sup>1,2</sup> resulting in a protein with a long polyglutamine tract that has a toxic effect on neuronal populations.<sup>3,4</sup> Signs and symptoms

include motor, cognitive, and emotional dysfunction.<sup>5,6</sup> Genetic testing can identify subjects at risk of HD many years before the onset of the disease when subjects are still in the prodromal or premanifest phase. In addition, CAG expansion length is inversely related to the age of disease onset, thereby allowing approximate prediction of the time to onset of motor dysfunction. Sensitive and robust imaging-based surrogate biomarkers are needed to monitor disease progression and response to possible treatment.

A well-studied MR imaging-based biomarker for disease progression in advanced and premanifest HD is brain atrophy,

in part, by a grant from Philips Healthcare. This arrangement has been approved by Johns Hopkins University in accordance with its conflict of interest policies.

Please address correspondence to Jiri van Bergen, MSc, Division of Psychiatry Research, University of Zurich, Wagistr 12, 8952 Schlieren, Switzerland; e-mail: Jiri.vanbergen@uzh.ch

Indicates open access to non-subscribers at [www.ajnr.org](http://www.ajnr.org)

Indicates article with supplemental on-line photo.

<http://dx.doi.org/10.3174/ajnr.A4617>

Received August 6, 2015; accepted after revision September 22.

From the Departments of Radiology and Radiological Sciences (J.M.G.v.B., J.H., I.A.L.L., C.K.J., P.C.M.v.Z., X.L.), Psychiatry and Behavioral Sciences (P.G.U., R.L.M., C.A.R.), and Neurology (R.L.M., C.A.R.), Johns Hopkins University School of Medicine, Baltimore, Maryland; F.M. Kirby Research Center for Functional Brain Imaging (J.M.G.v.B., J.H., I.A.L.L., C.K.J., P.C.M.v.Z., X.L.), Kennedy Krieger Institute, Baltimore, Maryland; and Division of Psychiatry Research and Psychogeriatric Medicine (P.G.U.), University of Zurich, Zurich, Switzerland.

This project was supported by the National Center for Research Resources and the National Institute of Biomedical Imaging and Bioengineering of the National Institutes of Health through resource grant P41 EB015909, with educational funding from a National Institutes of Health Training Grant for Interdisciplinary Training in Psychiatry and Neuroscience T32 MH015330. In addition, a grant from the Huntington's Disease Society of America—Centers of Excellence and a grant from the David Mahoney Neuroimaging Program from the Dana Foundation supported this work. Dr Peter van Zijl is a paid lecturer for Philips Healthcare and is the inventor of technology that is licensed to Philips Healthcare. Dr Xu Li's salary is supported,

mainly in the striatum, but other subcortical structures such as the globus pallidus (GP), thalamus, hippocampus, and amygdala were also found to be affected to a certain extent in HD.<sup>7,8</sup> Volumetric changes have been systematically reported in all stages of the disease, with atrophy starting around 12 years before predicted onset of motor dysfunction.<sup>7-9</sup> In addition to structural changes, iron level change has also been suggested to play an important role in HD pathophysiology, likely preceding structure changes, and may serve as a potential biomarker for early diagnosis and monitoring of a response to a therapeutic approach. Previous studies have indicated that the mutated huntingtin protein increases intracellular calcium levels, which activate the Rhes protein, leading to an influx of intercellular iron through the divalent metal transporter 1, which further leads to increased oxidative damage.<sup>10,11</sup> Such huntingtin-induced increased uptake of iron into the cells damages the neurons, inducing inflammation and neuronal loss, leading to degradation of striatopallidal projections.<sup>12,13</sup>

Another relevant pathologic model proposes that increased vulnerability of GABAergic medium spiny neurons in the early stages of HD could lead to the striatal iron accumulation and progressive volume loss.<sup>14</sup> In fact, animal studies of advanced HD have shown significantly higher levels of iron in the basal ganglia structures.<sup>15</sup> In addition, a postmortem study of advanced HD showed an increase in crude iron concentration of almost 150% in the putamen (PT) and GP.<sup>16</sup> Rosas et al<sup>17</sup> measured increased iron of 25%–30% in the same structures. These studies in advanced HD have sparked interest in investigating potentially abnormal iron accumulation during the earlier stages of the disease. Several recent studies by using transverse relaxation rate ( $R2^*$ ) measurements<sup>18,19</sup> or magnetic susceptibility–related measures, such as phase,<sup>20</sup> magnetic field correlation,<sup>21</sup> and field shift,<sup>17</sup> have indeed suggested that brain iron levels are increased in premanifest or patients with early-stage HD.

Previous MR imaging techniques for measuring tissue iron have been based on either relaxation or other indirect measures of tissue magnetic susceptibility, which could be masked by multiple confounding effects. For example, a major confounding effect in relaxation-based measures, including  $R2$  and  $R2^*$ , is the change of water content. Contributions from the macroscopic background field, which have no relationship to local tissue iron, may also contaminate  $R2^*$ -based iron measures. Previous magnetic susceptibility–based measures such as phase or field shift are known to be nonlocal (ie, affected by the susceptibility values of surrounding tissue and the position of the head)<sup>22</sup>; thus, this feature makes them hard to interpret and less specific for measuring tissue iron. Recent developments in quantitative susceptibility mapping (QSM) techniques<sup>23-27</sup> have made it possible to directly map brain tissue magnetic susceptibility. Compared with previous techniques, QSM is believed to give a more accurate and specific measure of tissue magnetic susceptibility, which has been shown to correlate well with tissue iron concentration in most brain gray matter regions.<sup>23,24,28-30</sup>

In the present study, QSM was used to assess and expand on previous findings<sup>31</sup> of differences in magnetic susceptibility between healthy controls and patients with premanifest HD in the basal ganglia, focusing on regions that have shown altered iron

content in advanced HD (ie, the caudate nucleus [CN], PT, GP,<sup>17</sup> and other deep gray matter structures that have shown certain atrophy and may possibly be affected in HD [ie, amygdala, hippocampus, and thalamus]).<sup>8</sup> Some deep iron-rich nuclei related to movement and cognition, including the substantia nigra and red nucleus, were also included in our analysis. To compare with previous studies, we also calculated  $R2^*$  as another susceptibility-related measure for the 2 groups. In addition, we tested possible correlations between magnetic susceptibility and structure volume and the genetic burden of the CAG repeats. It is hypothesized that brain iron concentration changes in subjects with premanifest HD will affect the local tissue magnetic susceptibility, which may, therefore, serve as a potential biomarker for HD progression.

## MATERIALS AND METHODS

### Subjects

Fifteen subjects with premanifest HD (5 men, 10 women; mean age,  $42.4 \pm 8.7$  years) were recruited through the Baltimore Huntington's Disease Center at the Johns Hopkins University School of Medicine. Inclusion criteria for the premanifest HD group were a CAG repeat length in the *HTT* gene higher than 40 and a Unified Huntington's Disease Rating Scale<sup>32</sup> motor score below 15. Of the subjects with premanifest HD, 7 were scanned in 2010, and 8, in 2013. Additionally, 16 age-matched healthy controls (8 men, 8 women; mean age,  $43.3 \pm 11.7$  years) were recruited through Johns Hopkins University. Consent was obtained according to the Declaration of Helsinki and approved by the Johns Hopkins University Institutional Review Board.

The age of onset of HD correlates strongly with CAG-repeat length. To quantify the genetic burden at the time of the scan, we calculated the CAG-age product scaled (CAPs) score<sup>33</sup> as  $CAPs = \text{Age} \times (\text{CAG} - 33.66) / 432.3326$ . This indicates a probability of disease onset within 5 years of  $<.5$ ,  $0$ , and  $>.5$  for CAPs scores  $<1$ ,  $1$ , and  $>1$ , respectively.

Clinical personnel, trained in neuropsychological subject evaluation, performed the following interviews and tests on the day of scanning for all gene-positive subjects: the Unified Huntington's Disease Rating Scale test to determine the total motor score, the Hamilton Depression Rating Scale,<sup>34</sup> the Montreal Cognitive Assessment<sup>35</sup> to screen for mild cognitive dysfunction, and the National Adult Reading Test<sup>36</sup> as an estimate of premorbid intelligence. Subjects with premanifest HD with a known acute neuropsychiatric disease, severe cognitive impairment, affective disorders, or other acute medical disorders were excluded from the study. Because the mean age of the subjects with premanifest HD is below prevalence rates of sporadic neurodegenerative disease and vascular dementia, we did not expect subjects with these disorders. Healthy controls were recruited from a different study in which their status as healthy was determined by interviews and scores on the Montreal Cognitive Assessment, Mini-Mental State Examination, and memory tests (immediate and delayed recall).

### MR Imaging Protocol

Subjects were imaged by using a 7T Achieva scanner (Philips Healthcare, Best, the Netherlands) equipped with a 1TX-32RX quadrature transmit head coil (Nova Medical, Wilmington, Mas-

sachusetts) and a 32-channel phased array receive coil. A T1-weighted MPRAGE image (TR/TE = 4.8/2.1 ms, resolution =  $0.6 \times 0.6 \times 0.6 \text{ mm}^3$ , scan time = 6 minutes 32 seconds) was acquired for anatomic referencing and automated image segmentation. MR phase measurements used for QSM calculation were acquired by using a multiecho 3D gradient recalled-echo (GRE) sequence. Two types of scan parameters were used. For 8 subjects with premanifest HD and all healthy controls, multiecho 3D GRE scans with 8 echoes (TR/TE/ $\Delta$ TE = 68/4/2 ms, flip angle =  $9^\circ$ , voxel size =  $1 \times 1 \times 1 \text{ mm}^3$ , FOV =  $220 \times 220 \times 100 \text{ mm}^3$ , bandwidth = 1529 Hz/voxel, scan time = 7 minutes 13 seconds) were acquired. For the other 7 patients, multiecho 3D GRE scans with 22 echoes (TR/TE/ $\Delta$ TE = 61/2/2 ms, flip angle =  $19^\circ$ , voxel size =  $1 \times 1 \times 1 \text{ mm}^3$ , FOV =  $212 \times 212 \times 80 \text{ mm}^3$ , bandwidth = 1213 Hz/voxel, scan time = 6 minutes 12 seconds) were acquired. Images were inspected (by P.G.U.) for any imaging artifacts or abnormalities, but no additional inspections were performed for small white matter hyperintensities or vascular disease.

Although MR phase measurements depend on the B0 field and echo time, the tissue magnetic susceptibility calculated by using QSM is expected to be affected by scanning parameters to a small extent as long as the same TE range is used. To evaluate possible differences and variations in the calculated susceptibility values caused by the 2 scanning parameters used in this study, we scanned 4 healthy subjects (2 men, 2 women; age range, 27–36 years) with both scan settings and compared the corresponding susceptibility quantities. For all the GRE scans, the 5 echoes with a TE in the range of 10–18 ms were used to calculate magnetic susceptibility to obtain a good signal-to-noise ratio and minimize the effect of nonlinear phase evolution at short TEs (ie, with TE < 10 ms).<sup>37</sup>

### Quantitative Susceptibility and R2\* Mapping

Multiple processing steps were performed to calculate the quantitative susceptibility maps from acquired MR phase images. First, phase unwrapping was performed by using Laplacian-based phase unwrapping.<sup>27</sup> A brain mask was then obtained by skull-stripping the GRE magnitude image acquired at a TE of 10 ms. The unwrapped phase images were then divided by  $2\pi \times \text{TE}$  to obtain an image of the frequency shift in hertz for each echo. Subsequently, background fields were eliminated with the variable spheric kernel size sophisticated harmonic artifact reduction for the phase-data (V-SHARP)<sup>29</sup> approach with a maximum radius of 4 mm and a regularization parameter of 0.05.<sup>38</sup> After removal of background fields, we averaged the resulting images of all 5 echoes to obtain a higher signal-to-noise ratio compared with single-echo reconstruction.<sup>39</sup> Inverse dipole calculations to obtain the susceptibility maps were performed by using a Least Squares with QR factorization-based minimization.<sup>27</sup> The central CSF region in the lateral ventricles of each subject was selected as a reference region for the final susceptibility quantification. All susceptibility values have been reported relative to the mean susceptibility value of this reference region for each subject. R2\* maps were calculated by nonlinear fitting of a monoexponential curve to the square of the magnitude data at all available echoes in each voxel by using the power method.<sup>23</sup>

**Table 1: Demographic data and clinical assessment scores for controls and subjects with premanifest HD<sup>a</sup>**

	Healthy Controls	Premanifest HD
No.	16	15
Sex (male/female)	8:8	5:10
Age (yr)	43.3 ± 11.7	42.4 ± 8.7
Education (yr)	18.1 ± 2.7	15.5 ± 2.6
CAG length	—	43.5 ± 2.6
CAPs score	—	0.9 ± 0.2
Unified Huntington's Disease Rating Scale motor score	—	7.2 ± 5.4
Hamilton Depression Rating Scale	—	4.7 ± 3.9
Montreal Cognitive Assessment	29.1 ± 0.7	26.0 ± 4.1
Full-scale intelligence quotient	—	111.0 ± 8.2
Verbal intelligence quotient	—	109.8 ± 9.2

**Note:** — indicates results were not available for all subjects.

<sup>a</sup> Data are presented as means.

### Image Segmentation

The T1-weighted MPRAGE image was coregistered to the GRE magnitude image at a TE of 10 ms. The coregistered T1 image was then segmented by using a multiatlas matching approach developed as part of the Johns Hopkins University brain atlas.<sup>40</sup> After this atlas-based segmentation, ROIs in the CN, PT, GP, amygdala, hippocampus, and thalamus were extracted. Manual corrections on ROIs in the substantia nigra and red nucleus were performed on the basis of magnetic susceptibility contrast, because they show little or no contrast on T1-weighted images and the ROIs generated from the automated segmentation process based on T1 contrast generally deviate from the true anatomic locations.<sup>24</sup> From each ROI, the volume of the structure was determined in an automated way by multiplying the amount of voxels in that ROI and the known voxel size. To account for different brain sizes across subjects, we corrected individual structural volume with the following approach: Corrected Structure Volume = Original Structure Volume  $\times$  (Group Mean Intracranial Volume/Subject Intracranial Volume). Each of the ROIs was eroded by 2 pixels in 3D to eliminate partial volume effects and then was used as a mask to calculate average susceptibility and R2\* values per region.

### Statistics

To examine the differences between the controls and the premanifest HD group, we performed 1-way MANCOVA with the mean magnetic susceptibility, R2\*, or tissue volume of each brain structure as the outcome variable, while controlling for age and sex. The *P* value after post hoc Bonferroni correction was considered significant at *P* ≤ .05.

To test how magnetic susceptibility, R2\*, and tissue volume in the selected gray matter structures were correlated with clinical measures in the premanifest HD group, we performed a Pearson partial correlation analysis, controlling for age and sex. The outcome variable was set as the susceptibility value, R2\*, or volume of each brain structure, and the predictor was set as the CAPs, Unified Huntington's Disease Rating Scale motor score, or Montreal Cognitive Assessment score. The CAPs score is a function of age; therefore, the correlation analysis of CAPs with susceptibility, R2\*, and ROI volume was not corrected for age.

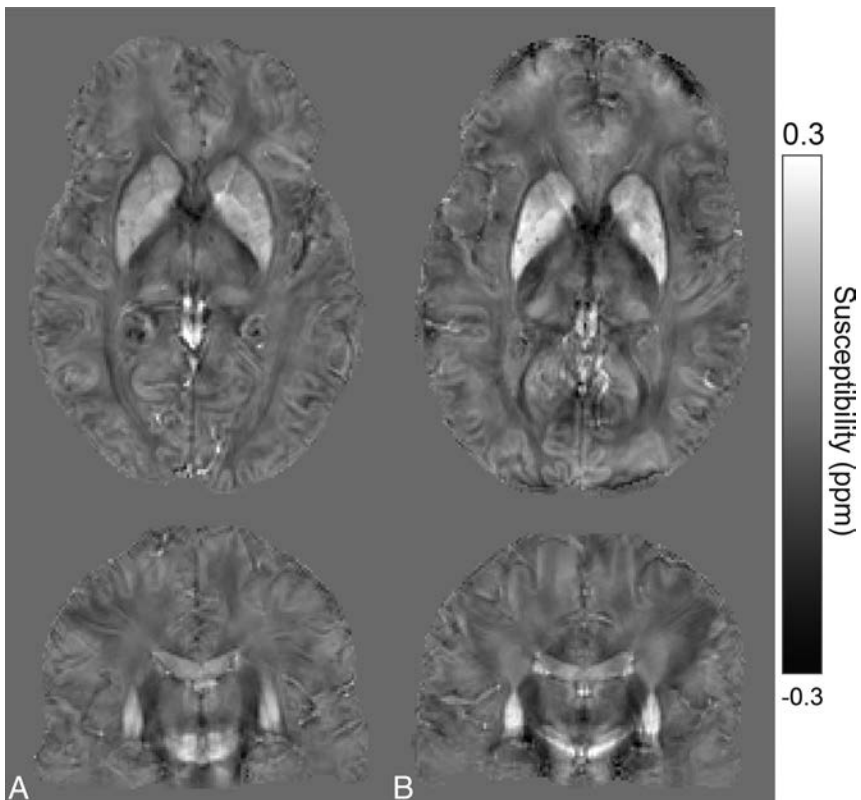


**FIG 1.** Sample axial and coronal QSM sections of a 41-year-old healthy subject (A). Similar sections in a 41-year-old subject with premanifest HD (B). Increased susceptibility values are visible in iron-rich deep gray matter structures, such as the caudate nucleus, putamen, and globus pallidus.

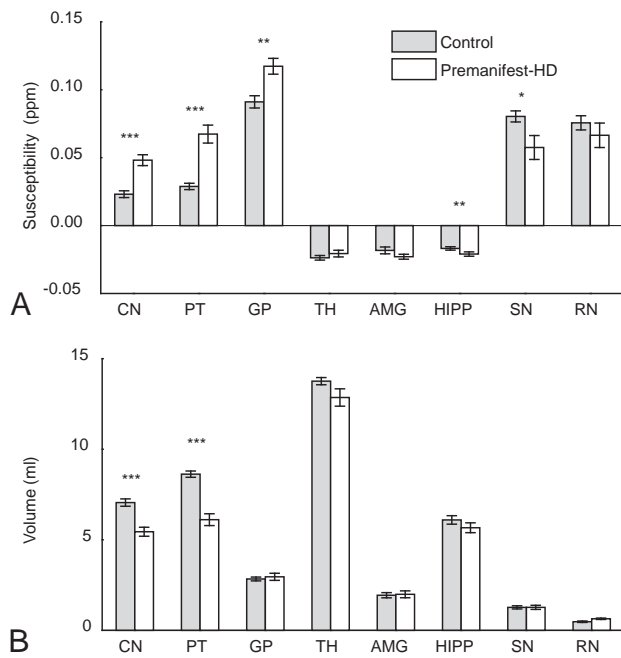


**FIG 2.** Average susceptibility values (A) and average volumes (B) in each ROI of the control and premanifest HD groups. Error bars represent standard error (SE). One asterisk indicates a significant difference with  $P < .05$ ; double asterisks, a significant difference with  $P < .01$ ; triple asterisks, a significant difference with  $P < .001$ ; TH, thalamus; AMG, amygdala; HIPP, hippocampus; SN, substantia nigra; RN, red nucleus.

## RESULTS

The demographic information for all the subjects and the clinical test results on all patients with premanifest HD are summarized in Table 1. Sample susceptibility maps of a healthy control and a subject with premanifest HD are shown in Fig 1. Compared with the healthy control (Fig 1A), susceptibility increases in the PT, part of the GP, and CN can be seen in the subject with premanifest HD (Fig 1B). The On-line Figure shows selected ROIs generated by using the atlas-based segmentation overlaid on the QSM images of a healthy control subject. The comparison between the 2 GRE scan settings showed no significant differences in the calculated mean susceptibility values and SDs in any selected ROI; thus, combining the 2 datasets for susceptibility analysis is valid and should not give significant bias to our conclusion.

Controlling for age, group comparison between controls, and premanifest HD shows a significant susceptibility increase (Fig 2A and Table 2) in the CN, PT ( $P < .001$ ), and GP ( $P < .01$ ). The substantia nigra ( $P < .05$ ) and hippocampus ( $P < .01$ ) show a significant susceptibility decrease, with a similar trend also observed in the red nucleus and amygdala.

Splitting the analysis by sex did not alter the results, with both male and female groups showing statistically significant differences in similar regions (data not shown).  $R2^*$  values were found to be increased in the CN and PT ( $P < .01$ ) (Table 2). In addition to susceptibility changes, a significant volume decrease was also observed in the CN and PT ( $P < .001$ ) (Fig 2B and Table 2).

Correlation analysis with the predictor as the Unified Huntington's Disease Rating Scale motor score or Montreal Cognitive Assessment score did not result in significant correlations between those metrics and magnetic susceptibility or  $R2^*$  in any selected ROI. In the CN and PT, strong inverse correlations were found between susceptibility and ROI volume (Fig 3A). The CAPs directly correlated with the susceptibility and inversely correlated with ROI volume in the CN and PT (Fig 3B, -C and Table 2). Using  $R2^*$ , we observed a correlation with CAPs in the PT ( $P < .05$ ,  $r = 0.52$ ).

## DISCUSSION

This cross-sectional study found significantly increased magnetic susceptibility values in the CN, PT, and GP of subjects with premanifest HD compared with control subjects. Due to the previously demonstrated strong direct correlation of susceptibility values with tissue iron levels in brain gray matter,<sup>24,30</sup> such increase is attributed predominantly to an HD-related increase of tissue iron content in these regions. Such increased iron levels in the CN, PT, and GP in patients with premanifest HD are, in general, con-

**Table 2: Summary of average susceptibility ( $\chi$ ), average R2\* values, and average volume for each selected ROI**

	$\chi$ (ppm) $\pm$ SE		R2* (s <sup>-1</sup> ) $\pm$ SE		Corrected Volume (mL) $\pm$ SE	
	Controls	Premanifest HD	Controls	Premanifest HD	Controls	Premanifest HD
Caudate nucleus	0.023 $\pm$ 0.002	0.048 $\pm$ 0.004 <sup>a,b,c</sup>	43.69 $\pm$ 0.88	49.35 $\pm$ 1.63 <sup>c,d</sup>	7.1 $\pm$ 0.8	5.4 $\pm$ 0.9 <sup>a,b</sup>
Putamen	0.029 $\pm$ 0.002	0.067 $\pm$ 0.007 <sup>a,b,c</sup>	52.59 $\pm$ 1.39	64.21 $\pm$ 2.55 <sup>b,c,d</sup>	8.6 $\pm$ 0.7	6.1 $\pm$ 1.3 <sup>a,b</sup>
Globus pallidus	0.091 $\pm$ 0.005	0.117 $\pm$ 0.007 <sup>d</sup>	84.48 $\pm$ 2.64	92.75 $\pm$ 3.35	2.8 $\pm$ 0.4	3.0 $\pm$ 0.8
Thalamus	-0.024 $\pm$ 0.002	-0.021 $\pm$ 0.002	40.22 $\pm$ 0.70	40.07 $\pm$ 0.79	13.8 $\pm$ 0.8	12.9 $\pm$ 1.5
Amygdala	-0.018 $\pm$ 0.003	-0.023 $\pm$ 0.002	29.82 $\pm$ 0.78	31.59 $\pm$ 1.64	1.9 $\pm$ 0.6	2.0 $\pm$ 0.7
Hippocampus	-0.017 $\pm$ 0.001	-0.021 $\pm$ 0.002 <sup>d</sup>	31.32 $\pm$ 0.54	30.47 $\pm$ 1.12	6.1 $\pm$ 0.9	5.7 $\pm$ 1.1
Substantia nigra	0.080 $\pm$ 0.004	0.057 $\pm$ 0.009 <sup>e</sup>	75.45 $\pm$ 2.68	70.62 $\pm$ 3.05	1.3 $\pm$ 0.4	1.3 $\pm$ 0.4
Red nucleus	0.076 $\pm$ 0.005	0.066 $\pm$ 0.009	65.30 $\pm$ 2.71	67.00 $\pm$ 2.47	0.5 $\pm$ 0.2	0.6 $\pm$ 0.1

<sup>a</sup> Significant difference with  $P < .001$ .

<sup>b</sup> Significant correlation with CAPs score in subjects with premanifest HD.

<sup>c</sup> Significant correlation with ROI volume in subjects with premanifest HD.

<sup>d</sup> Significant difference with  $P < .01$ .

<sup>e</sup> Significant difference between controls and premanifest HD with  $P < .05$ .

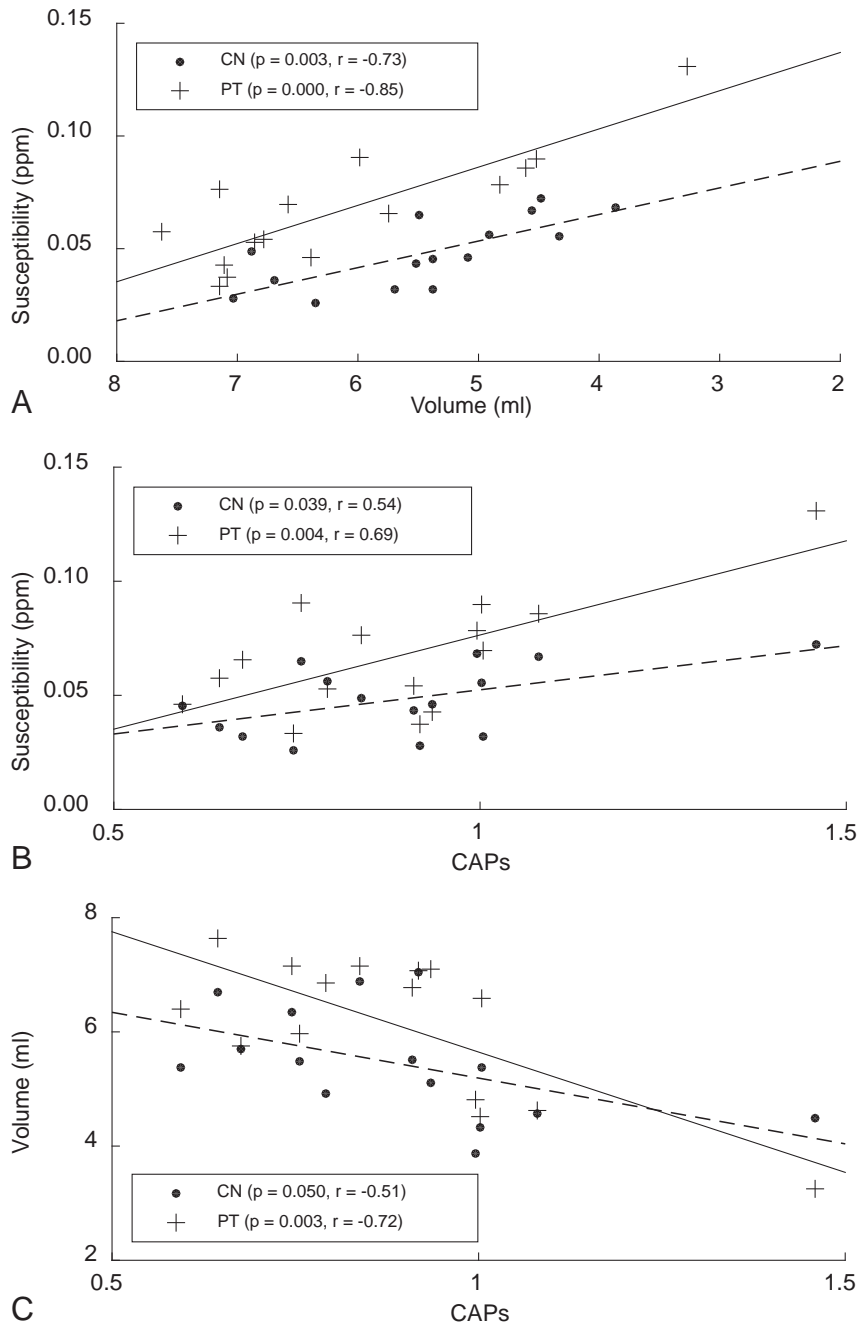


**FIG 3.** Correlation analysis of susceptibility and corrected structure volume while controlling for age (A), susceptibility with CAPs (B), and volume with CAPs (C).

sistent with the findings of other in vivo MR imaging studies of these patients and those with symptomatic HD,<sup>13,17,18,20,41</sup> indicating that altered iron homeostasis may be involved in HD pathophysiology and may happen at very early stages of the disease. Postmortem studies of the same regions in symptomatic HD also support these findings.<sup>16,17,42</sup> In addition, the more significant changes in the CN and PT compared with the GP found in this study are consistent with the general understanding that HD-related neuronal damage begins in the striatum and then spreads to the GP and other regions.<sup>6</sup> However, partly due to the use of different MR imaging-based iron measures, previous findings on iron level changes in HD have not always been consistent. For example, in comparison with the present study, Dumas et al,<sup>21</sup> using magnetic field correlation, could detect only elevated iron levels in early symptomatic patients with HD but not in the premanifest HD group. Such discrepancy may come from the lower sensitivity of magnetic field correlation in detecting HD-induced tissue iron changes, lower spatial resolution, and more stringent patient inclusion criteria used in that study (ie, with a Unified Huntington's Disease Rating Scale score cutoff point of 5 for the premanifest HD group).

The increased iron level in the striatum in the premanifest HD group is further confirmed by the increased R2\* in these regions. Given the strong correlation between R2\* and tissue iron,<sup>30,43</sup> the observation that susceptibility is more sensitive for detecting HD-related changes may hint at some other pathophysiological features of the disease such as loss of diamagnetic myelin.<sup>44</sup> Due to the microstructure of myelin and its diamag-

netic nature, it is known that demyelination would decrease R2\* and increase magnetic susceptibility. Similar higher sensitivity of susceptibility compared with R2\* has been observed previously in detecting tissue changes in multiple sclerosis, in which demyelination is a known disease hallmark.<sup>45</sup> In addition, some striatal demyelination and loss of tissue integrity in premanifest HD might also partly explain the increased mean diffusivity observed in another study.<sup>19</sup> In most of the deep gray matter regions investigated in this study, myelin content was not expected to be very high; therefore, iron change is still likely to be the dominant source of the observed susceptibility and R2\* increases in the premanifest HD group. Finally, R2\* as a parameter is more difficult to quantify reproducibly due to its dependence on magnetic field inhomogeneity and the orientation of the brain. This explanation may be an alternative one for the somewhat lower significance.

This study also found decreased levels of iron in other brain regions related to movement and memory, such as the hippocampus, substantia nigra, and red nucleus, in subjects with premanifest HD. Decreased iron concentration has been reported in certain cortical areas<sup>18</sup> and white matter regions<sup>44</sup> during the progress of HD. Such iron decreases are generally explained by the redistribution of brain iron after the increase of oligodendrocyte density, thus, iron concentration is an attempt to restore initial neural or myelin loss caused by HD.<sup>18,44</sup> The decrease in iron level in the hippocampus was previously observed as a nonsignificant trend by several *in vivo* studies<sup>21,44</sup>; however, to the best of our knowledge, there is no previous report on iron level changes in the substantia nigra in the premanifest HD group. The significant iron decrease in the substantia nigra and the decrease trend in the red nucleus may be caused by the iron redistribution processes or changes in myelin attenuation that are not yet fully understood. Increases in arterial blood volume could also be a cause of such a decrease because iron in deoxygenated venous blood has a strong effect on tissue susceptibility.<sup>30</sup> Decreased cerebral blood flow in the basal ganglia and hippocampus of patients with premanifest HD has been reported,<sup>46–48</sup> while increased arteriolar cerebral blood volume in the cortex has also been previously observed in patients<sup>49</sup> and animal models.<sup>50</sup>

As expected, significant volume decreases (atrophy) in the CN and PT were observed in patients with premanifest HD in the present study, but not in the GP, where atrophy often occurs later in the disease.<sup>6</sup> At this early stage, the significant iron-level difference observed in the GP may suggest that iron changes precede or have a greater magnitude than volume changes in the GP. In addition, iron levels were strongly inversely correlated with volumes in the CN and PT. Similar correlations were observed between R2\* and volume in the CN and PT in this study. Such correlations were observed in the PT and GP in a very recent study by using R2\*, but not in the CN.<sup>18</sup> No correlations with volume were observed by using magnetic field correlation<sup>21</sup> or phase imaging<sup>20</sup> as iron measures. Both volume and susceptibility in the CN and PT showed strong correlations with CAPs, suggesting that both measures are closely related to the disease process. Correlation with CAPs was only observed in the PT by using R2\*. Similar correlations in subjects with premanifest HD were observed previously only in the CN by using phase imaging<sup>20</sup> and in the PT by using R2\* measurements,<sup>18</sup> but no correlations were observed by using the magnetic field correlation.<sup>21</sup>

## CONCLUSIONS

Together with previous iron studies in premanifest and symptomatic HD, the present study suggests that disease-related iron increase in the striatum and GP happens in the early stage of HD and tissue magnetic susceptibility as obtained by QSM has a good potential to serve as a sensitive *in vivo* surrogate measure to track tissue iron changes in HD. However, due to the limited sample size used in the present study, the lack of a symptomatic HD group, and lack of controls for possible vascular diseases, quantitative susceptibility as biomarker of HD progression cannot be fully confirmed yet. Further investigation with a larger cohort and longitudinal follow-up is required in the future. In addition, tissue iron measures combined with other biomarkers sensitive to either macrostructure or microstructure impairment in a multimodal setup<sup>18,19</sup> would further help understand the pathophysiology of HD.

## ACKNOWLEDGMENTS

The authors thank Dr James Pekar, Dr Andreia Faria, Mr Joseph Gillen, Ms Terri Brawner, Ms Kathleen Kahl, Ms Ivana Kusevic, and Dr Raj Stewart for their assistance with data acquisition.

Disclosures: Issel Anne Lim—*RELATED: Grant:* National Institutes of Health Training Grant for Interdisciplinary Training in Psychiatry and Neuroscience (T32 MH015330). \**Craig Jones—RELATED: Grant:* Philips Healthcare. \**Comments:* My salary was paid, in part, by a grant to the Kennedy Krieger Institute from Philips Healthcare. Russell Margolis—*RELATED: Grant:* National Institutes of Health \*. *UNRELATED: Grants/Grants Pending:* National Institutes of Health, Prana, Auspex, Teva, Child Health and Development Institute. *Comments:* treatment trials and pathogenic studies of HD. Christopher Ross—*RELATED: Grant:* Huntington's Disease Society of America—Centers of Excellence. \**Peter van Zijl—RELATED: Grant:* Philips Healthcare (technical development grant)\*; *Support for Travel to Meetings for the Study or Other Purposes:* Philips Healthcare (supported travel to conferences); *UNRELATED: Payment for Lectures (including service on Speakers Bureaus):* Philips Healthcare. *Comments:* In the past, they have provided honoraria for lectures; *Patents (planned, pending or issued):* Philips Healthcare. \**Comments:* provided funds for patent licensing to the institution and also got income from such patent licenses; *Travel/Accommodations/Meeting Expenses Unrelated to Activities Listed:* Philips Healthcare. *Comments:* supported travel to conferences; *OTHER:* Dr Peter van Zijl is a paid lecturer for Philips Healthcare and is the inventor of technology that is licensed to Philips Healthcare. Xu Li—*RELATED: Grant:* Philips Healthcare. *Comments:* Dr Xu Li's salary is supported, in part, by a grant from Philips Healthcare. This arrangement has been approved by Johns Hopkins University in accordance with its conflict of interest policies. \*Money paid to the institution.

## REFERENCES

1. Ross CA, Aylward EH, Wild EJ, et al. **Huntington disease: natural history, biomarkers and prospects for therapeutics.** *Nat Rev Neurol* 2014;10:204–16 CrossRef Medline
2. **A novel gene containing a trinucleotide repeat that is expanded and unstable on Huntington's disease chromosomes: the Huntington's Disease Collaborative Research Group.** *Cell* 1993;72:971–83 CrossRef Medline
3. Gusella JF, Wexler NS, Conneally PM, et al. **A polymorphic DNA marker genetically linked to Huntington's disease.** *Nature* 1983;306:234–38 CrossRef Medline
4. Tabrizi SJ, Scahill RI, Durr A, et al; TRACK-HD Investigators. **Biological and clinical changes in premanifest and early stage Huntington's disease in the TRACK-HD study: the 12-month longitudinal analysis.** *Lancet Neurol* 2011;10:31–42 CrossRef Medline
5. Paulsen JS, Nopoulos PC, Aylward E, et al; PREDICT-HD Investigators and Coordinators of the Huntington's Study Group (HSG). **Striatal and white matter predictors of estimated diagnosis for Huntington disease.** *Brain Res Bull* 2010;82:201–07 CrossRef Medline

6. Ross CA, Tabrizi SJ. **Huntington's disease: from molecular pathogenesis to clinical treatment.** *Lancet Neurol* 2011;10:83–98 CrossRef Medline
7. Tabrizi SJ, Langbehn DR, Leavitt BR, et al; TRACK-HD investigators. **Biological and clinical manifestations of Huntington's disease in the longitudinal TRACK-HD study: cross-sectional analysis of baseline data.** *Lancet Neurol* 2009;8:791–801 CrossRef Medline
8. van den Bogaard SJ, Dumas EM, Acharya TP, et al; TRACK-HD Investigator Group. **Early atrophy of pallidum and accumbens nucleus in Huntington's disease.** *J Neurol* 2011;258:412–20 CrossRef Medline
9. Aylward EH, Li Q, Stine OC, et al. **Longitudinal change in basal ganglia volume in patients with Huntington's disease.** *Neurology* 1997;48:394–99 CrossRef Medline
10. Browne SE, Beal MF. **Oxidative damage in Huntington's disease pathogenesis.** *Antioxid Redox Signal* 2006;8:2061–73 CrossRef Medline
11. Muller M, Leavitt BR. **Iron dysregulation in Huntington's disease.** *J Neurochem* 2014;130:328–50 CrossRef Medline
12. Douaud G, Behrens TE, Poupon C, et al. **In vivo evidence for the selective subcortical degeneration in Huntington's disease.** *Neuroimage* 2009;46:958–66 CrossRef Medline
13. Dominguez DJ, Ng AC, Poudel G, et al. **Iron accumulation in the basal ganglia in Huntington's disease: cross-sectional data from the IMAGE-HD study.** *J Neurol Neurosurg Psychiatry* 2015 May 7. [Epub ahead of print] CrossRef Medline
14. Vonsattel JP. **Huntington disease models and human neuropathology: similarities and differences.** *Acta Neuropathol* 2008;115:55–69 Medline
15. Chen J, Marks E, Lai B, et al. **Iron accumulates in Huntington's disease neurons: protection by deferoxamine.** *PLoS One* 2013;8:e77023 CrossRef Medline
16. Chen JC, Hardy PA, Kucharczyk W, et al. **MR of human postmortem brain tissue: correlative study between T2 and assays of iron and ferritin in Parkinson and Huntington disease.** *AJNR Am J Neuroradiol* 1993;14:275–81 Medline
17. Rosas HD, Chen YI, Doros G, et al. **Alterations in brain transition metals in Huntington disease: an evolving and intricate story.** *Arch Neurol* 2012;69:887–93 Medline
18. Sánchez-Castañeda C, Squitieri F, Di Paola M, et al. **The role of iron in gray matter degeneration in Huntington's disease: a magnetic resonance imaging study.** *Hum Brain Mapp* 2015;36:50–66 CrossRef Medline
19. Sánchez-Castañeda C, Cherubini A, Elifani F, et al. **Seeking Huntington disease biomarkers by multimodal, cross-sectional basal ganglia imaging.** *Hum Brain Mapp* 2013;34:1625–35 CrossRef Medline
20. Apple AC, Possin KL, Sattris G, et al. **Quantitative 7T phase imaging in premanifest Huntington disease.** *AJNR Am J Neuroradiol* 2014;35:1707–13 CrossRef Medline
21. Dumas EM, Versluis MJ, van den Bogaard SJ, et al; TRACK-HD investigators. **Elevated brain iron is independent from atrophy in Huntington's disease.** *Neuroimage* 2012;61:558–64 CrossRef Medline
22. Salomir R, De Senneville BD, Moonen CT. **A fast calculation method for magnetic field inhomogeneity due to an arbitrary distribution of bulk susceptibility.** *Concept Magn Reson B* 2003;19B:26–34 CrossRef
23. Deistung A, Schäfer A, Schweser F, et al. **Toward in vivo histology: a comparison of quantitative susceptibility mapping (QSM) with magnitude-, phase-, and R2\*-imaging at ultra-high magnetic field strength.** *Neuroimage* 2013;65:299–314 CrossRef Medline
24. Lim IA, Faria AV, Li X, et al. **Human brain atlas for automated region of interest selection in quantitative susceptibility mapping: application to determine iron content in deep gray matter structures.** *Neuroimage* 2013;82:449–69 CrossRef Medline
25. Schweser F, Sommer K, Deistung A, et al. **Quantitative susceptibility mapping for investigating subtle susceptibility variations in the human brain.** *Neuroimage* 2012;62:2083–100 CrossRef Medline
26. Wharton S, Schäfer A, Bowtell R. **Susceptibility mapping in the human brain using threshold-based k-space division.** *Magn Reson Med* 2010;63:1292–304 CrossRef Medline
27. Li W, Wu B, Liu C. **Quantitative susceptibility mapping of human brain reflects spatial variation in tissue composition.** *Neuroimage* 2011;55:1645–56 CrossRef Medline
28. Schenck JF. **The role of magnetic susceptibility in magnetic resonance imaging: MRI magnetic compatibility of the first and second kinds.** *Medi Phys* 1996;23:815–50 CrossRef Medline
29. Schweser F, Deistung A, Lehr BW, et al. **Quantitative imaging of intrinsic magnetic tissue properties using MRI signal phase: an approach to in vivo brain iron metabolism?** *Neuroimage* 2011;54:2789–807 CrossRef Medline
30. Langkammer C, Schweser F, Krebs N, et al. **Quantitative susceptibility mapping (QSM) as a means to measure brain iron? A post mortem validation study.** *Neuroimage* 2012;62:1593–99 CrossRef Medline
31. Poynton CB, Lupo JM, Hess C, et al. **Quantitative susceptibility mapping of Huntington's disease at 7 Tesla.** In: *Proceedings of the Joint Annual Meeting of the International Society for Magnetic Resonance in Medicine and the European Society for Magnetic Resonance in Medicine*, Milan, Italy. May 10–16, 2014
32. **Unified Huntington's Disease Rating Scale: reliability and consistency—Huntington Study Group.** *Mov Disord* 1996;11:136–42 CrossRef Medline
33. Zhang Y, Long JD, Mills JA, et al; PREDICT-HD Investigators and Coordinators of the Huntington Study Group. **Indexing disease progression at study entry with individuals at-risk for Huntington disease.** *Am J Med Genet B Neuropsychiatr Genet* 2011;156B:751–63 CrossRef Medline
34. Hamilton M. **A rating scale for depression.** *J Neurol Neurosurg Psychiatry* 1960;23:56–62 CrossRef Medline
35. Nasreddine ZS, Phillips NA, Bedirian V, et al. **The Montreal Cognitive Assessment, MoCA: a brief screening tool for mild cognitive impairment.** *J Am Geriatr Soc* 2005;53:695–99 CrossRef Medline
36. Bright P, Jaldow E, Kopelman MD. **The National Adult Reading Test as a measure of premorbid intelligence: a comparison with estimates derived from demographic variables.** *J Int Neuropsychol Soc* 2002;8:847–54 CrossRef Medline
37. Wharton S, Bowtell R. **Fiber orientation-dependent white matter contrast in gradient echo MRI.** *Proc Natl Acad Sci U S A* 2012;109:18559–64 CrossRef Medline
38. Wu B, Li W, Guidon A, et al. **Whole brain susceptibility mapping using compressed sensing.** *Magnetic Reson Med* 2012;67:137–47 CrossRef Medline
39. Wu B, Li W, Avram AV, et al. **Fast and tissue-optimized mapping of magnetic susceptibility and T2\* with multi-echo and multi-shot spirals.** *Neuroimage* 2012;59:297–305 CrossRef Medline
40. Zhang Y, Zhang J, Hsu J, et al. **Evaluation of group-specific, whole-brain atlas generation using Volume-based Template Estimation (VTE): application to normal and Alzheimer's populations.** *Neuroimage* 2014;84:406–19 CrossRef Medline
41. Bartzokis G, Cummings J, Perlman S, et al. **Increased basal ganglia iron levels in Huntington disease.** *Arch Neurol* 1999;56:569–74 CrossRef Medline
42. Dexter DT, Carayon A, Javoy-Agid F, et al. **Alterations in the levels of iron, ferritin and other trace metals in Parkinson's disease and other neurodegenerative diseases affecting the basal ganglia.** *Brain* 1991;114:1953–75 CrossRef Medline
43. Langkammer C, Krebs N, Goessler W, et al. **Quantitative MR imaging of brain iron: a postmortem validation study.** *Radiology* 2010;257:455–62 CrossRef Medline
44. Bartzokis G, Lu PH, Tishler TA, et al. **Myelin breakdown and iron changes in Huntington's disease: pathogenesis and treatment implications.** *Neurochem Res* 2007;32:1655–64 CrossRef Medline

45. Langkammer C, Liu T, Khalil M, et al. **Quantitative susceptibility mapping in multiple sclerosis.** *Radiology* 2013;267:551–59 CrossRef Medline
46. Harris GJ, Codori AM, Lewis RF, et al. **Reduced basal ganglia blood flow and volume in pre-symptomatic, gene-tested persons at-risk for Huntington's disease.** *Brain* 1999;122:1667–78 CrossRef Medline
47. Hasselbalch SG, Oberg G, Sorensen SA, et al. **Reduced regional cerebral blood flow in Huntington's disease studied by SPECT.** *J Neurol Neurosurg Psychiatry* 1992;55:1018–23 CrossRef Medline
48. Chen JJ, Salat DH, Rosas HD. **Complex relationships between cerebral blood flow and brain atrophy in early Huntington's disease.** *Neuroimage* 2012;59:1043–51 CrossRef Medline
49. Hua J, Unschuld PG, Margolis RL, et al. **Elevated arteriolar cerebral blood volume in prodromal Huntington's disease.** *Mov Disord* 2014;29:396–401 CrossRef Medline
50. Lin C, Huang C, Lin M, et al. **Magnetic resonance microscopic angiography visualization of abnormal microvasculature in a transgenic mouse model of Huntington's disease.** In: *Proceedings of the ISMRM 18th Scientific Meeting and Exhibition*, Stockholm, Sweden. May 1–7, 2010

# Quantitative MRI for Rapid and User-Independent Monitoring of Intracranial CSF Volume in Hydrocephalus

J. Virhammar, M. Warntjes, K. Laurell, and E.-M. Larsson

## ABSTRACT

**BACKGROUND AND PURPOSE:** Quantitative MR imaging allows segmentation of different tissue types and automatic calculation of intracranial volume, CSF volume, and brain parenchymal fraction. Brain parenchymal fraction is calculated as (intracranial volume – CSF volume) / intracranial volume. The purpose of this study was to evaluate whether the automatic calculation of intracranial CSF volume or brain parenchymal fraction could be used as an objective method to monitor volume changes in the ventricles.

**MATERIALS AND METHODS:** A lumbar puncture with drainage of 40 mL of CSF was performed in 23 patients under evaluation for idiopathic normal pressure hydrocephalus. Quantitative MR imaging was performed twice within 1 hour before the lumbar puncture and was repeated 30 minutes, 4 hours, and 24 hours afterward. For each time point, the volume of the lateral ventricles was manually segmented and total intracranial CSF volume and brain parenchymal fraction were automatically calculated by using Synthetic MR postprocessing.

**RESULTS:** At 30 minutes after the lumbar puncture, the volume of the lateral ventricles decreased by  $5.6 \pm 1.9$  mL ( $P < .0001$ ) and the total intracranial CSF volume decreased by  $11.3 \pm 5.6$  mL ( $P < .001$ ), while brain parenchymal fraction increased by  $0.78\% \pm 0.41\%$  ( $P < .001$ ). Differences were significant for manual segmentation and brain parenchymal fraction even at 4 hours and 24 hours after the lumbar tap. There was a significant association using a linear mixed model between change in manually segmented ventricular volume and change in brain parenchymal fraction and total CSF volume, ( $P < .0001$ ).

**CONCLUSIONS:** Brain parenchymal fraction is provided rapidly and fully automatically with Synthetic MRI and can be used to monitor ventricular volume changes. The method may be useful for objective clinical monitoring of hydrocephalus.

**ABBREVIATIONS:** BPF = brain parenchymal fraction; CoV = coefficient of variation; ICV = intracranial volume; iNPH = idiopathic normal pressure hydrocephalus; QRAPMASTER = quantification of relaxation times and proton attenuation by multiecho acquisition of a saturation-recovery using turbo spin-echo readout; SyMRI = Synthetic MR

Standard MR imaging used in clinical practice is mainly qualitative, and morphologic evaluations are based on visual assessment. Quantitative MR imaging has the potential advantage of providing objective data on treatment effects and longitudinal follow-up data in neurologic conditions.<sup>1</sup>

One such neurologic condition is idiopathic normal pressure hydrocephalus (iNPH), with symptoms of gait disturbance, cognitive impairment, and urinary incontinence.<sup>2,3</sup> The brain morphology in iNPH is characterized by large ventricles, enlarged

Sylvian fissures, tight convexity sulci, and a small callosal angle.<sup>4-6</sup> The symptoms can be relieved by removal of CSF in patients with iNPH, either permanently by shunt implantation or temporarily by a lumbar puncture as a prognostic test (CSF tap test).<sup>7</sup> Radiologic evaluation of the size of the ventricles and sulci is also important in patients with other types of hydrocephalus (eg, secondary to a subarachnoid hemorrhage). However, with standard imaging, a reduction in ventricle size postshunting in patients with iNPH is difficult to detect with traditional morphologic measures such as the Evans index<sup>8</sup> or by visual inspection, even if the patient is clinically improved.<sup>9</sup> An objective, more sensitive quantitative measure of the CSF spaces, replacing the present visual estimation, would be advantageous, especially for longitudinal evaluation of treatment effects. Such a quantitative method must be rapid and easy to perform to be implemented in clinical practice.

The MR imaging sequence QRAPMASTER<sup>10</sup> provides a rapid simultaneous quantification of longitudinal relaxation time (T<sub>1</sub>),

Received July 28, 2015; accepted after revision October 25.

From the Departments of Neuroscience, Neurology (J.V.) and Surgical Sciences, Radiology (E.-M.L.), Uppsala University, Uppsala, Sweden; Center for Medical Imaging Science and Visualization (M.W.), Linköping University, Linköping, Sweden; SyntheticMR (M.W.), Linköping, Sweden; and Department of Pharmacology and Clinical Neuroscience (K.L.), Umeå University, Umeå, Sweden.

Please address correspondence to J. Virhammar, MD, PhD, Department of Neuroscience, Neurology, Uppsala University, Akademiska Sjukhuset, ing 85, 751 85 Uppsala, Sweden; e-mail: johan.virhammar@neuro.uu.se; @johanvirhammar

<http://dx.doi.org/10.3174/ajnr.A4627>

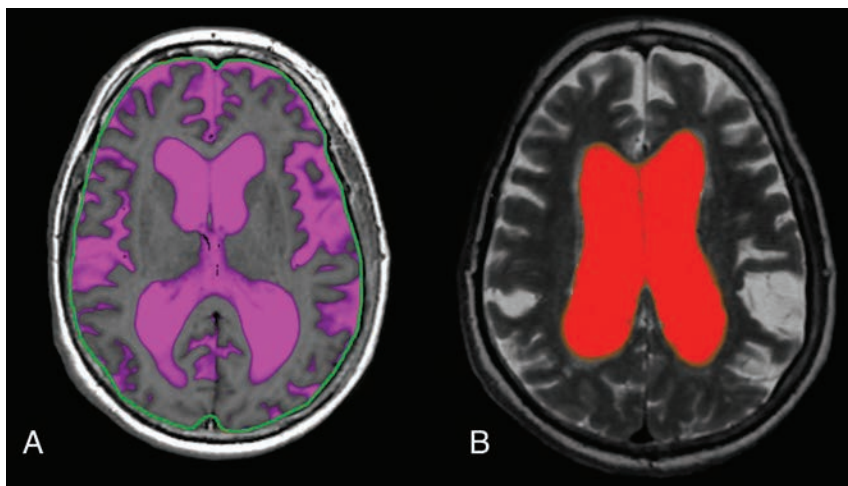


**FIG 1.** A, Fully automatic calculation of total intracranial CSF by using SyMRI. The green line is an intracranial mask used to automatically calculate the intracranial volume (the line was originally red but was colored green in external graphics-editing software to increase clarity). B, Manual segmentation of the lateral ventricles by using SyMRI.

the transverse relaxation time (T2), and proton density. The dedicated postprocessing software SyntheticMR (SyMRI; SyntheticMR, Linköping, Sweden) uses combinations of T1, T2, and proton density values to segment intracranial volume (ICV), GM, WM, and CSF. Summation of the tissues over the complete imaging volume automatically produces GM, WM, and CSF volumes (Fig 1A). SyMRI can be implemented in any PACS.

We reported in a previous study of patients with iNPH, by using a manual approach that is available in the same software, that the volume of the lateral ventricles decreases at 30 minutes and 4 hours following a lumbar puncture with removal of 40 mL of CSF (Fig 1B).<sup>11</sup> The drawback with the manual method is that it requires detailed anatomic knowledge and is rather time-consuming.

Potential alternatives to manual segmentation of the ventricular volume are calculation of total intracranial CSF volume or the brain parenchymal fraction (BPF). BPF is calculated as  $(ICV - CSF \text{ volume}) / ICV$ . The BPF value is regarded as a robust measure for monitoring the relative brain and CSF volumes, for example, in patients with multiple sclerosis.<sup>12</sup> Normalization with ICV has an advantage because it eliminates the effect of head size differences among patients and limits the impact of incomplete coverage of the imaging volume. Potentially, the use of BPF reduces the impact of signal voids due to a shunt because these artifacts would decrease both the CSF and ICV volumes, leaving the BPF relatively unaffected. Calculation of CSF volume and BPF is fully automated in SyMRI, with a postprocessing time of <2 minutes.<sup>13</sup>

Our aim was to evaluate whether the automatic calculation of intracranial CSF volume or BPF could be used as an objective method to monitor volume changes in the lateral ventricles.

## MATERIALS AND METHODS

### Patients

Twenty-six patients (15 men, 11 women) under evaluation for iNPH were consecutively included in the study. The median age was 73.5 years (range, 65–81 years). On the basis of the international iNPH

guidelines,<sup>14</sup> 17 patients were classified as having probable iNPH; 6, possible iNPH; and 3, unlikely iNPH. The inclusion process and demographics have been described in detail elsewhere.<sup>11</sup>

One patient classified as having unlikely iNPH did not fit into the MR imaging head coil and was excluded. Because of technical problems, quantitative MR imaging was not acquired in 2 patients, who were excluded. The remaining 23 patients were included in the statistical analysis. In 2 of the included patients, quantitative MR imaging data were missing for 1 investigation time point. The study was approved by the local ethics committee in Uppsala, and the site of the study was Uppsala University Hospital.

### Time Scheme

The first MR imaging scan (MR imaging 1) was performed between 8 and 10 AM. A second MR imaging (MR imaging 2) was performed 60 minutes after the first examination to assess the repeatability of the method. Between MR imaging 1 and MR imaging 2, the patients rested in the supine position in a quiet, isolated room next to the scanner. Immediately after MR imaging 2, a lumbar puncture was performed by using a 20-gauge needle, with patients in the lateral recumbent position, and a mean of  $40 \pm 2$  mL of CSF was removed. MR imaging 3 was performed 30 minutes after the lumbar puncture was completed; MR imaging 4 and MR imaging 5 were performed 4 and 24 hours after the CSF removal, respectively.

### Imaging Sequence

MR imaging was performed in a 3T Achieva scanner (Philips Healthcare, Best, the Netherlands).

The QRAPMASTER sequence was acquired with an FOV of 220 mm with an in-plane resolution of 1 mm and 30 sections of 4 mm. The sequence acquired signal intensities at 4 different saturation delay times (140, 540, 1870, and 3870 ms at a TR of 4000 ms) and 5 different TEs (17.5, 35.0, 52.5, 70.0, and 87.5 ms), resulting in a matrix of  $5 \times 4 = 20$  images with different T1 and T2 relaxation effects. The scan time for QRAPMASTER is less than 6 minutes.

### Image Postprocessing

The image data were processed to calculate the T1 and T2 relaxation times and proton density by using SyMRI 7.0 (SyntheticMR). On the basis of these maps, the same software automatically provided the ICV and estimated the partial volume content of WM, GM, and CSF according to tissue definitions in combination with a partial volume model.<sup>15</sup>

### Statistics

Baseline values were calculated by averaging the results of MR imaging 1 and MR imaging 2. The difference values for time

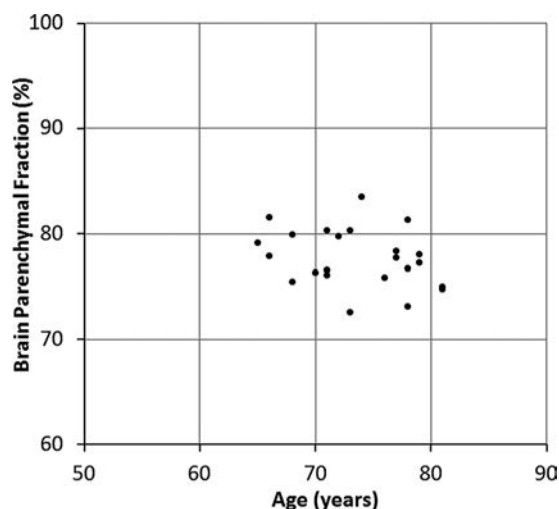


**FIG 2.** Baseline brain parenchymal fraction for all subjects as a function of age.

points 1–5 were calculated by subtracting all values from the baseline values. A multilevel linear mixed model was used to estimate the association between the difference in manually segmented ventricular volume and the difference in automatically estimated total CSF volume as well as the difference in automatically estimated BPF. The method was adjusted for repeated measurements in the same individuals by using a compound symmetry covariance structure. The slope and intercept with 95% confidence intervals were calculated. Linear regression was used to calculate the goodness of fit. Comparisons of differences in the volume of the lateral ventricles, total CSF volume, and BPF among subgroups were tested with the Mann-Whitney *U* test and the Kruskal Wallis test.

## RESULTS

At baseline, the manually segmented lateral ventricular volume of the patients was  $129 \pm 22$  mL. The automatically calculated mean ICV was  $1428 \pm 100$  mL, the mean automatic total CSF volume was  $319 \pm 49$  mL, and the mean BPF was  $77.7\% \pm 2.7\%$ . The mean difference between MR imaging 1 and MR imaging 2 was  $0.2 \pm 2.1$  mL for manual ventricular volume,  $1.1 \pm 7.8$  mL for automatic CSF volume, and  $0.1\% \pm 0.4\%$  for BPF, corresponding to  $0.14\% \pm 1.63\%$ ,  $0.34\% \pm 2.44\%$ , and  $0.14\% \pm 0.50\%$  of their mean values, respectively. The distribution of baseline BPF as a function of age is shown in Fig 2.

At 30 minutes after the lumbar puncture, the manually segmented lateral ventricular volume decreased by an average of  $5.6 \pm 1.9$  mL ( $P < .0001$ ; coefficient of variation [CoV] = 0.34). Simultaneously, a decrease in the automatically calculated total CSF volume of  $11.3 \pm 5.6$  mL was observed ( $P < .001$ ; CoV = 0.50). At 4 hours after the lumbar puncture, the manual ventricular volume difference was  $2.5 \pm 2.1$  mL ( $P < .001$ ) and the automatic CSF volume difference was  $0.5 \pm 6.3$  mL ( $P = .7$ ). At 24 hours after the CSF tap test, the difference was  $1.9 \pm 2.3$  mL ( $P < .001$ ) and  $3.0 \pm 5.3$  mL ( $P = .02$ ), respectively (Fig 3A).

The corresponding difference in BPF after the lumbar puncture is illustrated in Fig 3B. At 30 minutes after the CSF tap test, the BPF increased by  $0.78\% \pm 0.41\%$  with respect to baseline ( $P <$

$.001$ ; CoV = 0.53). At 4 hours after the lumbar puncture, the difference had decreased to  $0.15\% \pm 0.31\%$  ( $P = .03$ ), and at 24 hours after the lumbar puncture, the difference was  $0.14\% \pm 0.32\%$  ( $P = .05$ ).

There was no difference in changes of volume of the lateral ventricles, total CSF volume, or BPF among the diagnostic groups possible, probable, or unlikely iNPH, and there was no difference between patients with or without clinical improvement after the CSF removal.

The correlation between manual ventricular volume and automatic CSF volume is shown in Fig 4A. A linear mixed model showed a slope of 1.67 (intercept 0.37) (95% confidence interval, 1.35–2.00;  $P < .0001$ ). The correlation between manual ventricular volume and BPF is plotted in Fig 4B. A linear mixed model showed a slope of  $-0.104$  (intercept 0.008) (95% confidence interval,  $-0.125$  to  $-0.082$ ;  $P < .0001$ ). The goodness of fit was identical in both cases ( $R^2 = 0.45$ ).

## DISCUSSION

In this study, quantitative MR imaging was used to calculate and monitor changes in intracranial CSF after a lumbar puncture in patients with iNPH. Fully automatic volumetric functions and manual segmentation of the lateral ventricle volume were evaluated and compared. As methods for measuring changes in intracranial CSF, there was a significant association between the fully automatic calculation of intracranial CSF volume and BPF with manual segmentation of the lateral ventricular volume.

Both the manual and the automatic methods showed a significant change after the lumbar puncture. Manual segmentation was less variable than the fully automatic method, with lower CoV and *P* values, but it was more time-consuming and therefore not as advantageous in clinical practice.

The total intracranial CSF volume can be automatically calculated by using SyMRI. However, the volume differences after the lumbar puncture by using automatic CSF volume were not significantly changed at all time points. On the other hand, BPF increased significantly at all time points after the CSF removal and the repeatability was better for BPF than total intracranial CSF volume. In addition, the repeatability was better for BPF.

The BPF difference between MR imaging 1 and MR imaging 2 had an SD of 0.4%. With an ICV of 1428 mL, this corresponded to 5.6 mL, which was smaller than the difference for automatic CSF volume (7.8 mL).

There is no widely accepted reference method for calculation of BPF. Manual segmentation of the lateral ventricles performed in a previous study was used as a control method in the present study. In that study, segmentation was performed on every section that included the lateral ventricles.<sup>11</sup>

A risk associated with the use of total automatic CSF volume is incomplete brain coverage due to suboptimal planning or time limitations for special sequences. In other cases, a region of the brain may not be visualized, for example, due to shunt-related metal artifacts with signal loss. This potential error should be reduced by the use of BPF. An additional advantage of using BPF is that it largely removes differences in head size among subjects, potentially allowing the setting of a

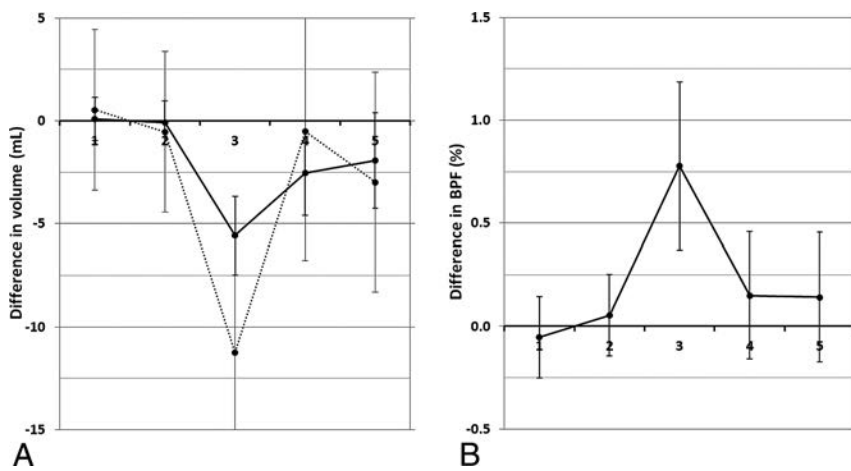


**FIG 3.** A, The mean difference in manually segmented lateral ventricular volume with respect to the baseline value (*solid line*) and the mean difference in automatically calculated total CSF volume with respect to the baseline value (*dotted line*) plotted at the 5 different time points. B, The mean difference of brain parenchymal fraction with respect to the baseline value at the same time points. Time point 1 and 2 are baseline investigations and the lumbar puncture with CSF removal was performed right after time point 2. The *error bars* indicate 1 SD.

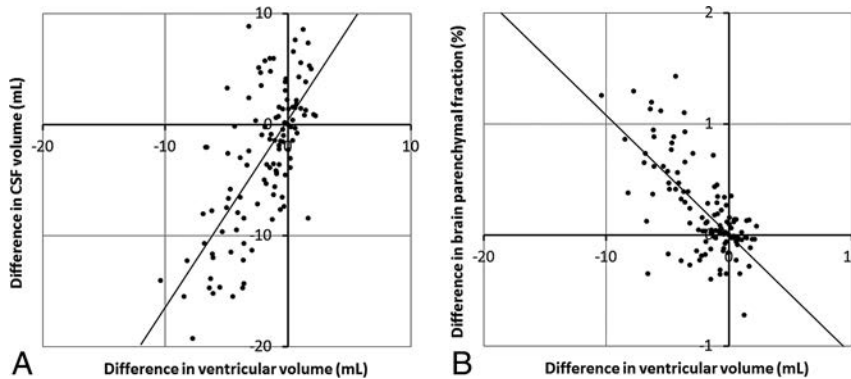


**FIG 4.** A, Correlation plot between the difference in ventricular volume and the difference in total CSF volume for all subjects at all time points. The *line* indicates a slope of 1.67 and intercept of 0.37. B, Correlation plot between the difference in ventricular volume and the difference in brain parenchymal fraction for all subjects at all time points. The *line* indicates a slope of  $-0.104$  and an intercept of 0.008.

range for normal and pathologic values. This could be useful for the evaluation of brain atrophy versus normal aging. Accuracy and repeatability of the automatic BPF measurement have been reported to be high.<sup>13,16</sup>

Another risk of using the total volume of CSF is that the acquisition volume can vary slightly between different investigations. An acquisition volume is normally placed by technical personnel and therefore is user-dependent. If part of the total CSF was not even acquired, for example, with a patient with a large head, it will be absent for the analysis, mimicking a loss of total CSF. The BPF, on the other hand, is a ratio, which is presumably rather similar for every acquisition section. Therefore, a suboptimal placement of the acquisition volume is not expected to alter the BPF values. This may explain the higher CoV and variability at baseline of total CSF volume compared with BPF.

As a tool to monitor brain atrophy, BPF has been used mainly in studies of multiple sclerosis<sup>17</sup> and dementia.<sup>18</sup> However, it is a robust measure of parenchymal volume and can be

applied to several diagnoses. The method could be useful for longitudinal evaluation of ventricular volume in all patients with hydrocephalus. It may, however, be difficult to apply in patients with brain tumors because the tumor volume changes with time, depending on disease progress or treatment effects, thereby affecting the BPF.

Other techniques, both manual and automatic, can be used to calculate BPF. Methods that provide good differentiation between brain parenchyma and CSF and reliable ICV measurement can be used, such as FreeSurfer (<http://surfer.nmr.mgh.harvard.edu/>). FreeSurfer and other quantitative MR imaging techniques have been tested in iNPH, mainly in research studies, but time-consuming postprocessing and the need for technical expertise limit the clinical usefulness of these methods. The advantage of SyMRI compared with FreeSurfer is that it provides BPF fully automatically within  $<2$  minutes and the reliability is high.<sup>13</sup> SyMRI can also be implemented in any PACS, which improves its clinical usefulness.

In patients with iNPH, the standard treatment is implantation of a ventriculo-peritoneal shunt. Having a reliable noninvasive measure of changes in intracranial CSF volume after shunting would be a great aid to the clinician to assess the patency of a shunt. In MR imaging, large artifacts surround the shunt valve. Whether BPF is a reliable measure

of CSF volume change after shunt surgery in patients with iNPH has not yet been investigated, to our knowledge, but is subject to future work. Some patients with congenital hydrocephalus are not treated with shunts when there are no clinical symptoms and no active progress in ventricular dilation. A sensitive quantitative method such as the one described in the present work could add important clinical value if an increase in CSF spaces is detected in time. Then the patient may be offered treatment before developing symptoms and irreversible injury to the brain has occurred. In a similar fashion, BPF could be used to follow the progress and eventual regress of ventriculomegaly after subarachnoid hemorrhage.

#### Limitations

SyMRI only provides 5-mm sections, and the in-plane resolution is slightly lower than that of standard 3T MR imaging. Slightly thicker sections will lead to partial volume effects, which may have an impact on BPF values. It has been reported, however, that the effect of image resolution on the brain segmentation results of

SyMRI is very small.<sup>15</sup> The sample studied was small, from a selected population with large ventricles. Therefore, it is not known whether the results could also be directly applied in a population with normal-sized ventricles. The automated method proposed in our study is also of more interest for use in patients with large ventricles (eg, for follow-up of progression or decrease of dilation of the ventricles of different etiologies).

## CONCLUSIONS

SyMRI was used to compare fully automatic calculations of intracranial CSF volume and BPF with manual segmentation of lateral ventricular volume as methods to monitor intracranial CSF changes after lumbar puncture. Both automatic CSF volume and BPF correlated equally well with manual segmentation, but BPF was less variable. Because BPF is rapid, it could be an expedient alternative for use in detecting and monitoring changes in intracranial CSF volume in patients with hydrocephalus.

Disclosures: Johan Virhammar—UNRELATED: Grants/Grants Pending: Independent Swedish Foundation Selanders Stiftelse grant 2013, approximately US \$11,700.\* Marcel Warntjes—UNRELATED: Employment: SyntheticMR, Comments: I am employed part-time at SyntheticMR; Stock/Stock Options: I have stock in SyntheticMR.\*Money paid to the institution.

## REFERENCES

1. Ma D, Gulani V, Seiberlich N, et al. **Magnetic resonance fingerprinting.** *Nature* 2013;495:187–92 CrossRef Medline
2. Adams RD, Fisher CM, Hakim S, et al. **Symptomatic occult hydrocephalus with “normal” cerebrospinal-fluid pressure; a treatable syndrome.** *N Engl J Med* 1965;273:117–26 CrossRef Medline
3. Hakim S, Adams RD. **The special clinical problem of symptomatic hydrocephalus with normal cerebrospinal fluid pressure: observations on cerebrospinal fluid hydrodynamics.** *J Neurol Sci* 1965;2:307–27 CrossRef Medline
4. Hashimoto M, Ishikawa M, Mori E, et al; Study of INPH on Neurological Improvement (SINPHONI). **Diagnosis of idiopathic normal pressure hydrocephalus is supported by MRI-based scheme: a prospective cohort study.** *Cerebrospinal Fluid Res* 2010;7:18 CrossRef Medline
5. Virhammar J, Laurell K, Cesarini KG, et al. **Preoperative prognostic value of MRI findings in 108 patients with idiopathic normal pressure hydrocephalus.** *AJNR Am J Neuroradiol* 2014;35:2311–18 CrossRef Medline
6. Virhammar J, Laurell K, Cesarini KG, et al. **The callosal angle measured on MRI as a predictor of outcome in idiopathic normal-pressure hydrocephalus.** *J Neurosurg* 2014;120:178–84 CrossRef Medline
7. Wikkelsö C, Andersson H, Blomstrand C, et al. **The clinical effect of lumbar puncture in normal pressure hydrocephalus.** *J Neurol Neurosurg Psychiatry* 1982;45:64–69 CrossRef Medline
8. Evans WA Jr. **An encephalographic ratio for estimating ventricular enlargement and cerebral atrophy.** *Arch Neuropsych* 1942;47:931–37 CrossRef
9. Meier U, Paris S, Gräwe, et al. **Is there a correlation between operative results and change in ventricular volume after shunt placement? A study of 60 cases of idiopathic normal-pressure hydrocephalus.** *Neuroradiology* 2003;45:377–80 CrossRef Medline
10. Warntjes JB, Leinhard OD, West J, et al. **Rapid magnetic resonance quantification on the brain: optimization for clinical usage.** *Magn Reson Med* 2008;60:320–29 CrossRef Medline
11. Virhammar J, Laurell K, Ahlgren A, et al. **Idiopathic normal pressure hydrocephalus: cerebral perfusion measured with pCASL before and repeatedly after CSF removal.** *J Cereb Blood Flow Metab* 2014;34:1771–78 CrossRef Medline
12. Rudick RA, Fisher E, Lee JC, et al. **Use of the brain parenchymal fraction to measure whole brain atrophy in relapsing-remitting MS: Multiple Sclerosis Collaborative Research Group.** *Neurology* 1999;53:1698–704 CrossRef Medline
13. Vågberg M, Lindqvist T, Ambarki K, et al. **Automated determination of brain parenchymal fraction in multiple sclerosis.** *AJNR Am J Neuroradiol* 2013;34:498–504 CrossRef Medline
14. Relkin N, Marmarou A, Klinge P, et al. **Diagnosing idiopathic normal-pressure hydrocephalus.** *Neurosurgery* 2005;57:S4–16; discussion ii–v Medline
15. West J, Warntjes JB, Lundberg P. **Novel whole brain segmentation and volume estimation using quantitative MRI.** *Eur Radiol* 2012;22:998–1007 CrossRef Medline
16. Ambarki K, Lindqvist T, Wählin A, et al. **Evaluation of automatic measurement of the intracranial volume based on quantitative MR imaging.** *AJNR Am J Neuroradiol* 2012;33:1951–56 CrossRef Medline
17. Bermel RA, Bakshi R. **The measurement and clinical relevance of brain atrophy in multiple sclerosis.** *Lancet Neurol* 2006;5:158–70 CrossRef Medline
18. Smith EE, Egorova S, Blacker D, et al. **Magnetic resonance imaging white matter hyperintensities and brain volume in the prediction of mild cognitive impairment and dementia.** *Arch Neurol* 2008;65:94–100 Medline

# Quantitative Intracranial Atherosclerotic Plaque Characterization at 7T MRI: An Ex Vivo Study with Histologic Validation

A.A. Hartevelde, N.P. Denswil, J.C.W. Siero, J.J.M. Zwanenburg, A. Vink, B. Pouran, W.G.M. Spliet, D.W.J. Klomp, P.R. Luijten, M.J. Daemen, J. Hendrikse, and A.G. van der Kolk



## ABSTRACT

**BACKGROUND AND PURPOSE:** In recent years, several high-resolution vessel wall MR imaging techniques have emerged for the characterization of intracranial atherosclerotic vessel wall lesions *in vivo*. However, a thorough validation of MR imaging results of intracranial plaques with histopathology is still lacking. The aim of this study was to characterize atherosclerotic plaque components in a quantitative manner by obtaining the MR signal characteristics ( $T1$ ,  $T2$ ,  $T2^*$ , and proton density) at 7T in ex vivo circle of Willis specimens and using histopathology for validation.

**MATERIALS AND METHODS:** A multiparametric ultra-high-resolution quantitative MR imaging protocol was performed at 7T to identify the MR signal characteristics of different intracranial atherosclerotic plaque components, and using histopathology for validation. In total, 38 advanced plaques were matched between MR imaging and histology, and ROI analysis was performed on the identified tissue components.

**RESULTS:** Mean  $T1$ ,  $T2$ , and  $T2^*$  relaxation times and proton density values were significantly different between different tissue components. The quantitative  $T1$  map showed the most differences among individual tissue components of intracranial plaques with significant differences in  $T1$  values between lipid accumulation ( $T1 = 838 \pm 167$  ms), fibrous tissue ( $T1 = 583 \pm 161$  ms), fibrous cap ( $T1 = 481 \pm 98$  ms), calcifications ( $T1 = 314 \pm 39$  ms), and the intracranial arterial vessel wall ( $T1 = 436 \pm 122$  ms).

**CONCLUSIONS:** Different tissue components of advanced intracranial plaques have distinguishable imaging characteristics with ultra-high-resolution quantitative MR imaging at 7T. Based on this study, the most promising method for distinguishing intracranial plaque components is T1-weighted imaging.

**ABBREVIATIONS:** CoW = circle of Willis; DESPOT1 = driven equilibrium single pulse observation of  $T1$ ; DESPOT2 = driven equilibrium single pulse observation of  $T2$ ; PD = proton density

Ischemic stroke is one of the major diseases in the Western world, associated with high morbidity and mortality.<sup>1,2</sup> Identifying the cause of ischemic stroke is of great clinical importance, not only for deciding the best treatment options for the individual

patient but also for possibly preventing future ischemic events, both recurrent and new.

Intracranial atherosclerosis is one of the main causes of ischemic stroke and TIA worldwide, accounting for approximately 9%–33% of all ischemic strokes and TIAs (depending on race-ethnicity) and is the major cause of cerebral ischemic events in the Asian population. Additionally, the risk of recurrent ischemic stroke is increased in patients with underlying intracranial atherosclerosis.<sup>3–8</sup> Similar to extracranial atherosclerosis, for intracranial atherosclerosis, the degree of luminal stenosis is currently the main factor determining whether an atherosclerotic plaque is symptomatic and/or treatment is necessary. In the past decade, plaque composition has become an additional important feature in extracranial atherosclerosis management, enabling identification of specific culprit lesions requiring treatment, even when not causing significant stenosis.<sup>9–12</sup> However, for intracranial atherosclerosis, this is not yet common practice, even though the literature suggests that also intracranially, stenosis grade is not always

Received August 19, 2015; accepted after revision October 27.

From the Departments of Radiology (A.A.H., J.C.W.S., J.J.M.Z., D.W.J.K., P.R.L., J.H., A.G.v.d.K.), Pathology (A.V., W.G.M.S.), Orthopedics (B.P.), and Rheumatology (B.P.), and Image Sciences Institute (J.J.M.Z.), University Medical Center Utrecht, Utrecht, the Netherlands; Department of Pathology (N.P.D., M.J.D.), Academic Medical Center, Amsterdam, the Netherlands; and Department of Biomedical Engineering (B.P.), Faculty of Mechanical, Maritime, and Materials Engineering, Delft University of Technology, Delft, the Netherlands.

This work was supported by the Netherlands Organization for Scientific Research under grant 91712322 (J.H.).

Please address correspondence to A.A. Hartevelde, MSc, Department of Radiology, University Medical Center Utrecht, Box 85500, 3508 GA Utrecht, the Netherlands, e-mail a.a.hartevelde-2@umcutrecht.nl

Indicates open access to non-subscribers at www.ajnr.org

Indicates article with supplemental on-line table.

<http://dx.doi.org/10.3174/ajnr.A4628>

**Table 1: Scan parameters of the 7T MRI protocol**

Pulse Sequence	DESPOT1	DESPOT2	T2* Map
TR/TE/TE2 (ms)	16/4.3/–	36/18/–	53/6/26
Flip angle	11°/44°	12°/62°	29°
No. of sections	153	153	153
FOV (mm)	150 × 150 × 20	150 × 150 × 20	150 × 150 × 20
Acquisition matrix	1152 × 1154	1152 × 1152	1152 × 1154
Acquired voxel size (mm)	0.13 × 0.13 × 0.13	0.13 × 0.13 × 0.13	0.13 × 0.13 × 0.13
Bandwidth (Hz/pixel)	165	41	101
TFE factor	1154	1152	1154
Repeated scans	4	3	1
Acquisition time	06 hr 21 min 28 sec	11 hr 07 min 34 sec	02 hr 00 min 53 sec

**Note:**—TFE indicates turbo field echo.

associated with a risk of ischemic events: In patients with a high-grade stenosis, only 1 in every 5–10 patients will have a recurrent ischemic stroke.<sup>5,6,13,14</sup> This implies that like in extracranial atherosclerosis, luminal information is not the only important marker for future cerebrovascular events.

In recent years, several high-resolution intracranial vessel wall imaging techniques using 3T and 7T MR imaging have emerged for the evaluation and characterization of atherosclerotic vessel wall lesions in vivo.<sup>15</sup> However, these in vivo techniques so far have not been validated with histopathology, due to poor accessibility of the intracranial arteries. Therefore, the question arises if these techniques are truly able—ie, have enough image contrast—to distinguish different atherosclerotic plaque components. In the past 2 years, 2 ex vivo correlation studies have been performed at 7T MR imaging to assess its ability to visualize different intracranial atherosclerotic plaque components.<sup>16,17</sup> These ex vivo studies showed that 7T MR imaging is capable of identifying focal thickening of the intracranial arterial vessel wall and distinguishing different plaque components within advanced intracranial atherosclerotic plaques with different image contrast weightings. Recently, a first case report was published demonstrating the correlation between certain intracranial atherosclerotic plaque components visualized in vivo at 3T and histologic validation of the plaque postmortem.<sup>18</sup> Those studies used qualitative MR images to score the atherosclerotic plaque signal heterogeneities. As a next step toward validation, quantitative assessment of MR signal characteristics of specific plaque components might enable more firm conclusions regarding the ability of T1-, T2-, T2\*-, and proton density (PD)-weighted sequences in characterizing intracranial atherosclerotic plaques. Once it is known which plaque components can be identified with ex vivo MR imaging sequences, a translation can be made to in vivo intracranial vessel wall MR imaging, by developing sequences based on the nuclear magnetic resonance tissue properties of the identified atherosclerotic plaque components. In the current study, a multiparametric ultra-high-resolution quantitative MR imaging protocol was performed to identify the MR signal characteristics of different intracranial atherosclerotic plaque components, and using histopathology for validation.

## MATERIALS AND METHODS

### Specimens

Human circle of Willis (CoW) specimens with a macroscopic presence of high atherosclerotic plaque burden were selected by

an experienced pathologist (A.V.) from >100 postmortem examinations that were performed in our institution. Material was handled in a coded manner that met the criteria of the Code of Conduct used in the Netherlands for the responsible use of human tissue in medical research ([www.federa.org/codes-conduct](http://www.federa.org/codes-conduct)), and institutional review board approval for this retrospective study was obtained.

### Specimen Preparation

All specimens had been stored in buffered formalin (4%). Preparation of the specimens for MR imaging and histologic sampling was performed according to the method previously described by van der Kolk et al.<sup>16</sup> Cactus spines were used as fiducials and placed at 15 locations in the agarose gel adjacent to an artery for histologic sampling, to enable spatial correlation with histology. The 15 locations were chosen to sample all major vessels of the CoW, including their branches (eg, A2 segment of the anterior cerebral artery), and the fiducials were placed at the location of a visible vessel wall abnormality (if present). The locations included the following: the anterior cerebral (A1 and A2 segments), middle cerebral (M1 segment), intracranial internal carotid (C7 segment), posterior cerebral (P2 segment), basilar (upper, middle, and lower part), and vertebral arteries (left and right if applicable).

### Imaging

The embedded specimens were scanned in a 7T whole-body system (Achieva; Philips Healthcare, Best, the Netherlands). A custom-made high density receive coil (16 channels per 70 cm<sup>2</sup>; High density surface array; MR Coils BV, Drunen, the Netherlands) was used for signal reception,<sup>19</sup> and a volume transmit/receive coil, for transmission (Quad TR; Nova Medical, Wilmington, Massachusetts). Each embedded specimen was imaged individually. The petri dish containing the embedded specimen was placed in the middle of the transmit coil on top of the receive coil; plastic filling was used to stabilize and secure the petri dish.

### Protocol

Imaging was performed at room temperature. The scan protocol had 3 sequences with different contrast weightings to image the specimens, from which quantitative MR parameter maps were calculated. For T1, T2, and PD mapping, the driven equilibrium single pulse observation of T1 (DESPOT1) and T2 (DESPOT2) sequences were used.<sup>20</sup> TR was chosen as short as allowed by the desired spatial resolution and FOV. We calculated optimal flip angle pairs for the DESPOT1 and DESPOT2 scans, assuming a range of T1 and T2 values of 150–650 ms and 10–30 ms, respectively. T2\* maps were obtained by using a dual-echo 3D T2\*-weighted scan. The applied scan parameters are presented in Table 1. A 3D B<sub>1</sub> map was acquired by using the actual flip angle method to correct for B<sub>1</sub> inhomogeneity during postprocessing of the MR images.<sup>21</sup> Total scan time was approximately 19.5 hours per specimen. All MR images were acquired with an isotropic resolution. This allowed reconstructions along arbitrary planes,

which enabled accurate matching of the MR images to the sectioning plane of the histologic sections.

### **MR Image Processing**

The MR images were processed by using Matlab, Version R2014b (MathWorks, Natick, Massachusetts). First, the DESPOT1 and DESPOT2 dynamic scans were coregistered to correct for small shifts between the matching images. Next, the parametric images ( $T1$ ,  $T2$ ,  $T2^*$  relaxation times and  $PD$  values) were calculated from the original MR imaging datasets according to the method previously described by Deoni et al.<sup>20</sup>  $B_1$  correction was performed during calculation of the parametric  $T1$  and  $T2$  maps, to correct for  $B_1$  inhomogeneity within the specimen.

### **Histopathology**

After MR imaging, 0.5-mm-thick tissue samples were taken from the 15 marked locations of each CoW specimen for histologic processing, which was performed by using an in-house-developed protocol, as previously described.<sup>16</sup> Classification of the histologic sections was performed according to the modified American Heart Association classification by Virmani et al,<sup>22</sup> a well-established method that is based on atherosclerotic characteristics as follows: 1) no anomaly; 2) early lesion, including intimal thickening (<50% smooth-muscle cells, no lipids, inflammatory cells), fatty streak, and pathologic intimal thickening (>50% smooth-muscle cells, rich in proteoglycans, foamy macrophages); and 3) advanced lesion, including fibrolipid plaque (>40% lipid), thin cap atheroma (<65- $\mu$ m thickness), fibrous plaque (<40% lipid), fibrocalcified plaque (>40% calcified), and calcified nodule (calcified element protruding the intima). When applicable, plaque complications (rupture, hemorrhage, or erosion) were also assessed. The histologic classification was performed by 1 experienced observer (N.P.D.), blinded to the MR imaging results.

### **Matching of MR and Histology Images**

Image reconstructions were made perpendicular to the relevant arteries (section thickness, 0.13 mm) at the locations of the fiducials seen on the MR images, by using the software program VesselMASS (Leiden University Medical Center, Leiden, the Netherlands). The MR images and the histologic sections were manually matched by 1 observer (A.A.H.) by using the marked locations with the fiducials in the MR images, the ink markings in the histologic sections, and gross morphologic features. Samples were excluded when no match was found or when air bubbles were present in the MR images.

### **Plaque Component Analysis**

To analyze different plaque components, we used only plaques histologically scored as advanced, therefore including several components, because a previous study showed no heterogeneity in qualitative signal intensity in early lesions.<sup>16</sup> The identified plaque components included fibrous tissue, fibrous cap, lipid accumulation (increasing mass of lipids [lipid retention] within the intimal area, which is defined as the "plaque"), intraplaque hemorrhage, and calcifications (deposition of extracellular calcium within the plaque). On the basis of the identified plaque compo-

nents in a histologic section, ROIs were drawn manually within the corresponding regions on  $T1$ -weighted MR images (DESPOT1 acquired with a flip angle of 44°, used for calculation of the quantitative maps) by 1 observer (A.A.H.). The ROIs were used to calculate the mean  $T1$ ,  $T2$ , and  $T2^*$  relaxation times and  $PD$  values for those regions in the MR parameter maps, by using the dedicated vessel wall analysis software VesselMASS.

### **Statistical Analysis**

All statistical analyses were performed by using SPSS statistics (Version 20.0; IBM, Armonk, New York). Because the data were normally distributed but the assumption of homogeneity of variance was not met, the Welch test was conducted to compare the mean ROI values of the different tissue components. Games-Howell post hoc tests were performed for pair-wise comparisons. A  $P$  value < .05 was statistically significant.

## **RESULTS**

Fifteen CoW specimens were selected for this study (9 men; mean age,  $68.7 \pm 13.3$  years). In total, 213 samples of CoW arteries were obtained (in 8 specimens,  $\geq 1$  vessel segment was absent;  $n = 12$  vessel segments); 8 of the 213 samples (3.8%) were excluded because they were not assessable for histologic classification (the samples could not be sliced properly), resulting in 205 samples available for histologic classification.

### **Histologic Classification**

Six samples (2.9%) were scored as nondiseased; 143 samples (69.8%) showed early lesions (intimal thickening,  $n = 97$ , pathologic intimal thickening,  $n = 19$ , and fatty streak,  $n = 27$ ); and 56 samples (27.3%) showed advanced plaques (fibrous plaque,  $n = 28$ , fibrolipid plaque,  $n = 25$ , and fibrocalcified plaque,  $n = 3$ ). No calcified nodules or thin cap atheromas were seen. Of the 56 advanced plaques, 18 (32%) were excluded due to lack of a match ( $n = 3$ ) or an air bubble present in the MR images ( $n = 15$ ), resulting in 38 MR imaging-matched advanced atherosclerotic plaques (20 fibrous plaques, 16 fibrolipid plaques, and 2 fibrocalcified plaques) that could be used for the ROI analysis. ROIs were drawn in the matched MR images of the advanced atherosclerotic plaques within the corresponding regions of the tissue components identified in the histologic sections: lipid accumulation ( $n = 17$ ), fibrous tissue ( $n = 24$ ), fibrous cap ( $n = 12$ ), calcifications ( $n = 5$ ), and vessel wall ( $n = 37$ ).

### **Quantitative MR Parameter Maps**

Figures 1–3 show examples of histologic sections with the matched MR parameter maps ( $T1$ ,  $T2$ ,  $T2^*$ , and  $PD$ ) of advanced plaques from the CoW specimens. Figure 4 and Table 2 show the results of the ROI analysis. For each quantitative MR parameter map, a significant difference was found among certain identified tissue components. In Fig 3B, the single sample containing intraplaque hemorrhage is shown. The hemorrhage can be distinguished from the surrounding fibrous tissue in the  $T1$  and  $PD$  maps. This sample was not included in the statistical analysis because only 1 sample contained an intraplaque hemorrhage in this study.

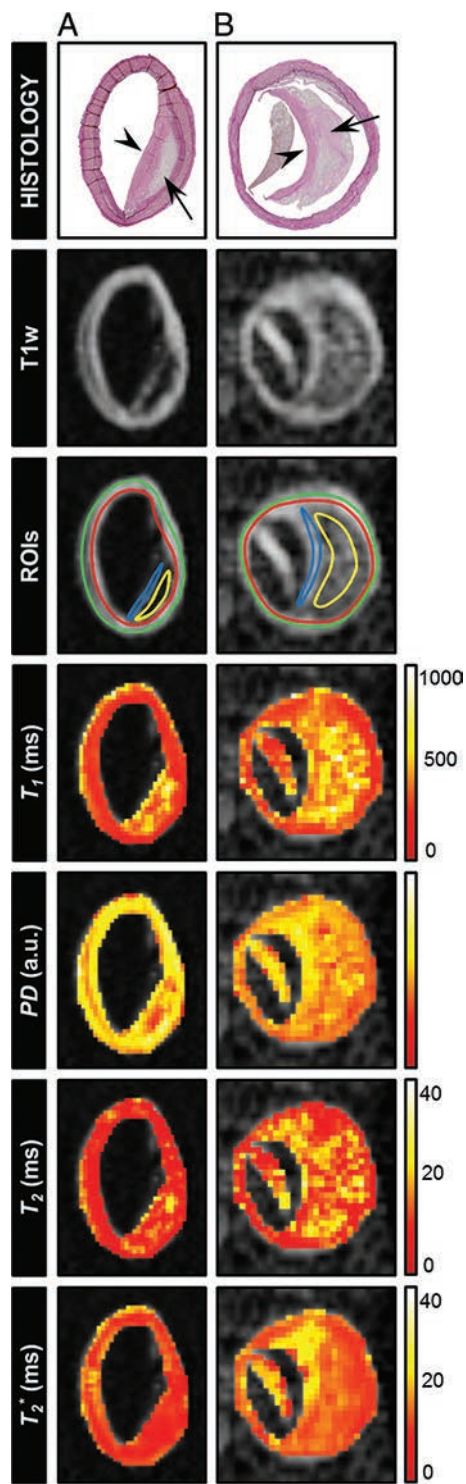


**FIG 1.** Histologic sections (Van Gieson elastic stain) of 2 different samples from the CoW specimens classified as fibrolipid plaques: (A) left vertebral artery and (B) left middle cerebral artery (*arrow* indicates lipid accumulation; *arrowhead*, fibrous cap). The corresponding T1-weighted image (T1w; DESPOT1 acquired with a flip angle of 44°) and the calculated parametric maps ( $T_1$ ,  $T_2$ ,  $T_2^*$ , and  $PD$ ) are shown. ROIs were drawn at the location of tissue components identified in the histologic section (yellow ROI indicates lipid accumulation; blue ROI, fibrous cap; green + red ROI, vessel wall) to calculate the mean  $T_1$ ,  $T_2$ ,  $T_2^*$ , and  $PD$  values for those regions. Lipid accumulation can be distinguished from the fibrous cap and the vessel wall in the  $T_1$ ,  $PD$ , and  $T_2$  maps. A, The lipid accumulation area has already developed into the beginning of a lipid core.

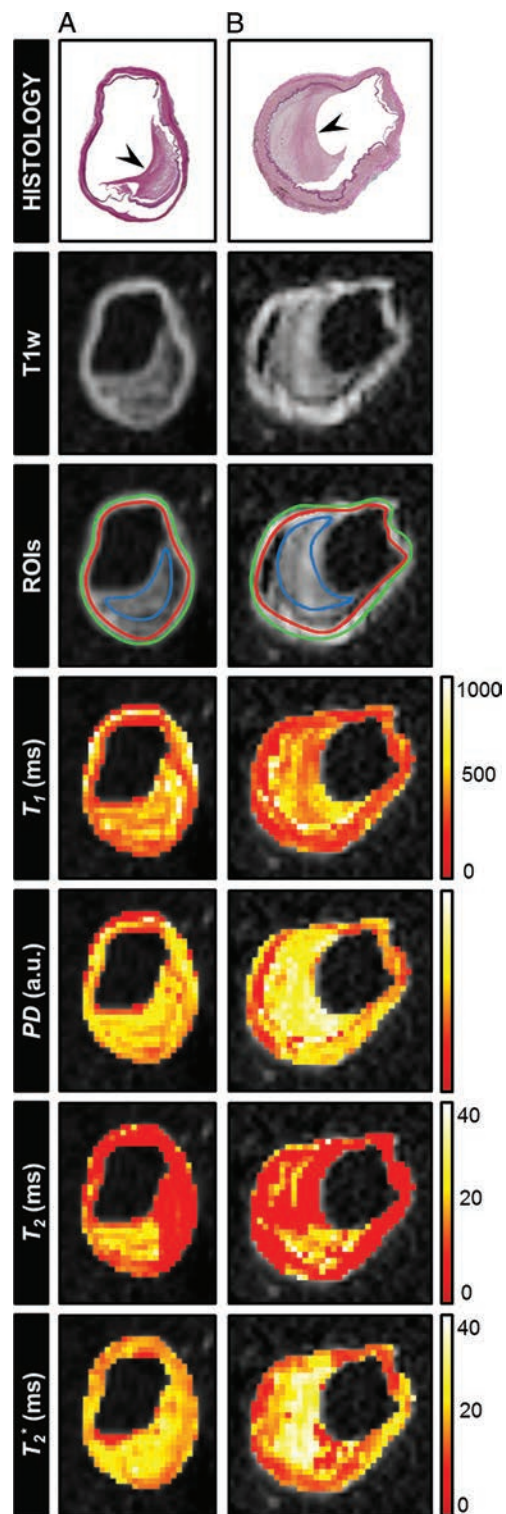


**FIG 2.** Histologic sections (Van Gieson elastic stain) of 2 different samples from the CoW specimens classified as fibrous plaques: (A) right middle cerebral artery and (B) left intracranial internal carotid artery (*arrowhead* indicates fibrous tissue). The corresponding T1-weighted image (DESPOT1 acquired with a flip angle of 44°) and the calculated parametric maps ( $T_1$ ,  $T_2$ ,  $T_2^*$ , and  $PD$ ) are shown. ROIs were drawn at the location of tissue components identified in the histologic section (blue ROI indicates fibrous tissue; green + red ROI, vessel wall) to calculate the mean  $T_1$ ,  $T_2$ ,  $T_2^*$ , and  $PD$  values for these regions. Here, fibrous tissue can be distinguished from the vessel wall in the  $T_1$  and  $T_2$  maps (partly) and, to a lesser extent, in the  $T_2^*$  map.

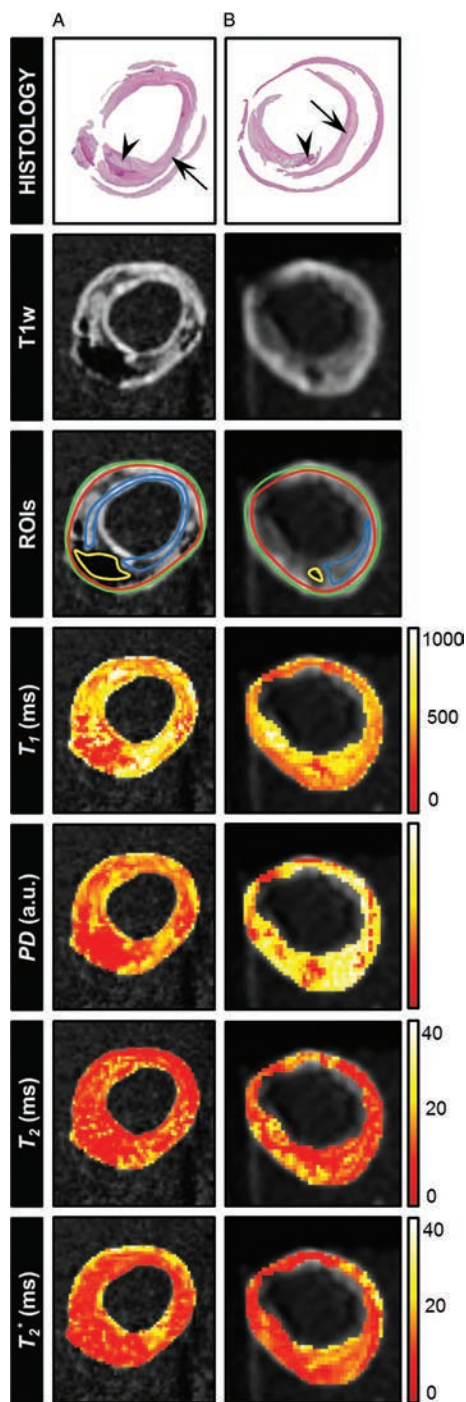


**FIG 3.** Histologic sections (H&E stain) of 2 different samples from the CoW specimens containing calcifications (A) and an intraplaque hemorrhage (B): right intracranial internal carotid artery (A), classified as fibrocalcified plaque, and middle part of the basilar artery (B), classified as fibrous plaque with an old hemorrhage (arrow indicates fibrous tissue, arrowhead: calcification, A, and hemorrhage, B). The corresponding T1-weighted image (DESPO1 acquired with a flip angle of 44°) and the calculated parametric maps ( $T_1$ ,  $T_2$ ,  $T_2^*$ , and PD) are shown. ROIs were drawn at the location of tissue components identified in the histologic section (yellow ROI indicates calcification, A, or intraplaque hemorrhage, B; blue ROI, fibrous tissue; green + red ROI, vessel wall) to calculate the mean  $T_1$ ,  $T_2$ ,  $T_2^*$ , and PD values for those regions. Here, the tissue area containing calcifications can be well distinguished in both the PD and  $T_1$  maps and, to a lesser extent, in the  $T_2$  and  $T_2^*$  maps. The intraplaque hemorrhage can be distinguished from the surrounding fibrous tissue in the  $T_1$  and PD maps.

### Post Hoc Analysis

The On-line Table gives an overview of the post hoc tests performed for pair-wise comparisons of mean ROI values of the identified tissue components, with the resulting  $P$  values.

### DISCUSSION

The current study focused on obtaining ex vivo quantitative  $T_1$ ,  $T_2$ , and  $T_2^*$  relaxation times and PD values for different intracranial atherosclerotic plaque components. Its goal was to provide detailed insight into the ability of MR imaging to characterize intracranial atherosclerotic plaque components. Our main results show that primarily,  $T_1$  relaxation times were significantly different between different plaque components; the other quantitative maps (PD,  $T_2$ , and  $T_2^*$ ) showed mostly nonsignificant differences between the individual tissue components present in the advanced intracranial plaques.

Thus far, atherosclerotic plaques have been extensively studied in extracranial carotid arteries with both in vivo<sup>23-25</sup> and ex vivo<sup>26-29</sup> MR imaging. These studies showed good correlation between MR imaging plaque characteristics and histologic findings. The advantage of extracranial carotid artery plaques is that in vivo MR imaging can be performed before a carotid endarterectomy procedure, allowing direct correlation with histopathology. However, extrapolation of MR signal characteristics of extracranial plaques to intracranial plaques may not be directly applicable because the intracranial arteries are smaller and have some unique histologic features.<sup>18,30-32</sup> Even so, several studies have recently reported visualization of different intracranial plaque components in vivo by using MR imaging, such as lipids,<sup>33</sup> fibrous cap,<sup>33-35</sup> and intraplaque hemorrhage.<sup>34,36-38</sup> These in vivo techniques, however, have not been validated thoroughly with histopathology, due to the poor accessibility of the intracranial arteries. Recently, Turan et al<sup>18</sup> published a first case report demonstrating the correlation between certain intracranial atherosclerotic plaque components visualized in vivo at 3T with histologic validation of the plaque postmortem. However, further correlations are needed to define additional plaque components and to increase the number of cases. As a first step toward MR imaging validation, 2 ex vivo correlation studies<sup>16,17</sup> assessed the ability of 7T MR imaging to image plaque components. These qualitative studies showed 7T to have sufficient image contrast to distinguish different plaque components within advanced plaques. As a second step toward validation, the current study quantitatively assessed intracranial atherosclerotic plaques to enable more firm conclusions regarding the ability of  $T_1$ -,  $T_2$ -,  $T_2^*$ -, and PD-weighted sequences to characterize intracranial atherosclerotic plaques.

Our results showed that the  $T_1$  relaxation times gave the most differences between individual tissue components of advanced intracranial plaques. Tissue components identified in the histologic sections as lipid accumulation, fibrous tissue, fibrous cap, calcifications, and vessel wall showed significant differences in  $T_1$  relaxation times, indicating that they can be distinguished from each other in a  $T_1$ -weighted sequence. Lipid accumulation showed the longest mean  $T_1$  relaxation time, indicating that this may appear as a hypo-isointense region in a  $T_1$ -weighted sequence. van der Kolk et al<sup>16</sup> also

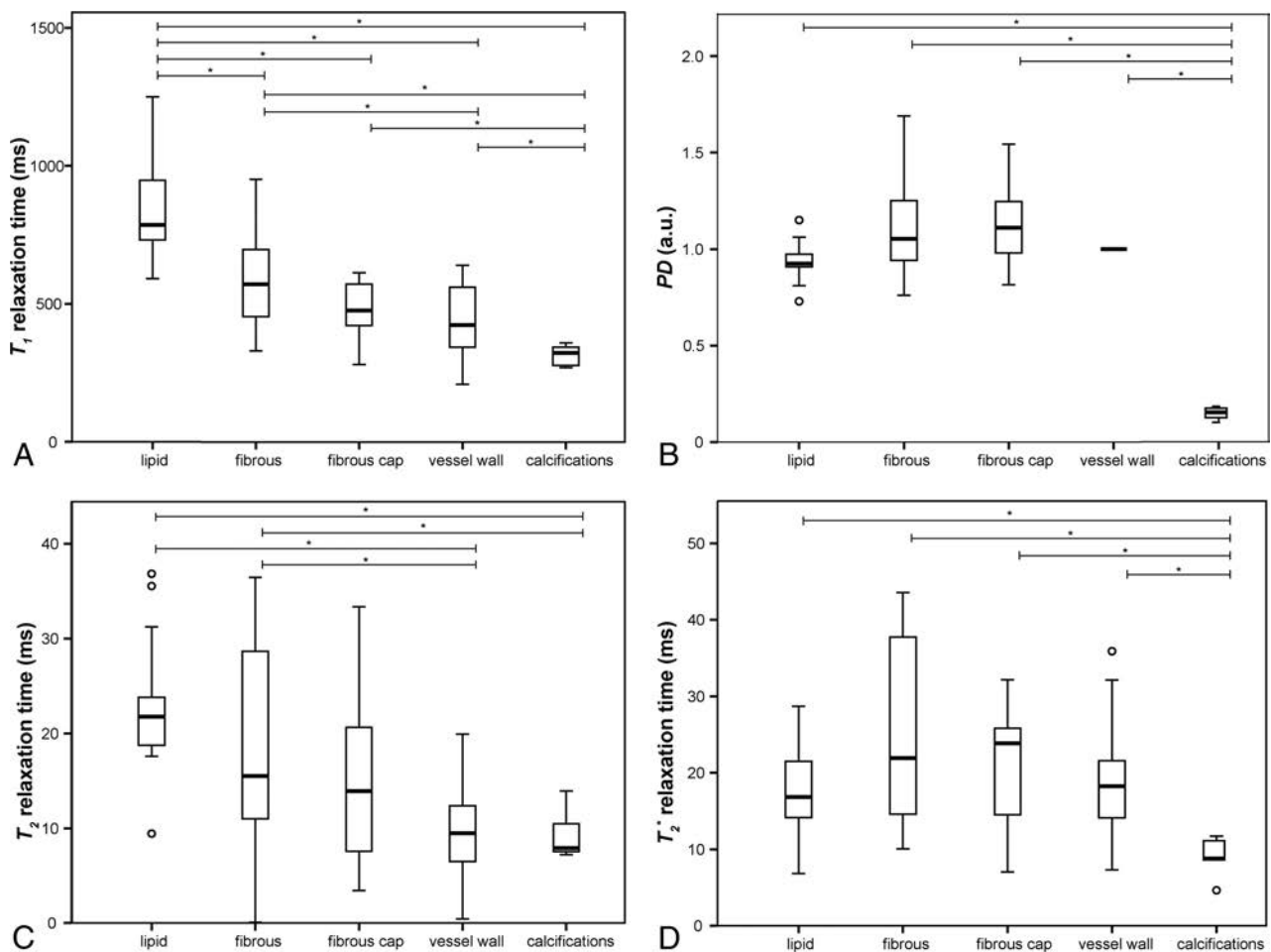


**FIG 4.** Boxplots showing the distribution of the mean ROI values of each identified tissue component determined in the quantitative  $T1$  (A),  $PD$  (B),  $T2$  (C), and  $T2^*$  (D) maps of each advanced plaque sample. The asterisk indicates post hoc pair-wise comparison ( $P < .05$ ).

**Table 2: NMR characteristics of different intracranial plaque tissue components<sup>a</sup>**

	Lipid Accumulation (n = 17)	Fibrous Tissue (n = 24)	Fibrous Cap (n = 12)	Calcifications (n = 5)	Vessel Wall (n = 37)
$T1$ (ms)	838 ± 167	583 ± 161	481 ± 98	314 ± 39	436 ± 122
$PD^b$	0.94 ± 0.10	1.10 ± 0.26	1.13 ± 0.21	0.15 ± 0.03	1.0 ± 0
$T2$ (ms)	22 ± 6.8	18 ± 10	15 ± 9.2	9.4 ± 2.8	10 ± 4.4
$T2^*$ (ms)	18 ± 6.2	25 ± 11	21 ± 8.4	8.9 ± 3.0	18 ± 6.5

**Note:**—NMR indicates nuclear magnetic resonance.

<sup>a</sup> For each identified plaque component the mean ± SD of the mean ROI values for all parameters ( $T1$ ,  $PD$ ,  $T2$ ,  $T2^*$ ) are given. Group differences between tissue components were tested with the Welch test; all maps showed a significant difference ( $P < .001$ ) between tissue components.

<sup>b</sup> Normalized to vessel wall.

showed the lipid-rich core to be hypointense on T1-weighted imaging of ex vivo CoW specimens at 7T, while Turan et al<sup>18</sup> demonstrated in vivo lipid and loose matrix to have an isointense signal intensity compared with the surrounding tissue on a T1-weighted image at 3T. However, both studies were based on a limited number of observations. Previous studies on carotid atherosclerotic plaques<sup>11,27,39</sup> have shown the lipid-rich core to be hyperintense on T1-weighted imaging. An explanation for this difference could be that the stage of development of the lipid-rich core in the current study might be earlier compared with the extracranial carotid artery studies. In the

current study, only 1 sample was identified showing the beginning of a lipid core (Fig 1A); all other samples that were classified as a fibrolipid plaque were still at the stage of lipid accumulation. Intracranial arteries showed more stable lesions and develop mainly as fibrous plaques.<sup>30</sup> Another explanation could be that lipids in an atherosclerotic plaque undergo a partially irreversible phase transition when cooled<sup>40</sup>; however, it is not clear whether this transition affects the MR imaging

properties of the lipids.<sup>27</sup>

The other quantitative maps ( $PD$ ,  $T2$ , and  $T2^*$ ) showed less significant differences among the mean ROI values of the individual tissue components present in the advanced intracranial plaques. The fibrous cap and fibrous tissue showed a larger mean  $PD$  value compared with lipid accumulation; however, these differences did not reach statistical significance. Chung et al<sup>34</sup> also found the fibrous cap to be hyperintense in  $PD$ -weighted imaging of intracranial plaques in vivo. Based on the  $T2$  relaxation time, a distinction can be made between lipids/fibrous tissue on the one hand and vessel wall/calcifications on the other. However, for

each analyzed tissue component, the  $T_2$  relaxation times showed a large relative SD. In addition, the  $T_2$  relaxation times were not consistently larger than the  $T_2^*$  relaxation times; this finding is in contrast to what is known from nuclear magnetic resonance theory. The DESPOT2 method for estimating the  $T_2$  relaxation times might be more sensitive to noise than the DESPOT1 method and might, thus, have been negatively affected by the limited SNR resulting from the high resolution used in the current study. Future studies specifically focused on plaque  $T_2$  relaxation times may show more significant results. For carotid plaque characterization, it has been shown that reviewing multiple contrast-weighted images provided the most comprehensive evaluation for certain plaque components (eg, intraplaque hemorrhage and lipid-rich necrotic core).<sup>27,41</sup>

Only at a few locations were intracranial calcified plaques detected. This finding is in agreement with the low prevalence of intracranial calcified plaques beyond the proximal segments of the ICA and vertebral artery.<sup>30,42</sup> The calcifications that were detected showed low values in all quantitative maps. The  $PD$  map showed the largest differences between calcifications and other plaque components and the intracranial vessel wall. It would be expected that this large difference would also be present on the  $T_2^*$  maps, due to the increased susceptibility effects; however, this difference was not seen in our small sample. This outcome could be due to the relatively lower SNR for the  $T_2^*$  maps (only 1 signal average was used for the  $T_2^*$ -weighted sequence). Also, the  $T_2^*$  of calcifications is known to be very short relative to the shortest TE of the current  $T_2^*$ -weighted sequence.<sup>43</sup> These factors can potentially impede accurate fitting of the  $T_2^*$  relaxation times. A sequence can be used that measures at even shorter TEs to overcome this impediment; however, this result would come at a price of attainable spatial resolution.

Plaque complications were very rare in this study: Only 1 sample with an intraplaque hemorrhage was found. Previous studies have shown a lower prevalence of intraplaque hemorrhage in intracranial compared with extracranial atherosclerosis, and the prevalence of intraplaque hemorrhage is higher in plaques of symptomatic patients (who experienced a cerebral infarct) compared with asymptomatic patients.<sup>30,31,38</sup> In the current study, the CoW specimens were selected on the basis of the macroscopic presence of a high atherosclerotic plaque burden, without knowledge of the clinical background of the patients. In addition, samples were taken at 15 marked locations per CoW specimen only. Increasing the number of samples per specimen and selecting specimens from symptomatic patients might increase the number of plaque complications found.

This study has several limitations. First, fixation effects of formalin have been shown to change relaxation parameters with time.<sup>44,45</sup> Compared with relaxation times in vivo for the vessel wall of the extracranial carotid arteries,<sup>46</sup> the relaxation times in the current ex vivo study are considerably shorter. Similar shortening was found in a previous postmortem study, in which the relaxation times for gray and white matter were measured in formalin-fixed human brains.<sup>47</sup> With an understanding of the effects of sample preparation, the MR imaging data can be correctly related to in vivo data.<sup>44</sup> Second, the MR imaging experiments were performed at room temperature instead of body temperature, which will have influenced the quantitative measurements in the

postmortem specimens.<sup>44</sup> The 7T MR imaging platform does not provide the possibility of performing temperature-controlled imaging. For now, this is the first study trying to identify specific intracranial plaque components in a quantitative manner to measure whether individual tissue components can be distinguished from each other on the basis of their nuclear magnetic resonance tissue properties. This might suggest which contrast weightings need further consideration, to offer the greatest potential to really discriminate different plaque components in vivo. A next step for future studies would be to validate the current findings in a new set of intracranial plaques with optimized MR imaging sequences, preferably of patients with cerebrovascular disease, by characterizing the plaque components on the basis of the MR images alone (with histologic validation afterward) and assessing the reliability of the measurements.

This study was performed to investigate which MR imaging relaxation times discriminate best among the different plaque components and, thereby, in essence, to predict which image contrast weighting would work best in vivo in characterizing atherosclerotic plaques. On the basis of this study, the  $T_1$  relaxation time seems to be the most promising parameter. For now, a direct translation of the quantitative sequences used in the current ex vivo setting to in vivo will be difficult due to the long scan times necessary to achieve the ultra-high resolution required to identify different plaque components. However, this study shows that  $T_1$ -weighted imaging is probably the best method for distinguishing intracranial plaque components ex vivo and therefore might be most promising for in vivo application. Now that it is known which plaque components can be identified with ex vivo MR imaging sequences, a translation can be made to in vivo intracranial vessel wall MR imaging by fine-tuning the current in vivo sequences on the basis of the nuclear magnetic resonance tissue properties of the identified atherosclerotic plaque components to obtain optimal image contrast between the different tissue components. Also, future developments in receive coil technology (increasing the number of receive elements) may provide significant improvement in SNR to make quantitative assessment of the intracranial arterial vessel wall possible in vivo. Furthermore, in vivo, we expect that quantitative assessment will first become feasible for the thicker arterial vessel wall of the more proximal intracranial arteries, including the distal carotid artery and the vertebrobasilar arterial vessel walls.

## CONCLUSIONS

We showed that different tissue components of advanced intracranial plaques have distinguishable imaging characteristics by using ultra-high-resolution quantitative MR imaging at 7T. Now that it is known which plaque components can be identified with ex vivo MR imaging sequences, a translation may be made to in vivo intracranial vessel wall MR imaging to obtain optimal image contrast between the different plaque components. Based on this study, the most promising method for distinguishing these plaque components is  $T_1$ -weighted imaging.

## REFERENCES

1. Go AS, Mozaffarian D, Roger VL, et al; American Heart Association Statistics Committee and Stroke Statistics Subcommittee. **Heart disease and stroke statistics—2014 update: a report from**

- the American Heart Association. *Circulation* 2014;129:e28–e292 CrossRef Medline
2. Lozano R, Naghavi M, Foreman K, et al. **Global and regional mortality from 235 causes of death for 20 age groups in 1990 and 2010: a systematic analysis for the Global Burden of Disease Study 2010.** *Lancet* 2012;380:2095–128 CrossRef Medline
  3. Arenillas JF. **Intracranial atherosclerosis: current concepts.** *Stroke* 2011;42:S20–23 CrossRef Medline
  4. Bos D, Portegies ML, van der Lugt A, et al. **Intracranial carotid artery atherosclerosis and the risk of stroke in whites: the Rotterdam Study.** *JAMA Neurol* 2014;71:405–11 CrossRef Medline
  5. Chimowitz MI, Lynn MJ, Derdeyn CP, et al; SAMMPRIS Trial Investigators. **Stenting versus aggressive medical therapy for intracranial arterial stenosis.** *N Engl J Med* 2011;365:993–1003 CrossRef Medline
  6. Chimowitz MI, Lynn MJ, Howlett-Smith H, et al. **Comparison of warfarin and aspirin for symptomatic intracranial arterial stenosis.** *N Engl J Med* 2005;352:1305–16 CrossRef Medline
  7. Gorelick PB, Wong KS, Bae HJ, et al. **Large artery intracranial occlusive disease: a large worldwide burden but a relatively neglected frontier.** *Stroke* 2008;39:2396–99 CrossRef Medline
  8. Qureshi AI, Caplan LR. **Intracranial atherosclerosis.** *Lancet* 2014;383:984–98 CrossRef Medline
  9. Hellings WE, Peeters W, Moll FL, et al. **Composition of carotid atherosclerotic plaque is associated with cardiovascular outcome: a prognostic study.** *Circulation* 2010;121:1941–50 CrossRef Medline
  10. Saam T, Hatsukami TS, Takaya N, et al. **The vulnerable, or high-risk, atherosclerotic plaque: noninvasive MR imaging for characterization and assessment.** *Radiology* 2007;244:64–77 CrossRef Medline
  11. Saba L, Anzidei M, Sanfilippo R, et al. **Imaging of the carotid artery.** *Atherosclerosis* 2012;220:294–309 CrossRef Medline
  12. Takaya N, Yuan C, Chu B, et al. **Association between carotid plaque characteristics and subsequent ischemic cerebrovascular events: a prospective assessment with MRI—initial results.** *Stroke* 2006;37:818–23 CrossRef Medline
  13. Kasner SE, Chimowitz MI, Lynn MJ, et al; Warfarin Aspirin Symptomatic Intracranial Disease Trial Investigators. **Predictors of ischemic stroke in the territory of a symptomatic intracranial arterial stenosis.** *Circulation* 2006;113:555–63 CrossRef Medline
  14. Leng X, Wong KS, Liebeskind DS. **Evaluating intracranial atherosclerosis rather than intracranial stenosis.** *Stroke* 2014;45:645–51 CrossRef Medline
  15. Dieleman N, van der Kolk AG, Zwanenburg JJ, et al. **Imaging intracranial vessel wall pathology with magnetic resonance imaging: current prospects and future directions.** *Circulation* 2014;130:192–201 CrossRef Medline
  16. van der Kolk AG, Zwanenburg JJ, Denswil NP, et al. **Imaging the intracranial atherosclerotic vessel wall using 7T MRI: initial comparison with histopathology.** *AJNR Am J Neuroradiol* 2015;36:694–701 CrossRef Medline
  17. Majidi S, Sein J, Watanabe M, et al. **Intracranial-derived atherosclerosis assessment: an in vitro comparison between virtual histology by intravascular ultrasonography, 7T MRI, and histopathologic findings.** *AJNR Am J Neuroradiol* 2013;34:2259–64 CrossRef Medline
  18. Turan TN, Rumboldt Z, Granholm AC, et al. **Intracranial atherosclerosis: correlation between in-vivo 3T high resolution MRI and pathology.** *Atherosclerosis* 2014;237:460–63 CrossRef Medline
  19. Petridou N, Italiaander M, van de Bank BL, et al. **Pushing the limits of high-resolution functional MRI using a simple high-density multi-element coil design.** *NMR Biomed* 2013;26:65–73 CrossRef Medline
  20. Deoni SC, Rutt BK, Peters TM. **Rapid combined T1 and T2 mapping using gradient recalled acquisition in the steady state.** *Magn Reson Med* 2003;49:515–26 CrossRef Medline
  21. Yarnykh VL. **Actual flip-angle imaging in the pulsed steady state: a method for rapid three-dimensional mapping of the transmitted radiofrequency field.** *Magn Reson Med* 2007;57:192–200 CrossRef Medline
  22. Virmani R, Kolodgie FD, Burke AP, et al. **Lessons from sudden coronary death: a comprehensive morphological classification scheme for atherosclerotic lesions.** *Arterioscler Thromb Vasc Biol* 2000;20:1262–75 CrossRef Medline
  23. Cai JM, Hatsukami TS, Ferguson MS, et al. **Classification of human carotid atherosclerotic lesions with in vivo multicontrast magnetic resonance imaging.** *Circulation* 2002;106:1368–73 CrossRef Medline
  24. Cai J, Hatsukami TS, Ferguson MS, et al. **In vivo quantitative measurement of intact fibrous cap and lipid-rich necrotic core size in atherosclerotic carotid plaque: comparison of high-resolution, contrast-enhanced magnetic resonance imaging and histology.** *Circulation* 2005;112:3437–44 CrossRef Medline
  25. Hofman JM, Branderhorst WJ, ten Eikelder HM, et al. **Quantification of atherosclerotic plaque components using in vivo MRI and supervised classifiers.** *Magn Reson Med* 2006;55:790–99 CrossRef Medline
  26. Coombs BD, Rapp JH, Ursell PC, et al. **Structure of plaque at carotid bifurcation: high-resolution MRI with histological correlation.** *Stroke* 2001;32:2516–21 CrossRef Medline
  27. Shinnar M, Fallon JT, Wehrli S, et al. **The diagnostic accuracy of ex vivo MRI for human atherosclerotic plaque characterization.** *Arterioscler Thromb Vasc Biol* 1999;19:2756–61 CrossRef Medline
  28. Serfaty JM, Chaabane L, Tabib A, et al. **Atherosclerotic plaques: classification and characterization with T2-weighted high-spatial-resolution MR imaging—an in vitro study.** *Radiology* 2001;219:403–10 CrossRef Medline
  29. Clarke SE, Hammond RR, Mitchell JR, et al. **Quantitative assessment of carotid plaque composition using multicontrast MRI and registered histology.** *Magn Reson Med* 2003;50:1199–208 CrossRef Medline
  30. Ritz K, Denswil NP, Stam OC, et al. **Cause and mechanisms of intracranial atherosclerosis.** *Circulation* 2014;130:1407–14 CrossRef Medline
  31. Chen XY, Wong KS, Lam WW, et al. **Middle cerebral artery atherosclerosis: histological comparison between plaques associated with and not associated with infarct in a postmortem study.** *Cerebrovasc Dis* 2008;25:74–80 CrossRef Medline
  32. Portanova A, Hakakian N, Mikulis DJ, et al. **Intracranial vasa vasorum: insights and implications for imaging.** *Radiology* 2013;267:667–79 CrossRef Medline
  33. Turan TN, Rumboldt Z, Brown TR. **High-resolution MRI of basilar atherosclerosis: three-dimensional acquisition and FLAIR sequences.** *Brain Behav* 2013;3:1–3 CrossRef Medline
  34. Chung JW, Kim BJ, Choi BS, et al. **High-resolution magnetic resonance imaging reveals hidden etiologies of symptomatic vertebral arterial lesions.** *J Stroke Cerebrovasc Dis* 2014;23:293–302 CrossRef Medline
  35. Yang WQ, Huang B, Liu XT, et al. **Reproducibility of high-resolution MRI for the middle cerebral artery plaque at 3T.** *Eur J Radiol* 2014;83:e49–55 CrossRef Medline
  36. Turan TN, Bonilha L, Morgan PS, et al. **Intraplaque hemorrhage in symptomatic intracranial atherosclerotic disease.** *J Neuroimaging* 2011;21:e159–61 CrossRef Medline
  37. Park JK, Kim SH, Kim BS, et al. **Imaging of intracranial plaques with black-blood double inversion recovery MR imaging and CT.** *J Neuroimaging* 2011;21:e64–68 CrossRef Medline
  38. Xu WH, Li ML, Gao S, et al. **Middle cerebral artery intraplaque hemorrhage: prevalence and clinical relevance.** *Ann Neurol* 2012;71:195–98 CrossRef Medline
  39. Yuan C, Mitsumori LM, Beach KW, et al. **Carotid atherosclerotic plaque: noninvasive MR characterization and identification of vulnerable lesions.** *Radiology* 2001;221:285–99 CrossRef Medline
  40. Lundberg B. **Chemical composition and physical state of lipid deposits in atherosclerosis.** *Atherosclerosis* 1985;56:93–110 CrossRef Medline
  41. Yuan C, Mitsumori LM, Ferguson MS, et al. **In vivo accuracy of**

- multispectral magnetic resonance imaging for identifying lipid-rich necrotic cores and intraplaque hemorrhage in advanced human carotid plaques. *Circulation* 2001;104:2051–56 CrossRef Medline
42. Homburg PJ, Plas GJ, Rozie S, et al. **Prevalence and calcification of intracranial arterial stenotic lesions as assessed with multidetector computed tomography angiography.** *Stroke* 2011;42:1244–50 CrossRef Medline
43. Sharma S, Boujraf S, Bornstedt A, et al. **Quantification of calcifications in endarterectomy samples by means of high-resolution ultra-short echo time imaging.** *Invest Radiol* 2010;45:109–13 CrossRef Medline
44. Thelwall PE, Shepherd TM, Stanisz GJ, et al. **Effects of temperature and aldehyde fixation on tissue water diffusion properties, studied in an erythrocyte ghost tissue model.** *Magn Reson Med* 2006;56:282–89 CrossRef Medline
45. Thickman DI, Kundel HL, Wolf G. **Nuclear magnetic resonance characteristics of fresh and fixed tissue: the effect of elapsed time.** *Radiology* 1983;148:183–85 CrossRef Medline
46. Koning W, de Rotte AA, Bluemink JJ, et al. **MRI of the carotid artery at 7 Tesla: quantitative comparison with 3 Tesla.** *J Magn Reson Imaging* 2015;41:773–80 CrossRef Medline
47. Pfefferbaum A, Sullivan EV, Adalsteinsson E, et al. **Postmortem MR imaging of formalin-fixed human brain.** *Neuroimage* 2004;21:1585–95 CrossRef Medline

# Mitotic Activity in Glioblastoma Correlates with Estimated Extravascular Extracellular Space Derived from Dynamic Contrast-Enhanced MR Imaging

S.J. Mills, D. du Plessis, P. Pal, G. Thompson, G. Buonacorsi, C. Soh, G.J.M. Parker, and A. Jackson



## ABSTRACT

**BACKGROUND AND PURPOSE:** A number of parameters derived from dynamic contrast-enhanced MR imaging and separate histologic features have been identified as potential prognosticators in high-grade glioma. This study evaluated the relationships between dynamic contrast-enhanced MRI–derived parameters and histologic features in glioblastoma multiforme.

**MATERIALS AND METHODS:** Twenty-eight patients with newly presenting glioblastoma multiforme underwent preoperative imaging (conventional imaging and T1 dynamic contrast-enhanced MRI). Parametric maps of the initial area under the contrast agent concentration curve, contrast transfer coefficient, estimate of volume of the extravascular extracellular space, and estimate of blood plasma volume were generated, and the enhancing fraction was calculated. Surgical specimens were used to assess subtype and were graded (World Health Organization classification system) and were assessed for necrosis, cell density, cellular atypia, mitotic activity, and overall vascularity scores. Quantitative assessment of endothelial surface area, vascular surface area, and a vascular profile count were made by using CD34 immunostaining. The relationships between MR imaging parameters and histopathologic features were examined.

**RESULTS:** High values of contrast transfer coefficient were associated with the presence of frank necrosis ( $P = .005$ ). High values of the estimate of volume of the extravascular extracellular space were associated with a fibrillary histologic pattern ( $P < .01$ ) and with increased mitotic activity ( $P < .05$ ). No relationship was found between mitotic activity and histologic pattern, suggesting that the correlation between the estimate of volume of the extravascular extracellular space and mitotic activity was independent of the histologic pattern.

**CONCLUSIONS:** A correlation between the estimate of volume of the extravascular extracellular space and mitotic activity is reported. Further work is warranted to establish how dynamic contrast-enhanced MRI parameters relate to more quantitative histologic measurements, including markers of proliferation and measures of vascular endothelial growth factor expression.

**ABBREVIATIONS:** DCE-MRI = dynamic contrast-enhanced MRI; EnF = enhancing fraction; GBM = glioblastoma multiforme; IAUC<sub>60</sub> = initial area under the contrast agent concentration curve;  $K^{trans}$  = contrast transfer coefficient;  $v_e$  = volume of the extravascular extracellular space per unit tissue volume; VEGF = vascular endothelial growth factor;  $v_p$  = volume of the blood plasma per unit tissue volume

**G**liomas are the most common primary cerebral tumor of adulthood. They are histologically classified according to the World Health Organization criteria into tumor grade and subtype,<sup>1</sup> which are important for determining appropriate treatment. Within given histologic subtypes and tumor grades, a num-

ber of additional descriptive histopathologic features have been identified as prognosticators, including mitotic activity,<sup>2-4</sup> microvascular density,<sup>5,6</sup> and certain vascular patterns.<sup>7,8</sup> Both proliferation markers, Ki-67<sup>2-4,7,9,10</sup> and expression of vascular endothelial growth factor (VEGF),<sup>3,5,11-14</sup> have also shown a relationship to survival.

Dynamic contrast-enhanced MR imaging (DCE-MR imaging) techniques generate a number of parameters that characterize the microvascular environment. The enhancing fraction (EnF) describes the proportion of perfused tumor tissue. CBV and CBF

Received July 6, 2015; accepted after revision October 6.

From the Departments of Neuroradiology (S.J.M., G.T., C.S., A.J.) and Neuropathology (D.d.P., P.P.), Salford National Health Service Foundation Trust, Salford, UK; and Imaging Science and Biomedical Engineering (S.J.M., G.T., G.B., G.J.M.P., A.J.), University of Manchester, Manchester, UK.

This work was funded as part of a Cancer Research UK Clinical Research Training Fellowship, reference C21247/A7473.

Please address correspondence to Samantha Mills, MD, Consultant Neuroradiologist, The Walton Centre, Fazakerley, Liverpool, L9 7LJ; e-mail: Samantha.Mills@thewaltoncentre.nhs.uk

Indicates open access to non-subscribers at www.ajnr.org

Indicates article with supplemental on-line table.

<http://dx.doi.org/10.3174/ajnr.A4623>

are commonly derived from dynamic susceptibility contrast techniques, while the volume transfer coefficient ( $K^{trans}$ ), fractional volume of the extravascular extracellular space ( $v_e$ ), and fractional blood plasma volume ( $v_p$ ) can be calculated from T1-weighted DCE-MR imaging.<sup>15</sup> In glioma,  $K^{trans}$ ,  $v_p$ , EnF, CBV, and CBF have been shown to relate to histologic grade and/or subtype of tumor.<sup>16-21</sup> In addition,  $K^{trans}$ , EnF, and CBV have been identified as potentially grade-independent prognosticators.<sup>22-25</sup> The number of studies examining the relationship between DCE-MR imaging parameters and more specific histopathologic features in glioma is currently small and this research predominantly focuses on vascular metrics such as blood volume and flow; however, significant correlations have been described between CBV and microvascular density,<sup>26-29</sup> VEGF expression,<sup>27,30</sup> cell density,<sup>29</sup> endothelial proliferation,<sup>31</sup> and mitotic activity<sup>31</sup> and between CBF and endothelial hyperplasia.<sup>32</sup>

More recent studies have focused on the potential of  $v_e$  as an imaging biomarker. In glioma, it has shown value in discriminating histologic grades,<sup>33,34</sup> but compared with other potential candidate biomarkers of the extravascular extracellular space volume (ADC), on a voxel by voxel basis, no correlation was seen between the 2 metrics, suggesting that these parameters provide independent information about extravascular extracellular space characteristics.<sup>35</sup> Two separate studies of patients with gliomas of various histologic grades have both reported significant correlations between both  $K^{trans}$  and  $v_e$  and vascular and microvascular density,<sup>33,34</sup> but neither study comments on the relationship with cellular density or mitotic activity. A high-field, 7T MR imaging study of rat xenografts showed an image-matched significant negative correlation between  $v_e$  and tumor cellularity.<sup>36</sup>

We hypothesized the following: 1) Larger, rapidly growing tumors would show higher mitotic activity and high angiogenic activity reflected by  $K^{trans}$  and EnF; and 2) more proliferative tumors would have a higher cellular density and mitotic activity associated with lower values of  $v_e$ .

## MATERIALS AND METHODS

### Patients

Ethical approval was obtained, and all patients gave informed consent. All tumors were histologically confirmed as glioblastoma multiforme (GBM) according to the World Health Organization criteria.<sup>1</sup> All imaging was preoperative, and patients received no treatment other than corticosteroids, which were administered for a minimum of 48 hours before imaging to allow stabilization of the effects of steroids on DCE-MR imaging measures.<sup>37</sup> Patients were excluded from the study if they had a history of renal dysfunction or low estimated glomerular filtration rate ( $<30$  mL/min/1.73 m<sup>2</sup>).

### MR Imaging Data Acquisition

Imaging was performed on a 3T Achieva system (Philips Healthcare, Best, the Netherlands) by using a sensitivity encoding head coil. DCE-MR imaging was acquired in a sagittal oblique orientation to allow improved definition of the arterial input function free from flow-related artifacts. Three precontrast T1 fast-field echo (radiofrequency spoiled gradient-echo) series (2°, 5°, 16°)

were acquired for calculation of baseline T1 maps (TR, 3.5 ms; TE, 1.1 ms; section thickness, 4.2 mm; matrix, 128 × 128; FOV, 230 × 230 × 105 mm) in the same geometry. A dynamic, contrast-enhanced acquisition series (TR, 3.5 ms; TE, 1.1 ms; flip angle, 16°; section thickness, 4.2 mm; matrix, 128 × 128; FOV, 230 × 230 × 105 mm) consisting of 100 volumes with temporal spacing of approximately 3.4 seconds followed. A bolus dose of 0.1 mmol/kg (body weight) of gadolinium-based contrast agent (gadodiamide; Gd-DTPA-BMA; Omniscan; GE Healthcare, Piscataway, New Jersey) was injected at a rate of 3 mL/s, after acquisition of the fifth image volume. Pre- and postcontrast T1-weighted imaging sequences (TR, 9.3 ms; TE, 4.6 ms) were acquired in the same sagittal oblique geometry for definition of the volume of interest of the whole tumor.

### MR Imaging Data Analysis

An experienced neuroradiologist (S.J.M.) manually defined VOIs for each tumor. The VOI corresponded to the enhancing tumor and all nonenhancing tissue contained within it on the postcontrast T1-weighted images. This technique of VOI definition has previously shown good interobserver agreement (intraclass correlation coefficient  $> 0.94$ ).<sup>38</sup> Pharmacokinetic analysis was performed on all pixels within the VOI that showed significant enhancement. Parametric maps of  $K^{trans}$ ,  $v_p$ ,  $v_e$ , and initial area under the contrast agent concentration curve (IAUC<sub>60</sub>) were produced by using in-house software (MaDyM; Manchester Dynamic Modeling, Manchester, UK) and the extended Tofts and Kermode pharmacokinetic model.<sup>15</sup> Automated arterial input functions were generated from an appropriately chosen section, which included the internal carotid artery.<sup>39</sup> Summary statistics for each parameter were generated for enhancing tumor tissue.

For each tumor, EnF initial area under the contrast agent concentration curve (EnF<sub>IAUC60>0</sub>) and thresholded EnF (EnF<sub>IAUC60>2.5</sub>) were calculated by dividing the enhancing volume (volume of voxels with IAUC<sub>60</sub>  $> 0$  mmol/s for EnF<sub>IAUC60>0</sub> and the volume of voxels with IAUC<sub>60</sub>  $> 2.5$  mmol/s for EnF<sub>IAUC60>2.5</sub>) by the total volume of the tumor VOI. The cutoff threshold of IAUC<sub>60</sub>  $> 2.5$  mmol/s for EnF<sub>IAUC60>2.5</sub> was previously identified as an optimal threshold for allowing the distinction of high- from low-grade gliomas.<sup>40</sup>

### Histopathologic Data Analysis

Two experienced neuropathologists (D.d.P. and P.P.) performed the histopathologic analysis. Histologic specimens were assessed for the following: necrosis (presence or absence of frank and/or geographic necrosis), cell density (3-point grading score), cell atypia (3-point grading score), mitotic activity (number of mitotic figures seen per 10 high-power-field units), infiltrates (presence or absence of lymphocytes and/or macrophages), tumor vascular pattern (presence or absence of the following features: endothelial hypertrophy and/or hyperplasia, glomeruloid structures, granulation tissue, large-vessel density, thrombosis, sclerosed vessels), an overall vascular density score (3-point grading score), and histologic pattern (fibrillar, gemistocytic, oligodendrocytes, sarcomatous, giant cells, and small cells) in conjunction with standard histopathologic subtyping and grading according to the World Health Organiza-

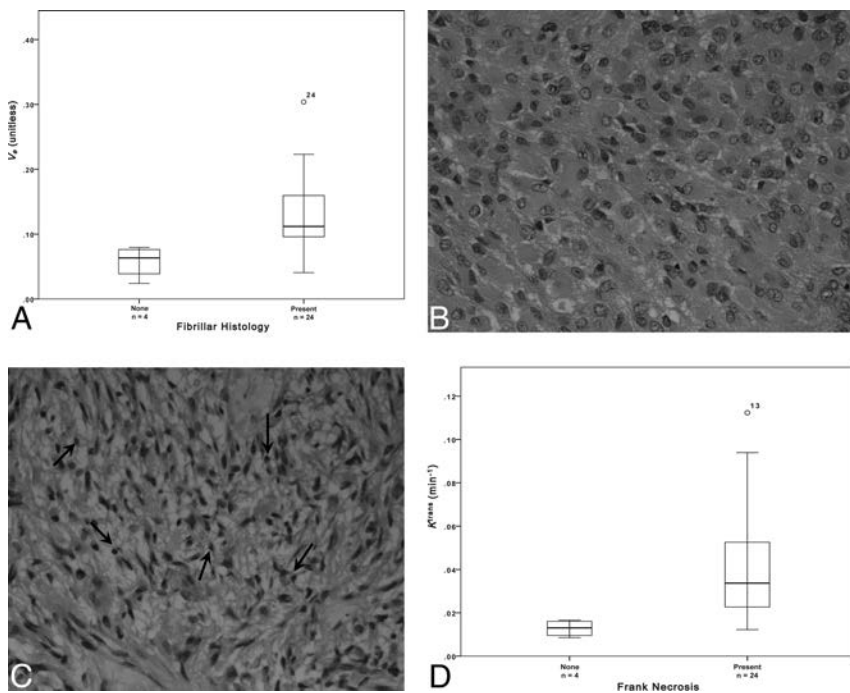


**FIG 1.** A, Boxplot of fibrillar histology and  $v_e$  (estimated  $P = .007$ ). Sample histologic specimens showing tumors without (B) and with (C) the presence of fibrils (small fibers measuring approximately 1 mm, black arrows, C). H&E stain  $\times 40$  magnification. D, Boxplot of frank necrosis and  $K^{trans}$  (estimated  $P = .005$ ).

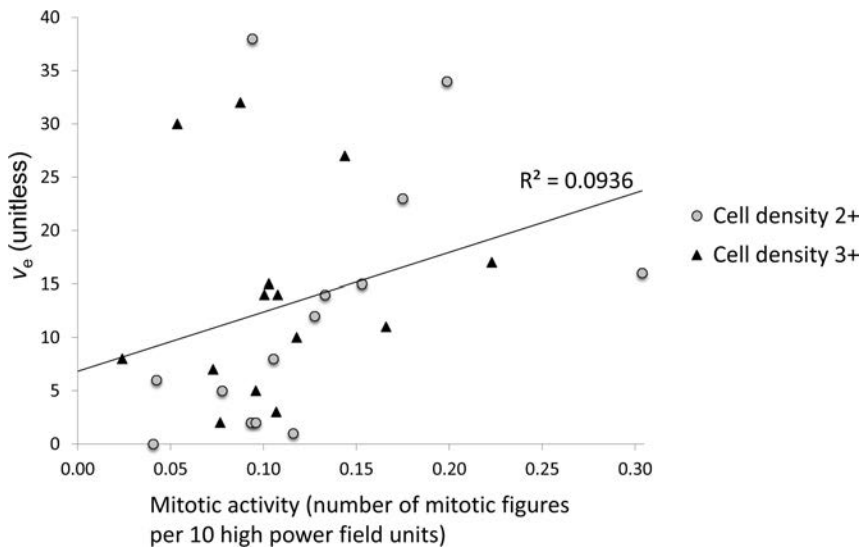


**FIG 2.** Scatterplot of mitotic activity versus  $v_e$  ( $P = .012$ ,  $\rho = 0.470$ ), marker shapes depict separate scores of cell density measures.

tion classification criteria.<sup>1</sup> Vascular and histologic features were not mutually exclusive; therefore,  $>1$  feature could be described in a given tumor specimen.

Quantitative measurement of the endothelial surface area, the vascular surface area, and the vascular profile count per square millimeter was made by using CD34 immunostaining and dedicated image-analysis software.

### Statistical Analysis

Statistical analysis was performed by using SPSS (Version 15.0; IBM, Armonk, New York) nonparametric statistical tests. While

histologic parameters produce a binary classification (necrosis, infiltrates, vascular patterns, and histologic patterns), Mann-Whitney  $U$  tests were performed to test the hypothesis that MR imaging parameter values did not differ among groups. While histologic features produce categorical scores (cell density, cell atypia, and overall vascular score), multivariate analysis of variance was used to test the hypothesis that MR imaging parameter values did not differ among groups. Spearman correlation analysis was performed to assess the relationship between quantitative histologic measures (mitotic activity, endothelial surface area, vascular surface area, and vascular profile count per square millimeter) and MR imaging parameters and to identify correlations among the individual MR imaging measurements. For Mann-Whitney  $U$  and ANOVA testing, a result was considered significantly different with  $P < .01$ , given the number of variables assessed. For the Spearman correlation analysis, significance was  $< .05$ .

### RESULTS

Twenty-eight untreated newly presented GBMs were included in the study (10 women; age range, 38–76 years; mean, 60 years). Histologic specimens were obtained from 12 biopsies and 16 surgical debulkings. The results of statistical analyses for comparisons of histologic and MR imaging measures are summarized in the On-line Table.

The presence of frank necrosis was associated with significantly higher values of  $K^{trans}$  ( $P < .01$ , Fig 1). Significantly higher values of  $v_e$  were seen in the presence of fibrillary histology (estimated  $P < .01$ , Fig 1). A positive correlation was found between  $v_e$  and mitotic activity ( $P < .05$ ,  $\rho = 0.470$ , Fig 2). No relationship was seen between mitotic

activity and any of the descriptive or semiquantitative histology measures, suggesting that the relationship between  $v_e$  and mitotic activity is independent of the relationship between  $v_e$  and the presence of fibrillary histology. No correlation was observed between  $v_e$  and cell density.

Cross-correlations between individual MR imaging parameters are summarized in Table 1. Positive correlations were found between  $K^{trans}$  and all other MR imaging parameters. Significant correlations were present between  $v_e$  and  $K^{trans}$  ( $P < .05$  and  $\rho = 0.450$ ) and between  $v_p$  and EnF. Mitotic activity did not correlate

**Table 1: Cross-correlations of MRI parameters<sup>a</sup>**

	Untreated GBM (n = 28)			
	$v_e$	$v_p$	$EnF_{IAUC60>0}$	$EnF_{IAUC60>2.5}$
$K^{trans}$	0.016, <sup>b</sup> $\rho = 0.450$	0.006, <sup>c</sup> $\rho = 0.507$	0.005, <sup>c</sup> $\rho = 0.513$	<0.001, <sup>c</sup> $\rho = 0.784$
$v_e$		0.105, $\rho = 0.313$	0.888, $\rho = 0.028$	0.059, $\rho = 0.361$
$v_p$			0.02, <sup>b</sup> $\rho = 0.437$	<0.001, <sup>c</sup> $\rho = 0.620$
$EnF_{IAUC60>0}$				<0.001, <sup>c</sup> $\rho = 0.825$

<sup>a</sup> Significance levels and Spearman  $\rho$  are shown.

<sup>b</sup> Significance was  $P < .05$ .

<sup>c</sup> Significance was  $P < .01$ .

**Table 2: Cross-correlations of quantitative histologic measures<sup>a</sup>**

	Untreated GBM (n = 28)		
	ESA Ratio	VSA Ratio	VPC/mm <sup>2</sup>
Mitotic activity	0.098, $\rho = 0.325$	0.066, $\rho = 0.358$	0.737, $\rho = 0.068$
ESA ratio		<0.001, <sup>b</sup> $\rho = 0.993$	0.04, <sup>c</sup> $\rho = 0.530$
VSA ratio			0.04, <sup>c</sup> $\rho = 0.532$

**Note:**—VPC indicates vascular profile count per square millimeter; VSA, vascular surface area; ESA, endothelial surface area.

<sup>a</sup> Significance levels and Spearman  $\rho$  are shown.

<sup>b</sup> Significance was  $P < .01$ .

<sup>c</sup> Significance was  $P < .05$ .

with any quantitative vascular measure, but cross-correlation was seen across all 3 histologic vascular metrics (Table 2). No other significant relationships were identified among histologic measures.

## DISCUSSION

While there has been considerable interest in the development of imaging biomarkers for use in clinical trials, most DCE-MR imaging studies have focused on identifying correlates of vascularity and angiogenesis.<sup>41</sup> This study identified an unexpected positive correlation between  $v_e$ , a parameter thought to reflect extravascular extracellular space volume, and mitotic activity. No relationships were identified among the previously described DCE-MR imaging prognosticators,  $K^{trans}$  and  $v_p$ , and mitotic activity or between vascular patterns and DCE-MR imaging measures.

The parameter  $v_e$  is often overlooked in DCE-MR imaging studies. In cerebral tumors, it has the potential to distinguish intra- from extra-axial tumors<sup>42,43</sup> and exhibits increased values with increasing tumor grade.<sup>33,34,42,44</sup> It has also demonstrated sensitivity in identifying changes in response to treatment with corticosteroids, with decreases in  $v_e$  presumably reflecting a reduction in interstitial edema.<sup>45,46</sup> In a study of vestibular schwannomas, meningiomas, and gliomas, no direct measure of the extravascular extracellular space or cell density measure was made, but  $v_e$  values in schwannoma were significantly larger than those in glioma, where cell density is higher.<sup>43</sup> In a study comparing  $v_e$  with ADC in glioma, no relationship was found between the 2 metrics, suggesting that these parameters may provide independent information about the extravascular extracellular space.<sup>35</sup> This may reflect the existence of separate extravascular leakage compartments characterized by fast and slow contrast exchange rates, possibly reflecting the presence of slow leakage/diffusion into and out of necrotic tumor spaces.<sup>42,47,48</sup> Previous studies have also reported correlations between microvascular density and both  $v_e$  and  $K^{trans}$ .<sup>33,34</sup> We did not find this correlation in our study, but there was a cross-correlation between the DCE-MR

imaging parameters  $v_e$  and  $K^{trans}$ , raising the possibility that the correlation reported in the previous studies reflects the relationship of  $v_e$  with  $K^{trans}$  rather than microvascular density. A previous rat xenograft study has reported a correlation between  $v_e$  and cellular density,<sup>36</sup> but our current study found no such relationship.

Histologic measures of cell density are often a count of the number of cell nuclei per unit area and without quantification of the amount of tissue the cells occupy; thus, an increase in histologic cell density may reflect an increase in the number of cells, but not necessarily a decrease in extravascular extracellular space if the cells are small. There are potential modeling problems associated with the calculation of  $v_e$ . Clearly it can be estimated only in perfused tissue where there is significant leakage of contrast agent.<sup>35</sup> This problem means that summary statistics presented in this and other studies reflect only perfused tissue with contrast agent leakage, in contrast to diffusion-weighted imaging, in which high ADC values are seen in association with necrosis. We have specifically excluded nonperfusing tissue from estimates of summary statistics, which could otherwise produce artificially low values of  $v_e$ . In addition, the relatively low dynamic sampling duration (6 minutes) will affect  $v_e$  estimates to some degree. First, model fitting errors (assuming that the model is correct) will result from undersampling, but modeling studies suggest that these fitting errors are likely to be very small.<sup>49</sup> Second, short sampling times will lead to relative underrepresentation of slow tissue exchange compartments, which would tend to reduce the impact of necrotic tissue on  $v_e$  estimations as described in several studies.<sup>42,47,48</sup> These potential model fitting errors and short sampling times imply that tumors with greater necrosis would have shown higher  $v_e$  values if sampling had continued for a longer time and that the measured values of  $v_e$  in this study are more likely to reflect the extravascular extracellular space fraction in viable tissue.

The positive correlation between  $v_e$  and mitotic activity is surprising. Tumors with larger  $v_e$  values exhibited more mitotic activity, the inverse of what one might expect (and the inverse of our initial hypothesis), whereby more proliferative tumors would be more densely packed with cells. Neither mitotic activity nor  $v_e$  related to the presence of necrosis, though the lack of a relationship between  $v_e$  and necrosis may, in part, reflect the relatively low dynamic collection period (see above). These observations suggest that the size of the extravascular extracellular space in perfused enhancing tumor tissue is truly related to mitotic rate and not simply a reflection of elevated measures of  $v_e$  due to increased necrosis in rapidly proliferating tumors.

This suggestion is initially counterintuitive. In normally developing tissues, mitotic activity is higher in areas of low cell packing due to the inhibition of proliferation in response to cell-to-cell contact, a process known as contact inhibition of proliferation in developing normal tissue.<sup>50</sup> No similar relationship has been described in malignant tissues, and loss of contact inhibition of mitosis is one of the hallmarks of the cancer cell.<sup>51</sup> This finding leads to the hypothesis, stated in the introduction, that rapidly proliferating

erating tumors will continue to proliferate, leading to increased cell density and a decreased size of the extravascular extracellular space and consequently of  $v_e$ . We have no evidence to explain why the observed relationship should exist. One possible explanation may be that tumors with high cellular density still have impaired responses to tumoral growth factors despite loss of contact inhibition of proliferation.<sup>52</sup> Another possible explanation is that tumors with short mitotic cycles are characterized by a reduced time for cellular maturation, resulting in smaller cells and reduced cell packing. Whatever the underlying biologic mechanism, this finding appears particularly interesting and requires further study.

The ability to obtain an MR imaging–based biomarker of mitotic activity and/or tumor cell proliferation is highly desirable. The findings presented here may be tumor-specific or reflect an unrecognized phenotype, but the possibility that  $v_e$  may be a potential marker of mitotic activity merits further evaluation.

The data also demonstrated a positive relationship between the presence of tumor cell fibrils within the histologic specimens and higher  $v_e$ , though the numbers were very small ( $n = 4$ ). Fibrillar cell processes are cell extensions containing cytoplasm, which are surrounded by cell membranes. These are visible through a microscope and allow tumor astrocytes to be recognized as “fibrillar.” A less cell-dense arrangement due to such cell extensions and/or intercellular edema facilitate its recognition via light microscopy. Thus, the ability to identify fibrillar cell processes suggests that the tumor cells are more loosely packed or that there is localized extracellular edema. No relationship was identified between fibrillar histology and mitotic activity, indicating that the relationships between  $v_e$  and these measures are independent.

Most previous work evaluating the relationship between specific histologic features and DCE-MR imaging has focused predominantly on CBV derived from DSC techniques with significant relationships seen among CBV and microvascular density,<sup>26–29</sup> VEGF expression,<sup>27,30</sup> cell density,<sup>29</sup> endothelial proliferation,<sup>31</sup> and mitotic activity.<sup>31</sup> No such relationships were identified between these latter 3 measures and  $v_p$  in this study. A study by Lüdemann et al<sup>53</sup> compared a variety of MR imaging techniques with  $H_2[^{15}O]$ -PET for measuring perfusion and found that while both DSC and T1-weighted DCE-MR imaging techniques correlated with the criterion standard  $H_2[^{15}O]$ -PET measure, only borderline correlation was seen between the DSC techniques and the T1-weighted technique, whereby DSC-derived blood volumes were generally lower than those derived from the T1-weighted DCE-MR imaging technique. This finding may account for the failure of  $v_p$  to relate to any of the histologic measures in this study.

The major limitation of the present work is the lack of stereotactic image–matched histologic specimens; therefore, correlation between the histology and the DCE-MR imaging measurements at a local level cannot be made. GBMs are notoriously heterogeneous tumors, and histologic analysis of small tumor specimens may lead to undergrading of a tumor if the sample is not a true reflection of the tumor as a whole. At the time of the study, image-matched histologic samples were not obtained and there was no concurrent postoperative imaging performed, which could have helped to identify the site of the histologic sample. All histologic specimens in this study did confirm the diagnosis of

GBM and therefore are considered representative samples. Previous nonimage-registered studies comparing  $v_e$  with histopathologic vascular measures have been reported, but these have been performed with a selection of 3–4 small ROIs, taking the maximal value of  $v_e$  and  $K^{trans}$ ,<sup>33,34</sup> which is unlikely to provide a representation of the tumor as a whole. In our current study, for the DCE-MR imaging measures  $K^{trans}$ ,  $v_e$ , and  $v_p$ , median values from whole-tumor VOIs were used. Studies using whole-tumor VOIs have previously identified significant differences in DCE-MR imaging parameters among tumor grades<sup>17</sup> and have been shown to convey important potential prognostic information.<sup>25</sup> Thus, a comparison between small histologic samples and DCE-MR imaging parameters from whole-tumor VOIs seems reasonable. Further work is required to confirm that the correlations identified in the current study hold true for image-matched stereotactic samples. In addition, some histologic features such as Ki-67 and VEGF expression, which have previously shown correlation with DSC-MR imaging–derived CBV,<sup>20,26–30</sup> were not available.

## CONCLUSIONS

The DCE-MR imaging–derived measure  $v_e$  has been identified as a potential correlate of mitotic activity in GBM. While this is an interesting result, our understanding of the biologic mechanisms responsible for this possible relationship is limited. Further work with the correlation of  $v_e$  to more precise measures of cell density, additional markers of cellular and vascular proliferation, and measures of VEGF expression is warranted.

Disclosures: Samantha J. Mills—RELATED: Grant: C21247/A7473 Cancer Research UK/RCR clinical training fellowship, September 2006 to March 2010.\* Giovanni Buonacorsi—RELATED: Grant: Cancer Research UK, Comments: salary paid by Cancer Research UK Programme grant via the University of Manchester; UNRELATED: Employment: Bioxydyn commenced since the completion of this work. Geoffrey J.M. Parker—UNRELATED: Board Membership: Bioxydyn, Comments: founder and CEO of Bioxydyn, a company with an interest in imaging biomarkers, including DCE-MRI, and their application to cancer and other conditions; Consultancy: GlaxoSmithKline, Comments: consultancy on advanced imaging methods for clinical trials; Employment: Bioxydyn, Comments: part-time employment as CEO of Bioxydyn, a company with an interest in imaging biomarkers, including DCE-MRI, and their application to cancer and other conditions; Grants/Grants Pending: Cancer Research UK,\* Engineering and Physical Sciences Research Council,\* Comments: Programme Grant and project grants to develop DCE-MRI and other MRI methods for use in cancer and neurologic conditions; Royalties: for DCE-MRI software, licensed via the University of Manchester; royalties shared between staff and the University; Stock/Stock Options: Bioxydyn, Comments: Bioxydyn is a company with an interest in imaging biomarkers, including DCE-MRI, and their application to cancer and other conditions. Alan Jackson—RELATED: Grant: Cancer Research UK.\* \*Money paid to the institution.

## REFERENCES

1. Louis DN, Ohgaki H, Wiestler OD, et al. **The 2007 WHO Classification of Tumours of the Central Nervous System.** *Acta Neuropathol* 2007;114:97–109 Medline
2. Struikmans H, Rutgers DH, Jansen GH, et al. **Prognostic relevance of MIB-1 immunoreactivity, S-phase fraction, 5-bromo-2'-deoxyuridine labeling indices, and mitotic figures in gliomas.** *Radiat Oncol Investig* 1999;7:243–48 Medline
3. Korshunov A, Golanov A, Sycheva R. **Immunohistochemical markers for prognosis of anaplastic astrocytomas.** *J Neurooncol* 2002;58:203–15 CrossRef Medline
4. Scott JN, Rewcastle NB, Brasher PM, et al. **Which glioblastoma multiforme patient will become a long-term survivor? A population-based study.** *Ann Neurol* 1999;46:183–88 Medline
5. Abdulrauf SI, Edvardsen K, Ho KL, et al. **Vascular endothelial**

- growth factor expression and vascular density as prognostic markers of survival in patients with low-grade astrocytoma. *J Neurosurg* 1998;88:513–20 CrossRef Medline
6. Yao Y, Kubota T, Takeuchi H, et al. Prognostic significance of microvessel density determined by an anti-CD105/endoglin monoclonal antibody in astrocytic tumors: comparison with an anti-CD31 monoclonal antibody. *Neuropathology* 2005;25:201–06 CrossRef Medline
  7. Preusser M, Gelpi E, Matej R, et al. No prognostic impact of survivin expression in glioblastoma. *Acta Neuropathol* 2005;109:534–38 CrossRef Medline
  8. Birner P, Piribauer M, Fischer I, et al. Vascular patterns in glioblastoma influence clinical outcome and associate with variable expression of angiogenic proteins: evidence for distinct angiogenic subtypes. *Brain Pathol* 2003;13:133–43 Medline
  9. Colman H, Giannini C, Huang L, et al. Assessment and prognostic significance of mitotic index using the mitosis marker phosphohistone H3 in low and intermediate-grade infiltrating astrocytomas. *Am J Surg Pathol* 2006;30:657–64 Medline
  10. Coleman KE, Brat DJ, Cotsonis GA, et al. Proliferation (MIB-1 expression) in oligodendrogliomas: assessment of quantitative methods and prognostic significance. *Appl Immunohistochem Mol Morphol* 2006;14:109–14 CrossRef Medline
  11. Flynn JR, Wang L, Gillespie DL, et al. Hypoxia-regulated protein expression, patient characteristics, and preoperative imaging as predictors of survival in adults with glioblastoma multiforme. *Cancer* 2008;113:1032–42 CrossRef Medline
  12. Karayan-Tapon L, Wager M, Guilhot J, et al. Semaphorin, neuropilin and VEGF expression in glial tumours: SEMA3G, a prognostic marker? *Br J Cancer* 2008;99:1153–60 CrossRef Medline
  13. Nam DH, Park K, Suh YL, et al. Expression of VEGF and brain specific angiogenesis inhibitor-1 in glioblastoma: prognostic significance. *Oncol Rep* 2004;11:863–69 Medline
  14. Oehring RD, Miletic M, Valter MM, et al. Vascular endothelial growth factor (VEGF) in astrocytic gliomas—a prognostic factor? *J Neurooncol* 1999;45:117–25 CrossRef Medline
  15. Tofts PS. Modeling tracer kinetics in dynamic Gd-DTPA MR imaging. *J Magn Reson Imaging* 1997;7:91–101 CrossRef Medline
  16. Law M, Yang S, Wang H, et al. Glioma grading: sensitivity, specificity, and predictive values of perfusion MR imaging and proton MR spectroscopic imaging compared with conventional MR imaging. *AJNR Am J Neuroradiol* 2003;24:1989–98 Medline
  17. Patankar TF, Haroon HA, Mills SJ, et al. Is volume transfer coefficient (K(trans)) related to histologic grade in human gliomas? *AJNR Am J Neuroradiol* 2005;26:2455–65 Medline
  18. Sugahara T, Korogi Y, Kochi M, et al. Correlation of MR imaging-determined cerebral blood volume maps with histologic and angiographic determination of vascularity of gliomas. *AJR Am J Roentgenol* 1998;171:1479–86 CrossRef Medline
  19. Roberts HC, Roberts TP, Brasch RC, et al. Quantitative measurement of microvascular permeability in human brain tumors achieved using dynamic contrast-enhanced MR imaging: correlation with histologic grade. *AJNR Am J Neuroradiol* 2000;21:891–99 Medline
  20. Roberts HC, Roberts TP, Bollen AW, et al. Correlation of microvascular permeability derived from dynamic contrast-enhanced MR imaging with histologic grade and tumor labeling index: a study in human brain tumors. *Acad Radiol* 2001;8:384–91 CrossRef Medline
  21. Law M, Young R, Babb J, et al. Comparing perfusion metrics obtained from a single compartment versus pharmacokinetic modeling methods using dynamic susceptibility contrast-enhanced perfusion MR imaging with glioma grade. *AJNR Am J Neuroradiol* 2006;27:1975–82 Medline
  22. Lev MH, Ozsunar Y, Henson JW, et al. Glial tumor grading and outcome prediction using dynamic spin-echo MR susceptibility mapping compared with conventional contrast-enhanced MR: confounding effect of elevated rCBV of oligodendrogliomas [corrected]. *AJNR Am J Neuroradiol* 2004;25:214–21 Medline
  23. Law M, Young RJ, Babb JS, et al. Gliomas: predicting time to progression or survival with cerebral blood volume measurements at dynamic susceptibility-weighted contrast-enhanced perfusion MR imaging. *Radiology* 2008;247:490–98 CrossRef Medline
  24. Cao Y, Tsien CI, Nagesh V, et al. Survival prediction in high-grade gliomas by MRI perfusion before and during early stage of RT [corrected]. *Int J Radiat Oncol Biol Phys* 2006;64:876–85 CrossRef Medline
  25. Mills SJ, Patankar TA, Haroon HA, et al. Do cerebral blood volume and contrast transfer coefficient predict prognosis in human glioma? *AJNR Am J Neuroradiol* 2006;27:853–58 Medline
  26. Cha S, Johnson G, Wadghiri YZ, et al. Dynamic, contrast-enhanced perfusion MRI in mouse gliomas: correlation with histopathology. *Magn Reson Med* 2003;49:848–55 CrossRef Medline
  27. Haris M, Husain N, Singh A, et al. Dynamic contrast-enhanced derived cerebral blood volume correlates better with leak correction than with no correction for vascular endothelial growth factor, microvascular density, and grading of astrocytoma. *J Comput Assist Tomogr* 2008;32:955–65 CrossRef Medline
  28. Liao W, Liu Y, Wang X, et al. Differentiation of primary central nervous system lymphoma and high-grade glioma with dynamic susceptibility contrast-enhanced perfusion magnetic resonance imaging. *Acta Radiol* 2009;50:217–25 CrossRef Medline
  29. Sadeghi N, D'Haene N, Decaestecker C, et al. Apparent diffusion coefficient and cerebral blood volume in brain gliomas: relation to tumor cell density and tumor microvessel density based on stereotactic biopsies. *AJNR Am J Neuroradiol* 2008;29:476–82 CrossRef Medline
  30. Maia AC Jr, Malheiros SM, da Rocha AJ, et al. MR cerebral blood volume maps correlated with vascular endothelial growth factor expression and tumor grade in nonenhancing gliomas. *AJNR Am J Neuroradiol* 2005;26:777–83 Medline
  31. Sadeghi N, Salmon I, Decaestecker C, et al. Stereotactic comparison among cerebral blood volume, methionine uptake, and histopathology in brain glioma. *AJNR Am J Neuroradiol* 2007;28:455–61 Medline
  32. Callot V, Galanaud D, Figarella-Branger D, et al. Correlations between MR and endothelial hyperplasia in low-grade gliomas. *J Magn Reson Imaging* 2007;26:52–60 CrossRef Medline
  33. Jia ZZ, Gu HM, Zhou XJ, et al. The assessment of immature microvascular density in brain gliomas with dynamic contrast-enhanced magnetic resonance imaging. *Eur J Radiol* 2015;84:1805–09 CrossRef Medline
  34. Li X, Zhu Y, Kang H, et al. Glioma grading by microvascular permeability parameters derived from dynamic contrast-enhanced MRI and intratumoral susceptibility signal on susceptibility weighted imaging. *Cancer Imaging* 2015;15:4 CrossRef Medline
  35. Mills SJ, Soh C, Rose CJ, et al. Candidate biomarkers of extravascular extracellular space: a direct comparison of apparent diffusion coefficient and dynamic contrast-enhanced MR imaging-derived measurement of the volume of the extravascular extracellular space in glioblastoma multiforme. *AJNR Am J Neuroradiol* 2010;31:549–53 CrossRef Medline
  36. Aryal MP, Nagaraja TN, Keenan KA, et al. Dynamic contrast enhanced MRI parameters and tumor cellularity in a rat model of cerebral glioma at 7 T. *Magn Reson Med* 2014;71:2206–14 CrossRef Medline
  37. Bastin ME, Carpenter TK, Armitage PA, et al. Effects of dexamethasone on cerebral perfusion and water diffusion in patients with high-grade glioma. *AJNR Am J Neuroradiol* 2006;27:402–08 Medline
  38. Thompson G, Cain J, Jackson A, et al. Interobserver agreement for cerebral glioma volumetrics on conventional MR imaging. In: *Proceedings of the 16th Scientific Meeting and Exhibition of the International Society for Magnetic Resonance in Medicine*, Toronto, Ontario, Canada. May 3–9, 2008
  39. Parker GJ, Jackson A, Waterton JC. Automated arterial input function extraction for T1-weighted DCE-MRI. In: *Proceedings of the 11th Scientific Meeting and Exhibition of the International Society for*

*Magnetic Resonance in Medicine*, Toronto, Ontario, Canada. July 10–16, 2003

40. Mills SJ, Soh C, O'Connor JP, et al. **Tumour enhancing fraction (EnF) in glioma: relationship to tumour grade.** *Eur Radiol* 2009;19:1489–98 CrossRef Medline
41. O'Connor JP, Jackson A, Parker GJM, et al. **DCE-MRI biomarkers in the clinical evaluation of antiangiogenic and vascular disrupting agents.** *Br J Cancer* 2007;96:189–95 CrossRef Medline
42. Lüdemann L, Grieger W, Wurm R, et al. **Quantitative measurement of leakage volume and permeability in gliomas, meningiomas and brain metastases with dynamic contrast-enhanced MRI.** *Magn Reson Imaging* 2005;23:833–41 CrossRef Medline
43. Zhu XP, Li KL, Kamaly-Asl ID, et al. **Quantification of endothelial permeability, leakage space, and blood volume in brain tumors using combined T1 and T2\* contrast-enhanced dynamic MR imaging.** *J Magn Reson Imaging* 2000;11:575–85 Medline
44. Lüdemann L, Grieger W, Wurm R, et al. **Comparison of dynamic contrast-enhanced MRI with WHO tumor grading for gliomas.** *Eur Radiol* 2001;11:1231–41 CrossRef Medline
45. Andersen C, Jensen FT. **Differences in blood-tumour-barrier leakage of human intracranial tumours: quantitative monitoring of vasogenic oedema and its response to glucocorticoid treatment.** *Acta Neurochir (Wien)* 1998;140:919–24 CrossRef Medline
46. Armitage PA, Schwindack C, Bastin ME, et al. **Quantitative assessment of intracranial tumor response to dexamethasone using diffusion, perfusion and permeability magnetic resonance imaging.** *Magn Reson Imaging* 2007;25:303–10 CrossRef Medline
47. Fluckiger JU, Loveless ME, Barnes SL, et al. **A diffusion-compensated model for the analysis of DCE-MRI data: theory, simulations and experimental results.** *Phys Med Biol* 2013;58:1983–98 CrossRef Medline
48. Lüdemann L, Hamm B, Zimmer C. **Pharmacokinetic analysis of glioma compartments with dynamic Gd-DTPA-enhanced magnetic resonance imaging.** *Magn Reson Imaging* 2000;18:1201–14 CrossRef Medline
49. Cheng HL. **Investigation and optimization of parameter accuracy in dynamic contrast-enhanced MRI.** *J Magn Reson Imaging* 2008;28:736–43 CrossRef Medline
50. McClatchey AI, Yap AS. **Contact inhibition (of proliferation) redux.** *Curr Opin Cell Biol* 2012;24:685–94 CrossRef Medline
51. Tumanishvili GD, Salamatina NV. **Action of nuclear and cytoplasmic fractions of liver homogenate on liver growth in the chick embryo.** *J Embryol Exp Morphol* 1968;20:53–71 Medline
52. Mayor R, Carmona-Fontaine C. **Keeping in touch with contact inhibition of locomotion.** *Trends Cell Biol* 2010;20:319–28 CrossRef Medline
53. Lüdemann L, Warmuth C, Plotkin M, et al. **Brain tumor perfusion: comparison of dynamic contrast enhanced magnetic resonance imaging using T1, T2, and T2\* contrast, pulsed arterial spin labeling, and H2(15)O positron emission tomography.** *Eur J Radiol* 2009;70:465–74 CrossRef Medline

# Identifying Significant Changes in Cerebrovascular Reactivity to Carbon Dioxide

O. Sobczyk, A.P. Crawley, J. Poubanc, K. Sam, D.M. Mandell, D.J. Mikulis, J. Duffin, and J.A. Fisher



## ABSTRACT

**BACKGROUND AND PURPOSE:** Changes in cerebrovascular reactivity can be used to assess disease progression and response to therapy but require discrimination of pathology from normal test-to-test variability. Such variability is due to variations in methodology, technology, and physiology with time. With uniform test conditions, our aim was to determine the test-to-test variability of cerebrovascular reactivity in healthy subjects and in patients with known cerebrovascular disease.

**MATERIALS AND METHODS:** Cerebrovascular reactivity was the ratio of the blood oxygen level–dependent MR imaging response divided by the change in carbon dioxide stimulus. Two standardized cerebrovascular reactivity tests were conducted at 3T in 15 healthy men ( $36.7 \pm 16.1$  years of age) within a 4-month period and were coregistered into standard space to yield voxelwise mean cerebrovascular reactivity interval difference measures, composing a reference interval difference atlas. Cerebrovascular reactivity interval difference maps were prepared for 11 male patients. For each patient, the test-retest difference of each voxel was scored statistically as z-values of the corresponding voxel mean difference in the reference atlas and then color-coded and superimposed on the anatomic images to create cerebrovascular reactivity interval difference z-maps.

**RESULTS:** There were no significant test-to-test differences in cerebrovascular reactivity in either gray or white matter (mean gray matter,  $P = .431$ ; mean white matter,  $P = .857$ ; paired  $t$  test) in the healthy cohort. The patient cerebrovascular reactivity interval difference z-maps indicated regions where cerebrovascular reactivity increased or decreased and the probability that the changes were significant.

**CONCLUSIONS:** Accounting for normal test-to-test differences in cerebrovascular reactivity enables the assessment of significant changes in disease status (stability, progression, or regression) in patients with time.

**ABBREVIATIONS:** BOLD = blood oxygen level–dependent; CO<sub>2</sub> = carbon dioxide; CVR = cerebrovascular reactivity; EC-IC = extracranial to intracranial; ID = interval difference; PaCO<sub>2</sub> = arterial partial pressure of carbon dioxide; PetCO<sub>2</sub> = end-tidal partial pressure of carbon dioxide

Knowledge of the repeatability of any test is crucial for assessing not only the progress of a disease with time but also the effects of any therapeutic intervention. Cerebrovascular reactivity (CVR) is a test indicating the magnitude of CBF responses to a

vasoactive stimulus. Reductions in CVR have been shown to indicate an enhanced risk of stroke<sup>1–3</sup> and reduced cognitive ability.<sup>4</sup> There are currently a number of techniques for mapping CVR. We have found blood oxygen level–dependent (BOLD) MR imaging signal intensity during arterial partial pressure of carbon dioxide (PaCO<sub>2</sub>) manipulation a reliable measure of CVR. Our CVR test is, in effect, a cerebrovascular “stress test,” in which occult regional limitations of hemodynamic reserve can be mapped using MR imaging of a stimulated global increase in CBF.<sup>5–7</sup>

### Clinical Aspects of CVR Maps

Clinically significant changes in CVR maps must be distinguishable from the normal variation in CVR due to equipment variability, artifacts such as patient movement, and normal day-to-day physiologic variability. If we consider a longitudinal study of a group of patients undergoing an intervention in which we wish to test the effectiveness of the intervention, performing a paired  $t$  test

Received July 22, 2015; accepted after revision October 23.

From the Institute of Medical Science (O.S., D.J.M., J.A.F.) and Department of Physiology (K.S., J.D., J.A.F.), University of Toronto, Toronto, Canada; and Joint Department of Medical Imaging and the Functional Neuroimaging Laboratory (A.P.C., J.P., K.S., D.M.M., D.J.M.) and Department of Anaesthesia and Pain Management (J.D., J.A.F.), University Health Network, Toronto, Canada.

J.A.F. is Chief Scientist and J.D. is Senior Scientist at Thornhill Research, a spin-off company from the University Health Network that developed the RespirAct. RespirAct is currently a noncommercial research tool assembled and made available by Thornhill Research to research institutions to enable CVR studies.

Please address correspondence to Olivia Sobczyk, MSc, Institute of Medical Science, Medical Sciences Building, One King's College Circle, University of Toronto, Toronto, ON, Canada, M5S 1A8; e-mail: o.pucci@mail.utoronto.ca

 Indicates article with supplemental on-line table.

 Indicates article with supplemental on-line photo.

<http://dx.doi.org/10.3174/ajnr.A4679>

would account for this background variability. In the case of a single patient whose improvement in CVR after an intervention is to be evaluated, we used a group of healthy control subjects to provide an equivalent statistical yardstick to test the significance of the measured change in CVR relative to the expected reproducibility of the test. To that end, we have standardized the PaCO<sub>2</sub> stimulus, a critical component for developing test-to-test reliability, MR imaging sequence parameters, and data analysis.<sup>8-10</sup> Once this step has been performed, quantization of the unavoidable background variability in CVR “noise” can be ascertained. We hypothesize that the variations in CVR outside the range of these normal test-to-test changes will be attributable to pathophysiologic changes.

### Study Aim

Therefore, our aim in this study was to develop and test a quantitative method for detecting significant within-subject changes in CVR with time. We created a voxelwise CVR test-to-test interval difference (ID) atlas for healthy subjects (CVR ID atlas). We used the SD of the CVR ID atlas to score the probability that the voxelwise differences between 2 CVR studies for a patient would exceed the normal variation (ie, z scores). We report on the use of this method to monitor the changes with time in CVR in 11 patients with intracranial steno-occlusive disease, most of whom had undergone revascularization procedures.

## MATERIALS AND METHODS

### Subjects and Ethics Approval

All studies conformed to the standards set by the latest revision of the Declaration of Helsinki and were approved by the Research Ethics Board of the University Health Network and Health Canada. All subjects gave written and informed consent. We recruited 15 healthy male subjects (mean age, 36.7 ± 16.1 years), with no history of neurologic or cardiovascular disease, who were non-smokers and were taking no medication, to generate the CVR ID atlas described below. They were asked not to engage in heavy exercise or drink caffeinated drinks on the day of the test. For the patient examples, we searched our database of the research ethics board–approved CVR studies in male subjects (to minimize hormonal effects on CVR) with chronic cerebrovascular disease (*n* = 11) who had undergone ≥2 CVR examinations.

### Experimental Protocol

**Hypercapnic Stimulus.** Subjects were fitted with a facemask and connected to a sequential gas-delivery breathing circuit.<sup>11</sup> The patterns of end-tidal partial pressure of carbon dioxide (PetCO<sub>2</sub>) and end-tidal partial pressure of oxygen were programmed into the automated gas blender (RespirAct; Thornhill Research, Toronto, Ontario, Canada) running the prospective gas-targeting algorithm of Slessarev et al.<sup>12</sup> A standardized step carbon dioxide (CO<sub>2</sub>) stimulus sequence was implemented, consisting of the following: a baseline PetCO<sub>2</sub> of 40 mm Hg for 60 seconds, step to a hypercapnia of 50 mm Hg for 45 seconds, baseline for 90 seconds, hypercapnia for 120 seconds, and return to baseline for 60 seconds, all during isoxic normoxia. The implementation of prospective end-tidal gas control is described in greater detail by Slessarev et al.<sup>12</sup>

**Table 1: Duration between CVR T1 scan and CVR T2 scan for each of the 15 healthy subjects in the ID CVR atlas**

Subject No.	Time between T1 and T2
1	12 Weeks
2	4 Weeks
3	8 Weeks
4	2 Weeks
5	4 Weeks
6	8 Weeks
7	16 Weeks
8	2 Weeks
9	4 Weeks
10	4 Weeks
11	16 Weeks
12	2 Weeks
13	4 Weeks
14	12 Weeks
15	2 Weeks

**Note:**—T1 indicates time point 1; T2, time point 2.

**MR Imaging Protocol and CVR Map Generation.** MR imaging was performed with a 3T scanner (Signa; GE Healthcare, Milwaukee, Wisconsin) with an 8-channel phased array head coil and consisted of BOLD acquisitions using a gradient-echo pulse sequence with an echo-planar readout (TR/TE, 2000/30 ms; FOV, 24 × 24 cm; matrix size, 64 × 64; number of temporal frames, 254; 39 sections; section thickness, 5 mm; no intersection gap; and flip angle, 85°). The acquired MR imaging and PetCO<sub>2</sub> data were analyzed using Analysis of Functional NeuroImages software (AFNI; <http://afni.nimh.nih.gov/afni>).<sup>13</sup> PetCO<sub>2</sub> data were time-shifted to the point of maximum correlation with the voxel showing the greatest positive BOLD signal change and were resampled at the TR. A linear, least-squares fit of the BOLD signal data series to the PetCO<sub>2</sub> data series was then performed on a voxel-by-voxel basis. BOLD images were then volume-registered and section-time corrected and coregistered to an axial 3D T1-weighted inversion recovery fast-spoiled gradient-recalled volume (TI/TR/TE, 450/8/3 ms; matrix size, 256 × 256; FOV, 22 × 22 cm; section thickness, 1 mm; and flip angle, 15°), which was acquired in the same imaging session.<sup>14</sup> The slope of the linear relation between the BOLD signal and the PetCO<sub>2</sub> was color-coded to a spectrum of colors corresponding to the direction (positive or negative) and the magnitude of the correlation and overlaid on the corresponding structural scans to form CVR maps. All voxels with correlation coefficients between −0.125 and +0.125 were thresholded from the maps. All subjects and patients had <3 mm head movement in any direction during the scanning.

### Analyzing the CVR Maps

**Repeatability and Construction of the ID CVR Atlas.** The 15 healthy subjects underwent 2 CVR measurements within a 4-month interval to mimic the times usually implemented for our patient CVR measurements pre- and postsurgical intervention (see Table 1 for between-study time intervals for the healthy subjects). Regional measures of CVR were obtained by segmenting the anatomic images into gray and white matter regions (SPM8 software; <http://www.fil.ion.ucl.ac.uk/spm/software/spm8>).

Construction of the CVR ID atlas proceeded by first coregistering all datasets into Montreal Neurological Institute standard

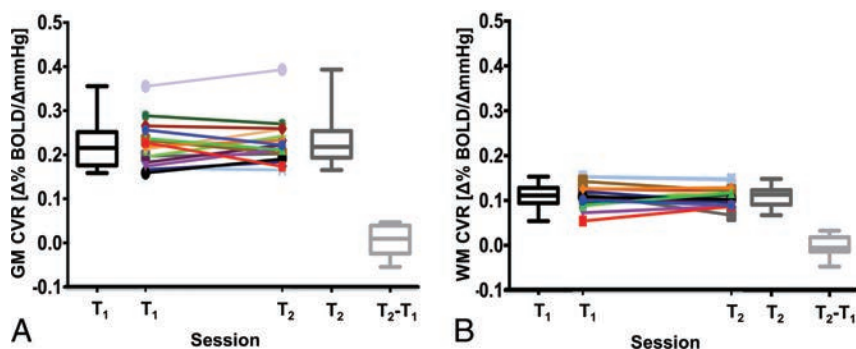


**FIG 1.** Comparison of CVR test 1 and CVR test 2 for gray matter (A) and white matter (B) for each of the 15 healthy subjects in the ID CVR atlas. There were no significant differences between tests (mean gray matter,  $P = .431$ ; mean white matter,  $P = .857$ ). The horizontal line in the box represents the median, the box represents the interquartile range (25% to 75%), and the whiskers represent the minimum and maximum values. T1 indicates time point session 1; T2, time point session 2.

**Table 2: Mean (SEM) CVR between days and mean (SEM) CV for the gray and white matter regions of the healthy cohort**

	Gray Matter	White Matter
Mean CVR ( $\Delta$ % BOLD/ $\Delta$ mm Hg)	0.228 (0.01)	0.117 (0.001)
Mean CV (%)	7.3 (1.33)	10.3 (2.19)

**Note:**—CV indicates coefficient of variation; SEM, standard error of the mean.

space (as defined by a T1-weighted Montreal Neurological Institute 152 standard template)<sup>15,16</sup> and then by calculating a voxel-wise difference in CVR values between the 2 time points in each of the 15 subjects. From these difference maps, a spatial smoothing of full width at half maximum at 5 mm was applied to each voxel. The difference, mean, and SD over all subjects for each voxel (AFNI software)<sup>13</sup> were calculated to produce the test-to-test CVR ID atlas. Comparisons with time for systematic differences in the CVR scans were evaluated by using paired Student  $t$  tests (significance,  $P < .05$ ). Coefficients of variation for gray and white matter were evaluated as estimates of repeatability (SigmaPlot 12.5; Systat Software, San Jose, California).

**CVR ID Z-Maps.** After spatial normalization, test-to-test CVR differences were calculated for 10 male patients who underwent repeated CVR studies within a year (On-line Figure) and 1 male patient who underwent 5 CVR scans during a 3-year period, to produce their CVR ID maps. Because CVR changes little with age, we did not expect systematic differences in CVR in healthy subjects during the 4-month range of repeat studies, and indeed there were none ( $P > .05$ , paired Student  $t$  test). The differences that we saw were due to small errors in coregistration, partial voluming effects, and day-to-day physiologic changes in the subjects and in the hardware. Because they do not represent real systematic differences, the mean ID values would trend to zero with larger subject cohorts. The assumption of zero as the sample mean difference produces an unbiased, estimate of the SD. The  $z$  scores for these patients were calculated voxel-by-voxel as the difference between the patient CVR ID values and those of the reference cohort (ie, zero) divided by the CVR ID atlas SD. The resulting CVR ID  $z$  scores indicate the statistical probability that the magnitude of the CVR interval differences was outside the normal range. These calculated CVR ID  $z$  scores were then color-coded (On-line Figure and On-line Table<sup>10</sup>) and superimposed on the anatomic images to produce CVR ID

$z$ -maps showing the distribution and statistical significance of changes in the patient CVRs with time.

## RESULTS

### Normal Repeatability

Figure 1 presents the distribution of the mean CVR values for both gray and white matter for each CVR test in the 15 control subjects. The overall mean CVR and coefficient of variation reproducibility measures for gray and white matter are presented in Table 2. On average, CVR measures were repeatable in both gray (coefficient of variation = 7.3%) and white matter (coefficient of variation = 10.3%), consistent with repeatability measurements found in a previous study using the same CVR measurement method.<sup>17</sup> The paired Student  $t$  test found no significant systematic differences between the CVR scans.

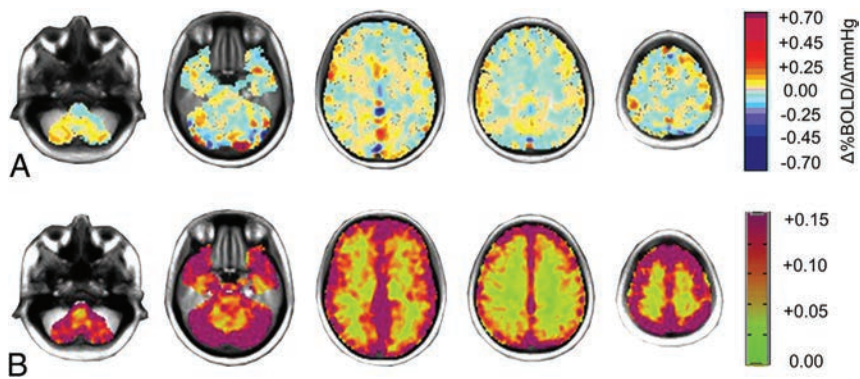
### ID Atlas Characteristics

Figure 2 shows the spatial distribution of the CVR ID atlas mean and SD test-to-test differences. The mean differences (Fig 2A) are close to zero, with the highest differences located in the superior sagittal sinus. Mean CVR differences ( $\pm$  standard error of the mean) in the ID atlas for gray matter were found to be  $0.0057 \pm 0.013$  and  $0.0047 \pm 0.010$  for white matter. Areas with the highest test-to-test differences in the CVR ID atlas (Fig 2B) were found in the cortex and regions with large veins.

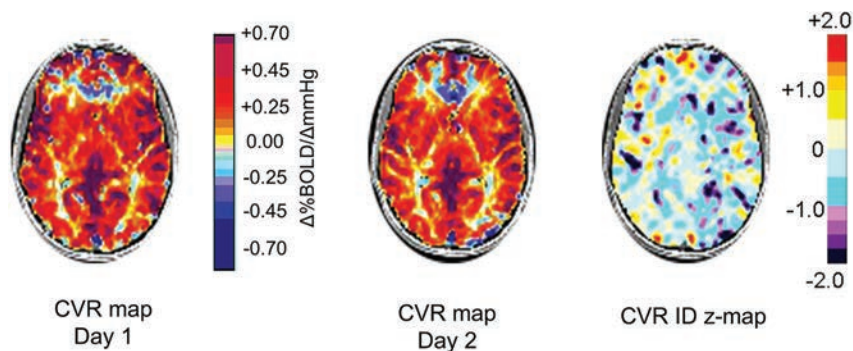
### ID Z-Map Examples

Figure 3 shows an application of the CVR ID atlas to assess changes in CVR with time in a healthy subject (not included in the CVR ID atlas).

Figure 4 shows the application of the CVR ID atlas to assess changes in CVR with time in a patient drawn from our data base (more patient examples are shown in the On-line Figure and On-line Table) with right extracranial to intracranial (EC-IC) bypass surgery. MR angiography shows complete right ICA occlusion and 90% left ICA stenosis preoperatively. Postoperatively, the patient continued to experience episodes of right hemisphere transient ischemic attacks. Their CVR map determined 1 month before surgery (Fig 4A) showed decreased CVR in the right hemisphere. CVR measured 4 months postoperatively (Fig 4B) shows improvement. The CVR ID  $z$ -map shows the distribution of the interval changes and indicates the probability that these changes are due to the normal test-to-test variability. The second follow-up CVR (Fig 4C) performed 3 months later shows regression of the CVR. Additional follow-up CVR studies (Fig 4D, -E) show that further changes in CVR were small and were mostly in the range of normal test-to-test variability. Figure 4F compares study A with study E, or the net change in CVR for the duration. It indicates that despite the regression of CVR in many areas following the operation, there are residual areas of increased CVR compared with the preoperative study.



**FIG 2.** Axial sections displaying the spatial distribution of the healthy cohort. A, The mean difference in CVR between the 2 CVR tests colored according to the scale shown on the right in percentage change of BOLD per millimeter-of-mercury change in PetCO<sub>2</sub>. B, The SD of CVR differences. The color scale is on the right.



**FIG 3.** An axial section from the midbrain of a healthy subject's CVR maps measured 2 months apart. These CVR measurements show the spatial distribution of CVR values colored according to the scale shown (percentage change of BOLD per millimeter-of-mercury change in PetCO<sub>2</sub>). The corresponding CVR ID z-map is shown on the right. The CVR ID z-map provides a perspective of the statistically normal differences in CVR with time.

## DISCUSSION

### Identifying Significant Changes with Time

In this article, we introduce a statistical analytic method for determining the voxelwise probability of a change in CVR between 2 scans: the CVR ID z-map. We minimized the test-to-test variability by standardizing what has previously been a major source of variability: the vasoactive stimulus.<sup>18</sup> With most methods, the partial pressure of CO<sub>2</sub> of the hypercapnic stimulus varies widely.<sup>19,20</sup> In this study, the stimulus was a precisely ( $\pm 2$  mm Hg) repeatable change in PaCO<sub>2</sub>. In a previous study, a patient's CVR scan was scored relative to a reference atlas to identify abnormal regions.<sup>8</sup> That was a cross-sectional atlas designed to score the probability of CVR values differing from normal in a single patient; in contrast, the present CVR ID atlas provides the significance of CVR changes between  $\geq 2$  tests in a single patient with time. This capability of identifying changes between CVR tests is necessary for longitudinal studies, such as following the progress of disease and determining the effects of interventions.

### Minimizing Variability in CVR Tests due to Variation in the Stimulus

Mapping cerebrovascular reactivity requires a vasoactive stimulus that applies to the entire brain. Infusing pharmacologic vasoactive agents such as acetazolamide results in a variability of blood levels with time and between subjects—even with standardized doses;

there is even a variation of the vasodilatory response to a given blood level (see Fierstra et al<sup>19</sup> for a discussion). By contrast, using hypercapnia as the vasoactive stimulus<sup>21</sup> can result in a more reliable response. The drawback of using hypercapnia as the vasoactive stimulus is the difficulty in repeatedly attaining a target PaCO<sub>2</sub>. Infusing CO<sub>2</sub> into a face mask,<sup>22</sup> inhaling a fixed concentration of CO<sub>2</sub>,<sup>23</sup> or simply breath-holding<sup>24</sup> do not produce a reproducible stimulus and cannot even provide a reliable measure of the change in the PaCO<sub>2</sub>.<sup>18,25</sup> Therefore, we used a computer-controlled gas blender in this study to prospectively target a PetCO<sub>2</sub> that was equilibrated with PaCO<sub>2</sub>.<sup>26</sup>

This methodology enabled repeat administration of a standardized stimulus (from baseline PetCO<sub>2</sub> at  $40.2 \pm 1.1$  mm Hg to  $49.9 \pm 1.5$  mm Hg) and thereby minimized the stimulus variability in the atlas and individual patient CVR tests. Our test is focused on showing that the repeatability of a CVR test provides the potential for clinical application, regardless of the type of stimulus used. The greater the variability in the stimulus, the larger the SD is for each voxel in the ID atlas and the lower the sensitivity for detecting changes in CVR. The versatility in this approach is that each institution,

by standardizing its own acquisition sequences and vasoactive stimulus, can obtain its own custom reference atlas, and the z scores of the institution would be comparable with those of any other institution.<sup>27</sup>

### Accounting for Variability in CVR Tests due to Signal Variation

Despite the precise designation of the MR imaging sequences and data analysis, there are nevertheless technical causes for variation in the CVR measurements. During acquisition, the BOLD signal can be affected by drift that has no consistent pattern or direction with time. In addition, there is day-to-day physiologic variability in vascular reactivity. The CVR ID atlas incorporates these variabilities so that CVR ID z-maps provide a confidence interval for identifying changes other than those attributable to these factors. The choice of thresholds for test-to-test difference determines the balance between sensitivity and specificity.

### Change in CVR with Time in Patients with Cerebrovascular Disease

In the patients we studied (On-line Figure and On-line Table), the symptoms were mild and transient. In contrast, the obstructions to the vessels as seen on angiography were severe. The CVR mea-

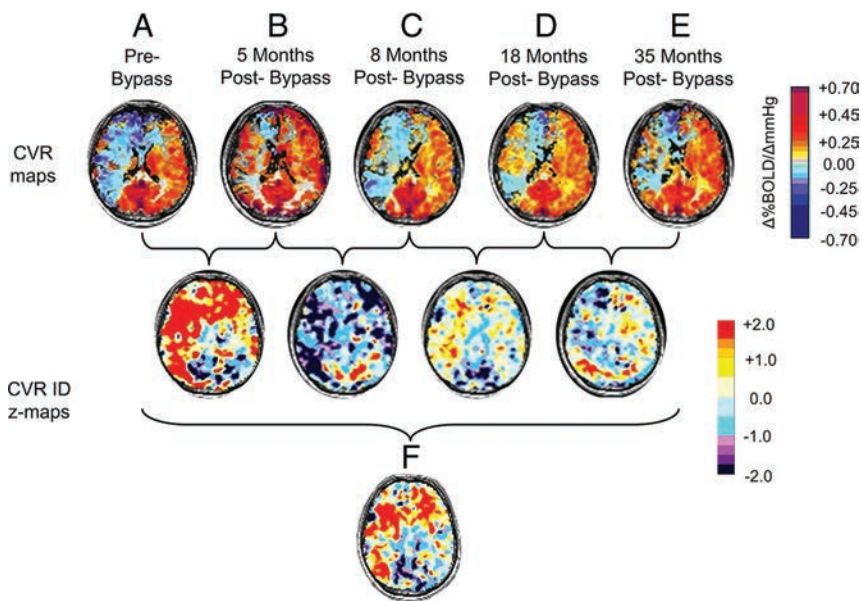


**FIG 4.** Longitudinal changes in CVR for a 56-year-old man with bilateral ICA stenosis who underwent right EC-IC bypass. Axial sections of CVR maps (*upper row*) with the color scale are shown on the right (percentage change of BOLD per millimeter-of-mercury change in  $\text{PetCO}_2$ ). A, CVR map 1 month prior to surgery; B, CVR measured 4 months postoperatively; C, second follow-up CVR measured 8 months postoperatively; D and E, additional follow-up CVR maps measured 18 and 35 months postoperatively. Their corresponding CVR ID z-maps are found in the *second and third rows*, as indicated by the *brackets*. F is an ID z-map that compares study A with study E, or the net change in CVR for the entire duration. See text for interpretations.

measurements were more physiologic in nature, reflecting the balance of blood flow resulting from the establishment of spontaneously developing and surgically established collateral blood flow. In these patients, the CVR ID z-maps indicated the significant changes in CVR with time, adding to the assessment of the success of surgical interventions. This ability is well-illustrated in the patient shown in Fig 4. In this patient, bypass revascularization surgery transiently improved CVR, but not to normal values. Thereafter, however, the CVR ID z-maps showed the degree and extent to which CVR progressively declined to a stable level at the final follow-up scan. The patient continuing to be symptomatic is also consistent with the CVR scans.

### Limitations

Accurate measurement of CBF in advanced cerebrovascular disease is difficult. PET remains the criterion standard, and current MR imaging vendor implementations of arterial spin-labeling have yet to be proved/validated for clinical use.<sup>28</sup> The use of BOLD as a surrogate measure of CBF is common and has been shown to correlate well with other modalities, including FAIR arterial spin-labeling<sup>29</sup> (also see Duffin et al<sup>9</sup> and Tancredi et al<sup>30</sup> for discussions). Nevertheless, the relationship between blood flow and BOLD is nonlinear.<sup>31,32</sup> The atlas approach helps to mitigate this issue. In this article, the z scores account for the limitations of BOLD reflecting CBF because this measure of CBF was used in both the patient studies and the atlas. As improved methods of measuring CBF become available, the same analysis methodology can also be applied.

Within-subject variability of CVR may differ more with age and sex than in the men in our reference cohort.<sup>33</sup> In this study, we examined male subjects and used only men for our reference

atlas. Nevertheless, we note that the between-day differences in CVR in women studied with a methodology similar to ours found no significant interval differences.<sup>17</sup> Our reference CVR ID atlas was not selected for a specific age group (mean age,  $36.7 \pm 16.1$ ), and neither was our patient cohort. The effect of age on CVR is unclear. Some studies found reductions in CVR<sup>34,35</sup>; we and others found no correlation between age and CVR.<sup>27,36</sup> However, the question is not whether age is a factor in CVR but whether age is a factor in test-retest differences obtained within a matter of a few months. There is no reason to suppose that interval differences in healthy subjects differ greatly with age.

Another limitation to the sensitivity of this study is the variation in the time differences between measurements. Test-to-test differences due to the variable duration between tests are probably of the same order of magnitude as those due to discrepancies in sex, comorbidities, or other anthropomorphic factors. Such unaccounted for discrepancies will

further reduce the sensitivity and increase specificity of the atlas by reducing the ID z-values.

In our CVR ID z-map approach, it is assumed that the range of test-to-test variability in CVR found in the abnormal areas of our patient group is the same as that in healthy tissue. We therefore assume that any changes in the abnormal tissue CVR with time due to a pathological process will be greater than changes in normal tissue, ensuring the ability of the CVR ID z-maps to distinguish true pathologic changes in abnormal areas. Nevertheless, further investigation may be required to determine the “normal” variability in abnormal areas. For this measurement, patient scans should be repeated within a short time (eg, <1 week), within which no substantial change would be expected in, for example, patients who are stable and not candidates for revascularization. Their CVR ID z-maps would reflect the normal variability in abnormal areas. Such measurements are shown in Fig 4, where CVR ID z-maps show no changes between C and D, and D and E.

Finally, a key confounding factor that affects CVR interpretation is blood pressure.<sup>37</sup> However, we were not able to measure blood pressure due to the constraints imposed by the MR imaging environment on this measurement. Accurate frequent blood pressure sampling in the MR imaging environment would aid in assessing the sensitivity of the CVR ID z scoring in the future.

### CONCLUSIONS

CVR ID z-maps are a secondary analysis of CVR maps that provides a statistical approach to separate test-to-test differences due to technical and physiologic changes with time from those due to changes in the underlying pathophysiology, informing the clinical assessment of disease activity and the response to treatment. The patients we present underwent considerable

changes in CVR. The lower the likelihood that these changes represent test-to-test variability, the more likely they are to represent underlying pathophysiology, despite few overt changes in symptoms. We therefore suggest that the advanced analysis of the CVR data by using CVR ID z-maps introduced in this article can improve assessment of longitudinal subclinical pathophysiologic changes that are difficult to gauge by using angiography and CVR maps alone.

## ACKNOWLEDGMENTS

The authors thank Toronto Western Hospital MR imaging technologist Eugen Hlasny for his help in acquiring the MR imaging data and clinical coordinator Abby Skanda for her help with study organization.

Disclosures: Olivia Sobczyk—UNRELATED: Consultancy/Employment: I am a consultant (part-time) of Thornhill Research, whose parent company owns intellectual property on the RespirAct device used in the study. James Duffin—UNRELATED: Employment, Patents (planned, pending or issued), Stock/Stock Options: Thornhill Research. Joseph A. Fisher—RELATED: Consulting Fee or Honorarium: The device that was used to control blood gases in the CVR experiments in this study is a custom prototype built by Thornhill Research, which is a spin-off of the University Health Network. I am also one of the inventors of this device and the chief scientist at Thornhill Research.

## REFERENCES

- Markus H, Cullinane M. Severely impaired cerebrovascular reactivity predicts stroke and TIA risk in patients with carotid artery stenosis and occlusion. *Brain* 2001;124:457–67 CrossRef Medline
- Ogasawara K, Ogawa A, Yoshimoto T. Cerebrovascular reactivity to acetazolamide and outcome in patients with symptomatic internal carotid or middle cerebral artery occlusion: a xenon-133 single-photon emission computed tomography study. *Stroke* 2002;33:1857–62 CrossRef Medline
- Sasoh M, Ogasawara K, Kuroda K, et al. Effects of EC-IC bypass surgery on cognitive impairment in patients with hemodynamic cerebral ischemia. *Surg Neurol* 2003;59:455–60; discussion 460–63 CrossRef Medline
- Silvestrini M, Viticchi G, Falsetti L, et al. The role of carotid atherosclerosis in Alzheimer's disease progression. *J Alzheimers Dis* 2011;25:719–26 CrossRef Medline
- Han JS, Mandell DM, Poublanc J, et al. BOLD-MRI cerebrovascular reactivity findings in cocaine-induced cerebral vasculitis. *Nat Clin Pract Neurol* 2008;4:628–32 CrossRef Medline
- Fierstra J, Poublanc J, Han JS, et al. Steal physiology is spatially associated with cortical thinning. *J Neurol Neurosurg Psychiatry* 2010;81:290–93 CrossRef Medline
- Mandell DM, Han JS, Poublanc J, et al. Quantitative measurement of cerebrovascular reactivity by blood oxygen level-dependent MR imaging in patients with intracranial stenosis: preoperative cerebrovascular reactivity predicts the effect of extracranial-intracranial bypass surgery. *AJNR Am J Neuroradiol* 2011;32:721–27 CrossRef Medline
- Sobczyk O, Battisti-Charbonney A, Fierstra J, et al. A conceptual model for CO<sub>2</sub>-induced redistribution of cerebral blood flow with experimental confirmation using BOLD MRI. *Neuroimage* 2014;92:56–68 CrossRef Medline
- Duffin J, Sobczyk O, Crawley AP, et al. The dynamics of cerebrovascular reactivity shown with transfer function analysis. *Neuroimage* 2015;114:207–16 CrossRef Medline
- Poublanc J, Crawley AP, Sobczyk O, et al. Measuring cerebrovascular reactivity: the dynamic response to a step hypercapnic stimulus. *J Cereb Blood Flow Metab* 2015;35:1746–56 CrossRef Medline
- Sommer LZ, Iscoe S, Robicsek A, et al. A simple breathing circuit minimizing changes in alveolar ventilation during hyperpnoea. *Eur Respir J* 1998;12:698–701 CrossRef Medline
- Slessarev M, Han J, Mardimae A, et al. Prospective targeting and control of end-tidal CO<sub>2</sub> and O<sub>2</sub> concentrations. *J Physiol* 2007;581:1207–19 CrossRef Medline
- Cox RW. AFNI: software for analysis and visualization of functional magnetic resonance neuroimages. *Comput Biomed Res* 1996;29:162–73 CrossRef Medline
- Saad ZS, Glen DR, Chen G, et al. A new method for improving functional-to-structural MRI alignment using local Pearson correlation. *Neuroimage* 2009;44:839–48 CrossRef Medline
- Ashburner J, Friston K. Multimodal image coregistration and partitioning: a unified framework. *Neuroimage* 1997;6:209–17 CrossRef Medline
- Ashburner J, Friston KJ. Nonlinear spatial normalization using basis functions. *Hum Brain Mapp* 1999;7:254–66 Medline
- Kassner A, Winter JD, Poublanc J, et al. Blood-oxygen level dependent MRI measures of cerebrovascular reactivity using a controlled respiratory challenge: reproducibility and gender differences. *J Magn Reson Imaging* 2010;31:298–304 CrossRef Medline
- Mark CI, Slessarev M, Ito S, et al. Precise control of end-tidal carbon dioxide and oxygen improves BOLD and ASL cerebrovascular reactivity measures. *Magn Reson Med* 2010;64:749–56 CrossRef Medline
- Fierstra J, Sobczyk O, Battisti-Charbonney A, et al. Measuring cerebrovascular reactivity: what stimulus to use? *J Physiol* 2013;591:5809–21 CrossRef Medline
- Tancredi FB, Hoge RD. Comparison of cerebral vascular reactivity measures obtained using breath-holding and CO<sub>2</sub> inhalation. *J Cereb Blood Flow Metab* 2013;33:1066–74 CrossRef Medline
- Kety SS, Schmidt CF. The effects of altered arterial tension of carbon dioxide and oxygen on cerebral blood flow and cerebral oxygen consumption of normal young men. *J Clin Invest* 1948;27:484–92 CrossRef Medline
- Markus HS, Harrison MJ. Estimation of cerebrovascular reactivity using transcranial Doppler, including the use of breath-holding as the vasodilatory stimulus. *Stroke* 1992;23:668–73 CrossRef Medline
- van der Zande FH, Hofman PA, Backes WH. Mapping hypercapnia-induced cerebrovascular reactivity using BOLD MRI. *Neuroradiology* 2005;47:114–20 CrossRef Medline
- Silvestrini M, Vernieri F, Troisi E, et al. Cerebrovascular reactivity in carotid artery occlusion: possible implications for surgical management of selected groups of patients. *Acta Neurol Scand* 1999;99:187–91 CrossRef Medline
- Prisman E, Slessarev M, Azami T, et al. Modified oxygen mask to induce target levels of hyperoxia and hypercarbia during radiotherapy: a more effective alternative to carbogen. *Int J Radiat Biol* 2007;83:457–62 CrossRef Medline
- Ito S, Mardimae A, Han J, et al. Non-invasive prospective targeting of arterial P(CO<sub>2</sub>) in subjects at rest. *J Physiol* 2008;586:3675–82 CrossRef Medline
- Sobczyk O, Battisti-Charbonney A, Poublanc J, et al. Assessing cerebrovascular reactivity abnormality by comparison to a reference atlas. *J Cereb Blood Flow Metab* 2015;35:213–20 CrossRef Medline
- Grade M, Hernandez Tamames JA, Pizzini FB, et al. A neuroradiologist's guide to arterial spin labeling MRI in clinical practice. *Neuroradiology* 2015;57:1181–202 CrossRef Medline
- Mandell DM, Han JS, Poublanc J, et al. Mapping cerebrovascular reactivity using blood oxygen level-dependent MRI in patients with arterial steno-occlusive disease: comparison with arterial spin labeling MRI. *Stroke* 2008;39:2021–28 CrossRef Medline
- Tancredi FB, Lajoie I, Hoge RD. Test-retest reliability of cerebral blood flow and blood oxygenation level-dependent responses to hypercapnia and hyperoxia using dual-echo pseudo-continuous arterial spin labeling and step changes in the fractional composition of inspired gases. *J Magn Reson Imaging* 2015;42:1144–57 CrossRef Medline
- Davis TL, Kwong KK, Weisskoff RM, et al. Calibrated functional MRI: mapping the dynamics of oxidative metabolism. *Proc Natl Acad Sci U S A* 1998;95:1834–39 CrossRef Medline
- Hoge RD, Atkinson J, Gill B, et al. Investigation of BOLD signal

- dependence on cerebral blood flow and oxygen consumption: the deoxyhemoglobin dilution model. *Magn Reson Med* 1999;42:849–63 Medline
33. Kastrup A, Thomas C, Hartmann C, et al. **Sex dependency of cerebrovascular CO<sub>2</sub> reactivity in normal subjects.** *Stroke* 1997;28:2353–56 CrossRef Medline
34. Flück D, Beaudin AE, Steinback CD, et al. **Effects of aging on the association between cerebrovascular responses to visual stimulation, hypercapnia and arterial stiffness.** *Front Physiol* 2014;5:49 CrossRef Medline
35. Mark CI, Mazerolle EL, Chen JJ. **Metabolic and vascular origins of the BOLD effect: implications for imaging pathology and resting-state brain function.** *J Magn Reson Imaging* 2015;42:231–46 CrossRef Medline
36. Schwertfeger N, Neu P, Schlattmann P, et al. **Cerebrovascular reactivity over time course in healthy subjects.** *J Neurol Sci* 2006;249:135–39 CrossRef Medline
37. Regan RE, Fisher JA, Duffin J. **Factors affecting the determination of cerebrovascular reactivity.** *Brain Behav* 2014;4:775–88 CrossRef Medline

# Cough-Associated Changes in CSF Flow in Chiari I Malformation Evaluated by Real-Time MRI

R.A. Bhadelia, S. Patz, C. Heilman, D. Khatami, E. Kasper, Y. Zhao, and N. Madan



## ABSTRACT

**BACKGROUND AND PURPOSE:** Invasive pressure studies have suggested that CSF flow across the foramen magnum may transiently decrease after coughing in patients with symptomatic Chiari I malformation. The purpose of this exploratory study was to demonstrate this phenomenon noninvasively by assessing CSF flow response to coughing in symptomatic patients with Chiari I malformation by using MR pencil beam imaging and to compare the response with that in healthy participants.

**MATERIALS AND METHODS:** Eight symptomatic patients with Chiari I malformation and 6 healthy participants were studied by using MR pencil beam imaging with a temporal resolution of ~50 ms. Patients and healthy participants were scanned for 90 seconds (without cardiac gating) to continuously record cardiac cycle–related CSF flow waveforms in real-time during resting, coughing, and postcoughing periods. CSF flow waveform amplitude, CSF stroke volume, and CSF flow rate (CSF Flow Rate = CSF Stroke Volume × Heart Rate) in the resting and immediate postcoughing periods were determined and compared between patients and healthy participants.

**RESULTS:** There was no significant difference in CSF flow waveform amplitude, CSF stroke volume, and the CSF flow rate between patients with Chiari I malformation and healthy participants during rest. However, immediately after coughing, a significant decrease in CSF flow waveform amplitude ( $P < .001$ ), CSF stroke volume ( $P = .001$ ), and CSF flow rate ( $P = .001$ ) was observed in patients with Chiari I malformation but not in the healthy participants.

**CONCLUSIONS:** Real-time MR imaging noninvasively showed a transient decrease in CSF flow across the foramen magnum after coughing in symptomatic patients with Chiari I malformation, a phenomenon not seen in healthy participants. Our results provide preliminary evidence that the physiology-based imaging method used here has the potential to be an objective clinical test to differentiate symptomatic from asymptomatic patients with Chiari I malformation.

**ABBREVIATIONS:**  $A_{CSF}$  = CSF flow waveform amplitude; CMI = Chiari I malformation;  $FR_{CSF}$  = CSF flow rate; PBI = pencil beam imaging;  $SV_{CSF}$  = CSF stroke volume

Although the diagnosis of Chiari I malformation (CMI) by MR imaging can be easily made by using a simple definition of >5-mm downward displacement of the cerebellar tonsils through the foramen magnum, management of this condition remains challenging and controversial.<sup>1-6</sup> The issue under debate is that

some patients who meet the MR imaging criteria for CMI diagnosis are asymptomatic and some with <5-mm tonsillar herniation may have typical symptoms of CMI.<sup>5-8</sup> Therefore, in the absence of an objective assessment test for CMI that correlates well with the severity of the clinical findings, a decision for surgery is often based entirely on the clinical judgment and management philosophy of the treating neurosurgeon. This scenario is believed to have led to overuse of surgical treatment.<sup>9</sup>

Many of the symptoms and signs associated with CMI are due to abnormal CSF circulation between the head and spine, secondary to foramen magnum obstruction produced by herniated cerebellar tonsils.<sup>10-18</sup> During the past 2 decades, attempts have been made to use cine phase contrast MR imaging to noninvasively assess CSF flow abnormalities in patients with CMI and to provide an objective test for assessment of disease severity.<sup>3,4,11-13,15</sup> Despite success in showing group differences in CSF flow between symptomatic and asymptomatic patients with CMI,<sup>3,4,15,19</sup> criti-

Received September 8, 2015; accepted after revision October 27.

From the Department of Radiology (R.A.B., D.K.), Beth Israel Deaconess Medical Center, Boston, Massachusetts; Department of Radiology (S.P.), Brigham and Women's Hospital, Boston, Massachusetts; Departments of Neurosurgery (C.H.) and Radiology (N.M.), Tufts Medical Center, Boston, Massachusetts; Department of Neurosurgery (E.K.), Beth Israel Deaconess Medical Center, Boston, Massachusetts; and Phillips Healthcare (Y.Z.), Boston, Massachusetts.

This work was supported by a grant from the Conquer Chiari Foundation.

Please address correspondence to Rafeeqe A. Bhadelia, MD, Department of Radiology, Beth Israel Deaconess Medical Center, WCB90, 330 Brookline Ave, Boston, MA 02115; e-mail: rbhadelia@bidmc.harvard.edu; @rbhadeliaMD



Indicates article with supplemental on-line photo.

<http://dx.doi.org/10.3174/ajnr.A4629>

cal questions remain concerning the management of an individual patient with CMI presenting for treatment, such as whether and when surgery should be performed and how a patient without typical clinical or MR imaging features should be managed.<sup>6,9</sup>

Symptoms experienced by patients with CMI can be induced or exaggerated by physiologic alterations such as coughing or the Valsalva maneuver.<sup>16,18</sup> This result is believed to be related to transient alterations in CSF flow across the foramen magnum. Therefore, it is logical to propose that an imaging test for patients with CMI include an assessment of the CSF flow response after a physiologic challenge. However, this is difficult, even with a very fast version of the cine phase contrast sequence, because it produces images that are weighted averages of the phasic behavior over many cardiac cycles and is therefore unable to show transient changes in CSF flow that result from a physiologic challenge and in which the duration of the transient changes is just a few cardiac cycles.<sup>20</sup> Therefore, we have chosen to assess CSF flow with the real-time MR imaging technique, pencil beam imaging (PBI).

Previously performed simultaneous invasive cranial and spinal pressure monitoring showed that in symptomatic patients with CMI, immediately after coughing or Valsalva maneuver, dissociation develops between intracranial and intraspinal pressures. During this pressure dissociation, a higher intracranial pressure compared with intraspinal pressure pushes the already herniated tonsils downward and further narrows the foramen magnum and thereby transiently reduces the CSF flow across it.<sup>18,20-23</sup> The purpose of this exploratory study was to demonstrate this phenomenon noninvasively by assessing CSF flow response to coughing in patients with CMI by using PBI and to compare the response with that in healthy participants.

## MATERIALS AND METHODS

### Patients and Healthy Subjects

Eight patients with CMI (mean age,  $41.1 \pm 7.6$  years; 7 women) and 6 healthy participants (mean age,  $38.8 \pm 13.3$  years; 4 women) underwent MR imaging on a 3T scanner (Achieva; Philips Healthcare, Best, the Netherlands). Institutional review board approval was obtained for this Health Insurance Portability and Accountability Act-compliant prospective study, and each patient and participant signed an informed consent. All patients with CMI were consecutive patients presenting for treatment who agreed to a research MR imaging study and were assessed by a neurosurgeon as having typical features of symptomatic CMI<sup>3</sup>: severe cough-associated headache ( $n = 6/8$ ), syringomyelia ( $n = 2/8$ ), and objective neurologic signs such as brisk reflexes, muscle weakness, and nystagmus ( $n = 4/8$ ). Healthy participants were recruited by local advertisement, and none had cardiovascular or neurologic disorders.

### CSF Flow Imaging Technique

PBI excites a narrow cylinder or “pencil” region and has been described in detail previously.<sup>20,24,25</sup> For this investigation, a 25-mm-diameter and 64-mm-length cylinder was excited by using a 2D spatially localized radiofrequency pulse with 8-turn spiral excitations, followed by a bipolar velocity-encoding gradient and a readout gradient applied along the axis of the cylinder.<sup>20</sup> A veloc-

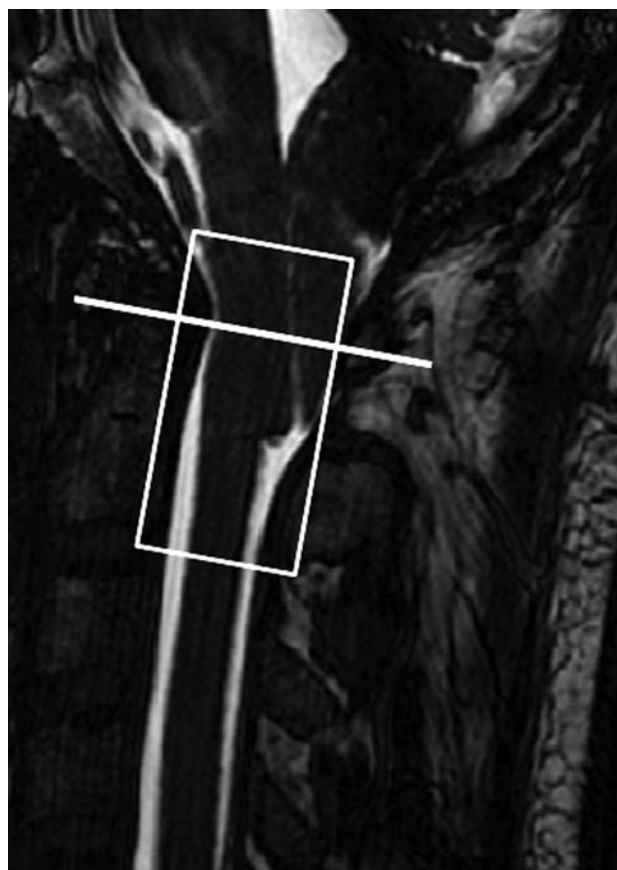


**FIG 1.** Position of the PBI cylinder (white rectangle) and location of CSF flow evaluation (white line) are shown in a patient with CMI.

ity-encoding of 5 cm/s along the superior-to-inferior direction was used. Other imaging parameters were the following: TR, 25–28 ms; TE, 3.8 ms; and flip angle, 10°. The effective temporal resolution was  $2 \times TR$  (ie, 50–56 ms). Heart rate and respiratory movements were continuously monitored by using the physiologic recording system of the scanner. Cardiac gating was not required for this PBI study, which recorded pulsatile CSF flow motion in real-time and, therefore, was able to acquire data much faster than the gated cine phase contrast sequence.

### MR Imaging

Sagittal 3D T2-weighted images were obtained to provide anatomic details. For PBI, the pencil beam was positioned along the long axis of the cervical spinal canal, extending from just above the level of the foramen magnum to the C2–3 disc level (Fig 1). Using multiplanar image reformatting, we positioned the pencil beam to cover the entire thecal sac.<sup>20</sup> The PBI scan was acquired for approximately 90 seconds, during which the participant was asked to do the following: 1) breathe quietly for the first 15–20 seconds (by counting from 1 to 20); 2) then cough as forcefully as possible consecutively 6 times; and 3) breathe quietly again after the end of coughing. Each ~90-second scan session was repeated 3 times.

### Image Analysis

3D anatomic images were used to determine the degree of tonsillar herniation below the level of the foramen magnum. CSF flow

analysis was performed off-line by using custom software developed in Matlab (MathWorks, Natick, Massachusetts), which allows simultaneous display of 3D anatomic and physiologic PBI data along with the heart rate and respiration. Anatomic images allow selection of a position along the pencil beam cylinder for assessment of CSF flow (Fig 1 and On-line Figure). By determining the area of the thecal sac on axial images at the position selected, the software then calculates CSF flow in milliliters per second by multiplying average velocity by area and plots the CSF flow on the y-axis versus time (seconds) on the x-axis, thereby depicting cardiac cycle-related CSF flow pulsations over the entire 90-second data acquisition. For further quantitative analysis, we determined 3 CSF flow parameters: 1) peak-to-peak CSF flow waveform amplitude ( $A_{CSF}$  in units of milliliters per minute: sum

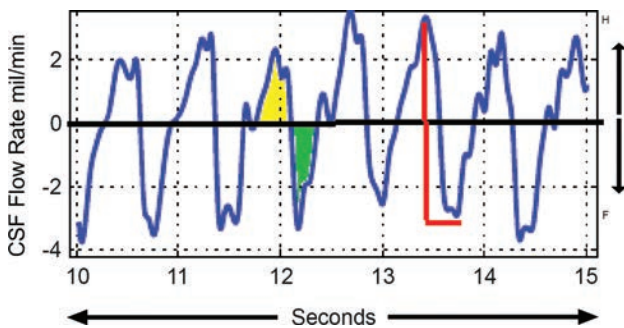


**FIG 2.** CSF flow waveforms from a healthy participant during a 5-second period: craniocaudal CSF flow (green) and caudocranial CSF flow (yellow).  $A_{CSF}$  is shown in red;  $SV_{CSF}$  is the average of absolute flow from yellow and green areas.

of the absolute values of peak craniocaudal and caudocranial flow rates), 2) CSF stroke volume ( $SV_{CSF}$  in milliliters: average of the absolute values of integrated craniocaudal and caudocranial CSF flows), and 3) CSF flow rate ( $FR_{CSF} = (SV_{CSF} \times \text{Heart Rate})$ ), with units of milliliters per minute, as shown in Fig 2.  $FR_{CSF}$  was calculated to eliminate any possible difference attributable to changes in heart rate after coughing.

The average CSF flow parameters were calculated during 2 separate 5-second periods (see horizontal blue and green color bars in Fig 3 showing resting and postcoughing periods). For postcoughing assessment, the 5-second period was selected approximately 5 seconds after the end of coughing to allow sufficient time for motion-related coughing to subside (Fig 3). While it is possible to assess CSF flow at multiple levels along the PBI cylinder, for this exploratory study, our assessment was limited to the C1 vertebral level for both patients and healthy participants (Fig 1). The phase images from each PBI acquisition were reviewed to determine whether there were any phase discontinuities indicating aliasing from velocities exceeding the encoding value of 5 cm/s. No aliasing was observed at the C1 level in either the patients with CMI or healthy participants.

#### Data Analysis

Resting and immediate postcoughing values for  $A_{CSF}$ ,  $SV_{CSF}$ , and  $FR_{CSF}$  were determined and compared between patients with CMI and healthy participants. Furthermore, postcoughing values of all 3 CSF flow parameters were expressed as a percentage of

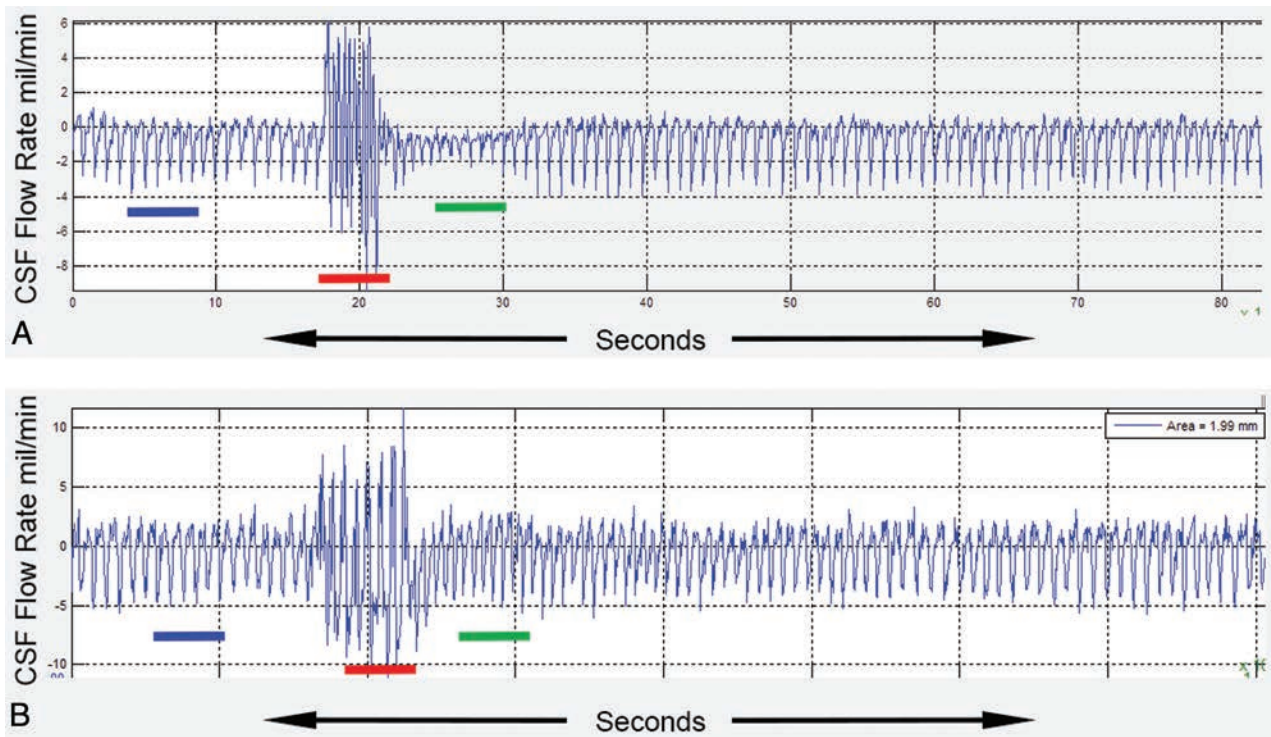


**FIG 3.** The effect of coughing on cardiac cycle-related CSF flow waveforms is seen in a patient with CMI (A) and a healthy participant (B). Left-to-right resting (blue), coughing (red), and immediate postcoughing (green) periods are seen. In the patient with CMI, the CSF flow-pulsation magnitude in the immediate postcoughing period decreases to  $\sim 50\%$  of the resting value before gradually returning to the resting level. In contrast, for the healthy participant, the CSF flow-pulsation magnitude immediately postcoughing is not significantly different compared with that of the resting period. X-axis indicates time in seconds; y-axis, CSF flow rate in milliliters per minute.

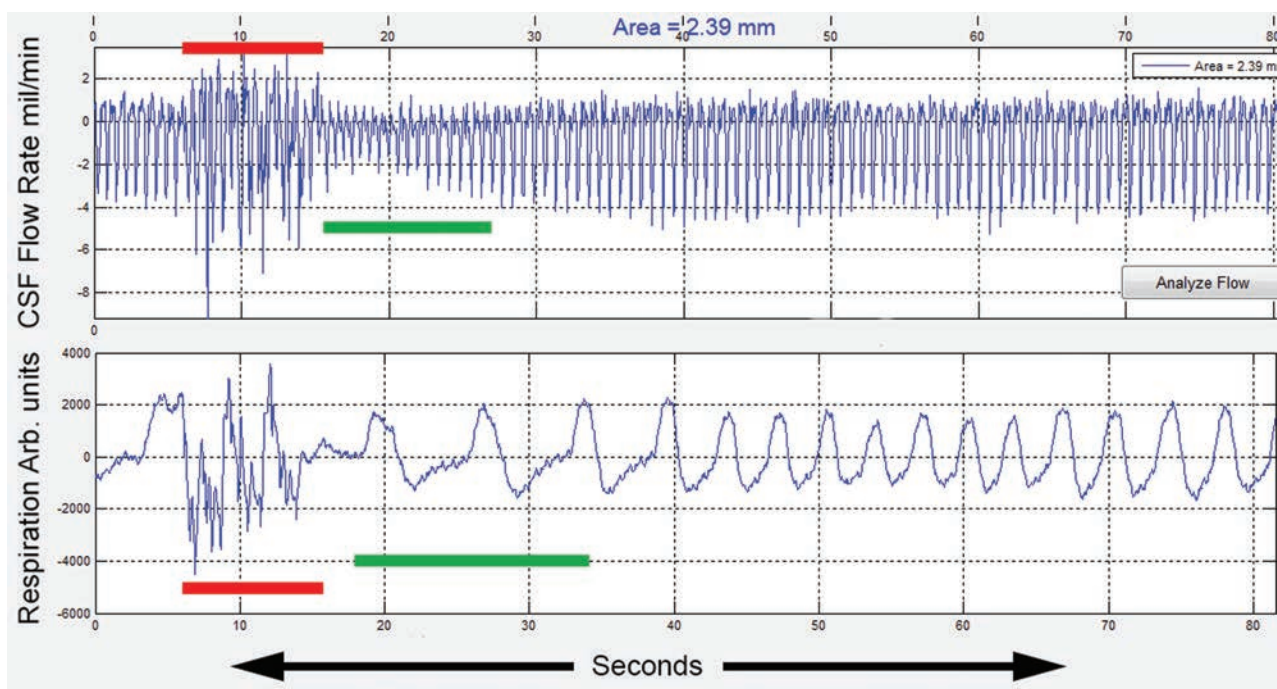


**FIG 4.** CSF flow waveforms (upper trace) and simultaneous recordings of respiratory motion (lower trace) in a patient with CMI (the patient is different from the one shown in Fig 3). The coughing period (red bar) is seen as irregular respiratory motion (lower trace) with almost simultaneous haphazard motion in the CSF flow waveform (upper trace). In the immediate postcoughing period, respiratory motion is regular but larger in magnitude (green bar). The decrease in CSF flow waveform magnitude is seen in the postcoughing period (green bar in the upper trace). CSF flow waveforms depict flow in milliliters per minute, and respiratory motion is recorded in arbitrary units (Arb). Mil indicates milliliters.

**Table 1: CSF flow parameters in resting and after coughing in patients with CMI compared with healthy participants<sup>a</sup>**

CSF Flow Parameter	Resting			Postcough		
	CMI (n = 8)	Healthy (n = 6)	P Value	CMI (n = 8)	Healthy (n = 6)	P Value
A <sub>CSF</sub> (mL/min)	3.85 ± 1.55	3.5 ± 1.9	NS	1.65 ± 1.01	3.95 ± 2.2	.007
SV <sub>CSF</sub> (mL)	0.38 ± 0.15	0.43 ± 0.21	NS	0.17 ± 0.11	0.37 ± 0.19	NS
FR <sub>CSF</sub> (mL/min)	31.1 ± 14.1	30.1 ± 16.2	NS	16.5 ± 11.3	32.2 ± 21	NS

**Note:**—NS indicates not significant.

<sup>a</sup> All values of CSF variables are shown as means. P values were assessed with the Mann-Whitney U test.

resting values and compared between patients with CMI and healthy participants. A Mann-Whitney U test was used for all comparisons. All statistical analyses were performed with SPSS software (IBM, Armonk, New York).

## RESULTS

There was no significant difference in age ( $P = .68$ ) or sex distribution ( $\chi^2$ ,  $P = .34$ ) between the patients with CMI and healthy participants. In all patients with CMI, tonsillar herniation was  $>5$  mm below the level of foramen magnum (mean,  $14.5 \pm 5.5$  mm; range, 9–22-mm). None of the healthy participants had tonsils below the level of foramen magnum.

Representative real-time cardiac cycle–related CSF flow waveforms from a patient with CMI and a healthy participant are shown in Fig 3A, -B. In both, minimal heartbeat-to-heartbeat variation in the magnitude of the CSF flow waveforms is seen during the resting period (blue color bar) with high-amplitude haphazard motion during the coughing period (red color bar). However, in the immediate postcoughing period (green color bar), CSF flow waveforms are markedly decreased in magnitude in the patient with CMI for up to 10 seconds before returning to

the resting magnitude (Fig 3A). As opposed to this result, in the healthy participant, the magnitude of the CSF waveforms immediately returns to resting values (Fig 3B). Figure 4 shows simultaneous recordings of CSF flow waveform (top) and respiratory motion (bottom, obtained with a respiratory bellows) in a patient with CMI (a different patient than the one shown in Fig 3). The respiratory tracing shows irregular motion during the coughing period with almost simultaneous haphazard motion in the CSF flow waveforms (red lines) followed by a decrease in CSF flow waveform magnitude in the immediate postcoughing period (green line).

The resting and postcoughing values of A<sub>CSF</sub>, SV<sub>CSF</sub>, and FR<sub>CSF</sub> in patients with CMI and healthy participants are shown in Table 1. There was no difference between patients with CMI and healthy participants in resting values. However, when postcoughing values were compared between patients with CMI and healthy participants, a significant difference was observed in A<sub>CSF</sub> ( $P = .007$ ), but the difference in SV<sub>CSF</sub> and FR<sub>CSF</sub> was not significant. We also compared the postcoughing heart rate between patients with CMI and healthy participants and did not find any significant difference ( $P = .43$ ).

For each subject group (ie, the CMI group and the healthy

**Table 2: Postcoughing CSF flow parameters expressed as a percentage of the resting value in patients with CMI and healthy participants<sup>a</sup>**

CSF Flow Variable (% of Resting)	Healthy Participants		P Value
	CMI (n = 8)	(n = 6)	
A <sub>CSF</sub>	45.5 ± 16.8	114.7 ± 22.2	<.001
SV <sub>CSF</sub>	44.1 ± 14.9	83.3 ± 13.6	<.001
FR <sub>CSF</sub>	51.8 ± 16.9	106.5 ± 20.7	<.001

<sup>a</sup> All values are shown as means. P values were assessed with the Mann-Whitney U test.

group), Table 2 shows postcoughing A<sub>CSF</sub>, V<sub>CSF</sub>, and FR<sub>CSF</sub> values as a percentage of resting values. There was a significant difference in the percentage of postcoughing change in A<sub>CSF</sub> (P < .001), SV<sub>CSF</sub> (P < .001), and FR<sub>CSF</sub> (P < .001) in patients with CMI compared with healthy participants.

## DISCUSSION

A significant decrease in CSF flow across the foramen magnum was observed in response to coughing only in symptomatic patients with CMI, a finding that was not seen in healthy participants. These observations are consistent with previous experiments performed by Williams<sup>18,22,23</sup> using simultaneous invasive measurements of CSF pressures in the head and spine. In his experiments, Williams observed that in patients with CMI immediately after coughing, dissociation developed between intracranial and intraspinal pressures due to the presence of tonsillar herniation. During this pressure dissociation, a higher intracranial pressure compared with intraspinal pressure pushes the already herniated tonsils in patients with CMI downward, further narrowing the foramen magnum and thereby transiently reducing the CSF flow across it. In healthy subjects without herniated tonsils, pressure dissociation does not develop and CSF flow across the foramen magnum does not significantly change with coughing. We believe that this is the first study to noninvasively demonstrate this phenomenon in patients with CMI.

Anatomic MR imaging provides some information about foramen magnum narrowing in patients with CMI through assessment of the degree of tonsillar herniation and crowding of the neural structures, but the findings are poorly correlated with the severity of symptoms.<sup>3,6,9,10</sup> This result has led investigators to assess CSF circulation abnormalities at the foramen magnum by using physiologic means, such as invasive pressure measurements<sup>14,16,18,22</sup> or noninvasive motion-sensitive MR imaging.<sup>3,4,10-13,15,19</sup> Although simultaneous invasive pressure measurements in the head and spinal canal during coughing or Valsalva maneuver can quantitatively assess the degree of foramen magnum obstruction in patients with CMI by assessing pressure dissociation, this method has not gained widespread acceptance and is rarely used as a diagnostic test. Using MR imaging CSF flow measurements obtained only in resting conditions has its limitations in an individual patient with CMI for clinical decision-making because of the wide variation in quantitative estimates of CSF flow between individuals due to the confounding effects of cerebral arterial and venous flow amplitudes, intracranial compliance, and the anatomy of posterior fossa and CSF pathways.<sup>3,8,10,26</sup> Results presented in Table 1 confirm this notion by showing a lack of significant differences in CSF flow parameters between patients with CMI and healthy participants when their resting values were

directly compared, and the postcoughing difference was seen only in the A<sub>CSF</sub>.

The major benefit of our approach is that using a physiologic challenge such as coughing assesses an individual patient's ability to handle compensatory CSF flow across the foramen magnum. By comparing the CSF flow-pulsation magnitudes with and without a physiologic challenge, one eliminates the effect of other confounding variables described above by using a patient as her or his own control. The strength of this method is highlighted in Table 2. Here, a significant difference in a percentile change between resting and postcoughing values of all 3 CSF flow parameters is seen in patients with CMI compared with the healthy participants. In this study, we have also shown that the dynamic quantitative information that was previously only available through invasive means can now be available to neurosurgeons through a noninvasive physiologic MR imaging method. In addition, unlike the invasive pressure measurements used to study CSF physiology, our approach can be used in a large number of patients with CMI and healthy participants to establish a normative data base, which can help develop an objective assessment test for differentiating patients with CMI who may need surgery from those who may not benefit from it.

Several limitations of this exploratory study need to be addressed in the future. First, the physiologic maneuver (coughing) used here was not quantified. The patients were simply asked to cough as forcibly as possible; this request can induce variability in the CSF flow response. While this did not affect the results in this exploratory study, which assessed only the symptomatic patients, for wider use in patients with CMI of different disease severity, the coughing effort will have to be quantified so that the CSF flow response can be appropriately scaled. We are currently exploring different options to address this issue. Second, given the small sample size, we could not determine the relationship between the degree of tonsillar herniation and CSF flow response to coughing. Finally, most patients examined had cough-associated headache. In a small number of patients with CMI in this study without cough-associated headache (n = 2), CSF flow response to coughing was similar to that in those with cough-associated headache. However, given the small sample size, this similarity needs to be further assessed in future studies.

We believe that on the basis of this exploratory study, a larger study can be designed to prospectively study patients with CMI of different disease severities to develop a quantitative noninvasive analysis tool for the evaluation of these patients. Our overall goal is to develop a protocol that will guide clinical management of patients with CMI. By adding a physiology-based quantitative assessment of CSF flow in patients with CMI to routine anatomic imaging, clinicians will be able to make an assessment of a patient's ability to handle altered CSF flow under conditions of stress that are known to produce symptoms in these patients. This objective assessment of CSF flow obstruction in patients with CMI can help their clinical management in 2 different ways. First, the presence of a significant dynamic foramen magnum obstruction, even in the absence of typical radiologic features, will provide supporting evidence that an operation is indicated. Second, the absence of a dynamic foramen magnum obstruction in patients who are asymptomatic or have atypical clinical features will pro-

vide objective evidence to clinicians that these patients will likely not benefit from the operation and should be managed by non-surgical means.

## CONCLUSIONS

Our results provide preliminary evidence that the physiology-based imaging method using real-time CSF flow imaging with PBI has the potential to be an objective clinical test to differentiate symptomatic from asymptomatic patients with CMI.

Disclosures: Rafeeqe A. Bhadelia—*RELATED: Grant: Conquer Chiari Foundation.\* Comments: A grant was provided to perform MRI scans and develop an analysis program for the project. Samuel Patz—RELATED: Consulting Fee or Honorarium: Beth Israel Deaconess Medical Center, Comments: I was a consultant on a grant awarded to R. Bhadelia (first author) from the Conquer Chiari Foundation. The grant was awarded to Beth Israel Deaconess Medical Center with Dr Bhadelia as the Principal Investigator. The consultant fees were paid to me directly by Beth Israel Deaconess Medical Center. Yansong Zhao—UNRELATED: Employment: I am a Clinical Scientist of Philips Healthcare North America. Neel Madan—RELATED: Grant: Conquer Chiari Foundation.\* Comments: Seed grant, with money to pay for MRI acquisitions and to give a small amount of money to subjects. \*Money paid to the institution.*

## REFERENCES

1. Elster AD, Chen MY. **Chiari I malformations: clinical and radiologic reappraisal.** *Radiology* 1992;183:347–53 CrossRef Medline
2. Alden TD, Ojemann JG, Park TS. **Surgical treatment of Chiari I malformation: indications and approaches.** *Neurosurg Focus* 2001; 11:E2 Medline
3. Alperin N, Loftus JR, Oliu CJ, et al. **MRI measures of posterior cranial fossa morphology and CSF physiology in Chiari malformation type I.** *Neurosurgery* 2014 Jul 18. [Epub ahead of print] Medline
4. Hofkes SK, Iskandar BJ, Turski PA, et al. **Differentiation between symptomatic Chiari I malformation and asymptomatic tonsillar ectopia by using cerebrospinal fluid flow imaging: initial estimate of imaging accuracy.** *Radiology* 2007;245:532–40 CrossRef Medline
5. Meadows J, Kraut M, Guarnieri M, et al. **Asymptomatic Chiari type I malformations identified on magnetic resonance imaging.** *J Neurosurg* 2000;92:920–26 CrossRef Medline
6. Voelker R. **Chiari conundrum: researchers tackle a brain puzzle for the 21st century.** *JAMA* 2009;301:147–49 CrossRef Medline
7. Sekula RF Jr, Arnone GD, Crocker C, et al. **The pathogenesis of Chiari I malformation and syringomyelia.** *Neurol Res* 2011;33: 232–39 CrossRef Medline
8. Tubbs RS, Beckman J, Naftel RP, et al. **Institutional experience with 500 cases of surgically treated pediatric Chiari malformation type I.** *J Neurosurg Pediatr* 2011;7:248–56 CrossRef Medline
9. Baisden J. **Controversies in Chiari I malformations.** *Surg Neurol Int* 2012;3(suppl 3):S232–37 CrossRef Medline
10. Alperin N, Kulkarni K, Loth F, et al. **Analysis of magnetic resonance imaging-based blood and cerebrospinal fluid flow measurements in patients with Chiari I malformation: a system approach.** *Neurosurg Focus* 2001;11:E6 Medline
11. Armonda RA, Citrin CM, Foley KT, et al. **Quantitative cine-mode magnetic resonance imaging of Chiari I malformations: an analysis of cerebrospinal fluid dynamics.** *Neurosurgery* 1994;35:214–23; discussion 223–24 Medline
12. Bhadelia RA, Bogdan AR, Wolpert SM, et al. **Cerebrospinal fluid flow waveforms: analysis in patients with Chiari I malformation by means of gated phase-contrast MR imaging velocity measurements.** *Radiology* 1995;196:195–202 CrossRef Medline
13. Haughton VM, Korosec FR, Medow JE, et al. **Peak systolic and diastolic CSF velocity in the foramen magnum in adult patients with Chiari I malformations and in normal control participants.** *AJNR Am J Neuroradiol* 2003;24:169–76 Medline
14. Oldfield EH, Muraszko K, Shawker TH, et al. **Pathophysiology of syringomyelia associated with Chiari I malformation of the cerebellar tonsils: implications for diagnosis and treatment.** *J Neurosurg* 1994;80:3–15 CrossRef Medline
15. Quigley MF, Iskandar B, Quigley ME, et al. **Cerebrospinal fluid flow in foramen magnum: temporal and spatial patterns at MR imaging in volunteers and in patients with Chiari I malformation.** *Radiology* 2004;232:229–36 CrossRef Medline
16. Sansur CA, Heiss JD, DeVroom HL, et al. **Pathophysiology of headache associated with cough in patients with Chiari I malformation.** *J Neurosurg* 2003;98:453–58 CrossRef Medline
17. Williams B. **Cerebrospinal fluid pressure changes in response to coughing.** *Brain* 1976;99:331–46 CrossRef Medline
18. Williams B. **Cough headache due to craniospinal pressure dissociation.** *Arch Neurol* 1980;37:226–30 CrossRef Medline
19. Krueger KD, Haughton VM, Hetzel S. **Peak CSF velocities in patients with symptomatic and asymptomatic Chiari I malformation.** *AJNR Am J Neuroradiol* 2010;31:1837–41 CrossRef Medline
20. Bhadelia RA, Madan N, Zhao Y, et al. **Physiology-based MR imaging assessment of CSF flow at the foramen magnum with a valsalva maneuver.** *AJNR Am J Neuroradiol* 2013;34:1857–62 CrossRef Medline
21. Tachibana S, Iida H, Yada K. **Significance of positive Queckenstedt test in patients with syringomyelia associated with Arnold-Chiari malformations.** *J Neurosurg* 1992;76:67–71 CrossRef Medline
22. Williams B. **Simultaneous cerebral and spinal fluid pressure recordings, 2: cerebrospinal dissociation with lesions at the foramen magnum.** *Acta Neurochir (Wien)* 1981;59:123–42 CrossRef Medline
23. Williams B. **Simultaneous cerebral and spinal fluid pressure recordings, I: technique, physiology, and normal results.** *Acta Neurochir (Wien)* 1981;58:167–85 CrossRef Medline
24. Hardy CJ, Pearlman JD, Moore JR, et al. **Rapid NMR cardiography with a half-echo M-mode method.** *J Comput Assist Tomogr* 1991;15: 868–74 CrossRef Medline
25. Maier SE, Hardy CJ, Jolesz FA. **Brain and cerebrospinal fluid motion: real-time quantification with M-mode MR imaging.** *Radiology* 1994;193:477–83 CrossRef Medline
26. Bhadelia RA, Bogdan AR, Kaplan RF, et al. **Cerebrospinal fluid pulsation amplitude and its quantitative relationship to cerebral blood flow pulsations: a phase-contrast MR flow imaging study.** *Neuroradiology* 1997;39:258–64 CrossRef Medline

# Imaging Findings Associated with Space-Occupying Edema in Patients with Large Middle Cerebral Artery Infarcts

A.D. Horsch, J.W. Dankbaar, T.A. Stemerink, E. Bennink, T. van Seeters, L.J. Kappelle, J. Hofmeijer, H.W. de Jong, Y. van der Graaf, and B.K. Velthuis; on behalf of the DUST investigators

## ABSTRACT

**BACKGROUND AND PURPOSE:** Prominent space-occupying cerebral edema is a devastating complication occurring in some but not all patients with large MCA infarcts. It is unclear why differences in the extent of edema exist. Better knowledge of factors related to prominent edema formation could aid treatment strategies. This study aimed to identify variables associated with the development of prominent edema in patients with large MCA infarcts.

**MATERIALS AND METHODS:** From the Dutch Acute Stroke Study (DUST), 137 patients were selected with large MCA infarcts on follow-up NCCT ( $3 \pm 2$  days after stroke onset), defined as ASPECTS  $\leq 4$ . Prominent edema was defined as a midline shift of  $\geq 5$  mm on follow-up. Admission patient and treatment characteristics were collected. Admission CT parameters used were ASPECTS on NCCT and CBV and MTT maps, and occlusion site, clot burden, and collaterals on CTA. Permeability on admission CTP, and day 3 recanalization and reperfusion statuses were obtained if available. Unadjusted and adjusted (age and NIHSS) odds ratios were calculated for all variables in relation to prominent edema.

**RESULTS:** Prominent edema developed in 51 patients (37%). Adjusted odds ratios for prominent edema were higher with lower ASPECTS on NCCT (adjusted odds ratio, 1.32; 95% CI, 1.13–1.55) and CBV (adjusted odds ratio, 1.26; 95% CI, 1.07–1.49), higher permeability (adjusted odds ratio, 2.35; 95% CI, 1.30–4.24), more proximal thrombus location (adjusted odds ratio, 3.40; 95% CI, 1.57–7.37), higher clot burden (adjusted odds ratio, 2.88; 95% CI, 1.11–7.45), and poor collaterals (adjusted odds ratio, 3.93; 95% CI, 1.78–8.69).

**CONCLUSIONS:** Extensive proximal occlusion, poor collaterals, and larger ischemic deficits with higher permeability play a role in the development of prominent edema in large MCA infarcts.

**ABBREVIATIONS:** ACA = anterior cerebral artery; ECASS = European Cooperative Acute Stroke Study

Prominent space-occupying edema can occur after acute large MCA ischemic stroke. The prominent space-occupying edema can cause herniation, increased intracranial pressure, and rapid neurologic deterioration. These occur in approximately 8% of MCA infarcts and have mortality rates of up to 80% with conservative treatment.<sup>1–3</sup> Current treatment options are limited; the only treatment of proved value is large hemicraniectomy within

48 hours after stroke onset.<sup>4–6</sup> The results from the hemicraniectomy trials showed a large decrease in mortality but with an increase in number of patients with severe disability.<sup>4</sup>

Although risk factors for prominent space-occupying edema have been identified, it is still unclear why only some patients with a large MCA infarct on follow-up develop prominent space-occupying edema.<sup>7</sup> Identification of associated variables is important to identify possible new targets for treatment development.<sup>8</sup>

The extent of the disturbance of the blood-brain barrier may play a role in the development of prominent space-occupying edema.<sup>9</sup> A measure of the BBB permeability is the permeability surface-area product, which can be obtained from an extended CTP acquisition.<sup>10</sup> Other known risk factors for the development of prominent space-occupying edema include proximal occlusion site, greater infarct size, involvement of  $>1$  vascular territory, basal ganglia involvement, increased ratio of CBV lesion volume/CSF volume, female sex, and higher NIHSS score on admission.<sup>9,11–14</sup>

Received July 8, 2015; accepted after revision October 30.

From the Departments of Radiology (A.D.H., J.W.D., T.A.S., E.B., T.v.S., H.W.d.J., B.K.V.) and Neurology (L.J.K.), Utrecht Stroke Center, University Medical Center Utrecht, Utrecht, the Netherlands; Department of Neurology (J.H.), Rijnstate Hospital, Arnhem, the Netherlands; and Julius Center for Health Sciences and Primary Care (Y.v.d.G.), Utrecht, the Netherlands.

This study was supported by grants from the Netherlands Heart Foundation (grant numbers 2008 T034 and 2012 T061) and the NutsOhra Foundation (grant number 0903-012).

Please address correspondence to Alexander D. Horsch, MD, MRCS, University Medical Center Utrecht, Heidelberglaan 100, HP E01132, 3584 CX Utrecht, the Netherlands; e-mail: alexanderhorsch@gmail.com

<http://dx.doi.org/10.3174/ajnr.A4637>

The aim of this study was to identify clinical and CT imaging variables that are associated with the development of prominent space-occupying edema in patients with large MCA infarcts on follow-up.

## MATERIALS AND METHODS

### Patient Selection

All patients participated in the Dutch Acute Stroke Study (DUST), and the study protocol has been published previously.<sup>15</sup> Patients were included in the DUST study if they had a NCCT, CTA, and CTP within 9 hours after stroke onset. The local medical ethics committees of the participating centers approved this study. All patients or their families gave signed informed consent unless a patient died before consent could be obtained; in that case, the need for consent was waived by the medical ethics committee.<sup>15</sup>

For the current study, patients were selected with a large infarct in the MCA territory defined as ASPECTS  $\leq 4$  on a follow-up NCCT performed  $3 \pm 2$  days after stroke onset.<sup>16</sup> Exclusion criteria were hemorrhagic transformation with substantial mass effect (European Cooperative Acute Stroke Study [ECASS] parenchymal hemorrhage type 2) and poor-quality admission CTP.<sup>17</sup> The selection process is clarified in the flow chart (Fig 1). We collected clinical data on age, sex, history of stroke or atrial fibrillation, admission NIHSS, IV-rtPA treatment, intra-arterial treatment, and time from symptom onset to admission CT.

### Imaging Protocol

NCCT and CTP of the brain and CTA of the cervical and cerebral arteries were performed on admission. Follow-up NCCT was planned at  $3 \pm 2$  days and in case of clinical deterioration. Additional follow-up CTA and CTP were also performed if possible. Multidetector row CT scanners were used, with the number of detectors ranging from 40 to 320 (LightSpeed VCT, GE Healthcare, Milwaukee, Wisconsin; Brilliance 40, Brilliance 64, and Brilliance iCT 256, Philips Healthcare, Best, the Netherlands; Sensation 64, Siemens, Erlangen, Germany; Aquilion ONE, Toshiba Medical Systems, Tokyo, Japan). NCCT was performed with 120 kV, 300–375 mAs, and a section thickness of 5 mm.

The CTP, performed before CTA, was acquired with 80 kV and 150 mAs per rotation and a section thickness of 5 mm and involved successive gantry rotations in cine mode (every 2 seconds for 50 seconds and 6 additional rotations 30 seconds apart) during intravenous administration of 40 mL of nonionic contrast material followed by 40 mL of saline with a flow of 6 mL/s. CTP coverage included at least the level of the basal ganglia to the lateral ventricles to allow assessment of both ASPECTS levels.<sup>16</sup> MTT and CBV maps were classified only with ASPECTS levels to ensure that uniform assessment on all CTP scans was performed, despite differences in scan range (40–320 sections).

CTA was acquired from the aortic arch to the vertex with 50–70 mL of contrast followed by 40 mL of saline, with a flow of 6 mL/s. The individual CTA scan delay after intravenous injection was calculated from time-to-peak arterial enhancement on CTP

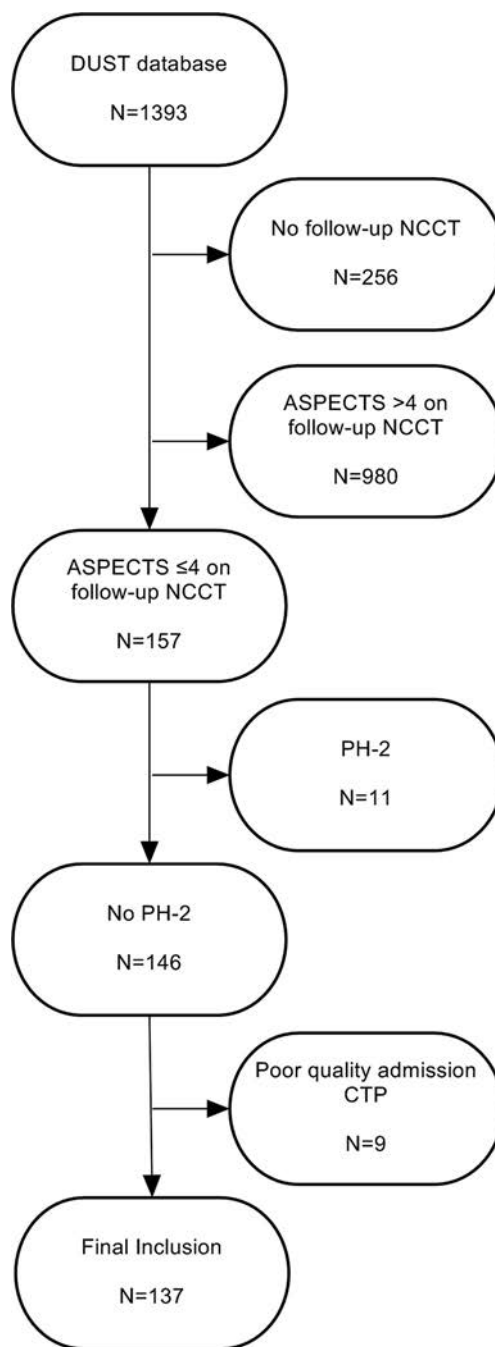


**FIG 1.** Inclusion flow chart. PH indicates parenchymal hemorrhage.

or by a trigger-based Hounsfield unit threshold measurement of contrast enhancement in the aortic arch.

### Imaging Analysis

**NCCT.** On the admission scan, we evaluated the ASPECTS score to quantify the presence of early CT signs of infarction.<sup>16</sup> On day  $3 \pm 2$  of follow-up, the infarct size was classified with ASPECTS and the presence of prominent space-occupying edema was defined as a midline shift of  $\geq 5$  mm (Fig 2).<sup>11,18,19</sup> Any hemorrhagic transformation on the follow-up scan was classified according to the ECASS criteria to identify patients with a parenchymal hemorrhage type 2 (hemorrhage of  $>30\%$  of the infarcted area with



**FIG 2.** Large MCA infarct on follow-up, with and without prominent space-occupying edema. Patient A (87-year-old man, follow-up day 5) has a large MCA infarct and generalized atrophy but does not show a midline shift. Patient B (58-year-old man, follow-up day 3) has a large MCA infarct with a midline shift of  $\geq 5$  mm, representing prominent space-occupying edema.

substantial space-occupying effect), because the midline shift in those patients is considered secondary to the large hemorrhage.<sup>17</sup>

**CTP.** CBF, CBV, MTT, and TTP were automatically calculated from CTP data using commercially available CTP software (Extended Brilliance Workstation 4.5; Philips Healthcare). The presence of a perfusion deficit on admission was defined as a focal asymmetry on the CBF, CBV, or MTT maps matching a part of or the complete MCA flow territory. MTT and CBV maps were classified with ASPECTS.<sup>20</sup> Involvement of the lentiform nucleus and additional anterior cerebral artery (ACA) vascular territory (including the caudate nucleus) was also evaluated separately.<sup>11,21</sup> Reperfusion was evaluated quantitatively by assessment of the change in MTT abnormality (Soares et al<sup>22</sup>) and categorized into reperfusion and no-reperfusion groups. Reperfusion was defined as a resolution of  $\geq 75\%$  of the abnormality on the MTT maps comparing admission and follow-up CTP.<sup>22</sup>

To estimate the permeability surface area, we used a nonlinear method, with a mathematic response model to describe an impulse response function obtained from the extended acquisition. The permeability surface area was calculated relative to the non-affected hemisphere.<sup>10</sup>

**CTA.** Admission CTA provided data on intracranial thrombus location, clot burden score, and collateral score.<sup>23-25</sup> Thrombus location was classified as the most proximal site of occlusion, unless there was a combined extracranial ICA occlusion and a more distal MCA occlusion with an open ICA top (tandem lesion), which was classified at the level of the MCA occlusion (proximal flow maintained through circle of Willis collaterals).<sup>26</sup> The clot burden score was obtained by evaluating the anterior circulation to the symptomatic hemisphere and subtracting segments with absent contrast opacification from the maximum score of 10, with 10 representing absence of any thrombus, and zero, a complete occlusion of all the segments. The score assigns 1 point to the infraclinoid ICA, the ACA, and each M2 branch (with a maximum of 2) and 2 points to the supraclinoid part of the ICA and the proximal and distal part of the M1 segment.<sup>23</sup>

The collateral score of the symptomatic hemisphere was evaluated by visual assessment of MIP images and the scoring system

applied by Tan et al.<sup>24</sup> Leptomeningeal collaterals were graded on admission CTA by the extent of collateral filling in the MCA territory of the affected hemisphere in comparison with the contralateral side: 0 = absent; 1 = filling  $\leq 50\%$ ; 2 = filling 50% to  $< 100\%$ ; 3 = filling 100%. For analysis, the scores were dichotomized into poor collaterals (0–1) and good collaterals (2–3). Tan et al found a very good interobserver correlation of 0.87 for this scoring system. Recanalization was evaluated by comparing admission and follow-up CTAs and was defined qualitatively as recanalization or no recanalization. This scoring system compares with a TIC1 score of 0–2a for the no-recanalization group and a TIC1 score of 2b or 3 for the recanalization group.<sup>27</sup>

All imaging data were collected and evaluated centrally by 1 of 3 observers (I.C. van der Schaaf, B.K.V., and J.W.D), all with at least 5 years of experience in stroke imaging. Only the symptomatic side was provided for the evaluation.

### Statistical Analysis

For all analyses, patients with prominent space-occupying edema were compared with patients without prominent space-occupying edema. The clinical variables were age, sex, history of stroke, history of atrial fibrillation, admission NIHSS, IV-rtPA treatment or intra-arterial treatment, and time to admission scan series. Imaging variables were the following: early CT signs of infarction (ASPECTS 0–10), decreased CBV (ASPECTS 0–10), prolonged MTT (ASPECTS 0–10), the presence of decreased CBV in the lentiform nucleus (yes/no), the presence of decreased CBV in the caudate nucleus and/or ACA vascular territory (yes/no), clot burden score (cutoff of  $\leq 6$ ), thrombus location (ICA/proximal M1 versus distal M1, M2, or  $>M2$ ), and collateral score (good or poor).<sup>24</sup> Permeability estimates, recanalization (recanalization versus no recanalization), and reperfusion (reperfusion versus no reperfusion) were analyzed in a subanalysis because these data were not available in all patients.

To compare variables, we used the  $\chi^2$  test, *t* test, or Mann-Whitney *U* test. The association between variables and prominent space-occupying edema was analyzed by using univariate and multivariate regression. Odds ratios were adjusted for age and admission NIHSS score (adjusted OR) with multivariate logistic regression. Significance was predefined at  $P < .05$ . Statistical computations were performed by using SPSS 23.0 (IBM, Armonk, New York).

### RESULTS

Inclusion criteria for this study were met in 137 patients. Not all patients in the DUST study underwent follow-up imaging, for the following reasons: no permission for follow-up, no follow-up due to discharge within 24 hours in patients with rapid recovery, poor condition of the patient, or impaired renal function. Admission NIHSS and 3-month mRS scores were not significantly different between patients with or without follow-up imaging.

Of the 137 patients with large MCA infarcts on follow-up, 51 (37%) developed prominent space-occupying edema. Their baseline clinical and imaging characteristics are shown in Table 1. Median onset time to imaging was 100 minutes, and most patients (88%) were imaged within 4.5 hours. Only 6% were imaged within the 6- to 9-hour range. The median time to follow-up was

**Table 1: Clinical and imaging characteristics<sup>a</sup>**

Characteristics	All Patients (N = 137)	Prominent Space-Occupying Edema (n = 51)	No Prominent Space-Occupying Edema (n = 86)	P Value
<b>Clinical parameters</b>				
Age (yr) (median) (IQR)	66 (53–73)	63 (52–72)	67 (54–73)	.31
Female sex (No.) (%)	48 (35)	19 (37)	29 (34)	.68
Prior stroke (No.) (%)	20 (15)	10 (20)	10 (12)	.18
Atrial fibrillation (No.) (%)	16 (12)	8 (16)	8 (9)	.27
NIHSS (median) (IQR)	15 (12–19)	18 (13–21)	14 (11–18)	.01 <sup>b</sup>
IV-rtPA (No.) (%)	94 (69)	32 (63)	62 (72)	.25
Intra-arterial treatment (No.) (%)	29 (21)	11 (22)	18 (21)	.93
<b>Imaging parameters</b>				
Time to admission scan (min) (median) (IQR)	100 (64–152)	106 (70–240)	91 (63–135)	.11
<b>NCCT</b>				
Early CT signs of infarction, ASPECTS, (median) (IQR)	8 (6–10)	7 (4–9)	9 (7–10)	.0001 <sup>b</sup>
<b>CTP</b>				
CBV deficit, ASPECTS (mean) (SD)	4.30 (2.57)	3.31 (2.32)	4.89 (2.54)	.001 <sup>b</sup>
MTT deficit, ASPECTS (median) (IQR)	1 (0–3)	1 (0–3)	2 (0–3)	.11
CBV deficit in lentiform nucleus (No.) (%)	72 (53)	32 (63)	40 (47)	.15
CBV deficit in caudate nucleus or ACA territory (No.) (%)	54 (39)	28 (55)	26 (30)	.004 <sup>b</sup>
Permeability ratio (median) (IQR) <sup>c</sup>	1.36 (1.13–1.88)	1.66 (1.24–2.60)	1.30 (1.09–1.54)	.002 <sup>b</sup>
<b>CTA</b>				
Clot burden score ≤6 (No.) (%)	99 (73)	44 (86)	55 (65)	.006 <sup>b</sup>
Thrombus location ICA/M1 proximal (No.) (%)	63 (48)	33 (67)	30 (36)	.001 <sup>b</sup>
Poor collateral score (No.) (%)	62 (46)	34 (68)	28 (33)	.0001 <sup>b</sup>
<b>Follow-up CTP and CTA</b>				
No recanalization <sup>c</sup>	26 (33)	6 (32)	20 (33)	.89
No reperfusion <sup>c</sup>	45 (62)	16 (76)	29 (56)	.10

**Note:**—IQR indicates interquartile range.

<sup>a</sup>  $\chi^2$  was used to compare categoric variables, and a *t* test or Mann-Whitney *U* test, continuous variables.

<sup>b</sup> All *P* < .05.

<sup>c</sup> The analysis of permeability ratio, recanalization, and reperfusion is a subanalysis on 101, 79, and 73 cases, respectively.

3.0 days (interquartile range, 2.0–4.0 days) and was not statistically different between patients with and without prominent space-occupying edema. Permeability estimates were only available in 101 patients; and recanalization and reperfusion data, in 79 and 73 patients, respectively.

Patients who developed prominent space-occupying edema had a higher NIHSS score on admission. In addition, early CT signs of infarction (lower ASPECTS), larger CBV deficit (lower ASPECTS), decreased CBV in the caudate nucleus or ACA territory, higher permeability estimates, ICA/proximal M1 occlusions, higher clot burden, and worse collateral scores were more often found in patients with prominent space-occupying edema (all, *P* < .05). Time to admission scan, percentage of patients treated with IV-rtPA or intra-arterial treatment, recanalization, and reperfusion were not significantly different between patients with large infarcts and prominent space-occupying edema and those without prominent space-occupying edema (Table 1). The ORs of univariate regression are summarized in Table 2.

After adjustment for age and NIHSS score, the adjusted OR (Table 2) for prominent space-occupying edema remained significantly higher, with more early CT signs of infarction, larger CBV deficit size, higher permeability estimates, more proximal thrombus location, higher clot burden, and poor collateral scores.

## DISCUSSION

The main finding of this study was that in patients with a large MCA infarct on follow-up, CT signs of infarction on admission NCCT, larger CBV deficits and higher permeability estimates on admission CTP, proximal thrombus location, a higher clot bur-

den, and worse collateral scores on admission CTA are significantly associated with the development of prominent space-occupying edema. These findings suggest that patients who develop prominent space-occupying edema already have an extensive proximal clot and poor collaterals on admission.

Space-occupying edema develops as a combination of swelling of ischemic brain cells (cytotoxic edema) and leakage of fluid through the BBB (vasogenic edema).<sup>28</sup> It is known that the balance between this edema formation and the brain regulatory systems (cerebrovascular autoregulation) that normally maintains cerebral perfusion pressure is impaired in patients with prominent space-occupying edema.<sup>29</sup> This imbalance possibly occurs because of early involvement of a large ischemic area.

This is supported by the more extensive early CT signs of infarction and larger CBV deficits on admission in patients with prominent space-occupying edema, while the time to scanning was not significantly different from that in patients without prominent space-occupying edema. We suggest that the early development of a large ischemic area in patients with prominent space-occupying edema is a consequence of an extensive proximal clot in combination with poor leptomeningeal collateral status, thereby causing a larger ischemic deficit and increased permeability.

The large MCA infarcts on follow-up in patients without prominent space-occupying edema are presumably the result of a more gradually occurring process. The initial thrombus in these patients is located more distally, and this thrombus may extend more proximally with time. Therefore, areas that still maintained

**Table 2: Univariate and multivariate regression**

	OR (95% CI)	aOR (95% CI)
<b>Clinical parameters</b>		
Age (per yr)	0.99 (0.96–1.01)	NA
Female sex	1.17 (0.57–2.40)	0.88 (0.41–1.90)
Prior stroke	1.90 (0.73–4.95)	2.08 (0.74–5.91)
Atrial fibrillation	1.79 (0.63–5.11)	2.74 (0.86–8.70)
NIHSS (per point)	1.12 (1.04–1.21) <sup>a</sup>	NA
IV-rtPA	0.65 (0.31–1.36)	0.56 (0.25–1.22)
Intra-arterial treatment	1.04 (0.45–2.42)	1.03 (0.42–2.49)
<b>Imaging parameters</b>		
Time to admission scan (per min)	1.002 (0.997–1.007)	1.003 (0.999–1.006)
<b>NCCT</b>		
Early CT signs of infarction, ASPECTS (0–10)	1.32 (1.14–1.53) <sup>a</sup>	1.32 (1.13–1.55) <sup>a</sup>
<b>CTP</b>		
CBV deficit, ASPECTS (0–10)	1.30 (1.12–1.52) <sup>a</sup>	1.26 (1.07–1.49) <sup>a</sup>
MTT deficit, ASPECTS (0–10)	1.20 (0.98–1.46)	1.14 (0.93–1.41)
CBV deficit in lentiform nucleus	1.90 (0.93–3.85)	1.53 (0.72–3.22)
CBV deficit in caudate nucleus or ACA territory	2.81 (1.37–5.76) <sup>a</sup>	2.01 (0.93–4.32)
Permeability ratio <sup>b</sup>	2.08 (1.21–3.60) <sup>a</sup>	2.35 (1.30–4.24) <sup>a</sup>
<b>CTA</b>		
Clot burden score ≤6	3.43 (1.38–8.55) <sup>a</sup>	2.88 (1.11–7.45) <sup>a</sup>
Thrombus location	3.64 (1.73–7.69) <sup>a</sup>	3.40 (1.57–7.37) <sup>a</sup>
ICA/M1 proximal versus M1 distal, M2, or >M2		
Poor collateral score	4.33 (2.05–9.13) <sup>a</sup>	3.93 (1.78–8.69) <sup>a</sup>
<b>Follow-up CTP and CTA</b>		
No recanalization <sup>b</sup>	0.92 (0.31–2.79)	0.92 (0.30–2.81)
No reperfusion <sup>b</sup>	2.54 (0.81–7.96)	2.18 (0.67–7.07)

**Note:**—aOR indicates adjusted odds ratio (for age and NIHSS); NA, not applicable.

<sup>a</sup> All  $P < .05$ .

<sup>b</sup> The analysis of permeability ratio, recanalization, and reperfusion is a subanalysis on 101, 79, and 73 cases respectively.

sufficient cerebral perfusion on admission could become infarcted on NCCT on day 3. There was no significant association between treatment with IV-rtPA on admission and recanalization or reperfusion status at day 3 (though recanalization and reperfusion data were only available in 55%–74% of patients). This finding also suggests that the early large extent of the MCA infarct and not recanalization or reperfusion is of importance for the development of prominent space-occupying edema.<sup>30</sup> Moreover, thrombolytic treatment cannot influence the early cascade of events leading to prominent space-occupying edema.

Permeability estimates were a significant factor in univariate regression and after adjusting for age and admission NIHSS. This finding is in agreement with a retrospective study of 120 patients (with 12 patients treated with a hemicraniectomy for prominent space-occupying edema) that showed an association between increased infarct permeability surface area and prominent space-occupying edema occurrence.<sup>9</sup> A relation between the duration of ischemia and the extent of damage to the BBB has also been shown previously.<sup>31,32</sup> The time between symptom onset and the scan series was shorter in our data (100 minutes versus 310 minutes). This difference suggests that the BBB damage already occurred early in patients who developed prominent space-occupying edema.

The cause of prominent space-occupying edema in patients with large MCA infarction has not been clarified so far, to our knowledge. A study of 818 patients with 208 large MCA infarcts showed that atrial fibrillation was more frequent in these infarcts. The authors suggested that a cardiac embolus, in contrast to atherosclerotic thrombi from carotid stenosis, occludes a cerebral artery abruptly, leaving little time for collateral pathways to de-

velop.<sup>3</sup> Although our findings support the suggestion that collaterals are insufficiently present in patients who develop prominent space-occupying edema, we did not find a significant difference in the history of atrial fibrillation. There is still much controversy about the role of collaterals in both chronic and acute occlusive disease and whether cerebral collaterals can develop with time. Our study cannot provide answers for this discussion.

Jaramillo et al<sup>12</sup> showed, in a post-mortem analysis of 45 patients, that anterior cerebral artery territory infarcts were associated with prominent space-occupying edema. Moreover, another study reported that ACA involvement contributes to mortality as a mediator of collateral circulation.<sup>19</sup> Our results did not show a significant relation between additional ACA vascular territory, with or without caudate nucleus involvement, and prominent space-occupying edema. A major difference between our study and the study of Jaramillo et al is that their assessment was performed postmortem after a median of

18 days, while we assessed the admission CT scan obtained within 9 hours of symptom onset.<sup>12</sup> The ACA can infarct at a later time point, secondary to ACA compression caused by subfalcine herniation.<sup>33</sup> This scenario suggests that the ACA involvement in their study was a consequence, rather than a cause, of space-occupying edema formation.

Although age did not make a significant difference in the development of prominent space-occupying edema, generalized atrophy in older patients (as demonstrated in Fig 2A) could protect against the occurrence of substantial mass effect. However, we did not collect these data to investigate this variable.

Strengths of this study are the prospective collection of a large number of patients with prominent space-occupying edema and the combined use of clinical data with NCCT, CTA, and CTP data.

This study also has some limitations. First, our definition of prominent space-occupying edema was based on follow-up NCCT only. In other articles, clinical deterioration was quantified and also considered in the definition of prominent space-occupying edema or malignant MCA infarction.<sup>12,14,30</sup> It is, however, unlikely that patients with prominent space-occupying edema or substantial hemorrhage were missed because additional CT scans were always obtained in case of clinical deterioration during the hospital stay.

Second, the exact time of recanalization was unclear because follow-up scans were obtained after  $3 \pm 2$  days because we had to compromise between short- and long-term follow-up, to reduce potential radiation risks associated with multiple scans. This potential bias makes it necessary to interpret the results of our recanalization and reperfusion data with caution.

Third, 9 patients were excluded because of poor-quality CTP at admission due to technical issues ( $n = 4$ ) and patient movement ( $n = 5$ ). The 3-month mRS score between these 9 excluded patients and the 137 included patients was not significantly different, so it is unlikely that these exclusions caused any bias.

Fourth, patients with early spontaneous recanalization could potentially have influenced our results because CTP and CTA parameters may not always be accurate. However, in these patients, the ischemic changes on NCCT should still be indicative of the severity of the ischemia and thereby associated with prominent mass effect.

## CONCLUSIONS

In patients with large MCA infarctions on follow-up, early CT signs of infarction on admission NCCT, larger CBV deficits, and higher permeability estimates on admission CTP and more proximal thrombus location, higher clot burden, and worse collateral scores on admission CTA were significantly associated with prominent space-occupying edema. These findings suggest that the prominent space-occupying edema in these patients develops due to a combination of extensive proximal occlusion and poor collaterals, which rapidly leads to a large area of ischemia with increased permeability.

## ACKNOWLEDGMENTS

The DUST study investigators are the following: Academic Medical Center, Amsterdam, the Netherlands (Majoie CB, Roos YB); Catharina Hospital, Eindhoven, the Netherlands (Duijm LE, Keizer K); Erasmus Medical Center, Rotterdam, the Netherlands (van der Lugt A, Dippel DW); Gelre Hospitals, Apeldoorn, the Netherlands (Droogh-de Greve KE, Bienfait HP); Leiden University Medical Center, Leiden, the Netherlands (van Walderveen MA, Wermer MJ); Medical Center Haaglanden, The Hague, the Netherlands (Lycklama à Nijeholt GJ, Boiten J); Onze Lieve Vrouwe Gasthuis, Amsterdam, the Netherlands (Duyndam D, Kwa VI); Radboud University Nijmegen Medical Centre, Nijmegen, the Netherlands (Meijer FJ, van Dijk EJ); Rijnstate Hospital, Arnhem, the Netherlands (Kesselring FO, Hofmeijer J); St. Antonius Hospital, Nieuwegein, the Netherlands (Vos JA, Schonewille WJ); St. Elisabeth Hospital, Tilburg, the Netherlands (van Rooij WJ, de Kort PL); St. Franciscus Hospital, Rotterdam, the Netherlands (Pleiter CC, Bakker SL); VU Medical Center, Amsterdam, the Netherlands (Bot J, Visser MC); University Medical Center Utrecht, Utrecht, the Netherlands (Velthuis BK, van der Schaaf IC, Dankbaar JW, Mali WP, van Seeters T, Horsch AD, Niesten JM, Biessels GJ, Kappelle LJ, Luitse MJ, van der Graaf Y).

Disclosures: Birgitta K. Velthuis—RELATED: Grant: Dutch Heart Foundation (2008T034);\* NutsOhra Foundation (0903–012)\*; UNRELATED: Payment for Lectures (including service on Speakers Bureaus): regular presenter for Philips Healthcare.\* Jan W. Dankbaar—RELATED: Grant: Dutch Heart Foundation 2012T061. Edwin Bennink—RELATED: Grant: Netherlands Technology Foundation Stichting voor de Technische Wetenschappen (grant number 11632).\* L.J. Kappelle—UNRELATED: Consultancy: Boehringer Ingelheim, Bayer HealthCare, Bristol-Meyers Squibb; Payment for Lectures (including service on Speakers Bureaus): Boehringer Ingelheim, Bayer HealthCare, Bristol-Meyers Squibb.\* Money paid to the institution.

## REFERENCES

1. Hacke W, Schwab S, Horn M, et al. 'Malignant' middle cerebral artery territory infarction: clinical course and prognostic signs. *Arch Neurol* 1996;53:309–15 CrossRef Medline
2. Berrouschot J, Sterker M, Bettin S, et al. Mortality of space-occupying ('malignant') middle cerebral artery infarction under conservative intensive care. *Intensive Care Med* 1998;24:620–23 CrossRef Medline
3. Heinsius T, Bogousslavsky J, Van Melle G. Large infarcts in the middle cerebral artery territory: etiology and outcome patterns. *Neurology* 1998;50:341–50 CrossRef Medline
4. Vahedi K, Hofmeijer J, Juettler E, et al; DECIMAL, DESTINY, and HAMLET investigators. Early decompressive surgery in malignant infarction of the middle cerebral artery: a pooled analysis of three randomised controlled trials. *Lancet Neurol* 2007;6:215–22 CrossRef Medline
5. Hofmeijer J, Kappelle LJ, Algra A, et al; HAMLET investigators. Surgical decompression for space-occupying cerebral infarction (the Hemicraniectomy After Middle Cerebral Artery infarction with Life-threatening Edema Trial [HAMLET]): a multicentre, open, randomised trial. *Lancet Neurol* 2009;8:326–33 CrossRef Medline
6. Arch AE, Sheth KN. Malignant cerebral edema after large anterior circulation infarction: a review. *Curr Treat Options Cardiovasc Med* 2014;16:275 CrossRef Medline
7. Hofmeijer J, Algra A, Kappelle LJ, et al. Predictors of life-threatening brain edema in middle cerebral artery infarction. *Cerebrovasc Dis* 2008;25:176–84 CrossRef Medline
8. Rudolf J, Grond M, Stenzel C, et al. Incidence of space-occupying brain edema following systemic thrombolysis of acute supratentorial ischemia. *Cerebrovasc Dis* 1998;8:166–71 CrossRef Medline
9. Bektas H, Wu TC, Kasam M, et al. Increased blood-brain barrier permeability on perfusion CT might predict malignant middle cerebral artery infarction. *Stroke* 2010;41:2539–44 CrossRef Medline
10. Bennink E, Riordan AJ, Horsch AD, et al. A fast nonlinear regression method for estimating permeability in CT perfusion imaging. *J Cereb Blood Flow Metab* 2013;33:1743–51 CrossRef Medline
11. Sykora M, Steiner T, Rocco A, et al. Baroreflex sensitivity to predict malignant middle cerebral artery infarction. *Stroke* 2012;43:714–19 CrossRef Medline
12. Jaramillo A, Góngora-Rivera F, Labreuche J, et al. Predictors for malignant middle cerebral artery infarctions: a postmortem analysis. *Neurology* 2006;66:815–20 CrossRef Medline
13. Wartenberg KE. Malignant middle cerebral artery infarction. *Curr Opin Crit Care* 2012;18:152–63 CrossRef Medline
14. Minnerup J, Wersching H, Ringelstein EB, et al. Prediction of malignant middle cerebral artery infarction using computed tomography-based intracranial volume reserve measurements. *Stroke* 2011;42:3403–09 CrossRef Medline
15. van Seeters T, Biessels GJ, van der Schaaf IC, et al. Prediction of outcome in patients with suspected acute ischaemic stroke with CT perfusion and CT angiography: the Dutch Acute Stroke Trial (DUST) study protocol. *BMC Neurol* 2014;14:37 CrossRef Medline
16. Barber PA, Demchuk AM, Zhang J, et al. Validity and reliability of a quantitative computed tomography score in predicting outcome of hyperacute stroke before thrombolytic therapy: ASPECTS Study Group—Alberta Stroke Programme Early CT Score. *Lancet* 2000;355:1670–74 CrossRef Medline
17. Hacke W, Kaste M, Fieschi C, et al. Intravenous thrombolysis with recombinant tissue plasminogen activator for acute hemispheric stroke: the European Cooperative Acute Stroke Study (ECASS). *JAMA* 1995;274:1017–25 CrossRef Medline
18. Dohmen C, Galdiks N, Bosche B, et al. The severity of ischemia determines and predicts malignant brain edema in patients with large middle cerebral artery infarction. *Cerebrovasc Dis* 2012;33:1–87 CrossRef Medline
19. Walcott BP, Miller JC, Kwon CS, et al. Outcomes in severe middle cerebral artery ischemic stroke. *Neurocrit Care* 2014;21:20–26 CrossRef Medline

20. van Seeters T, Biessels GJ, Niesten JM, et al; Dust Investigators. **Reliability of visual assessment of non-contrast CT, CT angiography source images and CT perfusion in patients with suspected ischemic stroke.** *PLoS One* 2013;8:e75615 CrossRef Medline
21. Kasner SE, Demchuk AM, Berrouschot J, et al. **Predictors of fatal brain edema in massive hemispheric ischemic stroke.** *Stroke* 2001;32:2117–23 CrossRef Medline
22. Soares BP, Tong E, Hom J, et al. **Reperfusion is a more accurate predictor of follow-up infarct volume than recanalization: a proof of concept using CT in acute ischemic stroke patients.** *Stroke* 2010;41:e34–40 CrossRef Medline
23. Puetz V, Dzialowski I, Hill MD, et al; Calgary CTA Study Group. **Intracranial thrombus extent predicts clinical outcome, final infarct size and hemorrhagic transformation in ischemic stroke: the clot burden score.** *Int J Stroke* 2008;3:230–36 CrossRef Medline
24. Tan IY, Demchuk AM, Hopyan J, et al. **CT angiography clot burden score and collateral score: correlation with clinical and radiologic outcomes in acute middle cerebral artery infarct.** *AJNR Am J Neuroradiol* 2009;30:525–31 CrossRef Medline
25. Tan JC, Dillon WP, Liu S, et al. **Systematic comparison of perfusion-CT and CT-angiography in acute stroke patients.** *Ann Neurol* 2007;61:533–43 CrossRef Medline
26. El-Mitwalli A, Saad M, Christou I, et al. **Clinical and sonographic patterns of tandem internal carotid artery/middle cerebral artery occlusion in tissue plasminogen activator-treated patients.** *Stroke* 2002;33:99–102 CrossRef Medline
27. Tomsick T, Broderick J, Carrozella J, et al; Interventional Management of Stroke II Investigators. **Revascularization results in the Interventional Management of Stroke II trial.** *AJNR Am J Neuroradiol* 2008;29:582–87 CrossRef Medline
28. Heo JH, Han SW, Lee SK. **Free radicals as triggers of brain edema formation after stroke.** *Free Radic Biol Med* 2005;39:51–70 CrossRef Medline
29. Dohmen C, Bosche B, Graf R, et al. **Identification and clinical impact of impaired cerebrovascular autoregulation in patients with malignant middle cerebral artery infarction.** *Stroke* 2007;38:56–61 CrossRef Medline
30. Thomalla G, Hartmann F, Juettler E, et al; Clinical Trial Net of the German Competence Network Stroke. **Prediction of malignant middle cerebral artery infarction by magnetic resonance imaging within 6 hours of symptom onset: a prospective multicenter observational study.** *Ann Neurol* 2010;68:435–45 CrossRef Medline
31. Ito U, Go KG, Walker JT Jr, et al. **Experimental cerebral ischemia in Mongolian gerbils. III: behaviour of the blood-brain barrier.** *Acta Neuropathol* 1976;34:1–6 CrossRef Medline
32. Todd NV, Picozzi P, Crockard A, et al. **Duration of ischemia influences the development and resolution of ischemic brain edema.** *Stroke* 1986;17:466–71 CrossRef Medline
33. Grossman RI, Yousem DM. *Neuroradiology: The Requisites*. 2nd ed. Philadelphia: Mosby, Elsevier; 2003:261–63

## TICI and Age: What's the Score?

L.A. Slater, J.M. Coutinho, J. Gralla, R.G. Nogueira, A. Bonafé, A. Dávalos, R. Jahan, E. Levy, B.J. Baxter, J.L. Saver, and V.M. Pereira; for the STAR and SWIFT investigators

### ABSTRACT

**BACKGROUND AND PURPOSE:** Previous studies have suggested that advanced age predicts worse outcome following mechanical thrombectomy. We assessed outcomes from 2 recent large prospective studies to determine the association among TICI, age, and outcome.

**MATERIALS AND METHODS:** Data from the Solitaire FR Thrombectomy for Acute Revascularization (STAR) trial, an international multicenter prospective single-arm thrombectomy study and the Solitaire arm of the Solitaire FR With the Intention For Thrombectomy (SWIFT) trial were pooled. TICI was determined by core laboratory review. Good outcome was defined as an mRS score of 0–2 at 90 days. We analyzed the association among clinical outcome, successful-versus-unsuccessful reperfusion (TICI 2b–3 versus TICI 0–2a), and age (dichotomized across the median).

**RESULTS:** Two hundred sixty-nine of 291 patients treated with Solitaire in the STAR and SWIFT data bases for whom TICI and 90-day outcome data were available were included. The median age was 70 years (interquartile range, 60–76 years) with an age range of 25–88 years. The mean age of patients 70 years of age or younger was 59 years, and it was 77 years for patients older than 70 years. There was no significant difference between baseline NIHSS scores or procedure time metrics. Hemorrhage and device-related complications were more common in the younger age group but did not reach statistical significance. In absolute terms, the rate of good outcome was higher in the younger population (64% versus 44%,  $P < .001$ ). However, the magnitude of benefit from successful reperfusion was higher in the 70 years of age and older group (OR, 4.82; 95% CI, 1.32–17.63 versus OR 7.32; 95% CI, 1.73–30.99).

**CONCLUSIONS:** Successful reperfusion is the strongest predictor of good outcome following mechanical thrombectomy, and the magnitude of benefit is highest in the patient population older than 70 years of age.

**ABBREVIATIONS:** AIS = acute ischemic stroke; NASA = North American Solitaire Stent Retriever Acute Stroke; STAR = Solitaire FR Thrombectomy for Acute Revascularization; SWIFT = Solitaire FR With the Intention For Thrombectomy; TIMI = Thrombolysis in Myocardial Infarction

The clinical outcome after acute ischemic stroke is generally worse in the elderly compared with nonelderly populations.<sup>1,2</sup> Poorer outcomes are to be expected in the elderly population in all disease states; however, the effect of a therapy may still

afford a similar magnitude of benefit.<sup>3</sup> Results from the Third International Stroke Trial suggest that the therapeutic effect of IV-tPA is similar or even better in the elderly population.<sup>4,5</sup> With regard to stroke therapy, recanalization has been definitively related to good clinical outcomes.<sup>6–8</sup> However, it has been reported in multiple studies that despite similar rates of recanalization, the elderly have higher mortality rates and poorer outcomes than younger patients following intra-arterial treatment.<sup>7,9–13</sup> These studies were mostly retrospective, single-center series or used older generation devices with suboptimal reperfusion rates.<sup>7,9–13</sup> Recent clinical studies demonstrating the value of mechanical thrombectomy for acute ischemic stroke (AIS) did not include a significant number of elderly patients.<sup>14–17</sup> We performed a post

Received July 1, 2015; accepted after revision September 7.

From the Division of Neuroradiology (L.A.S., J.M.C., V.M.P.), Joint Department of Medical Imaging, Department of Medical Imaging, and Division of Neurosurgery (V.M.P.), Department of Surgery, Toronto Western Hospital, University Health Network, University of Toronto, Toronto, Ontario, Canada; Service of Neuroradiology (J.G.), Inselspital, University of Bern, Bern, Switzerland; Marcus Stroke and Neuroscience Center (R.G.N.), Department of Neurology, Grady Memorial Hospital, Emory University School of Medicine, Atlanta, Georgia; Department of Neuroradiology (A.B.), Hôpital Gui-de-Chauliac, Montpellier, France; Department of Neurosciences (A.D.), Hospital Universitario Germans Trias i Pujol, Barcelona, Spain; Division of Interventional Neuroradiology (R.J.), and Department of Neurology and Comprehensive Stroke Center (J.L.S.), David Geffen School of Medicine, University of California, Los Angeles, Los Angeles, California; Toshiba Stroke and Vascular Research Center (E.L.), State University of New York at Buffalo, Buffalo, New York; and Department of Radiology (B.J.B.), Erlanger Hospital at the University of Tennessee, Chattanooga, Tennessee.

Please address correspondence to Vitor Mendes Pereira, MD MSc, Toronto Western Hospital and University Health Network, 3MCL-436; 399 Bathurst St, Toronto, ON, M5T 2S8, Canada; e-mail: vitormpbr@hotmail.com

<http://dx.doi.org/10.3174/ajnr.A4618>

**Table 1: Demographics and baseline characteristics**

Characteristic	70 Years or Younger	Older Than 70 Years	P Value
No.	135	134	
Male	49% (66/135)	34% (45/134)	.013
NIHSS (median) (IQR)	18 (14–20)	17 (13–20)	.359
Prestroke mRS (categorical)			<.001
0	81% (95/118)	63% (71/113)	
1	15% (18/118)	17% (19/113)	
2	3% (3/118)	19% (21/113)	
3	2% (2/118)	2% (2/113)	
Occluded vessel			.101
ICA	21% (28/130)	7% (22/132)	
M1	70% (91/130)	64% (84/132)	
M2	8% (10/130)	18% (24/132)	
M3	1% (1/130)	2% (2/132)	
Baseline ASPECTS (mean)	8.1 ± 1.9 (133)	8.4 ± 1.4 (133)	.207
IV-tPA	63% (77/123)	58% (70/121)	.513
Baseline serum glucose level (mean)	127 ± 56 (130)	126 ± 56 (129)	.865
Atrial fibrillation	27% (36/135)	51% (68/134)	<.001
Hypertension	53% (72/135)	74% (99/134)	<.001
Coronary artery disease	21% (29/135)	25% (34/134)	.474
Diabetes	19% (25/135)	19% (25/134)	1
Hyperlipidemia	46% (62/135)	39% (52/134)	.267
Peripheral artery disease	1% (2/135)	0% (0/134)	.498
Smoking	24% (32/135)	4% (5/134)	<.001
Prior stroke or TIA	13% (17/135)	25% (34/134)	.008

Note:—IQR indicates interquartile range.

hoc analysis of 2 prospective core lab–reviewed studies assessing mechanical thrombectomy by using new-generation devices (stent retrievers) for AIS to determine whether the benefit of reperfusion was constant across age groups, including the older population.

## MATERIALS AND METHODS

### Study Design and Patient Selection

We pooled data from the Solitaire FR Thrombectomy for Acute Revascularization (STAR) study and the Solitaire arm of Solitaire FR With the Intention For Thrombectomy (SWIFT) trial. Details of both studies have been previously reported.<sup>18,19</sup> Briefly, STAR was a prospective, multicenter, single-arm study. Key inclusion criteria were presentation within 8 hours of onset of acute ischemic stroke, a proximal occlusion of an anterior circulation vessel, age between 18 and 85 years, and a National Institutes of Health Stroke Scale score of 8–30. All patients were treated in high-volume stroke centers with a Solitaire stent retriever (Covidien, Irvine, California) through a balloon-guided catheter.<sup>19</sup> SWIFT was a randomized open-label trial with blinded end point assessment comparing the Solitaire stent retriever with the Merci retriever (Concentric Medical, Mountain View, California). The study included patients 22–85 years of age with NIHSS scores of 8–30. Patients were either ineligible for or had not responded to intravenous rtPA.<sup>18</sup>

All data in the STAR and SWIFT studies were determined by an independent CT and MR imaging core laboratory, a separate angiography core laboratory, and an independent clinical events committee. The clinical events committee was responsible for the review and validation of all complications that occurred during the course of the studies and the subsequent classification of these complications related to the device or procedure. The study data were independently monitored; study management was provided

by the sponsor, Covidien. Clinical outcome was determined at 90 days with the modified Rankin Scale. Reperfusion results were reported by using the Thrombolysis in Cerebral Infarction score and was defined as ranging from no reperfusion (TICI = 0) to complete reperfusion (TICI = 3), including partial reperfusion of TICI 2, divided into 2a and 2b as less than and greater than 50%, respectively.<sup>20</sup> This definition is different from the original one in which 2a was defined as less than two-thirds perfusion of the distal territory, and 2b, as greater than two-thirds perfusion.<sup>21</sup> Intracranial hemorrhage was reported with the European Cooperative Acute Stroke Study classification.<sup>22</sup> For the current study, we excluded patients from both studies for whom no TICI score or 90-day mRS was available.

### Data Analysis

Based on the distribution of age, patients within the cohort were dichotomized into 2 groups across the median for age. We studied differences in baseline patient characteristics and treatment details between the age groups. For continuous variables, we used a *t* test or Wilcoxon test, and for discrete variables, a Fisher exact test. We then used multivariate logistic regression analysis to assess the effect of successful reperfusion (TICI 2b–3) versus unsuccessful reperfusion (TICI 0–2a) on clinical outcome in each age group. Good clinical outcome at 90 days was defined as a mRS score of 0–2.

We calculated odds ratios, adjusting for the following variables: atrial fibrillation, ASPECTS, NIHSS score at admission, dyslipidemia, sex, hypertension, location of occlusion, use of IV-tPA, prestroke mRS, and smoking.

## RESULTS

A total 269 of the 291 patients treated with the Solitaire device in the STAR and SWIFT trials were included in this analysis. Twenty-two patients were excluded because of missing mRS scores at 90 days (*n* = 7) or missing TICI scores (*n* = 15). The median age for the entire cohort was 70 years (interquartile range, 60–76 years), and the age range was 25–88 years. The mean age for patients 70 years or younger was 59 years, and for those older than 70, it was 77 years. The baseline characteristics are summarized in Table 1. The proportion of men was higher among the younger compared with the older patients (49% versus 34%, *P* = .013). The baseline NIHSS score did not differ between the groups (18 versus 17, *P* = .359). There was a significantly lower rate of atrial fibrillation (27% versus 51%, *P* < .001), hypertension (53% versus 74%, *P* < .001), and prior stroke or TIA (13% versus 25%, *P* = .008) in the younger group, while smoking was more common in the 70 years and younger group (24% versus 4%, *P* < .001). The proportion of patients with a prestroke mRS of zero was lower in

**Table 2: Details of endovascular procedure<sup>a</sup>**

	70 Years or Younger	Older Than 70 Years	P Value
No. of Solitaire passes (mean)	1.8 ± 1.0	1.7 ± 1.0	.420
Time from symptom onset to hospital arrival	178 (98–265)	172 (68–245)	.263
Time from groin puncture to balloon guiding catheter	11 (6–17)	12 (8–17)	.12
Time from symptom onset to groin puncture	253 (205–322)	255 (185–323)	.714
Time from groin puncture to reperfusion	46 (28–68)	42 (32–70)	.714
TICI 2b–3	87% (117/135)	83% (111/134)	.400
General anesthesia	67% (90/135)	65% (87/134)	.763
Conscious sedation	29% (39/135)	28% (38/134)	.763

Note:—IQR indicates interquartile range.

<sup>a</sup> All times are given as median minutes with IQR in parentheses.

**Table 3: Complications and outcome stratified by age**

	70 Years or Younger	Older Than 70 Years	P Value
Complication			
Symptomatic intracerebral hemorrhage	4% (5/135)	1% (2/134)	.447
PH-1 intracerebral hemorrhage	2% (3/135)	1% (2/134)	.1
PH-2 intracerebral hemorrhage	2% (3/135)	0% (0/134)	.247
SAH intracerebral hemorrhage	1% (2/135)	2% (3/134)	.684
IVH intracerebral hemorrhage	0% (0/135)	1% (1/134)	.498
Any intracerebral hemorrhage	19% (25/135)	14% (19/134)	.410
Vasospasm	27% (36/135)	17% (23/134)	.077
Device-related AE	16% (21/135)	14% (19/134)	.864
Outcome at 90 days			
All-cause mortality	8% (11/135)	12% (16/134)	.318
mRS 0–2	64% (87/135)	12% (59/134)	0.318

Note:—PH-1 indicates parenchymal hematoma type 1; PH-2, parenchymal hematoma type 2; IVH, intraventricular hemorrhage; AE, adverse events.

**Table 4: Rate of good outcome according to age and TICI score<sup>a</sup>**

Age Groups (yr)	TICI 2b–3	TICI 0–2a	Unadjusted OR (95% CI)	Adjusted OR (95% CI)
70 or younger	67.5% (79/117)	44.4% (8/18)	2.6 (0.95–7.11)	4.82 (1.32–17.63)
Older than 70	49.5% (55/111)	17.4% (4/23)	4.66 (1.49–14.59)	7.32 (1.73–30.99)

<sup>a</sup> The frequency of good clinical outcome is given according to age and TICI scores. For each age group, the OR is provided for good outcome in patients with successful reperfusion (TICI 2b–3) vs unsuccessful reperfusion (TICI 0–2a).

**Table 5: Rates of good outcome according to age quartiles and TICI score**

Age (yr)	TICI 0–2a	TICI 2b–3	P Value
60 or younger	75.0% (9/12)	87.0% (47/54)	.372
61–70	50.0% (3/6)	73.0% (46/63)	.346
71–77	46.7% (7/15)	74.1% (43/58)	.061
78 or older	25.0% (2/8)	67.9% (36/53)	.044

the older than 70 years of age group (81% versus 63%,  $P < .001$ ). Although not reaching statistical significance, the mean baseline ASPECTS was slightly lower in the 70 years and younger group (8.1 versus 8.4,  $P = .207$ ). There was a trend toward a higher proportion of M2 occlusions in the older than 70 years of age group (8% versus 18%,  $P = .101$ ).

There was no significant difference in the proportion of patients who received IV-tPA in the 2 groups (63% versus 58%,  $P = .513$ , Table 1). There was no significant difference in the mechanical thrombectomy and time metrics, with a similar number of Solitaire passes, times of onset to arrival at the hospital and groin punctures, and similar types of anesthesia used and number of TICI 2b–3 reperfusion (Table 2).

Complications including intracranial hemorrhage, vasospasm, and device-related problems are summarized in Table 3. Although not reaching statistical significance, intracranial hemorrhage (19% versus 14%,  $P = .410$ ) and vasospasm (27% versus 17%,  $P = .077$ ) occurred more often in the younger age group. Device-related complications were similar between the 2 groups (16% versus 14%,  $P = .864$ ). There was a trend toward higher overall 90-day mortality in the older group (8% versus 12%  $P = .318$ ). Good clinical outcome was achieved in 64% of the 70 years and younger and 44% of the 70 years and older groups ( $P < .001$ ).

The rates of good outcome according to TICI score and age are summarized in Table 4. Univariate analysis showed that the effect of successful reperfusion on good outcome was more pronounced in the older than 70 years of age group than in the 70 years of age or younger group (OR, 2.6; 95% CI, 0.95–7.11 versus 4.66; 95% CI, 1.49–14.59). The same trend was seen when dividing the patients into quartiles, with overall better outcomes in the younger patients but a greater differential between good outcomes for unsuccessful-versus-successful outcome as age increased (Table 5). After adjustment for potential confounders, the strength of the association between successful reperfusion and outcome increased in both age groups but remained stronger in the age group older than 70

years (OR, 4.82; 95% CI, 1.32–17.63;  $P = .018$  versus OR, 7.32; 95% CI, 1.73–30.99;  $P = .007$ ). Table 6 demonstrates multivariate analysis of the predictors of good outcome following mechanical thrombectomy in patients younger and older than 70 years.

## DISCUSSION

Our post hoc analysis of the STAR trial and the patients from the Solitaire arm of the SWIFT trial, 2 prospective core lab–reviewed studies evaluating these new-generation devices, demonstrates that successful reperfusion, as defined by a TICI score of 2b or 3, after endovascular treatment of AIS, is the most significant variable in achieving good clinical outcome and is more significant in the elderly population. When we dichotomized patients across the age median, similar rates of successful reperfusion (87% versus 83%  $P = .4$ ) were demonstrated in both groups of patients and higher rates of good clinical outcome, given successful reperfusion, were demonstrated in the younger patients (younger than 70 years of age = 67.5%, older than 70 years of age = 49.5%). However, the effect of successful reperfusion was more pronounced in the older patients, with a higher odds ratio of 7.32 for good out-

**Table 6: Predictors of good outcome following mechanical thrombectomy in younger and older patients**

Variable	70 Years or Younger			Older Than 70 Years		
	OR	95% CI	P Value	OR	95% CI	P Value
Afib	0.53	(0.18–1.61)	.265	1.5	(0.58–3.90)	.407
Baseline ASPECTS	1.16	(0.91–1.49)	.222	1.06	(0.73–1.54)	.752
Baseline NIHSS	0.88	(0.78–0.99)	.033	0.86	(0.78–0.96)	.006
Female	1.28	(0.49–3.33)	.617	1.07	(0.39–2.97)	.898
HTN	0.57	(0.20–1.63)	.296	1	(0.34–2.95)	.995
ICA	4.01	(0.88–18.33)	.073	0.35	(0.08–1.44)	.145
IV-tPA	1.06	(0.38–2.96)	.915	2.32	(0.89–6.06)	.086
Prestroke mRS score	0.53	(0.26–1.11)	.092	0.64	(0.38–1.10)	.104
TICI 2b–3	4.82	(1.32–17.63)	.018	7.32	(1.73–30.99)	.007

**Note:**—Afib indicates atrial fibrillation; HTN, hypertension.

come in the patients older than 70 years compared with the younger cohort for whom the odds ratio was 4.8. Recent randomized controlled trials demonstrated the benefit of mechanical thrombectomy by using stent retrievers in the treatment of AIS (Solitaire With the Intention for Thrombectomy as Primary Endovascular Treatment [SWIFT-PRIME], Endovascular Treatment for Small Core and Proximal Occlusion Ischemic Stroke [ESCAPE], Multicenter Randomized Clinical Trial of Endovascular treatment for Acute Ischemic Stroke in the Netherlands [MR CLEAN], and Extending the Time for Thrombolysis in Emergency Neurological Deficits–Intra-Arterial [EXTEND-IA] trials).<sup>14–17</sup> Patient selection and new treatment guidelines are crucial at this point.

Although there was a trend toward higher 90-day mortality in the older group, this did not reach statistical significance (8% versus 12%,  $P = .318$ ). These mortality rates were lower for both age groups than those reported in previous studies, with the North American Solitaire Stent Retriever Acute Stroke (NASA) registry reporting 27.3% 90-day mortality in the younger group and 43.9% in the older group.<sup>12</sup> Most interesting, Engelter et al<sup>9</sup> in their analysis of IV thrombolysis and Mono et al<sup>10</sup> in their analysis of intra-arterial thrombolysis reported lower rates of 90-day mortality compared with the NASA registry, with 12% and 22% mortality for younger cohorts, respectively, and 32% and 40% mortality in the older cohorts. The Engelter and Mono studies reviewed results using treatment methods with lower recanalization rates than stent retrievers, and the NASA registry had an older patient population. Additionally, in our study, there was no difference in intracranial hemorrhage rates of all types in the younger age group (19% versus 14%,  $P = .410$ ); moreover, hemorrhage did not have a significant impact on differences in clinical outcome or mortality rates between the 2 groups and is in keeping with previously published results.<sup>12</sup>

Singer et al<sup>22</sup> demonstrated the highest rates of good clinical outcome (mRS  $\leq 2$ ) in the youngest quartile (60%) and the lowest in the oldest quartile (17%). They then dichotomized the entire patient cohort into good and poor clinical outcomes and determined the proportion of patients within each group in whom successful reperfusion was achieved. Thrombolysis in Myocardial Infarction (TIMI) 2–3 was achieved in 95% and 75% of those with good and poor clinical outcomes, respectively.<sup>23</sup> Kurre et al<sup>13</sup> analyzed intra-arterial therapy in patients with AIS 80 years of age and older and reported successful recanalization as defined by

TICI 2b–3 in 87.9% of patients; however, only 17.4% of patients achieved functional independence. Castonguay et al<sup>12</sup> evaluated the data from the NASA registry and reported successful recanalization in 73.1% of the patients 80 years of age and younger and 69.2% of patients older than 80 years when evaluated by the TICI score and in 84% of the younger group and 83.3% of the older group when using TIMI, with rates of good outcomes of 45.4% and 27.3% in the younger and older populations,

respectively.

Mono et al<sup>10</sup> assessed treatment of AIS with intra-arterial thrombolysis and measured successful revascularization as TIMI 2–3; this was demonstrated in 71% of the younger patients and 65% of the older patients, with good clinical outcomes in 46% of the younger patients and 28% of the older patients.<sup>7</sup> Luedi et al<sup>7</sup> analyzed outcome in quartiles and demonstrated TIMI 2–3 recanalization achieved in 81.3% and good outcome in 64.7% of the patients in the youngest quartile and TIMI 2–3 achieved in 73.8% and good outcome achieved in 20.3% of the patients in the oldest quartile.<sup>7</sup> Although assessing IV thrombolysis, Engelter et al<sup>9</sup> also demonstrated poorer outcomes in the younger-versus-older groups (37% versus 29%) and revascularization rates were not reported; however, it would be expected that lower rates of successful revascularization would have been achieved given that no intra-arterial therapy was used.

These studies consistently demonstrated lower absolute rates of good outcome in the older age groups; and similar to results of studies using first-generation mechanical thrombectomy devices, high recanalization rates did not always equate to clinical benefit.<sup>21,24,25</sup> Furthermore, previous analysis of the STAR registry by using stratification by the Stroke Prognostication using Age and NIH Stroke Scale (SPAN) demonstrated poorer outcomes in patients with SPAN-100-positive scores, that is, patients with AIS in whom age + presentation NIHSS were  $> 100$ .<sup>26</sup> Of note, the baseline NIHSS score did not differ significantly between the older and younger groups in our study or indeed in the other studies comparing outcomes between the 2 age groups. This finding confirms the expectation that poorer outcomes are expected in older age groups unless good reperfusion is achieved.

Although our analysis also demonstrated lower rates of good outcomes in the older patients, the rates of good outcome were higher than those in previous series. The overall better outcomes may be due to faster procedure times, new-generation devices, and criteria for center selection for the trials requiring high volume and experienced stroke centers.<sup>18,19,27</sup> The mean time from symptom onset to groin puncture in the NASA registry was 364.7 minutes for the younger cohort and 358.9 minutes in the older cohort, compared with 253 minutes and 255 minutes in our study; and the mean time from groin puncture to reperfusion was 71.7 minutes and 93.1 minutes within the NASA registry and 46 minutes and 42 minutes in our series for the younger and older cohorts, respectively.<sup>12</sup> Additionally, well-defined imaging

criteria were used to select patients with both a large vessel occlusion and a favorable ASPECTS, and patient selection is likely to play a role in determining good outcome. Improved likelihood of good outcome in patients selected using imaging criteria was highlighted by an assessment of stroke therapy scoring grades performed by Marks et al,<sup>28</sup> in which better clinical outcomes were associated with TICI 2b–3 scores compared with TICI 0–2a and with TIMI 2 or 3 scores only when the patient had a target mismatch, suggesting that good outcome is dependent more on reperfusion than on recanalization. Furthermore, Daniere et al<sup>29</sup> found that despite higher ASPECTSs in the older age groups, they still had significantly poorer outcomes than the younger groups. The authors concluded that the elderly may benefit from thrombectomy when their core volume is small, and they suggested that an age-adjusted ASPECTS should be used to maximize the chance of good clinical outcome postintervention.

To our knowledge, our analysis is the first to use prospective core lab–reviewed data, including patients between 25 and 88 years of age. We have chosen to dichotomize the cohort across the median, reducing the mean age of our younger (59 years of age) and older (77 years of age) cohorts compared with some other series. However, we think that this limitation is somewhat countered by the robust nature of the data, and thus is still sufficient to illustrate the principle that age should not be the sole determinant of whether to treat and that if a patient qualifies for treatment, particularly in the older groups, attempts should be made to achieve TICI 2b–3 reperfusion because these patients are afforded the greatest benefit from successful reperfusion.

The results from the recently published Multicenter Randomized Clinical Trial of Endovascular Treatment for Acute Ischemic Stroke in the Netherlands (MR CLEAN) demonstrated the efficacy and safety of intra-arterial therapy for acute stroke; and in addition, in their subgroup analysis, the patients in the 80 years of age and older group showed a greater benefit with intervention than the younger than 80 years of age group.<sup>15</sup> Although this was an assessment of intervention overall rather than reperfusion alone, it further indicates that the elderly should not be denied intra-arterial stroke therapy on the basis of age alone. This finding is similar to those in studies of IV-tPA for AIS in which subgroup analyses have demonstrated that the elderly not only benefit from IV-tPA but may even benefit more than the younger population; therefore, patients presenting with AIS should not be excluded from receiving treatment on the basis of age alone.<sup>4,30</sup>

A limitation of this analysis and indeed from applying the results of the recently published trials to elderly patients is that for the most part, the proportion of patients older than 80 years of age was small, and it is conceivable that the benefit of reperfusion may have a ceiling effect. Now that there is proof of principle for mechanical thrombectomy and there is evidence suggesting that the older patients not only benefit but may benefit more significantly when successful reperfusion is achieved, further evaluation of endovascular therapy for AIS in the older population should be performed with a focus on revascularization. Given the aging population, particular attention should be paid to those older than 80 years of age either

in the form of well-documented registries or randomized controlled trials.

## CONCLUSIONS

Successful reperfusion is the strongest predictor of good outcome following mechanical thrombectomy, and the magnitude of benefit is highest in the patient population older than 70 years of age.

Disclosures: Jonathan M. Coutinho—UNRELATED: Payment for Lectures (including service on Speakers Bureaus); Boehringer Ingelheim.\* Comments: All lecturing fees have been donated to the Stichting Klinische Neurologie, a local foundation that supports research in the field of neurological disorders. Jan Gralla—UNRELATED: Consultancy: Covidien.\* Comments: Former Global Principal Investigator of the STAR study, consultant for Covidien. Alain Bonafé—UNRELATED: Consultancy: Covidien.\*; Payment for Lectures (including service on Speakers Bureaus): Covidien. Antoni Dávalos—RELATED: Grant: Covidien.\* Comments: unrestricted grant for the Endovascular Revascularization With Solitaire Device Versus Best Medical Therapy in Anterior Circulation Stroke Within 8 Hours trial. Reza Jahan—RELATED: Consulting Fee or Honorarium: Covidien; Support for Travel to Meetings for the Study or Other Purposes: Covidien; UNRELATED: Consultancy: Covidien; Payment for Lectures (including service on Speakers Bureaus): Covidien. Elad Levy—UNRELATED: Consultancy: Pulsar; Expert Testimony: renders medical/legal opinion as an expert witness; Payment for Lectures (including service on Speakers Bureaus): Covidien. Comments: honorarium for training and lectures; Payment for Development of Educational Presentations: Abbott Vascular. Comments: carotid training sessions for physicians; Stock/Stock Options: Intratech Medical Ltd/Blockade Medical LLC; Other: Covidien. Comments: National Principal Investigator for Solitaire with the Intention for Thrombectomy as Primary Endovascular Treatment for Acute Ischemic Stroke Trial. Blaise J. Baxter—UNRELATED: Consultancy: Covidien, Penumbra, Stryker, Silk Road; Payment for Lectures (including service on Speakers Bureaus): Covidien, Penumbra, Stryker, Silk Road; Patents (planned, pending or issued): United States patent 8622992, held by Advanced Catheter Therapies. Comments: No royalties received, not developed to commercialization; Travel/Accommodations/Meeting Expenses Unrelated to Activities Listed: Covidien, Penumbra, Stryker, Silk Road. Jeffrey L. Saver—RELATED: Grant: Covidien.\*; Consulting Fee or Honorarium: Covidien.\*; Support for Travel to Meetings for the Study or Other Purposes: Covidien.\*; UNRELATED: Consultancy: Stryker.\* Neuravi.\*; Payment for Lectures (including service on Speakers Bureaus): Covidien.\*; Patents (planned, pending or issued): University of California.\* Vitor Mendes Pereira—RELATED: Consulting Fee or Honorarium: Medtronic.\* Comments: Principal Investigator of the STAR trial. \*Money paid to the institution.

## REFERENCES

1. Fonarow GC, Reeves MJ, Zhao X, et al; Get With the Guidelines-Stroke Steering Committee and Investigators. **Age-related differences in characteristics, performance measures, treatment trends, and outcomes in patients with ischemic stroke.** *Circulation* 2010; 121:879–91 CrossRef Medline
2. Saposnik G, Cote R, Phillips S, et al; Stroke Outcome Research Canada (SORCan) Working Group. **Stroke outcome in those over 80: a multicenter cohort study across Canada.** *Stroke* 2008;39:2310–17 Medline
3. Fries JF. **Ageing, natural death, and the compression of morbidity.** *N Engl J Med* 1980;303:130–35 Medline
4. Sandercock P, Wardlaw JM, Lindley RI, et al; IST-3 collaborative group. **The benefits and harms of intravenous thrombolysis with recombinant tissue plasminogen activator within 6 h of acute ischaemic stroke (the third International Stroke Trial [IST-3]): a randomised controlled trial.** *Lancet* 2012;379:2352–63 CrossRef Medline
5. Chapman SN, Mehndiratta P, Johansen MC, et al. **Current perspectives on the use of intravenous recombinant tissue plasminogen activator (tPA) for treatment of acute ischemic stroke.** *Vasc Health Risk Manag* 2014;10:75–87 CrossRef Medline
6. Rha JH, Saver JL. **The impact of recanalization on ischemic stroke outcome: a meta-analysis.** *Stroke* 2007;38:967–73 Medline
7. Luedi R, Hsieh K, Slezak A, et al. **Age dependency of safety and outcome of endovascular therapy for acute stroke.** *J Neurol* 2014;261:1622–27 CrossRef Medline

8. Dávalos A, Pereira VM, Chapot R, et al; Solitaire Group. **Retrospective multicenter study of Solitaire FR for revascularization in the treatment of acute ischemic stroke.** *Stroke* 2012;43:2699–705 Medline
9. Engelter ST, Reichhart M, Sekoranja L, et al. **Thrombolysis in stroke patients aged 80 years and older: Swiss survey of IV thrombolysis.** *Neurology* 2005;65:1795–98 Medline
10. Mono ML, Romagna L, Jung S, et al. **Intra-arterial thrombolysis for acute ischemic stroke in octogenarians.** *Cerebrovasc Dis* 2012;33:116–22 CrossRef Medline
11. Shi ZS, Liebeskind DS, Xiang B, et al; Multi MERCI, TREVO, and TREVO 2 Investigators. **Predictors of functional dependence despite successful revascularization in large-vessel occlusion strokes.** *Stroke* 2014;45:1977–84 CrossRef Medline
12. Castonguay AC, Zaidat OO, Novakovic R, et al. **Influence of age on clinical and revascularization outcomes in the North American Solitaire Stent-Retriever Acute Stroke Registry.** *Stroke* 2014;45:3631–36 CrossRef Medline
13. Kurre W, Aguilar-Pérez M, Niehaus L, et al. **Predictors of outcome after mechanical thrombectomy for anterior circulation large vessel occlusion in patients aged  $\geq 80$  years.** *Cerebrovasc Dis* 2013;36:430–36 CrossRef Medline
14. Saver JL, Goyal M, Bonafé A, et al. **Solitaire<sup>TM</sup> With the Intention for Thrombectomy as Primary Endovascular Treatment for Acute Ischemic Stroke (SWIFT PRIME) trial: protocol for a randomized, controlled, multicenter study comparing the Solitaire revascularization device with IV tPA with IV tPA alone in acute ischemic stroke.** *Int J Stroke* 2015;10:439–48 CrossRef Medline
15. Berkhemer OA, Fransen PS, Beumer D, et al; MR CLEAN Investigators. **A randomized trial of intraarterial treatment for acute ischemic stroke.** *N Engl J Med* 2015;372:11–20 CrossRef Medline
16. Campbell BC, Mitchell PJ, Kleinig TJ, et al; EXTEND-IA Investigators. **Endovascular therapy for ischemic stroke with perfusion-imaging selection.** *N Engl J Med* 2015;372:1009–18 CrossRef Medline
17. Goyal M, Demchuk AM, Menon BK, et al; ESCAPE Trial Investigators. **Randomized assessment of rapid endovascular treatment of ischemic stroke.** *N Engl J Med* 2015;372:1019–30 CrossRef Medline
18. Saver JL, Jahan R, Levy EI, et al; SWIFT Trialists. **Solitaire flow restoration device versus the Merci Retriever in patients with acute ischaemic stroke (SWIFT): a randomised, parallel-group, non-inferiority trial.** *Lancet* 2012;380:1241–49 CrossRef Medline
19. Pereira VM, Gralla J, Dávalos A, et al. **Prospective, multicenter, single-arm study of mechanical thrombectomy using Solitaire Flow Restoration in acute ischemic stroke.** *Stroke* 2013;44:2802–07 CrossRef Medline
20. Tomsick T, Broderick J, Carrozella J, et al; Interventional Management of Stroke II Investigators. **Revascularization results in the Interventional Management of Stroke II trial.** *AJNR Am J Neuroradiol* 2008;29:582–87 Medline
21. Hacke W, Kaste M, Fieschi C, et al. **Intravenous thrombolysis with recombinant tissue plasminogen activator for acute hemispheric stroke: the European Cooperative Acute Stroke Study (ECASS).** *JAMA* 1995;274:1017–25 Medline
22. Singer OC, Haring HP, Trenkler J, et al. **Age dependency of successful recanalization in anterior circulation stroke: the ENDOSTROKE study.** *Cerebrovasc Dis* 2013;36:437–45 CrossRef Medline
23. Smith WS, Sung G, Saver J, et al. **Mechanical thrombectomy for acute ischemic stroke: final results of the Multi MERCI trial.** *Stroke* 2008;39:1205–12 Medline
24. Smith WS, Sung G, Starkman S, et al; MERCI Trial Investigators. **Safety and efficacy of mechanical embolectomy in acute ischemic stroke: results of the MERCI trial.** *Stroke* 2005;36:1432–38 Medline
25. Penumbra Pivotal Stroke Trial Investigators. **The Penumbra pivotal stroke trial: safety and effectiveness of a new generation of mechanical devices for clot removal in intracranial large vessel occlusive disease.** *Stroke* 2009;40:2761–68 CrossRef Medline
26. Almekhlafi MA, Dávalos A, Bonafé A, et al; STAR Registry Investigators. **Impact of age and baseline NIHSS scores on clinical outcomes in the mechanical thrombectomy using Solitaire FR in acute ischemic stroke study.** *AJNR Am J Neuroradiol* 2014;35:1337–40 CrossRef Medline
27. Menon BK, Almekhlafi MA, Pereira VM, et al; STAR Study Investigators. **Optimal workflow and process-based performance measures for endovascular therapy in acute ischemic stroke: analysis of the Solitaire FR Thrombectomy for Acute Revascularization study.** *Stroke* 2014;45:2024–29 CrossRef Medline
28. Marks MP, Lansberg MG, Mlynash M, et al; DEFUSE 2 Investigators. **Correlation of AOL recanalization, TIMI reperfusion and TIC1 reperfusion with infarct growth and clinical outcome.** *J Neurointerv Surg* 2014;6:724–28 CrossRef Medline
29. Danière F, Lobotesis K, Machi P, et al. **Patient selection for stroke endovascular therapy: DWI-ASPECTS thresholds should vary among age groups—insights from the RECAST study.** *AJNR Am J Neuroradiol* 2015;36:32–39 CrossRef Medline
30. Tanne D, Gorman MJ, Bates VE, et al. **Intravenous tissue plasminogen activator for acute ischemic stroke in patients aged 80 years and older: the tPA stroke survey experience.** *Stroke* 2000;31:370–75 Medline

# Validity of the Meyer Scale for Assessment of Coiled Aneurysms and Aneurysm Recurrence

A. Rouchaud, W. Brinjikji, T. Gunderson, J. Caroff, J.-C. Gentric, G. Lanzino, H.J. Cloft, and D.F. Kallmes

## ABSTRACT

**BACKGROUND AND PURPOSE:** Both the Meyer and Raymond scales are commonly used to report angiographic outcomes following coil embolization of intracranial aneurysms. The objectives of this study were the following: 1) to assess the interobserver agreement of the Meyer and Raymond scales, and 2) to evaluate and compare their performance in predicting major recurrence at follow-up.

**MATERIALS AND METHODS:** A retrospective series of 120 coiled aneurysms was included. Four investigators independently graded DSA images immediately posttreatment and at follow-up according to the Meyer and Raymond scales. On follow-up DSA, readers also evaluated recurrence outcome. Interobserver agreement was assessed via the intraclass correlation coefficient. The ability of posttreatment Meyer and Raymond scales to predict major recurrence was modeled by using logistic regression and assessed by using receiver operating characteristic analysis.

**RESULTS:** For the Meyer scale, interobserver intraclass correlation coefficients were 0.58 (95% CI, 0.46–0.68) on posttreatment and 0.78 (95% CI, 0.72–0.83) on follow-up evaluations. For the Raymond scale, interobserver intraclass correlation coefficients were 0.50 (95% CI, 0.39–0.61) and 0.69 (95% CI, 0.62–0.76), respectively, for posttreatment and follow-up. The areas under the curve for the receiver operating characteristic analyses regarding the performance to predict major recurrence at follow-up were 0.69 (95% CI, 0.60–0.79) for the Meyer and 0.70 (95% CI, 0.61–0.78) for the Raymond scale.

**CONCLUSIONS:** The Meyer scale appears consistent and reliable with observer agreement as high or higher than that of the Raymond scale. Performance of both scales in predicting the risk of major recurrence at follow-up is adequate, with no statistical difference between the scales.

**ABBREVIATIONS:** ICC = intraclass correlation coefficient; ROC = receiver operating characteristic

The most commonly used grading scale to assess aneurysm occlusion after coiling is the Raymond and Roy scale.<sup>1</sup> This grading scale divides the arteriographic outcomes of endovascularly treated saccular aneurysms into 3 categories: 1) complete occlusion, 2) residual neck, and 3) residual aneurysm.<sup>1</sup> However, despite its simplicity, its application in large clinical registries demonstrated important interobserver variability, which may limit its application and efficacy as an outcome-

assessment tool.<sup>2</sup> Moreover, important variability in aneurysm morphology and occlusion may occur within the same category by using this 3-category scale. To standardize the reporting on the degree to which volumetric occlusion has been achieved, a new consensual 6-point grading system, the Meyer scale, has been proposed jointly by multiple societies across neurointerventional radiology, neurosurgery, and neurology.<sup>3-6</sup> This proposed scale, published in 2012, was put forth to standardize the reporting of the degree of volumetric occlusion and to properly assess technical outcomes in a standardized report. The rationale for this new scale was that the commonly used Raymond scale demonstrated important interobserver variability that may limit its application and efficacy as an outcome-assessment tool.<sup>2</sup> However, despite the necessity for high reproducibility and interobserver rates, this new grading scale has never been evaluated, to our knowledge. As stated by the consensus writing group, there is no literature support for the proposed grading system, though this writing group believes it is the best available grading scale and

Received July 2, 2015; accepted after revision September 18.

From the Departments of Radiology (A.R., W.B., G.L., H.J.C., D.F.K.), Neurosurgery (G.L., H.J.C., D.F.K.), and Health Sciences Research, Division of Biomedical Statistics and Informatics (T.G.), Mayo Clinic, Rochester, Minnesota; Department of Interventional Neuroradiology (A.R., J.C.), Bicetre Hospital, Clichy, France; Department of Interventional Neuroradiology (J.-C.G.), Notre-Dame Hospital, Montreal, Quebec, Canada; and Department of Interventional Neuroradiology (J.-C.G.), CHU Cavale Blanche, Brest, France.

Please address correspondence to Aymeric Rouchaud, MD, Department of Radiology, Mayo Clinic, 200 First St SW, Rochester, MN 55901; e-mail: aymeric.rouchaud@gmail.com, Rouchaud.Aymeric@mayo.edu

<http://dx.doi.org/10.3174/ajnr.A4616>

offers a greater likelihood of reporting additional degrees of aneurysm recurrence.<sup>3-6</sup>

In addition, none of the scales have been validated as predictive of aneurysm recurrence.<sup>7,8</sup> Possible risk factors for reopening of a coiled aneurysm with time, such as the initial degree of occlusion,<sup>9</sup> seem to have an influence on the likelihood of recurrence, with subtotal initial treatment leading to remnant regrowth.<sup>10,11</sup>

Using a large retrospective series of patients with coiled aneurysms, the objectives of this current study were the following: 1) to assess interobserver agreement of the Meyer scale, and 2) to evaluate its performance in predicting recurrence at follow-up and compare the results with those of the Raymond scale.

## MATERIALS AND METHODS

### Study Cases

Mayo Clinic institutional review board approval was obtained for this retrospective study. Records for patients treated with endovascular coil embolization for either ruptured or unruptured aneurysms at our institution were evaluated. Some of the cases were used in a prior publication, but there is no overlap in scope with the current article.<sup>12</sup> These images of 120 cases of coiled aneurysms were compiled, de-identified, and placed into a 120-page PDF file. Each page included a DSA of the initial uncoiled aneurysm if available, the final postcoiling working-projection DSA, and the follow-up DSA. The PDF file was then distributed to 4 interventional neuroradiologists in different international centers. Two readers had 6 years' experience, and 2 readers had 4 years' experience.

### Angiographic Evaluations

The Meyer scale is a 6-point grading scale based on the percentage of the aneurysm filled by contrast on DSA. Grade zero indicates complete and total aneurysm occlusion without remnant or interstitial filling within the aneurysm. Grade 1 represents >90% volumetric occlusion of the aneurysm based on planar imaging assessment; grade 2, 70%–89% aneurysm occlusion; grade 3, 50%–69%; grade 4, 25%–49%; and grade 5, <25% volumetric aneurysm occlusion. Two other “modifier” criteria are combined with this scale: The modifier “I” may be used to describe interstitial opacification within the confines of the coil mass and the modifier “G” may be used to describe interval growth in the overall dimensions of the aneurysm as a separate phenomenon from coil compaction with recurrence of the aneurysm.

The Raymond scale is a commonly used outcome grading scale that divides the angiographic outcomes of endovascularly treated saccular aneurysms into 3 categories: complete occlusion, residual neck, and residual aneurysm.<sup>1</sup> Complete occlusion and residual neck are considered adequate occlusion; and residual aneurysm, inadequate occlusion.<sup>13-16</sup>

The 4 investigators independently and retrospectively examined each set of images of the posttreatment and follow-up DSAs to grade occlusion status according to the Raymond scale, the Meyer scale, and the modifier criteria. The investigators also evaluated the recurrence status of the aneurysm at follow-up DSA as follows: no recurrence, minor recurrence, or major recurrence. Major recurrence was defined as a theoretically or technically re-treatable aneurysm and was considered an unfavorable outcome.

To evaluate the performance of posttreatment DSA evaluation

to predict the risk for major recurrence, we used a consensus rating based on the most common grade among all readers. In case of disagreement among readers, 2 readers (A.R., W.B.) did a consensus reading.

### Statistical Analysis

Reader agreement was assessed via the intraclass correlation coefficient (ICC) by using the ICC method (2,1), as specified by Shrout and Fleiss,<sup>17</sup> for each of the 7 outcomes (posttreatment and follow-up Raymond scale, Meyer scale, Meyer modifier criteria, and recurrence status at follow-up). For the ICC description, we used the verbal description proposed by Portney and Watkins<sup>18</sup>: 0–.2, poor agreement; 0.3–0.4, fair agreement; 0.5–0.6, moderate agreement; 0.6–0.7, substantial agreement; 0.7–0.8, strong agreement; and >0.8, almost perfect agreement.

Aneurysm recurrence at follow-up was modeled as a function of either the Raymond scale or the Meyer scale (including the Meyer modifier criteria). Univariable (for Raymond) or multivariable (for Meyer) logistic regression by using the Firth penalized likelihood was performed by using the consensus rating of favorable or unfavorable recurrence at follow-up as the outcome. Aneurysm recurrence was modeled and receiver operating characteristic (ROC) curves were constructed both for each of the 4 raters individually and by using a consensus rating for each scale.

Statistical analyses for ICC were performed in SAS (Version 9.3; SAS, Cary, North Carolina). All other analyses were performed in R (Version 3.1.1; <http://www.r-project.org/>). Penalized logistic regression was performed by using the `logistf` package (version 1.21; <https://cran.r-project.org/web/packages/logistf/logistf.pdf>). ROC, area under the curve, and confidence interval estimates were obtained by using the `pROC` package (Version 1.7.3; <http://www.rdocumentation.org/packages/pROC/functions/pROC-package>).

## RESULTS

### Posttreatment Results

With the Raymond scale, we classified 165 (34%) of 480 readings as complete occlusion, 163 (34%) as neck remnants, and 152 (32%) as aneurysms remnants. The ICC for the Raymond scale was 0.50 (95% CI, 0.39–0.61), indicating moderate agreement among readers. Using the Meyer scale, we classified 159 (33%) of 480 readings as complete occlusion, 152 (32%) as grade 1, 112 (23%) as grade 2, 43 (9%) as grade 3, 11 (2%) as grade 4, and 3 (1%) as grade 5. The ICC for the Meyer scale was 0.58 (95% CI, 0.46–0.68), indicating moderate agreement among readers. Using the modifier criteria, we classified 213 (44%) of 480 readings as having interstitial opacification (modifier I). The ICC was 0.36 (95% CI, 0.26–0.47), indicating fair agreement among readers (range, 0.24–0.56).

### Follow-Up Results

The mean time between treatment and follow-up DSA was 37.8 months, with a median of 30.5 months (range, 0.37–166.0 months). Using the Raymond scale, we classified 138 (29%) of 480 readings as complete occlusion, 147 (31%) as neck remnants, and 195 (41%) as aneurysms remnants. The ICC for the Raymond scale was 0.69 (95% CI, 0.62–0.76), indicating substantial agree-

ment among readers. Using the Meyer scale, we classified 126 (26%) of 480 readings as complete occlusion, 107 (22%) as grade 1, 128 (27%) as grade 2, 82 (17%) as grade 3, 29 (6%) as grade 4, and 8 (2%) as grade 5. The ICC for the Meyer scale was 0.78 (95% CI, 0.72–0.83), indicating strong agreement among readers. Using the modifier criteria, we classified 113 (24%) of 480 readings with the interstitial opacification modifier (modifier I) and 35 (7%) with interval aneurysm growth (modifier G). The ICC was 0.37 (95% CI, 0.27–0.47), indicating fair agreement among readers.

### Assessment of Recurrence Status

The evaluation of the recurrence status yielded 43.8% ( $n = 210/480$  readings) of cases with no recurrence, 20.6% ( $n = 99$ ) with

### Interreader agreements

	Intraclass Correlation	Agreement Level
Posttreatment DSA		
Raymond	0.50 (0.39–0.61)	Moderate
Meyer	0.58 (0.46–0.68)	Moderate
Modifier	0.36 (0.26–0.47)	Fair
Follow-up DSA		
Raymond	0.69 (0.62–0.76)	Substantial
Meyer	0.78 (0.72–0.83)	Strong
Modifier	0.37 (0.27–0.47)	Fair
Recurrence	0.72 (0.66–0.79)	Strong

minor recurrence, and 35.6% ( $n = 171$ ) with major recurrence (unfavorable outcome). The ICC was 0.72 (95% CI, 0.66–0.79), indicating strong agreement among readers. ICCs are presented in the Table.

After consensual assessment, dichotomized evaluation yielded 65.0% ( $n = 78/120$  cases) good outcomes (no or minor recanalization) and 35.0% ( $n = 42/120$ ) bad outcomes (major recanalization).

### Prediction of Recurrence According to the Posttreatment Angiographic Evaluation

For the Raymond and Meyer evaluations, individual readers' ROC evaluations with areas under the curve are presented in Fig 1, and the ROC curve for the model by using the consensus reading is presented in Fig 2. According to the consensus reading, the area under the curve for the model using the Raymond scale was 0.70 (95% CI, 0.61–0.78). The area under the curve for the model using the Meyer scale was 0.69 (95% CI, 0.60–0.79). The confidence interval estimates overlap, and both of the scales have a fair performance to predict major recurrence.

### DISCUSSION

Our current study demonstrated that the Meyer scale has moderate interreader agreement immediately after treatment and strong agreement at follow-up, and for both immediate posttreatment

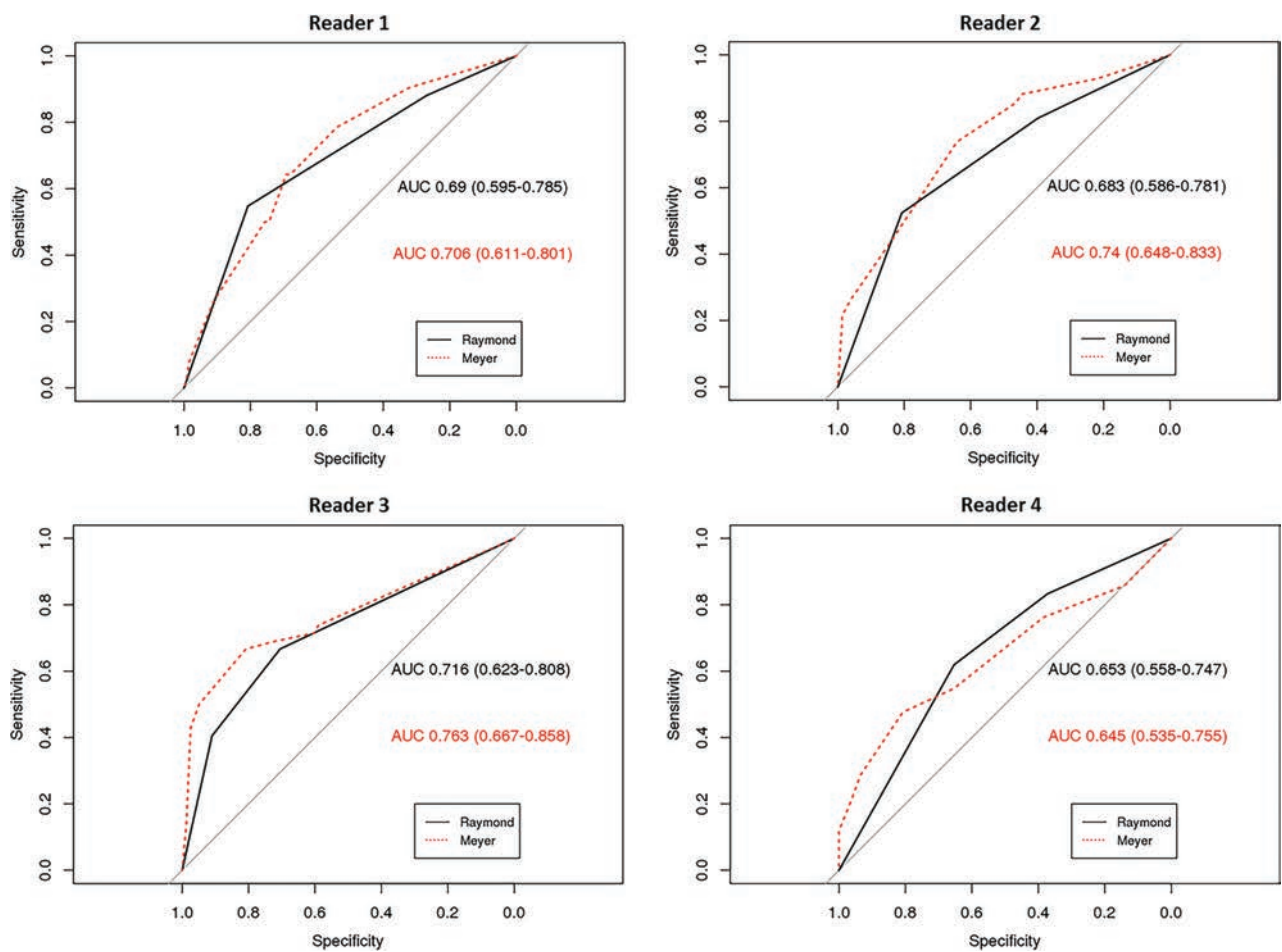


**FIG 1.** ROC curves per reader for the prediction of unfavorable outcome at follow-up (major recurrence) according to the posttreatment Raymond and Meyer scale evaluations.

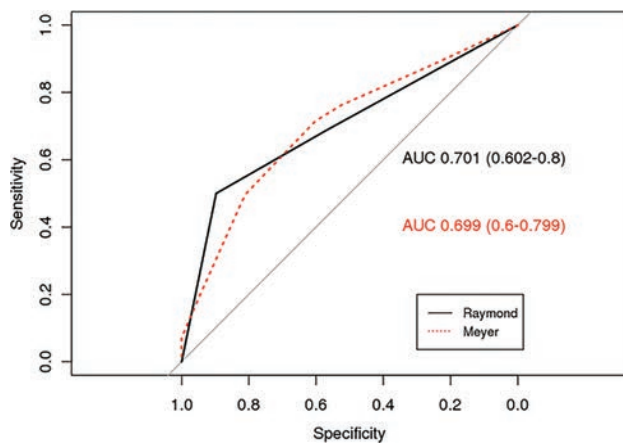


**FIG 2.** ROC curves for the prediction of unfavorable outcome at follow-up (major recurrence) according to the consensus posttreatment Raymond and Meyer scales evaluations.

and follow-up, the agreement for the Meyer scale is comparable with that of the Raymond scale. Furthermore, the performance of the Meyer and Raymond scales for predicting major recurrence risk, based on immediate posttreatment results, was fair and similar between scales. These data indicate that the Meyer and Raymond scales have similar performance and consistency levels for aneurysm occlusion evaluation and prediction of a major recurrence.

The interobserver agreement in our study for the Raymond scale is higher than that previously reported by Tollard et al,<sup>19</sup> who reported a fair  $\kappa$  statistic at 0.276. Interobserver agreement statistics for the Raymond scale ranged from 0.28 to 0.83 in prior studies.<sup>19-24</sup> Most interesting, the Meyer scale agreement score was higher than that of the Raymond scale despite the higher chance for better agreement when grading with fewer responses.<sup>8</sup> This outcome is likely because the Meyer score allows a little more flexibility in the assessment of angiographic occlusion. For example, in a case in which an aneurysm is well-occluded with the exception of filling in the interstices, some may mark the status as complete occlusion on the Raymond scale and others may mark the status as aneurysm remnant. However, with the Meyer scale, a visual assessment of the percentage of angiographic filling may be more reproducible. The interstitial opacification criteria have previously been taken into account in the recently introduced modified Raymond scale, with a higher performance in predicting recurrence at follow-up.<sup>20</sup>

Beyond assessing an adequate or inadequate operator result, grading aneurysm occlusion at the end of the coiling is of interest for predicting the long-term outcome and managing follow-up. Subtotal initial treatment leads to a higher likelihood of potential bleeding risk.<sup>10,11</sup> Raymond et al<sup>22</sup> reported major recurrence rates of 9% for aneurysms initially completely occluded, 23% for aneurysms with a residual neck, and 47% for aneurysms with residual aneurysm. Thornton et al<sup>25</sup> reported a recurrence rate of 1.8% for aneurysms that were 100% occluded and 26% for aneurysms with a residual neck. To our knowledge, this study is the first to evaluate the Meyer scale for predicting the risk of major recurrence at follow-up. Both the Raymond and the Meyer scales, combined with the interstitial opacification criteria, have a fair

performance level in predicting the risk of unfavorable outcome at follow-up. This is important because in cases of an inadequate posttreatment angiographic results, given the higher risk for major recurrence, physicians could plan to perform surveillance angiography earlier or more frequently.<sup>12,19,26,27</sup> Further studies are needed to determine a cutoff value for adequate-versus-inadequate posttreatment occlusion according to the Meyer scale. In our study, we focused on posttreatment angiographic grading, but this single criterion is not the only one that influences the recurrence outcome. Other factors such as aneurysm size,<sup>9,22</sup> smoking status,<sup>28,29</sup> and rupture status<sup>22</sup> should be taken into account to have a model for predicting recurrence.

### Limitations

Our study is limited by its retrospective nature and the use of only selected images for the DSA readers' assessment. Readers did not have access to the complete angiographic run when assessing angiographic occlusion. Another limitation of this study is that DSA was performed at different time points, which can modify the outcomes, depending on the length of follow-up.<sup>22</sup>

### CONCLUSIONS

This study highlights the consistency and the reliability of both the Meyer and Raymond occlusion scales for DSA evaluation of coiled aneurysms. Both scales have substantial interobserver agreement and fair performance levels in predicting major recurrence at follow-up. These findings are very important in managing patients at follow-up.

Disclosures: Giuseppe Lanzino—UNRELATED: Consultancy: Covidien.\* David F. Kallmes—UNRELATED: Grant: Sequent Medical.\* Comments: preclinical research; Support for Travel to Meetings for the Study or Other Purposes: Sequent Medical.\* Comments: travel to training for a clinical trial; UNRELATED: Board Membership: GE Healthcare.\* Comments: Cost-Effectiveness Board; Consultancy: ev3/Medtronic.\* Comments: Steering Committee membership for a clinical trial; Grants/Grants Pending: MicroVention.\* Surmodics.\* Sequent Medical.\* Codman.\* NeuroSigma.\* Royalties: University of Virginia Patent Foundation (Spine Fusion); Travel/Accommodations/Meeting Expenses Unrelated to Activities Listed: ev3/Medtronic.\* Comments: travel to FDA panel meeting. \*Money paid to the institution.

### REFERENCES

- Roy D, Milot G, Raymond J. Endovascular treatment of unruptured aneurysms. *Stroke* 2001;32:1998–2004 CrossRef Medline
- Sluzewski M, van Rooij WJ. Questionable interpretation of results of ACTIVE study on Matrix coils by Boston Scientific. *AJNR Am J Neuroradiol* 2005;26:1882–83 Medline
- Meyers PM, Schumacher HC, Higashida RT, et al; Joint Writing Group of the Technology Assessment Committee, Society of NeuroInterventional Surgery, Society of Interventional Radiology, Joint Section on Cerebrovascular Neurosurgery of the American Association of Neurological Surgeons and Congress of Neurological Surgeons, Section of Stroke and Interventional Neurology of the American Academy of Neurology. Reporting standards for endovascular repair of saccular intracranial cerebral aneurysms. *J Neurointerv Surg* 2010;2:312–23 CrossRef Medline
- Meyers PM, Schumacher HC, Higashida RT, et al. Reporting standards for endovascular repair of saccular intracranial cerebral aneurysms. *AJNR Am J Neuroradiol* 2010;31:E12–24 Medline
- Meyers PM, Schumacher HC, Higashida RT, et al; American Society of Interventional Neuroradiology, Society of Interventional Radiology. Reporting standards for endovascular repair of saccular intracranial cerebral aneurysms. *J Vasc Interv Radiol* 2009;20:S435–50 CrossRef Medline

6. Meyers PM, Schumacher HC, Higashida RT, et al. **Reporting standards for endovascular repair of saccular intracranial cerebral aneurysms.** *Stroke* 2009;40:e366–79 CrossRef Medline
7. Sluzewski M, van Rooij WJ. **Early rebleeding after coiling of ruptured cerebral aneurysms: incidence, morbidity, and risk factors.** *AJNR Am J Neuroradiol* 2005;26:1739–43 Medline
8. Cloft HJ, Kaufmann T, Kallmes DF. **Observer agreement in the assessment of endovascular aneurysm therapy and aneurysm recurrence.** *AJNR Am J Neuroradiol* 2007;28:497–500 Medline
9. Ferns SP, Sprengers ME, van Rooij WJ, et al. **Coiling of intracranial aneurysms: a systematic review on initial occlusion and reopening and retreatment rates.** *Stroke* 2009;40:e523–29 CrossRef Medline
10. Grunwald IQ, Papanagiotou P, Struffert T, et al. **Recanalization after endovascular treatment of intracerebral aneurysms.** *Neuroradiology* 2007;49:41–47 CrossRef Medline
11. Li MH, Gao BL, Fang C, et al. **Angiographic follow-up of cerebral aneurysms treated with Guglielmi detachable coils: an analysis of 162 cases with 173 aneurysms.** *AJNR Am J Neuroradiol* 2006;27:1107–12 Medline
12. McDonald JS, Carter RE, Layton KF, et al. **Interobserver variability in retreatment decisions of recurrent and residual aneurysms.** *AJNR Am J Neuroradiol* 2013;34:1035–39 CrossRef Medline
13. Pierot L, Cognard C, Anxionnat R, et al; CLARITY Investigators. **Endovascular treatment of ruptured intracranial aneurysms: factors affecting midterm quality anatomic results: analysis in a prospective, multicenter series of patients (CLARITY).** *AJNR Am J Neuroradiol* 2012;33:1475–80 CrossRef Medline
14. Johnston SC, Dowd CF, Higashida RT, et al; CARAT Investigators. **Predictors of rehemorrhage after treatment of ruptured intracranial aneurysms: the Cerebral Aneurysm Rerupture After Treatment (CARAT) study.** *Stroke* 2008;39:120–25 CrossRef Medline
15. Mortimer AM, Bradley MD, Mews P, et al. **Endovascular treatment of 300 consecutive middle cerebral artery aneurysms: clinical and radiologic outcomes.** *AJNR Am J Neuroradiol* 2014;35:706–14 CrossRef Medline
16. Ng P, Khangure MS, Phatouros CC, et al. **Endovascular treatment of intracranial aneurysms with Guglielmi detachable coils: analysis of midterm angiographic and clinical outcomes.** *Stroke* 2002;33:210–17 CrossRef Medline
17. Shrout PE, Fleiss JL. **Intraclass correlations: uses in assessing rater reliability.** *Psychol Bull* 1979;86:420–28 CrossRef Medline
18. Portney LG, Watkins MP. *Foundations of Clinical Research Applications to Practice.* New Jersey: Pearson Prentice; 2009
19. Tollard É, Darsaut TE, Bing F, et al. **Outcomes of endovascular treatments of aneurysms: observer variability and implications for interpreting case series and planning randomized trials.** *AJNR Am J Neuroradiol* 2012;33:626–31 CrossRef Medline
20. Mascitelli JR, Moyle H, Oermann EK, et al. **An update to the Raymond-Roy Occlusion Classification of intracranial aneurysms treated with coil embolization.** *J Neurointerv Surg* 2015;7:496–502 CrossRef Medline
21. Ogilvy CS, Chua MH, Fusco MR, et al. **Validation of a system to predict recanalization after endovascular treatment of intracranial aneurysms.** *Neurosurgery* 2015;77:168–73; discussion 173–74 CrossRef Medline
22. Raymond J, Guilbert F, Weill A, et al. **Long-term angiographic recurrences after selective endovascular treatment of aneurysms with detachable coils.** *Stroke* 2003;34:1398–403 CrossRef Medline
23. Singla A, Villwock MR, Jacobsen W, et al. **Aneurysm embolization grade: a predictive tool for aneurysm recurrence after coil embolization.** *Acta Neurochir (Wien)* 2013;155:231–36 CrossRef Medline
24. Urbach H, Dorenbeck U, von Falkenhausen M, et al. **Three-dimensional time-of-flight MR angiography at 3 T compared to digital subtraction angiography in the follow-up of ruptured and coiled intracranial aneurysms: a prospective study.** *Neuroradiology* 2008;50:383–89 CrossRef Medline
25. Thornton J, Debrun GM, Aletich VA, et al. **Follow-up angiography of intracranial aneurysms treated with endovascular placement of Guglielmi detachable coils.** *Neurosurgery* 2002;50:239–49; discussion 249–50 CrossRef Medline
26. Daugherty WP, Rad AE, White JB, et al. **Observer agreement regarding the necessity of retreatment of previously coiled recurrent cerebral aneurysms.** *AJNR Am J Neuroradiol* 2011;32:566–69 CrossRef Medline
27. Raymond J, White PM, Molyneux AJ. **Scales, agreement, outcome measures, and progress in aneurysm therapy.** *AJNR Am J Neuroradiol* 2007;28:501–02 Medline
28. Ortiz R, Stefanski M, Rosenwasser R, et al. **Cigarette smoking as a risk factor for recurrence of aneurysms treated by endosaccular occlusion.** *J Neurosurg* 2008;108:672–75 CrossRef Medline
29. Brinjikji W, Lingineni RK, Gu CN, et al. **Smoking is not associated with recurrence and retreatment of intracranial aneurysms after endovascular coiling.** *J Neurosurg* 2015;122:95–100 CrossRef Medline

# Pipeline Embolization Device in the Treatment of Recurrent Previously Stented Cerebral Aneurysms

 B. Daou,  R.M. Starke,  N. Chalouhi,  S. Tjoumakaris,  D. Hasan,  J. Khoury,  R.H. Rosenwasser, and  P. Jabbour



## ABSTRACT

**BACKGROUND AND PURPOSE:** The use of the Pipeline Embolization Device in the management of recurrent previously stented cerebral aneurysms is controversial. The aim of this study was to evaluate the efficacy and safety of the Pipeline Embolization Device in the treatment of recurrent, previously stented aneurysms.

**MATERIALS AND METHODS:** Twenty-one patients with previously stented recurrent aneurysms who later underwent Pipeline Embolization Device placement (group 1) were retrospectively identified and compared with 63 patients who had treatment with the Pipeline Embolization Device with no prior stent placement (group 2). Occlusion at the latest follow-up angiogram, recurrence and retreatment rates, clinical outcome, complications, and morbidity and mortality observed after treatment with the Pipeline Embolization Device were analyzed.

**RESULTS:** Patient characteristics were similar between the 2 groups. The mean time from stent placement to recurrence was 25 months. Pipeline Embolization Device treatment resulted in complete aneurysm occlusion in 55.6% of patients in group 1 versus 80.4% of patients in group 2 ( $P = .036$ ). The retreatment rate in group 1 was 11.1% versus 7.1% in group 2 ( $P = .62$ ). The rate of good clinical outcome at the latest follow-up in group 1 was 81% versus 93.2% in group 2 ( $P = .1$ ). Complications were observed in 14.3% of patients in group 1 and 9.5% of patients in group 2 ( $P = .684$ ).

**CONCLUSIONS:** The use of the Pipeline Embolization Device in the management of previously stented aneurysms is less effective than the use of this device in nonstented aneurysms. Prior stent placement can worsen the safety and efficacy profile of this device.

**ABBREVIATION:** PED = Pipeline Embolization Device

Since the introduction of detachable coils, cerebral aneurysm management has shifted considerably toward endovascular treatment. One of the main weaknesses of cerebral aneurysm coiling lies in the treatment of patients with large<sup>1,2</sup> wide-neck or fusiform aneurysms.<sup>3</sup> These aneurysms tend to have higher recurrence and retreatment rates after coiling. To make up for this deficiency, intracranial stents have emerged as an alternative in the management of this type of aneurysm. The most widely used stents include the Neuroform (Stryker Neurovascular, Kalamazoo, Michigan) and Enterprise self-expanding (Codman & Shurtleff, Raynham, Massachusetts) stents, which were approved for use as Humanitarian Use Devices in 2002 and 2007, respectively. Several techniques can be used with stents, including stent placement alone and stent-assisted coiling. Recanalization and retreatment rates are lower with stent placement and stent-assisted coiling than with coiling alone.<sup>4-6</sup> However, the initial occlusion rates are suboptimal, particularly in large aneurysms.<sup>7,8</sup>

The management of recurrent previously stented aneurysms remains controversial. There are no recommendations to indicate the most appropriate management strategy, to our knowledge. In 2011, the Pipeline Embolization Device (PED; Covidien, Irvine, California) was FDA-approved for the treatment of large and giant wide-neck aneurysms in the internal carotid artery, from the petrous to the superior hypophyseal segments.<sup>9</sup> The PED belongs to a family of devices known as flow diverters, which work by acting as a scaffold for endothelial overgrowth of the aneurysm neck.<sup>10</sup> The main structural differences from previous stents are the higher metal surface area coverage compared with previous

zoo, Michigan) and Enterprise self-expanding (Codman & Shurtleff, Raynham, Massachusetts) stents, which were approved for use as Humanitarian Use Devices in 2002 and 2007, respectively. Several techniques can be used with stents, including stent placement alone and stent-assisted coiling. Recanalization and retreatment rates are lower with stent placement and stent-assisted coiling than with coiling alone.<sup>4-6</sup> However, the initial occlusion rates are suboptimal, particularly in large aneurysms.<sup>7,8</sup>

Received June 9, 2015; accepted after revision September 16.

From the Department of Neurosurgery (B.D., N.C., S.T., J.K., R.H.R., P.J.), Thomas Jefferson University and Jefferson Hospital for Neuroscience, Philadelphia, Pennsylvania; Department of Neurological Surgery (R.M.S.), University of Virginia School of Medicine, Charlottesville, Virginia; and Department of Neurosurgery (D.H.), University of Iowa, Iowa City, Iowa.

Please address correspondence to Pascal Jabbour, MD, Division of Neurovascular Surgery and Endovascular Neurosurgery, Department of Neurological Surgery, Thomas Jefferson University Hospital, 901 Walnut St, 3rd Floor, Philadelphia, PA 19107; e-mail: pascal.jabbour@jefferson.edu

<http://dx.doi.org/10.3174/ajnr.A4613>

**Table 1: Baseline characteristics in patients with previous stent placement**

Patient	Age (yr)	Sex	Presented with SAH	Location	Aneurysm Form	Initial Size (mm)
1	45	Female	No	Cavernous ICA	Saccular	7
2	73	Female	No	VB	Saccular	11
3	80	Female	No	Cavernous ICA	Saccular	18
4	48	Female	No	VB	Fusiform	15
5	60	Female	No	CO	Saccular	5
6	54	Female	No	CO	Saccular	6
7	33	Male	No	VB	Saccular	27
8	44	Female	No	VB	Fusiform	22
9	48	Female	No	PcomA	Saccular	9
10	46	Male	Yes	VB	Pseudoaneurysm	2.5
11	61	Female	No	Cavernous ICA	Saccular	5
12	55	Male	No	VB	Fusiform	23
13	56	Female	No	Superior hypophyseal	Saccular	10
14	80	Female	Yes	Superior cerebellar	Saccular	9
15	64	Male	No	PcomA	Saccular	15
16	31	Female	Yes	CO	Saccular	11
17	51	Female	Yes	PcomA	Fusiform	10
18	56	Female	Yes	CO	Saccular	18
19	16	Female	No	Cavernous ICA	Pseudoaneurysm	6
20	24	Male	Yes	PcomA	Saccular	24
21	50	Female	Yes	Posterior wall ICA	Saccular	10

**Note:**—VB indicates vertebrobasilar artery; CO, carotid ophthalmic artery; PcomA, posterior communicating artery.

stents and the low porosity, which allows more flow reduction into the aneurysm neck.<sup>11,12</sup> The overall use of the PED has gained popularity mainly because of its high success rate in achieving aneurysm occlusion and low aneurysm recurrence and retreatment rates, especially compared with other endovascular interventions.<sup>13,14</sup> Early reports have questioned the efficacy and safety of the PED in treating previously stented aneurysms.<sup>15-17</sup> The aim of this study was to evaluate the role of the PED, both its efficacy and safety, in the treatment of recurrent, previously stented cerebral aneurysms.

## MATERIALS AND METHODS

### Patients

Patients with cerebral aneurysms treated with the PED between May 2011 and January 2015 at a single institution were reviewed. Twenty-one patients with previously stented aneurysms who later underwent PED placement for aneurysm recurrence were retrospectively identified (group 1). Blinded to outcome, we matched them with 63 patients who underwent treatment by using the PED without prior stent placement in a 3-to-1 ratio, on the basis of patient age and aneurysm size (group 2). PED treatment was offered for recurrent complex, wide-neck aneurysms, partially thrombosed aneurysms, and aneurysms with multiple recurrences treated unsuccessfully by other means. Baseline patient characteristics, aneurysm characteristics, and procedure characteristics were recorded. The study protocol was approved by the Thomas Jefferson University institutional review board.

### PED Procedure

Patients were started on clopidogrel and aspirin for at least 10 days before the intervention. An angiographic evaluation was performed to assess aneurysm dimensions. Treatment with the PED was performed with the patient under general anesthesia and neurophysiologic monitoring. After embolization, another angiogram was obtained. Patients were evaluated in the hospital for any complications. After discharge, patients were scheduled for clinical

and angiographic follow-up.<sup>18</sup> Patients continued taking both aspirin and clopidogrel for 6 months after the procedure, at which time clopidogrel was to be discontinued.

### Outcomes

The outcomes of interest in this study were the following: 1) the efficacy of the PED in the management of previously stented cerebral aneurysms evaluated for angiographic occlusion at the latest follow-up angiogram, recurrence and retreatment rates after PED placement, and clinical outcome as measured by the modified Rankin Scale at the latest available follow-up; and 2) the safety of the PED in the treatment of recurrent cerebral aneurysms with a stent in situ assessed by complications, morbidity, and mortality observed after treatment. Modified Rankin Scale scores of 0–2 were considered favorable outcomes, and mRS scores of 3–6 were considered poor outcomes. Modified Rankin Scale scores were assessed by the treating neurosurgeon on the basis of the last follow-up visit. Angiographic evaluations were obtained to monitor any recanalization or residual filling after PED treatment. Aneurysm occlusion at follow-up was evaluated by the treating neurosurgeon and was categorized as complete or incomplete.

### Statistical Analysis

Data are presented as mean and range for continuous variables and as frequency for categorical variables. Analysis was performed by using the Wilcoxon matched signed rank test and the McNemar test as appropriate. *P* values  $\leq .05$  were considered statistically significant. Statistical analysis was performed with STATA 10.0 (StataCorp, College Station, Texas).

## RESULTS

### Patient and Aneurysm Characteristics

In the 21 cases, the mean patient age was 51 years. Seven patients presented initially (before the first endovascular intervention) with a subarachnoid hemorrhage (33.3%) (Table 1). Aneurysm locations are detailed in Table 2. Fifteen aneurysms were saccular

(71.4%); 4, fusiform (19%); and 2, pseudoaneurysms (9.5%). The average initial aneurysm size before any attempted treatment was 12.5 mm. Before PED treatment, 12 patients had a recurrence on follow-up angiography, whereas 9 patients had aneurysm remnants that eventually grew.

Although patients with no stents were matched on the basis of age and aneurysm size, there was no statistical difference in other baseline characteristics between the 2 groups except for a higher percentage of patients who presented initially with SAH in group 1 ( $P = .004$ ) (Table 3).

### Treatment

In patients who had prior stent placement, the mean number of interventions before PED placement was 2.3, ranging from 1 prior intervention to 4 previous attempts (Table 4). Previous stent interventions included stent-assisted coiling in 57.1% and stent placement alone in 42.9% of patients. Sixteen aneurysms were initially coiled before stents were deployed (76%). Stents that were initially used included the Enterprise stent in 52% of patients and the Neuroform stent in 48% of patients.

The mean time from stent placement to recurrence was 23 months. The mean time from the initial treatment to PED placement was 40.4 months. The mean number of PEDs placed was 1.3, ranging from 1 to 4. The average procedure length for PED treatment of previously stented aneurysms was 66 minutes versus 58 minutes for nonstented aneurysms ( $P = .6$ ). Technical difficulties were observed in 5 patients with prior stent placement (23.8%). Technical difficulties were reported by the treating neurosurgeon and identified by reviewing the operative reports. In 1 patient, because of the prior stent placement, several catheter advance-

ments and several readjustments of the microcatheter and wire were required to achieve a good position for PED deployment. In another patient, the distal two-thirds of the PED was deployed with good wall apposition; however, because of prior stent placement, the proximal third did not open and good wall apposition was not achieved. In 2 patients, there were difficulties in placing the PED across the neck of the aneurysm and achieving appropriate overlap with the previous stent and covering the proximal tines of the stent. In another patient, 4 PEDs were required to span the proximal portion of the aneurysm and extend proximally to the pre-existing stent. On the other hand, technical difficulties were encountered in 3 patients with no prior stent placement (4.8%). There were difficulties in opening the proximal part of the PED during deployment in 2 patients who had a severe tortuosity of the inflow of the aneurysm, and a balloon was used to expand the device.

Preoperative P2Y12 reaction unit values were available in 19 patients in group 1 (mean, 128.1) and 51 patients in group 2 (mean, 127.6) ( $P = .98$ ). In-stent stenosis was observed in 2 of the 21 patients with previous stent placement (9.5%), one patient with 50% stenosis and the other with <50% stenosis.

### Efficacy of PED Treatment of Previously Stented Aneurysms

**Angiographic Occlusion.** In group 1, 3 patients did not have a follow-up angiographic evaluation because of loss to follow-up. Of the 18 patients who had follow-up angiograms, PED treatment resulted in complete aneurysm occlusion in 10 patients (55.6%) (Fig 1). In group 2, 7 patients did not have available angiograms, 3 patients because of death following the procedure and 4 patients who were lost to follow-up. Of the 56 patients with follow-up angiograms, 45 patients had complete aneurysm occlusion (80.4%). In group 1, 8 aneurysms (44.4%) were found to have incomplete occlusion with residual filling or recurrence after PED placement (Figs 2 and 3), whereas in group 2, 11 aneurysms were found to have incomplete occlusion (19.6%). This difference of 24.8% was statistically significant ( $P = .036$ ). The mean angiographic follow-up time from PED placement to the last angiogram was 10.4 months in group 1 and 10.6 months in group 2 ( $P = .816$ ).

The 8 aneurysms with incomplete occlusion in patients with prior stent placement had different characteristics. In general, 3 aneurysms were larger than the average size (12.5 mm) and 5 aneurysms were smaller. More specifically, incompletely occluded aneurysms included 3 vertebrobasilar aneurysms of >15 mm, 2 carotid ophthalmic aneurysms (6 and 9 mm), 2 aneurysms in the cavernous internal carotid artery (5 and 7 mm), and a 9-mm superior cerebellar artery aneurysm. Five aneurysms were previously coiled, and 3 were not.

The 11 incompletely occluded aneurysms in patients without prior stent placement included 3 cavernous ICA

**Table 2: Aneurysm location**

	Patients with Prior Stent (%)	Patients without Prior Stent (%)
ICA	23.8	35
Vertebrobasilar artery	28.6	9.5
Posterior communicating artery	19	4.8
Carotid ophthalmic artery	19	38
Superior hypophyseal artery	4.8	6.3
Superior cerebellar artery	4.8	0
Middle cerebral artery	0	4.8
Anterior choroidal artery	0	1.6

**Table 3: Comparison between patients with and without a prior stent**

	Patients with Prior Stent Placement	Patients without Prior Stent	P Value
Mean age (yr)	51.2	53.6	.523
Initial aneurysm size (mm)	12.5	12.2	.862
Sex (male/female)	76.2:23.8	85.7:14.3	.310
Smoking (%)	57.1	50	.571
Initial presentation with SAH (%)	33.3	8.06	.004
Aneurysm form (saccular/fusiform/pseudoaneurysm) (%)	71.4/19.05/9.5	80.95/15.87/3.17	.447
Average No. of PEDs used	1.33	1.39	.742
Retreatment post-PED (%)	11.11	7.14	.629
Complete aneurysm occlusion (%)	55.6	80.4	.036
Time of last follow-up angiogram (mo)	10.38	10.58	.816
Complications (%)	14.29	9.52	.684
Good clinical outcome (%)	80.95	93.22	.1
Time of last follow-up (months)	15.67	18.71	.278
Average preoperative PRU	128.1	127.6	.981

**Note:**—PRU indicates P2Y12 reaction units.

**Table 4: Treatment and outcomes in patients with previous stents**

Patient No.	No. of Interventions before PED	Time from Stenting to Pipeline (mo)	No. of PEDs Used	Occlusion on Follow-Up Angiogram	Complications	mRS at Latest Follow-Up	Retreatment Post-PED
1	1	3	1	Incomplete	No	0	No
2	1	38	2	Complete	No	0	No
3	3	54	2	Complete	No	0	No
4	3	74	1	Incomplete	No	0	No
5	3	25	1	Complete	Retinal emboli causing visual changes	1	No
6	2	22	1	Incomplete	No	1	No
7	1	13	4	Incomplete	No	4	Yes
8	3	52	1	Complete	No	0	No
9	4	49	1	Complete	No	0	No
10	2	3	1	Complete	No	0	No
11	3	75	1	Incomplete	No	0	No
12	2	44	3	Incomplete	PCA infarct	5	No
13	1	44	1	Complete	No	0	No
14	2	39	1	Incomplete	No	1	Yes
15	2	76	1	Complete	No	0	No
16	2	39	1	Incomplete	No	0	No
17	2	48	1	NA	No	0	NA
18	2	91	1	Complete	No	0	No
19	2	1	1	Complete	No	0	No
20	2	17	1	NA	No	3	NA
21	6	41	1	NA	ICH	6	NA

**Note:**—PCA indicates posterior cerebral artery; NA, not applicable; ICH, intracerebral hemorrhage.

aneurysms (10, 20, and 21 mm), 2 paraclinoid ICA aneurysms (9 and 16 mm), 3 carotid ophthalmic aneurysms (5, 10, and 13 mm), one 12-mm middle cerebral artery aneurysm, one 6-mm superior hypophyseal aneurysm, and one 7-mm posterior carotid wall aneurysm.

**Retreatment.** Two previously stented aneurysms managed with the PED required another retreatment, with placement of another PED (11.1%). No aneurysms required additional coiling or clipping. In patients with no prior stents, 4 patients required retreatment post-PED placement (7.1%). The rate of retreatment was nonsignificantly higher in patients with a prior stent ( $P = .62$ ).

**Clinical Outcome.** Mean follow-up was 15.7 months in group 1 and 18.7 months in group 2 ( $P = .278$ ). In patients with previous stent treatment, 17 patients had a good clinical outcome (mRS 0–2) at the latest follow-up (81%), with 14 patients having an mRS score of zero (66.7%) and 3 patients having an mRS score of 1 (14.3%). Four patients had an unfavorable outcome (19%), with 1 patient having an mRS score of 3, 1 patient with an mRS score of 4, 1 patient with an mRS of 5, and 1 patient with an mRS of 6. In patients with no prior stent placement, 93.2% had a good clinical outcome versus 6.8% with a poor clinical outcome. There was a trend toward worse clinical outcome in patients with prior stent placement (19%) as opposed to patients without prior stent treatment (6.8%) ( $P = .1$ ).

#### **Safety of PED Treatment of Previously Stented Aneurysms**

Complications within 30 days after treatment were observed in 3 patients (14.3%) in group 1 and 6 patients in group 2 (9.5%) ( $P = .684$ ). In group 1, 1 patient with a giant vertebrobasilar artery aneurysm had a posterior cerebral artery territory infarct and later developed hydrocephalus requiring ventriculoperitoneal shunt-

ing and then developed multiple shunt infections (mRS = 5). Another patient had retinal emboli causing visual changes (mRS = 1) after PED treatment of a carotid ophthalmic aneurysm, and another patient had a right intracerebral hemorrhage after PED treatment of a right ICA aneurysm and died (mRS = 6). Mortality was similar in both groups (4.76%). In group 2, 5/6 patients with complications had giant aneurysms. Complications in this group included 2 intracerebral hemorrhages, 3 MCA infarcts, and 1 basal ganglia stroke.

There were no statistically significant differences in the rate of complete occlusion (62% versus 50%,  $P = .7$ ), complications (10% versus 18%,  $P = .9$ ), or good clinical outcome (82% versus 80%,  $P = 1$ ) among patients who had prior Neuroform or Enterprise stent placement, respectively, though patients with prior Neuroform stents had better overall outcomes after PED deployment.

#### **DISCUSSION**

Our results show that stent placement negatively affects the efficacy of the PED in the management of recurrent aneurysms. The rate of complete aneurysm occlusion was significantly low (55.6%), especially compared with the high success rate of PED treatment reported in this study for subjects without prior stent placement (80.4%) and in other studies, with most reporting a high occlusion rate of >80%.<sup>12–14,19</sup> In addition, the rate of retreatment (11.1%) was considerably higher than that reported with PED treatment of nonstented aneurysms. Zanaty et al<sup>13</sup> reported a 5% rate of retreatment after PED placement.

The complication rate seen with PED treatment of recurrent previously stented aneurysms (14.3%) falls within the higher spectrum reported in the literature (0%–12%). Kallmes et al<sup>20</sup> reported a morbidity and mortality rate of 8.4% with PED treatment. Brinjikji et al<sup>19</sup>

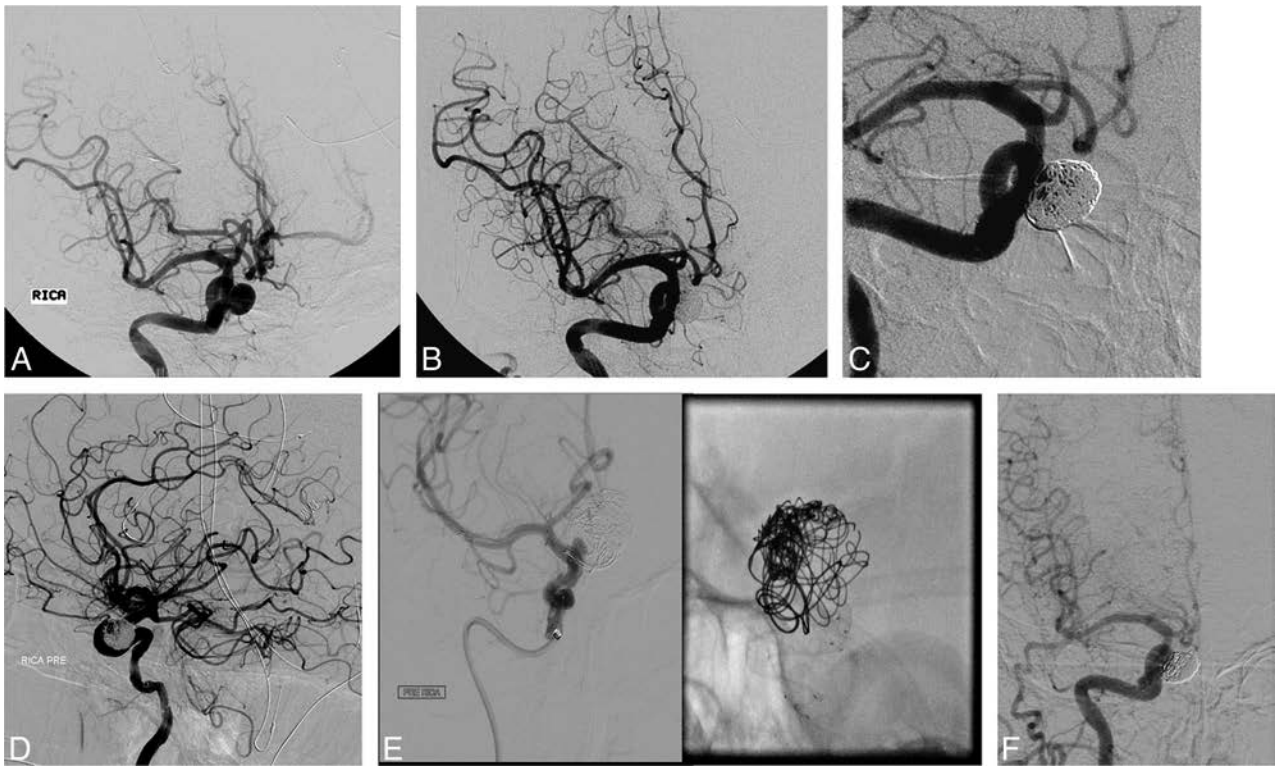


**FIG 1.** A, A 53-year-old woman who presented with headache and was found to have a 10-mm right superior hypophyseal artery aneurysm. B, Stent-assisted coiling was performed, and the control angiogram shows complete occlusion. C, A follow-up angiogram at 6 months shows complete occlusion of the aneurysm dome and minimal filling of the interstices. D, A follow-up angiogram after 2 years shows recurrence of the aneurysm. E, At that point, embolization by using the PED was performed. F, A 6-month follow-up angiogram shows complete occlusion of the aneurysm.

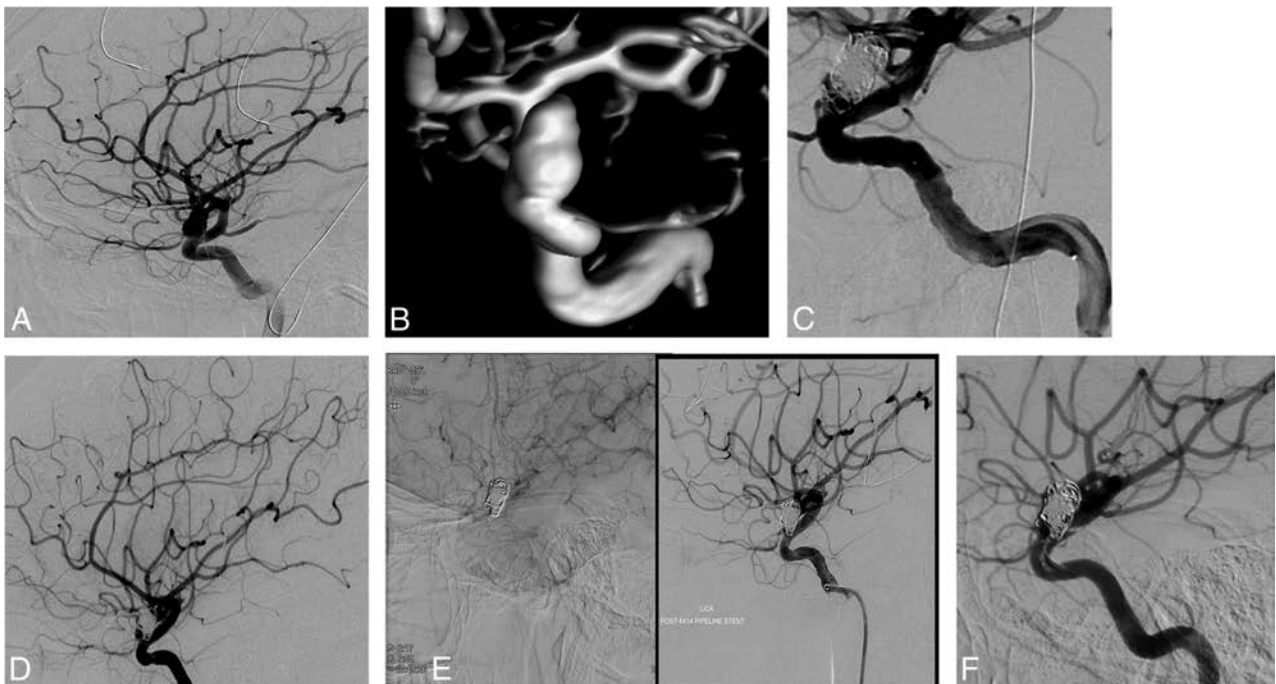


**FIG 2.** A and B, A 28-year-old woman who presented with subarachnoid hemorrhage resulting from a ruptured 11-mm left carotid ophthalmic artery aneurysm. C, Stent-assisted coiling was performed. This resulted in incomplete occlusion of the aneurysm. D, Three-year follow-up angiogram shows growth of the residual. E, Treatment with the PED was performed, with incomplete wall apposition. F, Six-month follow-up angiogram shows incomplete occlusion.

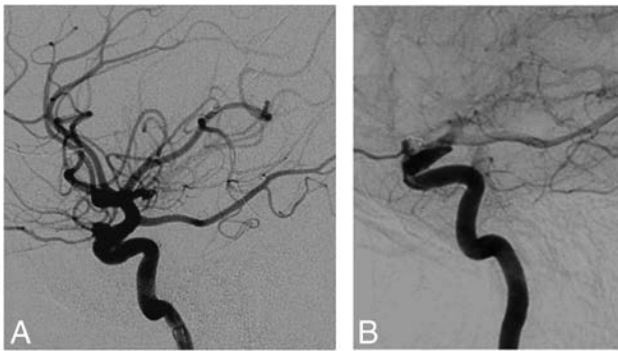


**FIG 3.** A, A 54-year-old woman with a 6-mm left carotid ophthalmic artery aneurysm, which was initially treated with stent-assisted coiling but recurred. B, Treatment with the PED was performed. A 12-month follow-up angiogram shows incomplete occlusion.

reported a procedure-related morbidity rate of 5%. In patients with prior stent treatment, 1 patient had a posterior cerebral artery infarct after PED treatment and then developed hydrocephalus requiring ventriculoperitoneal shunt placement and another patient developed emboli to the ophthalmic artery causing visual disturbances. Thromboembolic events are well-known complications of PED treatment.<sup>12,19,20</sup> Because this device consists of a bare metal stent that aids in neointimal tissue formation, it can lead to platelet activation causing local thrombosis and cerebral infarction or distal embolization. The large metal surface area coverage of the Pipeline Embolization Device and frequent use of multiple devices also contribute to the occurrence of thromboembolic events.

Treatment with the PED poses a risk for hemorrhagic complications as well. This was observed in 1 patient who had an intracerebral hemorrhage and died. The occurrence of intracerebral hemorrhage in patients treated with the PED can be due to multiple factors, including the dual-antiplatelet therapy that patients receive, hemorrhagic transformation of ischemic stroke, and hemodynamic changes related to placement of the PED. Furthermore, the presence of a prior Neuroform or Enterprise stent may increase the risk of both thromboembolic and hemorrhagic complications associated with PED placement because these stents act as foci of thrombus formation and patients are started on aspirin and clopidogrel (Plavix) before stent placement. Hemorrhagic and thromboembolic complications occurred at a nonsignificantly higher rate in previously stented aneurysms.

Since the initial reports about treatment with the PED, the use of this device has been controversial in the management of recurrent previously stented aneurysms. Fischer et al<sup>15</sup> criticized both the safety and efficacy of the PED in the treatment of aneurysms with prior stent placement in a series that included 30 lesions treated previously with conventional stents. They reported that adverse events occurred in only 1 of 54 patients (2%) without a previous stent placement after PED treatment and in 4 of 30 patients (13%) in whom a stent was previously placed before PED treatment. They added that the observed successful occlusion rate was lower for aneurysms with a previous stent placement (65%). The complication rate of 13% and the occlusion rate of 65% reported in their study are very much comparable with the rates obtained in our study (14.3% and 66.7%, respectively). They concluded that the presence of a previous stent may reduce the he-

modynamic effect of the PED. This negative interaction was attributed to a disruption of the process of wall apposition of the PED to the parent vessel, preventing the process of appropriate device endothelialization.

Nelson et al<sup>17</sup> reported that 1 of 2 aneurysms ( $n = 31$ ) not initially occluded with the PED was previously treated with another stent. They concluded as well that prior stent placement impairs effective apposition of the PED to the parent artery, thus slowing or preventing the neointimal formation and endothelialization processes and potentially inhibiting complete aneurysm occlusion. This outcome was indeed observed in our series in several patients with prior stent placement, in whom appropriate wall apposition was impeded by the previously placed stent.

Similarly, Lylyk et al<sup>16</sup> observed that of 63 aneurysms treated with the PED, the only aneurysm that remained patent at 12-month follow-up had been treated previously with stent-assisted coiling. They deduced that the presence of a pre-existing stent may have limited the efficacy of the PED by impairing the apposition of the PED to the wall of the parent artery, which led to endoleaks that maintained patency of the aneurysm and disrupted the endothelialization process over the surface of the PED. In addition, the presence of these devices can complicate the navigation of the delivery catheter into position and the actual deployment of the PED, increasing the technical difficulty of the procedure. Technical difficulties involving catheter advancements were encountered in our study as well. These increased the complexity of the procedure and the ability to properly deploy the PED.

Chalouhi et al<sup>21</sup> highlighted the technical difficulties observed with PED placement in aneurysms with a previous stent in situ. Because the PED should be deployed distal to the stent, the distal end of the PED may “catch” on the previously placed stent, which may cause anchoring and stretching of the device, leading to less effective results. They suggested that performing simultaneous balloon angioplasty may be useful in optimizing PED apposition to the vessel wall.

Given the negative association between stent placement and later PED treatment, physicians should be careful when selecting the primary intervention to treat large complex wide-neck cerebral aneurysms that are amenable to PED treatment and less likely to be cured with conventional endovascular procedures. If a stent was placed initially, recurrence would be less eligible for PED treatment and might require surgical clipping to achieve aneurysm occlusion.

The main limitations of this study include the single-center experience with a small number of aneurysms. Another important limitation is the retrospective nature of this study. Furthermore, the mean time of angiographic follow-up was limited (10 months).

## CONCLUSIONS

The use of the PED in the management of previously stented cerebral aneurysms is less effective than the use of this device in nonstented aneurysms. Prior stent placement may decrease the rate of aneurysm occlusion following treatment with the PED, may increase the rate of complications associated with the procedure, and may increase the chances of encountering technical difficulties during PED deployment. Initial management of large wide-neck complex cerebral aneurysms amenable to PED treat-

ment with conventional stents should be carefully planned because recurrence of stented aneurysms is less likely to respond to PED placement. More studies are required to determine the best treatment for recurrent previously stented aneurysms.

Disclosures: Stravropoula Tjoumakaris—UNRELATED: Consulting Fee or Honorarium: Covidien. Pascal Jabbour—UNRELATED: Consultancy: Covidien.

## REFERENCES

1. Raymond J, Guilbert F, Weill A, et al. **Long-term angiographic recurrences after selective endovascular treatment of aneurysms with detachable coils.** *Stroke* 2003;34:1398–403 CrossRef Medline
2. Ferns SP, Sprengers ME, van Rooij WJ, et al. **Coiling of intracranial aneurysms: a systematic review on initial occlusion and reopening and retreatment rates.** *Stroke* 2009;40:e523–29 CrossRef Medline
3. Ries T, Siemonsen S, Thomalla G, et al. **Long-term follow-up of cerebral aneurysms after endovascular therapy prediction and outcome of retreatment.** *AJNR Am J Neuroradiol* 2007;28:1755–61 CrossRef Medline
4. Piotin M, Blanc R, Spelle L, et al. **Stent-assisted coiling of intracranial aneurysms: clinical and angiographic results in 216 consecutive aneurysms.** *Stroke* 2010;41:110–15 CrossRef Medline
5. Nishido H, Piotin M, Bartolini B, et al. **Analysis of complications and recurrences of aneurysm coiling with special emphasis on the stent-assisted technique.** *AJNR Am J Neuroradiol* 2014;35:339–44 CrossRef Medline
6. King B, Vaziri S, Singla A, et al. **Clinical and angiographic outcomes after stent-assisted coiling of cerebral aneurysms with Enterprise and Neuroform stents: a comparative analysis of the literature.** *J Neurointerv Surg* Oct 28 2014 [Epub ahead of print] Medline
7. Santillan A, Greenberg E, Patsalides A, et al. **Long-term clinical and angiographic results of Neuroform stent-assisted coil embolization in wide-necked intracranial aneurysms.** *Neurosurgery* 2012;70:1232–37; discussion 1237 CrossRef Medline
8. Hong Y, Wang YJ, Deng Z, et al. **Stent-assisted coiling versus coiling in treatment of intracranial aneurysm: a systematic review and meta-analysis.** *PLoS One* 2014;9:e82311 CrossRef Medline
9. Becske T, Kallmes DF, Saatci I, et al. **Pipeline for uncoilable or failed aneurysms: results from a multicenter clinical trial.** *Radiology* 2013;267:858–68 CrossRef Medline
10. Kallmes DF, Ding YH, Dai D, et al. **A new endoluminal, flow-disrupting device for treatment of saccular aneurysms.** *Stroke* 2007;38:2346–52 CrossRef Medline
11. Fiorella D, Woo HH, Albuquerque FC, et al. **Definitive reconstruction of circumferential, fusiform intracranial aneurysms with the Pipeline embolization device.** *Neurosurgery* 2008;62:1115–20; discussion 1120–21 CrossRef Medline
12. D’Urso PI, Lanzino G, Cloft HJ, et al. **Flow diversion for intracranial aneurysms: a review.** *Stroke* 2011;42:2363–68 CrossRef Medline
13. Zanaty M, Chalouhi N, Starke RM, et al. **Flow diversion versus conventional treatment for carotid cavernous aneurysms.** *Stroke* 2014;45:2656–61 CrossRef Medline
14. Chalouhi N, Tjoumakaris S, Starke RM, et al. **Comparison of flow diversion and coiling in large unruptured intracranial saccular aneurysms.** *Stroke* 2013;44:2150–54 CrossRef Medline
15. Fischer S, Vajda Z, Aguilar Perez M, et al. **Pipeline embolization device (PED) for neurovascular reconstruction: initial experience in the treatment of 101 intracranial aneurysms and dissections.** *Neuroradiology* 2012;54:369–82 CrossRef Medline
16. Lylyk P, Miranda C, Ceratto R, et al. **Curative endovascular reconstruction of cerebral aneurysms with the Pipeline embolization device: the Buenos Aires experience.** *Neurosurgery* 2009;64:632–42; discussion 642–43; quiz N6 CrossRef Medline
17. Nelson PK, Lylyk P, Szikora I, et al. **The Pipeline embolization device for the intracranial treatment of aneurysms trial.** *AJNR Am J Neuroradiol* 2011;32:34–40 CrossRef Medline
18. Chitale R, Gonzalez LF, Randazzo C, et al. **Single center experience with Pipeline stent: feasibility, technique, and complications.** *Neurosurgery* 2012;71:679–91; discussion 691 CrossRef Medline
19. Brinjikji W, Murad MH, Lanzino G, et al. **Endovascular treatment of intracranial aneurysms with flow diverters: a meta-analysis.** *Stroke* 2013;44:442–47 CrossRef Medline
20. Kallmes DF, Hanel R, Lopes D, et al. **International retrospective study of the Pipeline embolization device: a multicenter aneurysm treatment study.** *AJNR Am J Neuroradiol* 2015;36:108–15 CrossRef Medline
21. Chalouhi N, Chitale R, Starke RM, et al. **Treatment of recurrent intracranial aneurysms with the Pipeline embolization device.** *J Neurointerv Surg* 2014;6:19–23 CrossRef Medline

# A Systematic Review and Meta-Analysis of Treatment and Outcome of Blister-Like Aneurysms

S. Peschillo, D. Cannizzaro, A. Caporlingua, and P. Missori



## ABSTRACT

**BACKGROUND AND PURPOSE:** Blister-like aneurysms are uncommon but challenging lesions. Their small size and atypical location often make the diagnosis difficult. Microsurgery and endovascular procedures have been used for their treatment, but there is no consensus on the best treatment technique. We conducted a systematic review and meta-analysis of treatments and outcomes of these vascular lesions.

**MATERIALS AND METHODS:** We reviewed English-language articles on “blood blister-like aneurysms” published between January 1997 and November 2014. All studies reporting patients with these aneurysms treated with surgery, endovascular procedures, or combined therapy with data on treatment modalities and clinical and/or angiographic outcomes were selected, including case reports and series. We performed a meta-analysis on the 2 largest treatment groups (surgery and endovascular management).

**RESULTS:** Sixty studies with 334 patients met our inclusion criteria. Surgery was performed in 114 patients (34.2%), and endovascular treatment, in 199 patients (59.5%). A combined treatment was used in 19 patients (5.7%). A favorable outcome (mRS 0–2) was reported in 67.4% and 78.9% of patients treated with surgery and with endovascular therapy, respectively ( $P = .034$ ).

**CONCLUSIONS:** Blister-like aneurysms are challenging vascular lesions. The choice of treatment method must be based on the initial clinical presentation and an analysis of the radiologic features of the lesion to select the best technique. Endovascular treatment seems to have lower morbidity and mortality and provides a better outcome compared with surgical approaches. Further prospective studies must be performed to confirm such interesting results.

**ABBREVIATION:** HH = Hunt and Hess

Blister-like aneurysms, described for the first time by Nakagawa et al<sup>1</sup> and Takahashi et al,<sup>2</sup> account for approximately 0.3%–1% of all intracranial aneurysms<sup>3</sup> and are a therapeutic challenge. They typically have thin, fragile walls and poorly defined necks, sometimes appearing as just a protrusion of the vessel wall. They are usually associated with diffuse subarachnoid hemorrhage and a severe clinical condition. These lesions can be dangerous because of their propensity to rupture intraoperatively and

postoperatively. Blister-like aneurysms are often not easily detected at the first angiography due to their small dimensions and unusual locations, but because of their rapid growth, they become more evident within a few days.

Originally, they were thought to occur exclusively in the internal carotid artery; however, recent studies have shown that this type of vascular lesion can be found anywhere in the circle of Willis. Specifically, there have been reports of blister-like aneurysms in the middle cerebral artery, anterior communicating artery, and vertebrobasilar circulation.<sup>4–7</sup>

The above characteristics make them particularly difficult to treat, and patients with these lesions often have a poor outcome. Numerous treatment methods have been proposed: microsurgery, including clipping techniques, titanium vascular miniclip internal carotid artery repair, vessel graft wrapping reinforced by clips, trapping, parent vessel occlusion, and revascularization; and endovascular approaches, which can be performed with coils, coils and stent placement, multiple stents, stent placement alone, or vessel occlusion. Flow-diverting stents have been used to treat these lesions with good early

Received July 14, 2015; accepted after revision September 8.

From the Department of Neurology and Psychiatry, Endovascular Neurosurgery/Interventional Neuroradiology (S.P.); and Neurosurgery (D.C., A.C., P.M.), “Sapienza” University of Rome, Rome, Italy.

S.P. had the conception and design of the work; all authors contributed equally to drafting and revising the manuscript and all gave final approval of the version published. D.C. selected the studies for inclusion.

Please address correspondence to Simone Peschillo, MD, PhD, Department of Neurology and Psychiatry, Endovascular Neurosurgery/Interventional Neuroradiology, “Sapienza” University of Rome, Rome, Italy; e-mail: simone.peschillo@gmail.com

Indicates open access to non-subscribers at www.ajnr.org

<http://dx.doi.org/10.3174/ajnr.A4606>

results, but their long-term safety has yet to be proved. The current literature describing surgical and endovascular interventions in blister-like aneurysms does not offer a clear consensus on the optimal treatment technique.<sup>8</sup>

The aim of this work was to perform a systematic review and meta-analysis of the various types of treatment to compare their efficacy and safety.

## MATERIALS AND METHODS

A comprehensive literature search of the PubMed and Scopus data bases was conducted by using the key words “blood blister-like aneurysm,” “blister-like aneurysm,” and “blister aneurysm.” The search was limited to articles published between January 1997 and November 2014 in English only. All studies reporting patients with blister-like aneurysms treated with surgery, endovascular procedures, or combined therapy were selected. Evaluation was performed according to the “Preferred Reporting Items for Systematic Reviews and Meta-Analyses” (PRISMA) statement, including methods of publication search, eligibility, data collection, extraction, analysis, and preparation of the systematic review report.

Case reports or series with available data on clinical and/or angiographic outcomes and details of the treatment modalities were included. One reviewer (D.C.) selected the studies for inclusion.

For each study, we extracted the following information: patient presentation described by using validated scales (Hunt and Hess [HH] and Fisher), treatment technique (endovascular, surgical, combined), and long-term neurologic outcome (a good neurologic outcome was defined as a modified Rankin Scale score of  $\leq 2$ ). When an mRS score was not available, good neurologic outcome was determined from the description of the clinical results (eg, terms such as “no morbidity” or “good recovery”).

For the analysis, we have defined angiographic occlusion status immediately after treatment and at the last follow-up as “complete,” “near-complete,” or “incomplete.”

The primary objective of this study was to determine the clinical and angiographic outcomes of patients treated with endovascular procedures or surgery (the group of patients that underwent combined treatment was excluded from the statistical analysis because of its small size [ $n = 19$ ]). The secondary objective was to determine perioperative, intraoperative, and postoperative complications in the endovascular and surgical groups, morbidity at the last follow-up, and the clinical outcome in relation to the technique used.

### Literature Review

Our literature search initially yielded 103 articles; 43 articles were excluded either because the patients did not have blister-like aneurysms or because the patients’ presentations or angiographic outcomes were not described. In total, 60 studies with 334 patients met our inclusion criteria.

### Statistical Analysis

Statistical analyses were performed by using SPSS, Release 15.0 (IBM, Armonk, New York). All included studies were non-

**Table 1: Distribution of locations of blister-like aneurysms**

Topography	(%)
Internal carotid artery	91.6
Anterior communicating artery	2.8
Middle cerebral artery	1.9
Posterior cerebral artery	1.6
Basilar artery	1.6
Anterior cerebral artery	0.3
Total	100

comparative. From each cohort, we estimated the cumulative incidence (event rate) and 95% confidence interval for each outcome. Event rates for each intervention were pooled in a meta-analysis across studies. Frequencies of categorical variables of pooled data were compared by using the  $\chi^2$  test. Finally, a multivariable binary logistic analysis was performed to evaluate variables predictive of clinical outcome. Variables included in the model were age, sex, treatment (surgery/endovascular), and Fisher and HH grades. The coefficients obtained from the logistic regression were expressed in terms of odds ratios with 95% confidence intervals. All tests were 2-sided, and statistical significance was set at  $P < .05$ .

## RESULTS

We selected 60 studies, including retrospectively collected case series and case reports, evaluating 334 patients. A preponderance of females was noted: There were 246 females (73%) and 88 males. The average age of the patients in these studies was 48.5 years (range, 14–87 years). The median HH grade at admission was 3; 59 patients had an HH grade of  $\geq 4$  on admission (44 patients had grade 4; 15 had grade 5). More than 90% of the blister-like aneurysms were located along nonbranching sites of the internal carotid artery (91.6%); all of those arising from intracranial arteries other than the internal carotid artery were classified as “atypical.” The sites are presented in Table 1. A treatment was offered to nearly all patients evaluated; only 2 patients were managed conservatively (0.6%). Surgery was performed in 114 patients (34.2%); an endovascular approach was preferred in 199 cases (59.5%), while a combined approach (either a pure combined approach or salvage therapy following failure of the initial therapeutic technique) was used in 19 patients (5.7%). For statistical purposes, we focused on the 2 more frequently used types of treatment (surgery and endovascular procedures).

As mentioned before, the primary objective of this study was to determine the clinical and angiographic outcomes of patients treated with endovascular approaches or surgery. Regarding outcome, based on a division of the mRS scores into 2 groups (0, 1, or 2 and 3, 4, 5, or 6), 70% of patients with HH grade  $\leq 3$  in the group treated with surgery had a positive outcome (mRS 0–2), compared with 84.9% of the patients in the endovascularly treated group ( $P = .008$ ). Among the patients with HH grade  $\geq 4$ , only 59.1% of the surgical group had a positive outcome (mRS 0–2), and the percentage in the endovascularly treated group was even lower at 40.7% ( $P = .251$ ) (Table 2).

Considered together, including patients with all HH grades, 67.4% of the group treated with surgery had an mRS score of 0, 1, or 2, while 32.6% had an mRS score of 3, 4, 5, or 6. The corre-

sponding percentages in the endovascular group were 78.9% and 21.1% ( $P = .034$ ) (Table 2).

When we analyzed the outcome of patients divided on the basis of the Fisher scale and treatment received, among the pa-

**Table 2: Clinical outcomes according to type of treatment and presentation**

	Surgery-Only Group Outcome (mRS Score)		Endovascular Group Outcome (mRS Score)		P
	0, 1, 2	3, 4, 5, 6	0, 1, 2	3, 4, 5, 6	
Hunt Hess					
All subjects	67.4%	32.6%	78.9%	21.1%	.034 <sup>a</sup>
HH ≤3	70.0%	30.0%	84.9%	15.1%	.006 <sup>a</sup>
HH ≥4	59.1%	40.9%	40.7%	59.3%	.251
Fisher					
All subjects	67%	33%	77.8%	22.2%	.054 <sup>a</sup>
Fisher 1–2	77.1%	22.9%	88.8%	11.2%	.081
Fisher 3–4	61.4%	38.6%	61.1%	38.9%	.973

<sup>a</sup> Significant.

**Table 3: Multivariable binary logistic analysis to evaluate variables predictive of clinical outcome**

Variable	$\beta \pm SE$	P Value	OR (95% CI)
Treatment (surgery/endovascular)	$-0.20 \pm 0.31$	.516	0.82 (0.45–1.49)
Sex (female/male)	$-0.07 \pm 0.35$	.840	1.02 (0.99–1.05)
Age (yr)	$0.02 \pm 0.01$	.197	0.93 (0.47–1.85)
Fisher grade	$0.44 \pm 0.20$	.031 <sup>a</sup>	1.55 (1.04–2.30)
HH grade	$0.38 \pm 0.19$	.041 <sup>a</sup>	1.47 (1.02–2.12)

Note:—SE indicates standard error.

<sup>a</sup> Significant.

tients with Fisher grade  $\leq 2$ , the outcome was good (mRS 0–2) in 77.1% of patients in the surgery group and in 88.8% of those in the endovascular group ( $P = .081$ ). In contrast, among the patients with Fisher grade  $\geq 3$ , the percentages of patients with a good outcome were essentially the same (61.4% in the surgery group versus 61.1% in the endovascular group;  $P = .973$ ). In multivariable analysis (Table 3), both the HH and Fisher grade were clear predictors of outcome ( $P = .041$  and  $P = .031$ , respectively).

Concerning angiographic outcome, the frequencies of early occlusion status (complete, near-complete, and incomplete) were 96.4%, 3.6%, and 0.0%, respectively, in the surgery group and 44.5%, 41.0%, and 14.5%, respectively, in the endovascular group ( $P < .001$ ). The frequencies of follow-up occlusion status were 97.3%, 2.7%, and 0.0%, respectively, in the surgery group and 76.9%, 18.1%, and 5.0%, respectively, in the endovascular group ( $P < .001$ ).

Regarding morbidity and mortality, perioperative morbidity occurred in 7.0% (95% CI, 3.0%–19.0%) of the endovascular group and 20.0% (95% CI, 6.0%–49.0%) of the surgery group. Perioperative death occurred in 9.0% (95% CI, 5.0%–13.0%) of the endovascular group and 10.7% (95% CI, 5.0%–16.4%) of the surgery group. However, when the population was split into 2 subgroups according to HH grade, among subjects with an HH grade of  $< 4$ , the mortality rate was significantly higher in the surgery group than in the endovascular group (14.3% versus 4.6%, respectively;  $P = .009$ ); on the other hand, for patients with an HH grade of  $> 3$ , the mortality was higher in the endovascular group (37.0% versus 9.1%,  $P = .043$ ).

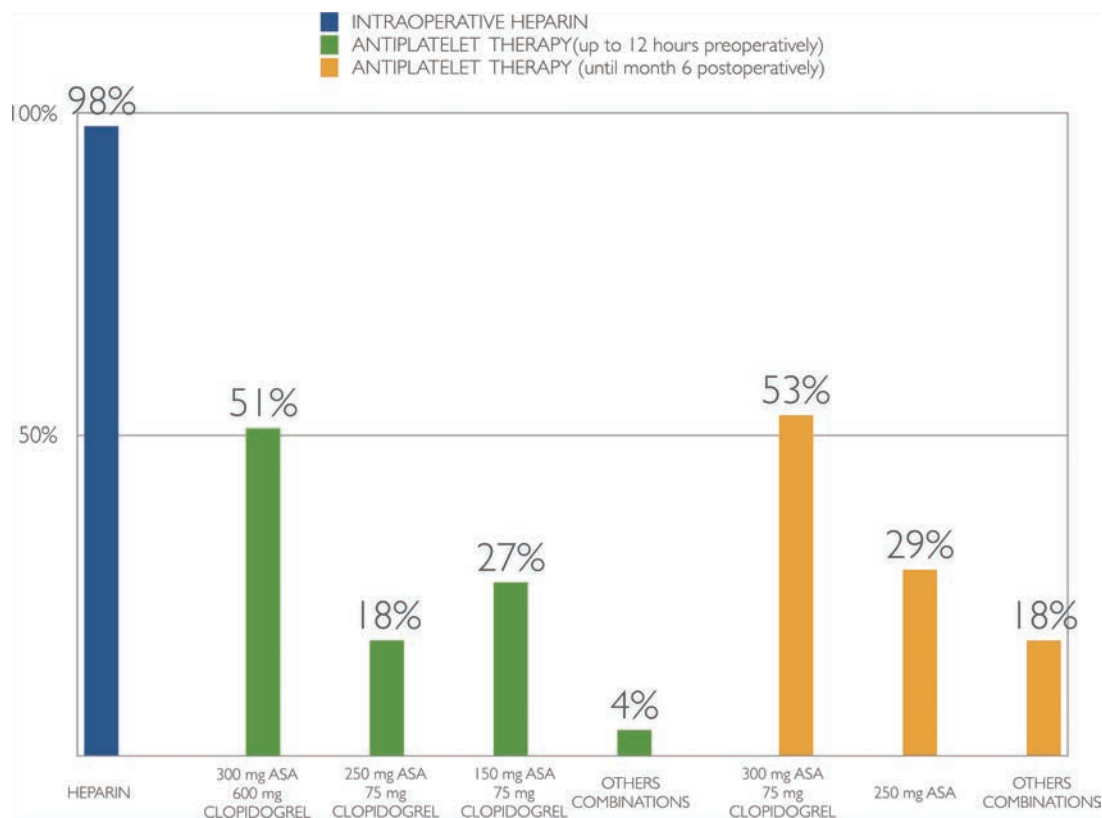


**FIG 1.** The graph shows the different data concerning antiplatelet therapy administered to patients treated with flow-diverter stents intraoperatively, up to 12 hours before the procedure, and during the first 6 postoperative months. Note that in some cases, this information was missing. These statistics are based on the available data. ASA indicates aspirin.

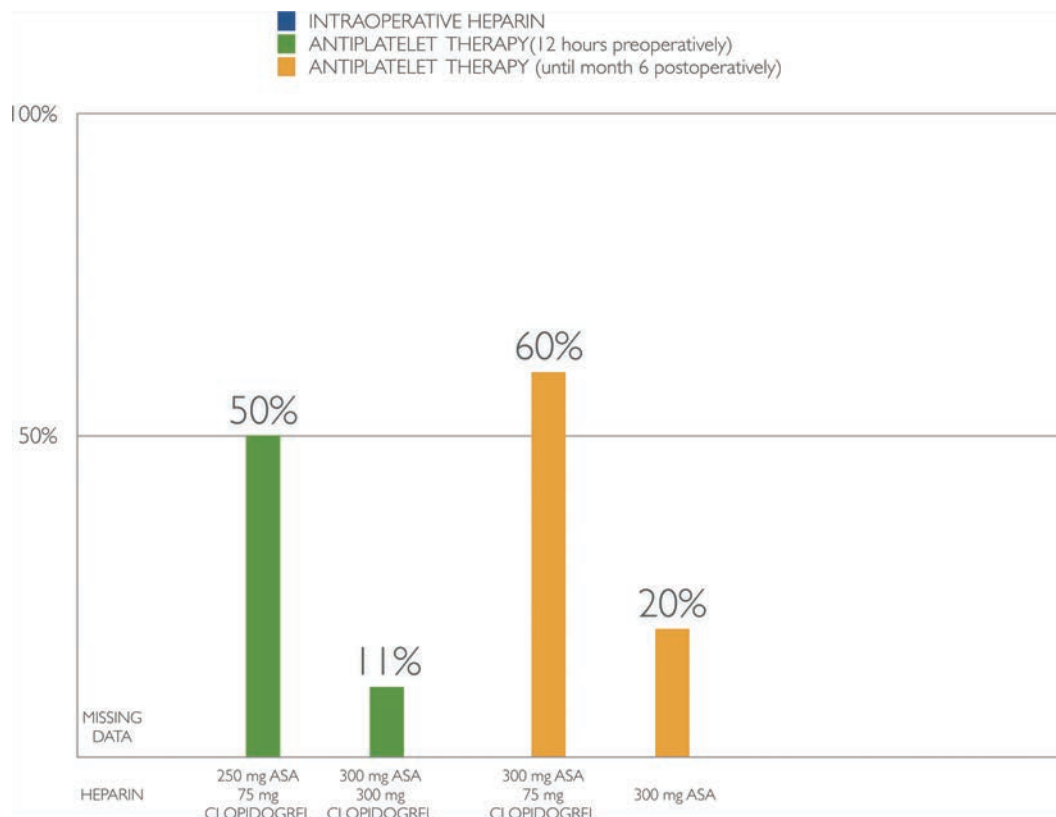


**FIG 2.** The graph shows the different data concerning antiplatelet therapy administered to patients treated with no flow-diverter stent up to 12 hours before the procedure, and during the first 6 postoperative months. Note that in some cases this information was missing. These statistics are based on the available data.

Intraprocedural complications occurred more frequently in the surgery group (24.1%) than in the endovascular group (10.5%) ( $P < .001$ ). The most frequent complication in the surgery group was rupture (81.5%). In the endovascular group, the most feared complications were thromboembolic events (33.3%), followed by vasospasm (19%); in particular, thromboembolic events were much more frequent in flow-diverter procedures (50%).

Concerning antiplatelet treatment in the endovascular group, it is worth considering the experiences of various authors when flow-diverter stents were or were not used (Figs 1 and 2).

Postprocedural complications were reported in 35.7% of the surgery group and 21.1% of the endovascular group ( $P < .001$ ). The most frequent complications in the surgery group were hydrocephalus and stroke in 20.0% and vasospasm in 17.5%, while the most common complications in the endovascular group were recanalization and hemorrhage, which occurred in 54.8% and 14.3%, respectively.

The outcomes in the endovascular group differed according to the endovascular technique used, with the highest percentages of patients having a good outcome being among those treated with stents (86.4%), stent-assisted coiling (85.2%), and flow diverters (82.2%); the subgroup with the lowest rate of good outcomes (mRS 0–2) was treated with coils (52.9%) ( $P = .266$ ) (Table 4). In the surgery group, the highest rates of good outcomes were found in the subgroups managed with trapping + radial artery bypass (92.3%), wrapping + clipping (82.9%), and clipping + arteriotomy (68.4%) ( $P = .12$ ) (Table 5). These dif-

**Table 4: Clinical outcome of patients treated with endovascular techniques**

	Outcome (mRS Score)				Total	(%)
	$(P = .266)$					
	0, 1, 2		3, 4, 5, 6			
(No.)	(%)	(No.)	(%)			
Balloon-assisted coils	6	75.0	2	25.0	8	4
Coil	9	52.9	8	47.1	17	9
Coil + stent, no FD	41	71.9	16	28.1	57	29
FD	37	82.2 <sup>a</sup>	8	17.8 <sup>a</sup>	45	23
FD + coils	3	100.0	0	0.0	3	2
FD + stent	1	100.0	0	0.0	1	1
Multistent	2	100.0	0	0.0	2	1
PAO	8	88.9	1	11.1	9	5
SAC	23	85.2 <sup>a</sup>	4	14.8 <sup>a</sup>	27	14
SAC + FD	1	100.0	0	0.0	1	1
Stent	19	86.4 <sup>a</sup>	3	13.6 <sup>a</sup>	22	11
Stent in stent	3	100.0	0	0.0	3	2
Trapping with coil	4	100.0	0	0.0	4	2
Total	157		42		199	104

**Note:**—FD indicates flow diverter; PAO, parent artery occlusion; SAC, stent-assisted coiling.

<sup>a</sup>Results for the largest groups.

ferences were not statistically significant and should, therefore, be interpreted with caution.

## DISCUSSION

Blister-like aneurysms were first described by Nakagawa et al<sup>1</sup> and Takahashi et al.<sup>2</sup> The pathogenesis of these vascular disorders remains unclear, but several mechanisms have been proposed, in-

**Table 5: Clinical outcome of patients treated with surgical techniques**

	Outcome (mRS Score) ( <i>P</i> = .12)				Total	Total (%)
	0, 1, 2		3, 4, 5, 6			
	(No.)	(%)	(No.)	(%)		
Bypass	1	100.0	0	0.0	1	0.9
Clip	4	66.7	2	33.3	6	5.3
Clip + arteriotomy	26	68.4 <sup>a</sup>	12	31.6 <sup>a</sup>	38	33.6
Clip + bypass	3	100.0	0	0.0	3	2.7
PAO	0	0.0	1	100.0	1	0.9
Proximal ligation + RA bypass	0	0.0	1	100.0	1	0.9
Sutured	2	66.7	1	33.3	3	2.7
Trapping	2	22.2	7	77.8	9	8.0
Trapping + RA bypass	12	92.3 <sup>a</sup>	1	7.7 <sup>a</sup>	13	11.5
Wrapping + bypass + PAO	1	100.0	0	0.0	1	0.9
Wrapping + clip	29	82.9 <sup>a</sup>	6	17.1 <sup>a</sup>	35	31.0
Wrapping	1	50.0	1	50.0	2	1.8
Total	81		32		113	100

Note:—RA indicates radial artery; PAO, parent artery occlusion.

<sup>a</sup>Results for the largest groups.

**Table 6: Characteristics of blister-like aneurysms**

Characteristic	Description
Localization	Nonbranching site, proximal
Dimension	Small, <3 mm (within 24 hours of SAH)
Shape	Conical, wide-neck
Appearance	Dissecting
Tendency to rebleed	High, due to friable walls
Tendency to grow	High

cluding atherosclerosis, hemodynamic stress related to hypertension, and arterial dissection creating a pseudoaneurysm. A postmortem pathologic study performed by Ishikawa et al<sup>3</sup> demonstrated blister-like aneurysms that arose in an atherosclerotic carotid artery in the junction between the sclerotic and normal carotid wall; there was degeneration of the internal elastic lamina associated with a lack of normal adventitia and fibrinous tissue at this site, leading to laceration of the internal carotid wall, suggesting that these kinds of vascular lesions may be a subtype of dissecting aneurysms or pseudoaneurysms.<sup>3,9</sup>

Although a definitive diagnosis can only be made from histologic studies, numerous features define blister-like aneurysms. According to the literature, we can define these as a small aneurysm (<3 mm, within 24 hours from subarachnoid hemorrhage), located at a nonbranching site, and proximal to the circle of Willis, which can evolve during a brief period. This type of aneurysm has friable walls, making the risk of intraoperative and postoperative bleeding high. It is conical and wide-necked with a dissecting/nonsaccular appearance (Table 6). It is frequently unrecognized at initial digital subtraction angiography.

Numerous treatments have been proposed, including microsurgical and endovascular techniques, without a unanimous consensus on the best method having been reached, probably because of the rarity of these lesions, which account for <1% of all intracranial aneurysms.

The aim of this meta-analysis was an overall analysis of this type of lesion and the various treatment options to gain a better understanding of the preferable therapeutic choices.

As reported in the “Results,” endovascular treatment was associated with a higher rate of favorable outcomes if the patients presented with an HH grade of ≤3; however, in more severe cases (HH ≥4), the outcome was better in the group treated with surgery. Overall, including patients with all HH grades, 67.4% in the group treated surgically had a good outcome (mRS 0–2), while 32.6% had a less satisfactory outcome (mRS 3–6) (Table 2). The corresponding percentages in the group treated with endovascular approaches were 78.9% and 21.1% (*P* = .034) (Table 2). The Fisher grade is also a good predictor of outcome; in fact, of the patients with Fisher grade ≤2, 77.1% in the surgery group had a positive outcome (mRS 0–2) as did 88.8% in the endovascular group (*P* = .081). Both HH and Fisher grades remained clear predictors of outcome in the multivariable analysis (*P* = .041 and *P* = .031, respectively) (Table 3).

Concerning angiographic outcome, surgery was more likely to achieve early, complete occlusions, whereas there was an improvement of 32.4% between the early occlusion status and the follow-up occlusion status in the endovascular group. This difference did not, however, seem to influence the outcome; it appears clear that the clinical status at the outset has a much greater effect than complete occlusion of the aneurysm.

Intraprocedural complications were more frequent in the surgery group than in the endovascular one (24.1% versus 10.5%, respectively; *P* < .001); the most feared complication in the surgery group was rupture of the aneurysm (81.5%). This is probably related to handling the sac and the surgical dissection. In contrast, the most feared complications of endovascular management were thromboembolic events (33.3%), followed by vasospasm (19%). There is not a unanimous consensus regarding the use of antiplatelet treatment in the endovascular group (Figs 1 and 2): Every group has set up their own protocol, probably based on their clinical experience or derived from other specialties. The differences, associated with the use of stents in the acute stage, may explain why thromboembolic events are quite common in patients managed with flow-diverter procedures.

However, in the setting of acute SAH, dual antiplatelet therapy is still controversial; the risk-benefit profile of potential hemorrhagic and thromboembolic complications should be considered carefully in deciding when to initiate such therapy.

Postprocedural complications were also more frequent after surgery (35.7%) than after endovascular treatment (21.1%) (*P* < .001); considering these data together, we can state that endovascular treatment is generally associated with fewer complications.

The different treatment groups (endovascular and surgical) were also compared in an attempt to determine whether the type of treatment affects the outcome in some way (Tables 4 and 5).

Considering the numerically larger subgroups, the percentage of good outcomes (mRS 0–2) in the endovascular group was high using flow diverters (82%), stent-assisted coiling (85.2%), and non-flow-diverter stents (86.4%), though the best results were obtained with parent artery occlusion (88.9%) (*P* = .266). Within the group treated surgically, clipping, trapping with bypass, and wrapping with clipping were the more successful techniques (*P* = .12). These analyses were not statistically significant because of the marked fragmentation of the groups investigated; the other percentages could not be considered reliable because of the small

sizes of the subgroups. In multivariable analysis, the type of treatment did not seem to influence the outcome (Table 3).

## CONCLUSIONS

Blister-like aneurysms are challenging lesions to treat whether by an open surgery or endovascular techniques. These complex aneurysms often require multiple treatments and have a high incidence of rebleeding. No single approach is clearly superior for these vascular lesions, but several options exist; endovascular treatment seems to be associated with lower morbidity and mortality compared with surgical approaches. The only parameters that seem to influence the outcome are HH and Fisher grades. Larger and homogeneous cohorts of patients will help to elucidate the optimal treatment for patients with subarachnoid hemorrhage due to blister-like aneurysms.

## ACKNOWLEDGMENTS

The authors thank Enrico Di Stasio, MD, for statistical analysis.

Disclosures: Simone Peschillo—UNRELATED: Consultancy: Educational Proctor for Penumbra.

## REFERENCES

1. Nakagawa F, Kobayashi S, Takemae T, et al. **Aneurysms protruding from the dorsal wall of the internal carotid artery.** *J Neurosurg* 1986; 65:303–08 Medline
2. Takahashi A, Suzuki J, Fujiwara S, et al. **Surgical treatment of chiasm (blood blister-like) aneurysm at c2 portion of internal carotid artery** [in Japanese]. *Surg Cereb Stroke* 1988;16:72–77
3. Ishikawa T, Nakamura N, Houkin K, et al. **Pathological consideration of a “blister-like” aneurysm at the superior wall of the internal carotid artery: case report.** *Neurosurgery* 1997;40:403–05; discussion 405–06 Medline
4. Peschillo S, Missori P, Piano M, et al. **Blister-like aneurysms of middle cerebral artery: a multicenter retrospective review of diagnosis and treatment in three patients.** *Neurosurg Rev* 2015;38:197–202; discussion 202–03 CrossRef Medline
5. Peschillo S, Cannizzaro D, Missori P, et al. **Reconstructive endovascular treatment of a ruptured blood blister-like aneurysm of anterior communicating artery.** *J Neurosurg Sci* 2014 Jun 10. [Epub ahead of print] Medline
6. Andaluz N, Zuccarello M. **Blister-like aneurysms of the anterior communicating artery: a retrospective review of diagnosis and treatment in five patients.** *Neurosurgery* 2008;62:4:807–11; discussion 811 CrossRef Medline
7. Peschillo S, Miscusi, M, Caporlingua A, et al. **Blister-like aneurysms in atypical locations: a single-center experience and comprehensive literature review.** *World Neurosurg* 2015;84:1070–79 CrossRef Medline
8. Gonzalez AM, Narata AP, Yilmaz H, et al. **Blood blister-like aneurysms: single center experience and systematic literature review.** *Eur J Radiol* 2014;83:197–205 CrossRef Medline
9. Mizutani T, Miki Y, Kojima H, et al. **Proposed classification of non-atherosclerotic cerebral fusiform and dissecting aneurysms.** *Neurosurgery* 1999;45:253–59; discussion 259–60 Medline

# Endovascular Treatment of Very Small Intracranial Aneurysms: Meta-Analysis

V.N. Yamaki, W. Brinjikji, M.H. Murad, and G. Lanzino

## ABSTRACT

**BACKGROUND AND PURPOSE:** Outcomes of endovascular treatment of very small intracranial aneurysms are still not well-characterized. Recently, several series assessing coil embolization of tiny aneurysms have presented new promising results. Thus, we performed a systematic review and meta-analysis of studies evaluating endovascular treatment of very small intracranial aneurysms.

**MATERIALS AND METHODS:** We conducted a computerized search of Scopus, Medline, and the Web of Science for studies on endovascular treatment of very small ( $\leq 3$  mm in diameter) intracranial aneurysms published between January 1996 and May 2015. Using a random-effects model, we evaluated clinical and angiographic outcomes.

**RESULTS:** Twenty-two studies with 1105 tiny aneurysms (844 ruptured and 261 unruptured) endovascularly treated were included. Postoperative and long-term complete occlusion was achieved in 85% (95% CI, 78%–90%) and 91% (95% CI, 87%–94%) of aneurysms, respectively. The recanalization rate was 6% (95% CI, 4%–11%) and retreatment occurred in 7% (95% CI, 5%–9%) of cases. Seventy-nine percent (95% CI, 64%–89%) of patients had good neurologic outcome at long-term follow-up. Intraprocedural rupture occurred in 7% (95% CI, 5%–9%) of the coiling procedures, while thromboembolic complications occurred in 4% (95% CI, 3%–6%).

**CONCLUSIONS:** Coil embolization of very small intracranial aneurysms can be performed safely and effectively. In the case of unruptured aneurysms, procedure-related complications are not negligible. Patients and providers should consider such risks when engaged in a shared decision-making process.

**ABBREVIATION:** IA = intracranial aneurysm

Endovascular treatment is now the standard of care for most intracranial aneurysms (IAs).<sup>1,2</sup> Despite endovascular treatment being safe with low morbidity and mortality rates, in certain groups of aneurysms, a detailed risk-benefit assessment of this treatment must be considered.<sup>3</sup> Coil embolization of very small IAs ( $\leq 3$  mm) is particularly challenging due to the thin fragile wall of small IAs, with limited space to obtain a stable microcatheter position for coil deployment.<sup>4-6</sup> In the Barrow Ruptured Aneurysm Trial, very small aneurysm size was one of the main rea-

sons for the high crossover rate from the coiling to the clipping group.<sup>2</sup> A previous meta-analysis that included only 7 studies observed a relatively high complication rate, especially in terms of periprocedural rupture risk.<sup>7</sup> Since then, several technologic improvements, including better microcatheters and steerable soft microguidewires, compliant and easier-to-navigate balloons, and the availability of newer distal access catheters and very small endovascular coils have been developed, which may have enhanced our ability in coiling very small aneurysms. Since publication of the previous meta-analysis, many recent series have outlined results and complications in this specific subset of aneurysms.

In an attempt to examine the current safety and efficacy of endovascular treatment of tiny intracranial aneurysms, we performed an updated systematic review and meta-analysis of the literature addressing the endovascular treatment of very small intracranial aneurysms. We also compared results from studies included in a previously published meta-analysis from 2010<sup>7</sup> with more recently published studies to determine whether there have been improvements in outcomes with time. We hypothesized that

Received August 18, 2015; accepted after revision November 10.

From the Coordenação de Aperfeiçoamento de Pessoal de Nível Superior Foundation (V.N.Y.), Ministry of Education of Brazil, Brasília, Brazil; and Department of Radiology (W.B.), Center for Science of Healthcare Delivery (M.H.M.), and Department of Neurosurgery (G.L.), Mayo Clinic, Rochester, Minnesota.

Contributorship statement: Vitor N. Yamaki, Waleed Brinjikji, Mohammad H. Murad, and Giuseppe Lanzino participated in drafting the article and revising it critically for important intellectual content. These authors made substantial contributions to conception and design, acquisition of data, and analysis and interpretation of data. All authors provided final approval of the version to be published.

Please address correspondence to Waleed Brinjikji, MD, Mayo Clinic, OL 1-115, 200 SW First St, Rochester, MN 55905; e-mail brinjikji.waleed@mayo.edu; @wbrinjikji

<http://dx.doi.org/10.3174/ajnr.A4651>

recently published studies would demonstrate lower intraoperative rupture rates and higher rates of aneurysm occlusion.

## MATERIALS AND METHODS

### Literature Search

Studies were identified by a search of Scopus, Medline, and the Web of Science for studies on the endovascular treatment of very small ( $\leq 3$  mm in diameter) intracranial aneurysms published between January 1996 and May 2015. The search was performed by using the following keywords: “cerebral aneurysm,” “intracranial aneurysm,” “coil,” “small,” “tiny,” and “endovascular” in both AND and OR combinations. The eligibility assessment of the articles was initially performed independently by 2 authors (W.B. and V.N.Y.). In case of disagreement, a third author (G.L.) was consulted for a final decision. Reference lists of included articles were scanned as an additional means of identifying articles.

### Study Selection

Consecutive case series studying the endovascular treatment of very small intracranial aneurysms ( $\leq 3$  mm in diameter) with  $\geq 10$  patients were included in this meta-analysis. Participants of any age with very small saccular IAs were considered. Studies addressing dissecting or “blister” IAs were excluded because these lesions have unique natural histories and pathologic characteristics. Series studying IAs in a specific location were also excluded to avoid selection bias.

Patients were divided into 3 groups: 1) unruptured coiled aneurysms, 2) ruptured coiled aneurysms, and 3) stent-assisted coiled aneurysms, ruptured and unruptured. Patients who received a stent without coiling were added to the stent-assisted group. In 1 article, 1 patient was treated with Onyx (Covidien, Irvine, California), thus excluding the article from our analysis. No patients were treated with flow-diverting stents.

### Data Abstraction

Information was extracted through a prespecified data-extraction protocol. From each included study, we collected the following data: 1) immediate and long-term angiographic occlusion, 2) technical success, 3) recanalization rate, 4) retreatment rate, 5) morbidity and mortality related to the procedure, 6) procedure-related rupture, 7) procedure-related thromboembolism, 8) long-term neurologic outcome, and 9) neurologic outcome at discharge.

The angiographic outcome data were divided into 2 groups: complete or near-complete angiographic occlusion and incomplete occlusion. Results reporting the angiographic findings by using the Raymond grading system (class 1, complete obliteration; class 2, neck remnant; class 3, aneurysm remnant) were translated to our methods as follows: Classes 1 and 2 were considered complete or near-complete angiographic occlusion, and class 3 was included in the incomplete-occlusion group.

The technical success was assessed in only prospective analysis or studies that reported failure of the endovascular treatment attempt. Hemorrhagic or ischemic events were not imputed to rupture or thromboembolism related to the procedure if they were not clearly described as a consequence of the procedure. With

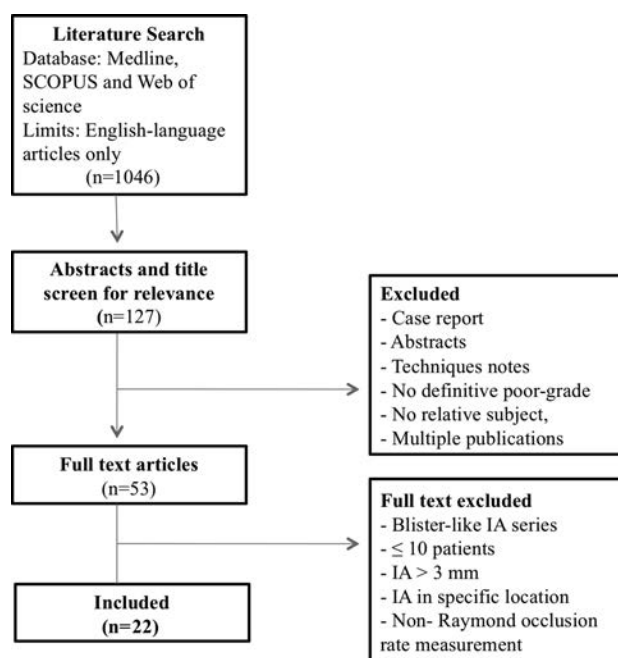


FIG 1. Flow diagram of the search strategy and study selection.

regard to the clinical outcome, only studies using the Glasgow Outcome Scale or the modified Rankin Scale were included. Good neurologic outcome was considered for grades 4 and 5 in the Glasgow Outcome Scale and for grades 0 and 1 in the mRS. Procedure-related morbidity and mortality were defined as morbidity or mortality related to thromboembolic or bleeding complications that occurred during the procedure.

We also compared results from studies included in a previously published meta-analysis from 2010 (time period 1) with more recently published studies (time period 2) to determine whether there were improvements in outcomes with time.<sup>7</sup> For this comparison, we studied only outcomes of the pooled ruptured/unruptured group.

### Statistical Analysis

All included studies were noncomparative. We estimated from each cohort the cumulative incidence (event rate) and 95% confidence interval for each outcome. Event rates for each intervention were pooled in a meta-analysis across studies by using the random-effects model.<sup>8</sup> Anticipating heterogeneity among studies, we chose this model a priori because it incorporates within-study variance and between-study variance. Heterogeneity of the treatment effect across studies was evaluated by using the  $I^2$  statistic.<sup>9</sup> We considered an  $I^2$  statistic of  $>50\%$  to indicate substantial heterogeneity. We were unable to test for publication bias due to the noncomparative nature of the studies. The meta-analysis was performed by using the statistical software package Comprehensive Meta-Analysis, Version 3.0 (Englewood, New Jersey).

## RESULTS

### Characteristics of Included Studies

The literature search yielded 1046 articles, of which 22 met our inclusion criteria. A summary of the literature search process is

**Table 1: Summary of studies evaluating the endovascular treatment of very small intracranial aneurysms**

Study	No. of Patients	Patient Age Range (yr)	Sex (M/F)	IA Size (mm) (Mean)	Follow-Up (mo) (Mean)	No. of Ruptured IAs	No. of Unruptured IAs	Total No. of IAs
Suzuki et al, 2006 <sup>22</sup>	21	31–86	5:16	2.6	25	21	0	21
Nguyen et al, 2008 <sup>4</sup>	60	24–92	–	2.7	–	60	0	60
Chen et al, 2008 <sup>23</sup>	11	26–73	8:3	2.7	5.3	10	1	11
van Rooji et al, 2009 <sup>10</sup>	187	11–78	51:136	≤3	6	149	47	196
Yang et al, 2009 <sup>24</sup>	12	23–88	4:8	2.6	13.4	12	0	12
Brinjikji et al, 2010 <sup>7</sup>	71	37–86	10:61	2.7	10.6	24	47	71
Pierot et al, 2010 <sup>25</sup>	51	–	10:41	≤3	–	0	51	51
Chae et al, 2010 <sup>26</sup>	30	28–81	11:19	≤3	13.3	5	26	31
Ioannidis et al, 2010 <sup>15</sup>	94	27–80	27:67	≤3	23	85	12	97
Fang et al, 2010 <sup>27</sup>	19	38–63	5:14	2.8	14.1	20	0	20
Zang et al, 2010 <sup>28</sup>	11	25–55	1:10	≤3	7.4	10	1	11
Hwang et al, 2011 <sup>29</sup>	38	24–70	12:26	2.5	14.8	23	20	43
Hong et al, 2011 <sup>30</sup>	51	17–71	22:29	2.4	14	51	0	51
Iskandar and Nepper-Rasmussen, 2011 <sup>3</sup>	107	–	34:73	≤3	9	87	24	111
Lu et al, 2012 <sup>11</sup>	46	27–83	22:24	2.5	46.7	29	23	52
Mohammadian et al, 2013 <sup>31</sup>	21	19–72	22:18	≤3	15	21	0	21
Chung et al, 2013 <sup>32</sup>	72	–	24:48	2.8	–	72	0	72
Starke et al, 2012 <sup>14</sup>	91	–	26:65	2.8	9.5	91	0	91
Li et al, 2014 <sup>33</sup>	16	33–62	7:9	1.7	7.7	16	0	16
Dalfino et al, 2014 <sup>18</sup>	20	27–80	5:15	2.7	17	17	3	20
Jindal et al, 2015 <sup>34</sup>	12	19–70	2:10	2.25	9.25	6	6	12
Yu et al, 2015 <sup>17</sup>	35	41–68	23:12	2.6	12–24	35	0	35
Total	1076					844	261	1105

provided in Fig 1. All 22 studies included were single-center case series. Nine studies provided data on only ruptured IAs, 2 provided data on only unruptured IAs, and 11 included both ruptured and unruptured aneurysms. A total of 1105 intracranial aneurysms that received endovascular treatment (844 ruptured and 261 unruptured) were included in this meta-analysis. Stent-assisted coil embolization was performed in 86 cases. Table 1 provides a summary of included studies.

### Study Outcomes

**Coil Embolization: Technical Success and Angiographic Outcomes.** Technical success for endovascular treatment was achieved in 92% of the coiled IAs (95% CI, 88%–95%). Immediate postoperative angiography demonstrated a complete occlusion rate of 85% (95% CI, 78%–90%). At long-term (≥6-month) angiographic follow-up, 91% (95% CI, 87%–94%) of aneurysms had complete or near-complete occlusion. The recanalization rate was 6% (95% CI, 4%–11%). The retreatment rate was 7% (95% CI, 5%–9%).

When we compared coiled ruptured and unruptured IAs, results from immediate postcoiling angiography demonstrated similar rates of occlusion, with 85% (95% CI, 77%–91%) for the unruptured coiled group and 88% (95% CI, 79%–93%) for ruptured aneurysms. For long-term (≥6-month) angiographic outcome, 86% (95% CI, 80%–90%) of ruptured aneurysms had complete or near-complete occlusion. Overall recanalization and retreatment rates were 6% and 7%, respectively. Overall long-term (≥6-month) occlusion rates were 91% (95% CI, 85%–94%).

**Coil Embolization: Clinical Outcomes and Complications.** Neurologic outcomes were reported at the time of discharge and at

long-term (≥6-month) follow-up. Eighty-two percent (95% CI, 64%–91%) of patients were discharged in good neurologic condition. Long-term (≥6-month) good neurologic outcome was 79% (95% CI, 64%–89%). For patients with ruptured IAs, the rate of good neurologic outcome at discharge was 65% (95% CI, 30%–89%) and the rate of long-term (≥6-month) good neurologic outcome was 74% (95% CI, 59%–85%). Not enough data were available for individual analysis of unruptured IAs for neurologic outcomes.

With regard to procedure-related complications, intraprocedural rupture was identified in 7% (95% CI, 5%–9%) of the coiling procedures, while thromboembolic complications occurred in 4% (95% CI, 3%–6%) of cases. Coiled ruptured aneurysms had procedure-related rupture in 9% (95% CI, 6%–12%) of cases and thromboembolic events in 4% (95% CI, 2%–9%). For unruptured IAs, the rate of rupture during coil embolization was 6% (95% CI, 3%–12%) and thromboembolic complications occurred in 4% (95% CI, 1%–13%). The mortality rate related to the coil embolization was 3% (95% CI, 2%–5%), while the morbidity rate was 2% (95% CI, 2%–4%). For patients with ruptured IAs, the procedure-related mortality and morbidity were 4% (95% CI, 2%–7%) and 3% (95% CI, 2%–5%), respectively. For patients with unruptured aneurysms, procedure-related morbidity was 2% (95% CI, 1%–12%) and procedure-related mortality was 2% (95% CI, 1%–13%). These data are summarized in Table 2.

**Stent-Assisted Coil: Outcomes.** Among patients treated with stent-assisted coiling, immediate complete occlusion occurred in 70% (95% CI, 52%–84%) of cases. Long-term (≥6-month) complete occlusion was 93% (95% CI, 81%–98%). For ruptured IAs, angiographic outcomes showed immediate and

**Table 2: Meta-analysis outcomes**

	Unruptured Aneurysms, (%) (95% CI)	I <sup>2</sup>	Ruptured Aneurysms, (%) (95% CI)	I <sup>2</sup>	All Aneurysms, (%) (95% CI)	I <sup>2</sup>
Complete angiographic occlusion						
Initial	85 (77–91)	40	88 (79–93)	71	85 (78–90)	76
Long-term	90 (44–99)	49	86 (80–90)	45	91 (87–94)	45
Periprocedural outcomes						
Rupture	6 (0–13)	0	9 (6–12)	0	7 (5–9)	0
Thromboembolism	4 (1–8)	NA	4 (2–9)	0	4 (3–6)	0
Morbidity	2 (1–12)	NA	3 (2–5)	0	2 (2–4)	0
Mortality	2 (1–13)	NA	4 (2–7)	0	3 (2–5)	0
Long-term favorable neurologic outcome	–	–	74 (59–85)	NA	79 (64–89)	83
Recanalization	–	–	9 (5–17)	28	6 (4–11)	54
Retreatment	–	–	7 (3–14)	12	7 (5–9)	14

Note:—NA indicates not available.

**Table 3: Outcomes by time period**

	Time Period 1 % (95% CI)	Time Period 2 % (95% CI)	P Value
Initial complete/near complete occlusion	89.0 (82.0–96.0)	85.0 (79.0–91.0)	.004
Initial incomplete occlusion	9.0 (2.0–16.0)	15.0 (9.0–21.0)	.002
Long-term complete/near complete occlusion	93.0 (90.0–97.0)	94.0 (90.0–97.0)	.12
Long-term good neurologic outcome	85.0 (74.0–95.0)	77.0 (53.0–100.0)	.12
Procedure-related morbidity	2.0 (0.0–3.0)	2.0 (1.0–3.0)	.94
Procedure-related mortality	2.0 (0.0–3.0)	2.0 (0.0–3.0)	.81
Procedure-related rupture	7.0 (4.0–10.0)	3.0 (2.0–4.0)	.007
Procedure-related thromboembolism	1.0 (0.0–3.0)	3.0 (2.0–5.0)	.06
Recanalization	2.0 (0.0–4.0)	5.0 (2.0–9.0)	.004
Retreatment	5.0 (3.0–8.0)	4.0 (2.0–5.0)	.93

long-term complete occlusion rates of 68% (95% CI, 49%–82%) and 93% (95% CI, 79%–98%), respectively. Intraprocedural rupture rates were 6% (95% CI, 1%–34%), and thromboembolism occurred in 13% (95% CI, 4%–33%) of cases. The incidence of IA recanalization with stent deployment was 14% (95% CI, 4%–43%), and the retreatment rate was 3% (95% CI, 0%–34%).

**Comparison of Outcomes across Time.** When we compared outcomes between studies included in the prior meta-analysis and those included in the current meta-analysis, angiographic outcomes were superior in studies included in the prior meta-analysis because initial complete/near-complete angiographic occlusion rates were 89.0% compared with 85.0% in recently published series ( $P = .004$ ).<sup>7</sup> Long-term ( $\geq 6$ -month) good clinical outcome rates were similar between studies (93.0% for time period 1 and 94.0% for time period 2). Procedure-related rupture rates were significantly lower in more recent studies (7.0% versus 3.0%,  $P = .007$ ). Retreatment rates were similar between time periods (5.0% for time period 1 and 4.0% for time period 2,  $P = .93$ ). These data are summarized in Table 3.

### Study Heterogeneity

No  $I^2$  statistics were higher than 50%, indicating substantial heterogeneity, for any outcomes in unruptured aneurysms or in stent-assisted coil-treated aneurysms.  $I^2$  statistics were higher than 50%, indicating substantial heterogeneity, for the following outcomes in ruptured aneurysms: complete/near-complete initial occlusion and good neurologic outcome at discharge.  $I^2$  statistics were higher than 50%, indicating substantial heterogeneity, for the following outcomes in all aneurysms: initiation complete/

near-complete occlusion, long-term good neurologic outcome, and recanalization. These data are summarized in Table 2.

### DISCUSSION

Our updated meta-analysis of endovascular coiling of very small intracranial aneurysms demonstrated that coil embolization is effective, with angiographic occlusion rates of  $>90\%$ . However, complications rates were not negligible at 6.5% for ruptured and 5% for unruptured aneurysms. Intraoperative rupture rates have decreased with time suggesting that technologic improvements may be enhancing patient outcomes. When we compared earlier experiences with more recent ones, there has been some improvement in complication rates as a result of newer technologic advances<sup>5</sup> and increased experience, which makes endovascular coil embolization a safe treatment technique in patients with ruptured very small aneurysms. Our results suggest that endovascular treatment of very small unruptured aneurysms should be pursued only in exceptional cases, given the very low risk of rupture of these aneurysms.

Our results showed high rates of complete or near-complete occlusion, both immediately following treatment and at follow-up. Technical success was achieved in 92% of patients, and recanalization rates were low. Only 7% of aneurysms were retreated with coiling or microsurgical clipping. In the prior meta-analysis including 7 studies, we reported slightly higher occlusion rates at short- and long-term, possibly due to factors related to publication and selection bias.<sup>7</sup> Recently published series are reporting complete occlusion rates as high as 96% in the immediate postoperative setting and 94% in the long-term.<sup>10</sup> Our report might be influenced by different treatment strategies adopted in the included studies. For example, Lu et al<sup>11</sup> suggested that complete coil occlusion of the aneurysm sac is not necessary to achieve good long-term outcomes. For challenging aneurysms with a very high rate of intraprocedural rupture, they suggested an initial partial occlusion, allowing progressive stable thrombus formation and complete occlusion in the long-term.

Intraprocedural rupture is a feared complication in the endovascular treatment of tiny aneurysms.<sup>4,7,12</sup> Nguyen et al<sup>4</sup> found a relative risk of intraprocedural rupture of 5.2 (95% CI, 2.2–12.8)

when comparing IAs of  $\leq 3$  mm versus  $> 3$  mm. However, there have been improvements in the procedural rupture rates with time. In a prior study, we reported an intraprocedural rupture rate of 10.7% of the ruptured IAs during the coiling procedure compared with 9% in the current study.<sup>7</sup> The first large series addressing the endovascular treatment of tiny IAs reported an 11% rate of procedure-related rupture, 5 times higher compared with larger IAs.<sup>4</sup> However, recent reports have demonstrated considerably lower risk, with rates of approximately 3%–4%. Improvements in technologies with smaller and softer coils, in addition to increased operator experience, have likely contributed to this finding.<sup>5</sup> New strategies and decisions by operators to avoid procedural rupture, such as partial initial occlusion of the sac as the treatment goal<sup>11</sup> and a lower threshold to convert to microsurgical clipping,<sup>13,14</sup> may be contributing to decreasing complication rates as well.

High rates of procedural rupture are expected in the treatment of tiny IAs. The smaller size of the aneurysm sac limits the movement of the microcatheter; thus, any unexpected movement during catheter positioning or coil deployment can result in rupture of the aneurysm sac.<sup>10,15</sup> Cases of intraprocedural perforation are generally managed through reversal of anticoagulation followed by coiling of the aneurysm. The placement of a balloon at the side of the IA neck to stop hemorrhage has been advocated; however, the use of additional adjunctive devices during treatment of very small intracranial aneurysms has been associated with increased complication rates in some studies.<sup>4,10,16</sup>

Although very helpful in packing coils and, in some cases, diverting flow from the aneurysmal sac,<sup>17</sup> stent placement has been associated with higher periprocedural complication rates in the endovascular treatment of tiny IAs, as demonstrated in our study.<sup>4,18</sup> Lower rates of immediate angiographic occlusion were likely due to the less attenuated tamponade required for satisfactory results in stent-coiling procedures. Most interesting, recanalization rates were higher for aneurysms treated with stent-assisted coiling. The higher recanalization rate in the stent-assisted group might be related to antiplatelet therapy required with the use of intraluminal stents and the wider neck size of aneurysms requiring stent-assisted treatment.

In the management of very small unruptured intracranial aneurysms, it is very important to consider the natural history of these aneurysms. Sonobe et al,<sup>19</sup> reported an annual risk of rupture of 0.34% and 0.95% for single and multiple unruptured small aneurysms, respectively. Moreover, on the basis of the Population, Hypertension, Age, Size of Aneurysm, Earlier Subarachnoid Hemorrhage from Another Aneurysm, and Site of (PHASES) Aneurysm score,<sup>20</sup> patients with aneurysms of  $< 7$  mm in diameter were subject to 0%–7% risk of rupture within 5 years according to the patient's risk factors. Therefore, the very low probability of rupture in these aneurysms must be considered against the risk of procedural complications and the morbidity/mortality rates related to treatment. Given the low risk of rupture, very small unruptured aneurysms should not be treated except in selected cases.<sup>21</sup>

### Limitations

Our study has limitations. Fifteen of 22 included studies were retrospective; this feature might influence the outcomes pre-

sented and increase the publication bias. A wide methodologic variability was found among studies, especially in assessing angiographic and clinical outcomes. Thus, for certain analyses, a limited number of studies were included. Moreover, lack of details about patients also hindered our analysis. The specific locations of IAs were not assessed in this meta-analysis due to lack of available data. Finally, the long-term angiographic and clinical outcomes were evaluated at different times in the studies analyzed. Publication bias is another limitation of this study. Nevertheless, our meta-analysis is currently the largest study assessing the endovascular treatment of very small intracranial aneurysms with  $> 1000$  included patients.

### CONCLUSIONS

On the basis of our results, we conclude that the coiling of very small intracranial aneurysms can be performed safely and effectively with favorable long-term angiographic and neurologic outcomes. However, complications rates were not negligible at 6.5% for ruptured and 5% percent for unruptured aneurysms. These findings highlight the importance of individualized decision-making based on aneurysm natural history and treatment risks.

Disclosures: Giuseppe Lanzino—Consultancy: Edge Therapeutics, Covidien/Medtronic\*; Payment for Development of Educational Presentations: Covidien/ev3\*; Travel/Accommodations/Meeting Expenses Unrelated to Activities Listed: Boston Biomedical Associates. Waleed Brinjikji—UNRELATED: grant funding from Brain Aneurysm Foundation, Society of Interventional Radiology, and Society of Neurointerventional Surgery.\* \*Money paid to the institution.

### REFERENCES

1. Molyneux AJ, Birks J, Clarke A, et al. **The durability of endovascular coiling versus neurosurgical clipping of ruptured cerebral aneurysms: 18 year follow-up of the UK cohort of the International Subarachnoid Aneurysm Trial (ISAT).** *Lancet* 2015;385:691–97 CrossRef Medline
2. Spetzler RF, McDougall CG, Zabramski JM, et al. **The Barrow Ruptured Aneurysm Trial: 6-year results.** *J Neurosurg* 2015;123:609–17 CrossRef Medline
3. Iskandar A, Nepper-Rasmussen J. **Endovascular treatment of very small intracranial aneurysms.** *Interv Neuroradiol* 2011;17:299–305 Medline
4. Nguyen TN, Raymond J, Guilbert F, et al. **Association of endovascular therapy of very small ruptured aneurysms with higher rates of procedure-related rupture.** *J Neurosurg* 2008;108:1088–92 CrossRef Medline
5. Lim YC, Kim BM, Shin YS, et al. **Structural limitations of currently available microcatheters and coils for endovascular coiling of very small aneurysms.** *Neuroradiology* 2008;50:423–27 CrossRef Medline
6. Singh V, Gress DR, Higashida RT, et al. **The learning curve for coil embolization of unruptured intracranial aneurysms.** *AJNR Am J Neuroradiol* 2002;23:768–71 Medline
7. Brinjikji W, Lanzino G, Cloft HJ, et al. **Endovascular treatment of very small (3 mm or smaller) intracranial aneurysms: report of a consecutive series and a meta-analysis.** *Stroke* 2010;41:116–21 CrossRef Medline
8. DerSimonian R, Laird N. **Meta-analysis in clinical trials revisited.** *Contemp Clin Trials* 2015;45(pt A):139–45 CrossRef Medline
9. Higgins JP, Thompson SG, Deeks JJ, et al. **Measuring inconsistency in meta-analyses.** *BMJ* 2003;327:557–60 CrossRef Medline
10. van Rooij WJ, Keeren GJ, Peluso JP, et al. **Clinical and angiographic results of coiling of 196 very small ( $< \text{or} = 3$  mm) intracranial aneurysms.** *AJNR Am J Neuroradiol* 2009;30:835–39 CrossRef Medline
11. Lu J, Liu JC, Wang LJ, et al. **Tiny intracranial aneurysms: endovas-**

- cular treatment by coil embolisation or sole stent deployment. *Eur J Radiol* 2012;81:1276–81 CrossRef Medline
12. Sluzewski M, Bosch JA, van Rooij WJ, et al. **Rupture of intracranial aneurysms during treatment with Guglielmi detachable coils: incidence, outcome, and risk factors.** *J Neurosurg* 2001;94:238–40 CrossRef Medline
  13. Bruneau M, Amin-Hanjani S, Koroknay-Pal P, et al. **Surgical clipping of very small unruptured intracranial aneurysms: a multicenter international study.** *Neurosurgery* 2015 Aug 26. [Epub ahead of print] Medline
  14. Starke RM, Chalouhi N, Ali MS, et al. **Endovascular treatment of very small ruptured intracranial aneurysms: complications, occlusion rates and prediction of outcome.** *J Neurointerv* 2013; 5(suppl 3):iii66–71 CrossRef Medline
  15. Ioannidis I, Lalloo S, Corkill R, et al. **Endovascular treatment of very small intracranial aneurysms.** *J Neurosurg* 2010;112:551–56 CrossRef Medline
  16. Lanzino G, Kallmes DF. **Endovascular treatment of very small ruptured intracranial aneurysms.** *J Neurosurg* 2008;108:1087 CrossRef Medline
  17. Yu M, Liu F, Jiang S, et al. **Stent-assisted coiling for the treatment of ruptured micro-intracranial wide-necked aneurysms.** *Interv Neuro-radiol* 2015;21:40–43 CrossRef Medline
  18. Dalfino J, Nair AK, Drazin D, et al. **Strategies and outcomes for coiling very small aneurysms.** *World Neurosurg* 2014;81:765–72 CrossRef Medline
  19. Sonobe M, Yamazaki T, Yonekura M, et al. **Small unruptured intracranial aneurysm verification study: SUAVE study, Japan.** *Stroke* 2010;41:1969–77 CrossRef Medline
  20. Greving JP, Wermer MJ, Brown RD Jr, et al. **Development of the PHASES score for prediction of risk of rupture of intracranial aneurysms: a pooled analysis of six prospective cohort studies.** *Lancet Neurol* 2014;13:59–66 CrossRef Medline
  21. Wiebers DO, Whisnant JP, Huston J 3rd, et al; International Study of Unruptured Intracranial Aneurysms Investigators. **Unruptured intracranial aneurysms: natural history, clinical outcome, and risks of surgical and endovascular treatment.** *Lancet* 2003;362:103–10 CrossRef Medline
  22. Suzuki S, Kurata A, Ohmomo T, et al. **Endovascular surgery for very small ruptured intracranial aneurysms: technical note.** *J Neurosurg* 2006;105:777–80 CrossRef Medline
  23. Chen Z, Feng H, Tang W, et al. **Endovascular treatment of very small intracranial aneurysms.** *Surg Neurol* 2008;70:30–35; discussion 35 CrossRef Medline
  24. Yang MS, Wong HF, Yang TH, et al. **Alternative option in the treatment of very small ruptured intracranial aneurysms.** *Surg Neurol* 2009;72(suppl 2):S41–46 CrossRef Medline
  25. Pierot L, Barbe C, Spelle L, et al. **Endovascular treatment of very small unruptured aneurysms: rate of procedural complications, clinical outcome, and anatomical results.** *Stroke* 2010;41:2855–59 CrossRef Medline
  26. Chae KS, Jeon P, Kim KH, et al. **Endovascular coil embolization of very small intracranial aneurysms.** *Korean J Radiol* 2010;11:536–41 CrossRef Medline
  27. Fang C, Li MH, Zhu YQ, et al. **The effectiveness and feasibility of endovascular coil embolization for very small cerebral aneurysms: mid- and long-term follow-up.** *Ann Vasc Surg* 2010;24:400–07 CrossRef Medline
  28. Zang P, Liang C, Shi Q. **Endovascular embolization of very small cerebral aneurysms.** *Neurol India* 2010;58:576–80 CrossRef Medline
  29. Hwang JH, Roh HG, Chun YI, et al. **Endovascular coil embolization of very small intracranial aneurysms.** *Neuroradiology* 2011;53: 349–57 CrossRef Medline
  30. Hong B, Yang PF, Zhao R, et al. **Endovascular treatment of ruptured tiny intracranial aneurysms.** *J Clin Neurosci* 2011;18:655–60 CrossRef Medline
  31. Mohammadian R, Asgari M, Sattarnezhad N, et al. **Endovascular treatment of very small and very large ruptured aneurysms of the anterior cerebral circulation: a single-center experience.** *Cerebro-vasc Dis* 2013;35:235–40 CrossRef Medline
  32. Chung KH, Herwadkar A, Laitt R, et al. **Rate and clinical impact of intra-procedural complications during coil embolisation of ruptured small (3 mm or less) cerebral aneurysms.** *Clin Neurol Neuro-surg* 2013;115:1356–61 CrossRef Medline
  33. Li CH, Su XH, Zhang B, et al. **The stent-assisted coil-jailing technique facilitates efficient embolization of tiny cerebral aneurysms.** *Korean J Radiol* 2014;15:850–57 CrossRef Medline
  34. Jindal G, Miller T, Beaty N, et al. **Ultra-small diameter coils for treatment of intracranial aneurysms.** *Interv Neuroradiol* 2015;21:50–54 CrossRef Medline

# Endovascular Treatment of Intracranial Aneurysms with the WEB Device: A Systematic Review of Clinical Outcomes

 X. Armoiry,  F. Turjman,  D.J. Hartmann,  R. Sivan-Hoffmann,  R. Riva,  P.E. Labeyrie,  G. Aulagner, and  B. Gory



## ABSTRACT

**BACKGROUND AND PURPOSE:** Despite the improvement in technology, endovascular treatment of bifurcation intracranial wide-neck aneurysms remains challenging, mainly due to the difficulty of maintaining coils within the aneurysm sac without compromising the patency of bifurcation arteries. The Woven EndoBridge (WEB) device is a recent intrasaccular braided device specifically dedicated to treating such aneurysms with a wide neck by disrupting the flow in the aneurysmal neck and promoting progressive aneurysmal thrombosis.

**MATERIALS AND METHODS:** Using several health data bases, we conducted a systematic review of all published studies of WEB endovascular treatment in intracranial aneurysms from 2010 onward to evaluate its efficacy and safety profile.

**RESULTS:** The literature search identified 6 relevant studies (7 articles) including wide-neck bifurcation aneurysms in  $\geq 80\%$  of cases. Clinical data supporting the efficacy and safety of the WEB are limited to noncomparative cohort studies with large heterogeneity from a methodologic standpoint. The WEB deployment was feasible with a success rate of 93%–100%. Permanent morbidity (mRS of  $>1$  at last follow-up) and mortality were measured at 2.2%–6.7% and 0%–17%, respectively. The adequate occlusion rate (total occlusion or neck remnant) varied between 65% and 85.4% at midterm follow-up (range, 3.3–27.4 months).

**CONCLUSIONS:** Endovascular treatment of bifurcation wide-neck aneurysms with the WEB device is feasible and allows an acceptably adequate aneurysm occlusion rate; however, the rate of neck remnants is not negligible. The WEB device needs further clinical and anatomic evaluation with long-term prospective studies, especially of the risk of WEB compression. Prospective controlled studies should be encouraged.

**ABBREVIATIONS:** CE = Conformité Européenne; PRISMA = Preferred Reporting Items for Systematic Reviews and Meta-Analyses; WEB = Woven EndoBridge; WEB-DL = Woven EndoBridge Dual-Layer; WEB-SL = Woven EndoBridge Single-Layer; WEB-SLS = Woven EndoBridge Single-Layer Sphere

With the emergence of detachable coils and results of the International Subarachnoid Aneurysm Trial and Barrow Ruptured Aneurysm Trial,<sup>1,2</sup> endovascular coiling has become the first-line option for ruptured intracranial aneurysms. It is also a widely accepted option for unruptured aneurysms

that are anatomically suitable for endovascular approaches.<sup>3</sup> However, coiling of large and wide-neck intracranial aneurysms is associated with low initial complete obliteration, a high incidence of recanalization (up to 20% at 12 months), and a 10% rate of retreatment.<sup>4</sup> Promising technologies like flow-diverter stents have the potential to overcome some of the limitations of standard coiling for sidewall aneurysms,<sup>5–7</sup> but the management of large wide-neck bifurcation aneurysms remains challenging. Balloon and stent-assisted techniques have widened the indications for endovascular treatment of aneurysms with a wide neck and/or unfavorable anatomy that were otherwise unsuitable for coiling.<sup>8–10</sup> However, endovascular treatment of such complex intracranial aneurysms requires the use of complex endovascular techniques with double-stent placement in Y and X configurations. Bartolini et al<sup>11</sup> suggested that Y and X stent-assisted coiling was associated with a high rate of complications, 10% procedure-related permanent morbidity, and 1% mortality rate.

In this context, a new endovascular device, the intrasaccular

Received September 8, 2015; accepted after revision October 8.

From the Délégation à la Recherche Clinique et à l'Innovation (X.A.), Hospices Civils de Lyon, Cellule Innovation, Lyon, France; CNRS 5510/MATEIS (X.A., D.J.H., P.E.L., G.A.), Lyon, France; Service de Neuroradiologie Interventionnelle (F.T., R.S.-H., R.R., B.G.), DHU IRIS, Hôpital Neurologique Pierre Wertheimer, Hospices Civils de Lyon, Lyon, France; Université Lyon 1 (F.T., D.J.H., G.A., B.G.), Lyon, France; Centre de Neurosciences Cognitives (F.T., B.G.), CNRS, UMR 5229, Lyon, France; Galilee Medical Center (R.S.-H.), Nahariya, Israel; Serine Proteases and Pathophysiology of the Neurovascular Unit (P.E.L.), INSERM UMR-S U919, Caen, France; and Service Pharmaceutique (G.A.), Hospices Civils de Lyon, Groupe-ment Hospitalier Est, Lyon, France.

Please address correspondence to Benjamin Gory, MD, MSc, DHU IRIS, Department of Interventional Neuroradiology, Hospices Civils de Lyon, Hôpital Neurologique Pierre Wertheimer, 59 Boulevard Pinel, 69677 Bron, France; e-mail: benjamin.gory@chu-lyon.fr

 Indicates article with supplemental on-line table.

<http://dx.doi.org/10.3174/ajnr.A4611>

flow disruptor Woven EndoBridge (WEB; Sequent Medical, Aliso Viejo, California), specifically designed to treat wide-neck bifurcation intracranial aneurysms, has emerged in the past 5 years.<sup>12-14</sup> There is an emerging body of literature on the use of the WEB device, but to our knowledge, no study has specifically reviewed the evidence on its use. We, therefore, performed a literature review of this technique in the management of wide-neck bifurcation intracranial aneurysms. Our specific aims were to evaluate its feasibility, safety, and effectiveness to finally discuss its place in the endovascular treatment of bifurcation intracranial aneurysms.

## **MATERIALS AND METHODS**

### **Description of the WEB Device**

The Woven EndoBridge system, known as the WEB aneurysm embolization system, is a self-expanding, oblate, braided nitinol mesh deployed in the aneurysm sac. The WEB device was originally released under a Dual-Layer configuration (WEB-DL) in which the first nitinol cage contains a proximally placed second nitinol braid. The inner and outer braids are made of 108 or 144 extremely fine nitinol wires (diameters from 19 to 38  $\mu\text{m}$ ). Therefore, the WEB-DL device has a total of 216 or 288 wires responsible for the intrasaccular blood flow disruption. The WEB-DL is available in several diameters (from 5 to 11 mm) and lengths (from 3 to 9 mm). Recently, the WEB device has evolved into a Single-Layer version (WEB-SL and Single-Layer Sphere [WEB-SLS]) not containing any inner braid. The WEB-SL has a higher number of nitinol wires (from 144 for the 4-mm diameter to 216 for the 11-mm diameter) providing a blood flow disruption while maintaining radial force. The WEB-SLS version has a more spheric shape compared with the WEB-SL. The WEB-SL device is available in several diameters (from 4 to 9 mm) and lengths (from 3 to 7 mm), whereas the WEB-SLS device is available in several diameters (from 4 to 11 mm) but only 1 length (4 mm). The WEB device is deployed in the aneurysmal sac through a  $\geq 0.027$ -inch internal diameter microcatheter and can be fully retrieved until final detachment, and it is finally implanted by using an instantaneous, electrothermal detachment system contained in a hand-held controller.

The WEB system obtained the Conformité Européenne (CE) certificates for the Dual-Layer and the Single-Layer (SL/SLS) in March 2010 and March 2013, respectively. According to the 93/42/EC Directive, the WEB implant is a class III device. As of October 2015, the WEB device is not approved by the US Food and Drug Administration.

### **Search Strategy and Search Terms**

The medical literature searches on the WEB device were undertaken up to September 2015 by using the MEDLINE, EMBASE, Cochrane Library, ClinicalTrials.gov, Database of Abstracts of Reviews of Effectiveness, and Health Technology Assessment data bases. The following key words were used in combination (by using “AND” and “OR”): “WEB,” “Woven EndoBridge,” “intracranial aneurysm (aneurysms),” “brain aneurysm (aneurysms).”

## **Inclusion and Exclusion Criteria**

**Type of Studies.** All types of study designs published in all languages from January 2010 to September 2015 were included except letters, commentaries, preclinical studies, case reports, and case series with fewer than 10 patients.

**Participants–Condition/Disease.** All patients with no limitation of age with  $\geq 1$  ruptured or unruptured bifurcation aneurysms were included.

### **Intervention**

The intervention of interest was endovascular treatment with the WEB device (WEB-DL, WEB-SL, or WEB-SLS).

### **Outcomes**

Feasibility was evaluated by the rate of technical success during the procedure. Effectiveness was evaluated by the percentage of patients with an adequate angiographic occlusion (total occlusion or neck remnant according to the 3-grade Montreal scale<sup>15</sup>) at the different follow-up times. Safety was assessed by the mortality rate, the rate of patients with a modified Rankin Scale score of  $> 1$  (permanent morbidity), and the type and the percentage of complications at the different follow-up times.

### **Study Selection Strategy and Data-Extraction Strategy**

Two authors (X.A. and B.G.) screened all identified bibliographic records for title/abstract and then for full text. The study flow and reasons for exclusion of full text articles were documented in a flow diagram (Fig 1), according to the Preferred Reporting Items for Systematic Reviews and Meta-Analyses (PRISMA) statement.<sup>16</sup> Among full text articles assessed for eligibility, an analysis of overlapping study populations was performed to exclude studies in which the same patient had been described several times. Two authors (X.A. and B.G.) were responsible for detecting articles with duplicate published cases on the basis of the following criteria: name of authors, location of participating centers, and time of patients' selection. In case of doubt, publications were retrieved from the list.

### **Individual Study Quality Assessment**

For the included studies that were uncontrolled, individual study quality was assessed by using a checklist published by the National Institutes of Health: “Quality Assessment Tool for Before-After (Pre-Post) Studies With No Control Group.”<sup>17</sup> This 12-item checklist enables an assessment of uncontrolled studies and provides an overall quality rating. Quality assessment was performed independently by 2 authors (X.A. and B.G.).

### **Data Synthesis**

Study, intervention, population, and outcome characteristics were summarized in the text and summary tables. Due to the presence of methodologic heterogeneity, data pooling was not appropriate.

## **RESULTS**

### **Search Results**

The flow chart presenting the process of identifying relevant articles is shown in Fig 1. After we removed duplicates, our search

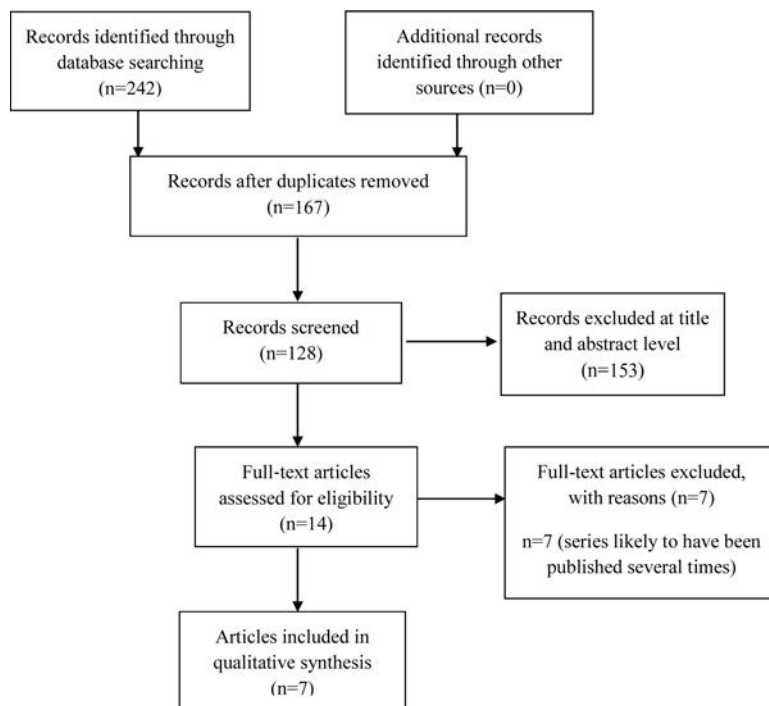


**FIG 1.** PRISMA study flow diagram.

identified 167 potentially relevant articles. One hundred fifty-three were excluded at the title and abstract level. Of the 14 articles identified, 7 were excluded because cohorts of patients were very likely to have been described several times or included in other cohorts. We finally presented the results of 6 studies (7 articles) that were all conducted in European centers (On-line Table). One article was the continuation of an already published article for the same study. We found no Health Technology Assessment report related to the WEB device.

### **Patient and Aneurysm Characteristics and Feasibility of the WEB Device**

The number of patients was between 45 and 90, depending on the study. Aneurysm locations were mainly the middle cerebral artery, anterior communicating artery, or basilar artery. The neck size was  $\geq 4$  mm in most cases (80%–100%), whereas the aneurysm size was mainly  $< 10$  mm. Five of the studies had selected patients with either ruptured or unruptured aneurysms, whereas 1 specifically reported outcomes of the WEB device on ruptured aneurysms. The implanted device was the WEB-DL in 2 studies and the WEB-SL in 1 study, whereas the other studies reported the use of the WEB-DL and the WEB-SL. The rate of technical success leading to a WEB implantation varied between 93% and 100%, depending on the study. Most interesting, the rate of additional treatment after the WEB deployment, whether anticipated or unplanned, was consistent between studies (8%–15%). It consisted of standard coiling, balloon-assisted coiling, or stent-assisted coiling. In most studies, authors reported the use of antiplatelet therapy (mainly single-antiplatelet therapy with aspirin or clopidogrel) after the procedure.

### **Safety Data**

At last follow-up, the percentage of patients with an mRS score of  $> 1$  varied between 2.2% and 6.7%. However, the average follow-up duration was limited (range, discharge to 6 months). The range of mortality rates at last follow-up was 0%–17%. A mortality rate of 17% corresponded only to patients with ruptured intracranial aneurysms.<sup>18</sup>

The range of complication rates was 11%–14% in 3 studies and 22%–34% in 3 studies. Most complications consisted of thromboembolic events (between 31% and 81% of complications), with an incidence of 7%–18%. Apart from thromboembolic events, device problem-related events have been described, such as detachment, WEB protrusion, or a WEB stuck in the microcatheter.<sup>19</sup> Intraoperative ruptures have been described rarely ( $< 2\%$ ).<sup>19</sup>

### **Efficacy Data**

Most studies reported an angiographic outcome of limited duration (between 3.2 and 6 months). In those studies, the rate of adequate occlusion (total occlusion or neck remnant according to the 3-grade Montreal scale<sup>15</sup>) varied between 65% and 85.4%. In 1 study,<sup>20</sup> the rate of adequate occlusion was reported at 84.2% after a mean duration of follow-up of 27.4 months.

### **Quality Assessment**

Four studies were retrospective, whereas 2 were prospective. All were noncomparative. Studies had large heterogeneity in terms of methods for the assessment of outcomes (the presence of an adjudication committee; presence of a centralized core laboratory; differences in the timeframes for end points; and modalities for anatomic evaluations). Using the prespecified tool, the quality rating of studies was considered good in 2 studies; the others were rated fair or poor. The main limitations of studies were as follows: no prespecification of selection criteria for the study population; no justification of sample size; no clear definition of outcome measures; and no consistent assessment of outcome measures across all study participants. Consequently, the risk of bias was high in all except 2 studies.

### **DISCUSSION**

Even though promising, the current knowledge on the WEB device is still limited. The WEB device emphasizes the great limitations of the current CE mark process in European countries. The current regulation on class III medical devices (2007/47/CE directive modifying the 93/42/CE) indicates that clinical evaluations are mandatory to comply with essential requirements needed for the CE marking. Most interesting, the first CE mark of the WEB device was obtained in March 2010, whereas the first report in humans was published in August 2011.<sup>12</sup> Five years after the CE

mark, a high number of articles on the WEB device have now been published. However, a high number were unfortunately excluded from our analysis because the same patients had likely been included in >1 published study or because the number of cases in that particular study was considered too small (<10 patients).

Despite the very specific population (wide-neck bifurcation aneurysms in  $\geq 80\%$  of cases), the 6 analyzed studies (7 articles) are convergent in showing that the WEB endovascular procedure is feasible (successful placement between 93% and 100%), though several authors stressed that adequate patient selection and precise sizing of the device are key issues to achieving technical success.<sup>21,22</sup> Because the WEB placement is challenging, most of the experiences reported here were still performed within the learning curve. Although the number of observations was limited, Behme et al<sup>23</sup> reported that patients obtained a more favorable angiographic result after a WEB procedure in their later experience in comparison with their earlier experience (75% of favorable angiographic outcome in 2014 versus 40% in 2012).

One study reported a complication rate of 34% in the most severe cases (ruptured aneurysms).<sup>18</sup> An exception in this study, the range of procedural complication rates was 12%–25%, and complications were mostly thromboembolic events with favorable outcome after treatment. The WEB treatment can therefore be considered as having an acceptable safety profile. The clinical outcome of patients treated with the WEB device is good (WEB treatment morbidity and mortality was between 2.2% and 6.7%, and 0.0% and 17.0%, respectively), but long-term data are clearly needed.

The currently available data on angiographic outcomes have shown promising results with immediate adequate occlusion rates (complete or neck remnant according to the 3-grade Montreal scale) of 65%–85% at 3.2–6 months. One study reported a complete occlusion rate of 84.2% at 27.4 months.<sup>20</sup> However, the follow-up concerned a limited number of cases (26 patients). Overall, long-term anatomic data on large prospective cohorts are needed to more accurately evaluate the efficacy of the WEB device. In fact, some authors have recently reported the risk of WEB compression with time. Cognard and Januel<sup>24</sup> reported similar findings in a series of 15 consecutive patients. Compression of the WEB cage (12 WEB-DLs and 3 WEB-SLs) was observed at first follow-up (3–6 months) in 8 of 14 (57.2%) and in an additional 3 of 7 cases (42.8%) at the second control (18  $\pm$  3 months). The last angiography showed complete occlusion in 1 of 14 (7.2%), neck remnant in 8 of 14 (57.2%), and residual aneurysm in 5 of 14 (35.7%) cases.

Sivan-Hoffmann et al<sup>25</sup> also reported similar findings recently. Of 8 aneurysms included, worsening of the aneurysm occlusion was observed in 2 aneurysms (25%) by compression of the WEB device. Although the recent article by Pierot et al<sup>26</sup> showed that the aneurysm occlusion was stable between midterm and long-term follow-up, the risk of WEB compression and aneurysm recanalization must be carefully assessed. In addition, the WEB-DL and the WEB-SL/SLS seem to have the same safety profile at 1 month, but the impact of the modification of the WEB shape on long-term angiographic outcome should be further investigated.<sup>19</sup>

From a methodologic standpoint, most of the currently pub-

lished articles have major limitations leading to a high risk of bias. First, the adjudication of end points (both adverse events and clinical outcomes) was performed in each participating center and not with an independent adjudication committee. Similarly, the angiographic parameters were mainly assessed by operators and not within an independent centralized core laboratory. In a recent meta-analysis, Rezek et al<sup>27</sup> demonstrated that core laboratories tend to report higher rates of unfavorable outcomes compared with self-reporting centers. In our opinion, the results of angiographic outcomes reported with the WEB device should be analyzed with caution. Among the European studies, only 2 were conducted according to good clinical practices (the French Observatory<sup>19</sup> and the WEB Clinical Assessment of Intracranial Aneurysm Therapy [WEBCAST] study<sup>26</sup>). No comparative data (either historical or prospective) are available to accurately determine the clinical and anatomic benefit of the WEB device in comparison with existing strategies. To our knowledge, no randomized clinical trial is either ongoing or planned to compare the WEB device with standard treatment, including endovascular coiling or surgical clipping. A prospective, multicenter, single-arm, cohort study (The WEB Intracranial Therapy Study [WEB-IT], ClinicalTrials.gov Identifier: NCT02191618) is being conducted in the United States to finally obtain FDA clearance.<sup>28</sup>

## CONCLUSIONS

Although the WEB device is a highly innovative technique for the endovascular treatment of bifurcation intracranial aneurysms with wide necks, to date, clinical data supporting the efficacy and safety of this new technology are limited to noncomparative cohort studies with extensive methodologic heterogeneity. According to the results of our literature review, WEB treatment of these intracranial aneurysms seems safe. However, no study comparing the safety and efficacy profiles of the WEB flow disruption technique with the balloon-assisted or stent-assisted coiling technique is available. The WEB device allows the treatment of wide-neck aneurysms with an acceptable adequate occlusion rate, but a not negligible rate of neck remnant. In addition, the risk of WEB compression and aneurysm recanalization must also be carefully assessed. Although it is promising for challenging wide-neck aneurysms, some issues are still unanswered regarding the benefit of the WEB long-term and its current positioning in comparison with existing strategies. The use of the WEB device may be considered in clinical situations with no acceptable therapeutic approach after discussion within a multidisciplinary team. Prospective controlled studies should be encouraged.

Disclosures: Francis Turjam—UNRELATED: Consultancy: Codman Neurovascular,\* Medtronic\*; Grants/Grants Pending: Medtronic\*; Payment for Development of Educational Presentations: Codman,\* Balt.\* \*Money paid to the institution.

## REFERENCES

1. Molyneux AJ, Birks J, Clarke A, et al. **The durability of endovascular coiling versus neurosurgical clipping of ruptured cerebral aneurysms: 18 year follow-up of the UK cohort of the International Subarachnoid Aneurysm Trial (ISAT).** *Lancet* 2015;385:691–97 CrossRef Medline
2. Zaidi HA, Montoure A, Elhadi A, et al. **Long-term functional outcomes and predictors of shunt-dependent hydrocephalus after treatment of ruptured intracranial aneurysms in the BRAT trial:**

- revisiting the clip vs coil debate. *Neurosurgery* 2015;76:608–13; discussion 613–14; quiz 614 CrossRef Medline
3. Gory B, Turjman F. **Endovascular treatment of 404 intracranial aneurysms treated with Nexus detachable coils: short-term and mid-term results from a prospective, consecutive, European multicenter study.** *Acta Neurochir (Wien)* 2014;156:831–37 CrossRef Medline
  4. Ferns SP, Sprengers ME, van Rooij WJ, et al. **Coiling of intracranial aneurysms: a systematic review on initial occlusion and reopening and retreatment rates.** *Stroke* 2009;40:e523–529 CrossRef Medline
  5. Gory B, Bonafé A, Pierot L, et al. **Safety and efficacy of flow-diverter stents in endovascular treatment of intracranial aneurysm: interest of the prospective DIVERSION observational study.** *J Neuroradiol* 2014;41:93–96 CrossRef Medline
  6. Armoiry X, Paysant M, Hartmann D, et al. **Interest of flow diversion prostheses in the management of unruptured intracranial aneurysms.** *Int J Vasc Med* 2012;2012:654627 CrossRef Medline
  7. Turjman F, Levrier O, Combaz X, et al. **EVIDENCE trial: design of a phase 2, randomized, controlled, multicenter study comparing flow diversion and traditional endovascular strategy in unruptured saccular wide-necked intracranial aneurysms.** *Neuroradiology* 2015; 57:49–54 CrossRef Medline
  8. Gory B, Kessler I, Seizem Nakiri G, et al. **Initial experience of intracranial aneurysm embolization using the balloon remodeling technique with Scepter C, a new double-lumen balloon.** *Interv Neuroradiol* 2012;18:284–87 Medline
  9. Gory B, Aguilar-Pérez M, Pomero E, et al. **pCONus device for the endovascular treatment of wide-neck middle cerebral artery aneurysms.** *AJNR Am J Neuroradiol* 2015;36:1735–40 CrossRef Medline
  10. Gory B, Rouchaud A, Saleme S, et al. **Endovascular treatment of middle cerebral artery aneurysms for 120 nonselected patients: a prospective cohort study.** *AJNR Am J Neuroradiol* 2014;35:715–20 CrossRef Medline
  11. Bartolini B, Blanc R, Pistocchi S, et al. **“Y” and “X” stent-assisted coiling of complex and wide-neck intracranial bifurcation aneurysms.** *AJNR Am J Neuroradiol* 2014;35:2153–58 CrossRef Medline
  12. Klisch J, Sychra V, Strasilla C, et al. **The Woven EndoBridge cerebral aneurysm embolization device (WEB II): initial clinical experience.** *Neuroradiology* 2011;53:599–607 CrossRef Medline
  13. Ding YH, Lewis DA, Kadirvel R, et al. **The Woven EndoBridge: a new aneurysm occlusion device.** *AJNR Am J Neuroradiol* 2011;32:607–11 CrossRef Medline
  14. Papagiannaki C, Spelle L, Januel AC, et al. **WEB intrasaccular flow disruptor—prospective, multicenter experience in 83 patients with 85 aneurysms.** *AJNR Am J Neuroradiol* 2014;35:2106–11 CrossRef Medline
  15. Raymond J, Guilbert F, Weill A, et al. **Long-term angiographic recurrences after selective endovascular treatment of aneurysms with detachable coils.** *Stroke* 2003;34:1398–403 CrossRef Medline
  16. Moher D, Liberati A, Tetzlaff J, et al. **Preferred Reporting Items for Systematic Reviews and Meta-Analyses: the PRISMA statement.** *PLoS Med* 2009;21;6:e1000097
  17. National Institutes of Health. National Heart, Lung and Blood Institute. Quality Assessment Tool for Before-After (Pre-Post) Studies With No Control Group. 2014. <http://www.nhlbi.nih.gov/health-pro/guidelines/in-develop/cardiovascular-risk-reduction/tools/before-after>. Accessed October 9, 2015
  18. Liebig T, Kabbasch C, Strasilla C, et al. **Intrasaccular flow disruption in acutely ruptured aneurysms: a multicenter retrospective review of the use of the WEB.** *AJNR Am J Neuroradiol* 2015;36:1721–27 CrossRef Medline
  19. Pierot L, Moret J, Turjman F, et al. **WEB treatment of intracranial aneurysms: feasibility, complications, and 1-month safety results with the WEB DL and WEB SL/SLS in the French Observatory.** *AJNR Am J Neuroradiol* 2015;36:922–27 CrossRef Medline
  20. Pierot L, Klisch J, Liebig T, et al. **WEB-DL endovascular treatment of wide-neck bifurcation aneurysms: long-term results in a European series.** *AJNR Am J Neuroradiol* 2015 Jul 30. [Epub ahead of print] CrossRef Medline
  21. Bozzetto Ambrosi P, Gory B, Sivan-Hoffmann R, et al. **Endovascular treatment of bifurcation intracranial aneurysms with the WEB SL/SLS: 6-month clinical and angiographic results.** *Interv Neuroradiol* 2015;21:462–69 CrossRef Medline
  22. Gherasim DN, Gory B, Sivan-Hoffmann R, et al. **Endovascular treatment of wide-neck anterior communicating artery aneurysms using WEB-DL and WEB-SL: short-term results in a multicenter study.** *AJNR Am J Neuroradiol* 2015;36:1150–54 CrossRef Medline
  23. Behme D, Berlis A, Weber W. **Woven EndoBridge intrasaccular flow disrupter for the treatment of ruptured and unruptured wide-neck cerebral aneurysms: report of 55 cases.** *AJNR Am J Neuroradiol* 2015; 36:1501–06 CrossRef Medline
  24. Cognard C, Januel AC. **Remnants and recurrences after the use of the WEB intrasaccular device in large-neck bifurcation aneurysms.** *Neurosurgery* 2015;76:522–30; discussion 530 CrossRef Medline
  25. Sivan-Hoffmann R, Gory B, Riva R, et al. **One-year angiographic follow-up after WEB-SL endovascular treatment of wide-neck bifurcation intracranial aneurysms.** *AJNR Am J Neuroradiol* 2015 Aug 20. [Epub ahead of print] CrossRef Medline
  26. Pierot L, Costalat V, Moret J, et al. **Safety and efficacy of aneurysm treatment with WEB: results of the WEBCAST study.** *J Neurosurg* 2015 Sep 18. [Epub ahead of print] CrossRef Medline
  27. Rezek I, Mousan G, Wang Z, et al. **Effect of core laboratory and multiple-reader interpretation of angiographic images on follow-up outcomes of coiled cerebral aneurysms: a systematic review and meta-analysis.** *AJNR Am J Neuroradiol* 2013;34:1380–84 CrossRef Medline
  28. ClinicalTrials.gov. The WEB-IT Clinical Study. <https://clinicaltrials.gov/ct2/show/NCT02191618?term=%22WEB%22+AND+%22aneurysm%22&rank=1> Cg. Accessed October 9, 2015
  29. Lubicz B, Klisch J, Gauvrit JY, et al. **WEB-DL endovascular treatment of wide-neck bifurcation aneurysms: short- and mid-term results in a European study.** *AJNR Am J Neuroradiol* 2014;35:432–38 CrossRef Medline
  30. Caroff J, Mihalea C, Klisch J, et al. **Single-layer WEBs: intrasaccular flow disrupters for aneurysm treatment—feasibility results from a European study.** *AJNR Am J Neuroradiol* 2015;36:1942–46 CrossRef Medline

# Endovascular Coiling versus Surgical Clipping for Poor-Grade Ruptured Intracranial Aneurysms: Postoperative Complications and Clinical Outcome in a Multicenter Poor-Grade Aneurysm Study

 B. Zhao,  X. Tan,  H. Yang,  Z. Li,  K. Zheng,  Y. Xiong, and  M. Zhong; for the AMPAS Group



## ABSTRACT

**BACKGROUND AND PURPOSE:** Endovascular coiling is an alternative to surgical clipping for ruptured intracranial aneurysms. However, no large multicenter prospective study has compared coiling and clipping in patients with poor-grade ruptured aneurysms. We aimed to determine differences in postoperative complications and clinical outcome between the 2 treatments in this group of patients.

**MATERIALS AND METHODS:** A Multicenter Poor-Grade Aneurysm Study was a prospective, multicenter, observational registry of consecutive patients who presented with poor-grade ruptured aneurysms. Three hundred sixty-six patients were enrolled from October 2010 to March 2012. “Poor-grade aneurysm” was defined as a World Federation of Neurosurgical Societies grade of IV or V at the time of aneurysm treatment. Two hundred sixty-two patients received aneurysm treatment within 21 days and were included. Clinical outcomes were assessed at discharge and at 6 and 12 months by the modified Rankin Scale.

**RESULTS:** One hundred thirty-three (50.8%) patients underwent endovascular coiling. Unadjusted analysis showed that the outcome rate (mRS 0–1 or mRS 0–2) at 6 and 12 months in patients undergoing coiling was higher than that in patients undergoing clipping. In adjusted analyses, there was no statistically significant difference in outcomes at 6 and 12 months between the 2 groups. The risk of radiologic hydrocephalus was higher in patients treated with coiling than that in those treated with clipping (adjusted OR, 3.36; 95% CI, 1.13–10.01;  $P = .030$ ).

**CONCLUSIONS:** The long-term outcome in selected patients was similar between endovascular coiling and clipping for poor-grade ruptured aneurysms. The risk of radiologic hydrocephalus was higher after endovascular treatment of poor-grade aneurysms.

**ABBREVIATIONS:** AMPAS = A Multicenter Poor-Grade Aneurysm Study; aSAH = aneurysmal subarachnoid hemorrhage; EVD = external ventricular drainage; GCS = Glasgow Coma Scale; WFNS = World Federation of Neurosurgical Societies; ISAT = International Subarachnoid Aneurysm Trial

Intracranial aneurysm rupture leading to aneurysmal subarachnoid hemorrhage (aSAH) is a devastating condition. Poor-grade ruptured aneurysms account for approximately 30% of all cases of aSAH.<sup>1,2</sup> Traditionally, patients with poor-grade aneurysms have been managed medically. In the past 2 decades, aggressive treatment has been proposed to improve outcomes in selected patients.<sup>1,3,4</sup> Despite recent advances in the treatment of

aSAH, patients with poor-grade aneurysms have high rates of long-term morbidity and mortality.<sup>1,3-6</sup>

The International Subarachnoid Aneurysm Trial (ISAT) has demonstrated that for ruptured aneurysms suitable for endovascular embolization and clipping, patients treated with coiling had better outcomes than those treated with clipping.<sup>7,8</sup> However, only a few patients (4.4%) in ISAT had poor-grade aneurysms. The results may not directly apply to poor-grade patients. Currently, case series have shown that endovascular coiling is a viable alternative to clipping for poor-grade aneurysms.<sup>5,9,10</sup> However, to date, no randomized, controlled study has been performed to evaluate the efficacy of coiling versus clipping for poor-grade ruptured aneurysms, to our knowledge. There has been no large multicenter prospective study regarding the effects of different treatments on postoperative complications and clinical outcome in these patients.

A Multicenter Poor-Grade Aneurysm Study (AMPAS) was a prospective, multicenter, observational registry of consecutive patients who presented with poor-grade ruptured aneurysm.<sup>11</sup> The primary purpose of this report was to determine differences

Received September 22, 2015; accepted after revision November 8.

From the Department of Neurosurgery (B.Z., X.T., Z.L., K.Z., Y.X., M.Z.), The First Affiliated Hospital of Wenzhou Medical University, Wenzhou, China; Department of Neurosurgery (B.Z.), Mayo Clinic, Rochester, Minnesota; and Department of Neurosurgery (H.Y.), The First Affiliated Hospital of Guizhou Medical University, Guiyang, China.

This work was supported by the Chinese Ministry of Health (grant WKJ2010-2-016), the Ministry of Science and Technology of China (grant 2011BAI08B06), and Wenzhou Bureau of Science and Technology (grant Y20090005). The funding organizations were not involved in the design and conduct of the study.

Please address correspondence to Ming Zhong, MD, Department of Neurosurgery, The First Affiliated Hospital of Wenzhou Medical University, Nanbai Xiang Town, 325000 Wenzhou, China; e-mail: zhongming158@sohu.com

 Indicates open access to non-subscribers at [www.ajnr.org](http://www.ajnr.org)

<http://dx.doi.org/10.3174/ajnr.A4649>

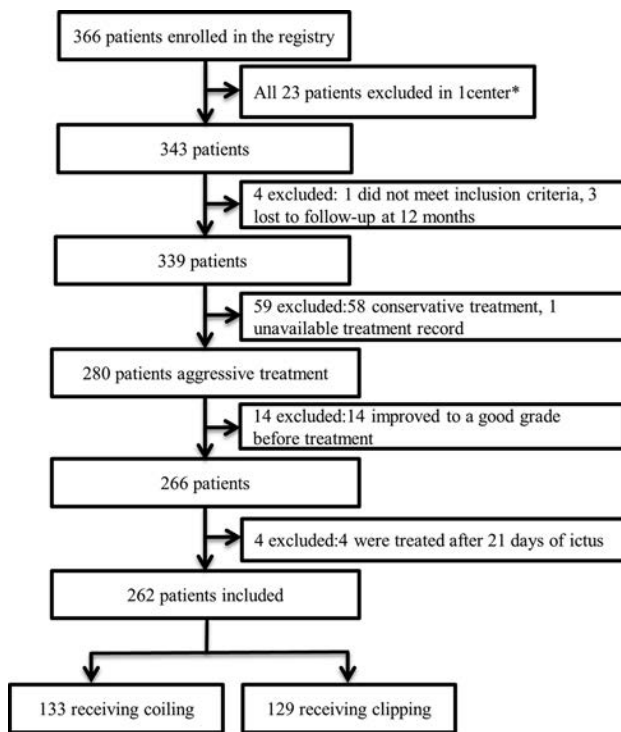


**FIG 1.** Study flow diagram. The asterisk indicates that 1 center was excluded because enrollment was not consecutive and 8 patients were lost to follow-up.

in postoperative complications and clinical outcome between patients treated with coiling and those treated with clipping in the AMPAS after adjustment for differences in baseline confounders.

## MATERIALS AND METHODS

### Study Design

The AMPAS protocol was approved by the Chinese Ethics Committee of Registering Clinical Trials (ChiECRCT-2010019) and was published elsewhere.<sup>11</sup> The study was registered with the Chinese Clinical Trial Registry (No. ChiCTR-TNRC-10001041). Between October 2010 and March 2012, 366 patients from 11 centers were enrolled in the registry. All informed consent was obtained from the patients' legal representatives. All patients were treated at tertiary referral centers (with >150 aSAH cases per year) with expertise in aneurysm coiling and clipping. "Poor-grade aneurysm" was defined as a World Federation of Neurosurgical Societies (WFNS) grade of IV or V after aSAH. Patients between 18 and 75 years of age were eligible for entry if they presented with poor-grade subarachnoid hemorrhage and had a ruptured aneurysm as confirmed by CT angiography or digital subtraction angiography. Patients were not enrolled if their family refused any treatment and they died in the emergency department. In this report, patients were excluded if they improved from an initial poor grade to a good grade (WFNS grade I or II or III) before aneurysm treatment and if they underwent aneurysm treatment after 21 days of poor-grade aSAH. Of the 366 patients, 262 patients were included in this study (Fig 1).

### Clinical Treatment Protocol

The treatment protocol included aggressive resuscitation, intensive critical care, early CT angiography or cerebral angiography if

the patient was clinically stabilized, multidisciplinary consensus, and early treatment.<sup>11-13</sup> The multidisciplinary team consisting of vascular neurosurgeons, interventional neuroradiologists, and anesthesiologists, made the treatment decision by considering patients' clinical conditions and radiologic findings. Surgical treatment was regularly performed in patients with associated large intracerebral hemorrhage (>30 mL), and endovascular coiling was performed in patients with posterior circulation aneurysms. Following aneurysm treatment, all patients were transferred to a neurointensive care unit and underwent aggressive management for vasospasm according to the individual institutional standards of practice.

### Data Collection and Definition

The data entry form included information on demographic characteristics, medical history, clinical presentation, neurologic examination, radiologic findings at the time of treatment, aneurysm characteristics, type and timing of treatment, postoperative complications during hospitalization, and outcomes at discharge and at 6 and 12 months. The Glasgow Coma Scale (GCS) and WFNS grade were the last assessment obtained before sedation or intubation if the patient was sedated or intubated. The Fisher grade and modified Fisher grade were determined by the last CT scan before treatment. The time of treatment was defined as the interval between the time of the poor-grade condition after ictus and the time of aneurysm treatment.

### Outcomes Measures

The outcome was assessed at each center by an independent neurosurgeon by using the modified Rankin Scale. They were not involved in the treatment of patients. The primary outcome measure was functional outcome at discharge and 6 and 12 months. The secondary outcomes were postoperative complications. Major complications included aneurysm rebleeding, cerebral infarction, symptomatic vasospasm, radiologic and clinical hydrocephalus, seizure, pneumonia, and renal failure. "Radiologic hydrocephalus" was defined as ventricular dilation with enlarged temporal horns ( $\geq 2$  mm wide) on postoperative CT,<sup>14,15</sup> and "clinical hydrocephalus" was defined as the presence of postoperative external ventricular drainage (EVD), ventriculoperitoneal shunt or lumbar drain placement, and the presence of radiologic hydrocephalus. "Cerebral infarction" was defined as a new hypodensity on posttreatment CT, and "symptomatic vasospasm" was defined as neurologic deterioration not explained by other causes such as seizure, hydrocephalus, edema, and a new hemorrhage.

### Statistical Analyses

Data were analyzed with SPSS, Version 22.0 (IBM, Armonk, New York). Differences in baseline characteristics were compared between the coiling and clipping groups. An independent-samples *t* test and Mantel-Haenszel,  $\chi^2$ , and Fisher exact tests were used to find variations in patient characteristics between the 2 groups. Crude and adjusted odds ratios with 95% confidence intervals were calculated with logistic regression analysis for major complications and outcomes (mRS 0-1, mRS 0-2, mRS 0-3, and death) at discharge and at 6 and 12 months for the different treatment

groups. All analyses were adjusted for smoking history, pretreatment GCS score, WFNS grade, Fisher grade, modified Fisher grade, brain herniation, ruptured aneurysm location, and postoperative EVD. In univariate analysis of the association between radiologic and clinical hydrocephalus and clinical characteristics, clinical variables with a  $P$  value  $\leq .05$  were entered into the multivariate analysis model by using the backward logistic regression method to identify independent risk factors for hydrocephalus. Receiver operating characteristic of area under the curve analysis was performed to test the prediction ability of the model. A  $P$  value  $< .05$  was considered statistically significant.

## RESULTS

### Patient Characteristics

Baseline characteristics of the 262 patients are shown in Table 1. According to multidisciplinary consensus, 133 (50.8%) patients received endovascular coiling within 21 days after poor-grade aSAH. Patients treated with coiling more often had a history of smoking ( $P = .035$ ), a higher GCS score ( $P < .001$ ), a WFNS grade of IV ( $P = .002$ ), a lower Fisher grade ( $P < .001$ ) and modified

Fisher grade ( $P = .001$ ), and a ruptured posterior circulation aneurysm ( $P < .001$ ) than those treated with clipping. Patients treated with clipping more commonly experienced brain herniation than did those treated with coiling ( $P < .001$ ). Postoperative EVD was more often performed in patients treated with coiling ( $P < .001$ ).

### Major Postoperative Complications

Major complications are shown in Table 2. There were no significant differences in aneurysm rebleeding, cerebral infarction, symptomatic vasospasm, seizure, pneumonia, and renal failure between the coiling and clipping groups. Patients treated with coiling had higher risks of radiologic and clinical hydrocephalus than those treated with clipping (unadjusted OR, 2.91;  $P = .021$ ; and unadjusted OR, 7.47;  $P = .009$ , respectively). The risk of radiologic hydrocephalus in the coiling group was higher than that in the clipping group (adjusted OR, 3.36;  $P = .030$ ), and there was a trend toward clinical hydrocephalus in the patients with coiling (adjusted OR, 5.15;  $P = .057$ ) when adjusting for the status of smoking, GCS score, WFNS grade, Fisher grade, modified Fisher grade, ruptured aneurysm location, brain herniation, and postoperative EVD (Table 2).

Univariate analysis of the association between hydrocephalus and clinical characteristics showed that higher modified Fisher grade ( $P = .019$ ), postoperative EVD ( $P = .004$ ), and endovascular treatment ( $P = .021$ ) were associated with radiologic hydrocephalus. Multivariate analysis showed that higher modified Fisher grade ( $P = .012$ ) and endovascular coiling ( $P = .035$ ) were independent risk factors for hydrocephalus (Table 3). The 2 variables predicted the risk of radiologic hydrocephalus with an area under the curve of 0.71 (95% CI, 0.60–0.81;  $P = .001$ ). The multivariate analysis for clinical hydrocephalus showed that postoperative EVD ( $P = .001$ ) was an independent predictor of clinical hydrocephalus (Table 3). The model combining coiling technique and postoperative EVD predicted clinical hydrocephalus with an area under the curve of 0.79 (95% CI, 0.66–0.91;  $P < .001$ ).

**Table 1: Baseline characteristics**

Variables	Coiling (n = 133)	Clipping (n = 129)	P Value
Age (yr)	54.5 (11.8)	54.4 (10.9)	.960
Women	62 (46.6%)	69 (53.5%)	.266
Hypertension	50 (37.6%)	63 (48.8%)	.066
Current smoking	49 (36.8%)	32 (24.8%)	.035
Diabetes mellitus	10 (7.5%)	4 (3.1%)	.168
Previous ischemic stroke	3 (2.3%)	4 (3.1%)	.719
Previous SAH	4 (3.0%)	9 (7.0%)	.163
GCS score	7.5 (2.6)	6.4 (2.4)	<.001
WFNS grade			.002
Grade IV	82 (61.7%)	55 (42.6%)	
Grade V	51 (38.3%)	74 (57.4%)	
Fisher grade	3.1 (0.9)	3.6 (0.7)	<.001
Modified Fisher grade	2.5 (1.1)	2.9 (0.9)	.001
Intraventricular hemorrhage	52 (39.1%)	51 (38.8%)	.955
Brain herniation	17 (12.8%)	51 (39.5%)	<.001
Multiple aneurysms	22 (16.5%)	24 (18.6%)	.661
Aneurysm size (mm)	5.7 (2.9)	6.0 (3.9)	.536
Ruptured aneurysm location			<.001
Anterior circulation	107 (80.5%)	128 (99.2%)	
Posterior circulation	26 (19.5%)	1 (0.8%)	
Preoperative EVD	10 (7.5%)	11 (8.5%)	.778
Postoperative EVD	37 (27.8%)	8 (6.2%)	<.001
Time to treatment			.544
0–72 hr	101 (75.9%)	102 (79.1%)	
73 hr to 21 days	32 (24.1%)	27 (21.1%)	
Hospital stay (days)	24.3 (20.7)	23.3 (21.4)	.721

<sup>a</sup> Data are mean (SD) or n/N (%).

**Table 2: Major complications associated with coiling compared with clipping**

Complications	Coiling	Clipping	Crude Analysis		Adjusted Analysis	
			OR (95% CI)	P Value	OR (95% CI)	P Value
Aneurysm rebleeding	6 (4.5%)	2 (1.6%)	3.00 (0.59–15.15)	.180	3.41 (0.55–21.27)	.189
Cerebral infarction	15 (11.3%)	23 (17.8%)	0.59 (0.29–1.18)	.140	0.62 (0.26–1.49)	.283
Symptomatic vasospasm	14 (10.5%)	13 (10.1%)	1.05 (0.47–2.33)	.910	0.53 (0.18–1.59)	.259
Radiologic hydrocephalus	19 (14.3%)	7 (5.4%)	2.91 (1.18–7.17)	.020	3.36 (1.13–10.01)	.030
Clinical hydrocephalus	14 (10.5%)	2 (1.6%)	7.47 (1.66–33.57)	.009	5.15 (0.95–27.89)	.057
Seizure	5 (3.8%)	6 (4.7%)	0.80 (0.24–2.69)	.720	0.72 (0.18–2.85)	.641
Pneumonia	31 (23.3%)	39 (30.2%)	0.70 (0.41–1.22)	.210	0.61 (0.30–1.24)	.173
Renal failure	2 (1.5%)	5 (3.9%)	0.38 (0.07–1.99)	.250	0.24 (0.02–2.45)	.230

### Outcome at Discharge

At discharge, 52 (19.8%) patients had an mRS score of 0 or 1, 78 (29.8%) had an mRS score of 0–2, 85 (32.4%) had an mRS score of 0–3, and 51 (19.5%) had died. Unadjusted analysis showed that the rate of outcome (mRS 0–2 or mRS 0–3) at discharge in the patients with coiling was higher than that in the patients with clipping. There was no significant difference in outcome at discharge after adjustment for the status of smoking, GCS score, WFNS grade, Fisher grade, modified Fisher grade, ruptured aneurysm location, brain herniation, and postoperative EVD (Table 4).

### Long-Term Outcomes

At 12 months, 95 (36.3%) patients had an mRS score of 0 or 1, 115 (43.9%) had an mRS of 0–2, 126 (48.1%) had an mRS of 0–3, and 103 (39.3%) had died. The outcomes at 12 months according to the WFNS grade and treatment technique are shown in Fig 2. Patients with a WFNS grade of V had worse outcomes than those with a WFNS grade of IV ( $P < .001$ ). Compared with outcomes at discharge, the rate of good outcome (mRS 0–2) increased to 39.3% at 6 months and 43.9% at 12 months. The outcome was improved after endovascular coiling or clipping with time (Table 4). Unadjusted analysis showed that the outcome rate (mRS 0–1 or mRS 0–2) at 6 and 12 months in patients with coiling was higher than that in the patients with clipping. However, there was no significant difference in outcomes at 6 months and 12 months between the 2 groups after adjustment for the status of smoking, GCS score, WFNS grade, Fisher grade, modified Fisher grade, ruptured aneurysm location, brain herniation, and postoperative EVD (Table 4).

### DISCUSSION

The AMPAS was a prospective, multicenter, observational registry of consecutive patients who presented with poor-grade ruptured aneurysm and was reflective of a real-world practice of multidisciplinary treatment of poor-grade aneurysms. Some patients experienced further clinical improvement with time. In this exploratory analysis, there was no significant difference in outcomes at 6 and 12 months between the 2 treatments. However, patients treated with coiling had a higher risk of radiologic hydrocephalus than those treated with clipping, and there was a trend toward clinical hydrocephalus in the patients with coiling.

Although numerous studies have reported outcomes in selected patients with poor-grade aneurysms,<sup>1,2,4,5,9,10</sup> interpretation of the results from case series or from single-center retrospective studies has been hampered by the use of different clinical grading scales (WFNS grade or Hunt and Hess scale) and outcome measurement scores and heterogeneity in the type of treatment and in the timing of outcome assessments.<sup>11</sup> In this study, standard neurologic scales, risk factor data, and functional outcome scores were prospectively collected in all sites. The registry dataset is also representative of the current practice for poor-grade aneurysms in high-volume centers. Our results are slightly better than those reported in older studies (good outcome of 38.3%–40.0%)<sup>1,2</sup> and are in agreement with current studies showing a good outcome of approximately 50%.<sup>10,16</sup> These findings might suggest that there is an increase in the proportion of patients experiencing good outcomes in recent years. In addition, our results also support the recent study showing that poor-grade patients have experienced delayed recovery with time.<sup>16</sup> Cerebral recovery may be attributable to cerebral plasticity.<sup>16</sup>

Since the ISAT study, endovascular coiling is more commonly used than clipping for ruptured aneurysms. Our results also show that most patients with a WFNS grade of IV and almost all patients with posterior circulation aneurysms received endovascular treatment. Unadjusted comparisons of outcomes showed that patients treated with coiling

**Table 3: Multivariate analysis of predictors of hydrocephalus**

Predictors	Univariate Analysis		Multivariate Analysis	
	OR (95% CI)	P Value	OR (95% CI)	P Value
Radiologic hydrocephalus				
Fisher grade	1.91 (1.00–3.66)	.050		
Modified Fisher grade	1.79 (1.10–2.92)	.019	1.88 (1.15–3.08)	.012
Endovascular coiling	2.91 (1.18–7.17)	.021	2.85 (1.08–7.57)	.035
Postoperative EVD	3.59 (1.51–8.55)	.004		
Clinical hydrocephalus				
Endovascular coiling	7.47 (1.66–33.57)	.009	4.27 (0.89–20.45)	.070
Postoperative EVD	10.05 (3.43–29.40)	<.001	6.79 (2.22–20.71)	.001

**Table 4: Clinical outcomes associated with coiling compared with clipping**

Outcomes	Coiling	Clipping	Crude Analysis		Adjusted Analysis	
			OR (95% CI)	P Value	OR (95% CI)	P Value
At discharge						
mRS (0–1)	30 (22.6%)	22 (17.1%)	1.42 (0.77–2.62)	.266	0.62 (0.28–1.38)	.241
mRS (0–2)	48 (36.1%)	30 (23.3%)	1.86 (1.09–3.20)	.024	0.74 (0.35–1.60)	.448
mRS (0–3)	51 (38.3%)	34 (26.4%)	1.74 (1.03–2.94)	.039	0.66 (0.31–1.39)	.273
Death	27 (20.3%)	24 (18.6%)	1.11 (0.60–2.06)	.729	1.88 (0.84–4.25)	.127
At 6 Mo						
mRS (0–1)	51 (38.3%)	29 (22.5%)	2.15 (1.25–3.69)	.006	1.34 (0.69–2.62)	.394
mRS (0–2)	61 (45.9%)	42 (32.6%)	1.76 (1.06–2.90)	.028	0.92 (0.48–1.79)	.808
mRS (0–3)	66 (49.6%)	54 (41.9%)	1.37 (0.84–2.23)	.208	0.64 (0.33–1.26)	.195
Death	47 (35.3%)	52 (40.3%)	0.81 (0.49–1.33)	.407	1.80 (0.91–3.54)	.091
At 12 Mo						
mRS (0–1)	58 (43.6%)	37 (28.7%)	1.92 (1.15–3.21)	.012	0.98 (0.51–1.91)	.961
mRS (0–2)	68 (51.1%)	47 (36.4%)	1.83 (1.11–2.99)	.017	0.75 (0.38–1.49)	.410
mRS (0–3)	71 (53.4%)	55 (42.6%)	1.54 (0.95–2.51)	.082	0.61 (0.31–1.22)	.162
Death	48 (36.1%)	55 (42.6%)	0.76 (0.46–1.25)	.279	1.70 (0.86–3.33)	.125

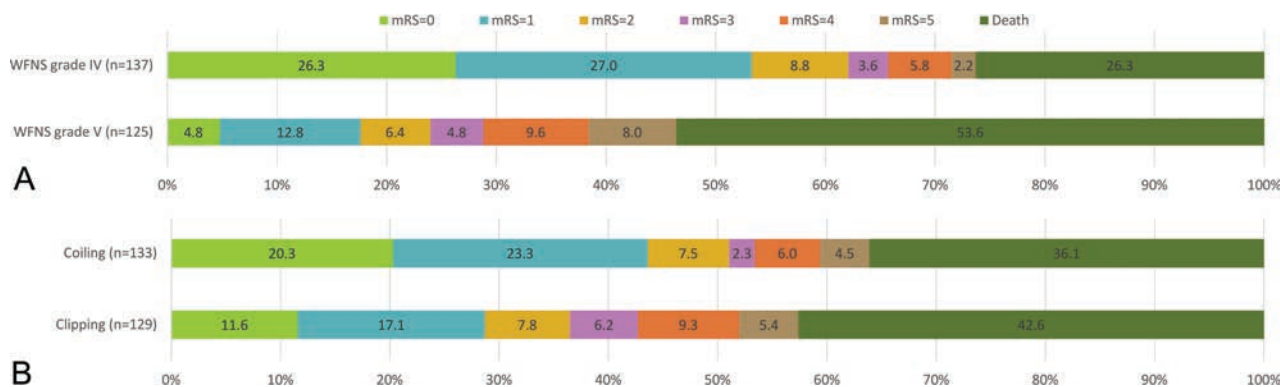


**FIG 2.** Outcome at 12 months in all patients. A, Outcome according to WFNS grade. B, Outcome by type of treatment in all patients.

had a better outcome than those treated with clipping at 6 and 12 months. Selected patients with a WFNS grade of IV were treated with coiling and might have a better outcome. After we adjusted for differences in baseline risk factors, these outcomes after coiling were similar to those after clipping. In a prospective data base of poor-grade aneurysms, Mocco et al<sup>2</sup> reported that 35 (35.7%) of 98 patients underwent coiling, and there was similar outcome between coiling and clipping. The current results at the 3- and 6-year follow-ups in the Barrow Ruptured Aneurysm Trial also showed that there was no significant difference in outcome between the 2 treatments for ruptured aneurysms.<sup>17,18</sup> These results suggest that both endovascular coiling and surgical clipping are viable treatment options for poor-grade ruptured aneurysms. Clinicians should make treatment decisions case-by-case, weighing the benefit of different treatments. Furthermore, with improvements in endovascular technology and surgical techniques, aneurysm treatment does not seem to make a big difference in the outcomes of selected patients.

Previously, no study focused on poor-grade aneurysms to determine the effects of coiling and clipping on the postoperative complications. In our study, radiologic hydrocephalus was used to make it more appropriate to assess these complications at all sites. Our results are in line with a meta-analysis showing a significantly higher risk for hydrocephalus after coiling than clipping for ruptured aneurysms.<sup>19</sup> Our study also showed a trend toward clinical hydrocephalus in the coiling group because open surgery may remove the clot and open cistern and result in less hydrocephalus.<sup>19</sup> However, Zaidi et al<sup>20</sup> reported no difference in hydrocephalus among patients treated by coiling or clipping. There is still a controversy regarding the effect of treatment technique on hydrocephalus, probably because of different diagnostic criteria of hydrocephalus and the time period observed. In addition, all patients had poor neurologic conditions, and systematic vasospasm could not be precisely detected. The long-term complications were also not determined because due to a high mortality in poor-grade patients, it might be difficult to properly compare these complications across time.

To the best of our knowledge, this is the first multicenter prospective report focused on the effects of postoperative complications and clinical outcome between the 2 treatments for poor-grade ruptured aneurysms. However, our study has several limitations. First, it was not a randomized study, and the drawback is that selected patients were included for the exploratory

analysis. All patients were treated according to the individual patient and aneurysm characteristics on the basis of multidisciplinary decision-making. Other factors such as family desires, relative treatment risk, and medical expenses may influence the decisions about treatment technique. Therefore, the decision regarding treatment of poor-grade aneurysms is complex and could not be defined in a registry study. Although we have adjusted for baseline imbalance between the 2 treatments, other unmeasured variables outside the analysis may contribute to selection bias. Therefore, no direct causal effect between treatment and complications and clinical outcome could be ascertained. Further studies focused on poor-grade aneurysms are needed to help guide treatment decisions. Second, we did not record laboratory findings and long-term imaging follow-up, and there may be other risk factors for outcome. Nevertheless, we found no difference in long-term outcomes between the 2 treatments by using a relatively large number of poor-grade patients, but the higher risk of radiologic hydrocephalus should be considered after endovascular coiling. These results may also help clinicians assess and treat the postoperative complications after both treatments.

## CONCLUSIONS

Unadjusted comparisons of outcomes showed that patients undergoing coiling had a better outcome than those undergoing clipping. Selected patients who were treated with coiling may have a better outcome. Adjusted analysis showed that the outcomes at 6 and 12 months were similar between the 2 treatments. A clinical trial focused on poor-grade ruptured aneurysms would be necessary to further assess the efficacy of different treatments. The higher risk of radiologic hydrocephalus was found in patients after endovascular coiling for poor-grade ruptured aneurysms. Meanwhile, there was a trend toward clinical hydrocephalus in patients treated with coiling.

## ACKNOWLEDGMENTS

AMPAS Study Investigators: Hongqi Zhang, MD, Xuan Wu Hospital, Capital Medical University; Chuansheng Liang, MD, The First Hospital of China Medical University; Huaizhang Shi, MD, The First Affiliated Hospital of Harbin Medical University; Jing Xu, MD, The Second Affiliated Hospital, School of Medicine, Zhejiang University; Li Pan, MD, Wuhan General Hospital of Guangzhou Command; Xin Zhang, MD, Nanjing General Hospital of Nanjing Command; Gang Zhu, MD, West South Hospital,

The Third Military Medical University; Jianping Deng, MD, Tang Du Hospital, The Fourth Military Medical University; and Zhigang Wang, MD, The Second Affiliated Hospital, School of Medicine, Shandong University.

Disclosures: Bing Zhao—RELATED: Grant: Chinese Ministry of Health,\* Comments: They were not involved in the data collection and analysis and the writing of the manuscript. Ming Zhong—RELATED: Grant: Chinese Ministry of Health,\* Wenzhou Bureau of Science and Technology,\* Comments: The funders were not involved in data collection, interpretation, and analysis. \*Money paid to the institution.

## REFERENCES

1. Le Roux PD, Elliott JP, Newell DW, et al. **Predicting outcome in poor-grade patients with subarachnoid hemorrhage: a retrospective review of 159 aggressively managed cases.** *J Neurosurg* 1996;85:39–49 CrossRef Medline
2. Mocco J, Ransom ER, Komotar RJ, et al. **Preoperative prediction of long-term outcome in poor-grade aneurysmal subarachnoid hemorrhage.** *Neurosurgery* 2006;59:529–38; discussion 529–38 CrossRef Medline
3. Huang AP, Arora S, Wintermark M, et al. **Perfusion computed tomographic imaging and surgical selection with patients after poor-grade aneurysmal subarachnoid hemorrhage.** *Neurosurgery* 2010;67:964–74; discussion 975 CrossRef Medline
4. Sandström N, Yan B, Dowling R, et al. **Comparison of microsurgery and endovascular treatment on clinical outcome following poor-grade subarachnoid hemorrhage.** *J Clin Neurosci* 2013;20:1213–18 CrossRef Medline
5. Pereira AR, Sanchez-Peña P, Biondi A, et al. **Predictors of 1-year outcome after coiling for poor-grade subarachnoid aneurysmal hemorrhage.** *Neurocrit Care* 2007;7:18–26 CrossRef Medline
6. Mitra D, Gregson B, Jayakrishnan V, et al. **Treatment of poor-grade subarachnoid hemorrhage trial.** *AJNR Am J Neuroradiol* 2015;36:116–20 CrossRef Medline
7. Molyneux AJ, Kerr RS, Yu LM, et al; International Subarachnoid Aneurysm Trial (ISAT) Collaborative Group. **International Subarachnoid Aneurysm Trial (ISAT) of neurosurgical clipping versus endovascular coiling in 2143 patients with ruptured intracranial aneurysms: a randomised comparison of effects on survival, dependency, seizures, rebleeding, subgroups, and aneurysm occlusion.** *Lancet* 2005;366:809–17 CrossRef Medline
8. Molyneux AJ, Birks J, Clarke A, et al. **The durability of endovascular coiling versus neurosurgical clipping of ruptured cerebral aneurysms: 18 year follow-up of the UK cohort of the International Subarachnoid Aneurysm Trial (ISAT).** *Lancet* 2015;385:691–97 CrossRef Medline
9. Suzuki S, Jahan R, Duckwiler GR, et al. **Contribution of endovascular therapy to the management of poor-grade aneurysmal subarachnoid hemorrhage: clinical and angiographic outcomes.** *J Neurosurg* 2006;105:664–70 CrossRef Medline
10. Taylor CJ, Robertson F, Brealey D, et al. **Outcome in poor grade subarachnoid hemorrhage patients treated with acute endovascular coiling of aneurysms and aggressive intensive care.** *Neurocrit Care* 2011;14:341–47 CrossRef Medline
11. Zhao B, Tan X, Yang H, et al. **A Multicenter Prospective Study of Poor-Grade Aneurysmal Subarachnoid Hemorrhage (AMPAS): observational registry study.** *BMC Neurol* 2014;14:1471–2377 CrossRef Medline
12. Zhao B, Tan X, Zhao Y, et al. **Variation in patient characteristics and outcomes between early and delayed surgery in poor-grade aneurysmal subarachnoid hemorrhage.** *Neurosurgery* 2015 Sep 29. [Epub ahead of print] Medline
13. Zhao B, Cao Y, Tan X, et al. **Complications and outcomes after early surgical treatment for poor-grade ruptured intracranial aneurysms: a multicenter retrospective cohort.** *Int J Surg* 2015;23:57–61 CrossRef Medline
14. Dorai Z, Hynan LS, Kopitnik TA, et al. **Factors related to hydrocephalus after aneurysmal subarachnoid hemorrhage.** *Neurosurgery* 2003;52:763–69; discussion 769–71 CrossRef Medline
15. Sheehan JP, Polin RS, Sheehan JM, et al. **Factors associated with hydrocephalus after aneurysmal subarachnoid hemorrhage.** *Neurosurgery* 1999;45:1120–27; discussion 1127–28 CrossRef Medline
16. Wilson DA, Nakaji P, Albuquerque FC, et al. **Time course of recovery following poor-grade SAH: the incidence of delayed improvement and implications for SAH outcome study design.** *J Neurosurg* 2013;119:606–12 CrossRef Medline
17. Spetzler RF, McDougall CG, Albuquerque FC, et al. **The Barrow Ruptured Aneurysm Trial: 3-year results.** *J Neurosurg* 2013;119:146–57 CrossRef Medline
18. Spetzler RF, McDougall CG, Zabramski JM, et al. **The Barrow Ruptured Aneurysm Trial: 6-year results.** *J Neurosurg* 2015;123:609–17 CrossRef Medline
19. de Oliveira JG, Beck J, Setzer M, et al. **Risk of shunt-dependent hydrocephalus after occlusion of ruptured intracranial aneurysms by surgical clipping or endovascular coiling: a single-institution series and meta-analysis.** *Neurosurgery* 2007;61:924–33; discussion 933–34 CrossRef Medline
20. Zaidi HA, Montoure A, Elhadi A, et al. **Long-term functional outcomes and predictors of shunt-dependent hydrocephalus after treatment of ruptured intracranial aneurysms in the BRAT trial: revisiting the clip vs coil debate.** *Neurosurgery* 2015;76:608–13; discussion 613–14; quiz 614 CrossRef Medline

# Inter- and Intrarater Agreement on the Outcome of Endovascular Treatment of Aneurysms Using MRA

S. Jamali, R. Fahed, J.-C. Gentric, L. Letourneau-Guillon, H. Raoult, F. Bing, L. Estrade, T.N. Nguyen, É. Tollard, J.-C. Ferre, D. Iancu, O. Naggara, M. Chagnon, A. Weill, D. Roy, A.J. Fox, D.F. Kallmes, and J. Raymond



## ABSTRACT

**BACKGROUND AND PURPOSE:** Patients treated with coiling are often followed by MR angiography. Our objective was to assess the inter- and intraobserver agreement in diagnosing aneurysm remnants and recurrences by using multimodality imaging, including TOF MRA.

**MATERIALS AND METHODS:** A portfolio composed of 120 selected images from 56 patients was sent to 15 neuroradiologists from 10 institutions. For each case, raters were asked to classify angiographic results (3 classes) of 2 studies (32 MRA-MRA and 24 DSA-MRA pairs) and to provide a final judgment regarding the presence of a recurrence (no, minor, major). Six raters were asked to independently review the portfolio twice. A second study, restricted to 4 raters having full access to all images, was designed to validate the results of the electronic survey.

**RESULTS:** The proportion of cases judged to have a major recurrence varied between 16.1% and 71.4% (mean, 35.0% ± 12.7%). There was moderate agreement overall ( $\kappa = 0.474 \pm 0.009$ ), increasing to nearly substantial ( $\kappa = 0.581 \pm 0.014$ ) when the judgment was dichotomized (presence or absence of a major recurrence). Agreement on cases followed-up by MRA-MRA was similarly substantial ( $\kappa = 0.601 \pm 0.018$ ). The intrarater agreement varied between fair ( $\kappa = 0.257 \pm 0.093$ ) and substantial ( $\kappa = 0.699 \pm 0.084$ ), improving with a dichotomized judgment concerning MRA-MRA comparisons. Agreement was no better when raters had access to all images.

**CONCLUSIONS:** There is an important variability in the assessment of angiographic outcomes of endovascular treatments. Agreement on the presence of a major recurrence when comparing 2 MRA studies or the MRA with the last catheter angiographic study can be substantial.

Time-of-flight MR angiography is a noninvasive, radiation-free follow-up technique that has been shown to be sensitive (>85%) and specific (>85%) in identifying incomplete aneurysm occlusion after endovascular treatment.<sup>1</sup> MRA is replacing conventional angiography in following patients after coiling in many centers.<sup>2,3</sup> Interobserver agreement in the diagnosis of a

residual or recurrent aneurysm has been reviewed recently.<sup>4</sup> Mean interrater agreement of the pooled studies was substantial ( $\kappa = 0.65$ ; 95% confidence interval, 0.60–0.69). However, authors concluded that because all 4 studies primarily focusing on reliability concerned conventional angiography, the reliability of MRA must still be considered unclear.<sup>4</sup>

Multiple MR angiographic scales have been proposed, but few have been tested for reliability.<sup>5</sup> Interobserver agreement by using a catheter angiographic scale directly applied to MR angiographic results has been reported as “substantial” and “similar” to angiography, but the number of readings was limited to duplicates.<sup>3,6</sup> A more rigorous evaluation of the agreement in the MR angiographic diagnoses of residual or recurrent aneurysms in patients treated by endovascular coiling by a larger number of observers with various expertise is needed to establish the reliability of MRA diagnoses.<sup>7</sup>

Please address correspondence to Jean Raymond, MD, Centre Hospitalier de l'Université de Montréal, Notre-Dame Hospital, Department of Radiology, 1560 Sherbrooke East, Pavillon Simard, Suite Z12909, Montreal, Quebec, Canada H2L 4M1; e-mail: jean.raymond@umontreal.ca

Indicates article with supplemental on-line tables and appendix.

<http://dx.doi.org/10.3174/ajnr.A4609>

Received July 23, 2015; accepted after revision September 14.

From the Department of Radiology (S.J., R.F., J.-C.G., L.L.-G., A.W., D.R., J.R.), Centre Hospitalier de l'Université de Montréal, Notre-Dame Hospital, Montreal, Quebec, Canada; Groupe d'étude de la Thrombose en Bretagne Occidentale (J.-C.G.), Brest, France; Service de radiologie et imagerie médicale (H.R., J.-C.F.), Centre Hospitalier Universitaire de Rennes, Rennes, France; Service imagerie médicale et interventionnelle (F.B.), Centre Hospitalier Anecy Genevois, St-Julien en Genevois, France; Service Imagerie, Médecine nucléaire et Explorations fonctionnelles (L.E.), Centre Hospitalier Régional Universitaire de Lille, Lille, France; Departments of Neurology, Neurosurgery, and Radiology (T.N.N.), Boston Medical Center, Boston, Massachusetts; Service d'Imagerie Médicale (E.T.), Centre Hospitalier Universitaire Hôpitaux de Rouen, Charles Nicolle, Rouen, France; Service of Diagnostic Imaging (D.I.), The Ottawa Hospital, Civic Campus, Ottawa, Ontario, Canada; Service d'Imagerie Morphologique et Fonctionnelle (O.N.), Centre Hospitalier Sainte Anne, Paris, France; Department of Mathematics and Statistics (M.C.), University of Montreal, Montreal, Quebec, Canada; Department of Medical Imaging (A.J.F.), University of Toronto, Toronto, Ontario, Canada; and Department of Neurointerventional Radiology (D.F.K.), Mayo Clinic, Rochester, Minnesota.

Robert Fahed is the recipient of a research scholarship delivered by the Fondation pour la Recherche Médicale, Paris, France (grant number DEA20140630151).

In clinical practice, the evolution of treated aneurysms is often followed by comparing the follow-up MRA with the final catheter angiogram of the embolization procedure. The reliability of the diagnoses of a stable occlusion or a recurrent lesion when the verdict depends on a comparison between 2 different imaging modalities (the MRA and the catheter angiographic results) has so far not been studied, to our knowledge.

Our objective was to assess inter- and intraobserver agreement in diagnosing aneurysm remnants and recurrences by using multimodality imaging, including DSA-MRA and MRA-MRA comparisons in close-to-clinical conditions.

## MATERIALS AND METHODS

The present report was written in compliance with the Guidelines for Reporting Reliability and Agreement studies.<sup>8</sup> The evaluation of the intra- and interobserver variability in adjudicating outcomes of endovascular treatment was primarily done by electronic survey by using a portfolio of selected images (DSA-MRA and MRA-MRA) to ease the participation of multiple readers from various backgrounds, institutions, and countries. A second study restricted to expert readers having full access to the set of angiographic and MRA data on the same patients on the hospital PACS system of a single institution was designed to validate the results of the electronic survey and resemble clinical working conditions.

### Cases

On the basis of Donner and Rotondi<sup>9</sup> (where for an expected  $K_0$  of 0.600 with a prevalence of 0.3 and 5 raters, 24 subjects are sufficient for the lower limit of a 95% 1-sided confidence limit to be no less than 0.400), we estimated that 24 cases per group (MRA-MRA and DSA-MRA comparisons for a total of 48 cases) would suffice to provide meaningful results. The number of cases was increased to 56 to account for potential missing responses and to include a spectrum of patients followed by using various follow-up methods. Images were retrieved from 52 patients with 56 coiled aneurysms (all platinum coils) followed between May 2012 and June 2013 in 1 center. Cases were selected to include at least 2 comparable images from 1.5T or 3T MRI or angiographic series either immediately following treatment or later. Two authors (J.-C.G. and S.J.) selected the cases, aiming to include approximately 50% of easily replicable verdicts (25% of large recurrences, 25% of stable occlusions) and 50% of less clear cases. Cases and proportions were chosen to mimic a typical endovascular case series and to aim for a prevalence of approximately 30%–40% major recurrences, to minimize paradoxes of  $\kappa$  statistics.<sup>10,11</sup> The characteristics of patients are summarized in Table 1. Detailed characteristics for each patient can be found in On-line Table 1.

### Portfolio of Images

A portfolio composed of 120 images from 56 cases (typically 1 pair of images per case) was assembled. On each page of the electronic survey, 1 postembolization and 1 follow-up image (at least) or 2 follow-up MRA images were displayed side by side. Most MR images ( $n = 92$ ) were time-of-flight source images, but 8 were 3D reconstructions.

**Table 1: Characteristics of patients**

	All Aneurysms ( $n = 56$ )	MRA-MRA Only ( $n = 32$ )
Male	14 (25%)	9 (28.1%)
Mean age (yr)	56.9 ± 10.6	57.6 ± 11.5
Unruptured aneurysms	37 (66.1%)	23 (71.8%)
Mean aneurysm size (mm)	12 ± 6.2	11.3 ± 6.5
Mean neck size (mm)	4.8 ± 1.7	4.4 ± 1.3
Mean FU1-FU2 delay (mo)	21.4 ± 15.4	24.6 ± 17.3
Anterior circulation aneurysm	37 (66.1%)	21 (65.6%)

**Note:**—FU1 indicates follow-up 1; FU2, follow-up 2.

There were 32 MRA-MRA pairs (22 comparing 1.5T–3T; three, 1.5T–1.5T; five, 3T–3T; and 2 comparing 3T–1.5T) and 24 DSA-MRA pairs (14 comparing DSA with 3T and 10 with 1.5T MRA). All MR imaging examinations were performed in 1 center; MR imaging protocols used for postcoiling surveillance included 3D TOF angiography of the circle of Willis on either a 1.5T Avanto (Siemens, Erlangen, Germany) or a 3T Achieva X system (Phillips Healthcare, Best, the Netherlands). The 1.5T 3D TOF sequence was performed with the following parameters: TR, 25 ms; TE, 7 ms; section thickness, 0.7 mm; FOV, 200 mm. The 3T 3D TOF sequence was performed with the following parameters: TR, 25 ms; TE, 3.5 ms; section thickness, 1.0 mm; FOV, 200 mm.

No clinical information was provided. Observers had to independently grade each image according to a 3-value scale (complete occlusion, residual neck, residual aneurysm), graphically displayed on each page.<sup>5,12</sup> They were also asked to make a final judgment regarding the presence of a recurrence, according to a 3-value scale (no recurrence, minor recurrence, major recurrence) by comparing the 2 images. The definition of a major recurrence was “a saccular recurrence of a size sufficient to allow retreatment.” Any other increase in the residuum was to be labeled a minor recurrence.<sup>5,13</sup> The portfolio was provided electronically (On-line Appendix).

### Raters

The portfolio was sent to 15 participants, selected because they had served as a core lab for endovascular trials ( $n = 5$ ), participated in ongoing trials ( $n = 5$ ), or were on lists of potential participants ( $n = 5$ ). There were 14 interventionists (13 neuroradiologists) working in 10 different centers from 3 different countries (United States, France, and Canada). There were 8 senior (4 with >10 and 4 with >20 years; maximum, 40 years of experience) and 7 junior observers (<10 years of experience; minimum, 3 years).

The portfolio was sent twice electronically at least 3 months apart to 6 raters, blinded to their previous responses, who agreed to participate in the intraobserver agreement study.

### PACS Study

Because agreement on judgments based on pairs of selected images differs from the normal clinical context, the same cases were independently reviewed, in a random order provided by another investigator, by 4 observers (all interventional neuroradiologists) having access to all images. Two senior observers also independently assessed the same cases twice on the PACS system >3 months apart in a different random order.

**Table 2: Summary of agreements on the electronic survey**

	FU1 Imaging	FU2 Imaging	Final Result	Final Result (Dichotomized)	Final Result (Dichotomized + MRA-MRA only)
Interrater agreement					
Mean $\kappa \pm$ SE ( $n = 15$ )	0.398 $\pm$ 0.010	0.534 $\pm$ 0.010	0.474 $\pm$ 0.009	0.581 $\pm$ 0.014	0.601 $\pm$ 0.018
Mean $\kappa \pm$ SE (seniors, $n = 8$ )	0.367 $\pm$ 0.020	0.471 $\pm$ 0.019	0.425 $\pm$ 0.019	0.501 $\pm$ 0.027	0.579 $\pm$ 0.130
Mean $\kappa \pm$ SE (juniors, $n = 7$ )	0.451 $\pm$ 0.023	0.591 $\pm$ 0.022	0.496 $\pm$ 0.022	0.660 $\pm$ 0.031	0.652 $\pm$ 0.062
Intrarater agreement					
Mean $\kappa \pm$ SE ( $n = 6$ )	0.563 $\pm$ 0.174	0.606 $\pm$ 0.091	0.470 $\pm$ 0.175	0.534 $\pm$ 0.149	0.660 $\pm$ 0.152

Note:—FU1 indicates follow-up 1; FU2, follow-up 2; SE, standard error.

**Table 3: Summary of agreement on PACS reading**

	FU1 Imaging	FU2 Imaging	Final Result	Final Result (Dichotomized)
Interrater agreement				
Mean $\kappa \pm$ SE ( $n = 4$ )	0.354 $\pm$ 0.241	0.567 $\pm$ 0.105	0.374 $\pm$ 0.091	0.398 $\pm$ 0.136
Intrarater agreement				
$\kappa \pm$ SE (1st reader)	0.225 $\pm$ 0.105	0.674 $\pm$ 0.081	0.687 $\pm$ 0.083	0.778 $\pm$ 0.846
$\kappa \pm$ SE (2nd reader)	0.616 $\pm$ 0.098	0.687 $\pm$ 0.089	0.317 $\pm$ 0.128	0.347 $\pm$ 0.157

Note:—FU1 indicates follow-up 1; FU2, follow-up 2; SE, standard error.

### Statistics

The interrater agreement regarding the angiographic results (in 3 categories at 2 points in time [A and B]) and the final judgment regarding the presence of a recurrence (no, minor, or major recurrence) for the 15 raters by using the portfolio were estimated by using generalized  $\kappa$ . The 95% confidence intervals are reported. Stratified analyses according to follow-up imaging methods (DSA-MRA or MRA-MRA) or experience (all, seniors, juniors) were performed. For the 6 judges with a replicated judgment on the portfolio, intrarater agreement was also estimated by using  $\kappa$  statistics. The observed minimum, median, and maximum values of  $\kappa$  statistics are reported, including the 95% confidence interval. Because the primary angiographic end point of many trials has been the occurrence of a major recurrence, agreement was also analyzed in 2 categories (major recurrence, yes or no). For the PACS study, the inter- and intrarater agreement was estimated similarly by using  $\kappa$  statistics. All analyses were performed by using SAS, Version 9.2 (SAS Institute, Cary, North Carolina). All categories, such as “fair,” “moderate,” or “substantial” agreement, were qualified according to Landis and Koch.<sup>14</sup>

### RESULTS

Detailed statistical results can be found in On-line Tables 2–6.

#### Angiographic Results and Final Judgment on the Electronic Survey

There was a wide variability in angiographic results, with 2–23 cases (3.6%–41.1%) being judged as having a residual aneurysm on the first posttreatment evaluation. On the second set of images, between 12 and 39 cases (21.4%–69.6%) were judged as presenting a residual aneurysm. The proportion of portfolio cases judged to have a major recurrence at follow-up MRA varied between 16.1% and 71.4% (mean, 35.0%  $\pm$  12.7%) (On-line Table 2).

#### Interrater and Intrarater Agreement on the Electronic Survey

Interrater agreement regarding the 3 different categories of angiographic results for the 2 sets of images is summarized in On-line Tables 3–6. The category showing a lesser degree of agreement

was “residual neck.” Agreement regarding the presence of a recurrence (3 categories) varied greatly between raters from slight ( $\kappa = 0.156 \pm 0.069$  [95% CI, 0.021–0.292]) to almost perfect agreement ( $\kappa = 0.874 \pm 0.049$  [95% CI, 0.777–0.971]). There was moderate overall agreement among raters regarding the final verdict ( $\kappa = 0.474 \pm 0.009$ ); the category showing a lesser degree of

agreement was “minor recurrence.” Agreement improved to nearly substantial ( $\kappa = 0.581 \pm 0.014$ ) when the judgment was dichotomized as the presence or absence of a major recurrence (Table 2). Overall agreement regarding dichotomized verdicts on cases followed-up by MRA-MRA comparisons was similarly substantial ( $\kappa = 0.601 \pm 0.018$ ).

Agreement regarding a final dichotomized judgment among experienced raters ( $\geq 10$  years;  $n = 8$ ;  $\kappa = 0.501 \pm 0.027$ ) was no better than the agreement among less experienced observers (0–9 years of experience;  $n = 7$ ;  $\kappa = 0.660 \pm 0.031$ ).

The intrarater agreement regarding final angiographic verdicts varied between fair ( $\kappa = 0.257 \pm 0.093$  [95% CI, 0.074–0.440]) and substantial ( $\kappa = 0.699 \pm 0.084$  [95% CI, 0.534–0.864]), improving with a dichotomized judgment, becoming moderate to almost perfect when a dichotomized judgment concerned MRA-MRA comparisons (Table 2). Three of 6 raters reached a “substantial” level of agreement between 2 interpretations.

#### PACS Reading

Raters having access to all images on the PACS system found major recurrences in 13.2%–57.4% of cases (mean, 32.4%  $\pm$  15.3%). Agreement was no better when raters had full access to all images than among raters having access to only the selected images of the portfolio (Table 3). Interobserver agreement regarding the presence or absence of a major recurrence varied from slight to substantial, with a median  $\kappa$  of 0.455. Examples are illustrated in Fig 1.

#### MRA-MRA Comparisons

Inter- and intrarater agreement regarding the presence of a recurrence in the subgroup of 32 cases that were studied twice with MRA was very similar to the overall results (Table 2). Power was insufficient to study whether agreement differed with MRAs of different field strengths.

### DISCUSSION

There was wide variability in the adjudication of outcomes of endovascular coiling on selected images from catheter angio-

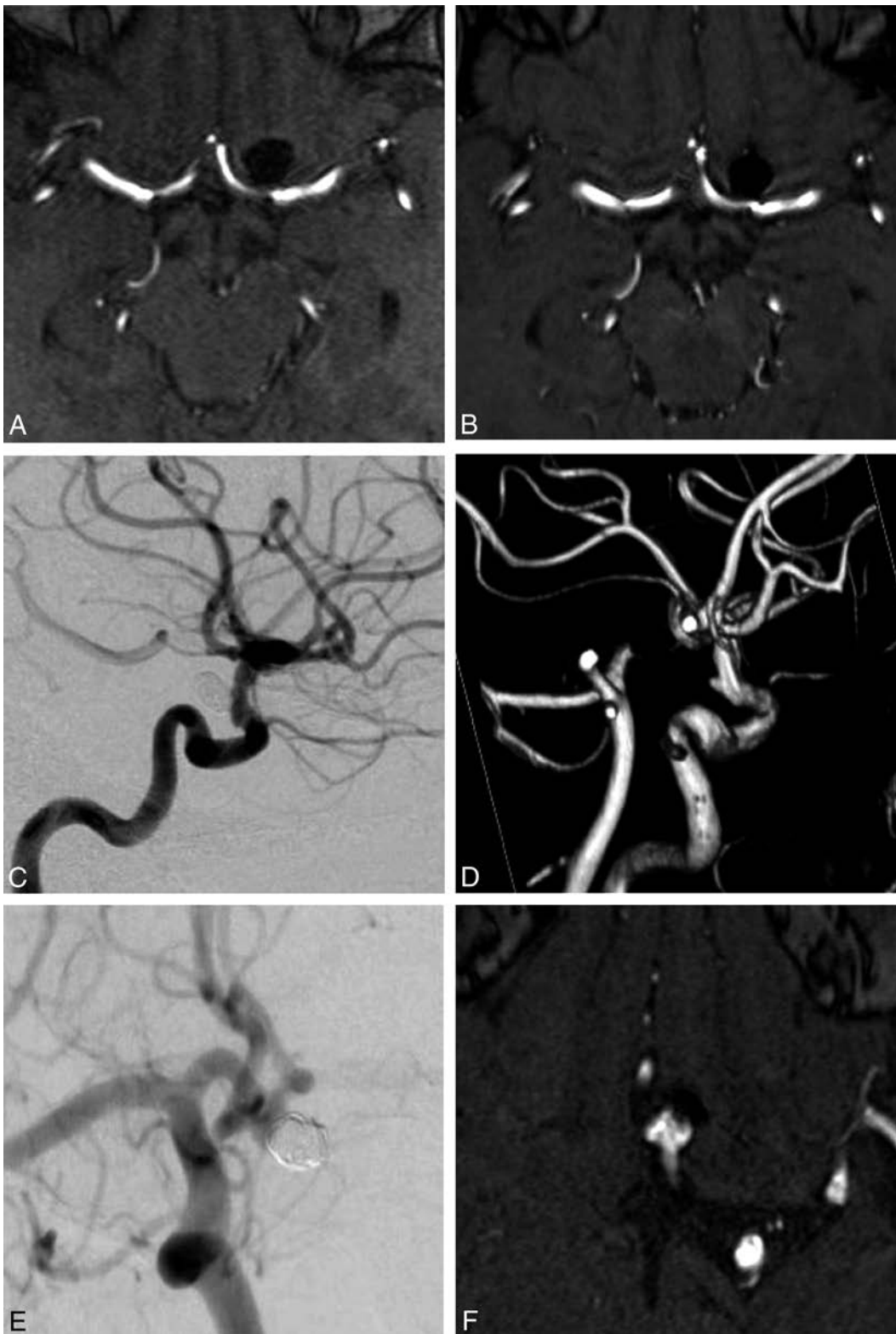


**FIG 1.** Illustrative cases from the electronic survey. Case number 10 is a 66-year-old woman with an unruptured aneurysm of the left ICA bifurcation. All 15 readers agreed on score A (complete occlusion) on first follow-up 1.5T MRA (A) and second follow-up 3T MRA (B). All 15 readers agreed on the final result, “no recurrence.” Case number 31 is a 59-year-old woman with an unruptured aneurysm of the left ICA. All 15 readers agreed on score A (complete occlusion) on first follow-up DSA (C), and 13/15 readers agreed on score B (residual neck) on second follow-up 3T MRA (D). Finally, 14/15 readers agreed on the final result “minor recurrence.” Case number 53 is a 61-year-old woman with an unruptured aneurysm of the anterior communicating artery. On the first follow-up DSA (E), 10/15 readers answered “residual neck” (score B), and 5/15 readers, “residual aneurysm” (score C). On the second follow-up 3T MRA (F), 7/15 readers answered “residual neck” (score B), and 8/15 readers, “residual aneurysm” (score C). The final angiographic result was “no recurrence” for 2/15 readers, “minor recurrence” for 6/15 readers, and “major recurrence” for 7/15 readers.

graphic or TOF MRA studies. Agreement was moderate at best and did not improve with rater experience. Disagreement among observers is not explained by divergences in the interpretations of the meaning of the various categories of the scale because agreement between 2 observations from the same raters was also fair to moderate in most cases. Reassuringly, agreement nearly reached a “substantial” level ( $\kappa \geq 0.600$ ) when the final verdict regarding the presence of a major recurrence was dichotomized (present-absent). Agreement when comparing the last angiographic result with the first MRA follow-up study (DSA-MRA), as commonly performed in clinical practice, was similar to MRA-MRA agreement. Agreement was not improved when raters had full access to all images.

### **Use of MRA for Aneurysm Follow-Up**

Previous studies on the reliability of postcoiling follow-up imaging studies have been systematically reviewed.<sup>4</sup> The overall diagnostic reliability was substantial ( $\kappa = 0.65$ ), but there was significant heterogeneity. Furthermore, the reliability of MRA follow-up examinations, now frequently replacing catheter angiographic studies, was not severely tested, for the primary aim of most studies was to assess diagnostic accuracy; interobserver agreement and reliability were conducted with few raters and reported as secondary quality measures.<sup>4</sup>

By contrast, our primary aim was to test the reproducibility of angiographic outcomes as they are assessed in clinical practice with a variety of modalities (DSA, 1.5T and 3T TOF MRA) that are actually used in realistic cases selected to mimic a clinical series. Although Pierot et al<sup>6</sup> have proposed that contrast-enhanced MRA performed better than TOF-MRA, most studies did not find a significant difference in accuracy between modalities or field strengths (3T or 1.5T), and for pragmatic reasons, patients cannot always be followed on the same equipment. The strengths of the present study also include a large number of observers with various experience and from various institutions and the inclusion of DSA-MRA comparisons that are often used in clinical practice.

### **Purpose of Follow-Up after Coiling**

Endovascular treatment of ruptured intracranial aneurysms was shown to improve patient outcomes compared with surgery.<sup>15</sup> It is also commonly used to treat unruptured aneurysms, even though it has not been shown superior to clipping or to conservative management.<sup>16</sup>

Angiography is a pragmatic way to assess the results of treatment of unruptured aneurysms because trials powered to show a decreased incidence of clinical ruptures would necessitate a large number of patients followed for a long time.<sup>16</sup> The main drawback of coiling, compared with surgery, is the risk of angiographic recurrence, reported to occur in 10%–20% of patients.<sup>17–19</sup> Second-generation coils<sup>20–25</sup> and, in some centers, stents and flow diverters<sup>26</sup> have been proposed to improve the stability of treatment. Angiographic results are still the main surrogate end point of ongoing trials on modified coils<sup>27,28</sup> or of other studies performed for the approval of endovascular devices.<sup>29</sup> However, the clinical significance of angiographic recurrences remains controversial.<sup>30</sup> Aneurysm ruptures have been rare, and whether treated patients should even be followed has recently been questioned.<sup>30</sup>

Some authors believe that most recurrences occur early and that follow-up imaging of aneurysms shown to be stable at 6 months is not necessary.<sup>2,31</sup>

A randomized trial, following versus not following patients with imaging, may be indicated to settle the issue. What to do when a recurrence is identified is even more controversial. There is little agreement regarding indications for retreatment,<sup>32</sup> though substantial agreement between decisions based on MRA and conventional angiography has been shown in 1 study.<sup>33</sup>

### **Various Scales**

At least 21 different grading scales have been reported,<sup>4</sup> but most can be translated into the 3-value scale we have previously proposed.<sup>11,34</sup> It has been observed that agreement increases as the number of categories is decreased.<sup>35</sup> Other ways to improve the reliability of angiographic judgments have been proposed, by using volumetric measurements of residual lesions,<sup>4</sup> or by increasing the precision of nominal definitions,<sup>24</sup> but the success of such strategies remains to be demonstrated. The present work supports the idea that agreement among observers can reach an acceptable level when the scale is translated into a simple dichotomous verdict (presence or absence of a major recurrence).

### **Limitations**

Our study has several limitations. First, we were careful to include a wide variety of cases that would test agreement in circumstances that were close to clinical conditions with multimodality imaging, but the selection of cases, images, and image parameters was artificial; a different set of cases could have led to different results. Second, we did not include patients treated with stents or stent-assisted coiling; this choice may affect MRA interpretations. Third, aneurysms were, on average, larger; and posterior circulation aneurysms were more frequent than those in typical endovascular series, perhaps because we included a sufficient number of major recurrences to minimize the paradoxes of  $\kappa$  statistics.<sup>10,11</sup> The variability we observed in judging the extent of angiographic occlusion of treated aneurysms and the presence of a recurrence at follow-up was probably underestimated by the portfolio method we used to multiply the number of raters. Many potential sources of discrepancies (selection of images, series, or sequences; diverse techniques; and equipment from various centers) were absent. Nevertheless, the substudy on a smaller number of readers having access to all images from the PACS yielded similar results. Finally, how seriously observers worked to come to verdicts can always be questioned, and the context of assessment certainly differed from the normal clinical context.

### **CONCLUSIONS**

There is an important variability in the assessment of angiographic outcomes of endovascular treatments. Agreement on the presence of a major recurrence when comparing 2 MRA studies or the MRA with the last catheter angiographic study can be substantial.

Disclosures: Robert Fahed—RELATED: Grant: Fondation pour la Recherche Médicale, grant number DEA20140630151, Comments: The research grant was accorded to me (Dr. Robert Fahed) from November 2014 to October 2015 as a full-time research

year. Laurent Letourneau-Guillon—UNRELATED: *Payment for Lectures (including service on Speakers Bureaus)*: Societe Canadienne Francaise de Radiologie, *Comments*: honorarium for 1 educational lecture at a radiology meeting. Allan J. Fox—UNRELATED: *Expert Testimony*: occasional medicolegal case (not relevant to the topic in question); *Stock/Stock Options*: none related to companies on this topic. David F. Kallmes—UNRELATED: *Board Membership*: GE Healthcare (Cost-Effectiveness Board membership)\*; *Consultancy*: Medtronic (planning and implementing clinical trials)\*; *Grants/Grants Pending*: MicroVention,\* Medtronic,\* Codman,\* Sequent Medical,\* NeuroSigma,\* Surmodics\*; *Royalties*: University of Virginia Patent Foundation. Jean Raymond—UNRELATED: *Grants/Grants Pending*: Canadian Institutes of Health research (Canadian UnRuptured Endovascular Versus Surgery Trial)\*; Codman (Does Embolization With Larger Coils Lead to Better Treatment of Aneurysms Trial)\* \*Money paid to the institution.

## REFERENCES

- van Amerongen MJ, Boogaarts HD, de Vries J, et al. **MRA versus DSA for follow-up of coiled intracranial aneurysms: a meta-analysis.** *AJNR Am J Neuroradiol* 2014;35:1655–61 CrossRef Medline
- Sprengers ME, Schaafsma J, van Rooij WJ, et al. **Stability of intracranial aneurysms adequately occluded 6 months after coiling: a 3T MR angiography multicenter long-term follow-up study.** *AJNR Am J Neuroradiol* 2008;29:1768–74 CrossRef Medline
- Schaafsma JD, Velthuis BK, Majoie CB, et al. **Intracranial aneurysms treated with coil placement: test characteristics of follow-up MR angiography—multicenter study.** *Radiology* 2010; 256:209–18 CrossRef Medline
- Ernst M, Yoo AJ, Kriston L, et al. **Is visual evaluation of aneurysm coiling a reliable study end point? Systematic review and meta-analysis.** *Stroke* 2015;46:1574–81 CrossRef Medline
- Tollard E, Darsaut TE, Bing F, et al. **Outcomes of endovascular treatments of aneurysms: observer variability and implications for interpreting case series and planning randomized trials.** *AJNR Am J Neuroradiol* 2012;33:626–31 CrossRef Medline
- Pierot L, Portefaix C, Gauvrit JY, et al. **Follow-up of coiled intracranial aneurysms: comparison of 3D time-of-flight MR angiography at 3T and 1.5T in a large prospective series.** *AJNR Am J Neuroradiol* 2012;33:2162–66 CrossRef Medline
- Bankier AA, Levine D, Halpern EF, et al. **Consensus interpretation in imaging research: is there a better way?** *Radiology* 2010;257:14–17 CrossRef Medline
- Kottner J, Audigé L, Brorson S, et al. **Guidelines for Reporting Reliability and Agreement Studies (GRRAS) were proposed.** *J Clin Epidemiol* 2011;64:96–106 CrossRef Medline
- Donner A, Rotondi MA. **Sample size requirements for interval estimation of the kappa statistic for interobserver agreement studies with a binary outcome and multiple raters.** *Int J Biostat* 2010;6: Article 31 Medline
- Feinstein AR, Cicchetti DV. **High agreement but low kappa, I: the problems of two paradoxes.** *J Clin Epidemiol* 1990;43:543–49 CrossRef Medline
- Cicchetti DV, Feinstein AR. **High agreement but low kappa, II: resolving the paradoxes.** *J Clin Epidemiol* 1990;43:551–58 Medline
- Roy D, Milot G, Raymond J. **Endovascular treatment of unruptured aneurysms.** *Stroke* 2001;32:1998–2004 CrossRef Medline
- Raymond J, Guilbert F, Weill A, et al. **Long-term angiographic recurrences after selective endovascular treatment of aneurysms with detachable coils.** *Stroke* 2003;34:1398–403 CrossRef Medline
- Landis JR, Koch GG. **The measurement of observer agreement for categorical data.** *Biometrics* 1977;33:159–74 CrossRef Medline
- Molyneux A, Kerr R, Stratton I, et al. **International Subarachnoid Aneurysm Trial (ISAT) of neurosurgical clipping versus endovascular coiling in 2143 patients with ruptured intracranial aneurysms: a randomized trial.** *Lancet* 2002;360:1267–74 CrossRef Medline
- Darsaut TE, Findlay JM, Raymond J. **The design of the Canadian UnRuptured Endovascular versus Surgery (CURES) trial.** *Can J Neurol Sci* 2011;38:236–41 CrossRef Medline
- Crobeddu E, Lanzino G, Kallmes DF, et al. **Review of 2 decades of aneurysm-recurrence literature, part 1: reducing recurrence after endovascular coiling.** *AJNR Am J Neuroradiol* 2013;34:266–70 CrossRef Medline
- Crobeddu E, Lanzino G, Kallmes DF, et al. **Review of 2 decades of aneurysm-recurrence literature, part 2: managing recurrence after endovascular coiling.** *AJNR Am J Neuroradiol* 2013;34:481–85 CrossRef Medline
- Lecler A, Raymond J, Rodriguez-Régent C, et al. **Intracranial aneurysms: recurrences more than 10 years after endovascular treatment: a prospective cohort study, systematic review, and meta-analysis.** *Radiology* 2015;277:173–80 CrossRef Medline
- White PM, Lewis SC, Gholkar A, et al; HELPS trial collaborators. **Hydrogel-coated coils versus bare platinum coils for the endovascular treatment of intracranial aneurysms (HELPS): a randomised controlled trial.** *Lancet* 2011;377:1655–62 CrossRef Medline
- White PM, Lewis SC, Nahser H, et al; HELPS Trial Collaboration. **HydroCoil Endovascular Aneurysm Occlusion and Packing Study (HELPS trial): procedural safety and operator-assessed efficacy results.** *AJNR Am J Neuroradiol* 2008;29:217–23 CrossRef Medline
- McDougall CG, Claiborne Johnston S, Gholkar A, et al; MAPS Investigators. **Bioactive versus bare platinum coils in the treatment of intracranial aneurysms: the MAPS (Matrix and Platinum Science) trial.** *AJNR Am J Neuroradiol* 2014;35:935–42 CrossRef Medline
- Coley S, Sneade M, Clarke A, et al. **Cerecyte coil trial: procedural safety and clinical outcomes in patients with ruptured and unruptured intracranial aneurysms.** *AJNR Am J Neuroradiol* 2012;33: 474–80 CrossRef Medline
- Molyneux AJ, Clarke A, Sneade M, et al. **Cerecyte coil trial: angiographic outcomes of a prospective randomized trial comparing endovascular coiling of cerebral aneurysms with either Cerecyte or bare platinum coils.** *Stroke* 2012;43:2544–50 CrossRef Medline
- Rezek I, Lingineni RK, Sneade M, et al. **Differences in the angiographic evaluation of coiled cerebral aneurysms between a core laboratory reader and operators: results of the Cerecyte coil trial.** *AJNR Am J Neuroradiol* 2014;35:124–27 CrossRef Medline
- Brinjikji W, Murad MH, Lanzino G, et al. **Endovascular treatment of intracranial aneurysms with flow diverters: a meta-analysis.** *Stroke* 2013;44:442–47 CrossRef Medline
- Raymond J, Klink R, Chagnon M, et al; PRET Collaborative Group. **Patients prone to recurrence after endovascular treatment: periprocedural results of the PRET randomized trial on large and recurrent aneurysms.** *AJNR Am J Neuroradiol* 2014;35:1667–76 CrossRef Medline
- ClinicalTrials.gov. **Hydrogel Endovascular Aneurysm Treatment Trial (HEAT).** <https://clinicaltrials.gov/ct2/show/NCT01407952>. Accessed July 23, 2015
- Becske T, Kallmes DF, Saatci I, et al. **Pipeline for uncoilable or failed aneurysms: results from a multicenter clinical trial.** *Radiology* 2013; 267:858–68 CrossRef Medline
- Molyneux AJ, Birks J, Clarke A, et al. **The durability of endovascular coiling versus neurosurgical clipping of ruptured cerebral aneurysms: 18 year follow-up of the UK cohort of the International Subarachnoid Aneurysm Trial (ISAT).** *Lancet* 2015;385:691–97 CrossRef Medline
- van Rooij WJ, Sluzewski M. **Opinion: imaging follow-up after coiling of intracranial aneurysms.** *AJNR Am J Neuroradiol* 2009;30: 1646–48 CrossRef Medline
- McDonald JS, Carter RE, Layton KF, et al. **Interobserver variability in retreatment decisions of recurrent and residual aneurysms.** *AJNR Am J Neuroradiol* 2013;34:1035–39 CrossRef Medline
- Schaafsma JD, Velthuis BK, van den Berg R, et al. **Coil-treated aneurysms: decision making regarding additional treatment based on findings of MR angiography and intraarterial DSA.** *Radiology* 2012;265:858–63 CrossRef Medline
- Raymond J, Roy D, Bojanowski M, et al. **Endovascular treatment of acutely ruptured and unruptured aneurysms of the basilar bifurcation.** *J Neurosurg* 1997;86:211–19 CrossRef Medline
- Cloft HJ, Kaufmann T, Kallmes DF. **Observer agreement in the assessment of endovascular aneurysm therapy and aneurysm recurrence.** *AJNR Am J Neuroradiol* 2007;28:497–500 Medline

# Endovascular Cooling Catheter for Selective Brain Hypothermia: An Animal Feasibility Study of Cooling Performance

G. Cattaneo, M. Schumacher, C. Maurer, J. Wolfertz, T. Jost, M. Büchert, A. Keuler, L. Boos, M.J. Shah, K. Foerster, W.-D. Niesen, G. Ihorst, H. Urbach, and S. Meckel



## ABSTRACT

**BACKGROUND AND PURPOSE:** Therapeutic hypothermia represents a promising neuroprotective treatment in acute ischemic stroke. Selective cerebral hypothermia applied early, prior to and during endovascular mechanical recanalization therapy, may be beneficial in the critical phase of reperfusion. We aimed to assess the feasibility of a new intracarotid cooling catheter in an animal model.

**MATERIALS AND METHODS:** Nine adult sheep were included. Temperature probes were introduced into the frontal and temporal brain cortices bilaterally. The cooling catheter system was introduced into a common carotid artery. Selective blood cooling was applied for 180 minutes. Systemic and local brain temperatures were measured during cooling and rewarming. Common carotid artery diameters and flow were measured angiographically and by Doppler sonography.

**RESULTS:** The common carotid artery diameter was between 6.7 and 7.3 mm. Common carotid artery blood flow velocities increased moderately during cooling and after catheter removal. Maximum cerebral cooling in the ipsilateral temporal cortex was  $-4.7^{\circ}\text{C}$  (95% CI,  $-5.1$  to  $-4.0^{\circ}\text{C}$ ). Ipsilateral brain temperatures dropped significantly faster and became lower compared with the contralateral cortex with maximum temperature difference of  $-1.3^{\circ}\text{C}$  (95% CI,  $-1.5$  to  $-1.0^{\circ}\text{C}$ ;  $P < .0001$ ) and compared with systemic temperature ( $-1.4^{\circ}\text{C}$ ; 95% CI,  $-1.7$  to  $-1.0^{\circ}\text{C}$ ;  $P < .0001$ ).

**CONCLUSIONS:** Sheep proved a feasible animal model for the intracarotid cooling catheter. Fast induction of selective mild hypothermia was achieved within the cooled cerebral hemisphere, with stable temperature gradients in the contralateral brain and systemic blood. Further studies are required to demonstrate any therapeutic benefit of selective cerebral cooling in a stroke model.

**ABBREVIATIONS:** BW = body weight; CCA = common carotid artery;  $\Delta T$  = temperature drop; MT = mechanical thrombectomy; TH = therapeutic hypothermia

Therapeutic hypothermia (TH) is an established neuroprotective therapy in patients after cardiac arrest<sup>1</sup> and in neonates with severe asphyxia.<sup>2</sup> Recently, the feasibility and safety of TH in patients with acute ischemic stroke was proved in controlled studies,<sup>3–6</sup> and 2 multicenter, randomized clinical

trials (EuroHYP-1 and ICTuS 2/3)<sup>7,8</sup> are currently underway to study its efficacy.

Patients with stroke with large-artery occlusions benefit from endovascular recanalization by mechanical thrombectomy (MT).<sup>9–13</sup> However, reperfusion of ischemic brain tissue may induce additional damage and hemorrhagic transformation, potentially limiting the benefits of recanalization. Current systemic cooling approaches involve long induction times, so the time window for TH during the critical reperfusion phase may still be missed for many patients.<sup>14</sup>

Recently, we have developed an intracarotid cooling catheter system for combined MT and selective TH treatment.<sup>15</sup> It simultaneously serves as an access for the intracranial MT procedure and enables early cooling of the ischemic penumbra via collaterals before recanalization, to then provide a “cold reperfusion” of the ischemic core during and after MT treatment. The latter is expected to be a critical determinant of clinical outcome.<sup>7</sup> Moreover, selective cooling may reduce systemic adverse events from TH.

Received June 26, 2015; accepted after revision October 21.

From Acandis (G.C., J.W., T.J., M.B.), Pforzheim, Germany; and Departments of Neuroradiology (M.S., C.M., A.K., L.B., H.U., S.M.), Neurosurgery (M.J.S.), Neurology (W.-D.N.), and University Heart Center (K.F.), and University Study Center (G.I.), University Hospital Freiburg, Freiburg, Germany.

This work was supported by Federal Ministry of Education and Research, Germany (grant 13GW0015B).

Paper previously presented in part at: Ninth World Stroke Congress, October 22–25, 2014; Istanbul, Turkey; and 24th European Stroke Conference, May 13–15, 2015; Vienna, Austria.

Please address correspondence to Stephan Meckel, MD, Department of Neuroradiology, Neurocenter, University Hospital Freiburg, Breisacher Str 64, D-79106 Freiburg, Germany; e-mail: stephanmeckel@gmail.com

Indicates open access to non-subscribers at www.ajnr.org

<http://dx.doi.org/10.3174/ajnr.A4625>

In this study, we aimed to assess the feasibility of the new cooling catheter in a large animal model with continuous monitoring of systemic and local cortical brain temperatures.

## MATERIALS AND METHODS

### Balloon Cooling Catheter System

The in vitro development and optimization of the intracarotid balloon cooling catheter system (Acandis, Pforzheim, Germany) was previously described.<sup>15</sup> In this study, the device and its functional properties were extensively outlined, including photographic and schematic images of the balloon cooling system. It consists of 4 serially arranged balloons at the catheter tip (diameter, 4 mm; length, 20 mm each) perfused with coolant (0.9% sodium chloride) that connect to a closed-loop inner-catheter cooling circuit without direct blood contact. The latter is kept constant at  $\sim 6^{\circ}\text{C}$  provided by an external thermostat and circulated by a roller pump. A third lumen (diameter, 1 mm) allows passage of a 2.5F microcatheter and thus distal access for MT.

### Animal Studies

Animal experiments with 9 sheep were approved by the local ethics committee (Freiburg, Germany) and performed in accordance with the German animal protection law and the animal care guidelines of the European Community (2010/63/EU).

Under general anesthesia (see protocol below), temperature probes (MP00991; Dräger Medical, Lübeck, Germany) were introduced into the frontal and temporal brain cortices bilaterally by neurosurgical burr-hole craniotomies. Via transfemoral arterial access, the cooling catheter system was introduced through an 8F 90-cm sheath (Flexor Shuttle Guiding Sheath; Cook, Bloomington, Indiana) into the common carotid artery (CCA) under systemic heparinization (70 IU/kg body weight [BW]) and fluoroscopic guidance. Selective intracarotid blood cooling was applied by coolant circulation and maintained for 60 minutes in the first sheep and 180 minutes in the remaining 8 sheep. Cortical brain, nasal, and systemic (inferior vena cava) temperatures were measured at 10-second intervals during cooling and 30 minutes after catheter removal. CCA diameters were measured by Doppler sonography and DSA before catheter insertion. During cooling and after catheter removal, the patency and flow of the CCA and side branches were assessed on DSA at 30-minute intervals. Blood temperature distal (1, 5, and 10 cm) to the cooling catheter was measured by using a self-made microprobe at 30-minute intervals. Mean blood-flow velocities were measured in mid-CCA on Doppler sonography before cooling catheter insertion, during cooling, and after cooling catheter removal. Positioning of brain temperature probes was analyzed on postprocedural CT.

### Protocol of Animal Anesthesia

Adult sheep ( $80.2 \pm 7.4$  kg BW) were premedicated with intramuscular midazolam (0.5 mg/kg BW) and ketamine hydrochloride (20 mg/kg BW) and anesthetized intravenously with propofol (2–4 mg/kg BW). Following endotracheal intubation, 12–15 breaths/min were provided by a volume-controlled ventilator at a 10–15 mL/kg BW tidal volume, 5-mbar positive end-expiratory pressure, with setting adjustments to normalize oxygen and carbon dioxide tension and pH values. Anesthesia was maintained

intravenously with propofol (15–18 mg/kg BW/h) and fentanyl (2–3  $\mu\text{g}/\text{kg}$  BW/h). Fluid requirements were substituted with Ringer solution (10 mg/kg BW/h). Electrocardiogram, blood pressure, and oxygen saturation were monitored continuously. At the end of the experiment, sheep were sacrificed in deep anesthesia with an intravenous dose of potassium chloride.

### Statistical Analysis

Statistical analyses were performed by using SAS 9.2 (SAS Institute, Cary, North Carolina) for data from 8 sheep with a 3-hour cooling phase. For each animal and temperature probe, temperature drops ( $\Delta T = \text{recorded temperature} - \text{baseline temperature}$ ) were calculated. Baseline temperatures were defined as time-averaged temperatures over 20 minutes before initiation of cooling. Temperature drops were averaged over the cooling phase and were compared within a linear regression model, accounting for repeated measurements by using the generalized estimating equation method for parameter estimation, with an exchangeable working correlation. The standard generalized estimating equation methodology provides robust standard error estimates that are reported here. We compared the cooled hemisphere versus the noncooled hemisphere (averaged frontal and temporal measurements), the cooled hemisphere versus the inferior vena cava, and the cooled hemisphere versus the nasal temperature. Mean temperature gradients (95% CI) were calculated between the cooled hemisphere and the noncooled hemisphere and systemic references during cooling and after 30 minutes of rewarming. Times needed to reach temperature drops of  $-1^{\circ}\text{C}$  and  $-2^{\circ}\text{C}$  were compared between measurement sites by using the Student *t* test.

## RESULTS

The mean CCA diameters were  $7.3 \pm 1.0$  mm proximally and  $6.7 \pm 1.0$  mm distally on DSA and  $6.3 \pm 0.6$  mm in the midsegment on sonography. Mean CCA blood flow velocity was  $36.9 \pm 8.2$  cm/s,  $51.9 \pm 18.7$  cm/s, and  $55.8 \pm 13.7$  cm/s before cooling catheter insertion, after the start of cooling, and after balloon catheter removal, respectively. Mean baseline temperatures varied between  $37.0^{\circ}\text{C} \pm 1.4^{\circ}\text{C}$  and  $37.2^{\circ}\text{C} \pm 1.7^{\circ}\text{C}$  (3/9 sheep were shorn). During selective cooling, temperatures decreased significantly more in the cooled brain hemisphere versus the noncooled brain hemisphere ( $P < .0001$ ) and versus central venous temperature ( $P < .0001$ ) (Fig 1). The mean maximum  $\Delta T$  was higher in the temporal cortex with  $-4.5^{\circ}\text{C}$  (95% CI,  $-5.1$  to  $-4.0^{\circ}\text{C}$ ) than in the frontal cortex with  $-4.2^{\circ}\text{C}$  (95% CI,  $-4.7$  to  $-3.7^{\circ}\text{C}$ ). The mean maximum systemic venous and nasal  $\Delta T$ s were  $-3.5^{\circ}\text{C}$  (95% CI,  $-3.9$  to  $-3.2^{\circ}\text{C}$ ) and  $-4.0^{\circ}\text{C}$  (95% CI,  $-4.7$  to  $-3.4^{\circ}\text{C}$ ), respectively.

The mean maximum temperature gradient among the cooled-versus-noncooled hemisphere, systemic inferior vena cava, and nasal temperatures was  $-1.28^{\circ}\text{C}$  (95% CI,  $-1.54$  to  $-1.02^{\circ}\text{C}$ ),  $-1.37^{\circ}\text{C}$  (95% CI,  $-1.71$  to  $-1.04^{\circ}\text{C}$ ), and  $-0.79^{\circ}\text{C}$  (95% CI,  $-1.08$  to  $-0.49^{\circ}\text{C}$ ), respectively. After initiation of selective cooling, these temperature gradients increased rapidly to then remain relatively constant during the remaining cooling period (Fig 2). Immediately after cooling catheter system removal, the mean interhemispheric and hemispheric-systemic temperature gradients started to equalize with  $-0.15^{\circ}\text{C}$  (95% CI,  $-0.40$  to  $0.09^{\circ}\text{C}$ ) and

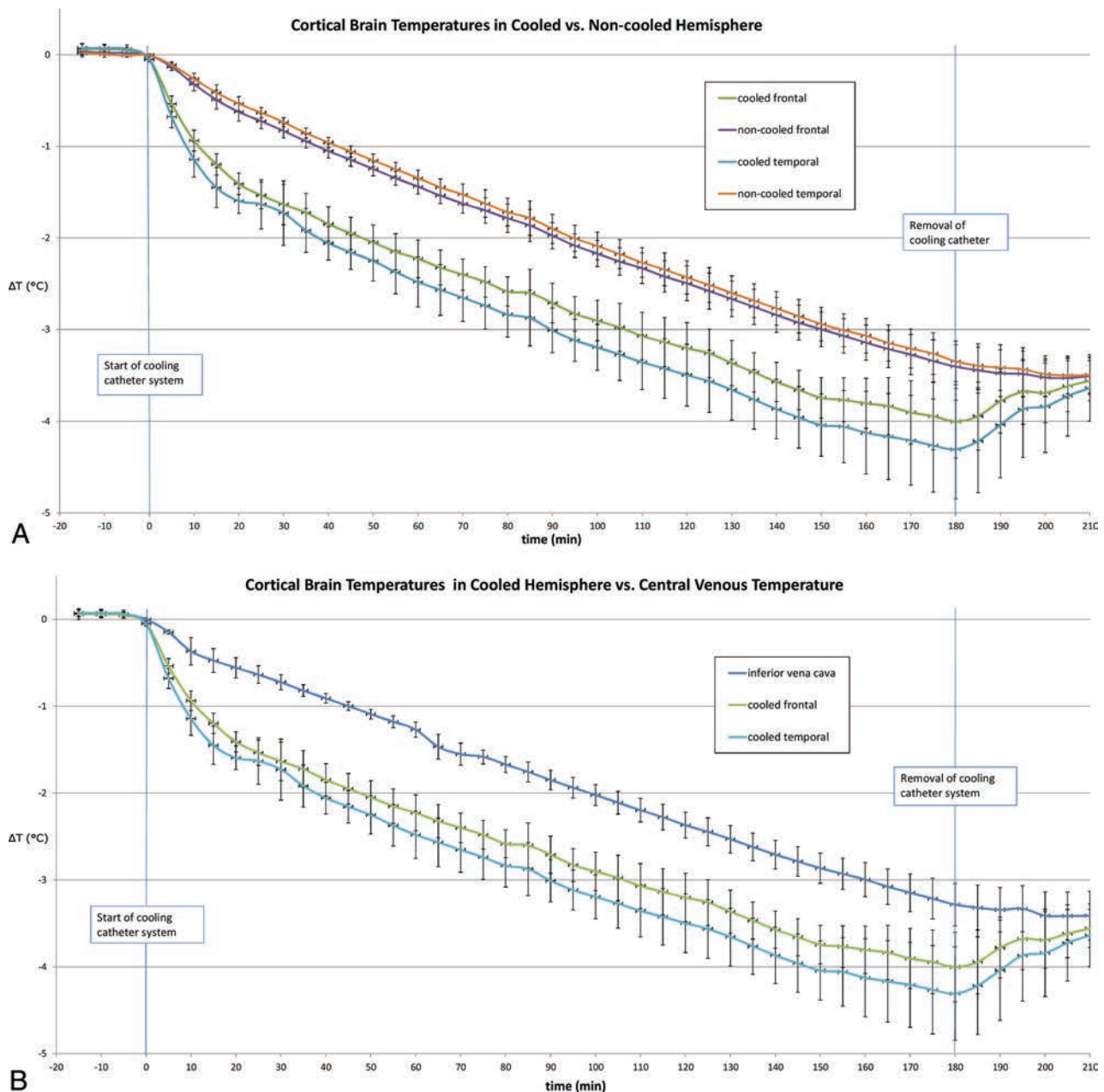


**FIG 1.** Temperature recordings from 9 sheep (mean  $\Delta T$  and 95% CI, plotted at 5-minute intervals) that were measured during (0–180 minutes) and after (180–210 minutes) selective intracarotid blood cooling in the frontal and temporal cortical probes of the cooled-versus-noncooled hemisphere (A) and cooled-versus-central venous temperature (B), respectively.

–0.21°C (95% CI, –0.46 to 0.05°C), respectively, measured after 30 minutes of rewarming, while the systemic temperatures remained below –3°C to baseline temperature.

The velocity of cooling was initially the highest (pronounced in the temporal cortex) and then remained relatively constant during the cooling phase (Table). The times to reach –1°C and –2°C were significantly shorter in the cooled hemisphere compared with both the noncooled hemisphere ( $P < .0001$ ) and the systemic venous temperature ( $P < .0001$ ) and were marginally shorter compared with the nasal temperature ( $P = .48$  and  $P = .03$ , respectively). Blood temperature at a 10-cm distance to the cooling catheter tip closely matched the cooled brain temperature during the later steady-state cooling phase (after  $\approx 60$  minutes, Fig 3).

On DSA, no evidence of CCA flow stagnation/occlusion or thromboembolic side branch occlusion was present. In 1 case, a superficial temporal branch occlusion related to the temporal craniotomy procedure was evident. In another case, the tip of the cooling catheter was accidentally engaged into a small muscular side branch of the CCA, resulting in branch occlusion after catheter withdrawal and major CCA vasospasm, whereas the latter resolved completely during further controls. In 6/9 sheep (66.7%), mild luminal changes compatible with vasospasm related to cooling catheter balloons (5/9) or tip (1/9) were found. Technical problems were the following: 1 temperature probe recording failure and, in 2 cases, short episodic rewarming ( $\approx 10$  minutes) due to a torqued cooling catheter connection and shivering from shallow sedation.

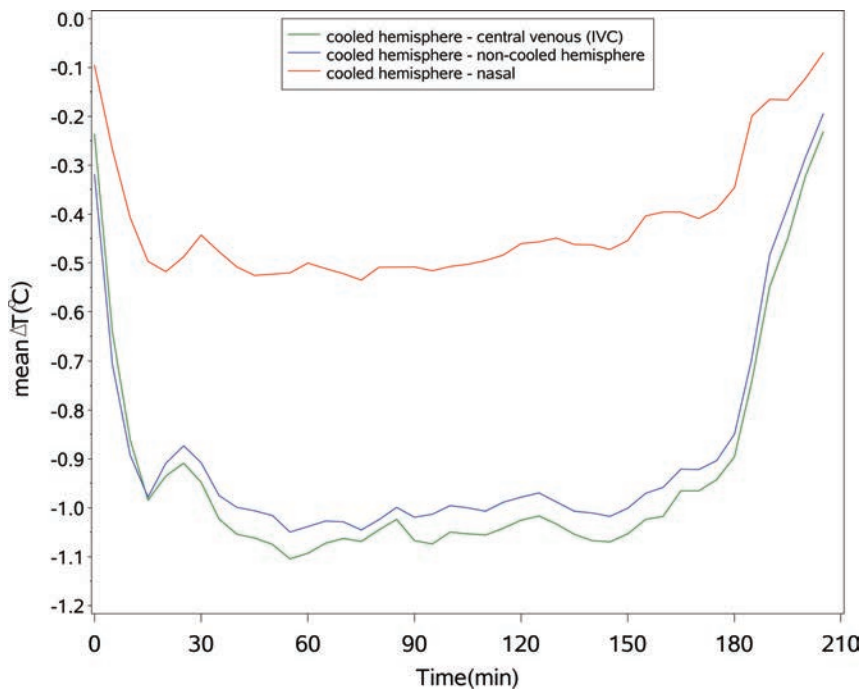


**FIG 2.** Mean temperature gradients (averaged over 8 sheep) among the cooled hemisphere and the central venous temperature, noncooled hemisphere, and nasal temperature, respectively, during 180 minutes of cooling and 30 minutes of rewarming (time-averaged at 5-minute intervals).

#### Velocity of selective brain cooling

	Cooled Temporal Cortex (median time) (range) (min)	Cooled Frontal Cortex (median time) (range) (min)
-1°C	8.5 (3.8–12.5)	11.5 (7.5–14.0)
-2°C	29.4 (11.7–70.3)	40.7 (27.0–70.0)
-3°C	85.7 (59.8–137.6)	100.5 (84.3–140.3)
-4°C	142.1 (109.3–180.0) <sup>a</sup>	158.3 (148.8–180.0) <sup>a</sup>

<sup>a</sup> -4°C was not reached in 2/8 sheep in both temporal and frontal cortices.

CT analysis of brain temperature probes showed optimal positioning of probes in 22/27 (81.5%); 2/27 (7.4%) were close to the craniotomy site; and 3/27 (11.1%) were close to midline. None were dislocated extracranially or crossed the midline.

#### DISCUSSION

In this *in vivo* study, we demonstrated the feasibility of selective cerebral hypothermia by using a newly developed intracarotid blood-cooling catheter system. The sheep is a suitable large-animal model with CCA diameters comparable with those of humans. The selective brain hemispheric temperature drop was induced significantly faster compared with the noncooled hemisphere and systemic temperature. The target temperature of 35° for mild TH (assuming a baseline temperature of 37°C) was achieved within a practical timeframe of 30–40 minutes for an MT procedure. Thus, these results may support the use of this catheter system in combination with MT for large-vessel occlusions to achieve an enhanced neuroprotective effect during the reperfusion phase (“cold reperfusion”). The latter concept remains to be proved in humans; however, various preclinical animal studies have indicated an increased benefit of TH when initiated early during the intra-ischemic period compared with delayed induction in the postischemic period.<sup>16–19</sup> In particular,

selective intracarotid cooling applied in the reperfusion phase has achieved a faster and deeper intracortical temperature reduction and an enhanced neuroprotective effect in a rat model compared with systemic blood cooling.<sup>14,20</sup>

Mack et al<sup>21</sup> used a similar closed-loop cooling catheter system (without a central “working” lumen) for systemic venous hypothermia (target temperature of 32°C, maintained for 6 hours) in a primate surgical large-artery occlusion and reperfusion stroke model. In their study, cooling was initiated 2 hours after reperfusion (3 hours after the start of ischemia) without any demonstrated neurologic benefit. These negative clinical results may also support the hypothesis that selective early TH with the concept of “cold reperfusion” may be more beneficial in patients with acute stroke.

Besides selectivity, systemic cooling due to cold venous return also had an additive effect on the brain temperature drop, decreasing the catheter blood inlet

temperature in our series. The lower cooling effect in the frontal-versus-temporal brain cortex can be attributed to blood mixing via the anterior communicating artery. The nasal temperature may only act as an imperfect surrogate of cooled brain temperature because it was measured in between the cortical brain temperatures of the cooled hemisphere and the systemic temperature, likely due to a mixture of cooled and noncooled blood supply via the ipsilateral and contralateral external carotid arteries.

Previous numeric modeling of selective brain cooling demonstrated the superiority of carotid artery blood cooling over external head-cooling devices.<sup>22,23</sup> Likewise, intracarotid cold saline infusion has been proposed for selective brain hypothermia by mathematic models,<sup>24,25</sup> and its effect was investigated on the jugular venous blood temperature in 18 patients undergoing diagnostic cerebral angiography.<sup>26</sup> The measured temperature drop (~0.8°C after 10 minutes of 7°C cold saline infusion at 33 mL/min) probably underestimates the true brain temperature due to blood mixing within the jugular venous return. We consider this technique an interesting alternative method for selective brain hypothermia and suppose that increasing the inflow rate of the coolant would increase the cooling performance. However, cold saline infusion may cause hemodilution and hypervolemia. The mathematic models cited above showed a decrease of the local hematocrit from 42% to 30.6% and ~20% after 60 minutes and 3 hours of saline infusion with a flow rate of 30 mL/min, respectively. In a randomized study of Kim et al<sup>27</sup> in patients with out-of-hospital cardiac arrest, 2 L of intravenous coolant at 4°C was given before hospitalization as soon as possible after return of spontaneous circulation in the hypothermia group. This resulted in an 11% higher rate of pulmonary edema and lower oxygen saturation on emergency department arrival. Although patients

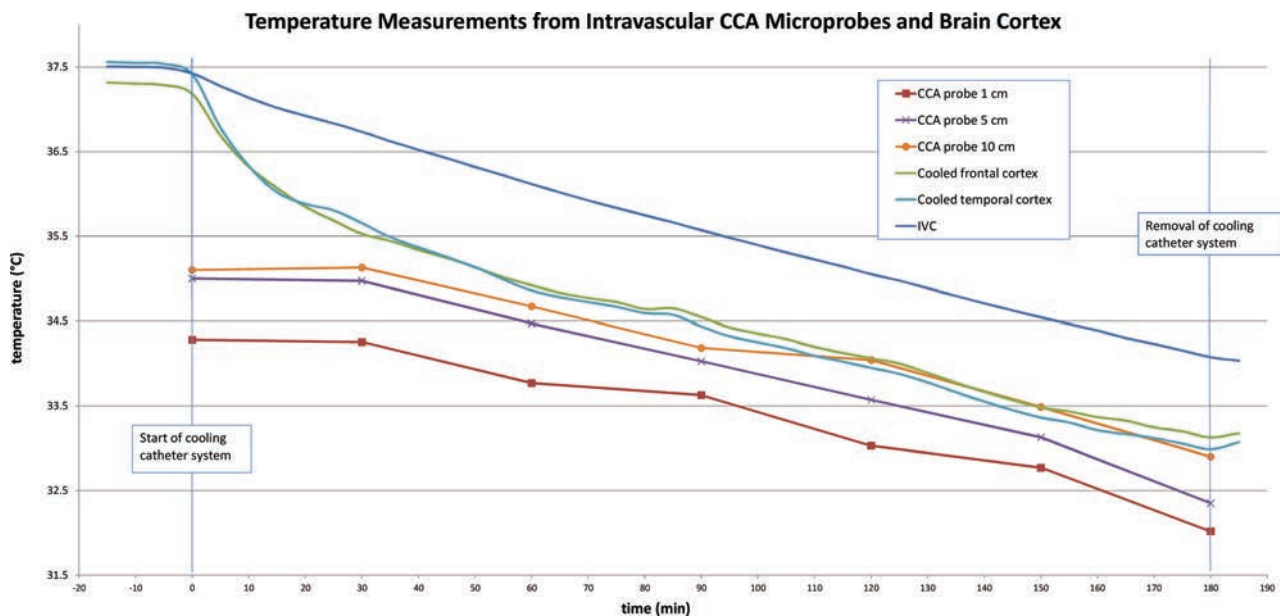


**FIG 3.** Microprobe temperature measurements performed at 30-minute intervals during the cooling phase at predefined distances to the cooling catheter tip (1, 5, and 10 cm) in comparison with continuously recorded ipsilateral brain cortex and central venous (IVC) temperatures.

with acute stroke may present with different clinical problems than those with cardiac arrest and the infusion rate may be kept lower, hemodilution and hypervolemia should be considered as possible relevant complications of cold saline infusions.

A recent study examined the induction of selective brain cooling (up to  $<30^{\circ}\text{C}$  within 25 minutes) by means of a coaxial catheter system in a focal MCA branch occlusion stroke model in swine.<sup>28</sup> With this approach, the CCA was occluded by an inflated balloon catheter and isolated from the aorta. Intra-aortic blood was removed via the outer catheter, cooled, and pumped back into the CCA via the inner catheter lumen by an extracorporeal pump. Resultant infarct size (on MR imaging and histology) was significantly reduced in the hypothermia group. Schwartz et al<sup>29</sup> presented a different method of extracorporeal blood cooling in which the blood was withdrawn from the femoral artery and reperfused into the proximally occluded carotid artery. With this technique, selective brain hypothermia up to  $25^{\circ}\text{C}$  was induced with simultaneous maintenance of the systemic temperature at  $36^{\circ}\text{C}$  by warm water blankets and a substantial reduction of infarct size was demonstrated in a surgical ICA and anterior cerebral artery occlusion model with baboons.<sup>30</sup> We suppose that the large-bore catheters that were used in both approaches of endovascular intracarotid blood cooling<sup>28,29</sup> are needed for recirculation of the extracorporeally cooled blood and, therefore, are incompatible with simultaneous access to MT treatment. Thus, cooling may only be applied as a stand-alone treatment or delayed in the postreperfusion phase with these techniques. Hence, the latter represent major limitations in the context of MT treatment, which has become the standard of care for patients with acute large-artery occlusions. Moreover, the required high-dose heparinization during the 12-hour period of extracorporeal blood cooling and the artificial pump circulation through a proximally occluded CCA, potentially leading to detrimental cerebral hyperperfusion, may be further disadvantages of such approaches in the treatment of patients with acute stroke.

Our tested cooling catheter system may potentially overcome several limitations of other previously proposed approaches for selective TH: 1) closed-loop coolant circulation that avoids hemodilution and could allow longer cooling times compared with intracarotid cold saline infusion; 2) a central catheter lumen enabling access for MT of occluded intracranial arteries for patients with large cerebral artery occlusions, and 3) simultaneous “cold reperfusion” therapy without affecting cerebral perfusion pressures compared with extracorporeal blood cooling. The optimal target temperature of TH in acute ischemic stroke is still a matter of debate, whereas emphasis is put on the time window more than on the depth of cooling, with neuroprotection being proved at  $35^{\circ}\text{C}$ .<sup>7</sup> Otherwise, the variable flow conditions and collateral perfusion in patients with stroke with major artery occlusion and the different times to mechanical recanalization, which are very dependent on anatomy, will influence the temperature at and after reperfusion and cause a variability of the neuroprotective effect of the proposed method.

With regard to safety, no critical blood flow impairment or thromboembolic events were observed. The single dissection of a muscular side branch of the CCA was a procedural complication, which is rather unlikely to occur in the human CCA due to anatomic differences (no direct small CCA side branches).

We observed an increase of CCA blood flow velocities after insertion of the cooling catheter system, which was sustained (by approximately 50%) after removal of the catheter system. The former may be explained by a combination of blood flow obstruction due to the introduction of the catheter system itself and hypothermia, whereas, the latter is likely related directly to a vasodilation effect of the central arteries from hypothermia, which is in line with a study by Mahmood et al,<sup>31</sup> which showed an increase in MCA blood flow velocities in healthy volunteers after mild externally induced hypothermia ( $34.5^{\circ}\text{C}$ ). These findings are also supported by another experimental study demonstrating a cooling-induced reversible graded vasodilation of the rabbit ca-

rotid artery.<sup>32</sup> By contrast, studies of TH in patients with acute brain injury from hypoxia after cardiac arrest, severe MCA infarct, or severe traumatic brain injury or in patients with poor-grade subarachnoid hemorrhage and delayed cerebral ischemia mostly showed a reduction of cerebral blood flow.<sup>33–37</sup> However, under all latter pathologic conditions, a clear distinction between hypothermia-related and direct pathology-related effects on the CBF is impossible; this finding relativizes this discrepancy to our blood flow measurements in cooled but otherwise healthy animals.

A major limitation of our study was the testing of the cooling catheter system under physiologic blood flow conditions without ischemia from a cerebral large-artery occlusion. We have chosen such a nonischemic large-animal model to determine the in vivo feasibility and capacity for selective brain hypothermia of the developed cooling catheter system. For this application, the sheep model was found ideal because the catheter system may only be inserted into the carotid arteries of similar anatomic dimensions to a human CCA. Thereby, the risks and time of the surgical procedure were limited because the rete mirabile, which is the only access to the cerebral circulation in sheep, prevents the use of a clot for generating an MCA occlusion.<sup>38,39</sup> Moreover, the variability of collaterals may affect flow conditions under MCA occlusion among the animals, thus increasing the complexity of the model and complicating the interpretation of the temperature development under selective hypothermia. After successful demonstration of selective brain hypothermia, we will test the safety and efficacy of this technique for neuroprotection in a future surgical model of temporary MCA occlusion on sheep. Thus, our catheter-based, selective intracarotid cooling technique may also be compared with a control group undergoing systemic venous cooling.

## CONCLUSIONS

Selective endovascular intracarotid blood cooling during 3 hours by using a new balloon cooling catheter system was able to achieve mild hypothermia ( $\approx -4.5^{\circ}\text{C}$ ) in a sheep model with a faster and significantly deeper temperature drop in targeted brain hemisphere compared with contralateral brain and systemic temperatures. This selective intracarotid TH approach offers combined MT access in patients with acute stroke due to large-artery occlusion. Thus, it enables cooling of penumbral tissue as well as “cold reperfusion” during and after the MT procedure. As a next step, we will test the efficacy of selective TH in a modified sheep model of acute ischemic stroke due to middle cerebral artery occlusion.

Disclosures: Giorgi Cattaneo—RELATED: Grant: Federal Ministry of Education and Research\*; UNRELATED: Employment: Acandis GmbH & Co KG, Martin Schumacher—RELATED: Grant: Federal Ministry of Education and Research (governmental grant)\*; Fees for Participation in Review Activities, such as Data Monitoring Boards, Statistical Analysis, Endpoint Committees, and the Like: Federal Ministry of Education and Research (governmental grant)\* Julia Wolfertz, Tobias Jost, Michael Büchert—RELATED: Grant: German Federal Ministry of Education and Research\*; UNRELATED: Employment: Acandis GmbH & Co KG, Andreas Keuler—RELATED: Support for Travel to Meetings for the Study or Other Purposes: Acandis GmbH & Co KG, Comments: support for visiting the Hypothermia Congress 2014 in Edinburgh, Scotland. Wolf-Dirk Niesen—UNRELATED: Travel/Accommodations/Meeting Expenses Unrelated to Activities Listed: Fresenius Medical Care travel expense. Stephan Meckel—RELATED: Grant: Federal Ministry of Education and Research, Germany\*; Consulting Fee or Honorarium: Acandis GmbH & Co KG, Comments: member of scientific advisory board; Support for Travel to Meetings for the Study or

Other Purposes: Acandis GmbH & Co KG; UNRELATED: Travel/Accommodations/Meeting Expenses Unrelated to Activities Listed: Covidien/Medtronic, Stryker, MicroVention. \*Money paid to the institution.

## REFERENCES

- Bernard SA, Gray TW, Buist MD, et al. **Treatment of comatose survivors of out-of-hospital cardiac arrest with induced hypothermia.** *N Engl J Med* 2002;346:557–63 CrossRef Medline
- Shankaran S, Laptook AR, Ehrenkranz RA, et al; National Institute of Child Health and Human Development Neonatal Research Network. **Whole-body hypothermia for neonates with hypoxic-ischemic encephalopathy.** *N Engl J Med* 2005;353:1574–84 CrossRef Medline
- Piironen K, Tiainen M, Mustanoja S, et al. **Mild hypothermia after intravenous thrombolysis in patients with acute stroke: a randomized controlled trial.** *Stroke* 2014;45:486–91 CrossRef Medline
- Hemmen TM, Raman R, Guluma KZ, et al; ICTuS-L Investigators. **Intravenous thrombolysis plus hypothermia for acute treatment of ischemic stroke (ICTuS-L): final results.** *Stroke* 2010;41:2265–70 CrossRef Medline
- De Georgia MA, Krieger DW, Abou-Chebl A, et al. **Cooling for Acute Ischemic Brain Damage (COOL AID): a feasibility trial of endovascular cooling.** *Neurology* 2004;63:312–17 CrossRef Medline
- Kammersgaard LP, Rasmussen BH, Jørgensen HS, et al. **Feasibility and safety of inducing modest hypothermia in awake patients with acute stroke through surface cooling: a case-control study—the Copenhagen Stroke Study.** *Stroke* 2000;31:2251–56 CrossRef Medline
- van der Worp HB, Macleod MR, Kollmar R, et al; European Stroke Research Network for Hypothermia (EuroHYP). **Therapeutic hypothermia for acute ischemic stroke: ready to start large randomized trials? J Cereb Blood Flow Metab** 2010;30:1079–93 CrossRef Medline
- Wu TC, Grotta JC. **Hypothermia for acute ischaemic stroke.** *Lancet Neurol* 2013;12:275–84 CrossRef Medline
- Berkhemer OA, Fransen PS, Beumer D, et al. **A randomized trial of intraarterial treatment for acute ischemic stroke.** *N Engl J Med* 2015;372:11–20 CrossRef Medline
- Saver JL, Goyal M, Bonafe A, et al; SWIFT PRIME Investigators. **Stent-retriever thrombectomy after intravenous t-PA vs. t-PA alone in stroke.** *N Engl J Med* 2015;372:2285–95 CrossRef Medline
- Campbell BC, Mitchell PJ, Kleinig TJ, et al; EXTEND-IA Investigators. **Endovascular therapy for ischemic stroke with perfusion-imaging selection.** *N Engl J Med* 2015;372:1009–18 CrossRef Medline
- Goyal M, Demchuk AM, Menon BK, et al; ESCAPE Trial Investigators. **Randomized assessment of rapid endovascular treatment of ischemic stroke.** *N Engl J Med* 2015;372:1019–30 CrossRef Medline
- Jovin TG, Chamorro A, Cobo E, et al; REVASCAT Trial Investigators. **Thrombectomy within 8 hours after symptom onset in ischemic stroke.** *N Engl J Med* 2015;372:2296–306 CrossRef Medline
- Pan J, Konstas AA, Bateman B, et al. **Reperfusion injury following cerebral ischemia: pathophysiology, MR imaging, and potential therapies.** *Neuroradiology* 2007;49:93–102 CrossRef Medline
- Cattaneo G, Schumacher M, Wolfertz J, et al. **Combined selective cerebral hypothermia and mechanical artery recanalization in acute ischemic stroke: in vitro study of cooling performance.** *AJNR Am J Neuroradiol* 2015;36:2114–20 CrossRef Medline
- van der Worp HB, Sena ES, Donnan GA, et al. **Hypothermia in animal models of acute ischaemic stroke: a systematic review and meta-analysis.** *Brain* 2007;130:3063–74 CrossRef Medline
- Dietrich WD, Busto R, Alonso O, et al. **Intraischemic but not post-ischemic brain hypothermia protects chronically following global forebrain ischemia in rats.** *J Cereb Blood Flow Metab* 1993;13:541–49 CrossRef Medline
- Maier CM, Sun GH, Kunis D, et al. **Delayed induction and long-term effects of mild hypothermia in a focal model of transient cerebral ischemia: neurological outcome and infarct size.** *J Neurosurg* 2001;94:90–96 CrossRef Medline
- Laszark I, Winkelheide U, Thal SC, et al. **Mild hypothermia has no**

- long-term impact on postischemic neurogenesis in rats. *Anesth Analg* 2009;109:1632–39 CrossRef Medline
20. Ding Y, Li J, Luan X, et al. **Local saline infusion into ischemic territory induces regional brain cooling and neuroprotection in rats with transient middle cerebral artery occlusion.** *Neurosurgery* 2004; 54:956–64; discussion 964–65 CrossRef Medline
  21. Mack WJ, Huang J, Winfree C, et al. **Ultraslow, convection-enhanced intravascular hypothermia: a feasibility study in nonhuman primate stroke.** *Stroke* 2003;34:1994–99 CrossRef Medline
  22. Sukstanskii AL, Yablonskiy DA. **Theoretical limits on brain cooling by external head cooling devices.** *Eur J Appl Physiol* 2007;101:41–49 CrossRef Medline
  23. Keller E, Mudra R, Gugl C, et al. **Theoretical evaluations of therapeutic systemic and local cerebral hypothermia.** *J Neurosci Methods* 2009;178:345–49 CrossRef Medline
  24. Konostas AA, Neimark MA, Laine AF, et al. **A theoretical model of selective cooling using intracarotid cold saline infusion in the human brain.** *J Appl Physiol* 2007;102:1329–40 Medline
  25. Neimark MA, Konostas AA, Laine AF, et al. **Integration of jugular venous return and circle of Willis in a theoretical human model of selective brain cooling.** *J Appl Physiol* 2007;103:1837–47 CrossRef Medline
  26. Choi JH, Marshall RS, Neimark MA, et al. **Selective brain cooling with endovascular intracarotid infusion of cold saline: a pilot feasibility study.** *AJNR Am J Neuroradiol* 2010;31:928–34 CrossRef Medline
  27. Kim F, Nichol G, Maynard C, et al. **Effect of prehospital induction of mild hypothermia on survival and neurological status among adults with cardiac arrest: a randomized clinical trial.** *JAMA* 2014; 311:45–52 CrossRef Medline
  28. Mattingly TK, Denning LM, Siroen KL, et al. **Catheter based selective hypothermia reduces stroke volume during focal cerebral ischemia in swine.** *J Neurointerv Surg* 2015 Feb 12. [Epub ahead of print] CrossRef Medline
  29. Schwartz AE, Stone JG, Finck AD, et al. **Isolated cerebral hypothermia by single carotid artery perfusion of extracorporeally cooled blood in baboons.** *Neurosurgery* 1996;39:577–81; discussion 581–82 Medline
  30. Schwartz AE, Finck AD, Stone JG, et al. **Delayed selective cerebral hypothermia decreases infarct volume after reperfused stroke in baboons.** *J Neurosurg Anesthesiol* 2011;23:124–30 CrossRef Medline
  31. Mahmood MA, Voorhees ME, Parnell M, et al. **Transcranial Doppler ultrasonographic evaluation of middle cerebral artery hemodynamics during mild hypothermia.** *J Neuroimaging* 2005;15:336–40 CrossRef Medline
  32. Mustafa S, Thulesius O. **Cooling-induced carotid artery dilatation: an experimental study in isolated vessels.** *Stroke* 2002;33:256–60 CrossRef Medline
  33. Bisschops LL, van der Hoeven JG, Hoedemaekers CW. **Effects of prolonged mild hypothermia on cerebral blood flow after cardiac arrest.** *Crit Care Med* 2012;40:2362–67 CrossRef Medline
  34. Kawamura S, Suzuki A, Hadeishi H, et al. **Cerebral blood flow and oxygen metabolism during mild hypothermia in patients with subarachnoid haemorrhage.** *Acta Neurochir (Wien)* 2000;142:1117–21; discussion 1121–22 CrossRef Medline
  35. Keller E, Steiner T, Fandino J, et al. **Changes in cerebral blood flow and oxygen metabolism during moderate hypothermia in patients with severe middle cerebral artery infarction.** *Neurosurg Focus* 2000; 8:e4 Medline
  36. Seule M, Muroi C, Sikorski C, et al. **Therapeutic hypothermia reduces middle cerebral artery flow velocity in patients with severe aneurysmal subarachnoid hemorrhage.** *Neurocrit Care* 2014;20: 255–62 CrossRef Medline
  37. Shiozaki T, Sugimoto H, Taneda M, et al. **Effect of mild hypothermia on uncontrollable intracranial hypertension after severe head injury.** *J Neurosurg* 1993;79:363–68 CrossRef Medline
  38. Qian Z, Climent S, Maynar M, et al. **A simplified arteriovenous malformation model in sheep: feasibility study.** *AJNR Am J Neuroradiol* 1999;20:765–70 Medline
  39. Wells AJ, Vink R, Blumbergs PC, et al. **A surgical model of permanent and transient middle cerebral artery stroke in the sheep.** *PLoS One* 2012;7:e42157 CrossRef Medline

# WEB in Partially Thrombosed Intracranial Aneurysms: A Word of Caution

G. Anil, A.J.P. Goddard, S.M. Ross, K. Deniz, and T. Patankar



## ABSTRACT

**SUMMARY:** Despite the proved safety and efficacy of Woven EndoBridge (WEB) flow disruption in conventional intracranial saccular aneurysms, the literature on its use in partially thrombosed intracranial aneurysms is scarce. We report a series of 4 patients in whom partially thrombosed intracranial aneurysms were treated with the WEB. The 2 patients who received additional intraluminal treatment with conventional stents made a good clinical recovery. Meanwhile, those patients who were treated with the WEB alone had fatal rupture of the aneurysm at short- to medium-term follow-up. This small, select case series demonstrates that WEB placement with adjunctive stent placement may be an effective treatment in the management of partially thrombosed intracranial aneurysms, which merits further validation. However, exclusive intrasaccular flow disruption may have an adverse influence on the natural history of this disease.

**ABBREVIATIONS:** WEB = Woven EndoBridge; WEB-DL = Woven EndoBridge Dual-Layer

Partially thrombosed intracranial aneurysms are distinct from conventional saccular aneurysms and difficult to treat. It is generally accepted that exclusive endosaccular treatment of a partially thrombosed intracranial aneurysm without parent vessel occlusion or stent placement has limited value.<sup>1</sup> Nonetheless, there is some evidence that exclusive endosaccular coiling can stabilize the disease process, provide clinical recovery, and reduce the mass effect in some patients.<sup>2,3</sup> Besides coil embolization, in recent years, intrasaccular flow disruption with the Woven EndoBridge aneurysm embolization system (WEB; Sequent Medical, Aliso Viejo, California) has emerged as a safe and efficient endosaccular technique for treating intracranial aneurysms.<sup>4</sup> However, literature on its role in the management of partially thrombosed intracranial aneurysm is scarce.<sup>5</sup>

### Case Series

Between May 2013 and August 2015, 40 patients underwent WEB flow disruption at a tertiary referral center in United Kingdom. Four (On-line Table) had a saccular partially thrombosed intra-

cranial aneurysm. With approval of the institutional review board, the aneurysm size, location, clinical and procedural details, imaging follow-up, and outcome of treatment in these 4 patients were retrospectively reviewed.

The patients received endovascular treatment following discussion in a multidisciplinary meeting. The circulating lumen of the 4 partially thrombosed aneurysms had a wide neck and morphology as well as dimensions suitable for WEB embolization. None of the patients had previous treatment. WEB flow disruption was performed with the patient under general anesthesia and systemic heparinization through a transfemoral access in 3 patients and a brachial artery access in 1 patient (patient 4). A carefully sized WEB was deployed through an appropriate catheter. All patients had been receiving aspirin for several months before treatment. Patients 1 and 3 have been kept on life-long aspirin therapy, and they received additional clopidogrel for 3 months after stent placement. Meanwhile, in patients 2 and 4, aspirin was continued for 6 weeks post-WEB embolization. All patients received a periprocedural short course of steroids.

**Case 1.** A 51-year-old man with left arm ataxia for 8 months presented with acute-onset diplopia, left arm weakness, and dizziness (Fig 1). On examination, he had dysconjugate gaze, grade 4/5 power, dysdiadochokinesis, and exaggerated reflexes in the left upper limb and left-sided past-pointing. CT demonstrated a partially thrombosed aneurysm near the basilar termination with hydrocephalus. MR imaging showed edema in the right thalamus and midbrain. There was some clinical recovery after ventriculoperitoneal shunt insertion.

Received August 18, 2015; accepted after revision September 22.

From the Departments of Neuroradiology (G.A., A.J.P.G., T.P.) and Neurosurgery (S.M.R., K.D.), Leeds Teaching Hospitals, National Health Service Trust, Leeds, UK; and Department of Diagnostic Imaging (G.A.), National University Hospital, Singapore.

Please address correspondence to Gopinathan Anil, MD, Department of Diagnostic Imaging, National University Hospital, 5 Lower Kentridge Rd, Singapore 119074; e-mail: ivyanil10@gmail.com

Indicates article with supplemental on-line table.

<http://dx.doi.org/10.3174/ajnr.A4604>

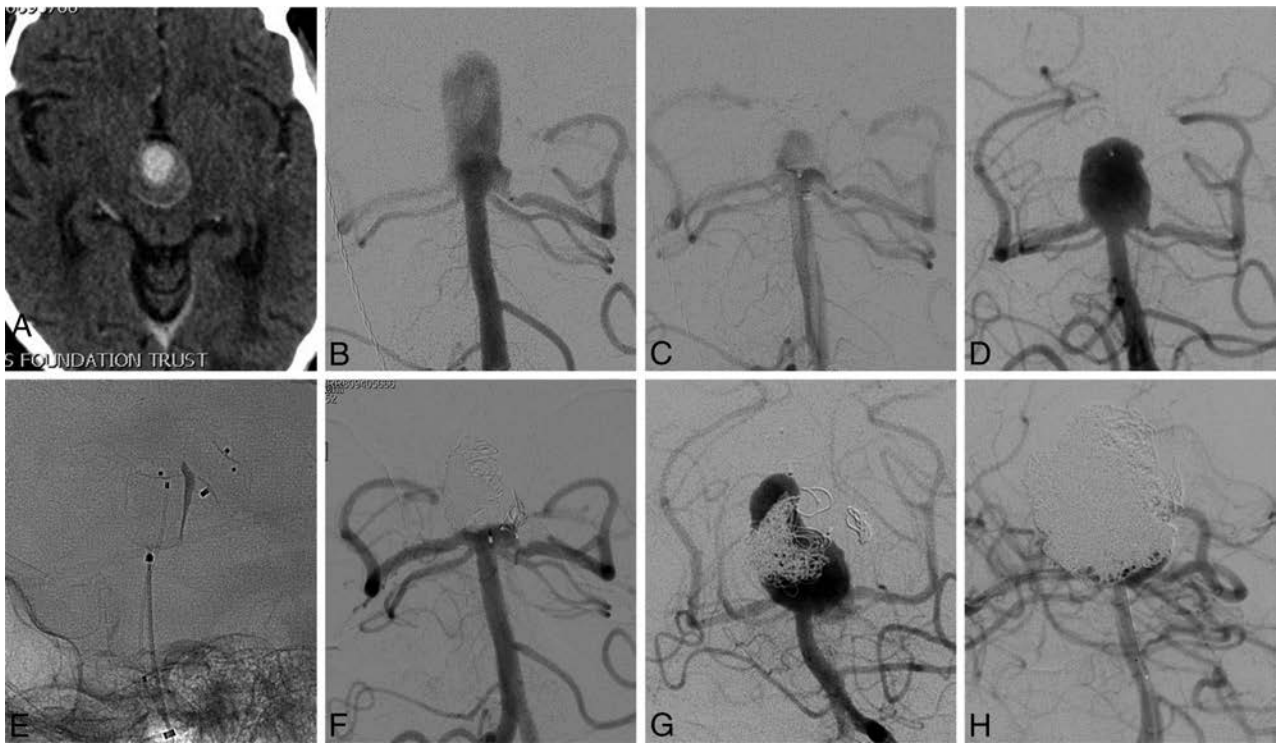


**FIG 1.** A, Axial CT angiographic image shows a partially thrombosed aneurysm. Pre- (B) and posttreatment (C) angiograms demonstrate technically successful placement of the WEB. D, A large recurrence is seen in this angiogram obtained 9 months following the initial treatment. E, The recurrence is being treated with another WEB device to protect the wide neck, while a microcatheter has been jailed within the aneurysm for coil embolization of the rest of the sac. Note the compaction of the initially deployed WEB. F, Complete occlusion of the recurrence following retreatment with the WEB and coils is seen here. G, The angiogram obtained 4 months later, when the patient presented with subarachnoid hemorrhage, shows a large recurrence with compaction of both the coils and the WEB. H, There is reasonable occlusion of the aneurysm following the second retreatment with balloon-assisted coiling.

Catheter angiography confirmed the aneurysm arising from the proximal P1 segment of the right posterior cerebral artery. The P1 segments were of near-equal size with noncontributory posterior communicating arteries. Angiography after WEB placement showed contrast filling the entire device with marked flow stasis, which continued beyond the venous phase. A small neck residue was not covered by the WEB. Therefore, a stent (LEO Baby; Balt Extrusion, Montmorency, France) was deployed in the right P1 across the neck of the aneurysm. The procedure was uneventful.

Two years from the initial treatment, the thrombosed component of the aneurysm had considerably decreased in size and surrounding edema had nearly resolved. At 28-month angiographic follow up, the residual neck of the aneurysm was stable, with no flow in the aneurysm sac or any thrombotic complications. The neurologic examination findings remained unremarkable.

**Case 2.** A 62-year-old man with a history of multidrug abuse was transferred to our institute following CT diagnosis of a giant partially thrombosed aneurysm causing triventricular hydrocephalus. He had diplopia and worsening frontal headache. On examination, there was left oculomotor palsy. MRA confirmed the diagnosis. There was extensive perilesional edema in the brain stem and both thalami. Both posterior cerebral arteries arose from the base of the aneurysm with equidominant P1 segments and hypoplastic posterior communicating arteries. A ventriculoperitoneal shunt was placed.

Following successful placement of a WEB within the aneurysm, there was immediate flow stasis with contrast gradually filling up to the proximal two-thirds of the WEB, consistent with satisfactory hemodynamic decoupling of the sac and parent vessel. The aneurysm was stable with minimal filling at the neck on 3-month follow-up MRA. At 6-month follow-up, the aneurysm had circumferentially grown, now measuring  $30 \times 29 \times 26$  mm with the WEB eccentrically buried within the thrombus. The recurrent patent sac measured  $11 \times 10$  mm in width and 15 mm in height with an 8-mm wide neck. The previously deployed WEB was distorted and compacted. The patient refused stent placement. However, he was agreeable to repeat endosaccular treatment.

Retreatment was performed via bifemoral access. Through the left vertebral artery, an  $11 \times 9$  mm WEB-Dual-Layer (DL) was placed (without detaching) in the proximal sac of the aneurysm, straddling the wide neck, while a microcatheter through the right vertebral artery was jailed in the distal sac. Before the WEB was detached, the patent sac around it was densely packed with coils through the jailed microcatheter. Angiographic exclusion of the aneurysm was complete with no visible intrasaccular flow. MRA performed 2 weeks later showed stable occlusion.

Four months from retreatment, he presented with World Federation of Neurosurgical Societies grade IV SAH. At CT, the aneurysm demonstrated an overall enlargement in size with luminal recurrence. The previously placed coils and WEBs were displaced

and compacted peripherally in the thrombus. Balloon-assisted coiling was performed to secure this acutely ruptured aneurysm. However, due to the wide neck, complete occlusion could not be achieved. The procedure was concluded with the intention of performing a delayed stent-assisted coiling. Unfortunately, his clinical deterioration continued, and 2 weeks later he died following yet another rebleed.

**Case 3.** A partially thrombosed anterior communicating artery aneurysm was reported in a 56-year-old male patient who had a CT scan for acute delirium. He had a short-term memory deficit. Comorbidities included hypertension, hypertriglyceridemia, peripheral vascular disease, diabetes mellitus, and ischemic heart disease. He was on life-long aspirin therapy.

At angiography, the left anterior cerebral artery supplied both anterior cerebral artery territories with a hypoplastic right A1 segment. The aneurysm was located at the A1 bifurcation, straddling the origin of both A2 segments. The initial WEB placement was slightly oblique to the long axis of the aneurysm, leaving the left edge of the neck uncovered. Further attempts to resheath the WEB not only failed but tilted it more. The device encroached into the proximal right A2 and occluded it. The WEB was deployed in that position. Attempts to cannulate the right A2 for placing a stent failed. The patient was given intravenous aspirin. Although there was no antegrade flow into the right A2, a right carotid angiogram showed modest retrograde filling of the right anterior cerebral artery. At the end of the procedure, there was a small residual neck along the left edge with the WEB satisfactorily occluding the rest of the aneurysm. The patient awoke without new neurologic deficits. He was hypertensive (mean, >120 mm Hg) and was started on clopidogrel besides aspirin. The same evening, he developed right arm sensory and motor weakness with right facial droop. MR imaging revealed multiple small cortical infarcts in the right anterior cerebral artery territory. The right arm weakness fully recovered within 48 hours while the facial weakness improved gradually.

Follow-up MRA, 3 months postprocedure showed an increase in the size of the residual neck, while both A2 segments were patent. The displaced and compacted WEB was more transverse within the thrombus. This early recurrence was successfully treated by stent-assisted coiling with a 3.5 × 20 mm Acclino-flex (Acandis, Pforzheim, Germany) stent deployed from the right A2 to the left A1. The procedure was uneventful. At the 17-month follow-up MRA, the partially thrombosed intracranial aneurysm had slightly decreased in size with no evidence of intrasaccular flow, while the patient's neurologic function remained stable

**Case 4.** A partially thrombosed superior cerebellar artery aneurysm was detected on CT in a 59-year-old woman with multiple episodes of TIA for 2 years. She was started on aspirin therapy and referred to our institution. She had been completely cured of breast cancer 12 years earlier.

The angiographic outcome of the WEB embolization of the aneurysm was excellent. Contrast filled the entire WEB with stasis. There was no flow beyond or around the device and no procedure-related complications. The patient was asymptomatic at 6-week postprocedural clinical evaluation. She defaulted from further follow-up. Thirteen months later, she was admitted to a

peripheral hospital with a World Federation of Neurosurgical Societies grade V SAH and died there. A CT performed following the bleed showed that the treated aneurysm had grown, measuring 23 × 22 × 19 mm with the patent lumen much larger than at the time of presentation. The compacted WEB was lying eccentrically, buried in the mural thrombus.

## DISCUSSION

Partially thrombosed intracranial aneurysms are a diverse group associated with organized thrombus formation. The thrombus could be intraluminal or intramural. Intraluminal thrombosis is the function of a critical ratio between the volume of the aneurysm and its neck diameter.<sup>6</sup> Hence, larger aneurysms are more likely to thrombose. Meanwhile, intramural thrombus is thought to result from recurrent nontransmural dissections that lead to subadventitial bleeding and organized hematoma formation.<sup>1</sup> The adventitial aspect of a partially thrombosed aneurysm is believed to be the epicenter of the pathology.<sup>7</sup> Partially thrombosed intracranial aneurysms mostly (60%–91%) present with symptoms of mass effect.<sup>2,8,9</sup> In comparison, embolic phenomena are infrequent.<sup>9</sup> Several patients had nonspecific symptoms, with headache being most common. Some symptoms mimicked SAH, a presentation postulated to be secondary to intramural dissection.<sup>8</sup> True SAH is rare with partially thrombosed intracranial aneurysms (0%–10%).<sup>1,2,8,9</sup>

Complete excision of the lesion and reconstruction of the vessel wall would be the ideal treatment for a partially thrombosed intracranial aneurysm; however, it is seldom feasible. Treatments such as direct clipping of the neck, parent vessel occlusion with or without bypass, endosaccular coil embolization with or without stent placement, and parent vessel flow diversion have been described with variable results.<sup>8–10</sup> Following occlusion of partially thrombosed aneurysms with exclusive endosaccular coiling, high recanalization rates (60%–75%) and failure of relief from symptoms of mass effect have been reported, often mandating retreatment.<sup>9,10</sup>

Meanwhile, a few other small case series found these aneurysms to be much less vulnerable to recanalization (approximately 30%) following coil embolization.<sup>2,8</sup> They also reported relief of symptoms and stabilization of the clinical evolution of the disease after coiling. Surgery was ruled out in our patients with aneurysms in the posterior circulation, due to their location, size, and circumferential thrombus. Meanwhile, in the patient with an anterior circulation aneurysm, the risk of an operation could not justify its use as the first treatment option. Parent vessel occlusion was unacceptable because it would have required sacrifice of the solitary A1 in patient 3 and the distal basilar artery in the remaining patients. We did not use flow diverters due to the high risk of perforator infarcts in the distal basilar artery in patients 1, 2, and 4, and in patient 3, a flow diverter could potentially occlude one of the A2 segments. Intracranial stents with their ability to modify the hemodynamic forces and effect a reconstruction of the parent artery, within certain limits, have been useful in the treatment of partially thrombosed intracranial aneurysms.<sup>11,12</sup> We had considered this option for all the patients from this series. Patients 2 and 3 with bifurcation aneurysms were potential candidates for double-stent placement in a Y-shaped configuration. However, in

view of patient factors and the clinical scenario, we offered the least aggressive management of exclusively endosaccular treatment and close surveillance as the first option. Patient 2 had refused to consent to stent placement, and he was unlikely to comply with long-term antiplatelet therapy. In patient 3, although the primary aneurysm was at the left anterior cerebral artery bifurcation, the recurrence was eccentric and had a sidewall aneurysm-like configuration. Hence, it could be satisfactorily treated with a single stent-assisted coiling.

In conventional aneurysms, the efficiency and safety of WEB flow disruption is comparable with coil embolization.<sup>4</sup> Because the aneurysms from our study had a wide neck, complete occlusion with coils was not possible without stent assistance. Conceptually, the WEB combines the advantage of flow diversion (diseased arterial wall treatment and stable occlusion) and selective intrasaccular embolization without the need for long-term antiplatelet therapy.<sup>13</sup> With the WEB, the surface exposed at the neck is smoother, compared with coils, providing potentially better support for neoendothelialization. These attributes prompted us to use the WEB in partially thrombosed intracranial aneurysms. Because the thrombus toward the luminal aspect in these aneurysms is considered old and organized, we thought it would adequately buttress the WEB. Unfortunately, despite the satisfactory immediate angiographic outcome, exclusive intrasaccular flow disruption did not provide stability to the aneurysm in any of the 3 cases as noted from their early recurrence. The WEB was displaced from its initial position in all of them. This could be secondary to lysis of the thrombus after treatment.<sup>13</sup> It may be argued that the device displacement would not have happened if we had allowed further oversizing of the WEB. However, the concerns of potential distortion of the device geometry and device protrusion into the parent vessel prevented us from deviating too much from the manufacturer's sizing recommendation.

All the recurrences were in the region corresponding to the previously treated neck and proximal sac that now appeared more bulbous than at the time of treatment. Hence, we believe that early growth at the neck of the aneurysm could have contributed to the recurrence. Before complete thrombosis and neoendothelialization, even a marginal increase in the size of the patent sac can result in loss of wall approximation of the WEB and make it susceptible to migrating into the thrombus with arterial pulsation ("water-hammer effect"). This mechanism of failure of flow disruption due to the movement of the WEB could explain the dismal performance of exclusive endosaccular treatment with the WEB compared with coils.<sup>8,9</sup> Because the WEB is a single composite plug, loss of wall approximation even over a small area can allow the whole device to move en masse. Meanwhile, a coil mass is made up of several individual coils, with each potentially interacting with the wall of the aneurysm at innumerable points along their lengths. Probably, an increase in the size of the sac has a greater impact on the WEB than on coils.

We are curious about the fatal SAH in both patients who did not receive adjunctive stent placement. Partially thrombosed intracranial aneurysms have a low propensity to bleed, and following treatment, SAH is almost unknown.<sup>1,2,8,9</sup> Even exclusive coil embolization delivers this favorable effect. On the contrary, our case series seems to suggest that exclusive endosaccular treatment

with the WEB has an unfavorable impact on the natural history of this disease. We suspect the earlier described potential for the WEB to move en masse within the partially thrombosed intracranial aneurysm following recurrence might have contributed to the mechanism of rupture. Alternatively, a ball valve mechanism, in which the WEB acts like a trapdoor that allows blood to enter the sac but not escape (or escape partially), may have been operational. Theoretically, a flow disruptor like the WEB is an intrasaccular version of a flow-diverter stent, and a comparable principle operates in the way it achieves occlusion of an aneurysm.<sup>13</sup> Hence, an aggressive thrombus-associated autolysis of the aneurysm wall, as described before with flow diverters, cannot be ruled out.<sup>14</sup> It would not be unreasonable to expect interplay of several or all of these postulated factors as the cause of SAH in patients from this series.

Unlike patients 2 and 4, the 2 patients who received adjunctive stent placement had excellent outcomes. This observation seems to suggest that WEB flow disruption in a partially thrombosed intracranial aneurysm could be an extremely promising treatment option when combined with parent vessel remodeling with stents. Stents provide the scaffold for endothelial growth and vessel healing. Besides metallic coverage that disrupts the flow into an aneurysm, the hemodynamic changes secondary to stent-induced alteration in vessel geometry can also reduce the inflow. From our limited experience, it appears that the light flow-diverter effect of the stent complements the intrasaccular flow disruption by the WEB.

Notwithstanding the limitations of the small sample size and the anecdotal nature of this case series, exclusive intrasaccular flow disruption does not seem to be an appropriate treatment for partially thrombosed intracranial aneurysms. Although the mechanism is not clear, it can probably have an unfavorable influence on the natural history of this disease, which has not been reported before with other treatment options. However, combining intrasaccular flow disruption with adjunctive stent placement may be a novel method of treating this complex disease with favorable long-term outcome. Further research is required to better evaluate this endovascular therapeutic option for partially thrombosed intracranial aneurysms.

Disclosures: Anthony J.P. Goddard—UNRELATED: Consultancy: Codman, Comments: for stent retriever development work, educational lectures, and advice on product development; Payment for Lectures (including service on Speakers Bureaus): Codman; Travel/Accommodations/Meeting Expenses Unrelated to Activities Listed: Codman, Stryker, Comments: travel to international meetings along with accommodations. Tunil Patankar—UNRELATED: Payment for Lectures (including service on Speakers Bureaus): Medtronic, Sequent Medical, Comments: lecture at Medtronic annual meeting; Travel/Accommodations/Meeting Expenses Unrelated to Activities Listed: Sequent Medical, Comments: Travel grant to present at Val d'Isere, France, 2013, and Cerebrovascular Complications Conference meeting, Jackson Hole, Wyoming, 2014; Other: proctor for Sequent Medical, Codman, and Stryker, Comments: proctor for the WEB and the PulseRider and Surpass stents.

## REFERENCES

1. Krings T, Alvarez H, Reinacher P, et al. **Growth and rupture mechanism of partially thrombosed aneurysms.** *Interv Neuroradiol* 2007; 13:117–26 Medline
2. Roccatagliata L, Guédin P, Condette-Auliac S, et al. **Partially thrombosed intracranial aneurysms: symptoms, evolution, and therapeutic management.** *Acta Neurochir (Wien)* 2010;152:2133–42 CrossRef Medline

3. van Rooij WJ, Sluzewski M. **Unruptured large and giant carotid artery aneurysms presenting with cranial nerve palsy: comparison of clinical recovery after selective aneurysm coiling and therapeutic carotid artery occlusion.** *AJNR Am J Neuroradiol* 2008;29:997–1002 CrossRef Medline
4. Papagiannaki C, Spelle L, Januel AC, et al. **WEB intrasaccular flow disruptor: prospective, multicenter experience in 83 patients with 85 aneurysms.** *AJNR Am J Neuroradiol* 2014;35:2106–11 CrossRef Medline
5. Pierot L, Liebig T, Sychra V, et al. **Intrasaccular flow-disruption treatment of intracranial aneurysms: preliminary results of a multicenter clinical study.** *AJNR Am J Neuroradiol* 2012;33:1232–38 CrossRef Medline
6. Black SP, German WJ. **Observations on the relationship between the volume and the size of the orifice of experimental aneurysms.** *J Neurosurg* 1960;17:984–90 CrossRef Medline
7. Schubiger O, Valavanis A, Wichmann W. **Growth-mechanism of giant intracranial aneurysms: demonstration by CT and MR imaging.** *Neuroradiology* 1987;29:266–71 CrossRef Medline
8. Cho YD, Park JC, Kwon BJ, et al. **Endovascular treatment of largely thrombosed saccular aneurysms: follow-up results in ten patients.** *Neuroradiology* 2010;52:751–58 CrossRef Medline
9. Yang K, Park JC, Ahn JS, et al. **Characteristics and outcomes of varied treatment modalities for partially thrombosed intracranial aneurysms: a review of 35 cases.** *Acta Neurochir (Wein)* 2014;156:1669–75 CrossRef Medline
10. Ferns S, van Rooij W, Sluzewski W, et al. **Partially thrombosed intracranial aneurysms presenting with mass effect: long-term clinical and imaging follow-up after endovascular treatment.** *AJNR Am J Neuroradiol* 2010;31:1197–205 CrossRef Medline
11. Cekirge HS, Yavuz K, Geyik S, et al. **A novel “Y” stent flow diversion technique for the endovascular treatment of bifurcation aneurysms without endosaccular coiling.** *AJNR Am J Neuroradiol* 2011;32:1262–68 CrossRef Medline
12. Fischer S, Vajda Z, Aguilar Perez M, et al. **Pipeline embolization device (PED) for neurovascular reconstruction: initial experience in the treatment of 101 intracranial aneurysms and dissections.** *Neuroradiology* 2012;54:369–82 CrossRef Medline
13. Mine B, Pierot L, Lubicz B. **Intrasaccular flow-diversion for treatment of intracranial aneurysms: the Woven EndoBridge.** *Expert Rev Med Devices* 2014;11:315–25 CrossRef Medline
14. Kulcsár Z, Houdart E, Bonafé A, et al. **Intra-aneurysmal thrombosis as a possible cause of delayed aneurysm rupture after flow-diversion treatment.** *AJNR Am J Neuroradiol* 2011;32:20–25 CrossRef Medline

# Different Functional and Microstructural Changes Depending on Duration of Mild Cognitive Impairment in Parkinson Disease

N.-Y. Shin, Y.S. Shin, P.H. Lee, U. Yoon, S. Han, D.J. Kim, and S.-K. Lee



## ABSTRACT

**BACKGROUND AND PURPOSE:** The higher cortical burden of Lewy body and Alzheimer disease–type pathology has been reported to be associated with a faster onset of cognitive impairment of Parkinson disease. So far, there has been a few studies only about the changes of gray matter volume depending on duration of cognitive impairment in Parkinson disease. Therefore, our aim was to evaluate the different patterns of structural and functional changes in Parkinson disease with mild cognitive impairment according to the duration of parkinsonism before mild cognitive impairment.

**MATERIALS AND METHODS:** Fifty-nine patients with Parkinson disease with mild cognitive impairment were classified into 2 groups on the basis of shorter (<1 year,  $n = 16$ ) and longer ( $\geq 1$  year,  $n = 43$ ) durations of parkinsonism before mild cognitive impairment. Fifteen drug-naïve patients with de novo Parkinson disease with intact cognition were included for comparison. Cortical thickness, Tract-Based Spatial Statistics, and seed-based resting-state functional connectivity analyses were performed. Age, sex, years of education, age at onset of parkinsonism, and levodopa-equivalent dose were included as covariates.

**RESULTS:** The group with shorter duration of parkinsonism before mild cognitive impairment showed decreased fractional anisotropy and increased mean and radial diffusivity values in the frontal areas compared with the group with longer duration of parkinsonism before mild cognitive impairment (corrected  $P < .05$ ). The group with shorter duration of parkinsonism before mild cognitive impairment showed decreased resting-state functional connectivity in the default mode network area when the left or right posterior cingulate was used as a seed, and in the dorsolateral prefrontal areas when the left or right caudate was used as a seed (corrected  $P < .05$ ). The group with longer duration of parkinsonism before mild cognitive impairment showed decreased resting-state functional connectivity mainly in the medial prefrontal cortex when the left or right posterior cingulate was used as a seed, and in the parieto-occipital areas when the left or right caudate was used as a seed (corrected  $P < .05$ ). No differences in cortical thickness were found in all group contrasts.

**CONCLUSIONS:** Resting-state functional connectivity and WM alterations might be useful imaging biomarkers for identifying changes in patients with Parkinson disease with mild cognitive impairment according to the duration of parkinsonism before mild cognitive impairment. The functional and microstructural substrates may topographically differ depending on the rate of cognitive decline in these patients.

**ABBREVIATIONS:** AD = Alzheimer disease; DMN = default mode network; MCI = mild cognitive impairment; PCC = posterior cingulate cortex; PD = Parkinson disease; PD-IC = PD with intact cognition; PD-MCI = PD with mild cognitive impairment; PD-MCI-LD = PD-MCI with  $\geq 1$  year of parkinsonism prior to MCI; PD-MCI-SD = PD-MCI with <1 year of parkinsonism prior to MCI; RSFC = resting-state functional connectivity

Parkinson disease (PD) has been considered, until recently, primarily a motor disorder. It is now recognized that a substantial portion of patients with PD have measurable cognitive deficits ranging from mild cognitive impairment (PD-

MCI) to dementia.<sup>1,2</sup> Although the exact pathologic substrates for cognitive impairment in PD are still under debate, limbic and cortical Lewy body– and Alzheimer disease (AD)–type pathology have been suggested as the main contributors to

Received July 20, 2015; accepted after revision October 26.

From the Department of Radiology (N.-Y.S.), Ewha Womans University School of Medicine, Seoul, Korea; Department of Psychology (Y.S.S., S.H.), Yonsei University, Seoul, Korea; Departments of Neurology (P.H.L.) and Radiology (N.-Y.S., D.J.K., S.-K.L.), Yonsei University College of Medicine, Seoul, Korea; and Department of Biomedical Engineering (U.Y.), College of Health and Medical Science, Catholic University of Daegu, Gyeongsan-si, South Korea.

Please address correspondence to Seung-Koo Lee, MD, PhD, Department of Radiology, Yonsei University College of Medicine, Integrated Neurocognitive Functional Imaging Center, Yonsei University, Seoul, Korea, 50-1 Yonsei-ro, Seodaemun-gu, Seoul 120-752, Korea; e-mail: slee@yuhs.ac

 Indicates article with supplemental on-line appendix and tables.

 Indicates article with supplemental on-line photos.

<http://dx.doi.org/10.3174/ajnr.A4626>

PD-MCI<sup>3-6</sup> as well as PD with dementia.<sup>7-9</sup> In terms of the rate of cognitive decline, a higher burden of these cortical pathologies<sup>9,10</sup> has been reported associated with a faster onset of cognitive impairment in PD.

In contrast to pathologic studies, imaging studies are noninvasive and useful for discovering biomarkers in living humans. However, only a few structural imaging studies<sup>11,12</sup> have been conducted thus far to define anatomic candidates influencing the rate of cognitive decline in PD. These studies have revealed atrophy of the posterior cingulate cortex (PCC)<sup>11</sup> and inferior parietal and orbitofrontal areas<sup>12</sup> in patients with PD with shorter durations of parkinsonism before dementia and MCI, compared with those with longer durations of parkinsonism. These regions show considerable overlap with the default mode network (DMN), which is well-known to be disrupted in patients with AD.<sup>13</sup> Some authors have suggested that impairment of axonal transport causes accumulation of axonally transported substances followed by cortical Lewy body formation.<sup>14,15</sup> In other words, alterations in WM, such as swelling and degeneration of the axonal projections, may precede cortical atrophy. Functional imaging is a more sensitive biomarker that detects earlier stages of disease than that seen structurally for both AD and PD.<sup>16-18</sup> However, there has been no study on the changes in WM integrity or resting-state functional connectivity (RSFC) according to the duration of parkinsonism before cognitive impairment in PD.

Therefore, we aimed to determine the structural and functional changes in patients with PD-MCI according to the duration of parkinsonism before MCI. During the resting-state fMRI analysis, we particularly focused on the DMN, which is highly associated with cognitive dysfunction in patients with AD<sup>13</sup> and other neurodegenerative disorders.<sup>19</sup> Furthermore, we also analyzed the corticostriatal loop, which is considered one of the primary areas of cognitive dysfunction in patients with PD.<sup>17</sup>

## MATERIALS AND METHODS

### Subjects

This retrospective study was approved by the Yosei University Health System institutional review board, and a waiver of informed consent was obtained. The patients were selected from a prospectively collected single-institution movement disorders and dementia outpatient clinic data base. From August 2011 to February 2014, consecutive patients with PD who underwent both MR imaging and neuropsychological tests within a 2-month interval were recruited. PD was diagnosed according to the clinical diagnostic criteria of the United Kingdom Parkinson's Disease Society Brain Bank.<sup>20</sup>

Assessment of parkinsonian motor symptoms was performed by using the Unified Parkinson's Disease Rating Scale, Part III. Total medication dosages for PD were calculated in levodopa equivalents.<sup>21</sup> The self-rating Beck Depression Inventory was used to assess depressive symptoms in patients with PD.<sup>22</sup> Patients with focal brain lesions, diffuse white matter hyperintensities outside the normal range, or multiple lacunar infarcts in the basal ganglia on MR imaging were excluded. Patients with other neurodegenerative diseases and medical comorbidities that might account for cognitive dysfunction were also excluded. Only patients who displayed decreased dopamine transporter uptake in

the posterior putamen on a [<sup>18</sup>F] N-3-fluoropropyl-2- $\beta$ -carboxymethoxy-3- $\beta$ -(4-iodophenyl) nortropane (FP-CIT) PET scan were included in this study, to ensure clinical diagnostic accuracy.

Information about memory problems or other subjective cognitive deficits was gathered by interviews with the patients or caregivers. The cognitive status diagnosis in patients with PD was assigned by consensus among 2 neurologists and 1 neuropsychologist on the basis of a neuropsychological battery and the physician-administered neurologic examination. The Seoul Neuropsychological Screening Battery was used to determine the cognitive status,<sup>23</sup> and its details are described in On-line Appendix 1. According to the diagnostic criteria recommended by the Movement Disorder Society Task Force,<sup>24</sup> PD-MCI was diagnosed when results of at least 2 tests for each of the attention, executive, memory, and visuospatial function domains, except for the language domain (level 2), or in 5 domains (level 1) were abnormal. Patients with PD-MCI were split into 2 groups by disease duration before MCI: PD-MCI with <1 year of parkinsonism before MCI (PD-MCI-SD) and PD-MCI with  $\geq$ 1 year of parkinsonism before MCI (PD-MCI-LD). Drug-naïve patients with de novo PD with intact cognition (PD-IC) were also included as control group.

### Image Acquisition

All scans were acquired by using a 3T scanner (Achieva; Philips Healthcare, Best, the Netherlands) with a 32-channel head coil. Head motion was minimized with restraining foam pads provided by the manufacturer.

**Structural Image Acquisition.** We used a 3D-T1-turbo field echo sequence with the following parameters: axial acquisition with FOV = 220 mm; voxel size =  $0.98 \times 0.98 \times 1.2$  mm<sup>3</sup>; TE = 4.6 ms; TR = 9.6 ms; flip angle = 8°; section gap = 0 mm; and total acquisition time = 5 minutes 29.3 seconds.

**DTI Acquisition.** A single-shot EPI acquisition was performed with the following parameters: FOV = 220 mm; voxel size =  $1.72 \times 1.72 \times 2$  mm<sup>3</sup>; TE = ~70 ms; TR = ~8000 ms; flip angle = 90°; section gap = 0 mm; NEX = 1; b factor = 600 s/mm<sup>2</sup>; noncardiac gating; and 70 axial sections. We acquired diffusion-weighted images from 32 noncollinear, noncoplanar directions with a baseline image without diffusion-weighting. Total acquisition time was 5 minutes 44.6 seconds.

**Resting-State fMRI Acquisition.** We used a T2\*-weighted single-shot EPI sequence. For each subject, 165 axial volume scans were obtained with the following parameters: FOV = 220 mm<sup>2</sup>; voxel size =  $2.75 \times 2.75 \times 4.5$  mm<sup>3</sup>; TE = 30 ms; TR = 2000 ms; and section number = 31 (interleaved). During each scan, subjects were instructed to rest and keep their eyes closed without moving, sleeping, or thinking about anything in particular for 5 minutes 38 seconds.

### Image Analysis

**Cortical Thickness Analysis.** Automated anatomic pipeline image processing steps were applied for cortical thickness measurement by using T1-weighted images. Details for measuring cortical

thickness are described in On-line Appendix 2. The localized regional differences of cortical thickness among groups were analyzed by applying ANCOVA, with age, sex, years of education, age at onset of parkinsonism, and levodopa-equivalent dose entered as covariates.

**Tract-Based Spatial Statistics Analysis.** DTI data preprocessing was performed by using the FMRIB Software Library (FSL; <http://www.fmrib.ox.ac.uk/fsl>) program. Details for Tract-Based Spatial Statistics (<http://fsl.fmrib.ox.ac.uk/fsl/fslwiki/TBSS>) analysis are described in On-line Appendix 3. In the ANCOVA analysis, age, sex, years of education, age at onset of parkinsonism, and levodopa-equivalent dose were included as covariates.

**Seed-Based RSFC Analysis.** Data were first preprocessed according to the Data Processing Assistant for Resting-State fMRI toolbox (<http://www.restfmri.net>) preprocessing pipeline implemented in Matlab (MathWorks, Natick, Massachusetts). Images were corrected for section timing, realigned, normalized by using the EPI template provided by SPM8 software (<http://www.fil.ion.ucl.ac.uk/spm/software/spm8>), and smoothed by using a 4-mm full width at half maximum Gaussian kernel. After normalization, to remove long-term drift and irrelevant oscillations in the signal, we detrended and bandpass filtered (0.01–0.08 Hz) data. Nuisance covariates, including head-motion parameters, global mean signals, WM signals, and CSF signals, were regressed out.

To perform seed-based analysis, an Automated Anatomical Labeling template (<http://www.gin.cnrs.fr/AAL>) defined 90 seed ROIs. Among them, 4 ROI seeds were selected to study the association of cognition and resting-state functional networks in patients with PD. First, the bilateral PCC seeds were chosen to investigate alterations within the DMN. Second, the bilateral caudate seeds, which are known to be key subcortical structures in the cognitive corticostriatal loop, were also selected. RSFC from each ROI seed was estimated and used to configure a statistical map. Two sample *t* tests were performed on each pair of the group's statistical images by using the SPM8 toolbox. The assumptions of unequal variance and independence among all groups were made on *t* tests. To exclude possible confounding factors, we covariated out age, sex, years of education, age at onset of parkinsonism, and levodopa-equivalent doses in the statistical test after normalization across 2 groups of interest by using the *z* score function in Matlab. The threshold for statistical analysis was set to corrected  $P < .05$  by using the Monte Carlo simulations with custom software implemented in Matlab.<sup>25</sup>

### **Correlation Analysis**

Two-tailed Pearson correlation analyses were performed to assess the relationship between the duration of parkinsonism before MCI and RSFCs, which showed remarkable differences between the PD-MCI-SD and PD-MCI-LD groups (left hippocampus and left medial frontal gyrus with the left PCC seed and left middle frontal gyrus with the left caudate seed). For each ROI, *z* values were extracted from correlation maps with a 4-mm radius sphere centered at the peak. Then, the correlation coefficients between the *z* values and the patients' duration of parkinsonism before MCI were computed.

### **Statistical Analysis**

Clinical characteristics and neuropsychological data were compared among the 3 groups. The Kolmogorov-Smirnov test was used to determine whether the data were normally distributed. Accordingly, data that had normal distribution are presented as means  $\pm$  SDs, and quantitative variables were compared by using an ANOVA. Otherwise, for comparing quantitative values, data are presented as medians with ranges and the Kruskal-Wallis test was used. Qualitative data were analyzed by using the  $\chi^2$  test or Fisher exact test when appropriate. Post hoc analysis was also performed by using a Bonferroni-corrected Student *t* test, Mann-Whitney *U* test,  $\chi^2$  test, or Fisher exact test when appropriate with correction for multiple comparisons. Statistical analyses were performed by using SPSS, Version 19.0 (IBM, Armonk, New York), and 2-tailed  $P < .05$  was considered significant.

## **RESULTS**

### **Demographic and Clinical Characteristics**

Among 239 patients with PD who underwent both MR imaging and neuropsychological tests, 59 patients with PD-MCI who met the inclusion criteria were analyzed in this study. Fifteen drug-naïve patients with de novo PD with intact cognition were also included for comparison. The demographic and clinical data of the patients are summarized in Table 1. The median duration of parkinsonism in the PD-MCI-SD group ( $n = 16$ ) was 5 months and it was 25 months in the PD-MCI-LD group ( $n = 43$ ). Patients in the PD-MCI-SD group had significantly older age at onset than those in the PD-MCI-LD group ( $68.5 \pm 7.3$  years versus  $61.6 \pm 9.0$  years;  $P = .016$ ). No significant differences were found in neuropsychological data between the 2 PD-MCI groups (On-line Table 1).

### **Group Comparisons of Cortical Thickness**

No difference in cortical thickness was found among all groups.

### **Group Comparisons of WM Alterations**

Compared with the de novo PD-IC group, the PD-MCI-SD group showed increased mean diffusivity in the bilateral anterior and superior corona radiata, genu and body of corpus callosum, right cingulum, and right superior longitudinal fasciculus and increased radial diffusivity in the right anterior and superior corona radiata, genu and body of the corpus callosum, right cingulum, and right superior longitudinal fasciculus (On-line Fig 1). The PD-MCI-LD group did not show significant WM alterations compared with the PD-IC group. In direct comparison between the PD-MCI-SD and PD-MCI-LD groups, the PD-MCI-SD group showed significantly decreased fractional anisotropy values in the right superior longitudinal fasciculus and corticospinal tract compared with the PD-MCI-LD group. More extensive changes were found in mean diffusivity and radial diffusivity values, showing a significant increase in the bilateral anterior and superior corona radiata, bilateral superior longitudinal fasciculus, genu and body of corpus callosum, right cingulum, and anterior and posterior limbs of the right internal capsule in the PD-MCI-SD group (Fig 1). No significant difference was found in axial diffusivity among groups.

**Table 1: Demographic and clinical characteristics of the patients<sup>a</sup>**

	De Novo PD-IC (n = 15)	PD-MCI-SD (n = 16)	PD-MCI-LD (n = 43)	P Value <sup>b</sup>	Post Hoc Analysis		
					P1 <sup>c</sup>	P2 <sup>d</sup>	P3 <sup>e</sup>
Age (yr)	65.7 ± 6.4	69.1 ± 7.2	64.9 ± 8.9	.221	–	–	–
Age at onset (yr)	64.9 ± 6.5	68.5 ± 7.3	61.6 ± 9.0	.017	.672	.555	.016
Male (No.) (%)	6 (40.0)	8 (50.0)	17 (39.5)	.604	–	–	–
Education duration (yr)	10.6 ± 4.7	8.8 ± 4.2	9.5 ± 5.2	.598	–	–	–
Parkinsonism duration (mo) (median) (range)	11 (2–18)	5 (1–11)	25 (12–120)	<.001	.015	<.001	<.001
UPDRS III	19.1 ± 8.3	25.4 ± 8.8	25.6 ± 11.2	.100	–	–	–
K-MMSE	28.6 ± 1.2	26.3 ± 1.5	26.9 ± 2.1	.002	.003	.009	.899
Levodopa-equivalent dose (mg) (median) (range)	0.0 (0.0–0.0)	0.0 (0.0–360.0)	25.0 (0.0–1050.0)	.008	.030	.006	1.000
BDI	11.7 ± 7.6	14.1 ± 8.7	14.8 ± 10.2	.543	–	–	–
Interval between MRI scan and NP test (day) (median) (range)	0 (0–34)	0 (0–49)	0 (0–50)	.266	–	–	–

**Note:**—BDI indicates Beck Depression Inventory; K-MMSE, the Korean version of the Mini-Mental State Examination; NP test, neuropsychological test; UPDRS III, Unified Parkinson's Disease Rating Scale, Part III; –, not significant.

<sup>a</sup> Unless otherwise indicated, data are means.

<sup>b</sup> P values for comparison among 3 groups.

<sup>c</sup> P values for comparison between de novo PD-IC and PD-MCI-SD groups.

<sup>d</sup> P values for comparison between de novo PD-IC and PD-MCI-LD groups.

<sup>e</sup> P values comparison between PD-MCI-SD and PD-MCI-LD groups.

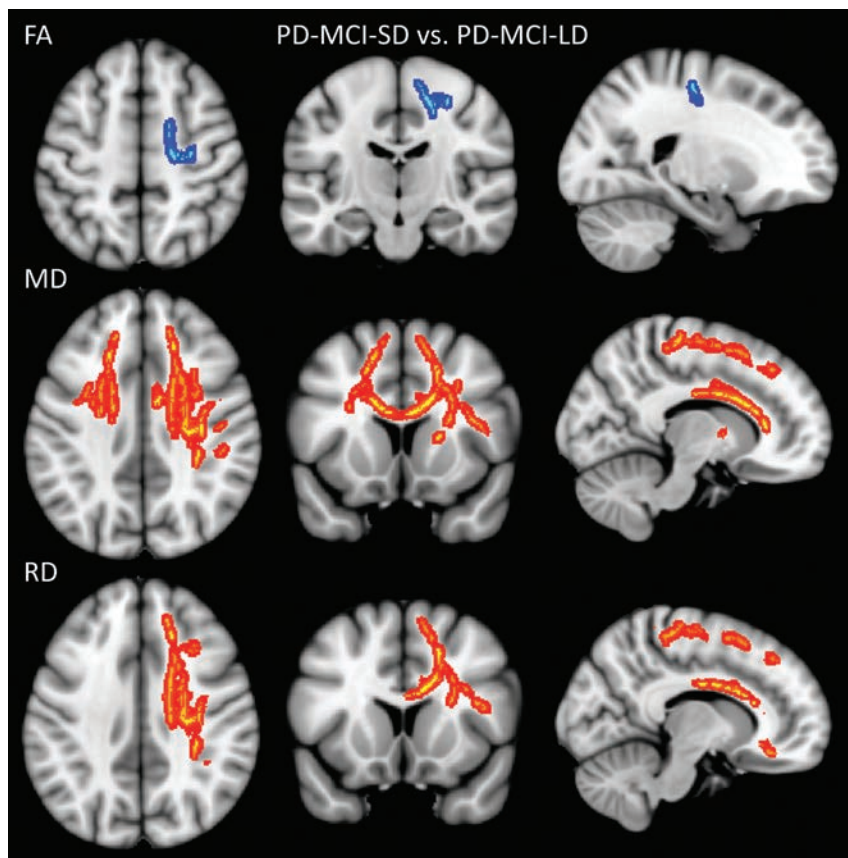


**FIG 1.** Tract-Based Spatial Statistics analysis in the PD-MCI groups. Warm colors indicate increased DTI values, and cool colors indicate decreased DTI values in the PD-MCI-SD group compared with PD-MCI-LD group ( $P < .05$ , family-wise error–corrected). Images are oriented according to neurological convention (right is right).

#### Group Comparisons of RSFC by Using the PCC Seeds

Compared with the de novo PD-IC group, the PD-MCI-SD group showed decreased RSFC in the parahippocampal gyrus, dorsolateral prefrontal areas, temporal areas, and precuneus, whereas increased RSFC was seen in the inferior frontal areas, primary motor area, and

occipital areas. The PD-MCI-LD group showed decreased RSFC in the medial frontal areas and middle cingulate cortex, while increased RSFC was seen mainly in the parietal and occipital areas, compared with the de novo PD-IC group. In direct comparison between the PD-MCI-SD and PD-MCI-LD groups, the PD-MCI-SD group showed decreased RSFC in the hippocampus, parietal areas, cuneus, and thalamus; on the contrary, the PD-MCI-LD group showed decreased RSFC in the medial and inferior frontal areas, primary motor area, cingulate cortex, inferior temporal area, and insula (Fig 2A, -B; On-line Fig 2 and On-line Table 2).

#### Group Comparison of RSFC by Using the Caudate Seeds

Compared with the de novo PD-IC group, the PD-MCI-SD group exhibited decreased RSFC in the putamen, temporal areas, precuneus, and insula and increased RSFC in the primary sensory motor areas. On the other hand, the PD-MCI-LD group showed decreased RSFC in the occipital area and thalamus and increased RSFC in the frontal areas, including the primary and supplementary motor areas, hippocampus/parahippocampal gyrus and other temporal areas, and the supramarginal gyri. In direct comparison between the PD-MCI-SD and PD-MCI-LD groups, the PD-MCI-SD group showed decreased RSFC in the putamen, globus pallidus, frontal and temporal areas, middle cingulate cortex, and insula, while the PD-MCI-LD group showed decreased RSFC mainly in the pari-

etal and occipital areas (Fig 2C, -D; On-line Fig 3 and On-line Table 3).

### Correlation Analysis

The RSFC between the left caudate and left middle frontal gyrus (Montreal Neurological Institute coordinates  $[-36, 33, 33]$ ) was significantly correlated with the duration of parkinsonism before MCI ( $r = 0.292, P = .025$ ). RSFCs between the left PCC and left hippocampus (Montreal Neurological Institute coordinates  $[-24, -36, -3]$ ) and the left PCC and left medial frontal gyrus (Montreal Neurological Institute coordinates  $[-6, 54, 24]$ ) were not significantly correlated with the duration of parkinsonism before MCI (Fig 3).

### DISCUSSION

The present study examined the different patterns of structural and functional changes in patients with PD-MCI according to the

duration of parkinsonism before MCI. First, the PD-MCI-SD group showed decreased frontostriatal RSFC, which was correlated with the duration of parkinsonism before MCI, and impaired frontal WM integrity compared with the PD-MCI-LD group. Second, the pattern of RSFC was topographically different between the 2 groups. The PD-MCI-SD group showed decreased RSFC in the DMN, while the PD-MCI-LD group showed decreased RSFC in the medial frontal areas with the PCC seeds. Third, no difference was found in cortical thickness among all group contrasts.

As mentioned earlier, the PD-MCI-SD group showed not only decreased frontostriatal RSFC but also decreased fractional anisotropy values and increased mean diffusivity and radial diffusivity values in the frontal WM compared with the PD-MCI-LD group. These functional and microstructural differences might be attributable to both striatal<sup>26,27</sup> and frontal<sup>28,29</sup> pathologies. Recently, some pathologic studies have suggested striatal  $\beta$ -amyloid<sup>26</sup> or  $\alpha$ -synuclein<sup>27</sup> deposits as a primary substrate for subcortical dementia in PD. Moreover, a higher degree of amyloid deposits in the striatum was found in patients with dementia with Lewy bodies than in those with PD with dementia, suggesting the possible role of amyloid deposition in the acceleration of cognitive decline in  $\alpha$ -synuclein-related cognitive disorders.<sup>30</sup> A previous imaging study also showed atrophy of the caudate nucleus and frontal cortex in patients with PD-MCI who subsequently converted to PD with dementia compared with those without conversion to PD with dementia.<sup>31</sup> Furthermore, our results showed that frontostriatal RSFC had significant correlation with the duration of parkinsonism before MCI. In other words, patients with more disrupted RSFC among these areas had MCI with a shorter interval after the onset of motor symptoms. Although the effort to determine which substrate has a primary role in accelerat-

ion of cognitive decline in  $\alpha$ -synuclein-related cognitive disorders.<sup>30</sup> A previous imaging study also showed atrophy of the caudate nucleus and frontal cortex in patients with PD-MCI who subsequently converted to PD with dementia compared with those without conversion to PD with dementia.<sup>31</sup> Furthermore, our results showed that frontostriatal RSFC had significant correlation with the duration of parkinsonism before MCI. In other words, patients with more disrupted RSFC among these areas had MCI with a shorter interval after the onset of motor symptoms. Although the effort to determine which substrate has a primary role in accelerat-

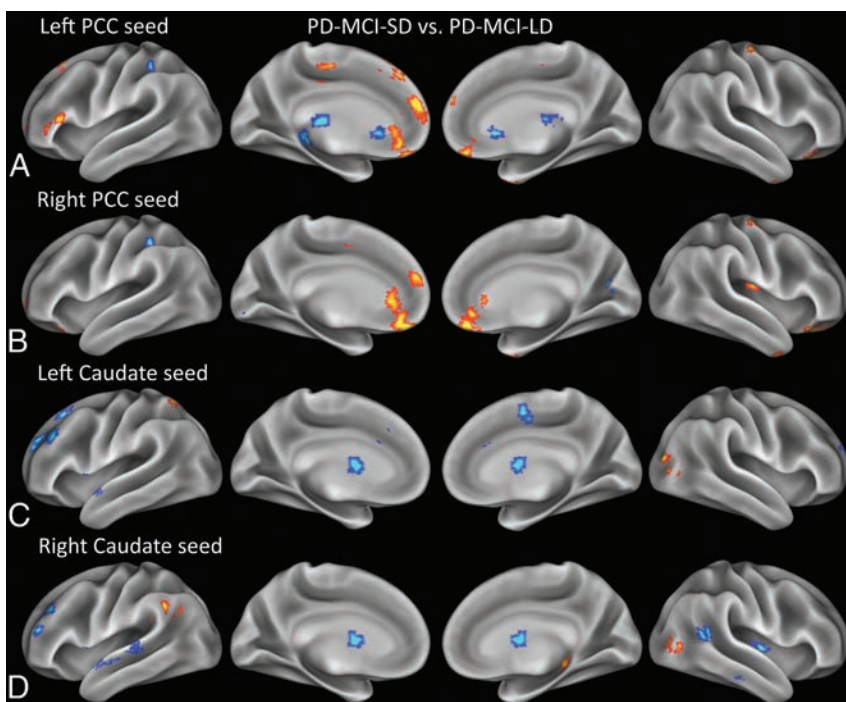


**FIG 2.** RSFC analysis in the PD-MCI groups by using the PCC and caudate as a seed. Warm colors indicate increased connectivity, and cool colors indicate decreased connectivity in PD-MCI-SD group compared with PD-MCI-LD group. All demonstrated clusters are significant at a  $P < .05$  level, with correction for multiple comparisons.

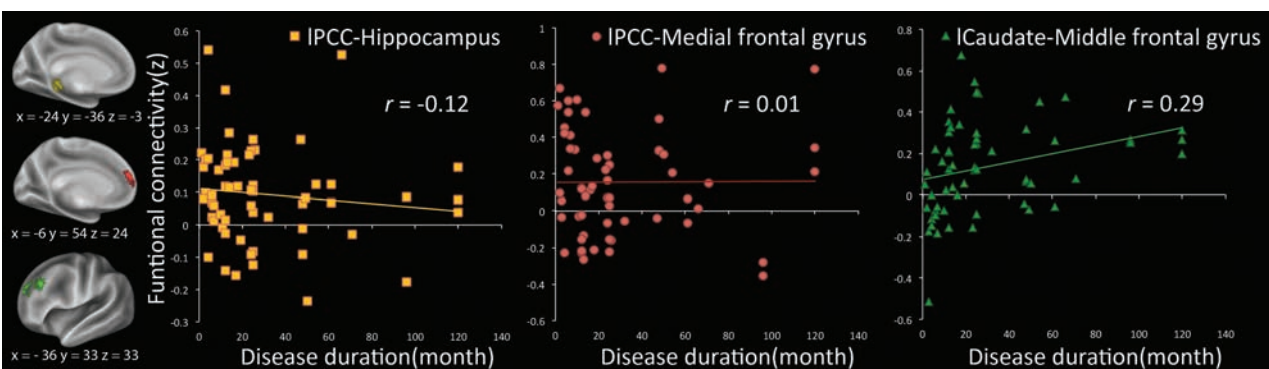


**FIG 3.** Correlation graph between the duration of parkinsonism before MCI and each ROI. The duration of parkinsonism before MCI is significantly correlated with only RSFC between the left caudate and left middle frontal gyrus ( $P = .025$ ).

ing cognitive decline should be continued, functional or microstructural alterations in the frontostriatal circuit may be a useful imaging biomarker for more rapid cognitive decline in patients with PD-MCI.

Compared with the PD-MCI-LD group, the PD-MCI-SD group also showed decreased RSFC in the DMN, including the hippocampus and inferior parietal lobule when PCC was used as a seed. Our results are in line with those in previous reports. According to previous imaging studies, patients with a shorter duration of parkinsonism before cognitive impairment in PD with dementia and PD-MCI had decreased GM volume in the PCC<sup>11</sup> and in the inferior parietal and orbitofrontal areas,<sup>12</sup> respectively. These areas substantially overlap with the DMN, which is susceptible to decline in patients with AD.<sup>13</sup> Moreover, a recent study reported AD pattern atrophy involving the hippocampus and temporal-parietal cortex as a predictor for 2-year future cognitive decline in PD,<sup>32</sup> suggesting that an AD imaging pattern is an important predictor for more rapid cognitive decline. Decreased RSFC between the PCC and the hippocampus has been observed in early AD and MCI.<sup>13,33</sup> In AD, tauopathy involving the medial temporal lobe, including the hippocampus, is considered a possible cause of the decreased connectivity.<sup>34</sup> Although this finding is less clear in PD,<sup>17,18</sup> pathologic evidence has suggested that the degree of Lewy body,<sup>35</sup> Lewy neurite,<sup>36</sup>  $\beta$ -amyloid, or neurofibrillary tangle deposit<sup>37</sup> in the entorhinal cortex or hippocampus is associated with cognitive dysfunction.

Most interesting, the PD-MCI-LD group had decreased RSFC primarily in the medial frontal areas and cingulate when using the PCC seeds compared with the PD-MCI-SD group. Braak et al<sup>38</sup> reported sequential topographic extension of Lewy neurite and Lewy body deposits in PD, with these areas showing substantial overlap with the affected areas in stage 5, which is the first stage of neocortical involvement. One pathologic study<sup>39</sup> found that among the patients who remained without dementia for a long time, the patients who had longer disease durations until death had more extensive Lewy body deposits, consistent with the PD stage of Braak et al. These patients had no or a low AD pathology burden. Therefore, decreased RSFC in these areas might be associated with cortical PD pathology accumulated for longer disease durations in the PD-MCI-LD group relative to the PD-MCI-SD group. In addition, when the caudate seeds were used, the PD-MCI-LD group showed decreased RSFC in mainly parieto-occipital areas compared with the PD-MCI-SD group. These areas, which are cognitive- and action-specific domains, have functional connection with the caudate tail, while the caudate head has a stronger functional connection with the prefrontal areas.<sup>40</sup> Further pathologic study is warranted to define different topographic areas involved within the caudate between the 2 groups.

Our study has several limitations. First, our cohort was not pathologically proved to have PD. Instead, we used dopamine transporter imaging to reduce the possibility of misdiagnosis. Second, the diagnosis of PD-MCI in this study did not fully satisfy the level 2 criteria of the Movement Disorder Society Task Force guideline for some patients.<sup>24</sup> Therefore, the possibility of patients with false-positive diagnoses in the PD-MCI group cannot be excluded. Third, although only the patients who underwent both MR imaging and neuropsychological tests within a 2-month

interval were included, there were 1- to 50-day intervals in 21 patients in our cohort. While the cognitive state might not change during this relatively short period, this range of intervals might have affected the results. Fourth, because we used seed-based RSFC analysis with only PCC and caudate seeds, the role of the remaining areas for cognitive decline rates could have been missed in patients with PD. Moreover, recent studies have suggested that dorsal attention<sup>41</sup> and frontoparietal networks<sup>41,42</sup> are associated with cognitive dysfunction in patients with PD-MCI. Therefore, future study with a data-driven approach of the whole brain should be conducted to consolidate our results and find other relevant networks influencing the cognitive decline rate in these patients. Fifth, it is still unclear what RSFC and DTI values exactly represent in the brain. Therefore, caution is needed to interpret our results until underlying pathologic evidence is elucidated. Finally, this study is a cross-sectional one, so our findings cannot be applied to predict the rate of development of cognitive decline. A prospective study with regular follow-up with comprehensive neuropsychological testing is warranted. However, we compared each PD-MCI group with the de novo PD-IC group, and areas showing decreased RSFC in these comparisons were similar to those in direct comparison between the 2 PD-MCI groups. Therefore, we hope that our results can provide an a priori hypothesis for future studies to define imaging biomarkers for the cognitive decline rate in drug-naïve patients with de novo PD-IC.

## CONCLUSIONS

Our results indicate that changes in RSFC and WM integrity in PD-MCI according to the duration of parkinsonism before MCI are more sensitive imaging biomarkers than cortical thickness. We also found topographically different functional and microstructural substrates corresponding to the timing of MCI in PD-MCI.

## REFERENCES

1. Emre M, Aarsland D, Brown R, et al. **Clinical diagnostic criteria for dementia associated with Parkinson's disease.** *Mov Disord* 2007;22:1689–707; quiz 837 Medline
2. Litvan I, Aarsland D, Adler CH, et al. **MDS Task Force on mild cognitive impairment in Parkinson's disease: critical review of PD-MCI.** *Mov Disord* 2011;26:1814–24 CrossRef Medline
3. Adler CH, Caviness JN, Sabbagh MN, et al. **Heterogeneous neuropathological findings in Parkinson's disease with mild cognitive impairment.** *Acta Neuropathol* 2010;120:827–28 CrossRef Medline
4. Jellinger KA. **Neuropathology in Parkinson's disease with mild cognitive impairment.** *Acta Neuropathol* 2010;120:829–30; author reply 31 CrossRef Medline
5. Alves G, Brønnick K, Aarsland D, et al. **CSF amyloid-beta and tau proteins, and cognitive performance, in early and untreated Parkinson's disease: the Norwegian ParkWest study.** *J Neurol Neurosurg Psychiatry* 2010;81:1080–86 CrossRef Medline
6. Montine TJ, Shi M, Quinn JF, et al. **CSF  $\beta$ (42) and tau in Parkinson's disease with cognitive impairment.** *Mov Disord* 2010;25:2682–85 CrossRef Medline
7. Compta Y, Pereira JB, Rios J, et al. **Combined dementia-risk biomarkers in Parkinson's disease: a prospective longitudinal study.** *Parkinsonism Relat Disord* 2013;19:717–24 CrossRef Medline
8. Compta Y, Ibarretxe-Bilbao N, Pereira JB, et al. **Grey matter volume correlates of cerebrospinal markers of Alzheimer-pathology in Parkinson's disease and related dementia.** *Parkinsonism Relat Disord* 2012;18:941–47 CrossRef Medline

9. Compta Y, Parkkinen L, O'Sullivan SS, et al. **Lewy- and Alzheimer-type pathologies in Parkinson's disease dementia: which is more important?** *Brain* 2011;134:1493–505 CrossRef Medline
10. Ballard C, Ziabreva I, Perry R, et al. **Differences in neuropathologic characteristics across the Lewy body dementia spectrum.** *Neurology* 2006;67:1931–34 CrossRef Medline
11. Song SK, Lee JE, Park HJ, et al. **The pattern of cortical atrophy in patients with Parkinson's disease according to cognitive status.** *Mov Disord* 2011;26:289–96 CrossRef Medline
12. Lee JE, Cho KH, Kim M, et al. **The pattern of cortical atrophy in Parkinson's disease with mild cognitive impairment according to the timing of cognitive dysfunction.** *J Neurol* 2012;259:469–73 CrossRef Medline
13. Greicius MD, Srivastava G, Reiss AL, et al. **Default-mode network activity distinguishes Alzheimer's disease from healthy aging: evidence from functional MRI.** *Proc Natl Acad Sci U S A* 2004;101:4637–42 CrossRef Medline
14. Katsuse O, Iseki E, Marui W, et al. **Developmental stages of cortical Lewy bodies and their relation to axonal transport blockage in brains of patients with dementia with Lewy bodies.** *J Neurol Sci* 2003;211:29–35 CrossRef Medline
15. Bellucci A, Zaltieri M, Navarria L, et al. **From alpha-synuclein to synaptic dysfunctions: new insights into the pathophysiology of Parkinson's disease.** *Brain Res* 2012;1476:183–202 CrossRef Medline
16. Frisoni GB, Fox NC, Jack CR Jr, et al. **The clinical use of structural MRI in Alzheimer disease.** *Nat Rev Neurol* 2010;6:67–77 CrossRef Medline
17. Seibert TM, Murphy EA, Kaestner EJ, et al. **Interregional correlations in Parkinson disease and Parkinson-related dementia with resting functional MR imaging.** *Radiology* 2012;263:226–34 CrossRef Medline
18. Tessitore A, Esposito F, Vitale C, et al. **Default-mode network connectivity in cognitively unimpaired patients with Parkinson disease.** *Neurology* 2012;79:2226–32 CrossRef Medline
19. Fox MD, Greicius M. **Clinical applications of resting state functional connectivity.** *Front Syst Neurosci* 2010;4:19 CrossRef Medline
20. Hughes AJ, Daniel SE, Kilford L, et al. **Accuracy of clinical diagnosis of idiopathic Parkinson's disease: a clinico-pathological study of 100 cases.** *J Neurol Neurosurg Psychiatry* 1992;55:181–84 CrossRef Medline
21. Tomlinson CL, Stowe R, Patel S, et al. **Systematic review of levodopa dose equivalency reporting in Parkinson's disease.** *Mov Disord* 2010;25:2649–53 CrossRef Medline
22. Beck AT, Ward CH, Mendelson M, et al. **An inventory for measuring depression.** *Arch Gen Psychiatry* 1961;4:561–71 CrossRef Medline
23. Kang Y, Na DL. *Seoul Neuropsychological Screening Battery.* Incheon: Human Brain Research & Consulting Co; 2003
24. Litvan I, Goldman JG, Troster AI, et al. **Diagnostic criteria for mild cognitive impairment in Parkinson's disease: Movement Disorder Society Task Force guidelines.** *Mov Disord* 2012;27:349–56 CrossRef Medline
25. Slotnick SD, Moo LR, Segal JB, et al. **Distinct prefrontal cortex activity associated with item memory and source memory for visual shapes.** *Brain Res Cogn Brain Res* 2003;17:75–82 CrossRef Medline
26. Kalaitzakis ME, Graeber MB, Gentleman SM, et al. **Striatal beta-amyloid deposition in Parkinson disease with dementia.** *J Neuropathol Exp Neurol* 2008;67:155–61 CrossRef Medline
27. Tsuboi Y, Uchikado H, Dickson DW. **Neuropathology of Parkinson's disease dementia and dementia with Lewy bodies with reference to striatal pathology.** *Parkinsonism Relat Disord* 2007;13(suppl 3):S221–24 CrossRef Medline
28. Mattila PM, Rinne JO, Helenius H, et al. **Alpha-synuclein-immunoreactive cortical Lewy bodies are associated with cognitive impairment in Parkinson's disease.** *Acta Neuropathol* 2000;100:285–90 CrossRef Medline
29. Mattila PM, Røyttä M, Lönnberg P, et al. **Choline acetyltransferase activity and striatal dopamine receptors in Parkinson's disease in relation to cognitive impairment.** *Acta Neuropathol* 2001;102:160–66 Medline
30. Jellinger KA, Attems J. **Does striatal pathology distinguish Parkinson disease with dementia and dementia with Lewy bodies?** *Acta Neuropathol* 2006;112:253–60 Medline
31. Lee JE, Cho KH, Song SK, et al. **Exploratory analysis of neuropsychological and neuroanatomical correlates of progressive mild cognitive impairment in Parkinson's disease.** *J Neurol Neurosurg Psychiatry* 2014;85:7–16 CrossRef Medline
32. Weintraub D, Dietz N, Duda JE, et al. **Alzheimer's disease pattern of brain atrophy predicts cognitive decline in Parkinson's disease.** *Brain* 2012;135:170–80 CrossRef Medline
33. Zhou Y, Dougherty JH Jr, Hubner KF, et al. **Abnormal connectivity in the posterior cingulate and hippocampus in early Alzheimer's disease and mild cognitive impairment.** *Alzheimers Dement* 2008;4:265–70 CrossRef Medline
34. Smith AD. **Imaging the progression of Alzheimer pathology through the brain.** *Proc Natl Acad Sci U S A* 2002;99:4135–37 Medline
35. Kövari E, Gold G, Herrmann FR, et al. **Lewy body densities in the entorhinal and anterior cingulate cortex predict cognitive deficits in Parkinson's disease.** *Acta Neuropathol* 2003;106:83–88 Medline
36. Churchyard A, Lees AJ. **The relationship between dementia and direct involvement of the hippocampus and amygdala in Parkinson's disease.** *Neurology* 1997;49:1570–76 Medline
37. Kalaitzakis ME, Christian LM, Moran LB, et al. **Dementia and visual hallucinations associated with limbic pathology in Parkinson's disease.** *Parkinsonism Relat Disord* 2009;15:196–204 CrossRef Medline
38. Braak H, Del Tredici K, Rüb U, et al. **Staging of brain pathology related to sporadic Parkinson's disease.** *Neurobiol Aging* 2003;24:197–211 Medline
39. Halliday G, Hely M, Reid W, et al. **The progression of pathology in longitudinally followed patients with Parkinson's disease.** *Acta Neuropathol* 2008;115:409–15 CrossRef Medline
40. Robinson JL, Laird AR, Glahn DC, et al. **The functional connectivity of the human caudate: an application of meta-analytic connectivity modeling with behavioral filtering.** *Neuroimage* 2012;60:117–29 CrossRef Medline
41. Baggio HC, Segura B, Sala-Llonch R, et al. **Cognitive impairment and resting-state network connectivity in Parkinson's disease.** *Hum Brain Mapp* 2015;36:199–212 CrossRef Medline
42. Amboni M, Tessitore A, Esposito F, et al. **Resting-state functional connectivity associated with mild cognitive impairment in Parkinson's disease.** *J Neurol* 2015;262:425–34 CrossRef Medline

# Impaired Cerebrovascular Reactivity Predicts Recurrent Symptoms in Patients with Carotid Artery Occlusion: A Hypercapnia BOLD fMRI Study

S.D. Goode, N. Altaf, S. Munshi, S.T.R. MacSweeney, and D.P. Auer

## ABSTRACT

**BACKGROUND AND PURPOSE:** A key factor in predicting recurrent ischemic episodes in patients with carotid artery occlusion is the presence of hemodynamic impairment. There is, however, no consensus on how to best assess this risk in terms of imaging modalities or thresholds used. Here we investigated whether a predefined threshold of hemispheric asymmetry in hypercapnia fMRI predicts recurrent symptoms in patients with carotid artery occlusion.

**MATERIALS AND METHODS:** We studied 23 patients (2 women) with a mean age of  $67.5 \pm 9$  years. Patients were assessed for recurrent ischemic events until lost to follow-up, study end, death, or recurrent ischemic event. Hypercapnia fMRI was used to assess the cerebrovascular reserve and quantify the percentage signal change in GM in the MCA territory and the hemispheric asymmetry index. Kaplan-Meier survival analysis and log-rank tests were performed to assess differences between patients with normal or abnormal hemispheric indices.

**RESULTS:** The median follow-up was 20 months. During this period, 8 patients experienced recurrent events, and 15 did not. The percentage signal change in GM in the MCA territory was significantly decreased in those patients with recurrent events compared with those without ( $2.39 \pm 0.22$  versus  $2.70 \pm 0.42$ ,  $P = .032$ ). The normal hemispheric index predicted event-free survival during follow-up (median, 20 months) for both the combined outcome (recurrent events and/or death, log-rank,  $P = .034$ ) and recurrent retinal or ipsilateral ischemic events only (log-rank,  $P = .012$ ).

**CONCLUSIONS:** The hemispheric asymmetry index derived from hypercapnia fMRI showed hemodynamic impairment in more than half of the studied patients with carotid occlusion, and those patients showed a higher risk of recurrent ischemic symptoms.

**ABBREVIATIONS:** BET = brain extraction tool; BOLD = blood oxygen level–dependent; CAO = carotid artery occlusion; CVR = cerebrovascular reserve; IC-IC = extracranial-intracranial; ETCO<sub>2</sub> = end-tidal carbon dioxide; HAI = hemispheric asymmetry index; PSC = percentage signal change

Of the 40% of patients presenting with stroke or TIA related to carotid atherosclerotic disease, 10%–15% are found to have an occluded carotid artery.<sup>1</sup> The rate of subsequent recurrent stroke in carotid artery occlusion (CAO) has been estimated between 2.4% and 7% per year.<sup>2–4</sup> This risk persists in the face of platelet inhibitory drugs and anticoagulation.<sup>5</sup> A key factor in

predicting recurrent ischemic episodes in CAO is the presence of hemodynamic impairment, whereby patients with an exhausted cerebrovascular reserve (CVR) and therefore impaired autoregulatory capacity are at higher risk of recurrent episodes of ischemia. In the subgroup of patients with symptomatic CAO and hemodynamic impairment, the risk of recurrent stroke may be as high as 12% per year.<sup>6</sup>

Various imaging techniques enable the assessment of cerebral hemodynamic status in patients with carotid artery disease, including PET, SPECT, transcranial Doppler, and, more recently, advanced MR imaging techniques.<sup>7,8</sup> These imaging modalities probe different pathophysiologic responses to falling cerebral perfusion pressure, but there is no consensus on their relative clinical relevance. Autoregulatory vasodilation is the primary compensation for a decrease in cerebral perfusion pressure, which can be assessed by increased cerebral blood volume or reduced cerebrovascular reserve to vasodilatory stimuli. When CBF no longer meets metabolic demand, the oxygen extraction frac-

Received February 22, 2015; accepted after revision September 1.

From the Sheffield Vascular Institute (S.D.G.), Northern General Hospital, Sheffield, UK; Department of Vascular Surgery (S.D.G., N.A., S.T.R.M.), Queens Medical Centre, Nottingham, UK; Department of Stroke Medicine (S.M.), Nottingham City Hospital, Nottingham, UK; and Department of Radiological Sciences (S.D.G., N.A., D.P.A.), Sir Peter Mansfield Imaging Centre, University of Nottingham, Nottingham, UK.

This work was supported by Nottingham University Hospitals NHS Trust, Royal College of Surgeons of England.

Please address correspondence to S.D. Goode, MD, Sheffield Vascular Institute, Northern General Hospital, Sheffield S5 7AU, UK; e-mail: s.goode@sheffield.ac.uk; Dorothee P. Auer, MD, Radiological Sciences, University of Nottingham, Queens Medical Centre, Nottingham, NG7 2UH, UK; e-mail: dorothee.auer@nottingham.ac.uk

<http://dx.doi.org/10.3174/ajnr.A4739>

**Table 1: Summary details of 8 patients with recurrent symptoms**

Patient No.	Age (yr)	Sex	Presenting Symptom	Contralateral		Days to Recurrent Event		Details of Recurrent Events
				Stenosis	hAI			
1	52	M	Stroke	0–30	19.6	2	Arm weakness	
2	72	M	TIA	80–99	15.4	24	Transient episode right arm/leg weakness	
3	83	F	TIA	60–69	10.1	676	Stroke	
4	51	M	Stroke	0–30	10.8	94	Recurrent episodes of weakness/collapse	
5	54	M	Stroke	0–30	12.2	154	Multiple episodes of collapse and loss of consciousness	
6	53	M	TIA	0–30	28.1	35	Recurrent left hand and face numbness/weakness	
7	84	M	TIA	50–59	8.4	169	Recurrent weakness	
8	70	M	TIA	0–30	11.6	715	Leg weakness	

tion increases, which is considered index misery perfusion or stage II hemodynamic impairment versus stage I when the oxygen extraction fraction is intact.<sup>1</sup> The concept of sequential progression of hemodynamic impairment was later challenged,<sup>9</sup> and CVR was found more sensitive to hemodynamic white matter ischemia than the oxygen extraction fraction.<sup>10</sup> In fact, both CVR and oxygen extraction fraction abnormalities were found to predict future strokes.<sup>5,11,12</sup> While PET is considered the most reliable technique to assess hemodynamic impairment, controversies remain regarding the best quantification method and threshold,<sup>13</sup> and the high cost may be prohibitive as a screening tool.<sup>14</sup>

A reliable MR imaging–based assessment of hemodynamic impairment would be desirable because it combines the advantage of noninvasiveness with spatial mapping and no radiation, has minimal operator-dependence, and could be integrated into the routine MR imaging work-up of patients with stroke/TIA. Hypercapnia blood oxygen level–dependent (BOLD) fMRI allows the assessment of CVR with high test-retest reproducibility.<sup>15</sup> Normalized CVR metrics derived from hypercapnia BOLD fMRI were found to be sufficiently sensitive to detect hemodynamic impairment in patients with carotid artery disease and to demonstrate CVR improvement after carotid endarterectomy.<sup>8,15</sup> We do, however, lack validation studies that investigate whether and how much hypercapnia BOLD-based CVR impairment predicts recurrent events.

To address this knowledge gap, we investigated whether a predefined threshold of hemispheric asymmetry in CVR predicts recurrent symptoms in patients with CAO who had previously experienced ipsilateral symptoms during the past 12 months. The threshold of CVR impairment was derived with hemispheric asymmetry from a previous study in healthy volunteers.<sup>15</sup> We focused on patients with CAO for 2 reasons: First, in carotid occlusion, there is no ipsilateral flow in the carotid artery; therefore, potential confounding issues of embolization from proximal carotid plaque or the cardiac source can be excluded. Second, in patients with CAO for whom the efficacy of recanalization therapies lacks evidence, there is a particular need to establish validated markers of clinically relevant hemodynamic impairment.

## MATERIALS AND METHODS

### Recruitment

Patients with transient ischemic attacks or stroke were prospectively and consecutively identified for 2.5 years at the vascular clinics of a tertiary referral acute hospital trust (Nottingham University Hospital NHS Trust). Eligibility criteria included CAO on

duplex scanning. All patients had experienced stroke, TIAs, or amaurosis fugax in the past 12 months. Participants gave written informed consent, and the study was approved by the hospital research and development department and the local research ethics committee (Queens Medical Centre, Nottingham).

We studied 23 patients with a mean age of  $67.5 \pm 9$  years; there were 21 men and 2 women. The contralateral ICA was stenosed in 9 patients: 50%–59% ( $n = 1$ ), 60%–69% ( $n = 2$ ), 70%–79% ( $n = 1$ ), 80%–95% ( $n = 4$ ), and 100% ( $n = 1$ ). Patients were assessed for recurrent ischemic events from 30 days before MR imaging to loss to follow-up, study end, or death. We chose this follow-up to avoid confounds from delays between the initial clinic visit and MR imaging scheduling, to ensure that we identified recurrent symptoms following the initial clinical events leading to presentation to the TIA/stroke clinic, but before MR imaging.

Fifteen patients had only a single symptomatic event, and the remaining 8 patients had recurrent symptomatic events following their initial episode (Table 1). By study end, 3 patients had died, all from noncerebrovascular causes. Five patients underwent contralateral carotid endarterectomy and were not followed-up beyond this time point because CVR is altered following surgical revascularization.<sup>8</sup>

### Hemodynamic Assessment

All subjects were asked not to consume alcohol or caffeine for 4 hours before the scanning session. MR imaging studies were performed on a clinical 1.5T scanner (Intera; Philip Healthcare, Best, Netherlands). A standard 8-channel head coil was used for imaging, with a standard gradient-echo echo-planar sequence (TR/TE, 3500/60 ms; flip angle, 90°; matrix size, 64 × 64; FOV, 192 mm; with 33 sections, 3 mm thick and no gap). A total of 160 volumes (approximately 9-minute acquisition time) were acquired for each experiment. End-tidal carbon dioxide (ETCO<sub>2</sub>) was controlled by using a standard nonbreathing anesthetic circuit by using two 1-way valves to prevent rebreathing. ETCO<sub>2</sub> was continuously monitored via a sampling tube at the mouthpiece level, with recordings being made during the whole experiment. Two periods of hypercapnia lasting 9 minutes were intercalated with 3 periods of normocapnia. We administered 10% CO<sub>2</sub>, aiming for an increase in ETCO<sub>2</sub> between 7 and 8 mm Hg for near-maximum cerebral vasodilation. Control of CO<sub>2</sub> gas flow was via an external source outside the MR imaging scanner. We continuously monitored the subject's blood pressure, pulse, and arterial oxygen saturation by using an MR imaging–compatible device (Invivo; Siemens, Erlangen, Germany).

## Data Analysis

All data were analyzed by using the FMRIB Software Library (FSL; <http://www.fmrib.ox.ac.uk/fsl>) and the FMRIB Expert Analysis Tool (FEAT; [http://fsl.fmrib.ox.ac.uk/fsl/feeds/data/fmri.feats/report\\_prestats.html](http://fsl.fmrib.ox.ac.uk/fsl/feeds/data/fmri.feats/report_prestats.html)) using standard preprocessing with high-pass filtering, smoothing, and motion correction by using an intramodal motion-correction tool (MCFLIRT; <http://fsl.fmrib.ox.ac.uk/fsl/fslwiki/MCFLIRT>) as previously described.<sup>8,15</sup> In brief, ETCO<sub>2</sub> data acquired during the scanning session were incorporated into the design matrix during the analysis. The FSL Brain Extraction Tool (BET; <http://fsl.fmrib.ox.ac.uk/fsl/fslwiki/BET>) was used to remove nonbrain structures from the anatomic T1-weighted scans. Following this step, the T1 images were segmented into gray and white matter by using the FMRIB Automated Segmentation Tool (FAST; <http://fsl.fmrib.ox.ac.uk/fsl/fslwiki/>).

BOLD signal changes were derived from individualized gray matter MCA territory masks by using the FSL FEAT query, following conversion from standard space into functional space. We used ETCO<sub>2</sub> as a regressor of no interest; thus, corrected BOLD responses were expressed as percentage signal change (PSC). To achieve higher robustness against technical and interindividual physiologic factors, we then normalized data to the contralateral hemisphere and expressed them as hemispheric asymmetry. The hemispheric asymmetry index (hAI) was determined according to  $hAI = 200 \times (PSC \text{ Asymptomatic Hemisphere} - PSC \text{ Symptomatic Hemisphere}) / (PSC \text{ Sum of Both Hemispheres})$  as reported.<sup>16</sup> The threshold to define abnormal CVR as the index of hemodynamic impairment was derived from the 95% confidence interval boundary from a group of previously studied healthy volunteers. We derived a level of  $hAI > 8$  as an impaired CVR, reflecting a 7.7% lower ipsilateral-than-contralateral BOLD response CO<sub>2</sub> challenge.<sup>15</sup>

## Statistical Analysis

Statistical calculations were performed by using the Statistical Package for the Social Sciences (SPSS, Version 16.0; IBM, Armonk, New York) software. Statistical significance was set as  $P < .05$ . *T* tests and *U* tests were performed for parametric and nonparametric variables, respectively. The effect of hemodynamic impairment on the rate of recurrent cerebral ischemic events was examined by using Kaplan-Meier survival analysis with the log-rank test.

## Group Analysis to Locate CVR Differences between Patients with CAO and Single versus Recurrent Events

To further investigate regional variation in CVR, we performed a second group-level analysis by using FMRIB Local Analysis of Mixed Effects (FLAME)<sup>17,18</sup> to derive group-averaged maps of the hypercapnia BOLD response separately for patients presenting with single versus those with recurrent symptoms. An additional step in the preprocessing was necessary for this analysis method, whereby the raw data from the patients with left hemispheric symptoms were flipped so that all images were “symptomatic” in the right hemisphere. Higher level group analysis was performed by using mixed-effect analysis (FLAME) with activation levels set at  $P < .05$ , uncorrected.

## RESULTS

Median follow-up was 20 months. During this period, 8 patients experienced recurrent events, and 15 did not. There was no sig-

**Table 2: Patient demographics according to new events or no events**

	No Events	New Events	P Value
Age (yr)	68	66	.64
Sex (%)			
Male	46	42	.63
Female	8	4	
Ipsilateral GM PSC (mean)	2.70 ± 0.41	2.40 ± 0.22	.03
Contralateral GM PSC (mean)	2.77 ± 0.49	2.74 ± 0.40	.91
hAI (mean)	3.98 ± 5.73	13.01 ± 7.58	.004
ETCO <sub>2</sub> change (mean)	7.0 ± 1.8	8.0 ± 3.3	.34
MAP (mean)	114.5 ± 12.4	104 ± 16.8	.11
Contralateral carotid disease			
0%–30%	9 (60%)	5 (62.5%)	
50%–70%	1 (6.7%)	2 (25%)	.651
70%–79%	1 (6.7%)	0	
80%–99%	3 (20%)	1 (12.5%)	
100%	1 (6.7%)	0	
Hypertension (%)	100	100	1
Ischemic heart disease	3 (21.4%)	1 (11%)	.52
Diabetes	3 (21%)	4 (44%)	.24
Smoking			
Nonsmoker	0	1 (12.5%)	
Ex-smoker	7 (50%)	3 (37.5%)	.37
Smoker	7 (50%)	4 (50%)	
Type of presenting symptoms			
Amaurosis fugax	4 (27%)	0	
Stroke	8 (53%)	4 (50%)	.158
TIA	3 (20%)	4 (50%)	

**Note:**—MAP indicates mean arterial pressure.

nificant difference in patient demographics between patients with single and recurrent events (Table 2). Twelve patients had an abnormal CVR defined as  $hAI \geq 8$ . Table 1 presents the details of patients who had recurrent events.

## CVR Comparison between Patients with Single and Recurrent Events

Normalized ipsilateral territorial PSC (GM MCA) was significantly decreased in those patients with recurrent events compared with those with single events ( $2.39 \pm 0.22$  versus  $2.70 \pm 0.42$ ,  $P = .032$ ). However, in the contralateral MCA territory, there was no difference in PSC ( $2.74 \pm 0.4$  versus  $2.77 \pm 0.5$ ,  $P = .91$ ). Mean hAI was significantly larger, reflecting significantly more lateralization to the contralateral hemisphere in patients with recurrent events ( $13 \pm 7.5$  versus  $4 \pm 5.7$ ; *t* test,  $P = .004$ ) than for those patients with only single events. Seven of the 8 patients who experienced recurrent events during the follow-up had abnormal hemodynamic status ( $hAI \geq 8$ ) compared with only 5/15 of those with single events.

## Survival Analysis

Kaplan-Meier analysis was performed for patients with no CVR impairment ( $hAI < 8$ ) versus those with CVR impairment ( $hAI \geq 8$ ). Normal CVR significantly predicted event-free survival during follow-up (median, 20 months) for both the combined outcome (recurrent events and/or death; log-rank,  $P = .034$ , Fig 1) and recurrent retinal or ipsilateral ischemic events only (log-rank,  $P = .012$ ).

## CVR Group Maps

Group-averaged maps illustrate only mild asymmetry in CVR expressed as hypercapnia-induced BOLD signal increase in patients

with single events (Fig 2B). There was also no apparent regional variation of CVR in patients with single episodes. In contrast, patients with recurrent symptoms showed an almost complete loss of CVR in the affected hemisphere (displayed on the right regardless of original side due to flipping of the brain during data analysis) distal to the CAO; in particular, there were no differences between territorial and watershed areas.

## DISCUSSION

Using noninvasive hypercapnia BOLD fMRI to assess CVR, we found a high rate of hemodynamic impairment in patients with symptomatic carotid artery occlusion. Most important, CVR reduction was more pronounced in patients with recurrent versus sin-

gle ischemic events, and the presence of hemodynamic impairment significantly shortened event-free survival during the follow-up.

More than half (12/23) of the patients with symptomatic CAO recruited for this study had hemispheric asymmetry indices outside the previously determined 95% CI from healthy volunteers. We chose this cutoff to define CVR reduction to reliably include patients with early (stage 1) hemodynamic impairment, while limiting inclusion of those within the upper distribution of physiologic variability. As seen for other modalities, this quantification of hemodynamic impairment can be achieved on the basis of hemispheric indices because confidence intervals are much wider for ipsilateral quantitative BOLD responsiveness, even after controlling for  $ETCO_2$ . We were able to complete hypercapnia fMRI in our patient cohort without complications, and the methodology was well-tolerated. For selected patients who might not tolerate the breathing mask setup well, the proposed CVR method could be easily adapted to a similar hemispheric asymmetry threshold test by using acetazolamide.

Patients with recurrent events showed ipsilateral reduced CVR and resulting increased hAI compared with those with single events. Moreover,  $hAI \geq 8$  allowed prediction of the risk of recurrent events. This finding adds to those in previous studies that investigated associations between impaired CVR and increased stroke risk.<sup>4,11,19-30</sup> Nine of 12 studies found a positive association of reduced or exhausted CVR and recurrent risk of future ischemic events or stroke by using a range of vasodilatory stimuli and CVR metrics. The negative findings may be explained by insufficient vasodilatory stimuli because 2 of the studies with negative findings<sup>3,4</sup> used carbogen (typically 5%  $CO_2$ ), whereas Markus and Cullinane<sup>11</sup> showed that exhausted CVR as assessed by hypercapnia transcranial Doppler with 6% or 8%  $CO_2$  independently predicted future stroke and that the prediction was stronger for 8%  $CO_2$  challenges.

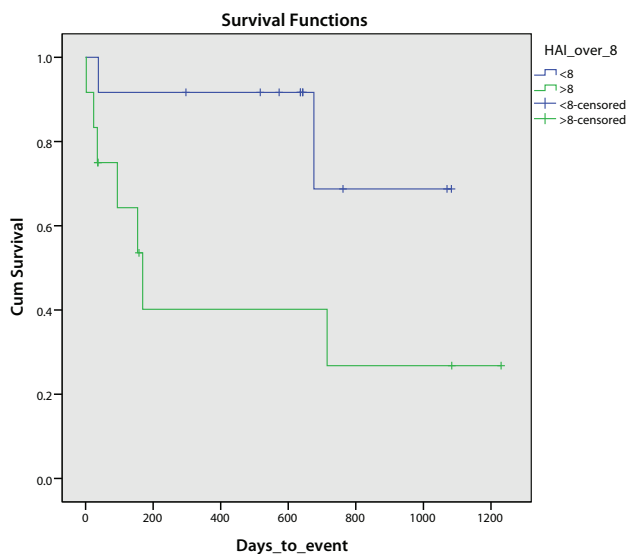


**FIG 1.** Kaplan-Meier graph showing recurrent ischemic events and death following the initial CVR scan (log-rank = 0.034).

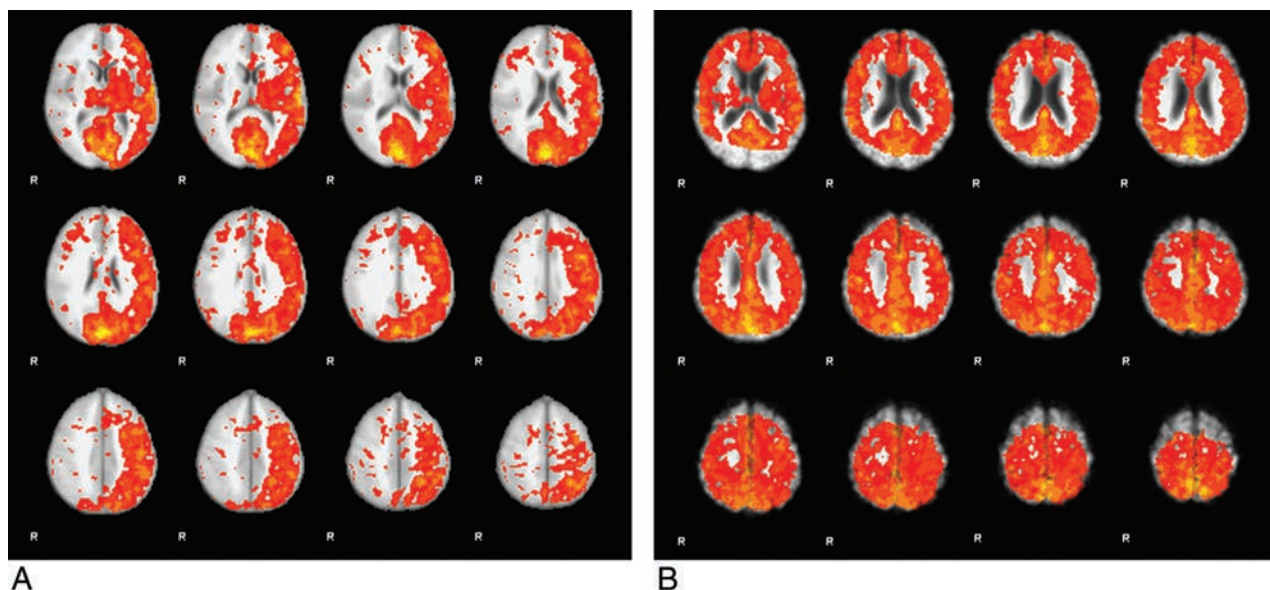


**FIG 2.** Hypercapnia BOLD response maps (threshold) in patients with symptomatic CAO. Color code for BOLD PSC shows that the higher the BOLD PSC the higher the CVR. Note that the symptomatic hemisphere is displayed on the left (right by radiologic convention). A, Patients who developed recurrent events during follow-up. B, Those who did not develop recurrent events during follow-up. Group-averaged CVR maps show mild asymmetry in CVR expressed as hypercapnia-induced BOLD signal changes in patients with recurrent events (A) and single events (B).

Our study was not powered to investigate the risk of future stroke, but any recurrent ischemic event was noted in 87% of patients with CAO and CVR impairment compared with 10% in those with intact CVR. This finding compares well with those in recent larger studies showing about 6-fold higher risk of recurrent events in patients with hemodynamic impairment: The stroke rate per year in patients with symptomatic CAO with medical management alone was about 18% compared with about a 3% yearly risk in patients with normal hemodynamics.<sup>31,32</sup> Prevention of subsequent stroke in patients with CAO remains a difficult challenge; revascularization techniques can be used to improve cerebral perfusion in an attempt to prevent ischemia, such as the extracranial-intracranial (EC-IC) bypass surgery or endovascular techniques.<sup>33</sup> EC-IC bypass has also been shown to improve the CVR of patients following intervention,<sup>34</sup> and Mandell et al,<sup>35</sup> by using CO<sub>2</sub> BOLD fMRI, showed that preoperative CVR measurements could predict the hemodynamic effects of EC-IC bypass surgery.

However, bypass surgery has been largely abandoned since the publication of a large negative randomized controlled trial in 1985, which showed no benefit to patients with CAO from a bypass operation.<sup>36</sup> This study received widespread criticism related to its design and implementation. During the past few years, 2 randomized controlled trials were set up to reassess the benefit of EC-IC bypass surgery in patients with hemodynamic compromise: the Japanese EC-IC Bypass Trial (JET) and the Carotid Occlusion Surgery Study (COSS),<sup>37,38</sup> with differing results. In these studies, patients with hemodynamically significant carotid occlusions were randomized to best medical therapy or to an operation and best medical therapy. The methods of hemodynamic assessment in these studies are SPECT for the JET study and PET for the COSS study. The second interim analysis from the JET study showed a significant benefit at 2 years for patients undergoing an EC-IC bypass surgery.<sup>37</sup>

However, more recently, the COSS study<sup>32</sup> was stopped due to an interim futility analysis suggesting that EC-IC bypass surgery plus medical therapy compared with medical therapy alone did not reduce the risk of recurrent ipsilateral ischemic stroke at 2 years. A core aspect of this study was the physiologic selection of patients with signs of hemodynamic impairment by using PET, but the chosen semi-quantitative oxygen extraction fraction has been criticized because it lacks validation to predict recurrent events.<sup>13</sup> More recently, the Randomized Evaluation of Carotid Occlusion and Neurocognition study published its results showing no improvement in cognition for patients undergoing EC-IC bypass for symptomatic carotid occlusion with an increased oxygen extraction fraction.<sup>39</sup>

In the future, it is likely that EC-IC bypass may be superseded by newer endovascular techniques for which there have been recent feasibility studies showing promising results by using a minimally invasive recanalization technique with proximal cerebral protection and stent placement for symptomatic acute and chronic carotid artery occlusion.<sup>33</sup>

One of the main problems of using nuclear medicine-based techniques such as PET and SPECT to assess hemodynamic impairment is the relatively large dose of ionizing radiation to the patient in addition to cost and access. A method for assessment of cerebral hemodynamics without radiation risks is obviously preferable.

Hypercapnia fMRI offers a potential alternative in this patient group without the use of radiation. Previous work shows the accuracy and reproducibility of our technique to assess CVR or stage I hemodynamic impairment<sup>15</sup> and also the changes in CVR following carotid endarterectomy.<sup>8</sup> Therefore, the ability to perform a quick and easy assessment of the hemodynamic status without the risk of ionizing radiation is particularly useful for the future of mainstream medical imaging.

We performed a group analysis of CVR maps to compare the pattern of hemodynamic impairment in patients with single versus recurrent events. There was a marked difference with almost complete loss of CVR capacity within the core MCA territory in addition to grossly altered watershed areas. This result highlighted the tissue at high risk for ischemic compromise with maximal dilation of the cerebral vessels and therefore no further dilating capacity to compensate for future cerebral autoregulatory demands. These maps provide us with a visual representation of anatomic CVR and thus allow us to assess individual areas at risk of hemodynamic impairment and could be further used to test the validity of CVR to predict hemodynamic tissue at risk. It will be of interest to further compare the location of CVR exhaustion with the location of future hemodynamic infarctions.

Our study is clearly limited by the small number of patients and the variable length of follow-up. We have only clinical follow-up on our patients, and we did not have any recurrent imaging. Further evaluation of patients' CVR with recurrent events is needed as a prospective study. A further limitation of this study is the lack of any reference imaging standard used for comparison; further studies are needed to evaluate and directly compare hypercapnia fMRI with the accepted imaging methods of CVR, such as PET or SPECT. There was heterogeneity in the patients' contralateral carotid disease within the study; however, we have found, from previous unpublished work, that different and increasing degrees of carotid disease do not necessarily correlate with increasing degrees of hemodynamic impairment.

## CONCLUSIONS

In this small study, we have shown that the hemispheric asymmetry index derived from hypercapnia BOLD fMRI demonstrated hemodynamic impairment in more than half of our patient cohort with carotid occlusion, and we found that those patients had an elevated risk of recurrent ischemic symptoms. This noninvasive technique may thus be helpful in selecting patients for recanalization with bypass treatment or endovascular revascularization.

Disclosures: Stephen D. Goode—RELATED: Grant: Royal College of Surgeons.\* Dorothee P. Auer—RELATED: Grant: Special Trustee, Nottingham University Hospital Trust.\* \*Money paid to the institution.

## REFERENCES

1. Powers WJ. **Cerebral hemodynamics in ischemic cerebrovascular disease.** *Ann Neurol* 1991;29:231–40 CrossRef Medline
2. Hankey GJ, Warlow CP. **Prognosis of symptomatic carotid artery occlusion: an overview.** *Cerebrovasc Dis* 1991;1:245–56 CrossRef
3. Klijn CJ, Kappelle LJ, van Huffelen AC, et al. **Recurrent ischemia in symptomatic carotid occlusion: prognostic value of hemodynamic factors.** *Neurology* 2000;55:1806–12 CrossRef Medline
4. Persoon S, Luitse MJ, de Borst GJ, et al. **Symptomatic internal ca-**

- rotid artery occlusion: a long-term follow-up study. *J Neurol Neurosurg Psychiatry* 2011;82:521–26 CrossRef Medline
5. Grubb RL Jr, Derdeyn CP, Fritsch SM, et al. **Importance of hemodynamic factors in the prognosis of symptomatic carotid occlusion.** *JAMA* 1998;280:1055–60 CrossRef Medline
  6. Klijn CJ, Kappelle LJ, Algra A, et al. **Outcome in patients with symptomatic occlusion of the internal carotid artery or intracranial arterial lesions: a meta-analysis of the role of baseline characteristics and type of antithrombotic treatment.** *Cerebrovasc Dis* 2001;12:228–34 CrossRef Medline
  7. Bokkers RP, van Osch MJ, van der Worp HB, et al. **Symptomatic carotid artery stenosis: impairment of cerebral autoregulation measured at the brain tissue level with arterial spin-labeling MR imaging.** *Radiology* 2010;256:201–08 CrossRef Medline
  8. Goode SD, Altaf N, Auer DP, et al. **Carotid endarterectomy improves cerebrovascular reserve capacity preferentially in patients with preoperative impairment as indicated by asymmetric BOLD response to hypercapnia.** *Eur J Vasc Endovasc Surg* 2009;38:546–51 CrossRef Medline
  9. Derdeyn CP, Videen TO, Yundt KD, et al. **Variability of cerebral blood volume and oxygen extraction: stages of cerebral haemodynamic impairment revisited.** *Brain* 2002;125:595–607 CrossRef Medline
  10. Nemoto EM, Yonas H, Kuwabara H, et al. **Identification of hemodynamic compromise by cerebrovascular reserve and oxygen extraction fraction in occlusive vascular disease.** *J Cereb Blood Flow Metab* 2004;24:1081–89 Medline
  11. Markus H, Cullinane M. **Severely impaired cerebrovascular reactivity predicts stroke and TIA risk in patients with carotid artery stenosis and occlusion.** *Brain* 2001;124:457–67 CrossRef Medline
  12. Yamauchi H, Fukuyama H, Nagahama Y, et al. **Significance of increased oxygen extraction fraction in five-year prognosis of major cerebral arterial occlusive diseases.** *J Nucl Med* 1999;40:1992–98 Medline
  13. Carlson AP, Yonas H, Chang YF, et al. **Failure of cerebral hemodynamic selection in general or of specific positron emission tomography methodology?: Carotid Occlusion Surgery Study (COSS).** *Stroke* 2011;42:3637–39 CrossRef Medline
  14. Garrett MC, Komotar RJ, Starke RM, et al. **Radiographic and clinical predictors of hemodynamic insufficiency in patients with atherosclerotic disease.** *J Stroke Cerebrovasc Dis* 2008;17:340–43 CrossRef Medline
  15. Goode SD, Krishan S, Alexakis C, et al. **Precision of cerebrovascular reactivity assessment with use of different quantification methods for hypercapnia functional MR imaging.** *AJNR Am J Neuroradiol* 2009;30:972–77 CrossRef Medline
  16. de Boorder MJ, van der Grond J, van Dongen AJ, et al. **SPECT measurements of regional cerebral perfusion and carbon dioxide reactivity: correlation with cerebral collaterals in internal carotid artery occlusive disease.** *J Neurol* 2006;253:1285–91 CrossRef Medline
  17. Beckmann CF, Jenkinson M, Smith SM. **General multilevel linear modeling for group analysis in fMRI.** *Neuroimage* 2003;20:1052–63 CrossRef Medline
  18. Woolrich MW, Behrens TE, Beckmann CF, et al. **Multilevel linear modelling for fMRI group analysis using Bayesian inference.** *Neuroimage* 2004;21:1732–47 CrossRef Medline
  19. Kleiser BW, Widder B. **Course of carotid artery occlusions with impaired cerebrovascular reactivity.** *Stroke* 1992;23:171–74 CrossRef Medline
  20. Yonas H, Smith HA, Durham SR, et al. **Increased stroke risk predicted by compromised cerebral blood flow reactivity.** *J Neurosurg* 1993;79:483–89 CrossRef Medline
  21. Widder B, Kleiser B, Krapf H. **Course of cerebrovascular reactivity in patients with carotid artery occlusions.** *Stroke* 1994;25:1963–67 CrossRef Medline
  22. Webster MW, Makaroun MS, Steed DL, et al. **Compromised cerebral blood flow reactivity is a predictor of stroke in patients with symptomatic carotid artery occlusive disease.** *J Vasc Surg* 1995;21:338–44; discussion 344–45 Medline
  23. Powers WJ, Tempel LW, Grubb RL Jr. **Influence of cerebral hemodynamics on stroke risk: one-year follow-up of 30 medically treated patients.** *Ann Neurol* 1989;25:325–30 CrossRef Medline
  24. Hasegawa Y, Yamaguchi T, Tsuchiya T, et al. **Sequential change of hemodynamic reserve in patients with major cerebral artery occlusion or severe stenosis.** *Neuroradiology* 1992;34:15–21 CrossRef Medline
  25. Yokota C, Hasegawa Y, Minematsu K, et al. **Effect of acetazolamide reactivity on [corrected] long-term outcome in patients with major cerebral artery occlusive diseases.** *Stroke* 1998;29:640–44 CrossRef Medline
  26. Ogasawara K, Ogawa A, Yoshimoto T. **Cerebrovascular reactivity to acetazolamide and outcome in patients with symptomatic internal carotid or middle cerebral artery occlusion: a xenon-133 single-photon emission computed tomography study.** *Stroke* 2002;33:1857–62 CrossRef Medline
  27. Vernieri FP, Pasqualetti P, Passarelli F, et al. **Outcome of carotid artery occlusion is predicted by cerebrovascular reactivity.** *Stroke* 1999;30:593–98 CrossRef Medline
  28. Kuroda S, Houkin K, Kamiyama H, et al. **Long-term prognosis of medically treated patients with internal carotid or middle cerebral artery occlusion: can acetazolamide test predict it?** *Stroke* 2001;32:2110–16 CrossRef Medline
  29. Isozaki M, Arai Y, Kudo T, et al. **Clinical implication and prognosis of normal baseline cerebral blood flow with impaired vascular reserve in patients with major cerebral artery occlusive disease.** *Ann Nucl Med* 2010;24:371–77 CrossRef Medline
  30. Kimiagar I, Bass A, Rabey JM, et al. **Long-term follow-up of patients with asymptomatic occlusion of the internal carotid artery with good and impaired cerebral vasomotor reactivity.** *Eur J Neurol* 2010;17:1285–90 CrossRef Medline
  31. Jeffrey RL, Stoodley MA. **STA-MCA bypass for symptomatic carotid occlusion and haemodynamic impairment.** *J Clin Neurosci* 2009;16:226–35 CrossRef Medline
  32. Powers WJ, Clarke WR, Grubb RL Jr, et al; COSS Investigators. **Extracranial-intracranial bypass surgery for stroke prevention in hemodynamic cerebral ischemia: the Carotid Occlusion Surgery Study randomized trial.** *JAMA* 2011;306:1983–92 CrossRef Medline
  33. Shojima M, Nemoto S, Morita A, et al. **Protected endovascular revascularization of subacute and chronic total occlusion of the internal carotid artery.** *AJNR Am J Neuroradiol* 2010;31:481–86 CrossRef Medline
  34. Gibbs JM, Wise RJ, Thomas DJ, et al. **Cerebral haemodynamic changes after extracranial-intracranial bypass-surgery.** *J Neurol Neurosurg Psychiatry* 1987;50:140–50 CrossRef Medline
  35. Mandell DM, Han JS, Poublanc J, et al. **Quantitative measurement of cerebrovascular reactivity by blood oxygen level-dependent MR imaging in patients with intracranial stenosis: preoperative cerebrovascular reactivity predicts the effect of extracranial-intracranial bypass surgery.** *AJNR Am J Neuroradiol* 2011;32:721–27 CrossRef Medline
  36. EC/IC Bypass Study Group. **Failure of extracranial-intracranial arterial bypass to reduce the risk of ischemic stroke: results of an international randomized trial.** *N Engl J Med* 1985;313:1191–200 CrossRef Medline
  37. JET Study Group. **Japanese EC-IC Bypass Trial (JET Study): the second interim analysis.** *Surg Cereb Stroke* 2002;30:434–37 CrossRef Medline
  38. Grubb RL Jr, Powers WJ, Derdeyn CP, et al. **The Carotid Occlusion Surgery Study.** *Neurosurg Focus* 2003;14:e9 Medline
  39. Marshall RS, Festa JR, Cheung YK, et al; RECON Investigators. **Randomized Evaluation of Carotid Occlusion and Neurocognition (RECON) trial: main results.** *Neurology* 2014;82:744–51 CrossRef Medline

# Imaging Features of Juvenile Xanthogranuloma of the Pediatric Head and Neck

 D.T. Ginat, S.O. Vargas, V.M. Silvera, M.S. Volk, B.A. Degar, and  C.D. Robson

## ABSTRACT

**BACKGROUND AND PURPOSE:** Juvenile xanthogranuloma is a non-Langerhans cell histiocytosis primarily affecting children. The purpose of this study was to characterize the imaging features of histologically confirmed pediatric head and neck juvenile xanthogranuloma.

**MATERIALS AND METHODS:** A retrospective review was performed of medical records and imaging of histologically confirmed head and neck juvenile xanthogranuloma.

**RESULTS:** Ten patients (6 girls, 4 boys) 1 month to 12 years of age were imaged with ultrasound only ( $n = 1$ ), CT only ( $n = 2$ ), CT and ultrasound ( $n = 1$ ), MR imaging only ( $n = 3$ ), or MR imaging and CT ( $n = 3$ ). Masses were solitary in 9 patients and multiple in 1. Solitary masses were located in the external auditory canal, infra-auricular region, infratemporal fossa with intracranial extension, frontal scalp, and subperiosteal space eroding the calvaria and along the dura. One patient with disseminated disease had scalp-, calvarial-, and dural-based masses. Clinical presentation included a mass or alteration in function. On sonography, juvenile xanthogranuloma appeared hypoechoic. On contrast-enhanced CT, masses appeared homogeneous and isoattenuating with muscle and sometimes eroded bone. On MR imaging, compared with the cerebral cortex, the masses appeared hyper- or isointense on T1 and hypo- or isointense on T2, had decreased diffusivity, and enhanced homogeneously. Juvenile xanthogranuloma was not included in the differential diagnosis in any case.

**CONCLUSIONS:** Head and neck juvenile xanthogranuloma has varied manifestations. Mild hyperintensity on T1, hypointensity on T2 compared with the cerebral cortex, decreased diffusivity, and homogeneous enhancement are characteristic. Awareness of these features should prompt radiologists to include juvenile xanthogranuloma in the differential diagnosis of pediatric head and neck masses.

**ABBREVIATIONS:** HN = head and neck; JXG = juvenile xanthogranuloma; LCH = Langerhans cell histiocytosis; US = ultrasound

Juvenile xanthogranuloma (JXG) is a non-Langerhans cell histiocytosis that typically presents as a well-circumscribed nodule or mass, containing attenuated infiltrates of histiocytes and a variable number of admixed multinucleate Touton giant cells and

inflammatory cells. The cell of origin in JXG is debated; the cells have immunohistochemical features of both macrophages and dendritic cells.<sup>1</sup> Approximately 20% of JXGs are noted at birth; 70%, in the first year of life; and only 10%, in adulthood. Localized dermal involvement is the most common presentation; two-thirds of the lesions are solitary.<sup>2</sup> Extracutaneous involvement is less common, with approximately 50% of lesions located within the head and neck (HN) region.<sup>2</sup> Extracutaneous HN JXG has been reported in locations such as the tympanic membrane, nasal cavity, tongue, orbit and paranasal sinus, subglottis, cervical spine, skull base including the temporal bone, intracranial compartment, and HN muscles.<sup>2-21</sup>

Cutaneous JXG typically presents as a solitary macule or papule with a flesh-colored, erythematous, or yellowish hue.<sup>2</sup> In such cases, radiographic imaging is not indicated. In extracutaneous sites, JXG is more difficult to diagnose and imaging can be misleading

Received November 1, 2014; accepted after revision November 10, 2015.

From the Departments of Radiology (D.T.G., V.M.S., C.D.R.), Pathology (S.O.V.), Otolaryngology (M.S.V.), and Pediatric Oncology (B.A.D.), Boston Children's Hospital, Boston, Massachusetts; Department of Pediatric Oncology (B.A.D.), Dana-Farber Cancer Institute, Boston, Massachusetts; and Harvard Medical School (S.O.V., V.M.S., M.S.V., B.A.D., C.D.R.), Boston, Massachusetts.

Current affiliation for D.T.G.: Department of Radiology, University of Chicago Medical Center, Chicago, Illinois.

Previously presented as a poster at: Annual Meeting of the American Society of Head and Neck Radiology, September 25–29, 2013; Milwaukee, Wisconsin.

Please address correspondence to Caroline D. Robson, MB, ChB, Department of Radiology, Boston Children's Hospital, 300 Longwood Ave, Boston, MA 02115; e-mail: caroline.robson@childrens.harvard.edu

<http://dx.doi.org/10.3174/ajnr.A4644>

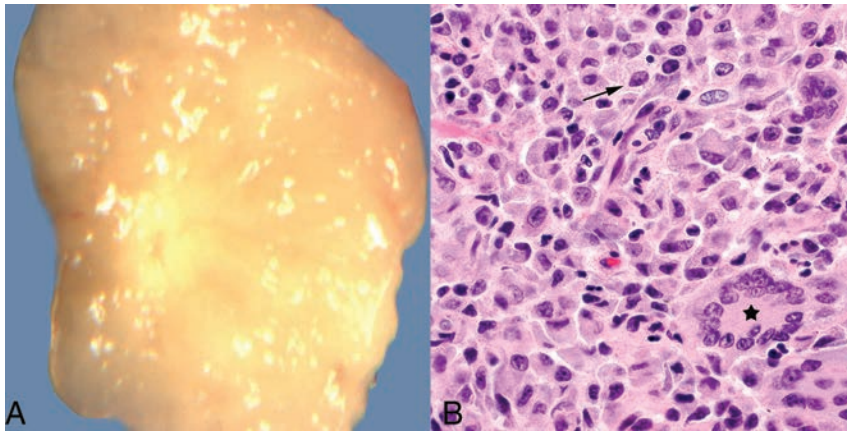


**FIG 1.** A, Grossly, juvenile xanthogranulomas are typically yellowish, due to their high lipid content. B, Hematoxylin-eosin stain, original magnification  $\times 600$ . Microscopically, abundant variably lipidized histiocytes are present (arrow), usually with admixed Touton giant cells (star) and scattered inflammatory cells (not shown on this image).

because an infiltrative appearance may mimic malignancy.<sup>2,22</sup> Previous reports detailing the radiographic features of JXG are limited to case reports and several small series or to a limited description of imaging within the context of a clinicopathologic report.<sup>2-21</sup>

The purpose of this study was to provide detailed characterization of the ultrasound (US), CT, and MR imaging features of JXG in the HN region.

## MATERIALS AND METHODS

Boston Children's Hospital institutional review board approval was obtained for a retrospective review of pathologically confirmed pediatric cases of JXG. The pathology data base at Boston Children's Hospital was searched for all reports containing the text "xanthog" in patients younger than 19 years of age from December 1997 to December 2013. Cases were included only if the incisional or excisional biopsy met histologic criteria for JXG. The site of each biopsy was recorded. Patients with biopsies showing JXG involving the HN were studied further by review of their pathology and radiology records. Pathology was reviewed by a pediatric pathologist. Radiology examinations were reviewed by a pediatric neuroradiologist with approximately 20 years of experience and a neuroradiology fellow. For patients who were imaged with sonography, CT, and/or MR imaging, original images were reviewed in detail. The maximum lesion diameter on the presenting imaging examination was recorded. The attenuation of the lesions was compared with that of muscle by visual inspection on available noncontrast and postcontrast CT images. MR imaging technical parameters were as follows: T1-weighted images: TR/TE, 427-667/10-25 ms; NEX, 2; matrix, 205-256  $\times$  256-512; FOV, 15-22  $\times$  18-27 cm; T2-weighted sequences: TR/TE, 2693-5800/86-120 ms; NEX, 1-2; matrix, 179-256  $\times$  320-512; FOV, 15-20  $\times$  18-25 cm; fast spin-echo inversion recovery sequences: TR/TE, 4000/45 ms; NEX, 2; matrix, 256  $\times$  512; FOV, 22  $\times$  28 cm; and diffusion-weighted sequences: TR/TE, 8300/93 ms; NEX, 1; matrix, 128  $\times$  128; FOV, 18-26  $\times$  22-32 cm; b-value, 1000). Contrast-enhanced images of extracranial lesions were obtained with similar parameters with fat-suppression. Lesion signal intensity on T1-weighted and fast spin-echo T2-weighted or fast spin-echo inversion recovery sequences was designated as hypointense,

isointense, or hyperintense with respect to the signal intensity of the cerebral cortex, based on visual inspection. The presence of enhancement on postcontrast T1-weighted sequences within the lesions was characterized as homogeneous versus heterogeneous. ADC maps were generated from diffusion-weighted images, and whole-lesion average ADC measurements were obtained by using a freehand ROI. The differential diagnosis provided on the original radiology reports was assessed for the 9 patients for whom the histopathologic diagnosis of JXG was not known at the time of imaging.

## RESULTS

During a 16-year period, there were 114 children with a histologic diagnosis of

JXG. Lesions involved the skin in 107 (94%) of these patients. Multiple lesions were present in 8 patients. Imaging was performed in 14 of 114 (12%) patients. Imaged lesions involved the skin and subcutaneous tissues (back, chest, neck, scalp, and groin), abdominal wall rectus sheath, paraspinous muscles, liver, neck, skull, and external auditory meatus. The HN was involved in 67 of 114 (59%) patients. Sites of cutaneous HN involvement included the forehead, cheek, nose, chin, ear, eyelid, lip, neck, and scalp. Review of pathologic features in all cases revealed diagnostic features of JXG (Fig 1). The features included an infiltrate of variably xanthomatized mononuclear histiocyte-like cells. Touton giant cells were seen in all except 1 case, and eosinophils and lymphocytes were seen in most cases.

Ten patients had imaging of HN lesions. The 6 female and 4 male patients ranged in age from 1 month to 12 years at the time of imaging, with 8 children younger than 1 year of age. Their clinical presentations and initial radiologic diagnoses based on the imaging findings are summarized in Table 1. US only was performed in 1 patient; US and CT, in 1 patient; CT only, in 2 patients; MR imaging only, in 3; and both MR imaging and CT, in 3. Imaging characteristics are summarized in Table 2. Lesions were solitary in 9 children and multiple in 1 patient who had disseminated disease. Maximum diameters of the lesions in the 10 patients ranged from 2 to 60 mm.

Doppler US examinations performed for evaluation of each of the superficial lesions, one adjacent to the coronal suture and the other in the infra-auricular region (Fig 2), revealed sharply defined, ovoid, slightly heterogeneous, hypoechoic masses without demonstrable internal blood flow.

On contrast-enhanced CT, the lesions appeared as homogeneous, solid soft-tissue masses without calcifications and isoattenuating compared with muscle (Fig 2). Bony erosion was present in 3 of 5 children (Figs 3 and 4). CT in 1 patient with a right parietal subperiosteal mass showed an irregular and somewhat aggressive-appearing erosion of the calvarial outer table with a peripheral periosteal reaction (Fig 4). CT in another patient showed mild, smooth, benign-appearing thinning of the frontal bone outer table in the midline above the nasofrontal suture. CT

**Table 1: Patient age and sex, clinical presentation, lesion location, and radiographic diagnosis**

Case	Age, Sex	Clinical Presentation	Location	Radiographic Diagnosis
1	10 yr, F	Mass and bloody otorrhea for 10 days	External auditory canal, polypoid mass	Polyp
2	4 mo, M	Mass and bloody discharge for 1 month	External auditory canal, subcutaneous tissues	Sebaceous cyst, dermoid or branchial cleft cyst
3	3 mo, M	Reddish-blue nodule for 2 days	Infra-auricular, subcutaneous, and cutaneous	Lymph node, pilomatrixoma, nontuberculous mycobacterial infection
4	1 mo, M	Facial weakness, otorrhea for 1 month	Infratemporal fossa, middle ear space, bony erosion, intracranial, temporal lobe edema	LCH, neuroblastoma
5	7 mo, F	Scalp mass for 2 weeks	Subperiosteal with outer table erosion, parietal bone	Neuroblastoma metastasis, LCH, fibromatosis, other malignant tumor
6	4 mo, F	Enlarging scalp mass for 6 weeks	Cutaneous edema, subcutaneous scalp mass over coronal suture	Dermoid
7	1 mo, F	Mass over nose since birth	Subcutaneous tissue, midline nasofrontal	Neuroglial heterotopia
8	10 mo, F	Enlarging mass over nose for 3 weeks	Subperiosteal with outer table erosion, midline frontal	LCH, metastasis such as neuroblastoma, other malignant tumor
9	12 yr, F	Tremor for 6 months, recent seizure	Intracranial, extra-axial; frontal lobe edema	Tumor not otherwise specified
10	9 mo, M	Multiple skin lesions since birth, occipital lesion for 4 weeks	Innumerable scalp lesions; occipital calvarial, epidural; intracranial parietal dural-based	Referred for imaging with known diagnosis of JXG

**Table 2: Lesion characteristics on CT and MR imaging**

Case	Size (mm)	US	CT Attenuation <sup>a</sup> without Contrast	CT Attenuation <sup>a</sup> with Contrast	Bony Erosion	Relative Signal Intensity on T1 <sup>b</sup>	Relative Signal Intensity on T2 <sup>b</sup>	Enhancement Postgadolinium	ADC ( $\times 10^{-3}$ mm <sup>2</sup> /s)
1	6	NA	NA	Iso	–	NA	NA	NA	NA
2	5	NA	NA	Iso	–	NA	NA	NA	NA
3	10	Hypoechoic	NA	Iso	–	NA	NA	NA	NA
4	43	NA	Iso	NA	+	Hyper	Hypo	Homogeneous	0.739
5	34	NA	Iso	NA	+	Hyper	Hypo	Homogeneous	NA
6	15	Hypoechoic	NA	NA	NA	NA	NA	NA	NA
7	27	NA	NA	Iso	+	Hyper	Hypo	Homogeneous	0.534
8	4	NA	NA	NA	+	Iso	Hypo	Homogeneous	0.596
9	8	NA	NA	NA	–	Iso	Iso	Homogeneous	NA
10	2–17	NA	NA	NA	+	Iso	Iso	Homogeneous	0.777 (largest)

**Note:**—Iso indicates isoattenuating; Hyper, hyperintense; Hypo, hypointense; –, absent; +, present; NA, not available.

<sup>a</sup> Compared with muscle.

<sup>b</sup> Compared with gray matter.

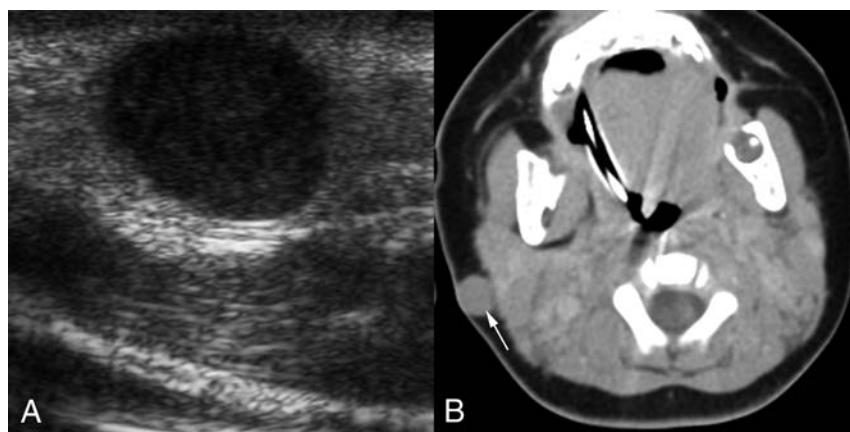


**FIG 2.** A 3-month-old boy with a reddish-blue infra-auricular nodule that had been noticed for 2 days (patient 3). *A*, Transverse sonographic image reveals a hypoechoic solid mass. The mass was mistaken for adenopathy. *B*, Axial contrast-enhanced CT image shows a sharply circumscribed subcutaneous mass (*arrow*) that also involves the skin. The mass is isoattenuating with muscle and has no distinguishing characteristics other than its location. The lack of calcification is unusual for pilomatrixoma, which is the most common tumor in this location in children. The lack of necrosis or parotid space adenopathy is atypical for nontuberculous mycobacterial infection, which is the most common infection in this location.

in a third patient showed lytic destruction of the temporal bone affecting the floor of the middle ear space, the tegmen tympani, and the lateral retroauricular mastoid cortex. There was also erosion of the ossicles and otic capsule region of the petrous bone (Fig 3). Bony erosion was not identified in 3 of 6 children. All of these children had small, nonspecific, enhancing soft-tissue masses projecting into the external auditory canal or involving the skin and subcutaneous tissues beneath the ear (Fig 2).

As suggested by the range of technical parameters, the MR imaging technique has evolved considerably during the study period, with a more recent trend toward imaging on 3T systems using multichannel phased array coils with an FOV optimized for the ROI and higher resolution imaging. Neverthe-

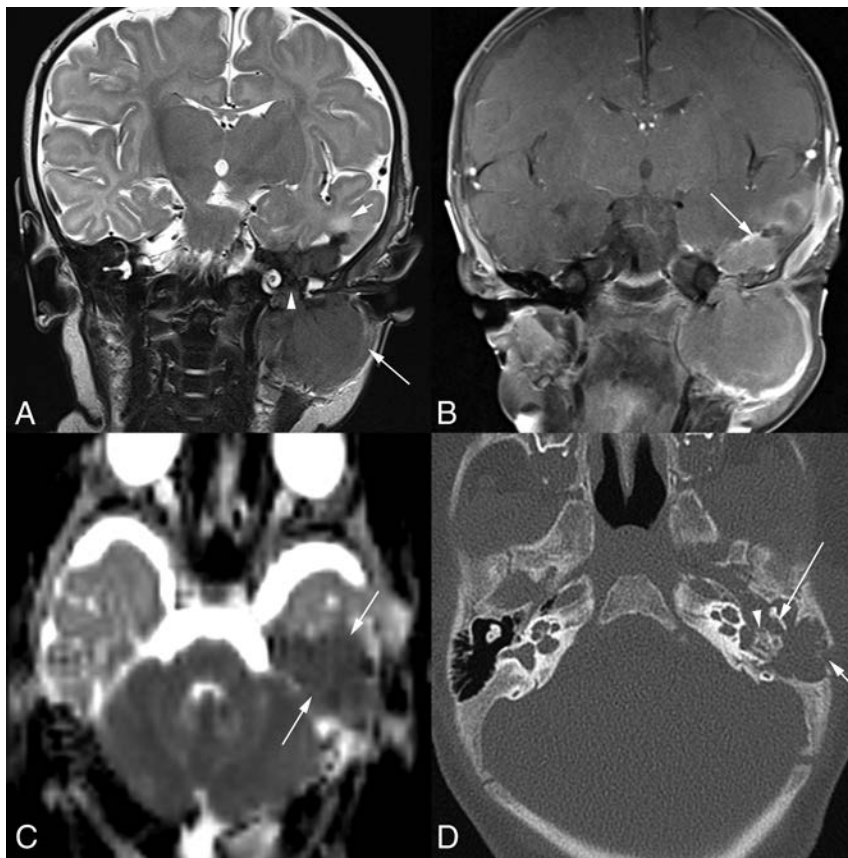


**FIG 3.** A 1-month-old boy with a 1-month history of left facial weakness and otorrhea (patient 4). **A**, Coronal T2-weighted MR image shows a mass that is hypointense compared with the cortex. Tumor involves the infratemporal fossa (*long arrow*), erodes the skull base and tegmen tympani, and involves the middle ear space (*arrowhead*) and epidural space in the middle cranial fossa. There is edema of the adjacent temporal lobe (*short arrow*). Scalp swelling is due to recent surgical debulking of the intracranial component at another institution. **B**, Coronal contrast-enhanced, fat-suppressed T1-weighted MR imaging shows the homogeneously enhancing mass extending into the middle ear space and the epidural space (*arrow*). **C**, On this axial DWI ADC image, the lesion (*arrows*) demonstrates decreased diffusivity. Axial CT image (**D**) shows lytic destruction of the mastoid temporal bone retroauricular cortex (*short arrow*). Tumor extends into the left middle ear space with erosion of the short process of the incus (*long arrow*) along its medial aspect and erosion of the otic capsule bone around the oval window and lateral semicircular canal (*arrowhead*).

less, on T2-weighted MR images, the JXG ranged from hypointense (3 of 6 patients) to isointense (3 of 6 patients) relative to gray matter (Figs 3–5), while on T1-weighted sequences before administration of contrast, the lesions ranged from isointense (3 of 6 patients) to hyperintense (3 of 6 patients) relative to gray matter (Figs 4 and 5). Diffusion-weighted imaging was available in 4 cases, and the lesions demonstrated decreased diffusivity (Figs 3 and 5), appearing hypointense relative to the cortex on ADC maps, with average ADC values of the lesions ranging from  $0.53$  to  $0.78 \times 10^{-3} \text{ s/mm}^2$ . Enhancement on postcontrast T1-weighted MR imaging was homogeneous in all patients (Figs 3–7).

Two patients had extra-axial lesions associated with edema in the adjacent brain parenchyma with seizures in one of these children (Figs 3 and 6). The other child presented a few weeks after birth with left facial weakness, and imaging revealed temporal bone erosion, as detailed earlier, with progressive enlargement in the soft-tissue components extending inferiorly into the infratemporal fossa and superiorly into the middle cranial fossa on serial imaging (Fig 3). One patient had disseminated disease with

innumerable cutaneous and subcutaneous lesions; a calvarial mass; and lobulated, plaque-like dural-based lesions (Fig 7). This patient also had abdominal visceral involvement.

A diagnosis of JXG before head and neck imaging was known in only 1 patient who had cutaneous lesions and disseminated disease. For the remaining 9 patients, the radiologic differential diagnosis provided for the tumor varied depending on the location of the tumor (Table 1). Proposed differential diagnoses included Langerhans cell histiocytosis (LCH) or neuroblastoma (masses with bony erosion), neuroglial heterotopia (midline nasofrontal mass), granulomatous inflammation, lymph node or nonmineralized pilomatixoma (subcutaneous infra-auricular lesion), epidermoid or dermoid (lesion over a coronal suture and external auditory canal lesion), and first branchial cleft cyst or polyp (external auditory canal lesion). Most interesting, JXG was not included in the initial radiologic differential diagnosis for any of these 9 patients.

## DISCUSSION

Our study confirmed that the HN is a favored location for both cutaneous and extracutaneous JXG; the latter included the calvaria, midline nasofrontal region, periauricular region, and temporal bone. Intracranial disease in our series manifested as a dural-based mass or masses. Multifocal disease is rarely encountered. A small but important proportion of all pediatric JXG cases (12%) of this classic pediatric disease undergo preoperative imaging. Our study demonstrated the range of US, CT, and MR imaging findings in primarily extracutaneous JXG of the pediatric HN. We also showed that while only a small fraction of all pediatric JXGs were imaged, this entity was seldom included by the radiologist in the differential diagnosis of HN masses.

Our findings, based on the evaluation of a very limited number of patients, suggest that on US, the presence of a solid, sharply circumscribed, superficial, nonmineralized mass should prompt consideration of JXG in the differential diagnosis. Hypoechoic and relatively avascular sonographic characteristics help distinguish JXG from lymph nodes. Bone erosion associated with JXG was not an uncommon finding in this series and could be depicted on both CT and MR imaging. Indeed, the presence of bone involvement has been described as a feature of JXG, but not of adult xanthogranuloma.<sup>17</sup> Tumors that demonstrated punched-out lytic destruction resembled LCH most closely. However, 1 tumor demonstrated irreg-

ular destruction of the temporal bone. Intracranial disease in our series manifested as a dural-based mass or masses. Multifocal disease is rarely encountered. A small but important proportion of all pediatric JXG cases (12%) of this classic pediatric disease undergo preoperative imaging. Our study demonstrated the range of US, CT, and MR imaging findings in primarily extracutaneous JXG of the pediatric HN. We also showed that while only a small fraction of all pediatric JXGs were imaged, this entity was seldom included by the radiologist in the differential diagnosis of HN masses.

ular calvarial destruction simulating a higher grade primary or metastatic tumor.

On CT, JXGs have been described as masses of soft-tissue attenuation with central areas of hypoattenuation in the muscles, lungs, kidney, liver, and adrenal glands and as small hypoattenuating nodules in the spleen.<sup>23</sup> In this series, the cases for which contrast-enhanced CT was performed were homogeneously isoattenuating compared with muscle, without central areas of

hypoattenuation. Because the examination protocol did not include precontrast imaging, the true determination of enhancement could not be made with certainty.

The MR imaging appearance of JXGs involving the extremities and CNS has been previously described. Intramuscular JXG may have slightly high signal intensity on T2-weighted images and isointense with muscle on T1-weighted images.<sup>24</sup> Likewise, the MR signal intensity of intracranial and spinal JXG has been reported as similar to that of neural

tissue with faint homogeneous enhancement after gadolinium administration.<sup>25</sup> The higher signal intensity on T1-weighted images compared with the cortex in many of the JXGs in our series is presumably attributable to the presence of lipid within these lesions. Lipid-rich zones correspond to xanthomatized areas that are seen histologically, characterized by abundant intracellular fat within histiocytes, and they occur as a variably prominent component of JXG.<sup>2</sup> The low signal intensity compared with the cortex on T2-weighted images may be attributable to attenuated cellularity, which is a common histologic feature, or collagenous matrix, which is thought to develop with time in JXG.<sup>26</sup> Decreased diffusivity is also likely attributable to attenuated cellularity and/or collagenous matrix, a feature that simulates higher grade lesions such as neuroblastomas or atypical teratoid/rhabdoid tumors. Ultimately, imaging is useful for delineating the extent of disease and for narrowing the differential diagnosis.<sup>17</sup>

Our review of radiology reports for differential diagnoses provided at the time of imaging highlighted some of the diagnostic pitfalls that can be posed by JXG. The size and location of the JXG

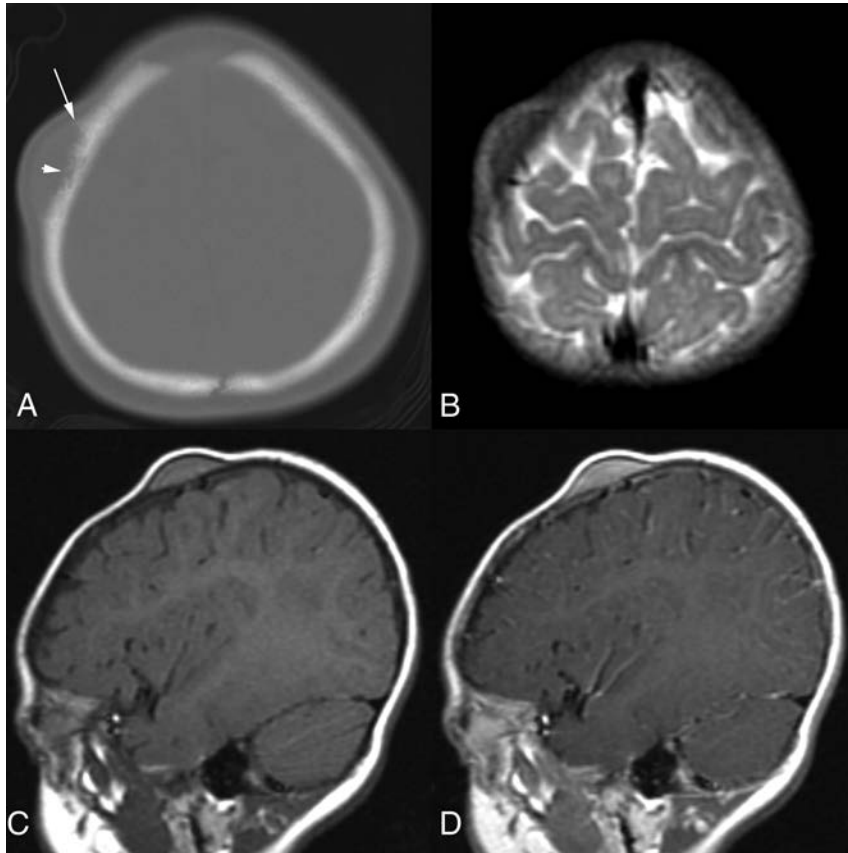


**FIG 4.** A 7-month-old girl with a 2-week history of a right frontal scalp mass that was clinically thought to represent a dermoid cyst (patient 5). *A*, Axial CT image shows a semilunar mass with irregular erosion of the calvarial outer table (*short arrow*) and periosteal reaction (*long arrow*). *B*, Axial T2-weighted MR image demonstrates that the mass is hypointense relative to the cerebral cortex. *C*, On this sagittal T1-weighted MR image, the mass is hyperintense relative to cerebral cortex. *D*, Sagittal gadolinium-enhanced T1-weighted MR image shows that the lesion enhances homogeneously.

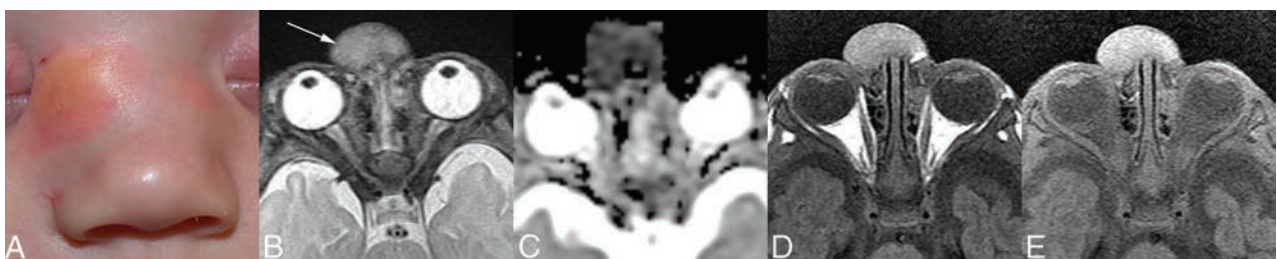


**FIG 5.** A male infant with a mass over the nose that had been present since birth (patient 7). *A*, A clinical photograph at 18 days of age demonstrates a raised, yellowish mass with surrounding erythema over the right side of the nasal bridge. Clinically, this was thought to represent a dermoid, neuroglial heterotopia, or cephalocele. *B*, Axial T2-weighted MR image at 1 month of age demonstrates that the mass (*arrow*) is isointense with the cerebral cortex with no intracranial connection. *C*, DWI ADC image shows that the mass has decreased diffusivity compared with the cortex. *D*, Axial T1-weighted image without contrast demonstrates that the tumor is hyperintense relative to the cortex. *E*, On the gadolinium-enhanced, fat-suppressed T1-weighted image, there is mild homogeneous enhancement, which is difficult to appreciate given the intrinsic hyperintensity on the nonenhanced T1-weighted images. Appreciation of the enhancement is helpful in excluding dermoid and cephalocele.

affected the radiographic differential diagnosis. For example, the small, nonerosive lesions projecting into the external auditory meatus simulated polyps or dermoids. The cutaneous and subcutaneous infra-auricular lesion was mistaken for a benign tumor of hair follicles or possibly a granulomatous infection. Two cases of midline nasal region JXGs mimicked neuroglial heterotopia, encephalocele, or dermoid/epidermoid on physical examination. One of these lesions was thought to be a neuroglial heterotopia at the time of imaging by virtue of the midline nasofrontal location and similar signal characteristics compared with the cortex. In retrospect, a clue as to the correct diagnosis lay in the relative high signal on T1-weighted imaging before contrast, the relatively low signal intensity on T2, and homogeneous enhancement following the administration of contrast. Three lesions (midline frontal, parietal, and infratemporal fossa eroding temporal bone) that demonstrated bony erosion were originally interpreted at the time of imaging as LCH, metastasis (eg, neuroblastoma), fibrous tumor, or other malignant tumor. Reinterpretation of the imaging for this study revealed intrinsic T1 shortening in 2 of 3 of these lesions

that again would have been atypical for entities mentioned in the differential diagnosis. Thus, imaging provides information for surgical planning and can be useful in differentiating JXG from other lesions in the clinical differential diagnosis or at least should prompt inclusion of JXG in the differential diagnosis.

Histologic misclassification can be a pitfall in studies requiring histologic-radiologic correlation. In the current study, we believe the histologic diagnoses to have been ascertained with a high level of certainty. When classic histologic features including Touton giant cells are observed, the microscopic findings in JXG are quite distinctive. When Touton giant cells are lacking, the histologic differential may sometimes expand to include other lesions that can show histiocytic differentiation, as can be observed in a subset of inflammatory myofibroblastic tumors and fibrous histiocytomas; however, immunohistologic and sometimes genetic information can be discriminating in these more difficult cases.

Intracranial involvement in JXG is uncommon and, in our limited experience, includes solitary or multiple dural-based lesions and secondary extension from extracranial sites, as demonstrated in the present series. In some cases, there may be parenchymal edema adjacent to the lesions, which can be associated with seizure activity. Multiple intraparenchymal and subarachnoid foci of JXG are rare but are also described in the literature.<sup>8</sup> Intracranial involvement in JXG is associated with increased mortality and morbidity.<sup>8</sup> The intracranial lesions tend to grow and require follow-up imaging.<sup>11</sup> While cutaneous lesions usually resolve spontaneously, extracutaneous lesions may require medical or surgical intervention.<sup>8</sup> Optimal treatment for unresectable, systemic disease is currently

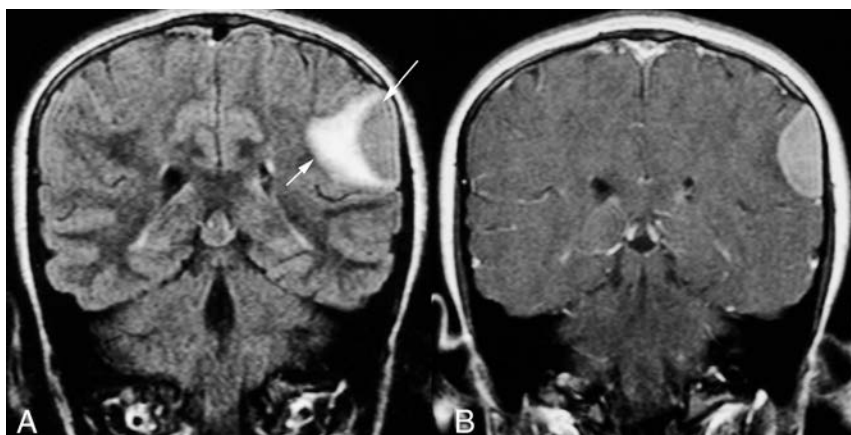


**FIG 6.** A 12-year-old girl with tremor and recent onset of seizures (patient 9). *A*, Coronal FLAIR MR image shows confluent hyperintensity due to edema in the brain parenchyma (*short arrow*) adjacent to the semilunar extra-axial left parietal mass (*long arrow*), which is isointense with the cortex. *B*, Contrast-enhanced T1-weighted MR image shows that the extra-axial lesion enhances homogeneously.



**FIG 7.** A 9-month-old boy with innumerable skin lesions, visceral lesions, and a diagnosis of disseminated JXG (patient 10). *A*, Sagittal contrast-enhanced T1-weighted MR image shows homogeneously enhancing, lobulated, parietal dural-based enhancing lesions (*arrows*). *B*, More medially, there is an erosive lesion within the occipital bone (*long arrow*) with contiguous plaque-like dural enhancement superiorly (*short arrow*). *C*, Axial contrast-enhanced T1-weighted MR image shows a homogeneously enhancing, dome-shaped dural-based lesion (*long arrow*) with tapered dural thickening and enhancement (*arrowheads*), also known as a “dural tail.”

undefined; however, treatment regimens similar to those used for LCH have been used successfully.<sup>27-29</sup>

## CONCLUSIONS

JXG of the HN has a variety of manifestations and can simulate LCH, fibrous tumors, and high-grade, highly cellular lesions such as neuroblastoma or other malignant neoplasms. The presence of a soft-tissue mass with intrinsically high signal intensity on T1-weighted images and relatively low signal intensity on T2-weighted MR images relative to the cerebral cortex, homogeneous enhancement, and decreased diffusivity may suggest the diagnosis of JXG. Familiarity with the common locations, typical imaging appearances, and recognized diagnostic pitfalls outlined herein may prompt radiologists to include JXG in the radiographic differential diagnosis for head and neck masses.

Disclosures: Sara O. Vargas—UNRELATED: Expert Testimony: Previous testimony as an expert witness for medical malpractice cases. Medical issues involved were unrelated to the topic of the current work.

## REFERENCES

1. Jaffe R, Fletcher CD, Burgdorf WH. **Disseminated juvenile xanthogranuloma**. In: Swerdlow SH, Campo E, Harris NL, et al, eds. *WHO Classification of Tumours of Haematopoietic and Lymphoid Tissues*. 4th ed. Lyon: IARC; 2008:366–67
2. Dehner LP. **Juvenile xanthogranulomas in the first two decades of life: a clinicopathologic study of 174 cases with cutaneous and extracutaneous manifestations**. *Am J Surg Pathol* 2003;27:579–93 CrossRef Medline
3. Konar S, Pandey P, Yasha TC. **Solitary juvenile xanthogranuloma in cervical spine: case report and review of the literature**. *Turk Neurosurg* 2014;24:102–07 CrossRef Medline
4. Baik FM, Andeen NK, Schmechel SC, et al. **A large juvenile xanthogranuloma within the tongue**. *Otolaryngol Head Neck Surg* 2014; 150:332–33 CrossRef Medline
5. Puerta P, Candela S, Rovira C, et al. **Juvenile xanthogranuloma of skull base: case report and review of the literature**. *Acta Neurochir (Wien)* 2013;155:1039–40 CrossRef Medline
6. Chiba K, Aihara Y, Eguchi S, et al. **Diagnostic and management difficulties in a case of multiple intracranial juvenile xanthogranuloma**. *Childs Nerv Syst* 2013;29:1039–45 CrossRef Medline
7. Chu MW, Werner A, Moody-Antonio SA. **Juvenile xanthogranuloma of the tympanic membrane: a case report**. *Ear Nose Throat J* 2012;91:364, 366, 368 Medline
8. Lalitha P, Reddy MCh, Reddy KJ. **Extensive intracranial juvenile xanthogranulomas**. *AJNR Am J Neuroradiol* 2011;32:E132–33 CrossRef Medline
9. Johnson TE, Alabiad C, Wei L, et al. **Extensive juvenile xanthogranuloma involving the orbit, sinuses, brain, and subtemporal fossa in a newborn**. *Ophthal Plast Reconstr Surg* 2010; 26:133–34 CrossRef Medline
10. Sun LP, Jin HM, Yang B, et al. **Intracranial solitary juvenile xanthogranuloma in an infant**. *World J Pediatr* 2009;5:71–73 CrossRef Medline
11. Kasliwal MK, Suri A, Rishi A, et al. **Symptomatic bilateral cerebellar mass lesions: an unusual presentation of intracranial xanthogranuloma**. *J Clin Neurosci* 2008;15:1401–04 CrossRef Medline
12. Cao D, Ma J, Yang X, et al. **Solitary juvenile xanthogranuloma in the upper cervical spine: case report and review of the literatures**. *Eur Spine J* 2008;17(suppl 2):S318–23 Medline
13. Margulis A, Melin-Aldana H, Bauer BS. **Juvenile xanthogranuloma invading the muscles in the head and neck: clinicopathological case report**. *Ann Plast Surg* 2003;50:425–28 CrossRef Medline
14. Behne K, Casey T. **Ulcerated juvenile xanthogranuloma of the scalp**. *Australas J Dermatol* 2003;44:74–75 CrossRef Medline
15. Thevasagayam MS, Ghosh S, O'Neill D, et al. **Isolated juvenile xanthogranuloma of the subglottis: case report**. *Head Neck* 2001;23: 426–29 CrossRef Medline
16. Saravanappa N, Rashid AM, Thebe PR, et al. **Juvenile xanthogranuloma of the nasal cavity**. *J Laryngol Otol* 2000;114:460–61 Medline
17. Miskiel KA, Sohaib SA, Rose GE, et al. **Radiological and clinicopathological features of orbital xanthogranuloma**. *Br J Ophthalmol* 2000;84:251–58 CrossRef Medline
18. Shapiro NL, Malis DJ, Charon CC, et al. **Giant juvenile xanthogranuloma of the tongue**. *Am J Otolaryngol* 1999;20:241–44 CrossRef Medline
19. Hidayat AA, Mafee MF, Laver NV, et al. **Langerhans' cell histiocytosis and juvenile xanthogranuloma of the orbit: clinicopathologic, CT, and MR imaging features**. *Radiol Clin North Am* 1998;36:1229–40, xii Medline
20. Tamir I, Davir R, Fellig Y, et al. **Solitary juvenile xanthogranuloma mimicking intracranial tumor in children**. *J Clin Neurosci* 2013;20: 183–88 CrossRef Medline
21. Deisch JK, Patel R, Koral K, et al. **Juvenile xanthogranulomas of the nervous system: a report of two cases and review of the literature**. *Neuropathology* 2013;33:39–46 CrossRef Medline
22. Cornips EM, Cox KE, Creyten DH, et al. **Solitary juvenile xanthogranuloma of the temporal muscle and bone penetrating the dura mater in a 2-month-old boy**. *J Neurosurg Pediatr* 2009;4:588–91 CrossRef Medline
23. Yeh BM, Nobrega KT, Reddy GP, et al. **Juvenile xanthogranuloma of the heart and liver: MRI, sonographic, and CT appearance**. *AJR Am J Roentgenol* 2007;189:W202–04 CrossRef Medline
24. David JK, Anupindi SA, Deshpande V, et al. **Intramuscular juvenile xanthogranuloma: sonographic and MR findings**. *Pediatr Radiol* 2003;33:203–06 CrossRef Medline
25. Rampini PM, Alimehmeti RH, Egidi MG, et al. **Isolated cervical juvenile xanthogranuloma in childhood**. *Spine (Phila Pa 1976)* 2001; 26:1392–95 CrossRef Medline
26. Patterson JW, Wick MR. *Nonmelanocytic Tumors of the Skin: AFIP Atlas of Tumor Pathology*. Washington: American Registry of Pathology; 2006:389–413
27. Auvin S, Cuvelier JC, Vinchon M, et al. **Subdural effusion in a CNS involvement of systemic juvenile xanthogranuloma: a case report treated with vinblastin**. *Brain Dev* 2008;30:164–68 Medline
28. Nakatani T, Morimoto A, Kato R, et al. **Successful treatment of congenital systemic juvenile xanthogranuloma with Langerhans cell histiocytosis-based chemotherapy**. *J Pediatr Hematol Oncol* 2004;26: 371–74 Medline
29. Simko SJ, Tran HD, Jones J, et al. **Clofarabine salvage therapy in refractory multifocal histiocytic disorders, including Langerhans cell histiocytosis, juvenile xanthogranuloma and Rosai-Dorfman disease**. *Pediatr Blood Cancer* 2014;61:479–87 CrossRef Medline

# Diffusion Tractography Biomarkers of Pediatric Cerebellar Hypoplasia/Atrophy: Preliminary Results Using Constrained Spherical Deconvolution

S. Fiori, A. Poretti, K. Pannek, R. Del Punta, R. Pasquariello, M. Tosetti, A. Guzzetta, S. Rose, G. Cioni, and R. Battini



## ABSTRACT

**BACKGROUND AND PURPOSE:** Advances in MR imaging modeling have improved the feasibility of reconstructing crossing fibers, with increasing benefits in delineating angulated tracts such as cerebellar tracts by using tractography. We hypothesized that constrained spherical deconvolution–based probabilistic tractography could successfully reconstruct cerebellar tracts in children with cerebellar hypoplasia/atrophy and that diffusion scalars of the reconstructed tracts could differentiate pontocerebellar hypoplasia, nonprogressive cerebellar hypoplasia, and progressive cerebellar atrophy.

**MATERIALS AND METHODS:** Fifteen children with cerebellar ataxia and pontocerebellar hypoplasia, nonprogressive cerebellar hypoplasia or progressive cerebellar atrophy and 7 controls were included in this study. Cerebellar and corticospinal tracts were reconstructed by using constrained spherical deconvolution. Scalar measures (fractional anisotropy and mean, axial and radial diffusivity) were calculated. A general linear model was used to determine differences among groups for diffusion MR imaging scalar measures, and post hoc pair-wise comparisons were performed.

**RESULTS:** Cerebellar and corticospinal tracts were successfully reconstructed in all subjects. Significant differences in diffusion MR imaging scalars were found among groups, with fractional anisotropy explaining the highest variability. All groups with cerebellar pathologies showed lower fractional anisotropy compared with controls, with the exception of cerebellar hypoplasia.

**CONCLUSIONS:** This study shows the feasibility of constrained spherical deconvolution to reconstruct cerebellar and corticospinal tracts in children with morphologic cerebellar pathologies. In addition, the preliminary results show the potential utility of quantitative analysis of scalars of the cerebellar white matter tracts in children with cerebellar pathologies such as cerebellar hypoplasia and atrophy. Further studies with larger cohorts of patients are needed to validate the clinical significance of our preliminary results.

**ABBREVIATIONS:** AD = axial diffusivity; CA = progressive cerebellar atrophy; CH = nonprogressive cerebellar hypoplasia; CPCT = corticopontocerebellar tract; CST = corticospinal tract; CTT = cerebellar-thalamic tract; dMRI = diffusion MR imaging; FA = fractional anisotropy; MD = mean diffusivity; PCH = pontocerebellar hypoplasia; RD = radial diffusivity

In past years, there has been an increasing interest in the application of advanced MR imaging techniques for in vivo investigation of WM microstructure by using diffusion MR imaging (dMRI).<sup>1</sup> dMRI provides image contrast based on differences in the magnitude of diffusion of water molecules in the brain.<sup>2</sup> By combining the directional information and magnitude of anisotropic diffusion of the individual voxels, the trajectories of the

main WM tracts in the brain can be reconstructed<sup>2,3</sup> and quantitative analysis of WM organization can be performed.<sup>2</sup> dMRI scalars can be measured in specific anatomic ROIs or within/along reconstructed WM tracts to measure tissue properties.<sup>2</sup> Several studies have shown that advanced fiber tractography algorithms provide invaluable qualitative and quantitative information on the brain WM microstructure that cannot be obtained with conventional structural neuroimaging sequences.<sup>2,4</sup>

Developments in high-angular-resolution diffusion imaging<sup>5,6</sup> and progress in postprocessing software that take into ac-

Received July 24, 2015; accepted after revision September 29.

From Istituto di Ricovero e Cura a Carattere Scientifico Stella Maris Foundation (S.F., R.D.P., R.P., M.T., A.G., G.C., R.B.), Pisa, Italy; Section of Pediatric Neuroradiology (A.P.), Division of Pediatric Radiology, Russell H. Morgan Department of Radiology and Radiological Science, The Johns Hopkins School of Medicine, Baltimore, Maryland; Commonwealth Scientific and Industrial Research Organization (K.P., S.R.), Centre for Computational Informatics, Brisbane, Australia; Department of Computing (K.P.), Imperial College London, London, United Kingdom; and Department of Clinical and Experimental Medicine (A.G., G.C.), University of Pisa, Pisa, Italy.

Please address correspondence to Simona Fiori, MD, Department of Developmental Neuroscience, IRCCS Stella Maris Foundation, Viale Del Tirreno 331, 56128 Calambrone, Pisa, Italy; e-mail: s.fiori@fsm.unipi.it

Indicates article with supplemental on-line table.

Indicates article with supplemental on-line photo.

<http://dx.doi.org/10.3174/ajnr.A4607>

count multiple fiber orientations in the same voxel have improved the correct anatomic reconstruction of WM tracts such as the afferent and efferent cerebellar pathways<sup>5-9</sup> by accommodating crossing fibers. Improvements in fiber tractography of the cerebellar pathways are important because a large number of congenital, acquired, or degenerative diseases of pediatric<sup>10-26</sup> and adult<sup>27-31</sup> populations affect the cerebellum.

Currently, the diagnosis of nonprogressive cerebellar hypoplasia (CH) and progressive cerebellar atrophy (CA) is based on qualitative criteria that take into account conventional, structural MR imaging sequences.<sup>32-35</sup> CH refers to a developmental (nonprogressive) reduction of cerebellar volume with preserved near-normal shape,<sup>32</sup> while CA is defined as progressive loss of cerebellar parenchyma, with secondary enlargement of the interfolia space.<sup>33</sup> In some diseases with prenatal onset, hypoplasia of the cerebellum may be associated with pontine hypoplasia (ie, pontocerebellar hypoplasia [PCH]<sup>17</sup>). Despite improvement of structural MR imaging techniques (eg, phased array and higher magnetic field), differentiation of CH and CA remains challenging, particularly when only 1 MR imaging study is available.<sup>32-35</sup> A correct distinction between CH and CA is important in terms of management, prognosis, and family counseling. Neuroimaging methods that may increase the sensitivity in the diagnosis of CH and CA are warranted.

We aimed to study the feasibility of constraint spherical deconvolution fiber tractography to reconstruct cerebellar WM tracts and corticospinal tracts (CSTs) in children with PCH, CH, and CA. We hypothesized that despite different degrees of reduction of cerebellar volumes, our approach could successfully reconstruct cerebellar tracts. In addition, we aimed to measure microstructural properties of cerebellar tracts and CSTs in patients and age-matched controls. We expected that the reconstructed WM tracts would show altered scalar metrics in patients compared with controls. Differences in dMRI scalars of the cerebellar tracts and CSTs among the 3 groups of patients may shed light on the underlying pathomechanism causing macroscopic cerebellar abnormalities and may facilitate the differentiation among the 3 groups of diseases.

## MATERIALS AND METHODS

### Subjects

Children with cerebellar ataxia for this prospective study were recruited at Stella Maris Scientific Institute from June 2013 to January 2015 and underwent MR imaging as part of their clinical diagnostic work-up. Inclusion criteria for this study were evidence of isolated PCH, CH, or CA on structural conventional MR imaging and the availability of 2 structural MR imaging studies at least 1 year apart to clearly differentiate CH and CA. On the basis of the 2 structural neuroimaging studies, all patients were classified into the following groups: CH, PCH, and CA.<sup>32-35</sup> Children with supratentorial abnormalities were excluded from the study. Age-matched typically developing children were recruited as controls. The institutional review board approved the study, and informed parental consent was obtained for all participants.

### Data Acquisition

MR imaging data were acquired by using a 1.5T MR imaging scanner (Signa Horizon 1.5; GE Healthcare, Milwaukee, Wisconsin). A high-resolution structural 3D T1 BRAVO sequence (GE Healthcare) was acquired by using the following parameters: section thickness, 0.9 mm; FOV, 25.6 × 31.5 cm; TR/TE, 12.36/5.18 ms; flip angle, 13°. The acquisition time was 4 minutes and 30 seconds. dMRI data were acquired by using an echo-planar multidirection diffusion-weighted sequence. The imaging parameters were the following: 45 axial sections; section thickness, 3 mm; FOV, 24 × 29.6 cm; acquisition matrix, 80 × 80 (in-plane resolution, 3.0 × 3.7 mm); TR/TE, 11,000/92 ms. dMRI data were acquired along 30 noncollinear directions by using a b-value of 1000 s/mm<sup>2</sup>, in which the encoding gradients were distributed in space by using the electrostatic approach. In addition, 1 measurement without diffusion weighting ( $b=0$  ss/mm<sup>2</sup>) was performed. The dMRI acquisition time was 6 minutes.

### Structural Image Analysis

Structural images were assessed by an experienced pediatric neuroradiologist (R.P.). All MR imaging studies were qualitatively evaluated for the presence of CH, PCH, or CA according to published diagnostic criteria.<sup>15,17</sup> Supratentorial structures were systematically assessed to exclude children with cerebral involvement.

### dMRI Data Analysis and Fiber Tractography

An extensive preprocessing procedure was performed to detect and correct image artifacts caused by involuntary head motion, cardiac pulsation, and intensity inhomogeneities, as previously described,<sup>23,36,37</sup> by using FSL tools (<http://www.fmrib.ox.ac.uk/fsl>),<sup>38</sup> ANTS (<http://picsl.upenn.edu/software/ants/>), and in-house tools. Constrained spherical deconvolution was used to estimate the fiber-orientation distribution for fiber tractography with the MRtrix package (<http://neuro.debian.net/pkgs/mrtrix.html>).<sup>6</sup> To facilitate manual ROI placement, we generated a short-track color-encoded track-density image by using 5 million streamlines of a maximum length of 2 cm seeded throughout the entire brain volume.<sup>23,36,37</sup> Cerebellar tracts were reconstructed on the basis of a multi-ROI approach (On-line Figure).

The corticopontocerebellar tract (CPCT) constitutes the main afferent pathway from the cerebral cortex to the cerebellum. To identify the CPCT, we placed a seeding ROI in the middle cerebellar peduncle (drawn on the coronal plane of the track-density image map in the green area [anteroposterior fiber direction]) and an inclusion ROI in the posterior limb of the internal capsule (drawn on the axial plane of the color-coded track-density image in the blue area [top-down fibers direction]). Frontal, parietal, and occipital projections to the cerebellum were included. ROIs were drawn separately for the right and left sides.

The cerebellar-thalamic tract (CTT) is the main efferent tract from the cerebellum. To identify the CTT, we placed a seeding ROI in the superior cerebellar peduncle (drawn on the coronal plane of the track-density image map in the light blue area [anteroposterior mixed with top-down fiber direction, more vertically displaced compared with CPCT]) separately on the right and left sides.

The CST originates from the precentral areas and descends through the centrum semiovale and ipsilateral posterior limb of internal capsule. To identify the CST, we chose the posterior limb of the internal capsule as the seeding ROI. An additional ROI was placed in the cerebral peduncle, on the right and left sides separately, on the axial plane of the color-coded track-density image, according to WM atlas mapping.<sup>3</sup>

Ten thousand streamlines were generated from the seeding ROIs. The maximum number of attempts (ie, number of seeded streamlines) was 1 million. Several exclusion ROIs were systematically placed to remove aberrant fibers.

Tracts were visually examined by 2 experienced raters (R.P. and S.F.) on all subjects to verify trajectory and anatomic landmarks described in the referenced atlas of human WM<sup>3</sup> and to check false-positive streamlines.

Fractional anisotropy (FA), mean diffusivity (MD), axial diffusivity (AD), and radial diffusivity (RD) were calculated as weighted mean values within each tract.

### Statistical Analysis

For all subjects, several dMRI scalars were calculated for each reconstructed tract. For each tract, a *t* test was used to compare dMRI scalars of the right and left sides. When no significant differences were found, the mean values of the right and left sides were averaged for further analysis.

A general linear model incorporating age as a covariate of no interest was used to determine the difference among groups for fiber tractography scalar measures (FA, MD, AD, RD). Post hoc pair-wise comparisons were performed to correct for multiple comparisons (Bonferroni-corrected *P* values).

Statistical analysis was performed by using SPSS, Version 2.0 (IBM, Armonk, New York), and all *P* values were 2-tailed. Results were considered significant at *P* < .05.

## RESULTS

### Subjects

Fifteen children (mean age, 8.8 ± 4.9 years; range, 4–16 years) with cerebellar abnormalities and 7 normally developing controls (mean age, 9.8 ± 4.2 years; range, 4–16 years) were recruited for this study. On the basis of structural MR imaging studies, patients were classified as follows: 5 children had CH (mean age, 14.2 ± 2.3 years; range, 11–17 years), 5 patients had PCH (mean age, 6.2 ± 4.3 years; range, 3–11 years), and 5 had CA (mean age, 6.2 ± 3.1 years; range, 3–9 years). Detailed demographic, clinical, and genetic information of the 15 patients are shown in On-line Table 1.

Tracts were successfully reconstructed in all subjects (Fig 1); however, fewer than 10,000 streamlines were generated in all groups for both the CPCT (mean number, 8050.89 ± 2076.61) and the CTT (mean number, 5236.67 ± 1731.02), with no differences across groups or controls. No significant differences emerged in scalar measures between the right and left sides. Averaged means and SD of dMRI scalars for each tract are reported in Table 1. Results for FA and MD are plotted in Fig 2. All pair-wise comparisons for averaged scalar measures of each tract are reported in Table 2.

### Corticopontocerebellar Tract

There were significant differences among the groups in FA (*P* < .001, *R*<sup>2</sup> = 0.89), MD (*P* = .005, *R*<sup>2</sup> = 0.59), and RD (*P* = .001, *R*<sup>2</sup> = 0.71). Post hoc analysis revealed that compared with controls, FA was reduced in PCH (Bonferroni-corrected *P* values < .001) and CA (Bonferroni-corrected *P* values = .002). PCH showed lower FA compared with CH (Bonferroni-corrected *P* values < .001) and CA (Bonferroni-corrected *P* values = .001). In addition, in PCH MD (Bonferroni-corrected *P* values = .005) and RD (Bonferroni-corrected *P* values < .001) values were higher compared with those of controls. No differences were found between controls and CH.

### Cerebellar-Thalamic Tract

There were significant differences between groups in FA (*P* < .001, *R*<sup>2</sup> = 0.80) and RD (*P* = .014, *R*<sup>2</sup> = 0.49). Post hoc analysis revealed that compared with controls, FA was significantly lower in PCH (Bonferroni-corrected *P* value < .001) and CA (Bonferroni-corrected *P* value < .001). PCH (Bonferroni-corrected *P* value = .001) and CA (Bonferroni-corrected *P* value = .019) showed lower FA compared with CH. Furthermore, PCH (Bonferroni-corrected *P* value = .041) and CA (Bonferroni-corrected *P* value = .028) showed higher RD compared with controls. No differences were detected between controls and CH.

### Corticospinal Tract

There were significant differences among groups in FA (*P* < .001, *R*<sup>2</sup> = 0.89), AD (*P* = .003, *R*<sup>2</sup> = 0.56), and RD (*P* < .001, *R*<sup>2</sup> = 0.75). Post hoc analysis revealed that compared with controls, FA was lower in PCH (Bonferroni-corrected *P* value < .001) and CA (Bonferroni-corrected *P* value < .001). PCH showed lower FA compared with CH (Bonferroni-corrected *P* value < .001) and CA (Bonferroni-corrected *P* value = .041). Furthermore, PCH showed higher MD compared with controls (Bonferroni-corrected *P* value = .005) and higher RD compared with both controls (Bonferroni-corrected *P* value < .001) and CA (Bonferroni-corrected *P* value = .045). Finally, CA showed lower AD (Bonferroni-corrected *P* value = .043) compared with controls. No differences were detected between controls and CH.

## DISCUSSION

This study shows a 100% success rate for fiber tractography reconstruction of afferent (CPCT) and efferent (CTT) cerebellar tracts and the CST in children with CH, PCH, and CA. We used probabilistic tractography with constrained spherical deconvolution to reconstruct the WM tracts. In adults with ataxic syndromes, previous studies showed that probabilistic tractography is more accurate and less variable compared with deterministic tractography in reconstructing WM tracts within the cerebellar peduncles.<sup>31</sup> However, our very high successful rate is not straightforward because traditional tensor techniques have serious limitations in regions of crossing fibers due to the inability to represent multiple, independent intravoxel orientations. The superior cerebellar peduncles are the main component of the CTT and cross the midline in the midbrain at the level of the inferior colliculus. The dorsomedial portion of the superior cerebellar peduncle and its ventral fibers are the first to decussate, while the middle part de-

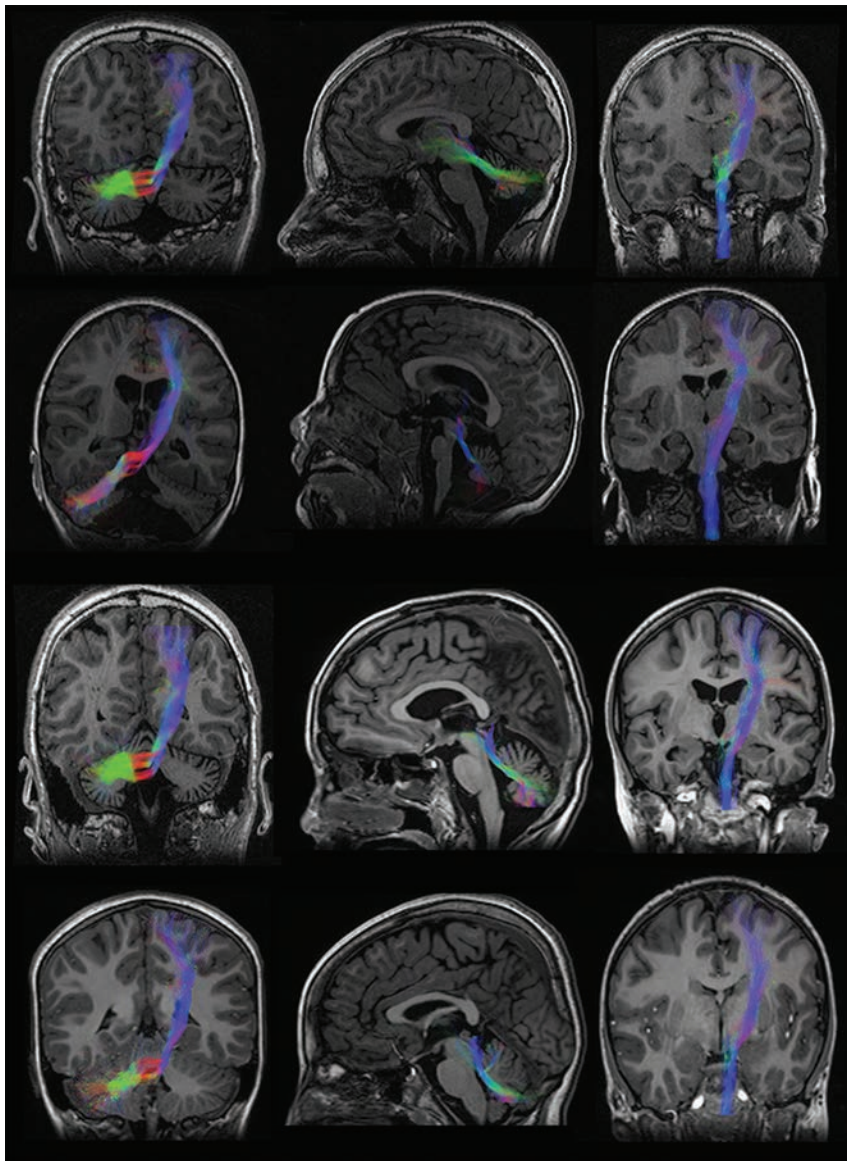


**FIG 1.** Reconstructed bundles for corticopontocerebellar (*left*), cerebellar-thalamic (*middle*), and corticospinal (*right*) tracts in subjects with (from *top to bottom*) CH, PCH, CA, and controls. Bundles are overlaid on T1-weighted images. Figures are representative of the global shape of the reconstructed bundles, irrespective of the cropping of the anatomic section.

**Table 1: Mean and SD of FA, MD, AD, and RD within the CPCT, CTT, and CST**

Tract/Group	FA Mean (SD)	MD Mean (SD) ( $10^{-3} \text{ mm}^2/\text{s}$ )	AD Mean (SD) ( $10^{-3} \text{ mm}^2/\text{s}$ )	RD Mean (SD) ( $10^{-3} \text{ mm}^2/\text{s}$ )
CPCT				
CH	0.42 (0.03)	0.98 (0.11)	1.42 (0.12)	0.76 (0.09)
PCH	0.27 (0.04)	1.14 (0.14)	1.41 (0.08)	0.99 (0.14)
CA	0.35 (0.03)	0.99 (0.03)	1.36 (0.03)	0.81 (0.04)
Control	0.44 (0.02)	0.88 (0.07)	1.37 (0.09)	0.66 (0.06)
CTT				
CH	0.28 (0.03)	1.39 (0.11)	1.79 (0.09)	1.26 (0.17)
PCH	0.19 (0.03)	1.49 (0.18)	1.79 (0.23)	1.39 (0.14)
CA	0.22 (0.02)	1.59 (0.14)	1.68 (0.21)	1.41 (0.15)
Control	0.29 (0.02)	1.29 (0.17)	1.81 (0.19)	1.27 (0.21)
CST				
CH	0.44 (0.02)	1.07 (0.29)	1.69 (0.16)	0.91 (0.11)
PCH	0.31 (0.03)	1.29 (0.13)	1.71 (0.19)	1.08 (0.11)
CA	0.36 (0.03)	1.06 (0.06)	1.46 (0.05)	0.86 (0.06)
Control	0.45 (0.02)	0.97 (0.04)	1.43 (0.06)	0.73 (0.04)

cussates at a more rostral level. The middle cerebellar peduncle represents the last portion of the CPCT. Middle cerebellar peduncles connect the brain stem nuclei with the contralateral cerebellar hemisphere and cross the midline at the level of the pons. Constrained spherical deconvolution is a new and innovative model of the diffusion signal that allows the resolution of crossing fibers in voxels containing multiple fiber orientations.<sup>6</sup> Compared with classic tensor models, it improves the estimated fiber orientations present in each voxel, which is especially important for fiber tractography of bundles with abundant crossing fibers, such as the cerebellar tracts, and allows a more accurate reconstruction of WM tracts.

High-order probabilistic fiber tractography models provide not only qualitative but also quantitative information, and dMRI scalars (FA, MD, AD, and RD) can be measured. The results of our study show differences in dMRI scalars of the cerebellar tracts and CST among the 3 groups of patients and controls. Our findings further support the high value of quantitative analysis of dMRI scalars to assess tissue microstructural properties in children with different cerebellar diseases.<sup>30,31</sup> dMRI scalars are derived from tensor eigenvalues and depend on WM characteristics such as axonal density and the size and degree of myelination.<sup>2,39,40</sup> AD describes water molecule mobility along the main fiber orientation axis (estimates axonal injury<sup>41</sup>), while RD describes water mobility perpendicular to the fiber axis (estimates myelin injury<sup>41</sup>). FA describes the relationship between AD and RD and is related to MD (eg, often a decrease in FA is associated with an increase in MD and RD). Each dMRI scalar, however, can be affected by different tissue properties.<sup>2</sup> In our study, FA values explained the highest amount of variability across groups, in agreement with previous studies.<sup>2,31,39,40</sup> MD changed consistently with FA as shown in Fig 2 but explained across-group variability to a lesser degree.

Post hoc analysis revealed differences in FA and RD values between children with cerebellar pathologies and controls, with the exception of patients with CH. Compared with controls, changes in MD reached statistical significance only in the

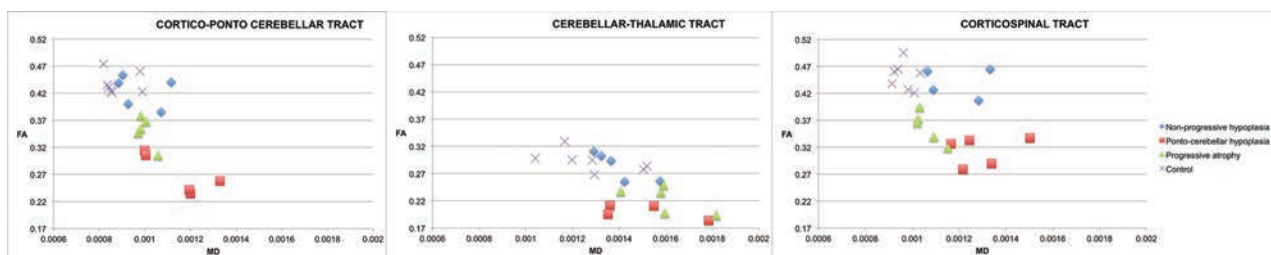


**FIG 2.** Plots of fractional anisotropy and mean diffusivity within the corticopontocerebellar, cerebellar-thalamic, and corticospinal tracts for CH, PCH, CA, and controls.

**Table 2: Pair-wise comparisons for averaged scalar measures of each tract**

	PCH	CA	Control
CPCT			
CH			
FA	(pB < .001) <sup>a</sup>	(pB = .242)	(pB = .714)
MD	(pB = 1.000)	(pB = 1.000)	(pB = .278)
AD	(pB = 1.000)	(pB = 1.000)	(pB = .297)
RD	(pB = .212)	(pB = 1.000)	(pB = .277)
PCH			
FA		(pB < 0.001) <sup>a</sup>	(pB < .001) <sup>a</sup>
MD		(pB = 0.149)	(pB = .005) <sup>a</sup>
AD		(pB = 1.000)	(pB = .952)
RD		(pB = .045) <sup>a</sup>	(pB < .001) <sup>a</sup>
CA			
FA			(pB = .002) <sup>a</sup>
MD			(pB = .821)
AD			(pB = 1.000)
RD			(pB = .289)
CTT			
CH			
FA	(pB = .001) <sup>a</sup>	(pB = .019) <sup>a</sup>	(pB = 1.000)
MD	(pB = 1.000)	(pB = 1.000)	(pB = 1.000)
AD	(pB = 1.000)	(pB = 1.000)	(pB = 1.000)
RD	(pB = 1.000)	(pB = 1.000)	(pB = .715)
PCH			
FA		(pB = .293)	(pB < .001) <sup>a</sup>
MD		(pB = 1.000)	(pB = .504)
AD		(pB = .914)	(pB = 1.000)
RD		(pB = 1.000)	(pB = .041) <sup>a</sup>
CA			
FA			(pB = .001) <sup>a</sup>
MD			(pB = .071)
AD			(pB = .315)
RD			(pB = .028) <sup>a</sup>
CST			
CH			
FA	(pB < .001) <sup>a</sup>	(pB = .082)	(pB = .492)
MD	(pB = .621)	(pB = 1.000)	(pB = 1.000)
AD	(pB = 1.000)	(pB = .289)	(pB = .143)
RD	(pB = .265)	(pB = 1.000)	(pB = .018)
PCH			
FA		(pB = .041) <sup>a</sup>	(pB < .001) <sup>a</sup>
MD		(pB = .221)	(pB = .005) <sup>a</sup>
AD		(pB = .040) <sup>a</sup>	(pB = .157)
RD		(pB = .045) <sup>a</sup>	(pB < .001) <sup>a</sup>
CA			
FA			(pB < .001) <sup>a</sup>
MD			(pB = 1.000)
AD			(pB = 1.000)
RD			(pB = .215)

**Note:**—pB indicates Bonferroni-corrected *P* value.

<sup>a</sup> Significant.

CPCT of children with PCH. However, boxplots showed a trend of changes in MD in children with CA matching FA changes across groups (reduction of FA corresponded to an increase of MD and RD<sup>2</sup>). Changes in dMRI scalars in cerebellar WM tracts may generally result from primary or secondary involvement. In WM tracts with primary involvement, myelin necrosis and axonal loss may lead to the formation of cystic spaces filled by CSF. The increased content of unhindered, isotropically diffusing water in these cavities is shown by a marked increase in MD.<sup>42</sup> On the contrary, in secondary WM involvement, there is neither substantial water accumulation in the interstitial spaces nor formation of cysts, even of microscopic dimensions, resulting in only a limited increase in MD.<sup>42</sup>

In children with PCH, we found a reduction of FA in all tracts compared with all groups, with the exception of CTT compared with children with CA. In addition, subjects with PCH showed higher MD and RD compared with controls in the CPCT and CST and higher RD in the CTT compared with controls. These findings support an involvement of WM tracts outside the cerebellum as previously shown by neuropathology studies.<sup>43</sup> In addition, neuropathology studies in PCH showed regressive (primary) changes with cystic formation in the cerebellar WM.<sup>44</sup> Degenerative cystic formation in the cerebellar WM causes an increase in isotropically diffusing water and, hence, a marked increase in MD as we found in the CPCT (including the middle cerebellar peduncle) of children with PCH. This explanation applies to at least 2 of the 5 patients with PCH. Three subjects with PCH had mutations in the *CASK* gene.<sup>45</sup> *CASK*-related PCH is rather of a malformative, not degenerative, nature. Neuropathology findings in a 2-week-old male patient revealed mainly GM involvement.<sup>46</sup> A more recent study, however, showed a role of *CASK* in axonal outgrowth and branching, supporting WM involvement as shown by our results.<sup>47</sup> Further studies including a larger and more homogeneous group of patients with PCH may elucidate the detailed pathomechanism leading to dMRI changes in GM or WM tracts within and outside of the cerebellum.

In children with CA, we found reduced FA compared with controls and CH in all reconstructed WM tracts and an increase in RD in the CTT, including the superior cerebellar peduncle. In neuronal ceroid lipofuscinosis and congenital disorders of glycosylation type 1a due to *PMM2* mutation, neuropathology studies showed that the primary involvement affected the cerebellar cortex with extensive loss of Purkinje cells and granule cells.<sup>48</sup> Neuropathology studies and our findings (decrease in FA and increase in RD without significant changes in MD) suggest that involvement of the cerebellar WM is most likely of a secondary nature

(Wallerian degeneration). In subjects with CA, we found dMRI changes not only within the cerebellar tracts but also in the CST. This finding may reflect a more diffuse involvement as shown in PCH. In neuronal ceroid lipofuscinosis, atrophy of the cerebral cortex and periventricular WM abnormalities have been reported.<sup>49</sup> Atrophy of the cerebral cortex and abnormalities of the subcortical WM have also been shown in congenital disorders of glycosylation type 1a.<sup>50</sup> Although no supratentorial abnormalities were detected in our patients on conventional MR imaging, changes in the CST may be secondary to ongoing injury of the cerebral cortex and subcortical WM.

In children with CH, we did not find differences in scalars compared with controls. This result is in contrast with the findings in CA and PCH. The lack of differences in dMRI scalars between children with CH and controls suggests that the microstructure of cerebellar WM tracts is preserved (eg, normal axonal packing, diameter, and myelination) and that a malformed cerebellum does not cause a secondary alteration of the connecting WM tracts (at least detectable by our approach). This finding is important for the primary or secondary role of the cerebellum in the pathogenesis of cognitive and affective impairment in children with CH. Distinction between CA and CH is not difficult in theory but can be problematic or impossible in practice on the basis of a single examination.<sup>32–35</sup> An accurate differentiation between CA and CH is important for a targeted diagnostic work-up, correct diagnosis, early institution of the correct therapy, prediction of the prognosis, and counseling of the family, including inheritance pattern and risk of recurrence. Our preliminary results suggest that FA values of the CTT may differentiate CA and CH on a single neuroimaging study. Our preliminary results, however, need to be validated in future studies, including larger cohorts of patients.

### Limitations

This study was performed in the context of a clinical MR imaging examination. Due to the need for a short acquisition time, we were able to apply only 30 gradient directions. This number of directions is too low to qualify the technique as high-angular-resolution diffusion imaging.<sup>5</sup> However, we believe that this number of directions is appropriate for a preliminary project to study the feasibility of advanced processing procedures with constrained spherical deconvolution in children with cerebellar pathologies. A higher number of gradient directions, measurement of DTI scalars along the white matter tracts (instead of 1 average value), and inclusion of additional white matter tracts (eg, spinocerebellar tracts) may provide additional important information and should be considered for future research studies, including a larger cohort of patients. The sample size is limited due to the inclusion criteria and the low prevalence of the included cerebellar pathologies in the pediatric population. However, the significant results, even in a small cohort of patients, are convincing.<sup>51</sup>

### CONCLUSIONS

Our study shows the feasibility of probabilistic tractography with constrained spherical deconvolution to reconstruct cerebellar tracts and the CST in children with morphologic cerebellar pathologies. In addition, our preliminary results show the potential

utility of quantitative analysis of scalars of the cerebellar WM tracts in children with cerebellar pathologies such as CH and CA. Further studies with larger cohorts of patients are needed to validate the clinical significance of our preliminary results.

### ACKNOWLEDGMENTS

We thank all children who took part in the study and their families.

### REFERENCES

1. Assaf Y, Pasternak O. **Diffusion tensor imaging (DTI)-based white matter mapping in brain research: a review.** *J Mol Neurosci* 2008;34:51–61 CrossRef Medline
2. Jones DK, Knösche TR, Turner R. **White matter integrity, fiber count, and other fallacies: the do's and don'ts of diffusion MRI.** *Neuroimage* 2013;73:239–54 CrossRef Medline
3. Mori S, Wakana S, Nagae-Poetscher LM, et al. *MRI Atlas of Human White Matter.* Amsterdam: Elsevier; 2005
4. Rollins NK. **Clinical applications of diffusion tensor imaging and tractography in children.** *Pediatr Radiol* 2007;37:769–80 CrossRef Medline
5. Tournier JD, Calamante F, Connelly A. **Determination of the appropriate b value and number of gradient directions for high-angular-resolution diffusion-weighted imaging.** *NMR Biomed* 2013;26:1775–86 CrossRef Medline
6. Tournier JD, Yeh CH, Calamante F, et al. **Resolving crossing fibers using constrained spherical deconvolution: validation using diffusion-weighted imaging phantom data.** *Neuroimage* 2008;42:617–25 CrossRef Medline
7. Palesi F, Tournier JD, Calamante F, et al. **Contralateral cerebello-thalamo-cortical pathways with prominent involvement of associative areas in humans in-vivo.** *Brain Struct Funct* 2015;220:3369–84 CrossRef Medline
8. Chokshi FH, Poretti A, Meoded A, et al. **Normal and abnormal development of the cerebellum and brainstem as depicted by diffusion tensor imaging.** *Semin Ultrasound CT MR* 2011;32:539–54 CrossRef Medline
9. Kamali A, Kramer LA, Frye RE, et al. **Diffusion tensor tractography of the human brain cortico-ponto-cerebellar pathways: a quantitative preliminary study.** *J Magn Reson Imaging* 2010;32:809–17 CrossRef Medline
10. Klingberg T, Vaidya CJ, Gabrieli JD, et al. **Myelination and organization of the frontal white matter in children: a diffusion tensor MRI study.** *Neuroreport* 1999;10:2817–21 CrossRef Medline
11. Saksena S, Husain N, Malik GK, et al. **Comparative evaluation of the cerebral and cerebellar white matter development in pediatric age group using quantitative diffusion tensor imaging.** *Cerebellum* 2008;7:392–400 CrossRef Medline
12. Leitner Y, Travis KE, Ben-Shachar M, et al. **Tract profiles of the cerebellar white matter pathways in children and adolescents.** *Cerebellum* 2015 Feb 4. [Epub ahead of print] CrossRef Medline
13. Boltshauser E. **Cerebellar imaging: an important signpost in paediatric neurology.** *Childs Nerv Syst* 2001;17:211–16 CrossRef Medline
14. Poretti A, Huisman TA, Scheer I, et al. **Joubert syndrome and related disorders: spectrum of neuroimaging findings in 75 patients.** *AJNR Am J Neuroradiol* 2011;32:1459–63 CrossRef Medline
15. Volpe JJ. **Brain injury in premature infants: a complex amalgam of destructive and developmental disturbances.** *Lancet Neurol* 2009;8:110–24 CrossRef Medline
16. Namavar Y, Barth PG, Kasher PR, et al. **Clinical, neuroradiological and genetic findings in pontocerebellar hypoplasia.** *Brain* 2011;134:143–56 CrossRef Medline
17. Widjaja E, Blaser S, Raybaud C. **Diffusion tensor imaging of midline posterior fossa malformations.** *Pediatr Radiol* 2006;36:510–17 CrossRef Medline
18. Huisman TA, Bosemani T, Poretti A. **Diffusion tensor imaging for**

- brain malformations: does it help?** *Neuroimaging Clin N Am* 2014; 24:619–37 CrossRef Medline
19. Bucci M, Mandelli ML, Berman JJ, et al. **Quantifying diffusion MRI tractography of the corticospinal tract in brain tumors with deterministic and probabilistic methods.** *Neuroimage Clin* 2013;3: 361–68 CrossRef Medline
  20. Poretti A, Boltshauser E, Loenneker T, et al. **Diffusion tensor imaging in Joubert syndrome.** *AJNR Am J Neuroradiol* 2007;28:1929–33 CrossRef Medline
  21. Fiori S, Pannek K, Pasquariello R, et al. **Corticopontocerebellar connectivity disruption in congenital hemiplegia.** *Neurorehabil Neural Repair* 2015;29:858–66 CrossRef Medline
  22. Law N, Bouffet E, Laughlin S, et al. **Cerebello-thalamo-cerebral connections in pediatric brain tumor patients: impact on working memory.** *Neuroimage* 2011;56:2238–48 CrossRef Medline
  23. Jeong JW, Asano E, Juhász C, et al. **Quantification of primary motor pathways using diffusion MRI tractography and its application to predict postoperative motor deficits in children with focal epilepsy.** *Hum Brain Mapp* 2014;35:3216–26 CrossRef Medline
  24. Lui YW, Law M, Chacko-Mathew J, et al. **Brainstem corticospinal tract diffusion tensor imaging in patients with primary posterior fossa neoplasms stratified by tumor type: a study of association with motor weakness and outcome.** *Neurosurgery* 2007;61:1199–1207; discussion 1207–08 CrossRef Medline
  25. Kovanlikaya I, Firat Z, Kovanlikaya A, et al. **Assessment of the corticospinal tract alterations before and after resection of brainstem lesions using diffusion tensor imaging (DTI) and tractography at 3T.** *Eur J Radiol* 2011;77:383–91 CrossRef Medline
  26. Law N, Greenberg M, Bouffet E, et al. **Visualization and segmentation of reciprocal cerebrocerebellar pathways in the healthy and injured brain.** *Hum Brain Mapp* 2015;36:2615–28 CrossRef Medline
  27. Rizzo G, Tonon C, Valentino ML, et al. **Brain diffusion-weighted imaging in Friedreich's ataxia.** *Mov Disord* 2011;26:705–12 CrossRef Medline
  28. Pagani E, Ginestroni A, Della Nave R, et al. **Assessment of brain white matter fiber bundle atrophy in patients with Friedreich ataxia.** *Radiology* 2010;255:882–89 CrossRef Medline
  29. Ying SH, Landman BA, Chowdhury S, et al. **Orthogonal diffusion-weighted MRI measures distinguish region-specific degeneration in cerebellar ataxia subtypes.** *J Neurol* 2009;256:1939–42 CrossRef Medline
  30. Yoon B, Kim JS, Lee KS, et al. **Early pathological changes in the cerebellum of patients with pure cerebellar syndrome demonstrated by diffusion-tensor imaging.** *Eur Neurol* 2006;56:166–71 CrossRef Medline
  31. Prakash N, Hageman N, Hua X, et al. **Patterns of fractional anisotropy changes in white matter of cerebellar peduncles distinguish spinocerebellar ataxia-1 from multiple system atrophy and other ataxia syndromes.** *Neuroimage* 2009;47(suppl 2):T72–81 CrossRef Medline
  32. Poretti A, Boltshauser E, Doherty D. **Cerebellar hypoplasia: differential diagnosis and diagnostic approach.** *Am J Med Genet C Semin Med Genet* 2014;166C:211–26 CrossRef Medline
  33. Poretti A, Wolf NI, Boltshauser E. **Differential diagnosis of cerebellar atrophy in childhood.** *Eur J Paediatr Neurol* 2008;12:155–67 CrossRef Medline
  34. Boltshauser E. **Cerebellar hypoplasias.** *Handb Clin Neurol* 2008;87: 115–27 CrossRef Medline
  35. Boltshauser E. **Cerebellum-small brain but large confusion: a review of selected cerebellar malformations and disruptions.** *Am J Med Genet A* 2004;126A:376–85 CrossRef Medline
  36. Pannek K, Raffelt D, Bell C, et al. **HOMOR: higher order model outlier rejection for high b-value MR diffusion data.** *Neuroimage* 2012;63:835–42 CrossRef Medline
  37. Pannek K, Boyd RN, Fiori S, et al. **Assessment of the structural brain network reveals altered connectivity in children with unilateral cerebral palsy due to periventricular white matter lesions.** *Neuroimage Clin* 2014;5:84–92 CrossRef Medline
  38. Jenkinson M, Beckmann CF, Behrens TE, et al. **FSL.** *Neuroimage* 2012;62:782–90 CrossRef Medline
  39. Kanai R, Rees G. **The structural basis of inter-individual differences in human behaviour and cognition.** *Nat Rev Neurosci* 2011;12: 231–42 CrossRef Medline
  40. Johansen-Berg H. **Behavioural relevance of variation in white matter microstructure.** *Curr Opin Neurol* 2010;23:351–58 CrossRef Medline
  41. Song SK, Sun SW, Ramsbottom MJ, et al. **Dysmyelination revealed through MRI as increased radial (but unchanged axial) diffusion of water.** *Neuroimage* 2002;17:1429–36 CrossRef Medline
  42. Pierpaoli C, Barnett A, Pajevic S, et al. **Water diffusion changes in Wallerian degeneration and their dependence on white matter architecture.** *Neuroimage* 2001;13:1174–85 Medline
  43. Namavar Y, Barth PG, Poll-The BT, et al. **Classification, diagnosis and potential mechanisms in pontocerebellar hypoplasia.** *Orphanet J Rare Dis* 2011;6:50 CrossRef Medline
  44. Barth PG, Aronica E, de Vries L, et al. **Pontocerebellar hypoplasia type 2: a neuropathological update.** *Acta Neuropathol* 2007;114: 373–86 CrossRef Medline
  45. Takanashi J, Arai H, Nabatame S, et al. **Neuroradiologic features of CASK mutations.** *AJNR Am J Neuroradiol* 2010;31:1619–22 CrossRef Medline
  46. Najm J, Horn D, Wimplinger I, et al. **Mutations of CASK cause an X-linked brain malformation phenotype with microcephaly and hypoplasia of the brainstem and cerebellum.** *Nat Genet* 2008;40: 1065–67 CrossRef Medline
  47. Kuo TY, Hong CJ, Chien HL, et al. **X-linked mental retardation gene CASK interacts with Bcl11A/CTIP1 and regulates axon branching and outgrowth.** *J Neurosci Res* 2010;15:88:2364–73 CrossRef Medline
  48. Anderson GW, Goebel HH, Simonati A. **Human pathology in NCL.** *Biochim Biophys Acta* 2013;1832:1807–26 CrossRef Medline
  49. Jadav RH, Sinha S, Yasha TC, et al. **Magnetic resonance imaging in neuronal ceroid lipofuscinosis and its subtypes.** *Neuroradiol J* 2012; 25:755–61 CrossRef Medline
  50. Feraco P, Mirabelli-Badenier M, Severino M, et al. **The shrunken, bright cerebellum: a characteristic MRI finding in congenital disorders of glycosylation type 1a.** *AJNR Am J Neuroradiol* 2012;33: 2062–67 CrossRef Medline
  51. Friston K. **Ten ironic rules for non-statistical reviewers.** *Neuroimage* 2012;61:1300–10 CrossRef Medline

# Cerebral Reorganization after Hemispherectomy: A DTI Study

 A. Meoded,  A.V. Faria,  A.L. Hartman,  G.I. Jallo,  S. Mori,  M.V. Johnston,  T.A.G.M. Huisman, and  A. Poretti



## ABSTRACT

**BACKGROUND AND PURPOSE:** Hemispherectomy is a neurosurgical procedure to treat children with intractable seizures. Postsurgical improvement of cognitive and behavioral functions is observed in children after hemispherectomy suggesting plastic reorganization of the brain. Our aim was to characterize changes in DTI scalars in WM tracts of the remaining hemisphere in children after hemispherectomy, assess the associations between WM DTI scalars and age at the operation and time since the operation, and evaluate the changes in GM fractional anisotropy values in patients compared with controls.

**MATERIALS AND METHODS:** Patients with congenital or acquired neurologic diseases who required hemispherectomy and had high-quality postsurgical DTI data available were included in this study. Atlas- and voxel-based analyses of DTI raw data of the remaining hemisphere were performed. Fractional anisotropy and mean, axial, and radial diffusivity values were calculated for WM and GM regions. A linear regression model was used for correlation between DTI scalars and age at and time since the operation.

**RESULTS:** Nineteen patients after hemispherectomy and 21 controls were included. In patients, a decrease in fractional anisotropy and axial diffusivity values and an increase in mean diffusivity and radial diffusivity values of WM regions were observed compared with controls ( $P < .05$ , corrected for multiple comparisons). In patients with acquired pathologies, time since the operation had a significant positive correlation with white matter fractional anisotropy values. In all patients, an increase in cortical GM fractional anisotropy values was found compared with controls ( $P < .05$ ).

**CONCLUSIONS:** Changes in DTI metrics likely reflect Wallerian and/or transneuronal degeneration of the WM tracts within the remaining hemisphere. In patients with acquired pathologies, postsurgical fractional anisotropy values correlated positively with elapsed time since the operation, suggesting a higher ability to recover compared with patients with congenital pathologies leading to hemispherectomy.

**ABBREVIATIONS:** ABA = atlas-based analysis; AD = axial diffusivity; CGC = cingulate bundle at the cortex; FA = fractional anisotropy; MD = mean diffusivity; RD = radial diffusivity; VBA = voxel-based analysis

**H**emispherectomy is a neurosurgical procedure to treat children with intractable seizures that start in childhood, arise diffusely from 1 hemisphere, and are associated with unihemispheric insults.<sup>1,2</sup> These include congenital (eg, hemimegalen-

cephaly and prenatal stroke) or postnatally acquired (eg, Rasmussen encephalitis and traumatic brain injury) lesions.<sup>1,3</sup>

Postsurgical improvement of cognitive and behavioral functions is observed in children after hemispherectomy.<sup>4-8</sup> Motor, cognitive, and behavioral outcomes after hemispherectomy, however, differ among children and depend on the etiology and time of onset of the underlying pathology and age of the child at neurosurgery.<sup>6,9-11</sup> These differences suggest that posthemispherectomy plastic reorganization of brain circuitry may differ on the basis of the underlying disease.

We used DTI to investigate the WM architecture of the re-

Received August 12, 2015; accepted after revision November 3.

From the Section of Pediatric Neuroradiology (A.M., T.A.G.M.H., A.P.), Division of Pediatric Radiology, Russell H. Morgan Department of Radiology and Radiological Sciences (A.V.F., S.M.), and Departments of Neurology (A.L.H., M.V.J.) and Neurosurgery (G.I.J.), The Johns Hopkins University School of Medicine, Baltimore, Maryland; and F.M. Kirby Research Center for Functional Brain Imaging (S.M.), Kennedy Krieger Institute (M.V.J.), Baltimore, Maryland.

Susumu Mori was funded by National Institutes of Health grants: P41EB015909 and R01 NS084957.

Please address correspondence to Andrea Poretti, MD, Section of Pediatric Neuro-radiology, Division of Pediatric Radiology, Russell H. Morgan Department of Radiology and Radiological Sciences, The Johns Hopkins University School of Medicine, Zayed Building Room 4174, 1800 Orleans St, Baltimore, MD 21287; e-mail: aporetti@jhmi.edu

 Indicates open access to non-subscribers at [www.ajnr.org](http://www.ajnr.org)

 Indicates article with supplemental on-line tables.

 Indicates article with supplemental on-line photos.

<http://dx.doi.org/10.3174/ajnr.A4647>

maintaining cerebral hemisphere in children after hemispherectomy. We performed the following: 1) characterization of the changes in DTI metrics in WM tracts of the remaining hemisphere in children after hemispherectomy, and 2) assessment of the associations between WM DTI scalars and age at and time since neurosurgery. We hypothesized the following: 1) a secondary degeneration of WM tracts in patients compared with controls, and 2) more severe changes in DTI scalars in patients with congenital compared with postnatally acquired pathologies. Finally, we evaluated the changes in GM fractional anisotropy (FA) values in patients compared with controls.

## MATERIALS AND METHODS

This retrospective study was approved by the Johns Hopkins University review board.

### Subjects

The inclusion criteria for this study were the following: 1) status post full anatomic hemispherectomy with sparing of only the basal ganglia and thalamus, and 2) availability of postsurgical DTI data without artifacts. Demographic data and detailed information about the etiology of intractable seizures leading to hemispherectomy (classified as “congenital” for cortical malformations and prenatally acquired lesions and “acquired” for postnatally acquired lesions), age at neurosurgery, and time interval between the operation and the DTI study were collected by a review of the clinical charts.

Controls were selected from our neuroimaging data base by using 3 criteria: 1) normal brain anatomy, 2) absence of neurologic disorders, and 3) availability of DTI raw data. MR imaging studies of the controls were acquired for clinical indications such as facial skin lesions or evaluation of soft-tissue pathologies confined to the head and neck region.

### DTI Acquisition

DTI data were acquired on two 1.5T scanners (Intera; Philips Healthcare, Best, Netherlands; and Avanto; Siemens, Erlangen, Germany). On the Philips scanner, a DTI dataset was acquired with a multisection, single-shot echo-planar (sensitivity encoding factor = 2.5) spin-echo sequence. Diffusion-weighting was applied along 32 directions with a b-value of 700 s/mm<sup>2</sup>. Five minimally weighted images (b-value = 33 s/mm<sup>2</sup>) were also acquired. For the acquisition of the DTI data, we used the following parameters: section thickness = 2.5 mm, FOV = 240 × 240 mm, and matrix size = 96 × 96 reconstructed/interpolated to a matrix of 256 × 256. The acquisition was repeated 3 times to enhance the SNR.

DTI parameters on the Siemens scanner were the following: 20 noncollinear directions and a high b-value of 1000 s/mm<sup>2</sup>. An additional measurement without diffusion-weighting ( $b = 0$  s/mm<sup>2</sup>) was performed. For the acquisition of the DTI data, we used the following parameters: section thickness = 2.5 mm, FOV = 240 × 240 mm, and matrix size = 192 × 192. We used parallel imaging (integrated parallel acquisition technique) = 2 with a generalized autocalibrating partially parallel acquisition reconstruction. The acquisition was repeated twice to enhance the SNR.

### DTI Postprocessing

DTI postprocessing was performed off-line by using MRI Studio software (Jiang H and Mori S, Johns Hopkins University; at [www.MriStudio.org](http://www.MriStudio.org)). The raw diffusion-weighted images were first coregistered to one of the least diffusion-weighted images and corrected for eddy current and subject motion. We generated the following map: FA, color-coded FA, trace of diffusion, axial diffusivity (AD) and radial diffusivity (RD), and mean B0. After skull-stripping, we subsequently normalized the images to the Montreal Neurological Institute coordinates by using B0 images for both the subject and the template. Two “half-brain templates,” including only 1 cerebral hemisphere (right and left, respectively), were previously created by using the JHU-MNI template (On-line Fig 1). Subsequently, a transformation by using a dual-contrast (FA and trace of diffusion) large deformation diffeomorphic metric mapping was applied.

As the next step, atlas-based analysis (ABA) was performed by using the WM parcellation map of the “half-brain JHU-MNI template” to parcellate the brain into 88 anatomic regions including both GM and WM. Because of the reciprocal nature of both linear and nonlinear transformations, the transformation results were used to warp the parcellation map to the original DTI data, thus automatically segmenting each brain into the 88 subregions. After exclusion of the extracerebral spaces by a trace of diffusion threshold at 0.0045, FA, mean diffusivity (MD), AD, and RD values were calculated for following categories of tracts: 1) projection tracts: posterior limb of the internal capsule; anterior, superior, and posterior corona radiata; 2) association tracts: cingulate bundle at the cortex (CGC), cingulate bundle–hippocampal part, superior longitudinal fasciculus, and superior fronto-occipital fasciculus; and 3) commissural tracts: genu, body, and splenium of the corpus callosum of the remaining hemisphere.<sup>12</sup> In addition, DTI metrics were collected for the following GM structures: superior parietal, frontal, temporal occipital, precentral, postcentral, and cingulate gyri and the thalamus and putamen. MD values were calculated using the formula:

$$MD = \text{Trace of Diffusion}/3.$$

After ABA, voxel-based analysis (VBA) was performed by a normalization of the subject data to the template by using the large deformation diffeomorphic metric mapping matrix. Statistical parametric mapping was used to assess DTI scalar differences between all patients and controls. VBA was performed with SPM8 (<http://www.fil.ion.ucl.ac.uk/spm/software/spm8>) for Matlab, Version 2011b (MathWorks, Natick, Massachusetts). After masking all images with the half-brain template and flipping all images to the left side, we smoothed the images with a 10-mm full width at half maximum filter. The postprocessed scans of the patient group were compared with the scans of controls by using a 2-sample *t* test, with scanner as a covariate. For the statistical analysis, an explicit WM mask (FA threshold of >0.2) created with ROI EDITOR (<http://cmrm.med.jhmi.edu/cmrm/forumMRI/forum.php?id=3>) was used. VBA was performed for FA, MD, AD, and RD maps. In our analyses, we used false discovery rate correction for multiple comparisons with  $P < .05$  and a 30-voxel extent threshold. Finally, after controlling for correlation for right and

**Table 1: Demographic and clinical data of all patients with hemispherectomy**

Patients	Sex	Age at Study (yr)	Age at Operation (yr)	Time since Operation (yr)	Diagnosis	Etiology Group
1	M	8.1	5.9	2.2	HME left	Congenital
2	M	3.3	1.1	2.2	HME left	Congenital
3	M	14.8	3.7	11.1	Cortical dysplasia right <sup>a</sup>	Congenital
4	M	2.2	0.9	1.3	HME left	Congenital
5	F	2.7	2.7	0.02	Cortical dysplasia right <sup>a</sup>	Congenital
6	M	12.9	5.7	7.2	Cortical dysplasia left <sup>a</sup>	Congenital
7	F	11.5	6.9	4.6	Cortical dysplasia right <sup>a</sup>	Congenital
8	F	0.9	0.8	0.1	HME left	Congenital
9	M	14.0	2.3	11.7	Prenatal stroke right	Congenital
10	F	8.9	4.1	4.8	Prenatal stroke left	Congenital
11	F	20.5	2.5	18.0	Prenatal stroke right	Congenital
12	F	8.7	2.2	6.5	Rasmussen right	Acquired
13	F	3.9	3.1	0.8	Rasmussen left	Acquired
14	F	18.1	9.8	8.3	Rasmussen right	Acquired
15	F	15.2	3.8	11.4	Rasmussen right	Acquired
16	F	12.2	4.1	8.1	Rasmussen right	Acquired
17	F	25.0	12.9	12.1	Rasmussen right	Acquired
18	F	20.7	4.4	16.3	Postnatal stroke right	Acquired
19	F	14.5	5.7	8.8	Postnatal stroke right	Acquired

**Note:**—HME indicates hemimegalencephaly.

<sup>a</sup> Includes an extensive unilateral malformation of cortical development affecting >1 cerebral lobe requiring full anatomic hemispherectomy rather than a more conservative neurosurgical approach.

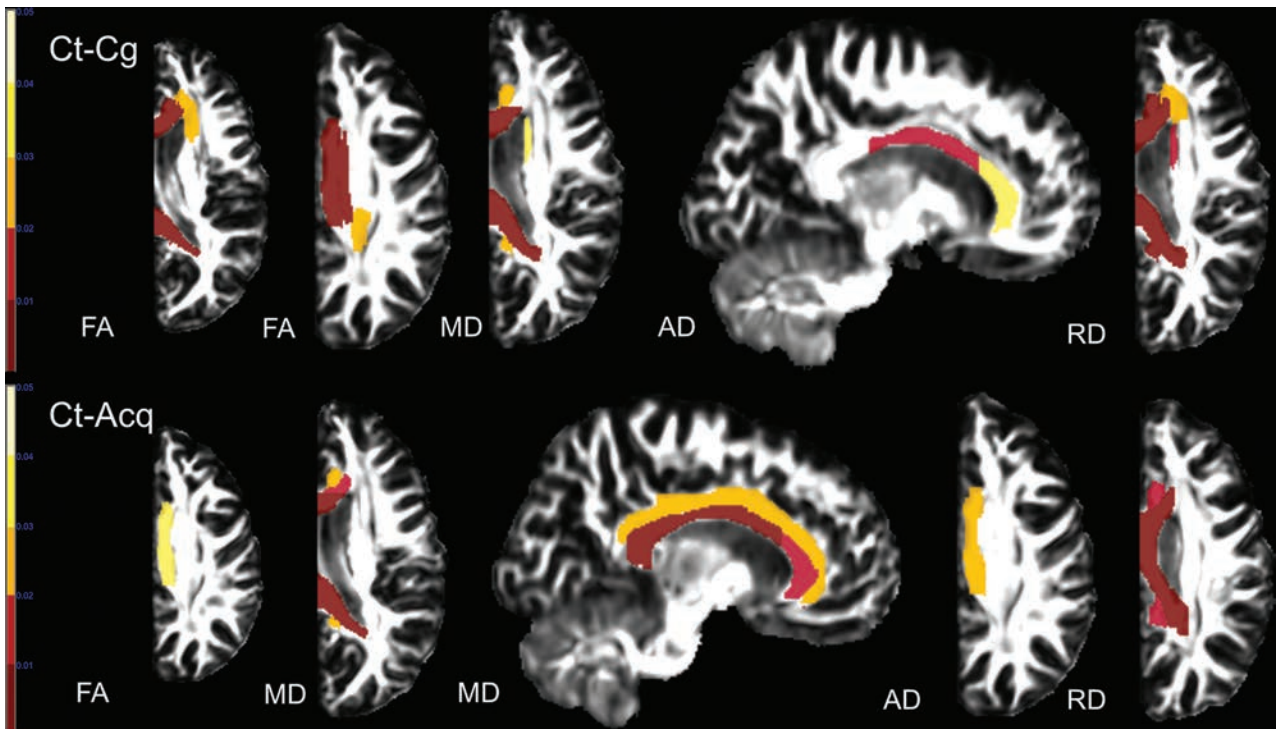


**FIG 1.** Results of ABA. Compared with controls (Ct), patients with anatomic hemispherectomy because of a congenital (Cg) and acquired (Acq) underlying etiology showed a decrease in FA and AD and an increase in MD and RD in multiple WM tracts. Only results that survived the Tukey significant difference test are depicted with  $P < .05$ . Color bars represent  $P = .001-.05$  with a color gradient from red to light yellow. Ct-Cg indicates differences between controls and patients with congenital etiology leading to hemispherectomy; Ct-Acq indicates differences between controls and patients with acquired etiology leading to hemispherectomy.

left structures in our controls, we flipped the right half-brain to the left for all patients and controls, so analysis was done on the left hemisphere.

**Statistical Analysis**

Statistical analyses were performed by using SPSS, Version 21 (IBM, Armonk, New York). Data obtained from ABA analysis was compared by using a 1-way ANCOVA with scanner type as a

covariate. Post hoc analyses were performed by using the Tukey significant difference test. To evaluate the associations between DTI scalars of the selected WM tracts and GM structures and age at the operation and time since the operation, we used a linear regression model in which age, sex, and disease duration were considered as covariates. In all our analyses, observed differences were considered statistically significant with  $P < .05$ .

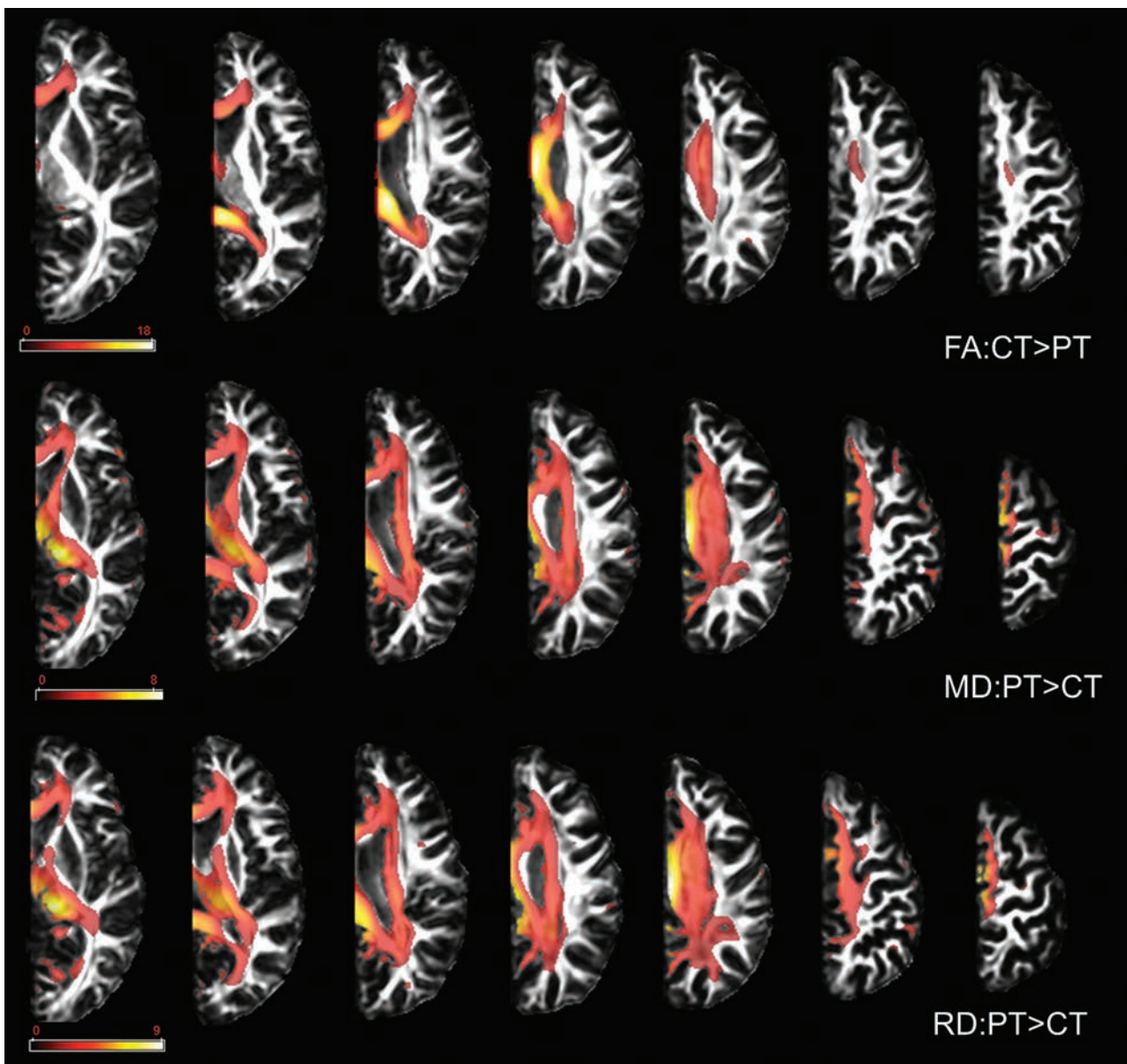


**FIG 2.** Results of the VBA. Compared with controls, patients showed a decrease in FA values and an increase in MD and RD values in all examined WM tracts. Only results that survived false discovery rate correction for multiple comparisons are depicted, with  $P < .05$ . Color bars represent the  $t$  statistics. PT indicates patients; CT indicates controls.

## RESULTS

### Subjects

There were 19 patients (13 females; median age at MR imaging, 12.2 years; range, 0.9–25.0 years) and 21 controls (14 females; median age at MR imaging, 12.2 years; range, 0.9–29.0 years). Median age at the operation and median time since the operation were 3.8 years (range, 0.8–12.9 years) and 7.2 years (range, 0.02–18.0 years), respectively. Eleven (5 females) patients had a congenital etiology leading to hemispherectomy; 8 patients (all females) had an acquired etiology (Table 1). The median age at MR imaging for the patients with a congenital etiology was 8.9 years (range, 0.9–20.5 years); median age at the operation, 2.7 years (range, 0.8–6.9 years); and median time since the operation, 4.6 years (range, 0.02–18.0 years). The median age at MR imaging for the patients with an acquired etiology was 14.9 years (range, 3.9–25.0 years); median age at the operation, 4.3 years (range, 2.2–12.9

years); and median time since the operation, 8.6 years (range, 0.8–16.3 years).

### Atlas-Based Analysis of WM Tracts

One-way ANOVA and post hoc analyses revealed significant changes in DTI scalars within the projection (anterior corona radiata and posterior corona radiata), association (CGC and superior fronto-occipital fasciculus), and commissural (genu of the corpus callosum, body of the corpus callosum, and splenium of the corpus callosum) tracts between patients after hemispherectomy and controls (On-line Tables 1 and 2). When significantly different, FA and AD values were lower, and MD and RD values, higher in patients after hemispherectomy compared with controls (Fig 1). DTI changes between both groups of patients and controls involved commissural and association tracts more than projection tracts. A higher number of differences in DTI scalars and WM

**Table 2: Significant correlations between DTI scalars in WM structures and clinical parameters in patients after hemispherectomy classified on the basis of the underlying etiology<sup>a</sup>**

Clinical Parameter/Etiology Group	DTI Scalars	WM Tracts	Pearson Correlation Coefficient	P Value	R <sup>2</sup>	Adjusted R <sup>2</sup>	
Age at the operation	Congenital	FA	CGC	0.840	.001	0.71	0.67
		FA	PLIC	-0.737	.037	0.54	0.47
	Acquired	RD	SCR	0.919	.001	0.84	0.82
		MD	PCR	0.884	.004	0.78	0.75
		RD	PCR	0.744	.034	0.55	0.48
Time since the operation	Congenital	FA	CGC	-0.632	.037	0.40	0.33
		FA	PLIC	0.805	.016	0.65	0.59
	Acquired	RD	PLIC	-0.792	.019	0.63	0.56
		RD	ACR	-0.802	.017	0.64	0.58
		RD	SCR	-0.906	.002	0.82	0.79
		MD	PCR	-0.788	.020	0.62	0.56
		MD	CGC	-0.728	.041	0.53	0.45
		FA	GCC	0.722	.043	0.52	0.44

**Note:**—ACR indicates anterior corona radiata; GCC, genu of the corpus callosum; PCR, posterior corona radiata; SCR, superior corona radiata; PLIC, posterior limb of internal capsule.

<sup>a</sup> Pearson correlation coefficient, *r*<sup>2</sup>, adjusted *r*<sup>2</sup>, and *P* value from multivariate linear regression analysis are shown.

tracts were found between patients with congenital pathologies and controls compared with patients with acquired pathologies and controls. Between patients with congenital and acquired pathologies, only FA values in the CGC were significantly higher in the acquired group (On-line Fig 2).

#### Voxel-Based Analysis of WM Tracts

VBA showed a decrease in FA and an increase in MD and RD values in patients after hemispherectomy compared with controls (Fig 2). Changes in FA values were similar between VBA and ABA, while changes in MD and RD were more prominent for VBA compared with ABA. Compared with ABA, VBA did not reveal significant changes in AD. Changes in DTI scalars involved commissural and association tracts more than projection tracts, confirming the ABA results.

#### Correlation between WM Tract DTI Scalars and Clinical Parameters

In patients with acquired pathologies, age at the operation showed a significant negative correlation with FA values and a significant positive correlation with MD and RD values in projection tracts (Table 2). In the same group of patients, time since the operation had a significant positive correlation with FA values and a significant negative correlation with MD and RD values in projection fibers, the cingulate bundle at the cortex, and the genu of the corpus callosum. In patients with congenital etiology, however, only FA values within the cingulate bundle at the cortex showed a significant positive correlation with age at the operation and a significant negative correlation with time since the operation.

#### Atlas-Based Analysis and Correlation Analysis of GM Regions

ABA of cortical GM regions revealed a significant reduction in FA values within the superior frontal, temporal, parietal, occipital, pre- and postcentral, and cingulate gyrus in all patients compared with controls (Fig 3). Within the putamen, however, FA values were significantly higher in the congenital group compared with both the acquired group and controls. MD, AD, and RD did not

show significant differences between patients and controls; statistically significant correlations with clinical measures were not observed.

#### DISCUSSION

The ability of the central nervous system to adapt and reorganize following injury early in life is remarkable but has been difficult to study systematically in human infants. Data have been mostly accumulated from case studies and suggest that lesions sustained in early childhood are associated with better recovery.<sup>13</sup> This finding indicates a prominent structural reorganization of the human brain.<sup>14-16</sup> The posthemispherectomy brain offers a unique opportunity for studying the structural and functional neuroanatomic reorganization that underlies plasticity. Previous studies in patients after hemispherectomy applied DTI to study the reorganization of the motor and sensory tracts.<sup>9,17,18</sup> These studies showed marked trophic and microstructural changes within the ipsilesional corticospinal tract, while no differences were seen between the ipsi- and contralesional medial lemnisci.

We studied the contralateral (remaining) cerebral hemisphere by using ABA and VBA.<sup>19</sup> These postprocessing approaches are considered complementary.<sup>20</sup> ABA groups voxel values within a segmentation, resulting in a marked reduction of information (from >1 million voxels within a brain to 176 anatomic regions). This reduction (voxel averaging) may lead to a higher statistical power, reduction of noise, and an easier biologic interpretation. VBA, however, has a higher sensitivity to detect subtle abnormalities that may remain undetected by ABA. For both ABA and VBA, we used a half-brain template to avoid inaccurate normalization due to ipsilateral brain tissue remnants after anatomic hemispherectomy (eg, the thalamus). The accuracy of the brain parcellation hinges on the accuracy of the image transformation and subsequent atlas warping. Previous studies have shown a high level of accuracy by using the large deformation diffeomorphic metric mapping algorithm for populations with marked anatomic distortions, various disease models, and different image conditions.<sup>21,22</sup> In our opinion, the use of a half-brain template and

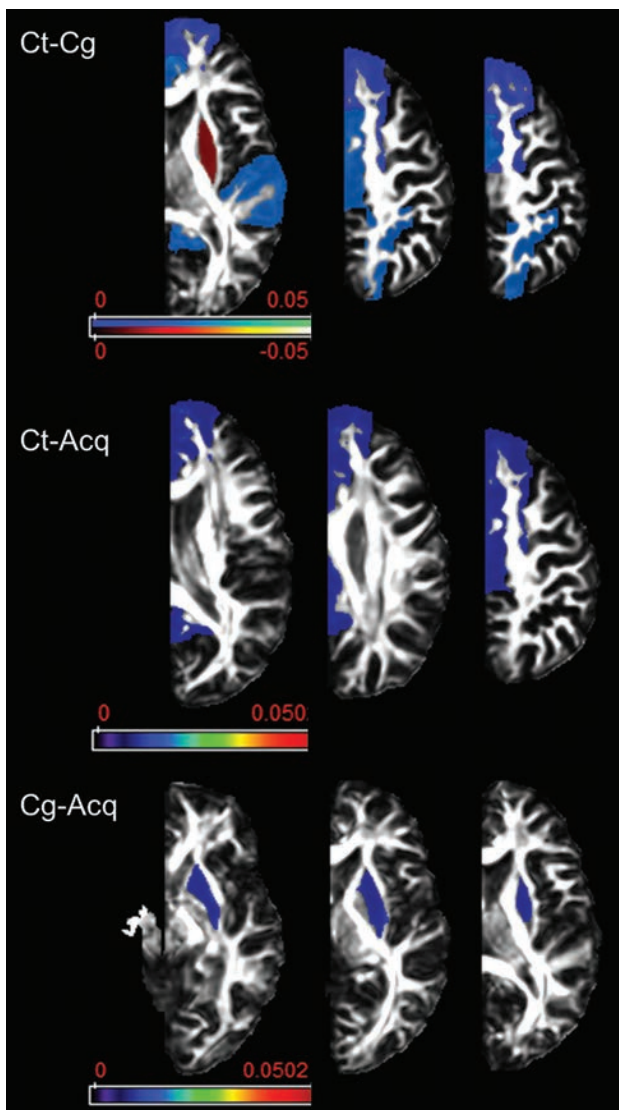


**FIG 3.** Results of atlas-based analysis of GM structures. Compared with controls, patients in both etiology groups showed decreased FA in all the examined cortical areas with the exception of the putamen, which showed increased FA in the congenital group. Only results that survived the Tukey significant difference test are depicted, with  $P < .05$ . The *Color bar* represents the  $P$  value: blue–light blue represents  $PT < CT$ , and red–light yellow represents  $CT < PT$ . PT indicates patients including Cg (congenital) and Acq (acquired) pathologies; CT, controls.

ABA as a low granularity filter helped to improve the parcellation accuracy in this study. Although state-of-the-art methods were used in all the steps, we cannot completely exclude minor inaccuracies within brain mapping.

In our study, ABA and VBA provided similar results, including a decrease in FA values and an increase in MD and RD values in the cerebral WM tracts of patients after hemispherectomy compared with controls. In addition, ABA revealed reduced AD values in cerebral WM tracts of patients compared with controls. Reduction in FA and AD associated with an increase in MD and RD is suggestive of secondary Wallerian and/or transneuronal degeneration.<sup>23</sup> These changes in DTI scalars may indicate an increase in isotropic tissue diffusion characteristics consistent with the presence of gliosis and the possible increase in extracellular ma-

trix as shown by histology in Wallerian and/or transneuronal degeneration.

Between patients with congenital and acquired pathologies, the only significant difference was found in FA values of the CGC, which were lower in the congenital group. A previous fMRI study showed activation in the cingulate cortex after passive foot dorsiflexion in patients after hemispherectomy.<sup>24</sup> This may suggest a role of the CGC in rewiring cortical regions after hemispherectomy and assuming new functions such as motor tasks. Higher FA values suggest a better reorganization in the acquired group, matching the better motor recovery in these patients.<sup>10</sup>

Highly different correlations were seen between both patient groups and age at the operation and time since the operation. In the acquired group, age at the operation negatively correlated with FA values but had a positive correlation with MD and RD values in various components of the corona radiata. This finding suggests a more severe degeneration of projection fibers in children who underwent the operation at an older age. In this group, an early operation may save the contralesional WM tracts from progressive degeneration and may support/promote the greatest postsurgical improvement with the application of rehabilitation techniques earlier during brain development.<sup>25</sup> Time since the operation, however, correlated well with an increase (normalization) of FA values and reduction of MD and RD values in WM tracts. This correlation suggests that patients with an acquired pathology have a progressive neuronal reorganization.

For the congenital group, we found less obvious results. Our structural findings match previous outcome studies that show poorer posthemispherectomy outcome in patients with congenital etiologies.<sup>5,10</sup> In patients with congenital pathologies, structural and functional abnormalities have been shown within the “healthy” cerebral hemisphere.<sup>26,27</sup> Our findings are contrary to the Kennard principle suggesting that the immature brain should be able to recover more easily from injury than the more developed brain.<sup>28</sup> More recent studies have shown that lesions occurring during critical phases of brain development may result in severe disabilities caused by disturbed development of the neuronal networks.

In cortical GM regions, ABA revealed a decrease in FA values in patients compared with controls. The reduction in anisotropy may reflect increased unoccupied intracellular space due to a change in neuronal cell attenuation and/or reduction of the cortical neuropil. However, the significance of FA in GM is still poorly understood. Compared with WM, various cell types (eg, neuronal cell bodies, randomly oriented axons, dendritic fibers, oligodendrocytes) and extracellular matrices are present in GM structures and may affect the diffusion properties and degree of anisotropy.<sup>29,30</sup> Putaminal FA values were significantly higher in the congenital group compared with both the acquired group and controls. This is an unexpected finding. Recently, increase in FA in GM structures after mild traumatic brain injury was shown to reflect progressive gliosis.<sup>31</sup> In this study, it is unclear whether an increase in putaminal FA may reflect pre- or postsurgical gliosis in patients with congenital etiologies.

We are aware of some limitations of our study. Prehemispherectomy DTI data were not available for this study. Accordingly, we cannot exclude the possibility that presurgical WM mi-

crostructural alterations may partially explain postsurgical DTI changes. The number of patients was rather small. However, few previous pediatric studies are available due to the rarity of the surgical procedure. The 2 groups of patients are of different median ages and have different age distributions. With progressing brain maturation, DTI scalars evolve. However, the most important age-related changes in DTI scalars occur within the first 4 years of life.<sup>32-34</sup> Both studied groups of patients were markedly older (median ages of 8.9 and 14.9 years, respectively). The retrospective nature of this study made it impossible to correlate longitudinally collected clinical parameters of motor and cognitive functions and DTI scalars. Future prospective studies should include presurgical DTI data and longitudinally collected clinical parameters of neurologic functions to evaluate neuroplasticity in children after anatomic hemispherectomy more accurately.

## CONCLUSIONS

DTI is an ideal tool to study brain reorganization and may shed light on the structural cerebral plasticity in patients after hemispherectomy. Changes in DTI metrics reflect Wallerian and/or transneuronal degeneration of the commissural, association, and projection WM tracts within the remaining hemisphere. In patients with acquired pathologies, postsurgical FA values tend to normalize with time, suggesting a higher potential for recovery compared with patients with congenital etiologies leading to hemispherectomy.

## ACKNOWLEDGMENTS

We are thankful to Amy Bastian, PhD, Kennedy Krieger Institute, Baltimore, Maryland, for sharing imaging data of some patients with us.

Disclosures: Andreia V. Faria—RELATED: Grant: National Institutes of Health National Institute of Biomedical Imaging and Bioengineering (R03 EB014357).\* Adam L. Hartman—UNRELATED: Board Membership: Wiley Publishers (Associate Editor for *Epilepsia*); Expert Testimony: medicolegal work; Grants/Grants Pending: National Institute of Neurological Disorders and Stroke.\* TEDCO.\* Johns Hopkins University.\* Harrington Foundation.\* Howard Hughes Medical Institute.\* Patents (planned, pending, or issued): Patent Cooperation Treaty filed (to be prosecuted in 2016); Royalties: Wiley, Wolters/Kluwer, Taylor & Francis; Travel/Accommodations/Meeting Expenses Unrelated to Activities Listed: American Academy of Pediatrics, American Epilepsy Society, George I. Jallo—UNRELATED: Expert Testimony: several defense malpractice cases; Royalties: Plural Publishing Inc, Thieme, Springer. Susumi Mori—UNRELATED: Consultancy: AnatomyWorks; Grants/Grants Pending: National Institutes of Health grants\*; Patents (planned, pending, or issued): patents. One issued patent about 3D tractograph reconstruction (this technology uses the results of DTI and 3D reconstructs white matter pathway; this technology was not used in this manuscript) and 12 invention disclosures related to postprocessing of MR images including quantitative analysis and feature extraction of MR images (these disclosures are related to quantitative analysis of MR images and extraction, storing, and comparison of anatomical features in the images; these disclosures include some approaches of structural labeling that have been used in this article); Royalties: Academic Press, Elsevier; Travel/Accommodations/Meeting Expenses Unrelated to Activities Listed: business travel paid by AnatomyWorks; OTHER RELATIONSHIPS: Cofounder of AnatomyWorks. \*Money paid to the institution.

## REFERENCES

- Vining EP, Freeman JM, Pillas DJ, et al. **Why would you remove half a brain? The outcome of 58 children after hemispherectomy—the Johns Hopkins experience: 1968 to 1996.** *Pediatrics* 1997;100:163–71 CrossRef Medline
- Grissensauer CJ, Salam S, Hendrix P, et al. **Hemispherectomy for treatment of refractory epilepsy in the pediatric age group: a systematic review.** *J Neurosurg Pediatr* 2015;15:34–44 CrossRef Medline
- Kossoff EH, Vining EP, Pillas DJ, et al. **Hemispherectomy for intractable unihemispheric epilepsy etiology vs outcome.** *Neurology* 2003; 61:887–90 CrossRef Medline
- Kossoff EH, Vining EP, Pyzik PL, et al. **The postoperative course and management of 106 hemidecortications.** *Pediatr Neurosurg* 2002;37: 298–303 CrossRef Medline
- Jonas R, Nguyen S, Hu B, et al. **Cerebral hemispherectomy: hospital course, seizure, developmental, language, and motor outcomes.** *Neurology* 2004;62:1712–21 CrossRef Medline
- Pulsifer MB, Brandt J, Salorio CF, et al. **The cognitive outcome of hemispherectomy in 71 children.** *Epilepsia* 2004;45:243–54 CrossRef Medline
- Battaglia D, Chieffo D, Lettori D, et al. **Cognitive assessment in epilepsy surgery of children.** *Childs Nerv Syst* 2006;22:744–59 CrossRef Medline
- Devlin AM, Cross JH, Harkness W, et al. **Clinical outcomes of hemispherectomy for epilepsy in childhood and adolescence.** *Brain* 2003; 126:556–66 CrossRef Medline
- Wakamoto H, Eluvathingal TJ, Makki M, et al. **Diffusion tensor imaging of the corticospinal tract following cerebral hemispherectomy.** *J Child Neurol* 2006;21:566–71 CrossRef Medline
- van der Kolk NM, Boshuisen K, van Empelen R, et al. **Etiology-specific differences in motor function after hemispherectomy.** *Epilepsy Res* 2013;103:221–30 CrossRef Medline
- Zhang J, Mei S, Liu Q, et al. **fMRI and DTI assessment of patients undergoing radical epilepsy surgery.** *Epilepsy Res* 2013;104:253–63 CrossRef Medline
- Wakana S, Jiang H, Nagae-Poetscher LM, et al. **Fiber tract-based atlas of human white matter anatomy.** *Radiology* 2004;230:77–87 CrossRef Medline
- Werth R. **Visual functions without the occipital lobe or after cerebral hemispherectomy in infancy.** *Eur J Neurosci* 2006;24:2932–44 CrossRef Medline
- Bittar RG, Ptito A, Reutens DC. **Somatosensory representation in patients who have undergone hemispherectomy: a functional magnetic resonance imaging study.** *J Neurosurg* 2000;92:45–51 CrossRef Medline
- Holloway V, Gadian DG, Vargha-Khadem F, et al. **The reorganization of sensorimotor function in children after hemispherectomy: a functional MRI and somatosensory evoked potential study.** *Brain* 2000;123(pt 12):2432–44 Medline
- Olausson H, Ha B, Duncan GH, et al. **Cortical activation by tactile and painful stimuli in hemispherectomized patients.** *Brain* 2001; 124:916–27 CrossRef Medline
- Mori H, Aoki S, Abe O, et al. **Diffusion property following functional hemispherectomy in hemimegalencephaly.** *Acta Radiol* 2004; 45:778–81 CrossRef Medline
- Choi JT, Vining EP, Mori S, et al. **Sensorimotor function and sensorimotor tracts after hemispherectomy.** *Neuropsychologia* 2010;48: 1192–99 CrossRef Medline
- Oishi K, Faria AV, Yoshida S, et al. **Quantitative evaluation of brain development using anatomical MRI and diffusion tensor imaging.** *Int J Dev Neurosci* 2013;31:512–24 CrossRef Medline
- Faria AV, Zhang J, Oishi K, et al. **Atlas-based analysis of neurodevelopment from infancy to adulthood using diffusion tensor imaging and applications for automated abnormality detection.** *Neuroimage* 2010;52:415–28 CrossRef Medline
- Oishi K, Faria A, Jiang H, et al. **Atlas-based whole brain white matter analysis using large deformation diffeomorphic metric mapping: application to normal elderly and Alzheimer's disease participants.** *Neuroimage* 2009;46:486–99 CrossRef Medline
- Djamanakova A, Faria AV, Hsu J, et al. **Diffeomorphic brain mapping based on T1-weighted images: improvement of registration accuracy by multichannel mapping.** *J Magn Reson Imaging* 2013;37: 76–84 CrossRef Medline
- Pierpaoli C, Barnett A, Pajevic S, et al. **Water diffusion changes in**

- Wallerian degeneration and their dependence on white matter architecture. *Neuroimage* 2001;13:1174–85 CrossRef Medline
24. de Bode S, Firestine A, Mathern GW, et al. **Residual motor control and cortical representations of function following hemispherectomy: effects of etiology.** *J Child Neurol* 2005;20:64–75 CrossRef Medline
  25. Fritz SL, Rivers ED, Merlo AM, et al. **Intensive mobility training postcerebral hemispherectomy: early surgery shows best functional improvements.** *Eur J Phys Rehabil Med* 2011;47:569–77 Medline
  26. Jahan R, Mischel PS, Curran JG, et al. **Bilateral neuropathologic changes in a child with hemimegalencephaly.** *Pediatr Neurol* 1997;17:344–49 CrossRef Medline
  27. Salamon N, Andres M, Chute DJ, et al. **Contralateral hemimicrocephaly and clinical-pathological correlations in children with hemimegalencephaly.** *Brain* 2006;129:352–65 Medline
  28. Dennis M. **Margaret Kennard (1899–1975): not a ‘principle’ of brain plasticity but a founding mother of developmental neuropsychology.** *Cortex* 2010;46:1043–59 CrossRef Medline
  29. Komlos ME, Horkay F, Freidlin RZ, et al. **Detection of microscopic anisotropy in gray matter and in a novel tissue phantom using double pulsed gradient spin echo MR.** *J Magn Reson* 2007;189:38–45 CrossRef Medline
  30. Yoshida S, Oishi K, Faria AV, et al. **Diffusion tensor imaging of normal brain development.** *Pediatr Radiol* 2013;43:15–27 CrossRef Medline
  31. Budde MD, Janes L, Gold E, et al. **The contribution of gliosis to diffusion tensor anisotropy and tractography following traumatic brain injury: validation in the rat using Fourier analysis of stained tissue sections.** *Brain* 2011;134:2248–60 CrossRef Medline
  32. Hermoye L, Saint-Martin C, Cosnard G, et al. **Pediatric diffusion tensor imaging: normal database and observation of the white matter maturation in early childhood.** *Neuroimage* 2006;29:493–504 CrossRef Medline
  33. Saksena S, Husain N, Malik GK, et al. **Comparative evaluation of the cerebral and cerebellar white matter development in pediatric age group using quantitative diffusion tensor imaging.** *Cerebellum* 2008;7:392–400 CrossRef Medline
  34. Cancelliere A, Mangano FT, Air EL, et al. **DTI values in key white matter tracts from infancy through adolescence.** *AJNR Am J Neuroradiol* 2013;34:1443–49 CrossRef Medline

# Quantitative Assessment of Neovascularization after Indirect Bypass Surgery: Color-Coded Digital Subtraction Angiography in Pediatric Moyamoya Disease

H.-H. Cho, J.-E. Cheon, S.-K. Kim, Y.H. Choi, I.-O. Kim, W.S. Kim, S.-M. Lee, S.K. You, and S.-M. Shin

## ABSTRACT

**BACKGROUND AND PURPOSE:** For the postoperative follow-up in pediatric patients with Moyamoya disease, it is essential to evaluate the degree of neovascularization status. Our aim was to quantitatively assess the neovascularization status after bypass surgery in pediatric Moyamoya disease by using color-coded digital subtraction angiography.

**MATERIALS AND METHODS:** Time-attenuation intensity curves were generated at ROIs corresponding to surgical flap sites from color-coded DSA images of the common carotid artery, internal carotid artery, and external carotid artery angiograms obtained pre- and postoperatively in 32 children with Moyamoya disease. Time-to-peak and area under the curve values were obtained. Postoperative changes in adjusted time-to-peak ( $\Delta$ TTP) and ratios of adjusted area under the curve changes ( $\Delta$ AUC ratio) of common carotid artery, ICA, and external carotid artery angiograms were compared across clinical and angiographic outcome groups. To analyze diagnostic performance, we categorized clinical outcomes into favorable and unfavorable groups.

**RESULTS:** The  $\Delta$ TTP at the common carotid artery increased among clinical and angiographic outcomes, in that order, with significant differences ( $P = .003$  and  $.005$ , respectively). The  $\Delta$ AUC ratio at the common carotid artery and external carotid artery also increased, in that order, among clinical and angiographic outcomes with a significant difference (all,  $P = .000$ ). The  $\Delta$ AUC ratio of ICA showed no significant difference among clinical and angiographic outcomes ( $P = .418$  and  $.424$ , respectively). The  $\Delta$ TTP for the common carotid artery of  $>1.27$  seconds and the  $\Delta$ AUC ratio of  $>33.5\%$  for the common carotid artery and  $504\%$  for the external carotid artery are revealed as optimal cutoff values between favorable and unfavorable groups.

**CONCLUSIONS:** Postoperative changes in quantitative values obtained with color-coded DSA software showed a significant correlation with outcome scores and can be used as objective parameters for predicting the outcome in pediatric Moyamoya disease, with an additional cutoff value calculated through the receiver operating characteristic curve.

**ABBREVIATIONS:** AUC = area under the curve; CCA = common carotid artery;  $\Delta$ AUC ratio = adjusted area under the curve changes;  $\Delta$ TTP = difference between preoperative and postoperative time-to-peak; ECA = external carotid artery; EDAS = encephaloduroarteriosynangiosis; MMD = Moyamoya disease

Moyamoya disease (MMD) is a cerebrovascular disease causing progressive steno-occlusive changes at the terminal portion of the ICAs or proximal areas of the anterior or middle cerebral arteries with compensatory development of a fine vascular network, the so-called “Moyamoya” vessels.<sup>1-4</sup> Surgical neo-

vascularization is considered the most successful means of improving cerebral hemodynamics and resolving clinical symptoms.<sup>1,2,4-7</sup> These surgical procedures can be categorized into 3 types: direct, indirect, or combined bypass.<sup>1,2,5-9</sup> Indirect bypass surgery using the parietal branch of the superficial temporal artery, encephaloduroarteriosynangiosis (EDAS), is preferred in pediatric patients with MMD because of the simple technique and the lower risk of temporary ischemia during the operation.<sup>5,10-12</sup> Additional bifrontal encephalogaleo(perioosteal)synangiosis can be performed to reinforce the anterior circulation.

After bypass surgery, it is essential to evaluate the degree of neovascularization via the external carotid artery (ECA) system and subsequent changes occurring in the ICAs. DSA is thought to be the most reliable imaging technique for these purposes and has been used for initial diagnosis and evaluation of neovascularization. However, evaluation of neovascularization after bypass sur-

Received July 27, 2015; accepted after revision September 15.

From the Department of Radiology (H.-H.C., J.-E.C., Y.H.C., I.-O.K., W.S.K., S.-M.L., S.K.Y.), Seoul National University Hospital, Seoul, Korea; Department of Radiology (J.-E.C., Y.H.C., I.-O.K., W.S.K.), Seoul National University College of Medicine, Seoul, Korea; Institute of Radiation Medicine (J.-E.C., I.-O.K., W.S.K.), Seoul National University Medical Research Center, Seoul, Korea; Division of Pediatric Neurosurgery (S.-K.K.), Seoul National University Children's Hospital, Seoul, Korea; and Department of Radiology (S.-M.S.), Seoul Metropolitan Government-Seoul National University, Boramae Medical Center, Seoul, Korea.

Please address correspondence to Jung-Eun Cheon, MD, Department of Radiology, Seoul National University Hospital, 101 Daehak-ro, Jongno-gu, Seoul, 110-744, Korea; e-mail: cheonje@snu.ac.kr

<http://dx.doi.org/10.3174/ajnr.A4614>

gery with DSA is usually subjective and could not provide the objective information for the postoperative revascularization status.

Recently, a color-coded postprocessing software program for the quantitative analysis of DSA was introduced<sup>13</sup> and used as guidance for thrombolytic therapy or embolization and for perfusion analysis in adult patients with MMD.<sup>14-16</sup> The purpose of this study was to quantitatively assess the neovascularization status after indirect bypass surgery in children with MMD by using postprocessing software.

## MATERIALS AND METHODS

### Patients

The institutional review board of Seoul National University Hospital approved this retrospective study; informed consent was waived. From August 2012 to March 2014, 198 patients underwent DSA for underlying MMD in our institution. We included patients with both preoperative and postoperative DSA after an initial unilateral EDAS. Ninety-one patients were excluded because there were no available preoperative ( $n = 23$ ) or postoperative ( $n = 68$ ) DSA images. Seventy-five patients were excluded because DSA images were obtained with a different protocol between the pre- and postoperative DSAs (no available common carotid artery [CCA] angiogram,  $n = 28$ ; different contrast media injection rate and volume,  $n = 35$ ; different magnification,  $n = 12$ ).

Finally, 32 patients (13 male and 19 female; mean age, 8.0 years; range, 3~18 years) were included. Initial symptoms included motor TIA in 22 patients (68.8%), seizures in 6 patients (18.8%), headache in 2 patients (6.3%), and sensory TIA in 2 patients (6.3%). Among these, 23 patients (71.9%) underwent EDAS and 9 patients (28.1%) underwent unilateral EDAS and bifrontal encephalogleo(perioosteal)synangiosis simultaneously. Selection of the side for the initial operation was determined on the basis of the dominant hemisphere of the patient, symptom severity, and perfusion alteration based on MR imaging. None suffered from postoperative complications, including hemorrhage or infarction involving the ipsilateral brain hemisphere, seen on the postoperative imaging studies such as CT or MR imaging.

### Conventional DSA

All enrolled patients underwent both preoperative and postoperative cerebral angiography in a dual-plane angiographic machine (Axiom Artis; Siemens, Erlangen, Germany) performed by 3 pediatric radiologists (Y.H.C., H.-H.C., and S.-M.L., with 10, 6, and 6 years of experience, respectively). A 4F or 5F Davis angiographic catheter (A&A Medical Device, Gyeonggi-do, Korea) was used according to the patient's femoral artery diameter. All procedures were performed with same catheter diameter for both preoperative and postoperative cerebral angiography. Conventional DSA images included anteroposterior and lateral ICA, ECA, and CCA angiograms. Diluted contrast media (iobitridol; Xenetix 350; Guerbet, Aulnay-sous-Bois, France) with a contrast-to-normal-saline ratio of 1:1 was used with an automatic injector (Angiomat Illumena; Liebel-Flarsheim, Cincinnati, Ohio). The injection rate and amount were determined by the operator on the basis of the

size of each vessel. The mean injection rates for patients younger than 5 years of age were 2 mL/s for the CCA, 1 mL/s for the ICA, and 1.5 mL/s for the ECA. The rates for patients older than 5 years were approximately 3 mL/s for the CCA, 1.5 mL/s for the ICA, and 2 mL/s for ECA angiography, and they were adjusted for each patient's circumstances. The injection duration of contrast material was fixed for 2 seconds. The same contrast injection rate and amount were used for pre- and postoperative DSA in each patient. The mean time interval between pre- and postoperative DSA was approximately 82.9 days (range, 72~103 days), and the mean time interval between the operation and postoperative DSA was approximately 76.2 days (range, 64~96). The stages of preoperative DSA were classified by using the criteria of Suzuki and Kodama<sup>17</sup>: stage 1 ( $n = 4$ ), stage 2 ( $n = 9$ ), and stage 3 ( $n = 19$ ).

### Postprocessing of DSA

Postprocessing of DSA images was performed by using syngo iFlow (Siemens). With this program, we could obtain a color-coded (range from red to blue) single image showing the history of contrast material passage through vessels, which reflected the time from injection. This color map provided flow velocity and total amount of injected contrast material passing through the vessels. We also obtained signal-intensity curves of the selected ROIs, adjusted with a reference ROI. Two pediatric radiologists (H.-H.C. and S.-M.L. with 6 years of experience each) drew a rectangular ROI (approximately 2500 mm<sup>2</sup>) to cover the EDAS flap in consensus. A round reference ROI was drawn within the proximal input artery (approximately 10 mm<sup>2</sup>) at the level of the atlas for maintenance of the identical location between the pre- and postinterventional DSAs (Fig 1A). A time-attenuation intensity curve was obtained automatically and summarized the maximum concentration of contrast passing through the ROI at that point (Fig 1B). Using the curve, the program automatically calculated the "peak time of contrast concentration," which corresponds to time-to-peak of perfusion MR imaging. The calculated area under the curve (AUC) is the total amount of contrast material passed, which corresponds to the cerebral blood volume of the perfusion MR imaging. The TTP difference ( $\Delta$ TTP) in seconds was calculated by subtracting the TTP of the preoperative DSA from the TTP of the postoperative DSA. For the AUC, the adjusted area under the curve changes ( $\Delta$ AUC ratio) in percentages were calculated by dividing the difference between post- and preoperative AUCs by the preoperative AUC values (Fig 1C):

$$\Delta\text{TTP} = \text{TTP}_{\text{preoperative}} - \text{TTP}_{\text{postoperative}}$$

$$\Delta\text{AUC Ratio} = (\text{AUC}_{\text{postoperative}} - \text{AUC}_{\text{preoperative}}) / \text{AUC}_{\text{preoperative}}$$

In this study, postprocessing of DSA was performed by using only a lateral projection because detection of the EDAS flap site was easier than in anteroposterior images. Likewise, the widely used angiographic staging method for MMD, the Matsushima classification, also used lateral images for evaluating neovascularization degree.<sup>18</sup>

### Angiographic Outcome Group

To classify postoperative neovascularization status, we used the Matsushima 3-grade method.<sup>18</sup> The "good group" was defined as

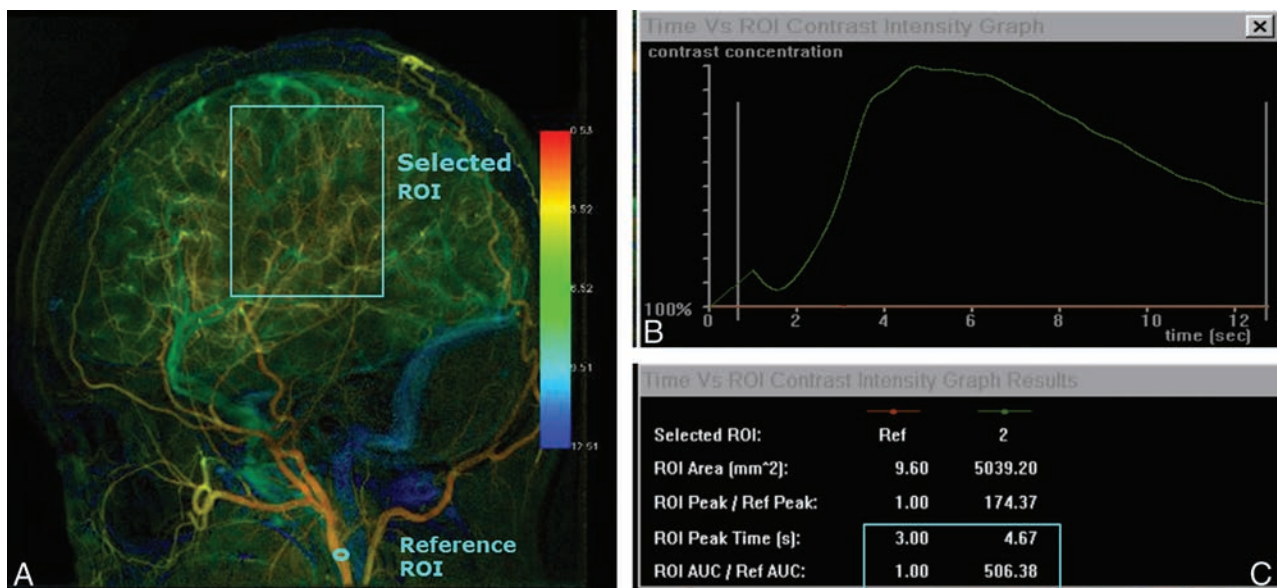


**FIG 1.** Postprocessing cascade of the DSA image. *A*, A color-coded single image is obtained from DSA images of CCA angiography; then, we draw selected ROIs along the estimated EDAS flap site. A reference ROI is drawn within the proximal input artery. *B*, The time-attenuation intensity curve is obtained automatically. The superior green line represents the time-attenuation intensity curve within the selected ROI, and the inferior red line represents that of the reference ROI. *C*, Using the time-attenuation intensity curve, we calculated the TTP and AUC within the selected ROI, adjusted by the reference ROI.

more than two-thirds of the MCA distribution supplied by neovascularization after surgery. The “fair group” was defined as a neovascularization area covering between two-thirds and one-third of the MCA distribution. The “poor group” was defined as only 1 cortical branch of the MCA covered through the bypass or no collateral circulation observed. Angiographic outcomes were classified by a radiologist after each procedure.

#### Clinical Outcome Group

Postoperative clinical outcomes were classified according to ipsilateral MCA symptoms (such as TIAs or seizures) by the clinician at the time of admission for the postoperative angiography, blinded to the results of imaging studies, including MR imaging, perfusion MR imaging, or DSA.<sup>6,19</sup> The “excellent group” represented total disappearance of symptoms (such as TIAs or seizures) without fixed neurologic deficits. The “good group” represented total disappearance of symptoms, but with neurologic deficits remaining. The “fair group” represented persistent symptoms, albeit less frequently. The “poor group” represented remaining unchanged or worsened symptoms. The excellent and good groups were considered favorable outcomes, and the fair and poor groups were considered unfavorable outcomes in receiver operating characteristic curve analysis. Anterior cerebral artery symptoms, such as paraparesis or urinary incontinence, were not considered in this study because it was designed for the evaluation of the neovascularization status of EDAS sites.

#### Statistical Analysis

Comparisons between AUC differences in CCA, ECA, and ICA angiograms and mean TTP differences in the CCA between pre- and postoperative studies in each clinical and angiographic outcome group were analyzed by using the Jonckheere-Terpstra test by using PASW software for Windows (Version 18.0; IBM, Ar-

monk, New York). To determine the diagnostic performance of parameters in each angiogram, we performed receiver operating characteristic analysis by using MedCalc for Windows (MedCalc Software, Mariakerke, Belgium). *P* values < .05 were statistically significant.

## RESULTS

### DSA Parameters and Clinical Outcome

Sixteen patients showed excellent; 4 patients, good; 8 patients, fair; and 4 patients, poor clinical outcomes. After neovascularization surgery, postoperative TTP decreased compared with preoperative TTP in CCA angiography in the excellent, good, and fair clinical outcome groups. In the poor clinical outcome group, postoperative TTP increased compared with preoperative TTP. The  $\Delta$ TTP values in CCA angiography were significantly different among clinical outcome groups (*P* = .003), and a gradual decrease of  $\Delta$ TTP was noted from the excellent-to-poor groups.

Calculated  $\Delta$ AUC ratios in CCA angiography showed a significant increase among clinical outcome groups in sequence from poor to excellent (*P* = .000). Mean  $\Delta$ AUC ratios in CCA angiography were 68.1% for excellent, 31.5% for good, 9.1% for fair, and -11.3% for poor. The  $\Delta$ AUC ratios of ECA angiography also showed a significant increase among clinical outcome groups in sequence from poor to excellent (*P* = .000). The  $\Delta$ AUC ratios in ECA angiography were 1119.8% for excellent, 768.2% for good, 279.5% for fair, and 248.7% for poor. Figures 2 and 3 show representative cases with pre- and postoperative DSA images in the excellent and poor clinical outcome groups. The  $\Delta$ AUC ratios in ICA angiography showed no significant difference among the clinical outcome groups (*P* = .418). The  $\Delta$ AUC ratios in ICA angiography were -41.0% for

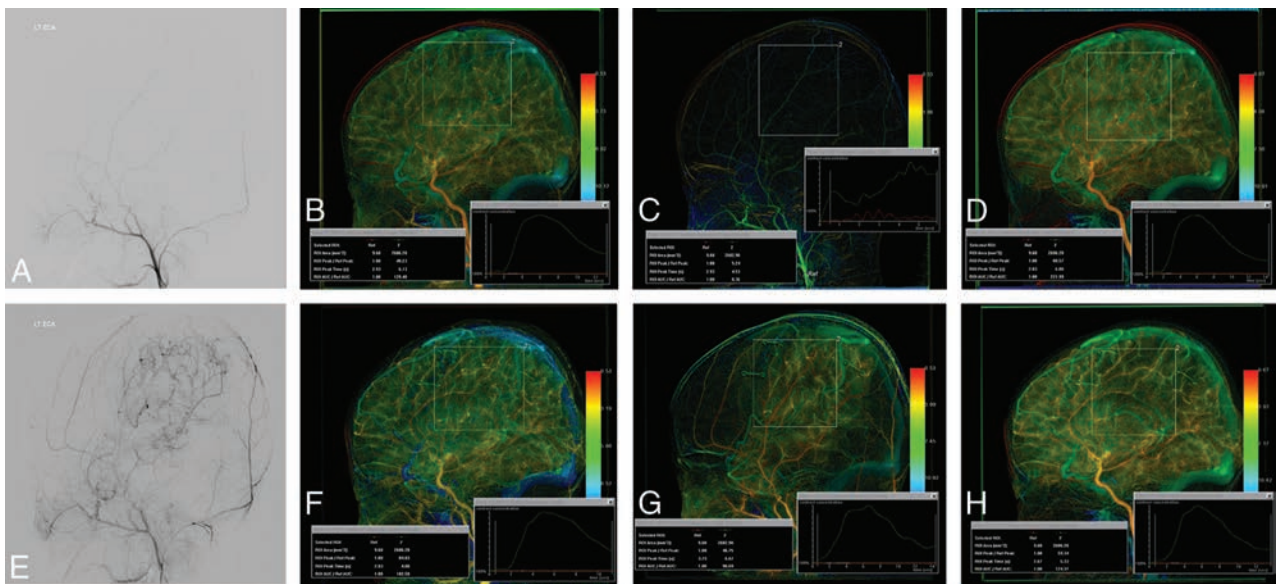


**FIG 2.** A 4-year-old boy with excellent clinical outcome after EDAS neovascularization. Comparing pre- (A) and post- (E) operative ECA angiograms shows good neovascularization after EDAS. Postprocessed pre- (B) and post- (F) operative CCA angiograms show shortening of TTP of approximately 2.3 seconds and an increase of the percentage of AUC difference of about 51.0% after the operation. Approximately a 1080.5% increment of the percentage of AUC difference after surgery is noted when comparing pre- (C) and post- (G) operative ECA angiograms, and an approximate 44.0% of AUC difference decrease is noted when comparing pre- (D) and post- (H) operative ICA angiograms.

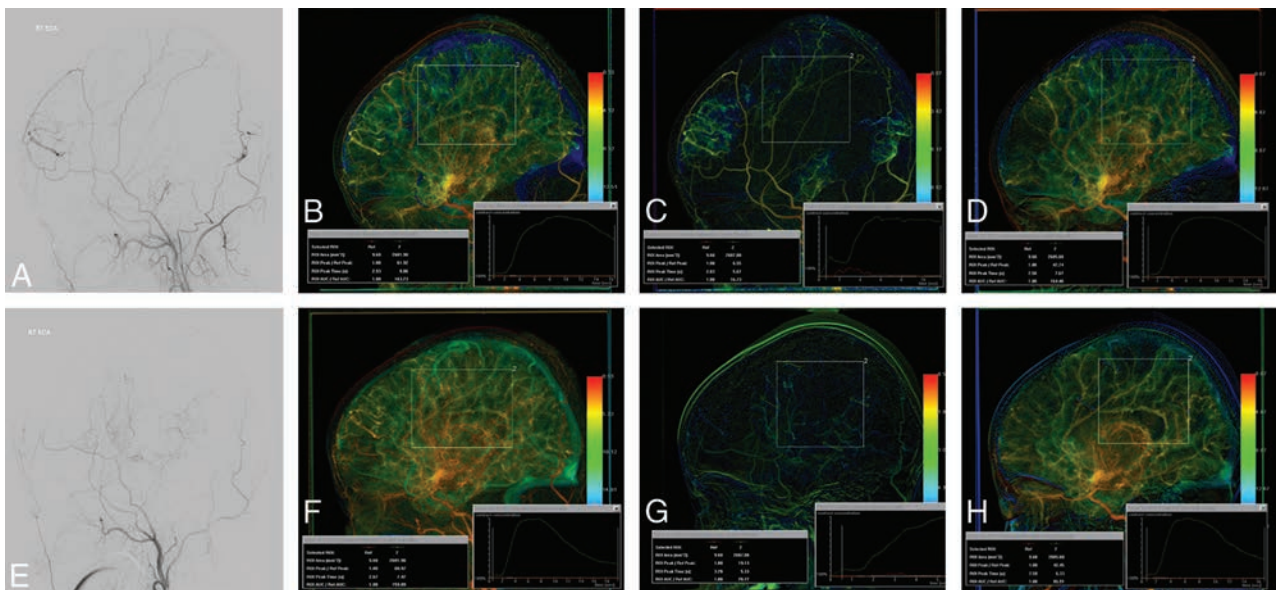


**FIG 3.** A 5-year-old boy with poor clinical outcome after EDAS neovascularization. Comparing pre- (A) and post- (E) operative ECA angiograms shows poor neovascularization after EDAS. Postprocessed pre- (B) and post- (F) operative CCA angiograms show no definite shortening of the TTP (0.0 seconds), with a decrease of the percentage of AUC difference of approximately 2.0% after the operation. About a 41.2% increase of the percentage of AUC difference after the operation is noted when comparing pre- (C) and post- (G) operative ECA angiograms, and about a 13.7% of AUC difference increase is noted when comparing pre- (D) and post- (H) operative ICA angiograms.

**Table 1: Relationships between DSA parameters and clinical outcomes**

Group	Excellent (n = 16)	Good (n = 4)	Fair (n = 8)	Poor (n = 4)	P Value
ΔTTP in CCA (sec)	2.02	1.0	0.80	-0.13	.003
ΔAUC ratio in CCA (%)	68.1	31.5	9.1	-11.3	.000
ΔAUC ratio in ECA (%)	1119.8	768.2	279.5	248.7	.000
ΔAUC ratio in ICA (%)	-41.0	-35.6	-44.2	-22.3	.418

excellent, -35.6% for good, -44.2% for fair, and -22.3% for poor (Table 1).

#### DSA Parameters and Angiographic Outcome

Angiographic outcome by using the Matsushima grade was good in 16, fair in 7, and poor in 9 patients. ΔTTP showed a statistically significant difference among angiographic outcome groups in CCA angiography ( $P = .005$ ), and a gradual decrease of ΔTTP was noted from good to poor.

**Table 2: Relationships between DSA parameters and angiographic outcomes**

Group	Good (n = 16)	Fair (n = 7)	Poor (n = 9)	P Value
ΔTTP in CCA (sec)	2.01	0.97	0.49	.005
ΔAUC ratio in CCA (%)	64.5	29.8	0.4	.000
ΔAUC ratio in ECA (%)	1065.9	753.1	210.5	.000
ΔAUC ratio in ICA (%)	-41.0	-42.4	-32.2	.424

**Table 3: Cutoff values between favorable and unfavorable groups**

Parameter	Criterion	Sensitivity (%)	Specificity (%)
ΔTTP in CCA (sec)	>1.27	81.4	91.7
ΔAUC ratio in CCA (%)	>33.5	81	100
ΔAUC ratio in ECA (%)	>504	85.3	92
ΔAUC ratio in ICA (%)	≤20.2	85.9	33.4

The ΔAUC ratios in CCA angiography showed a statistically significant difference among angiographic outcome groups in sequence from poor to excellent ( $P = .000$ ), being approximately 64.5% for good, 29.8% for fair, and 0.4% for poor. The ΔAUC ratios of ECA angiography also showed a statistically significant difference among the angiographic outcome groups in sequence from poor to excellent ( $P = .000$ ). The ΔAUC ratios in ECA angiography were noted as approximately 1065.9% for good, 753.1% for fair, and 210.5% for poor. The ΔAUC ratios of ICA angiography showed no significant difference among the angiographic outcome groups ( $P = .424$ ). The ΔAUC ratios in ICA angiography were approximately -41.0% for good, -42.4% for fair, and -32.2% for poor groups (Table 2).

The ΔTTP and ΔAUC ratio showed no significant difference between EDAS only and unilateral EDAS in the bifrontal encephalogaleo(periosteal)synangiosis groups ( $P = .76$ ).

#### **Cutoff Value between Favorable and Unfavorable Groups**

According to receiver operating characteristic analysis, an optimal cutoff value of 1.27 seconds was obtained for the difference between pre- and postoperative adjusted TTP in CCA angiography, with 81.4% sensitivity and 91.7% specificity between favorable and unfavorable groups. The optimal cutoff value for the difference ratio of the AUC in CCA angiography was 33.5%, with 81% sensitivity and 100% specificity, while that in ECA angiography was 504%, with 85.3% sensitivity and 92% specificity (Table 3).

#### **DISCUSSION**

The optimal goal for EDAS in pediatric patients with MMD is to re-establish cerebral blood flow to hypoperfused areas by using angiogenesis from parietal branches of the superficial temporal artery.<sup>20</sup> After the operation, collateral vessels from the superficial temporal artery develop at the flap site, along with simultaneous and sequential progression of steno-occlusive changes of the ICA and disappearance or diminishing of Moyamoya vessels.<sup>18,21</sup> Hemodynamic changes after the operation might be difficult to understand; likewise, estimating postoperative neovascularization status is challenging. Noninvasive imaging modalities such as perfusion MR imaging, single-photon emission CT, and positron-emission tomography

can demonstrate secondary hemodynamic changes.<sup>1-4,12,21-27</sup> However, these methods show only overall cerebral perfusion changes and cannot directly visualize fine parenchymal neovascularization itself following the operation.

Concerning the evaluation of postoperative neovascularization status, DSA is still the most reliable imaging technique and is widely used for the initial diagnosis and follow-up of MMD.<sup>1,9,19</sup> DSA also provides anatomic information of vessels and direct visualization of steno-occlusive changes and visualizes neovascularization status after the operation. However, it cannot provide the objective perfusion parameters. It might be difficult to compare the change in the DSA during longitudinal or postoperative follow-up. The decision for the postoperative stage might be made only by the operator.

In this study, to supplement these shortcomings of DSA, we used the postprocessing software syngo iFlow. This software calculates opacity changes within each pixel at each moment and then summarizes these to make a color-coded map of contrast flow. With this software, additional hemodynamic information can be obtained from serial DSA images without additional radiation exposure or contrast material, with a simplified method with little effort.

Although this study included only hemodynamic changes within the operative bed, we predicted that the increase of AUC with shortening TTP might be noted on CCA and ECA angiography. We also predicted that a decrease of AUC in ICA angiography might be noted after neovascularization surgery because ICA flows, including basal collaterals (Moyamoya vessels), are no longer required to function as collateral pathways. The actual results showed patterns similar to our estimations, except in the poor clinical outcome group. The largest ΔTTP, which represents the degree of shortening-delayed TTP due to neovascularization, was noted in the excellent clinical outcome group on CCA angiography. The largest increment of the ΔAUC ratio, which represents increased CBV through neovascularization, was also noted in the excellent clinical outcome group in CCA and ECA angiography. We suggest that the values obtained from CCA angiography provide real hemodynamic changes because those values might include both increased blood flow through neovascularization of the superficial temporal artery and diminished blood flow through the ipsilateral ICA.

With receiver operating characteristic analysis, improved TTP delay of >1.27 seconds and improved percentage AUC difference of >33.5% for CCA and 504% for ECA angiography are optimal cutoff values between favorable and unfavorable groups with reliable sensitivity and specificity. Using these cutoff values, we could provide additional information to predict patient outcomes; and for the unfavorable group, an additional operation for the contralateral side or bifrontal encephalogaleo(periosteal)synangiosis was considered earlier than in the favorable group. In addition, in these cases, shorter imaging and clinical follow-up were recommended.

The mean time interval between the operation and postoperative DSA was approximately 76.2 days (range, 64~96). Moreover, neovascularization after indirect bypass surgery was known to become well-developed after 3~6 months postoperatively.<sup>20,28-31</sup>

There are several study limitations. In some cases, postoperative DSA data might not be enough to provide real hemo-

dynamic status after neovascularization. However, previous studies explained that the neovascularization begins 2 weeks after surgery,<sup>21,32,33</sup> so the obtained data in this study could provide the near-complete status of the neovascularization. In addition, although the data obtained from the postoperative DSA might provide the earlier neovascularization status before completion, we thought they might provide the later outcome because the data showed good correlation with the outcomes in this study.

Although neovascularization after indirect bypass surgery develops along the flap site, accurate flap site drawing was difficult; thus, another limitation is that some neovascularization developing outside the flap site was not included in this study. However, the portion of neovascularization developing outside the flap site might be small and therefore negligible. We used a manufactured head fixator for maintenance of the head position during the study, so another limitation of the study could be that there was little difference between the pre- and postoperative DSA. We suggest that the standardized positioning might be helpful for a more exact comparison.

## CONCLUSIONS

Using simple postprocessing software might provide objective quantitative perfusion values based on obtained DSA images with significant correlation with clinical and angiographic outcomes for pediatric patients with MMD without additional radiation. Furthermore, the cutoff values obtained with receiver operating characteristic analysis may help in predicting patient outcomes after the operation and could affect the establishment of further additional treatment or follow-up plans.

## ACKNOWLEDGMENTS

We thank Hyung Bin Yu, the project manager of Siemens, Korea, for technical support.

## REFERENCES

1. Kuroda S, Houkin K. **Moyamoya disease: current concepts and future perspectives.** *Lancet Neurol* 2008;7:1056–66 Medline
2. Kim SK, Cho BK, Phi JH, et al. **Pediatric moyamoya disease: an analysis of 410 consecutive cases.** *Ann Neurol* 2010;68:92–101 CrossRef Medline
3. Suzuki J, Takaku A. **Cerebrovascular “moyamoya” disease: disease showing abnormal net-like vessels in base of brain.** *Arch Neurol* 1969;20:288–99 Medline
4. Fukui M. **Guidelines for the diagnosis and treatment of spontaneous occlusion of the circle of Willis (‘moyamoya’ disease): Research Committee on Spontaneous Occlusion of the Circle of Willis (Moyamoya Disease) of the Ministry of Health and Welfare, Japan.** *Clin Neurol Neurosurg* 1997;99(suppl 2):S238–40 Medline
5. Kim SK, Wang KC, Kim IO, et al. **Combined encephaloduroarteriosynangiosis and bifrontal encephalogaleo (periosteal) synangiosis in pediatric moyamoya disease.** *Neurosurgery* 2008;62:1456–64 Medline
6. Kim CY, Wang KC, Kim SK, et al. **Encephaloduroarteriosynangiosis with bifrontal encephalogaleo(periosteal)synangiosis in the pediatric moyamoya disease: the surgical technique and its outcomes.** *Child Nerv Syst* 2003;19:316–24 Medline
7. Mesiwala AH, Sviri G, Fatemi N, et al. **Long-term outcome of superficial temporal artery-middle cerebral artery bypass for patients with moyamoya disease in the US.** *Neurosurg Focus* 2008;24:E15 CrossRef Medline

8. Houkin K, Kuroda S, Ishikawa T, et al. **Neovascularization (angiogenesis) after revascularization in moyamoya disease: which technique is most useful for moyamoya disease?** *Acta Neurochir (Wien)* 2000;142:269–76 Medline
9. Goda M, Isono M, Ishii K, et al. **Long-term effects of indirect bypass surgery on collateral vessel formation in pediatric moyamoya disease.** *J Neurosurg* 2004;100:156–62 Medline
10. Yun TJ, Cheon JE, Na DG, et al. **Childhood moyamoya disease: quantitative evaluation of perfusion MR imaging—correlation with clinical outcome after revascularization surgery.** *Radiology* 2009;251:216–23 CrossRef Medline
11. Choi JU, Kim DS, Kim EY, et al. **Natural history of moyamoya disease: comparison of activity of daily living in surgery and non-surgery groups.** *Clin Neurol Neurosurg* 1997;99(suppl 2):S11–18 Medline
12. Kim SK, Wang KC, Oh CW, et al. **Evaluation of cerebral hemodynamics with perfusion MRI in childhood moyamoya disease.** *Pediatr Neurosurg* 2003;38:68–75 Medline
13. Strother CM, Bender F, Deuerling-Zheng Y, et al. **Parametric color coding of digital subtraction angiography.** *AJNR Am J Neuroradiol* 2010;31:919–24 CrossRef Medline
14. Lin CJ, Yu M, Hung SC, et al. **In-room assessment of cerebral blood volume for guidance during intra-arterial thrombolytic therapy.** *Interv Neuroradiol* 2012;18:463–68 Medline
15. Zhang XB, Zhuang ZG, Ye H, et al. **Objective assessment of transcatheter arterial chemoembolization angiographic endpoints: preliminary study of quantitative digital subtraction angiography.** *J Vasc Interv Radiol* 2013;24:667–71 CrossRef Medline
16. Hung SC, Liang ML, Lin CF, et al. **New grading of moyamoya disease using color-coded parametric quantitative digital subtraction angiography.** *J Chin Med Assoc* 2014;77:437–42 CrossRef Medline
17. Suzuki J, Kodama N. **Moyamoya disease: a review.** *Stroke* 1983;14:104–09 Medline
18. Matsushima T, Inoue T, Suzuki SO, et al. **Surgical treatment of moyamoya disease in pediatric patients: comparison between the results of indirect and direct revascularization procedures.** *Neurosurgery* 1992;31:401–05 Medline
19. Kim SK, Wang KC, Kim IO, et al. **Combined encephaloduroarteriosynangiosis and bifrontal encephalogaleo(periosteal)synangiosis in pediatric moyamoya disease.** *Neurosurgery* 2002;50:88–96 Medline
20. Matsushima T, Fujiwara S, Nagata S, et al. **Surgical treatment for paediatric patients with moyamoya disease by indirect revascularization procedures (EDAS, EMS, EMAS).** *Acta Neurochir (Wien)* 1989;98:135–40 Medline
21. Houkin K, Nakayama N, Kuroda S, et al. **How does angiogenesis develop in pediatric moyamoya disease after surgery? A prospective study with MR angiography.** *Childs Nerv Syst* 2004;20:734–41 Medline
22. Honda M, Kitagawa N, Tsutsumi K, et al. **Magnetic resonance angiography evaluation of external carotid artery tributaries in moyamoya disease.** *Surg Neurol* 2005;64:325–30 Medline
23. Ikezaki K, Matsushima T, Kuwabara Y, et al. **Cerebral circulation and oxygen metabolism in childhood moyamoya disease: a perioperative positron emission tomography study.** *J Neurosurg* 1994;81:843–50 Medline
24. So Y, Lee HY, Kim SK, et al. **Prediction of the clinical outcome of pediatric moyamoya disease with postoperative basal/acetazolamide stress brain perfusion SPECT after revascularization surgery.** *Stroke* 2005;36:1485–89 Medline
25. Hoshi H, Ohnishi T, Jinnouchi S, et al. **Cerebral blood flow study in patients with moyamoya disease evaluated by IMP SPECT.** *J Nucl Med* 1994;35:44–50 Medline
26. Mountz JM, Foster NL, Ackermann RJ, et al. **SPECT imaging of moyamoya disease using 99mTc-HM-PAO: comparison with computed tomography findings.** *J Comput Tomogr* 1988;12:247–50 Medline
27. Fujimura M, Mugikura S, Shimizu H, et al. **Diagnostic value of perfusion-weighted MRI for evaluating postoperative alteration of cerebral hemodynamics following STA-MCA anastomosis in patients with**

- moyamoya disease** [in Japanese]. *No Shinkei Geka* 2006;34:801–09 Medline
28. Fung LW, Thompson D, Ganesan V. **Revascularisation surgery for paediatric moyamoya: a review of the literature.** *Childs Nerv Syst* 2005;21:358–64 Medline
  29. Sakamoto H, Kitano S, Yasui T, et al. **Direct extracranial-intracranial bypass for children with moyamoya disease.** *Clin Neurol Neurosurg* 1997;99(suppl 2):S128–33 Medline
  30. Togao O, Mihara F, Yoshiura T, et al. **Cerebral hemodynamics in moyamoya disease: correlation between perfusion-weighted MR imaging and cerebral angiography.** *AJNR Am J Neuroradiol* 2006;27:391–97 Medline
  31. Kassner A, Zhu XP, Li KL, et al. **Neoangiogenesis in association with moyamoya syndrome shown by estimation of relative recirculation based on dynamic contrast-enhanced MR images.** *AJNR Am J Neuroradiol* 2003;24:810–18 Medline
  32. Kinugasa K, Mandai S, Kamata I, et al. **Surgical treatment of moyamoya disease: operative technique for encephalo-duro-arterio-myo-synangiosis, its follow-up, clinical results, and angiograms.** *Neurosurgery* 1993;32:527–31 Medline
  33. Kim SK, Seol HJ, Cho BK, et al. **Moyamoya disease among young patients: its aggressive clinical course and the role of active surgical treatment.** *Neurosurgery* 2004;54:840–44; discussion 844–46 Medline

# Brain Structural and Vascular Anatomy Is Altered in Offspring of Pre-Eclamptic Pregnancies: A Pilot Study

M.T. Rätsep, A. Paolozza, A.F. Hickman, B. Maser, V.R. Kay, S. Mohammad, J. Pudwell, G.N. Smith, D. Brien, P.W. Stroman, M.A. Adams, J.N. Reynolds, B.A. Croy, and N.D. Forkert



## ABSTRACT

**BACKGROUND AND PURPOSE:** Pre-eclampsia is a serious clinical gestational disorder occurring in 3%–5% of all human pregnancies and characterized by endothelial dysfunction and vascular complications. Offspring born of pre-eclamptic pregnancies are reported to exhibit deficits in cognitive function, higher incidence of depression, and increased susceptibility to stroke. However, no brain imaging reports exist on these offspring. We aimed to assess brain structural and vascular anatomy in 7- to 10-year-old offspring of pre-eclamptic pregnancies compared with matched controls.

**MATERIALS AND METHODS:** Offspring of pre-eclamptic pregnancies and matched controls ( $n = 10$  per group) were recruited from an established longitudinal cohort examining the effects of pre-eclampsia. Children underwent MR imaging to identify brain structural and vascular anatomic differences. Maternal plasma samples collected at birth were assayed for angiogenic factors by enzyme-linked immunosorbent assay.

**RESULTS:** Offspring of pre-eclamptic pregnancies exhibited enlarged brain regional volumes of the cerebellum, temporal lobe, brain stem, and right and left amygdalae. These offspring displayed reduced cerebral vessel radii in the occipital and parietal lobes. Enzyme-linked immunosorbent assay analysis revealed underexpression of the placental growth factor among the maternal plasma samples from women who experienced pre-eclampsia.

**CONCLUSIONS:** This study is the first to report brain structural and vascular anatomic alterations in the population of offspring of pre-eclamptic pregnancies. Brain structural alterations shared similarities with those seen in autism. Vascular alterations may have preceded these structural alterations. This pilot study requires further validation with a larger population to provide stronger estimates of brain structural and vascular outcomes among the offspring of pre-eclamptic pregnancies.

**ABBREVIATIONS:** MNI = Montreal Neurological Institute; PE = pre-eclampsia; PE-FI = offspring of pre-eclamptic pregnancy; PGF = placental growth factor; sFLT-1 = soluble fms-like tyrosine kinase 1

Pre-eclampsia (PE), a serious clinical gestational disorder, occurs in approximately 3%–5% of all pregnancies.<sup>1</sup> The current clinical definition of PE involves new-onset hypertension (>140/90 mm Hg) and at least 1 of the following: proteinuria (>300 mg/day), thrombocytopenia (platelet level <10<sup>5</sup>/μL), re-

nal insufficiency (serum creatinine level >1.1 mg/dL), impaired liver function (blood liver transaminases levels 2× normal), pulmonary edema, or cerebral or visual disturbances occurring after the 20th week of gestation.<sup>2</sup> PE is a severe acute disorder, requiring immediate action. Unfortunately, no effective treatments are available for PE, and the only course of action is delivery of the fetus and placenta, often prematurely, which terminates maternal symptoms. Although many theories have been proposed for the origins of PE, specific causes and mechanisms of pathogenesis are poorly understood. A very popular theory is centered on deficient

Received August 17, 2015; accepted after revision November 5.

From the Department of Biomedical and Molecular Sciences (M.T.R., A.F.H., B.M., V.R.K., S.M., G.N.S., J.N.R., B.A.C.) and Centre for Neuroscience Studies (A.P., D.B., P.W.S., M.A.A., J.N.R.), Queen's University, Kingston, Ontario, Canada; Department of Obstetrics and Gynecology (J.P., G.N.S.), Kingston General Hospital, Kingston, Ontario, Canada; and Department of Radiology and Hotchkiss Brain Institute (N.D.F.), University of Calgary, Calgary, Alberta, Canada.

This work was supported by the Harry Botterell Foundation for the Neurological Sciences Award from Kingston General Hospital Foundation, Canadian Institutes of Health Research; Heart and Stroke Foundation of Canada; and NeuroDevNet, which is funded by the Networks of Centers of Excellence, a federal government program to advance science and technology. B.A.C. is funded by the Canada Research Chairs program; M.T.R. is funded by a Frederick Banting and Charles Best Canada Graduate Scholarship from the Canadian Institutes of Health Research.

Please address correspondence to Matthew T. Rätsep, PhD, Department of Biomedical and Molecular Sciences, Queen's University, Room 926, Botterell Hall, 18 Stuart St, Kingston, ON, Canada, K7L3N6; e-mail: m.ratsep@queensu.ca; @MTRatsep

Indicates open access to non-subscribers at www.ajnr.org

Indicates article with supplemental on-line table.

<http://dx.doi.org/10.3174/ajnr.A4640>

uteroplacental angiogenesis and vessel remodeling, leading to increased vascular resistance, resulting in clinical signs. Many have posited systemic vascular endothelial dysfunction as the main factor underlying this deficient angiogenesis to explain the occurrence of the wide range of clinical indicators beyond hypertension.<sup>3,4</sup>

Given the strong association of PE with angiogenesis and vessel remodeling, numerous angiogenic biomarkers of PE have been proposed.<sup>5</sup> Most important, deficient expression of placental growth factor (PGF)<sup>6,7</sup> or overexpression of soluble endoglin<sup>7,8</sup> or soluble fms-like tyrosine kinase 1 (sFLT-1)<sup>6,7</sup> is strongly linked with the development of PE. In many cases, aberrant expression of these factors will precede clinical signs<sup>9</sup> and may predict a more severe form of the disorder.<sup>10</sup> Furthermore, women who experience a PE pregnancy with aberrant angiogenic factor expression will continue to exhibit an increased lifetime risk for cardiovascular disease.<sup>11,12</sup> The lifetime risk outcomes are also suboptimal for the offspring of pre-eclamptic pregnancies (PE-F1s), who display an elevated risk of cardiovascular disease and stroke<sup>13,14</sup> as well as impaired cognitive function<sup>15,16</sup> and increased depressive signs.<sup>17</sup> This finding raises the possibility that impairment in cerebral angiogenesis in PE-F1 fetuses leads to deficits in cognitive function while simultaneously increasing stroke risk. However, there appears to be no reported study on cerebrovascular anatomy in a PE-F1 population, to our knowledge.

Imaging of cerebral blood vessels can be achieved noninvasively with excellent quality, for example, by using TOF-MRA. With this method, high-resolution images of cerebral vasculature with a good blood-to-background contrast can be acquired without the administration of an exogenous contrast agent. In the current study, we have used high-resolution T1-weighted MR imaging to investigate regional brain volume alterations in combination with TOF-MRA for a quantitative analysis of the regional cerebral vasculature of children 7–10 years of age who were born of PE or uncomplicated pregnancies.

## MATERIALS AND METHODS

### Participants

All experimental procedures were reviewed and approved by the Human Research Ethics Board at Queen's University and Kingston General Hospital. Participants were recruited from the Pre-Eclampsia New Emerging Team study data base.<sup>18</sup> Briefly, pregnant women were recruited to the Pre-Eclampsia New Emerging Team study at Kingston General Hospital between September 2003 and October 2009. Women were diagnosed with PE if blood pressure was  $>140/90$  mm Hg and proteinuria level,  $>300$  mg/24 hours or  $\geq 2+$  on a repeat dipstick. Control women, with uncomplicated pregnancies, were enrolled and matched to test subjects for age, race, and parity. Women with a history of chronic hypertension, diabetes (including gestational diabetes), or renal disease were excluded. For this pilot study, women from the Pre-Eclampsia New Emerging Team data base were contacted between July 2014 and February 2015 to request participation of their child. PE-F1s 7–10 years of age ( $n = 10$ ; 5 male, 5 female) were matched as closely as possible for age and sex to a child born of an uncomplicated pregnancy ( $n = 10$ ; 5 male, 5 female). Following parental consent and participant assent, children underwent brain MR im-

aging as described below. During the same session, the child's parent or guardian completed a questionnaire encompassing demographics, socioeconomic variables, pregnancy and birth information, the child's current health status, and family history variables. The accuracy of pregnancy and birth information was confirmed through access of medical records. Socioeconomic status was calculated according to Hollingshead Four Factor Index of Social Status.<sup>19</sup> Participants received a Can\$25 gift card on completion of the testing session.

### MR Imaging

All MR imaging was performed on a 3T Magnetom Trio MR imaging scanner (Siemens, Erlangen, Germany) without administration of contrast media or sedation. Among others, a high-resolution TOF-MRA and a high-resolution anatomic T1-weighted MPRAGE sequence were acquired for each participant. TOF-MRA was acquired by using 4 slabs, each consisting of 40 sections with a thickness of 0.5 mm, a TE of 3.59 ms, a TR of 20 ms, a flip angle of 18°, and a spatial resolution of  $0.26 \times 0.26$  mm<sup>2</sup>. Because TOF-MRA imaging provides a good blood-to-background contrast of arteries but little anatomic information, high-resolution T1-weighted MPRAGE images were used as the basis for the regional vessel and brain volume analysis. The MPRAGE sequence was acquired in a single 160-section slab, by using a TE of 3.45 ms, a TR of 2180 ms, a flip angle of 15°, and an isotropic spatial resolution of 1.0 mm<sup>3</sup>.

### Data Analyses

For the vessel analyses, the cerebrovascular system was segmented in each TOF-MRA dataset by using an advanced multistep segmentation framework.<sup>20–22</sup> On the basis of the resulting vessel segmentation, the 3D vessel centerline representation and the corresponding vessel radius for each voxel of the vessel centerline were then calculated by using the method described by Forkert et al (Figure).<sup>23</sup> Due to different FOVs of the TOF-MRA acquisition and to enable an analysis of the regional vascular alterations, parcellation of each brain into anatomic substructures was required. First, the well-established Montreal Neurological Institute (MNI) adult brain atlas<sup>24</sup> was registered to the MNI pediatric atlas (7–11 years of age)<sup>25</sup> by optimizing the nonlinear transformation  $\varphi_A$ . Next, the MNI pediatric atlas was registered to each MPRAGE dataset by optimizing the nonlinear transformation  $\varphi_P$ . Finally, each MPRAGE dataset was registered to the corresponding TOF-MRA dataset of the same participant by optimizing the rigid transformation  $\varphi_M$ . All registrations were performed by using the NiftyReg software (<http://sourceforge.net/projects/niftyreg/>)<sup>26</sup> and were visually checked for quality control. A full intracranial brain volume segmentation, the MNI brain regions, and the Harvard-Oxford subcortical brain regions, as defined in the MNI adult brain atlas, were then transformed to each MPRAGE dataset by concatenating the 2 nonlinear transformations ( $\varphi_A \circ \varphi_P$ ) as well as to the TOF-MRA dataset by concatenating the 2 nonlinear and the rigid transformations ( $\varphi_A \circ \varphi_P \circ \varphi_M$ ) by using a nearest-neighbor interpolation.

After registration, the subject-specific full intracranial brain volume and the volume of each of the MNI and Harvard-Oxford subcortical brain regions, as defined by a probabilistic threshold

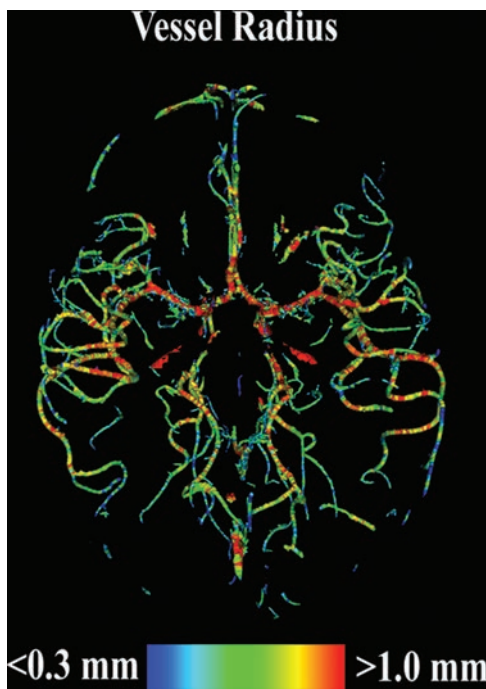


**FIGURE.** Visual 3D representation of the vessel radii calculated for a segmented TOF-MRA dataset of a single female, 8-year-old PE-FI participant who was born at 34 weeks of gestation.

of 50%, were extracted in T1 space. The full intracranial volume was used to calculate normalized regional brain volumes to account for different head geometries. Normalized regional brain volumes are expressed as a percentage of the full intracranial volume. The MNI brain regions extracted and quantified were the cerebellum, frontal lobe, occipital lobe, parietal lobe, and temporal lobe. The Harvard-Oxford brain regions extracted and quantified were the amygdalae, brain stem, caudate, cerebral cortex, cerebral white matter, lateral ventricles, pallidum, putamen, and thalamus. The volume of the Harvard-Oxford subcortical brain regions was calculated separately for the left and right hemispheres, except for the brain stem.

For the regional vessel analysis, the mean vessel radius and the vascular attenuation were calculated only for the larger MNI and Harvard-Oxford brain regions because smaller regions are too susceptible to noise artifacts. The MNI brain regions used for vessel analysis were the cerebellum, frontal lobe, occipital lobe, parietal lobe, and temporal lobe. Harvard-Oxford brain regions used for vessel analysis were the cerebral white matter and cerebral cortex. Vascular attenuation within each region was calculated by dividing the total volume of segmented vascular structures within a given region by the total volume of brain tissue in that same region. This value was then multiplied by 100 to be expressed as a percentage.

#### Enzyme-Linked Immunosorbent Assays

Pregnant women recruited to the Pre-Eclampsia New Emerging Team study were asked to give peripartum blood samples. Of the participants used in this study, 4 women with PE and 8 control women consented to blood sample donation. Samples were collected in heparin and were stored at  $-80^{\circ}\text{C}$  until used for analysis. Blood samples were assayed by enzyme-linked immunosorbent

assays for PGF, sFLT-1, and soluble endoglin by using purchased kits (Quantikine; R&D Systems, Minneapolis, Minnesota); enzyme-linked immunosorbent assays were performed according to the manufacturer's instructions. PE and control samples were diluted 1:1 for PGF, 1:25 for sFLT-1, and 1:4 for soluble endoglin.

#### Statistics

Equality of variances of continuous variables between groups was assessed by the *F* test. Differences in continuous variables between groups were analyzed by 2-tailed unpaired *t* tests for demographic and plasma protein data using the Satterthwaite approximation for unequal variances when appropriate. Differences in categorical variables between groups were analyzed by the  $\chi^2$  test or Fisher exact test when expected counts were  $<5$ . Differences in parameters extracted from MR imaging between groups were analyzed by multivariate analysis of covariance with consideration to age, height, and weight of the participants as covariates. The multivariate effect of each independent variable was assessed by the Wilks  $\lambda$ , which is a measure of the proportion of variance of the dependent variables that is accounted for by the independent variable. Adjusted means were calculated for each parameter on the basis of the linear models produced in the MANCOVA analysis. Pair-wise comparisons were corrected for multiple comparisons by the Bonferroni method. All data are expressed as mean  $\pm$  standard error, unless stated otherwise. Differences between groups were considered statistically significant at a *P* value  $< .05$ . Statistical analyses were conducted by using SAS, Version 9.3 (SAS Institute, Cary, North Carolina) and SPSS, Version 22 (IBM, Armonk, New York).

#### RESULTS

The characteristics of the study samples are displayed in Table 1. The PE-FI and control groups differed significantly in birth weight (control:  $3419.9 \pm 361.2$  g versus PE:  $2665.2 \pm 788.7$  g, *P* = .013). All other characteristics, including gestational age at birth, were not significantly different between the PE-FI and control groups.

The MANCOVA analysis showed no overall effect of PE status ( $\lambda = 0.058$ , *P* = .649). Similarly, none of the covariates displayed a significant overall effect on the extracted parameters (age:  $\lambda = 0.024$ , *P* = .448; height:  $\lambda = 0.020$ , *P* = .416; weight:  $\lambda = 0.041$ , *P* = .566). Post hoc analyses did reveal significant differences among pair-wise comparisons of individual extracted parameters. The MPRAGE imaging revealed no significant difference in total intracranial volume between the control and PE groups (control:  $1431.7 \pm 33.6$  mL versus PE:  $1495.5 \pm 33.6$  mL, *P* = .201; Table 2). The PE group displayed statistically significantly larger adjusted mean normalized volumes in 5 brain regions: cerebellum (control:  $8.72 \pm 0.21\%$  versus PE:  $9.58 \pm 0.21\%$ , *P* = .010; Table 2), temporal lobe (control:  $8.98 \pm 0.15\%$  versus PE:  $9.65 \pm 0.15\%$ , *P* = .007; Table 2), left amygdala (control:  $0.09 \pm 0.003\%$  versus PE:  $0.10 \pm 0.003\%$ , *P* = .023; Table 2), right amygdala (control:  $0.11 \pm 0.002\%$  versus PE:  $0.12 \pm 0.002\%$ , *P* = .012; Table 2), and brain stem (control:  $1.27 \pm 0.04\%$  versus PE:  $1.40 \pm 0.04\%$ , *P* = .015; Table 2). None of the other 21 brain regions analyzed displayed statistically significant differences (Table 2).

The analysis of the TOF-MRA datasets revealed significant

**Table 1: Study population characteristics**

Characteristics at Testing	Control (n = 10)	PE (n = 10)	P Value <sup>b</sup>
Age (yr) (mean) (SD)	9.79 (0.89)	9.66 (1.07)	.769 <sup>c</sup>
Male sex (No.) (%)	5 (50.0)	5 (50.0)	1.000 <sup>d</sup>
Height (m) (mean) (SD)	1.37 (0.09)	1.39 (0.14)	.644 <sup>c</sup>
Weight (kg) (mean) (SD)	30.12 (5.68)	30.66 (9.19)	.875 <sup>c</sup>
BMI (kg/m <sup>2</sup> ) (mean) (SD)	16.08 (1.93)	16.17 (5.45)	.962 <sup>c</sup>
Caucasian (No.) (%)	10 (100)	10 (100)	1.000 <sup>d</sup>
Household SES <sup>a</sup> (mean) (SD)	49.15 (9.07)	51.10 (9.10)	.637 <sup>c</sup>
Psychiatric disorder (No.) (%)			.303 <sup>d</sup>
Anxiety	0 (0)	2 (20)	
Depression	0 (0)	1 (10)	
ADHD	1 (10)	2 (20)	
Characteristics at birth			
Gestational age (wks) (mean) (SD)	39.47 (1.38)	37.16 (3.34)	.055 <sup>c</sup>
Birth weight (g) (mean) (SD)	3419.9 (361.2)	2665.2 (788.7)	.013 <sup>c</sup>
Length (cm) (mean) (SD)	51.38 (3.39)	48.50 (4.36)	.146 <sup>c</sup>
Head circumference (cm) (mean) (SD)	34.31 (0.59)	32.65 (3.01)	.120 <sup>c</sup>
Abdominal girth (cm) (mean) (SD)	32.69 (2.22)	29.81 (3.10)	.051 <sup>c</sup>
Delivery type (No.) (%)			.070 <sup>d</sup>
Vaginal	8 (80)	3 (30)	
Cesarean birth	2 (20)	7 (70)	
Maternal height (m) (mean) (SD)	1.64 (0.07)	1.65 (0.09)	.716 <sup>c</sup>
Maternal weight (kg) (mean) (SD)	80.44 (14.31)	84.80 (16.96)	.556 <sup>c</sup>
Maternal BMI (kg/m <sup>2</sup> ) (mean) (SD)	30.06 (6.26)	30.99 (5.41)	.735 <sup>c</sup>
Maternal age (yr) (mean) (SD)	32.27 (4.58)	30.59 (3.23)	.355 <sup>c</sup>

**Note:**—SES indicates socioeconomic status; ADHD, attention deficit/hyperactivity disorder; BMI, body mass index.

<sup>a</sup> Calculated according to Hollingshead Four Factor Index of Social Status.

<sup>b</sup> Bonferroni-corrected.

<sup>c</sup> Student t test.

<sup>d</sup> Fisher exact test.

**Table 2: Adjusted mean brain regional volumes (percentage of full intracranial volume)<sup>a</sup>**

Brain Region	Control (n = 10) (mean) (SE)	PE (n = 10) (mean) (SE)	P Value <sup>d</sup>
Full intracranial volume (mL)	1431.7 (33.6)	1495.5 (33.6)	.201
Cerebellum <sup>b</sup>	8.72 (0.21)	9.58 (0.21)	.010
Frontal lobe <sup>b</sup>	16.62 (0.39)	17.08 (0.39)	.422
Occipital lobe <sup>b</sup>	6.25 (0.18)	6.58 (0.18)	.213
Parietal lobe <sup>b</sup>	9.41 (0.26)	9.75 (0.26)	.364
Temporal lobe <sup>b</sup>	8.98 (0.15)	9.65 (0.15)	.007
Left accumbens <sup>c</sup>	0.03 (0.001)	0.03 (0.001)	.993
Right accumbens <sup>c</sup>	0.03 (0.001)	0.03 (0.001)	.986
Left amygdala <sup>c</sup>	0.09 (0.003)	0.10 (0.003)	.023
Right amygdala <sup>c</sup>	0.11 (0.002)	0.12 (0.002)	.012
Brain stem <sup>c</sup>	1.27 (0.04)	1.40 (0.04)	.015
Left caudate <sup>c</sup>	0.20 (0.01)	0.21 (0.01)	.843
Right caudate <sup>c</sup>	0.20 (0.01)	0.21 (0.01)	.490
Left cerebral cortex <sup>c</sup>	23.25 (0.41)	24.39 (0.41)	.071
Right cerebral cortex <sup>c</sup>	24.42 (0.46)	25.39 (0.46)	.158
Left cerebral white matter <sup>c</sup>	13.42 (0.37)	13.96 (0.37)	.320
Right cerebral white matter <sup>c</sup>	12.17 (0.33)	12.85 (0.33)	.168
Left hippocampus <sup>c</sup>	0.21 (0.01)	0.23 (0.01)	.166
Right hippocampus <sup>c</sup>	0.22 (0.01)	0.23 (0.01)	.247
Left lateral ventricle <sup>c</sup>	0.34 (0.07)	0.36 (0.07)	.873
Right lateral ventricle <sup>c</sup>	0.31 (0.05)	0.32 (0.05)	.941
Left pallidum <sup>c</sup>	0.11 (0.004)	0.12 (0.004)	.327
Right pallidum <sup>c</sup>	0.12 (0.004)	0.12 (0.004)	.257
Left putamen <sup>c</sup>	0.31 (0.01)	0.32 (0.01)	.446
Right putamen <sup>c</sup>	0.34 (0.01)	0.34 (0.01)	.594
Left thalamus <sup>c</sup>	0.36 (0.01)	0.38 (0.01)	.335
Right thalamus <sup>c</sup>	0.41 (0.01)	0.42 (0.01)	.396

**Note:**—SE indicates standard error.

<sup>a</sup> All means were adjusted for age (9.72 yr), height (1.38 m), and weight. (30.39 kg).

<sup>b</sup> Derived from the Montreal Neurological Institute brain atlas.

<sup>c</sup> Derived from the Harvard-Oxford subcortical atlas.

<sup>d</sup> Bonferroni-corrected.

differences in 2 regions: the occipital lobe and parietal lobe. In the occipital lobe, the mean vessel radius was significantly smaller in the PE group (control:  $0.50 \pm 0.01$  mm versus PE:  $0.45 \pm 0.01$  mm,  $P = .004$ ; Table 3). Similarly, in the parietal lobe, the mean vessel radius was significantly smaller in the PE group (control:  $0.55 \pm 0.01$  mm versus PE:  $0.52 \pm 0.01$  mm,  $P = .025$ ; Table 3). There were no significant differences in vessel radius between the PE and control groups for any of the other brain regions analyzed (Table 3). Additionally, there were no significant differences in vascular attenuation between the PE and control groups for any of the 7 brain regions analyzed (On-line Table).

Analysis of maternal plasma samples by enzyme-linked immunosorbent assay revealed that PE samples expressed significantly lower levels of PGF (control:  $221.0 \pm 46.6$  pg/mL versus PE:  $37.2 \pm 21.5$  pg/mL,  $P = .024$ ). PE samples did not display statistically significant different concentrations of sFLT-1 (control:  $12,272 \pm 3302$  pg/mL versus PE:  $23,596 \pm 13,630$  pg/mL,  $P = .479$ ) or soluble endoglin (control:  $13.34 \pm 3.40$  ng/mL versus PE:  $40.43 \pm 21.10$  ng/mL,  $P = .294$ ) compared with controls.

## DISCUSSION

Although numerous reports exist regarding cognitive function,<sup>15</sup> risk of depression,<sup>17</sup> or stroke<sup>14</sup> among PE-F1s, our study aimed to link these outcomes to potential underlying defects in structural development. Prematurity has long been known to adversely affect brain growth and development and is linked to increased likelihood of variation of the circle of Willis.<sup>27</sup> Although the effects of prematurity cannot be completely ruled out, the PE-F1s examined in this study were not born significantly earlier in gestation than the cohort-matched controls. Additionally, children of each group were not significantly different with respect to height or weight at the time of testing. Thus, long-term effects of PE on the growth trajectory are not apparent. Thus, the effects seen in the PE-F1s in this study can be attributed to the experience of gestation in a PE pregnancy. This would be consistent with previous findings of

**Table 3: Adjusted mean brain regional vascular diameters (mm)<sup>a</sup>**

Brain Region	Control (n = 10) (mean) (SE)	PE (n = 10) (mean) (SE)	P Value <sup>d</sup>
Cerebellum <sup>b</sup>	0.56 (0.01)	0.55 (0.01)	.417
Frontal lobe <sup>b</sup>	0.54 (0.01)	0.52 (0.01)	.112
Occipital lobe <sup>b</sup>	0.50 (0.01)	0.45 (0.01)	.004
Parietal lobe <sup>b</sup>	0.55 (0.01)	0.52 (0.01)	.025
Temporal lobe <sup>b</sup>	0.63 (0.01)	0.60 (0.01)	.128
Cerebral cortex <sup>c</sup>	0.57 (0.01)	0.55 (0.01)	.085
Cerebral white matter <sup>c</sup>	0.44 (0.02)	0.42 (0.02)	.454

<sup>a</sup> All means were adjusted for age (9.72 yr), height (1.38 m), and weight (30.39 kg).

<sup>b</sup> Derived from the Montreal Neurological Institute brain atlas.

<sup>c</sup> Derived from the Harvard-Oxford subcortical atlas.

<sup>d</sup> Bonferroni-corrected.

impairment among PE-F1s compared with offspring born of pregnancies complicated by gestational hypertension.<sup>15,16</sup>

As expected, the maternal plasma samples displayed an aberrant expression pattern of an angiogenic factor (ie, underexpression of the proangiogenic PGF). Unexpectedly, however, the PE-F1s displayed larger volumes in 5 brain regions (cerebellum, temporal lobe, brain stem, left and right amygdalae) but smaller vessel radii in the occipital and parietal lobes. In line with this finding, all other regions examined also displayed a nonsignificant trend for smaller vessel radii for PE-F1s compared with controls. This finding suggests that the aberrant maternal angiogenic signaling milieu common among PE pregnancies adversely affects brain vascular growth in the offspring. The described vessel measurements are mostly related to vessels in the sulci that are responsible for the blood supply of the brain tissue. Although these arteries are, strictly speaking, outside the brain regions used, they are still covered by the brain atlas regions because a probabilistic threshold of 50% was used for definition of the binary brain regions. Nevertheless, the reduction in brain vessel radii among PE-F1s does not appear to affect brain growth. This finding raises the question of how PE gestation leads to deficits in cognitive function and increased susceptibility to stroke in the offspring. The answer may lie in the disrupted general architecture of the brain, potentially causing imbalances in signaling between adjacent regions. This is a phenomenon seen in autism spectrum disorder and attention deficit/hyperactivity disorder, in which the growth trajectory of the brain is disrupted, particularly in early life.<sup>28,29</sup>

The regional brain volumetric alterations seen in this study may further shed light on the specific cognitive functional profile of PE-F1s. Enlarged left and right amygdalae are also commonly seen in autism spectrum disorder<sup>30</sup> and are associated with an increased incidence of temporal lobe epilepsy.<sup>31,32</sup> Most interesting, the temporal lobe was also enlarged in PE-F1s compared with controls. A commonly prescribed antiepileptic, valproic acid, can also induce hypertrophy of the amygdalae, leading to autistic-like behaviors in a rat model.<sup>33</sup> Additionally, early life stress has been shown to have an effect on amygdala hypertrophy in a macaque model, acting through serotonin signaling.<sup>34</sup> This is mirrored in a study of children, showing that enlarged amygdalae are associated with increased anxiety.<sup>35</sup> Cerebellar and brain stem enlargements are common among small-for-gestational-age neonates at term.<sup>36</sup> These enlargements correlated significantly with cluster scores from the Neonatal Behavioral Assessment Scale.<sup>36</sup> Additionally,

children born very preterm display delays in cortical thinning compared with children born at term.<sup>37</sup> Thus, the brain anomalies observed among PE-F1 in the present study may be caused by a combined effect of a PE gestation in addition to prematurity and fetal growth restriction. Further study will be necessary to separate the effects of each factor on brain development in these children.

Our data also agree well with studies of animal models of PE. In a mouse model of PE induced by pregnancy-specific lentiviral overexpression of sFLT-1, offspring displayed structural alterations in numerous brain regions.<sup>38</sup> In this case, many of the structural alterations were enlargements, with patterns of alterations differing between sexes. Furthermore, this model induced impairments in vestibular function, balance, and coordination in the offspring.<sup>39</sup> In both cases, maternal treatment with pravastatin prevented the structural and functional impairments seen in the offspring. Furthermore, brain developmental and functional impairments were displayed in the offspring of a rat model of PE induced by maternal treatment with *N* $\omega$ -nitro-L-arginine methyl ester, a potent nitric oxide synthase inhibitor.<sup>40</sup> The authors found that the *N* $\omega$ -nitro-L-arginine methyl ester-treated rat offspring displayed impaired neurogenesis but increased gliogenesis, which compensated for the reduction in neurogenesis to normalize brain weight. Therefore, although brain structural anatomy was essentially normal in the offspring of this model, the treatment led to functional deficits in spatial learning and memory.<sup>40</sup>

Our pilot study provides fresh insight into the well-documented cognitive functional outcomes among PE-F1s. By examining children rather than adults, though somewhat more challenging, our study results are less susceptible to confounding from long-term environmental exposures that may also deviate cognitive functioning. Additionally, we are able to detect anomalies in specific brain regions relatively early in life, when interventional strategies may still provide very profound beneficial long-term effects. Although sample size and range in childhood ages are limited, our findings are consistent with numerous previously published studies that have consistently shown impaired cognitive functions among PE-F1s.<sup>15</sup> Through this study, we have provided a foundation on which future studies can build. The focus within our group will be to increase participant recruitment for this study to provide more accurate estimates of how brain vascular and structural alterations may lead to functional deficits. Within this context, the results of this study need to be considered exploratory at this stage because of the rather small sample size. On the basis of the clear differences found in the vascular anatomy, it appears most fruitful to investigate the cerebrovascular system in more detail (eg, by investigating the branching index of vessels in different brain regions or even by developing vascular network analysis methods).<sup>41</sup>

## CONCLUSIONS

We have shown that PE-F1 as children display significant enlargement of the cerebellum, brain stem, temporal lobe, and right and left amygdalae. Additionally, PE-F1s display significantly reduced vessel radii in the occipital and parietal lobes. These structural and vascular anomalies may underlie the cognitive deficits reported in

PE-F1 populations and may contribute to an elevated lifetime risk of depression and stroke.

## ACKNOWLEDGMENTS

We thank the participants and their families for taking part in the study. We thank Mrs Aysha Tayab, Queen's University, for assistance in participant recruitment and acquiring questionnaire data, and Ms Janelle Zhan, Queen's University, for assistance in acquiring questionnaire data.

Disclosures: Matthew T. Rätsep—*RELATED: Grant:* Kingston General Hospital Foundation; Canadian Institutes of Health Research.\* Vanessa R. Kay—*RELATED: Grant:* Grant funding for the lab is disclosed on the Principal Investigator's disclosure form\*; *Support for Travel to Meetings for the Study or Other Purposes:* Travel Award from the Canadian Institutes of Health Research to attend the Gordon Research Conference on Angiogenesis (August 2015); *Other:* Canadian Institutes of Health Research.\* *Comments:* MD/PhD program funding support to the institution; the program provides me (a student) with stipend. Queen's University also provides stipend support. Michael A. Adams—*RELATED: Grant:* Canadian Institutes of Health Research.\* James N. Reynolds—*RELATED: Grant:* NeuroDevNet.\* *Comments:* NeuroDevNet is funded by the Networks of Centers of Excellence, a program of the Canadian federal government to advance science and technology; *UNRELATED: Grants/Grants Pending:* NeuroDevNet.\* *Comments:* NeuroDevNet is funded by the Networks of Centers of Excellence, a program of the Canadian federal government to advance science and technology. Barbara Anne Croy—*RELATED: Grant:* Harry Botterell Foundation for the Neurological Sciences Award.\* *Comments:* Internal Institutional award administered through Queen's University, Kingston, Ontario, for the Kingston General Hospital Research Foundation. The amount of the award was Can\$10,000. I was the Principal Investigator on the 1-year award made June 1, 2014. These funds covered the MRI user fees for the studies reported in the article; *UNRELATED: Employment:* I am an employee of Queen's University, *Comments:* The funds awarded were in an internal university competition, and a proposal was written and ranked by others in a peer review for this and all other Kingston General Hospital Foundation Awards; *Grants/Grants Pending:* Garfield Kelly and Harry Botterell Foundation for the Neurological Sciences.\* *Comments:* I received internal competitive funds of Can\$10,000 from my university for June 1, 2015 from the Garfield Kelly Award (Can\$2500) and the Botterell Foundation (Can\$7500). The former enabled the enzyme-linked immunosorbent assay studies reported in the article. The Botterell funds will permit us to access a second pregnancy cohort, the Oak (Ottawa and Kingston cohort), and support MRI user fees to study 4 more pairs of children.\* Money paid to the institution.

## REFERENCES

1. Roberts CL, Ford JB, Algert CS, et al. **Population-based trends in pregnancy hypertension and pre-eclampsia: an international comparative study.** *BMJ Open* 2011;1:e000101 CrossRef Medline
2. American College of Obstetricians and Gynecologists, Task Force on Hypertension in Pregnancy. **Hypertension in pregnancy: report of the American College of Obstetricians and Gynecologists' Task Force on Hypertension in Pregnancy.** *Obstet Gynecol* 2013;122:1122–31 CrossRef Medline
3. Brennan LJ, Morton JS, Davidge ST. **Vascular dysfunction in pre-eclampsia.** *Microcirculation* 2014;21:4–14 CrossRef Medline
4. Turner RJ, Bloemenkamp KW, Penning ME, et al. **From glomerular endothelium to podocyte pathobiology in preeclampsia: a paradigm shift.** *Curr Hypertens Rep* 2015;17:54 CrossRef Medline
5. Staff AC, Benton SJ, von Dadelzen P, et al. **Redefining preeclampsia using placenta-derived biomarkers.** *Hypertension* 2013;61:932–42 CrossRef Medline
6. Levine RJ, Maynard SE, Qian C, et al. **Circulating angiogenic factors and the risk of preeclampsia.** *N Engl J Med* 2004;350:672–83 CrossRef Medline
7. Powers RW, Jayabalan A, Clifton RG, et al; Eunice Kennedy Shriver National Institute of Child Health Human Development Maternal-Fetal Medicine Units Network. **Soluble fms-like tyrosine kinase 1 (sFlt1), endoglin and placental growth factor (PlGF) in preeclampsia among high risk pregnancies.** *PLoS One* 2010;5:e13263 CrossRef Medline
8. De Vivo A, Baviera G, Giordano D, et al. **Endoglin, PlGF and sFlt-1 as markers for predicting pre-eclampsia.** *Acta Obstet Gynecol Scand* 2008;87:837–42 CrossRef Medline
9. Thadhani R, Mutter WP, Wolf M, et al. **First trimester placental growth factor and soluble fms-like tyrosine kinase 1 and risk for preeclampsia.** *J Clin Endocrinol Metab* 2004;89:770–75 CrossRef Medline
10. Powers RW, Roberts JM, Plymire DA, et al. **Low placental growth factor across pregnancy identifies a subset of women with preterm preeclampsia: type 1 versus type 2 preeclampsia?** *Hypertension* 2012;60:239–46 CrossRef Medline
11. Melchiorre K, Sutherland GR, Liberati M, et al. **Preeclampsia is associated with persistent postpartum cardiovascular impairment.** *Hypertension* 2011;58:709–15 CrossRef Medline
12. Östlund E, Al-Nashi M, Hamad RR, et al. **Normalized endothelial function but sustained cardiovascular risk profile 11 years following a pregnancy complicated by preeclampsia.** *Hypertens Res* 2013;36:1081–87 CrossRef Medline
13. Davis EF, Lazdam M, Lewandowski AJ, et al. **Cardiovascular risk factors in children and young adults born to preeclamptic pregnancies: a systematic review.** *Pediatrics* 2012;129:e1552–61 CrossRef Medline
14. Kajantie E, Eriksson JG, Osmond C, et al. **Pre-eclampsia is associated with increased risk of stroke in the adult offspring: the Helsinki birth cohort study.** *Stroke* 2009;40:1176–80 CrossRef Medline
15. Tuovinen S, Eriksson JG, Kajantie E, et al. **Maternal hypertensive pregnancy disorders and cognitive functioning of the offspring: a systematic review.** *J Am Soc Hypertens* 2014;8:832–47.e1 CrossRef Medline
16. Tuovinen S, Räikkönen K, Pesonen AK, et al. **Hypertensive disorders in pregnancy and risk of severe mental disorders in the offspring in adulthood: the Helsinki Birth Cohort Study.** *J Psychiatry Res* 2012;46:303–10 CrossRef Medline
17. Tuovinen S, Räikkönen K, Kajantie E, et al. **Depressive symptoms in adulthood and intrauterine exposure to pre-eclampsia: the Helsinki Birth Cohort Study.** *BJOG* 2010;117:1236–42 CrossRef Medline
18. Smith GN, Walker MC, Liu A, et al. **A history of preeclampsia identifies women who have underlying cardiovascular risk factors.** *Am J Obstet Gynecol* 2009;200:58 e1–8 CrossRef Medline
19. Hollingshead AB. **Four Factor Index of Social Status.** *Yale J Sociology* 2011;8:21–51
20. Forkert ND, Schmidt-Richberg A, Fiehler J, et al. **Fuzzy-based vascular structure enhancement in time-of-flight MRA images for improved segmentation.** *Meth Inf Med* 2011;50:74–83 CrossRef Medline
21. Forkert ND, Schmidt-Richberg A, Fiehler J, et al. **3D cerebrovascular segmentation combining fuzzy vessel enhancement and level-sets with anisotropic energy weights.** *Magn Reson Imaging* 2013;31:262–71 CrossRef Medline
22. Forkert ND, Schmidt-Richberg A, Fiehler J, et al. **Automatic correction of gaps in cerebrovascular segmentations extracted from 3D time-of-flight MRA datasets.** *Meth Inf Med* 2012;51:415–22 CrossRef Medline
23. Forkert ND, Fiehler J, Suniaga S, et al. **A statistical cerebroarterial atlas derived from 700 MRA datasets.** *Meth Inf Med* 2013;52:467–74 CrossRef Medline
24. Mazziotta J, Toga A, Evans A, et al. **A probabilistic atlas and reference system for the human brain: International Consortium for Brain Mapping (ICBM).** *Philos Trans R Soc Lond B Biol Sci* 2001;356:1293–322 CrossRef Medline
25. Fonov V, Evans AC, Botteron K, et al; Brain Development Cooperative Group. **Unbiased average age-appropriate atlases for pediatric studies.** *Neuroimage* 2011;54:313–27 CrossRef Medline
26. Modat M, McClelland J, Ourselin S. **Lung registration using the NiftyReg package.** In: *Proceedings of the International Conference on Medical Image Computing and Computer Assisted Intervention*, Beijing, China. September 20–24, 2010
27. van Kooij BJ, Hendrikse J, Benders MJ, et al. **Anatomy of the circle**

- of Willis and blood flow in the brain-feeding vasculature in pre-maturely born infants. *Neonatology* 2010;97:235–41 CrossRef Medline
28. Courchesne E, Karns CM, Davis HR, et al. **Unusual brain growth patterns in early life in patients with autistic disorder: an MRI study.** *Neurology* 2001;57:245–54 CrossRef Medline
  29. Konrad K, Eickhoff SB. **Is the ADHD brain wired differently? A review on structural and functional connectivity in attention deficit hyperactivity disorder.** *Hum Brain Mapp* 2010;31:904–16 CrossRef Medline
  30. Nordahl CW, Scholz R, Yang X, et al. **Increased rate of amygdala growth in children aged 2 to 4 years with autism spectrum disorders: a longitudinal study.** *Arch Gen Psychiatry* 2012;69:53–61 CrossRef Medline
  31. Sone D, Ito K, Taniguchi G, et al. **Evaluation of amygdala pathology using (11)C-methionine positron emission tomography/computed tomography in patients with temporal lobe epilepsy and amygdala enlargement.** *Epilepsy Res* 2015;112:114–21 CrossRef Medline
  32. Lv RJ, Sun ZR, Cui T, et al. **Temporal lobe epilepsy with amygdala enlargement: a subtype of temporal lobe epilepsy.** *BMC Neurol* 2014;14:194 CrossRef Medline
  33. Olde Loohuis NF, Kole K, Glennon JC, et al. **Elevated microRNA-181c and microRNA-30d levels in the enlarged amygdala of the valproic acid rat model of autism.** *Neurobiol Dis* 2015;80:42–53 CrossRef Medline
  34. Coplan JD, Fathy HM, Jackowski AP, et al. **Early life stress and macaque amygdala hypertrophy: preliminary evidence for a role for the serotonin transporter gene.** *Front Behav Neurosci* 2014;8:342 CrossRef Medline
  35. Qin S, Young CB, Duan X, et al. **Amygdala subregional structure and intrinsic functional connectivity predicts individual differences in anxiety during early childhood.** *Biol Psychiatry* 2014;75:892–900 CrossRef Medline
  36. Sanz-Cortes M, Egaña-Ugrinovi G, Zupan R, et al. **Brainstem and cerebellar differences and their association with neurobehavior in term small-for-gestational-age fetuses assessed by fetal MRI.** *Am J Obstet Gynecol* 2014;210:452.e1–8 CrossRef Medline
  37. Mürner-Lavanchy I, Steinlin M, Nelle M, et al. **Delay of cortical thinning in very preterm born children.** *Early Hum Dev* 2014;90:443–50 CrossRef Medline
  38. Carver AR, Andrikopoulou M, Lei J, et al. **Maternal pravastatin prevents altered fetal brain development in a preeclamptic CD-1 mouse model.** *PLoS One* 2014;9:e100873 CrossRef Medline
  39. Carver AR, Tamayo E, Perez-Polo JR, et al. **The effect of maternal pravastatin therapy on adverse sensorimotor outcomes of the offspring in a murine model of preeclampsia.** *Int J Dev Neurosci* 2014;33:33–40 CrossRef Medline
  40. Liu X, Zhao W, Liu H, et al. **Developmental and functional brain impairment in offspring from preeclampsia-like rats.** *Mol Neurobiol* 2015 Jan 10. [Epub ahead of print] CrossRef Medline
  41. Hadjiiski LM, Tourassi GD, Galarreta-Valverde MA, et al. **Characterization of vascular tree architecture using the Tokunaga taxonomy.** In: *Proceedings of the Annual Meeting of the SPIE Medical Imaging Conference*, February 21–16. Orlando, Florida

# Diagnostic Value of Prenatal MR Imaging in the Detection of Brain Malformations in Fetuses before the 26th Week of Gestational Age

G. Conte, C. Parazzini, G. Falanga, C. Cesaretti, G. Izzo, M. Rustico, and A. Righini



## ABSTRACT

**BACKGROUND AND PURPOSE:** In several countries, laws and regulations allow abortion for medical reasons within 24–25 weeks of gestational age. We investigated the diagnostic value of prenatal MR imaging for brain malformations within 25 weeks of gestational age.

**MATERIALS AND METHODS:** We retrospectively included fetuses within 25 weeks of gestational age who had undergone both prenatal and postnatal MR imaging of the brain between 2002 and 2014. Two senior pediatric neuroradiologists evaluated prenatal MR imaging examinations blinded to postnatal MR imaging findings. With postnatal MR imaging used as the reference standard, we calculated the sensitivity, specificity, positive predictive value, and negative predictive value of the prenatal MR imaging in detecting brain malformations.

**RESULTS:** One-hundred nine fetuses (median gestational age at prenatal MR imaging: 22 weeks; range, 21–25 weeks) were included in this study. According to the reference standard, 111 malformations were detected. Prenatal MR imaging failed to detect correctly 11 of the 111 malformations: 3 midline malformations, 5 disorders of cortical development, 2 posterior fossa anomalies, and 1 vascular malformation. Prenatal MR imaging misdiagnosed 3 findings as pathologic in the posterior fossa.

**CONCLUSIONS:** The diagnostic value of prenatal MR imaging between 21 and 25 weeks' gestational age is very high, with limitations of sensitivity regarding the detection of disorders of cortical development.

**ABBREVIATIONS:** GA = gestational age; US = ultrasonography

Prenatal MR imaging of the brain is a technique increasingly used in clinical practice; it is generally performed as a second-look investigation in case of abnormal or suspicious findings at prenatal ultrasonography (US).<sup>1</sup>

Prenatal MR imaging is often advocated as an important tool in parental counseling and decision-making regarding the fate of the pregnancy.<sup>2</sup> In several countries, crucial decisions on pregnancy must be made before the 24th to 25th week of gestation because local laws and regulations allow abortion for medical reasons within this deadline. In these cases, a correct diagnosis should be reached early during pregnancy because performing

additional MR imaging follow-up is not compatible with legal time constraints. Moreover, an early correct diagnosis may have an important impact on the psychological well-being of the mother and may help the clinician in planning other diagnostic or therapeutic procedures.

To determine prenatal MR imaging accuracy, several studies have already compared its results with ones from postmortem examinations,<sup>3–5</sup> postnatal MR imaging,<sup>6–11</sup> or both postmortem examination and postnatal MR imaging.<sup>12,13</sup> However, these studies were performed in small cohorts of fetuses, and they were focused on a single specific class of anomalies or accounted for few fetuses younger than 24–25 weeks' gestational age (GA), thus providing little information about the diagnostic accuracy of prenatal MR imaging performed at an early GA.

The purpose of our study was to assess the diagnostic value of prenatal MR imaging in the diagnosis of brain malformations, in a large cohort of fetuses (109 cases) within 25 weeks of GA, by using postnatal MR imaging as the reference standard.

## MATERIALS AND METHODS

### Subjects

We retrospectively included in our study all fetuses that underwent prenatal MR imaging at the Children's Hospital Vittore

Received July 3, 2015; accepted after revision November 5.

From the Departments of Radiology and Neuroradiology (G.C., C.P., C.C., G.I., A.R.) and Gynecology and Obstetrics (M.R.), Children's Hospital Vittore Buzzi, Milan, Italy; Department of Health Sciences (G.C.), University of Milan, Milan, Italy; and Department of Biopathology and Medical and Forensic Biotechnologies (G.F.), Section of Radiological Sciences, University of Palermo, Palermo, Italy.

Please address correspondence to Giorgio Conte, MD, Radiology and Neuroradiology Department, Children's Hospital Vittore Buzzi, Via Castelvetro 32, Milan, 20154, Italy; e-mail: giorgioconte.unimed@gmail.com

 Indicates article with supplemental on-line table.

 Indicates article with supplemental on-line photos.

<http://dx.doi.org/10.3174/ajnr.A4639>

Buzzi from 2002 to 2014 and fulfilled the following criteria: 1) GA within 25 weeks at prenatal MR imaging examination; 2) neither termination of pregnancy, fetal death, nor stillbirth; and 3) at least 1 postnatal MR imaging examination of the brain performed at the Children's Hospital Vittore Buzzi or in other institutions and available for review. Mothers signed the specific informed consent for prenatal MR imaging in use in our institution, which also includes a disclaimer about data collection regarding clinical and imaging follow-up. The study complied with regulations in use in our institution for clinical review studies.

For each fetus, the US and/or clinical indications for the prenatal MR imaging, GA at prenatal MR imaging examination, and the child's age at postnatal MR imaging examination were recorded. Because our cases were referred from several different prenatal sonography centers, US was performed by operators with different experience levels. The US findings were collected from the examination reports. GA at prenatal MR imaging examination was determined by the mother's last menstrual period and by findings at first trimester US.

### Imaging Methods and Analysis

All prenatal MR imaging examinations were performed on a 1.5T system with a phased array abdominal or cardiac coil. Prenatal MR imaging protocol was standard clinical and state-of-the-art: It included T2-weighted single-shot FSE multiplanar sections (3- to 4-mm-thick sections; gap, 0.1 mm; TR/TE, 3000/180 ms; in-plane resolution, 1.1 mm<sup>2</sup>); balanced steady-state multiplanar sections (contiguous 2- to 3-mm-thick sections); T1-weighted FSE multiplanar sections (5.5-mm-thick sections; TR/TE, 300/14 ms; turbo factor, 3; in-plane resolution, 1.4 mm<sup>2</sup>); and, in some cases, DWI sections (5.5-mm-thick sections; TR/TE, 1000/90 ms; b factor, 0–600 s/mm<sup>2</sup>; FOV, 320 × 320 mm; matrix, 128 × 128).

Postnatal MR imaging sequences varied because they were performed at different institutions; however, all included sagittal T1-weighted images and T2-weighted images in at least 2 different anatomic planes with section thicknesses ranging from 3 to 5 mm. When >1 postnatal MR imaging examination was performed, the first postnatal one was used as the reference for this study.

Two senior pediatric neuroradiologists (A.R., C.P.) with 12 years of experience in fetal MR imaging (approximately 150 fetal cases assessed yearly) evaluated prenatal MR imaging examinations separately; in cases of disagreement, they reached consensus in a second reading. At the time of the review of prenatal MR imaging examinations for this study, both readers were blinded to the patient's name and postnatal MR imaging findings; however, they were aware of the US and/or clinical indications for prenatal MR imaging and the GA at prenatal MR imaging. The 2 readers evaluated the postnatal MR imaging examinations in consensus with knowledge of the prenatal MR imaging findings.

For each fetus, the readers assessed the images for the following categories of brain malformations: 1) midline malformations, 2) disorders of cortical development, 3) posterior fossa anomalies, 4) vascular malformations, and 5) ventricular/subarachnoid space anomalies.

**Table 1: Ultrasonographic and clinical indications for prenatal MR imaging**

Indications for MR Imaging	No.
Ventricular dilation at US	34
Midline malformation at US	20
Posterior fossa anomalies at US	17
CMV infection	14
TTS	14
Cysts at US	2
Vascular malformation at US	2
Brain anomalies in previous pregnancy	2
Cortical malformations at US	1
Toxoplasma infection	1
Polymalformation at US	1
Brain edema at US	1

**Note:**—TTS indicates twin-to-twin transfusion syndrome; CMV, cytomegalovirus.

### Statistical Analysis

With postnatal MR imaging used as the reference standard, we calculated the sensitivity, specificity, positive predictive value, and negative predictive value for each category of malformations on the basis of the final reading in consensus with the prenatal MR imaging. The agreement between the 2 readers in evaluating prenatal MR imaging was assessed by using the Cohen  $\kappa$  statistic. We reported discrepancies between the US and MR imaging findings without providing statistics because US was performed by several centers, thus preventing us from reliably calculating the US performance in the detection of brain malformations.

### RESULTS

Our study included 109 fetuses. The median GA at prenatal MR imaging examination was 22 weeks (range, 21–25 weeks). The median age at first postnatal MR imaging examination was 1 month (range, 0–60 months), corrected for delivery age <37 weeks. In 15 cases, a second postnatal MR imaging examination was performed at a median age of 8 months (range, 5–21 months).

US and clinical indications for prenatal MR imaging are summarized in Table 1.

According to the reference standard, 111 brain malformations were detected in 75 fetuses (median GA, 22 weeks; range, 19–25 weeks), while no brain malformation was detected in the remaining 34 fetuses (median GA, 22 weeks; range, 19–25 weeks). The brain malformations were categorized as follows: 27 midline malformations, 14 disorders of cortical development, 19 posterior fossa anomalies, 48 ventricular/subarachnoid space anomalies, and 3 vascular malformations (see Table 2 for details).

The prenatal MR imaging failed to detect correctly 11 of the 111 malformations: 3 midline malformations including 1 agenesis of septum pellucidum, 1 fused thalami (On-line Fig 1E), and 1 callosal hypoplasia; 5 disorders of cortical development including 3 focal polymicrogyrias and 2 periventricular nodular heterotopias (On-line Fig 2); 2 posterior fossa anomalies including 1 molar tooth malformation (On-line Fig 1A–C) and 1 Chiari type I malformation; and 1 vascular malformation consisting of a persistent falcine sinus. Prenatal MR imaging misdiagnosed 3 findings as pathologic (false-positives) in the posterior fossa: All were moderate (<25°) vermian cranial counterclockwise rotation angles

**Table 2: Brain malformations detected at postnatal MR imaging**

Malformation	No.
Midline malformations	
Complete callosal agenesis <sup>a</sup>	10
Callosal hypoplasia	9
Partial callosal agenesis	3
Septum pellucidum agenesis	2
Incomplete septum pellucidum	1
Fused thalami	1
Occipital meningocele	1
Disorders of cortical development	
Focal polymicrogyria	5
Heterotopias	3
Hemispheric polymicrogyria	2
Anomalous sulcations not of polymicrogyria type <sup>b</sup>	2
Arrhinencephaly	1
Schizencephaly	1
Posterior fossa anomalies	
Vermian hypoplasia	6
Cerebellar hypoplasia	4
Vermian counterclockwise rotation	4
Malformed brain stem	2
Chiari type I malformation	1
Molar tooth malformation	1
Beaking of the tectum	1
Vascular malformations	
Persistent falcine sinus	2
Dural sinus malformation	1
Ventricular/subarachnoid space anomalies	
Ventricular dilation	32
Ventricular and pericerebral space dilation <sup>c</sup>	6
Dysmorphic ventricles <sup>d</sup>	6
Pericerebral space dilation	4

<sup>a</sup> Median diameter of the atrium of the lateral ventricles: 11 mm (range, 9–12 mm).

<sup>b</sup> Dysmorphic gyration pattern, for example, large areas of shallower or deeper sulci without evidence of abnormally small and packed gyri.

<sup>c</sup> Pericerebral CSF space was considered enlarged when the difference between the right-left brain and skull diameters was >10 mm.<sup>29</sup>

<sup>d</sup> Ventricular shape anomalies, mostly of the frontal horns (On-line Fig 4).

with respect to the fourth ventricle floor from a midsagittal section (On-line Fig 3).

Performance of the prenatal MR imaging according to the categories of brain malformations is summarized in the On-line Table.

The interobserver agreement in evaluating prenatal MR imaging was optimum, with  $\kappa = 0.99$  (95% CI, 0.98–1.0), with reader disagreement in a case of arrhinencephaly.

Sonography failed to detect 28 of 111 malformations: 10 midline malformations (7 partial callosal agenesis, 1 septum pellucidum agenesis, 1 fused thalami, 1 complete callosal agenesis), 13 disorders of cortical development (7 polymicrogyrias, 3 periventricular nodular heterotopias, 2 anomalous sulcations not of polymicrogyria type, 1 arrhinencephaly), 4 posterior fossa anomalies (1 Chiari type I malformation, 1 molar tooth malformation, 1 beaking of the tectum, and 1 malformed brain stem), and 1 vascular malformation (persistent falcine sinus). Prenatal MR imaging detected 17 malformations more than sonography: 7 midline malformations (7 partial callosal agenesis), 8 disorders of cortical development (4 polymicrogyrias, 1 periventricular nodular heterotopia, 2 anomalous sulcations not of polymicrogyria type, and 1 arrhinencephaly), and 2 posterior fossa anomalies (1 beaking of the tectum and 1 malformed brain stem). Sonography did not add any findings to prenatal MR imaging.

## DISCUSSION

This study demonstrates that in the context of a large referral fetal imaging center, with the assessment of pediatric neuroradiologists with >10 years' experience in fetal neuroimaging, the diagnostic value of prenatal MR imaging within 25 weeks of GA was very high, with important limitations of sensitivity regarding early detection of disorders of cortical development and, to a lesser extent, posterior fossa anomalies. Our data complement previous studies that investigated the performance of prenatal MR imaging in large cohorts of fetuses, but with mean GAs well above 25 weeks.<sup>6,7,10,11</sup> Our study also showed an optimum interobserver agreement in evaluating prenatal MR imaging; however, this result may be because the 2 readers have worked together in the same hospital for >10 years. The readers were in disagreement in a case of arrhinencephaly studied at 23 weeks' GA. However, prenatal MR imaging can better depict olfactory sulci from 30 weeks' GA onward and olfactory bulbs from 30 to 34 weeks' GA.<sup>14</sup>

The median GA at prenatal MR imaging of our population reflects our national legislation that does not allow termination of pregnancy for medical reasons after the 23rd week of gestation. This highlighted the unmet need to investigate the effectiveness of prenatal MR imaging in detecting fetal malformations at an earlier gestational age because the counseling at this age range is a daily task of fetal medicine centers in our and other countries.

The range of children's ages at postnatal MR imaging was quite large, from 0 to 60 months, with a median value of 1 month. We can hypothesize that these data reflect the indications for postnatal MR imaging examinations being performed early because of abnormalities detected prenatally and others being performed later for an abnormal child development, such as seizure, neurodevelopment delay, and so forth. Fifteen children underwent a second postnatal MR imaging as a follow-up for the ventricular and/or pericerebral space enlargement. These second MR imaging examinations did not provide any findings in addition to the first MR imaging examinations and thus did not influence our analysis.

The main clinical and US indications for prenatal MR imaging were ventricular dilation ( $n = 34$ ), midline malformations ( $n = 20$ ), and posterior fossa anomalies ( $n = 17$ ), resulting in agreement with the practice guidelines for the safe and optimal performance of fetal MR imaging of the American College of Radiology and the Society for Pediatric Radiology.<sup>1</sup>

### Midline Malformations

Prenatal MR imaging demonstrated high sensitivity (88.9%) in detecting midline malformations, with only 3 false-negative findings among 27 cases in this category. The first false-negative finding was callosal hypoplasia in a fetus of 20 weeks, characterized by a clearly thinner-than-normal corpus callosum at postnatal control but with normal length, >16 mm in anteroposterior diameter (reference value from our internal normal pool) at prenatal examination. This example of a normally long but abnormally thin corpus callosum may highlight the specific limitations of fetal MR imaging in assessing corpus callosum thickness; abnormalities related to corpus callosum length would be more easily assessable. A previous study has already demonstrated discrepancies between prenatal and postnatal MR imaging related to the corpus callosal

morphology; however, it investigated a cohort of fetuses with more advanced GA (older than 25 weeks), and it took into account a coarser assessment for the distinction of complete-versus-partial (missing segment) corpus callosum agenesis.<sup>10</sup> The second false-negative finding was thalamic fusion over the midline in a fetus of 22 weeks. The third false-negative finding was a partial septum pellucidum defect in a fetus of 23 weeks. Despite its minuteness, the septum pellucidum is detectable in >90% of fetuses before 27 weeks' GA.<sup>15</sup> In our case, the incorrect depiction of the septum defect could also be attributed to the less-than-optimal quality of this examination. However, the intrinsic limited spatial resolution of prenatal MR imaging versus postnatal MR imaging, as suggested elsewhere,<sup>15</sup> is likely to play a pivotal role in all such missed diagnoses.

### **Disorders of Cortical Development**

In our study, prenatal MR imaging showed a moderate sensitivity (64.7%) in detecting disorders of cortical development at an early gestational age. In particular, prenatal MR imaging failed to detect 3 of the 7 polymicrogyrias and 2 of the 3 nodular periventricular heterotopias. Our data are substantially in agreement with those of a previous study by Glenn et al,<sup>11</sup> which reported sensitivities of 75% and 44% in detecting polymicrogyria and heterotopia, respectively, in fetuses younger than 24 weeks' GA. Our experience supports the literature reports that focal cortical anomalies (such as polymicrogyria) appear in their early phase as focal distortion of the cortical plate rim, standing out from an otherwise smooth hemispheric surface, allowing the diagnosis of early developing focal cortical anomalies.<sup>16,17</sup> The limited sensitivity in detecting heterotopic periventricular nodules is probably due to their very small size and their signal intensity similar to that of the adjacent germinal matrix remnants. Indeed, when the germinal matrix decreases in thickness with increasing gestational age, the heterotopic nodules may be more easily detected.<sup>11</sup> However, irregular borders of the lateral ventricles could be retrospectively detected in 1 (25 weeks' GA) of the 2 fetuses with periventricular nodular heterotopias undetected at prenatal MR imaging (On-line Fig 2A, -B). This finding suggests a possible ependymal-germinal layer insult, which evolved into a heterotopia on the postnatal MR imaging from an early triggered cell proliferation-migration deficit.

### **Posterior Fossa Anomalies**

The false-negative findings among posterior fossa anomalies were 1 molar tooth malformation and 1 Chiari type I malformation. Molar tooth malformation has been reported rarely in prenatal MR imaging literature, basically as single case reports.<sup>18-20</sup> No sensitivity data are available in this regard: the 2 relatively largest series (of 3 and 7 cases of molar tooth malformation), with a total of 4 cases with early diagnoses (before 25 weeks' GA) by MR imaging or US, were affected by a selection bias; because these cases were within a possible recurrence exclusion prospective protocol, the scanning technique and radiologist were likely to be particularly focused on highlighting minimal heralding signs.<sup>21,22</sup> At an early GA, besides the presence of a smaller vermis and abnormal fourth ventricle shape on midsagittal sections, the definitive evidence of a molar tooth footprint in the midbrain-superior

cerebellar peduncle complex may often be visible in only 1 single axial section, unless more axial acquisitions are acquired with different tilting though the brain stem under the guidance of an a priori hypothesis. In our fetus at 22 weeks' GA, we reported a smaller vermis according to the reference data,<sup>23</sup> with an antero-posterior diameter of 4 mm and a superior-inferior diameter of 7 mm, but we did not detect the molar tooth footprint in midbrain-superior cerebellar peduncles, which was visible on only 1 section (On-line Fig 1B and -C). The missed prenatal diagnosis of Chiari type I malformation in a fetus undergoing MR imaging for ventricular dilation on US is easy to explain because, to the best of our knowledge, this malformation has not been reported in prenatal imaging and neonatal cases are exceedingly rare.<sup>24</sup> The progressive herniation of cerebellar tonsils, characteristic of Chiari type I, seems indeed to be the result of a postnatal phenomenon.

Prenatal MR imaging misdiagnosed 3 cases of vermian counterclockwise cranial rotation as pathologic. In such cases, the vermian rotation was isolated and of mild-to-moderate range (<25°), with a normal-sized posterior fossa and normal tentorial insertion and vermian dimensions, thus suggesting a persistent Blake pouch cyst.<sup>25</sup> Sometimes the Blake pouch cyst disappears by the third trimester due to late fenestration, and the cranial vermian rotation could be detected only until 24-26 weeks. Therefore, isolated mild-to-moderate vermian rotation detected at an early GA does not necessarily indicate an adverse outcome, and in one-third of cases, it undergoes spontaneous resolution in utero,<sup>25</sup> explaining our false-positive findings. However, even if less common, vermian rotation is reported to be associated with other anomalies in up to 25% of cases, and in <10% of survivors, it is associated with abnormal postnatal neurologic development,<sup>26</sup> thus giving reason to include it among our prenatal MR imaging findings.

### **Ventricular/Subarachnoid Space Anomalies**

Our results demonstrated the high accuracy of prenatal MR imaging in depicting the ventricular and subarachnoid space condition due to the high contrast between the signal of the CSF and that of solid adjacent structures. Our results confirm that prenatal MR imaging plays an important role as an adjunctive tool to US in the evaluation of ventricular and subarachnoid spaces because it can rule out pathologic findings at US, confirm the findings, or add associated abnormalities not amenable to US diagnosis.<sup>27</sup>

### **Vascular Malformations**

Our results about the accuracy of the prenatal MR imaging in detecting vascular malformations are limited by the small incidence of this pathologic finding in general and in our cohort. The only false-negative finding refers to a persistent falcine sinus, not an uncommon incidental finding in the pediatric population.<sup>28</sup> This diagnostic error may be attributed to the low spatial resolution of the technique used. Furthermore, the falcine sinus normally closes before or shortly after birth, and the detection of this structure in the fetus does not always represent a pathologic finding, except in case of its association with other vascular anomalies such as a vein of Galen malformation or sinus thrombosis. In our case, the persistent falcine sinus was not

associated with additional vascular anomalies but with a midline malformation (fused thalami) and a cortical gyration disorder (polymicrogyria).

There are many limitations in our study. First, we included only fetuses with postnatal MR imaging, usually those with findings suspicious for malformations at prenatal MR imaging, thus resulting in an inflation of the true-positive rate and an underestimation of the true-negative rate. We decided to exclude the cases having undergone pathology for 2 main reasons: 1) The number of cases with pathologic assessment was very limited, and 2) pathology results are often difficult match with fetal MR imaging ones. In this regard, fetal brain pathology may have some paradoxical limitations with respect to fetal MR imaging, especially regarding younger fetal age as in our case. Sometimes, for example, an “agenesis of corpus callosum” is unexpectedly called by postmortem examination, while the corpus callosum had simply collapsed due to postmortem changes and intrapartum brain deformation.

Another limitation is that we relied for the diagnosis on the judgment of pediatric neuroradiologists with long experience in the field, whose learning curve was probably close to a plateau. However, as in other fields of diagnostic imaging, younger professionals should gain their skill working side by side with more experienced professionals before reaching a sufficient plateau of knowledge. Thus, we think that repeating our diagnostic accuracy test with less experienced observers would not match the practice in the main international prenatal MR imaging centers, which generally rely on experienced professionals to whom most cases should be referred, thus avoiding sporadic fetal MR imaging practice in smaller institutions. Furthermore, the readers were from the same institution, and local trends in assessing unclear findings (such as vermian abnormalities) may have influenced the results. We cannot rule out some variability in results if other institutions replicated our work. Finally, currently there are no internationally accepted criteria for referring fetal cases to MR imaging, such as in the case of twin-to-twin transfusion, and they may vary from center to center, so our data base population and our results would not necessarily overlap those of other clinics.

## CONCLUSIONS

The diagnostic value of prenatal MR imaging for brain malformations within 25 weeks of GA is very high, despite important limitations of sensitivity in the early detection of disorders of cortical development, such as polymicrogyrias and periventricular nodular heterotopias.

## REFERENCES

1. ACR-SPR practice guideline for the safe and optimal performance of fetal magnetic resonance imaging (MRI). American College of Radiology (ACR); 2010. 10 p. <http://www.guidelines.gov/content.aspx?id=32509>. Accessed October 1, 2010
2. Sharma G, Heier L, Kalish R, et al. **Use of fetal magnetic resonance imaging in patients electing termination of pregnancy by dilation and evacuation.** *Am J Obstet Gynecol* 2003;189:990–93 CrossRef Medline
3. de Laveaucoupet J, Audibert F, Guis F, et al. **Fetal magnetic resonance imaging (MRI) of ischemic brain injury.** *Prenat Diagn* 2001; 21:729–36 CrossRef Medline
4. Garel C, Delezoide AL, Elmaleh-Berges M, et al. **Contribution of fetal MR imaging in the evaluation of cerebral ischemic lesions.** *AJNR Am J Neuroradiol* 2004;25:1563–68 Medline
5. Tilea B, Delezoide AL, Khung-Savatovski S, et al. **Comparison between magnetic resonance imaging and fetopathology in the evaluation of fetal posterior fossa non-cystic abnormalities.** *Ultrasound Obstet Gynecol* 2007;29:651–59 CrossRef Medline
6. Blaicher W, Bernaschek G, Deutinger J, et al. **Fetal and early postnatal magnetic resonance imaging: is there a difference?** *J Perinat Med* 2004;32:53–57 Medline
7. Falip C, Blanc N, Maes E, et al. **Postnatal clinical and imaging follow-up of infants with prenatal isolated mild ventriculomegaly: a series of 101 cases.** *Pediatr Radiol* 2007;37:981–89 CrossRef Medline
8. Limperopoulos C, Robertson RL Jr, Khwaja OS, et al. **How accurately does current fetal imaging identify posterior fossa anomalies?** *AJR Am J Roentgenol* 2008;190:1637–43 CrossRef Medline
9. Senapati G, Levine D, Smith C, et al. **Frequency and cause of disagreements in imaging diagnosis in children with ventriculomegaly diagnosed prenatally.** *Ultrasound Obstet Gynecol* 2010;36: 582–95 CrossRef Medline
10. Dhoubib A, Blondiaux E, Moutard ML, et al. **Correlation between pre- and postnatal cerebral magnetic resonance imaging.** *Ultrasound Obstet Gynecol* 2011;38:170–78 CrossRef Medline
11. Glenn OA, Cuneo AA, Barkovich AJ, et al. **Malformations of cortical development: diagnostic accuracy of fetal MR imaging.** *Radiology* 2012;263:843–55 CrossRef Medline
12. Brisse H, Sebag G, Fallet C, et al. **Prenatal MRI of corpus callosum agenesis: study of 20 cases with neuropathological correlations [in French].** *J Radiol* 1998;79:659–66 Medline
13. Tang PH, Bartha AI, Norton ME, et al. **Agenesis of the corpus callosum: an MR imaging analysis of associated abnormalities in the fetus.** *AJNR Am J Neuroradiol* 2009;30:257–63 CrossRef Medline
14. Azoulay R, Fallet-Bianco C, Garel C, et al. **MRI of the olfactory bulbs and sulci in human fetuses.** *Pediatr Radiol* 2006;36:97–107 CrossRef Medline
15. Schmook MT, Brugger PC, Weber M, et al. **Forebrain development in fetal MRI: evaluation of anatomical landmarks before gestational week 27.** *Neuroradiology* 2010;52:495–504 CrossRef Medline
16. Righini A, Zirpoli S, Mrakic F, et al. **Early prenatal MR imaging diagnosis of polymicrogyria.** *AJNR Am J Neuroradiol* 2004;25: 343–46 Medline
17. Righini A, Parazzini C, Doneda C, et al. **Early formative stage of human focal cortical gyration anomalies: fetal MRI.** *AJR Am J Roentgenol* 2012;198:439–47 CrossRef Medline
18. Fluss J, Blaser S, Chitayat D, et al. **Molar tooth sign in fetal brain magnetic resonance imaging leading to the prenatal diagnosis of Joubert syndrome and related disorders.** *J Child Neurol.* 2006;21: 320–24 CrossRef Medline
19. Shen O, Ben-Sira L, Rosenak D, et al. **Early second-trimester molar tooth sign.** *Fetal Diagn Ther* 2014;36:259–62 CrossRef Medline
20. Iskender CT, Tarım E, Alkan O. **Joubert syndrome and related disorders, prenatal diagnosis with ultrasound and magnetic resonance imaging.** *J Turk Ger Gynecol Assoc* 2012;13:135–38 CrossRef Medline
21. Saleem SN, Zaki MS. **Role of MR imaging in prenatal diagnosis of pregnancies at risk for Joubert syndrome and related cerebellar disorders.** *AJNR Am J Neuroradiol* 2010;31:424–29 CrossRef Medline
22. Quarello E, Molho M, Garel C, et al. **Prenatal abnormal features of the fourth ventricle in Joubert syndrome and related disorders.** *Ultrasound Obstet Gynecol* 2014;43:227–32 CrossRef Medline
23. Parazzini C, Righini A, Rustico M, et al. **Prenatal magnetic resonance imaging: brain normal linear biometric values below 24 gestational weeks.** *Neuroradiology* 2008;50:877–83 CrossRef Medline
24. Righini A, Parazzini C, Doneda C, et al. **Fetal MRI features related to**

- the Chiari malformations.** *Neurol Sci* 2011;32(suppl 3):S279–81 CrossRef Medline
25. Robinson AJ. **Inferior vermian hypoplasia: preconception, misconception.** *Ultrasound Obstet Gynecol* 2014;43:123–36 CrossRef Medline
26. Gandolfi Colleoni G, Contro E, Carletti A, et al. **Prenatal diagnosis and outcome of fetal posterior fossa fluid collections.** *Ultrasound Obstet Gynecol* 2012;39:625–31 CrossRef Medline
27. Saleem SN. **Fetal MRI: an approach to practice—a review.** *J Adv Res* 2014;5:507–23 CrossRef Medline
28. Smith A, Choudhary AK. **Prevalence of persistent falcine sinus as an incidental finding in the pediatric population.** *AJR Am J Roentgenol* 2014;203:424–25 CrossRef Medline
29. Garel C. *MRI of the Fetal Brain: Normal Development and Cerebral Pathologies.* Berlin: Springer-Verlag; 2004

# Normal Development and Measurements of the Occipital Condyle-C1 Interval in Children and Young Adults

P. Smith, L.L. Linscott, S. Vadivelu, B. Zhang, and J.L. Leach

## ABSTRACT

**BACKGROUND AND PURPOSE:** Widening of the occipital condyle-C1 interval is the most specific and sensitive means of detecting atlanto-occipital dislocation. Recent studies attempting to define normal measurements of the condyle-C1 interval in children have varied substantially. This study was performed to test the null hypothesis that condyle-C1 interval morphology and joint measurements do not change as a function of age.

**MATERIALS AND METHODS:** Imaging review of subjects undergoing CT of the upper cervical spine for reasons unrelated to trauma or developmental abnormality was performed. Four equidistant measurements were obtained for each bilateral condyle-C1 interval on sagittal and coronal images. The cohort was divided into 7 age groups to calculate the mean, SD, and 95% CIs for the average condyle-C1 interval in both planes. The prevalence of a medial occipital condyle notch was calculated.

**RESULTS:** Two hundred forty-eight joints were measured in 124 subjects with an age range of 2 days to 22 years. The condyle-C1 interval varies substantially by age. Average coronal measurements are larger and more variable than sagittal measurements. The medial occipital condyle notch is most prevalent from 1 to 12 years and is uncommon in older adolescents and young adults.

**CONCLUSIONS:** The condyle-C1 interval increases during the first several years of life, is largest in the 2- to 4-year age range, and then decreases through late childhood and adolescence. A single threshold value to detect atlanto-occipital dissociation may not be sensitive and specific for all age groups. Application of this normative data to documented cases of atlanto-occipital injury is needed to determine clinical utility.

**ABBREVIATION:** CCI = occipital condyle-C1 interval

Widening or asymmetry of the occipital condyle-C1 interval (CCI) on CT has been shown to be the most specific and sensitive means of detecting atlanto-occipital dislocation in the pediatric population.<sup>1</sup> A prior study of the normal CCI measurements in children suggested that CCI joint measurements do not differ substantially from birth to early adulthood.<sup>2</sup> However, more recent studies evaluating the CCI by using different measurement techniques<sup>3,4</sup> and our own experience at a large tertiary care children's hospital suggest otherwise. The purpose of this

study was to assess normative CCI measurements in the largest nontraumatic cohort to date and test the null hypothesis that CCI morphology and joint space measurements do not change with age.

## MATERIALS AND METHODS

### Subject Identification

This retrospective study was approved by our institutional review board and was performed at a tertiary care children's hospital. A retrospective review was performed of subjects undergoing imaging of the cervical spine for reasons unrelated to trauma or developmental abnormality of the spine. Using a radiology data base search engine (Softtek Illuminate; <https://www.softekinc.com/illuminate/>), we searched for imaging modalities that included postprocessed true sagittal and coronal reconstructions of the craniocervical junction, including sinus, temporal bone, and head CT.

Criteria for inclusion in the study were age younger than 23 years and subjects who had undergone CT that included the occipital condyle-C1 joint in its entirety. Clinical exclusion criteria included a history of recent head/neck trauma, genetic/syndromic

Received June 3, 2015; accepted after revision August 3.

From the Departments of Radiology (P.S., L.L.L., J.L.L.), Neurosurgery (S.V.), and Epidemiology and Biostatistics (B.Z.), Cincinnati Children's Hospital Medical Center, University of Cincinnati Medical School, Cincinnati, Ohio.

Paper previously presented as an oral presentation at: American Society of Neuroradiology Annual Meeting and the Foundation of the ASNR Symposium, April 25–30, 2015; Chicago, Illinois.

Please address correspondence to Luke Linscott, MD, Cincinnati Children's Hospital Medical Center, 3333 Burnet Ave, ML 5031, Cincinnati, OH 45229; e-mail: [luke.linscott@cchmc.org](mailto:luke.linscott@cchmc.org); @LukeLinscott

<http://dx.doi.org/10.3174/ajnr.A4543>

diagnosis, or connective tissue disorder. Exclusion criteria based on imaging included the following: developmental abnormalities of the craniocervical junction or cervical spine, craniosynostosis, or other evidence of genetic/syndromic abnormalities. Patient demographics and clinical indications for the examination were tabulated.

### Imaging

All CT examinations were performed on either an Aquilion 64 or Aquilion ONE CT scanner (Toshiba Medical Systems, Tokyo, Japan) with detector widths of 0.375 mm. The kilovolt(peak) was between 80 and 120 mA and was age-dependent. All sinus, head, and temporal bone CT examinations were performed by using a helical acquisition. 3D head examinations were performed by using a volume acquisition on the Aquilion ONE or a helical acquisition on the Aquilion 64. Sagittal and coronal reconstructions were performed by the CT technologist at section thicknesses of  $\leq 2$  mm.

### Image Analysis

Each imaging examination was reviewed by 1 of 2 examiners. The first investigator (L.L.L.) had 7 years of experience reviewing CT and is an attending pediatric neuroradiologist. The second investigator (P.S.) was a postgraduate year 1 resident who received detailed instructions and initial supervision in the appropriate measurements. Each investigator examined approximately two-thirds of all the subjects, with 45 subjects (36%) being examined by both examiners to calculate interobserver variance. For those 45 subjects evaluated by both investigators, the measurements were averaged in the final analysis. The investigators were included in the multiple regression analysis to detect any independent association of the investigator with average CCI measurements.

The investigators tabulated the following measurements and imaging features: clivus-dens angle; coronal, axial, and sagittal plane reconstruction angle; CCI in the sagittal and coronal planes; and the presence of a medial occipital condyle notch in the midjoint on sagittal images.

The clivus-dens angle was calculated as the angle between lines drawn along the dorsal cortex of the clivus and the posterior cortex of the dens. This angle was calculated to test whether the degree of flexion or extension of the joint was associated with differences in joint space measurements. The coronal reconstruction plane angulation was calculated to evaluate whether differences in reconstruction angulation between varying types of examinations were associated with differences in CCI measurements. The coronal reconstruction plane angulation was calculated from sagittal images as the angle between the coronal reconstruction plane and a line drawn along the posterior aspect of the dens. To reduce measurement variation secondary to rotation and tilt of the head in relation to the upper cervical spine, axial and sagittal plane angulations were calculated. The axial plane angulation was calculated as the angle between the skull base (drawn along the midline skull base) and a line drawn between the midline anterior and posterior arches of C1. Examinations with axial angulation  $>10^\circ$  were excluded. The sagittal reconstruction plane angulation was calculated from the coronal images as the angle between a vertical

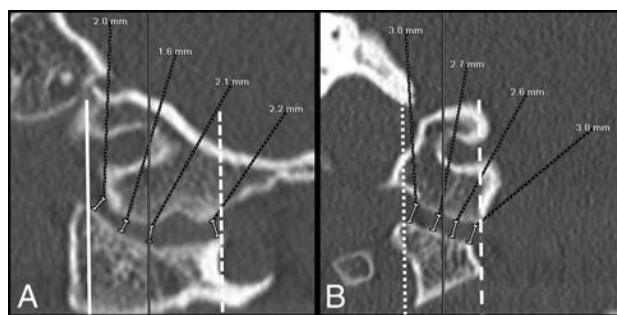


**FIG 1.** Method used to make sagittal (A) and coronal (B) CCI measurements in an 8-year-old boy. Note the use of localizer lines (solid black lines midjoint) to avoid the notch when selecting the appropriate coronal image from which to obtain measurements. On sagittal images (A), the anteriormost measurement is taken beginning at the anterior margin of the C1 joint (solid white line) and the posteriormost measurement is taken beginning at the posterior margin of the C1 joint (dashed line). On coronal images, the medialmost measurement is taken beginning at the margin of the foramen magnum (dashed white line) and the lateralmost measurement is taken where the superior aspect of the C1 lateral mass goes from a rounded contour to a flat articular plane (dotted line).

plumb line and a line drawn through the center of the C2 body and the dens. Examinations with sagittal reconstruction plane angulation of  $>5^\circ$  were excluded.

To calculate the average CCI, the investigators used the method of Pang et al,<sup>2</sup> except that localizer lines were used in the sagittal plane rather than the axial plane to select coronal images to allow confident exclusion of the medial occipital condyle notch in younger children. Four equidistant measurements were made for each bilateral CCI in both the sagittal and coronal planes perpendicular to the articular surfaces (Fig 1). In the coronal plane, measurements from a section localized to the midjoint on sagittal images were obtained, taking special care to avoid the medial occipital condyle notch, if present. The medialmost measurement was taken beginning at the margin of the foramen magnum, and the lateralmost measurement was taken where the superior aspect of the C1 lateral mass goes from a rounded contour to a flat articular plane. In the sagittal plane, measurements were obtained from a section localized to the midjoint on coronal images. When measuring the CCI on sagittal images with the medial occipital condyle notch present, the examiners took special care to avoid measurements within the medial occipital notch. The anteriormost measurement was taken beginning at the anterior margin of the C1 joint, and the posteriormost measurement was taken beginning at the posterior margin of the C1 joint. These 4 measurements for each joint space were then averaged, giving 2 average coronal and 2 average sagittal CCI values for each patient.

### Statistical Analysis

The cohort was divided into 7 age groups to calculate the mean, SD, and 95% confidence intervals for average coronal and sagittal CCIs. Multivariate logistic regression models were used to evaluate the independent effects of subject age, sex, investigator (L.L.L. and P.S.), coronal reconstruction angle, and the clivus-dens angle on average CCIs. Model selection under a stepwise criterion was performed to avoid multicollinearity. The mean absolute difference between left and right coronal and sagittal average CCI was

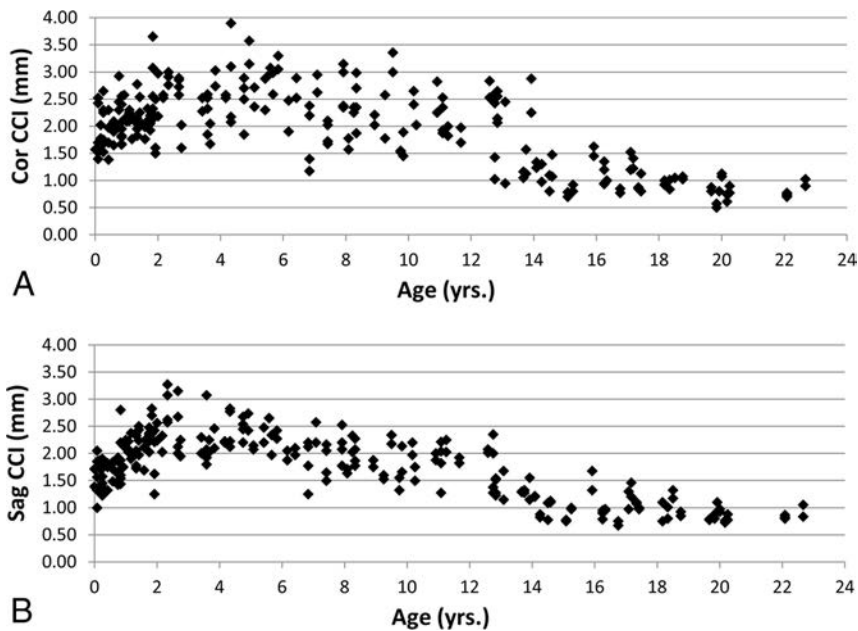


**FIG 2.** Scatterplots representing each of the 248 joint spaces in the coronal (A) and sagittal (B) planes.

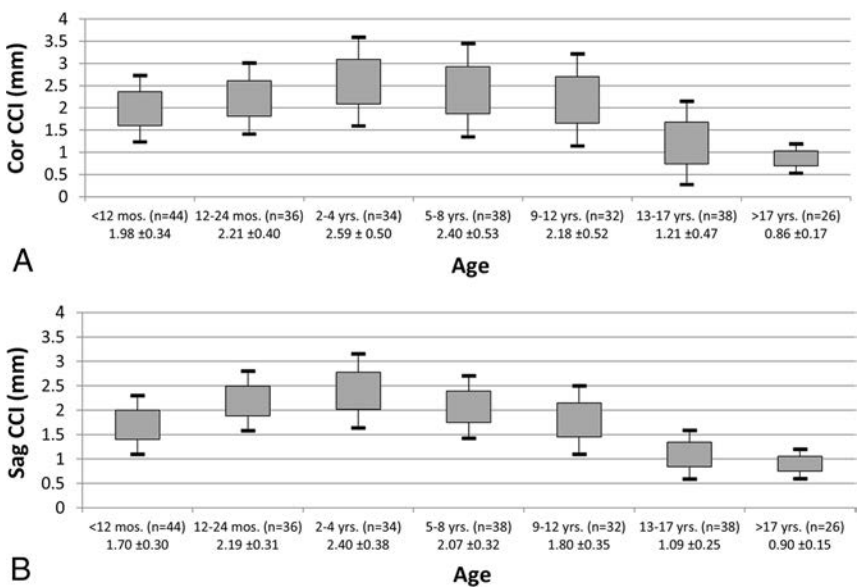


**FIG 3.** Average CCI by age group in the coronal (A) and sagittal (B) planes. The gray box represents  $\pm 1$  SD, and the bars represent  $\pm 2$  SDs from the mean.

calculated. The variance in measurements at different locations within the joint was calculated for the entire population to determine whether some locations within the joint are more reliable measures from one subject to the next. Stepwise comparison between the variance of the most lateral CCI measurement and the 3 more medial CCI measurements (coronal plane) and the most anterior CCI measurement and the 3 more posterior measurements (sagittal plane) was performed. Quantitative morphologic changes with time in the coronal plane were investigated by measuring the mean difference between the lateralmost and medialmost coronal occipital condyle-CI joint space measurements for each age group. The mean absolute variance in joint space measurement by the investigator was calculated by using

2.41–2.76 mm) in the coronal plane. Beyond the 2- to 4-year age group, CCI decreased throughout development. In the 17-years of age and older group, CCI was 0.90 mm (95% CI, 0.84–0.96 mm) in the sagittal plane and 0.86 mm (95% CI, 0.80–0.93 mm) in the coronal plane. This age-dependent change in CCI was statistically significant with a quadratic relationship ( $P < .001$ ) (Figs 2 and 3). The mean clival-dens angle was  $30^\circ$  ( $1^\circ$  to  $58^\circ$ ). The mean coronal reconstruction plane angle was  $5.6^\circ$  ( $-17^\circ$  to  $54^\circ$ ). Multivariate logistic regression analysis revealed no significant relationship between mean sagittal/coronal CCI and subject sex, investigator, clival-dens angle, or coronal reconstruction angle.

The mean absolute variance in measurement between the investigators for the 45 subjects measured by both investigators was

measurements for the 45 subjects examined by both investigators. A subset analysis of investigator variance for those subjects 14 years and older and a second group younger than 14 years was also performed. A  $\chi^2$  or Fisher exact test was used to assess the relationship between subject age and the presence of the medial occipital condyle notch.  $P < .05$  was considered significant. All analyses were performed by using SAS statistical software, Version 9.3 (SAS Institute, Cary, North Carolina).

## RESULTS

One hundred twenty-four subjects (248 joint spaces) were identified as appropriate according to inclusion and exclusion criteria. The mean age of the cohort was 7.8 years (range, 2 months to 22 years). The cohort included 62 females and 62 males. CT examination types were as follows: routine sinus ( $n = 90$ ), routine head ( $n = 21$ ), 3D head ( $n = 6$ ), and temporal bone ( $n = 7$ ). Clinical indications for the examinations were sinusitis ( $n = 53$ ), abnormal head shape ( $n = 13$ ), fever ( $n = 10$ ), mass/tumor ( $n = 9$ ), cough ( $n = 8$ ), seizure ( $n = 8$ ), headache ( $n = 3$ ), leukemia ( $n = 3$ ), hearing loss ( $n = 2$ ), and other ( $n = 15$ ).

Scatterplots reveal the distribution of all data by age for the 248 joints in the sagittal and coronal planes (Fig 2). Results were aggregated into 7 age groups, with a range of 26–44 joint spaces in each age group. With a multivariate logistic regression, subject age was found to be statistically associated with average coronal and sagittal CCIs (Fig 3). The mean sagittal and coronal CCIs increased during the first 2 years of life and were largest in the 2- to 4-year age group at 2.4 mm (95% CI, 2.26–2.53 mm) in the sagittal plane and 2.59 mm (95% CI,

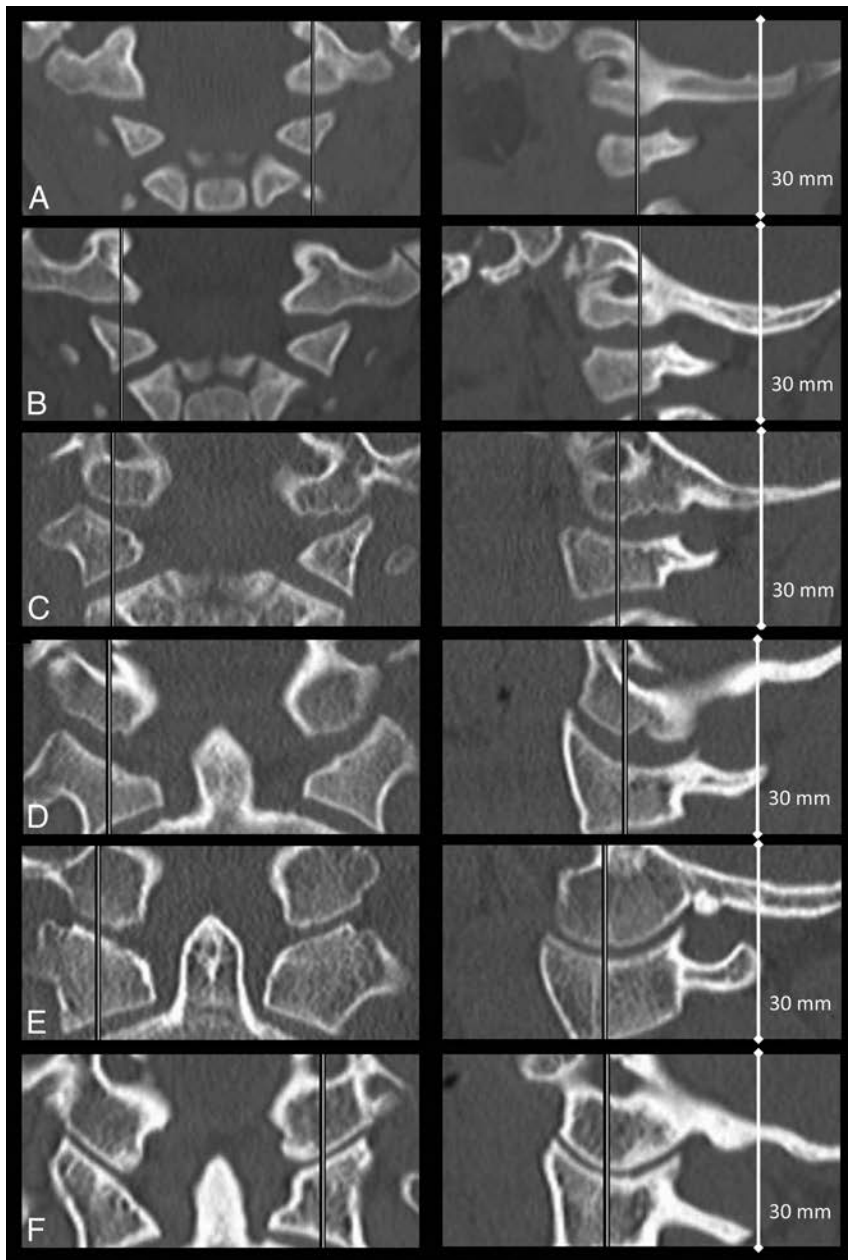


**FIG 4.** Coronal (*left*) and sagittal (*right*) images of the CCI in subjects of the following ages: 3 months (A), 1.5 years (B), 4 years (C), 9 years (D), 17 years (E), and 22 years (F).

$0.19 \pm 0.17$  mm in the sagittal plane and  $0.27 \pm 0.28$  mm in the coronal plane. Subset analysis of measurement variance in younger (13 years or younger) versus older (14 years and older) subjects revealed an SD of 0.18 versus 0.09 mm ( $P = .001$ ) in the sagittal plane and 0.30 versus 0.09 mm ( $P < .001$ ) in the coronal plane, respectively.

Across all subjects, the mean absolute difference (ie, asymmetry) between the right and left CCI in the sagittal plane was 0.218 mm (95% CI, 0.186–0.249 mm) and the mean difference between the right and left CCI in the coronal plane was 0.252 mm (95% CI, 0.208–0.296 mm).

Analysis of measurement variance based on measurement location within the joint space in the sagittal plane showed a trend toward greater variability in the posterior measurement (0.56

mm) compared with the anterior measurement (0.39 mm), but the trend was not statistically significant ( $P = .06$ ). The same analysis in the coronal plane showed significantly greater variability of the medial measurements (1.53 mm) compared with the lateral measurements (0.32 mm) in the coronal plane ( $P = .001$ ).

To evaluate the morphologic changes that occur in the coronal plane, the examiners calculated the difference between lateralmost and medialmost measurements by age group and revealed the following: <12 months (1.39 mm,  $P < .001$ ), 12–24 months (1.84 mm,  $P < .001$ ), 2–4 years (2.07 mm,  $P < .001$ ), 5–8 years (1.56 mm,  $P < .001$ ), 9–12 years (1.21 mm,  $P < .001$ ), 13–17 years (0.42 mm,  $P < .001$ ), and older than 17 years (0.115 mm;  $P = .078$ ). Examples from this study of the age-related changes in the morphology of the occipital condyle and occipital condyle-C1 articulation throughout childhood and young adulthood are given in Fig 4.

The medial occipital condyle notch (Fig 5) was first detected in a subject at 12 months of age and was very uncommon after 13 years of age. The prevalence of the notch peaked in the 2- to 4-year (85.3%) and 5- to 8-year age groups (84%) and became less frequent throughout life (Fig 6). The prevalence of the notch was age-dependent ( $P < .001$ ).

## DISCUSSION

In our clinical practice, we have been frequently asked by our neurosurgical colleagues to evaluate the CCI in patients with trauma and have often identified joint spaces in young subjects that were much larger than those in older patients, contradicting prior studies.<sup>2</sup> In addition, we noted that the occipital condyle and CCI interval undergo significant morphologic changes throughout development (Fig 4), making it challenging to apply previously published normative data. All prior investigations into the normative values and age-related changes in the CCI in the pediatric population<sup>2–4</sup> have some limitations (Table), decreasing widespread applicability in children.

Prior studies of the CCI interval have primarily assessed patients with trauma,<sup>2–4</sup> leaving whether these are truly representative of a normative population up to debate. Bertozzi et al<sup>3</sup> and Vachhrajani et al<sup>4</sup> both focused on myriad craniocervical junction anatomic measurements, with less focus on the CCI. Both of these

studies included measurements of the joint in only a single plane (Bertozzi et al, sagittal; Vachhrajani et al, coronal), and in the case of Vachhrajani et al, only a single measurement in the center of the joint was used. Pang et al<sup>2</sup> had the most rigorous investigation of the CCI, with 4 measurements in each plane. The average CCI varied substantially among these 3 studies, with nearly a 2-fold

difference between the results of Pang et al (1.28 mm) and Vachhrajani et al (2.4 mm).

We were unable to reproduce the findings of Pang et al,<sup>2</sup> who demonstrated no significant age-related changes in the CCI. According to our findings, the CCI morphology and average measurements change substantially with development, with an increase in the first several years of life before a steady decline in the later childhood and early teenage years. The etiology of this initial increase is not completely understood but corresponds to increased prevalence of the medial occipital notch. Despite meticulous effort in our study to exclude the notch, its presence may contribute to this initial increase, particularly in the coronal plane. We hypothesize that the notch has a fanlike shape, with the more medial part of the notch having a greater anteroposterior dimension than the lateral aspect of the notch. This would explain the large difference between medialmost and lateralmost CCI joint space measurements in the coronal plane. The progressive decrease in average CCI joint space from the 2- to 4-year period until the later teenage years is a common trajectory for most joints of the human body.<sup>5-8</sup> As with most synovial joint spaces in the body, the occipital condyle and C1 lateral mass components of the CCI undergo progressive ossification of cartilage, leading to a decrease in the “osseus” joint space detected on CT.

While the scatterplots and age group data give an overall sense

of the change in average CCI with time, examination of specific parts of the joint (ie, medial versus lateral) is also very informative. Figure 4 shows the striking change in morphology of the CCI that occurs during the early months and years of human development. Anecdotally, one of the most apparent features of the CCI that changes with time is the difference between medial and lateral joint space in the coronal plane. Our measurement data bear this out, with the average medialmost coronal measurement being significantly greater and more variable than the lateralmost measurement in younger age groups. In contrast to the younger subjects, within the oldest age group, the variance and measurement difference between the medialmost and lateralmost joint spaces are

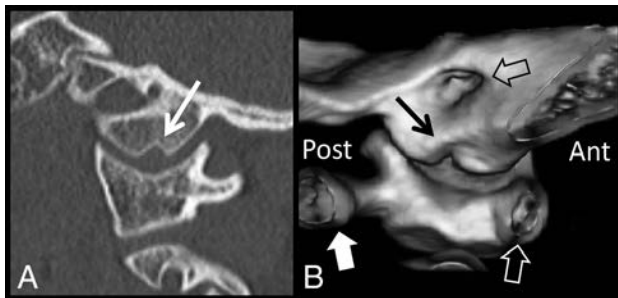


**FIG 5.** Sagittal CT (A) demonstrates the medial occipital condyle notch (white arrow) in an 8-year-old boy. A 3D surface-rendered reconstruction image (B) with a medial-to-lateral perspective demonstrates the 3D contour of the occipital condyle notch (black arrow). For orientation, the anterior arch of C1 (white hollow arrow) is to the right and the posterior arch of C1 (white block arrow) is to the left. The internal auditory canal is shown by a hollow black arrow. Note how the notch is wider at its medial aspect compared with the lateral aspect. Ant indicates anterior; post, posterior.

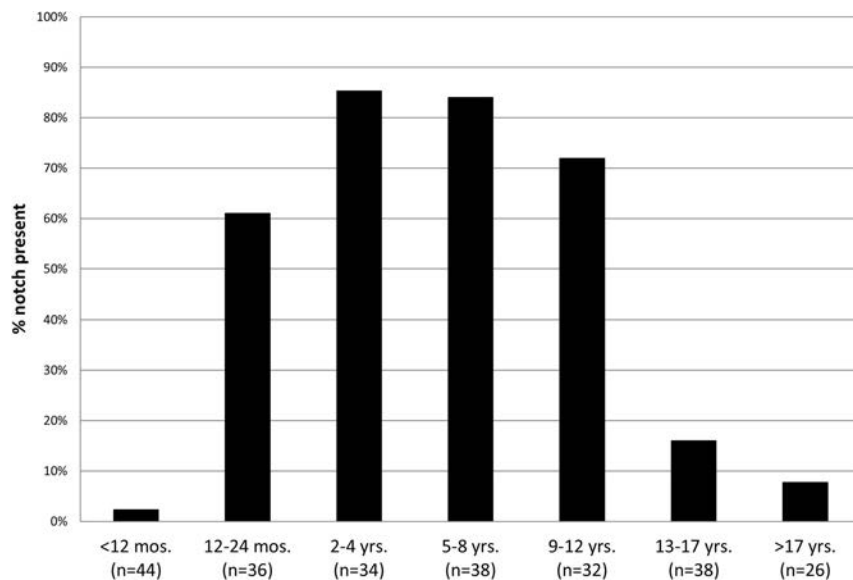


**FIG 6.** Prevalence of the medial occipital condyle notch by age group.

#### Comparison of investigations of the normal CCI to date, including this study

Investigator	Cohort Size	Mean CCI (mm)	Mean Age (Range)	Age-Dependent?	Sag/Cor Measure	Subjects with Trauma
Pang et al <sup>1</sup> (2007)	89	1.28	56 Months (6 months to 17.1 years)	No	Sag/Cor (avg. 4 measures)	80%
Bertozzi et al <sup>3</sup> (2009)	117	1.6	56 Months (2 months to 10 years)	Not examined	Sag (avg. 5 measures)	100%
Vachhrajani et al <sup>4</sup> (2014)	42	2.38	100 Months (1 month to 17.8 years)	Yes	Cor (1 measure)	86%
Current study (2015)	124	0.90–2.4	94 Months (2 months to 22 years)	Yes	Sag/Cor (avg. 4 measures)	0%

**Note:**—Sag indicates sagittal; cor, coronal; avg., average.

small. With this understanding in mind, it is not surprising that Vachhrajani et al<sup>4</sup> found this large mean CCI measurement with high variability, considering that they only made a single measurement in the coronal plane.

Prior work by Pang et al<sup>2</sup> examining the clinical utility of the CCI measurement found it to be a specific and sensitive means for detecting atlanto-occipital dislocation, with a cutoff value of 4 mm. In their investigation, Pang et al assumed no change in the CCI measurements with age, which does not agree with the findings of our study. Most interesting, a more recent investigation by Gire et al<sup>9</sup> advocated an even more aggressive abnormal CCI cutoff value of 2.5 mm to detect AOD in all age groups, but this study did not include any control subjects less than 18 years of age to define the false-positive rate in children. Our study would suggest a very high false-positive rate in the age range of 1–12 years by using a cutoff value of 2.5 mm, given that this value is within 1 or 2 SDs of the mean for these age groups. Our data would support using the more conservative abnormal cutoff of 4 mm (Pang et al) for infants and children younger than 13 years, to avoid false-positives, while in older teens and young adults, the more aggressive abnormal cutoff of 2.5 mm proposed by Gire et al may be valid.

This study underscores the need for surgeons and imaging professionals to understand the normal dynamic changes that the occipital condyle-C1 joint space undergoes in the early years of life. Using medial occipital condyle-C1 joint space measurements in the coronal plane in young children will inevitably result in false-positives if the aforementioned cutoff values of 2.5 and 4 mm are applied. We recommend using multiple measurements obtained in the sagittal plane at the midjoint, with special care to exclude the medial occipital condyle notch to avoid such false-positives.

Additionally, an understanding of medial occipital condyle notch prevalence can help the imaging professional avoid falsely identifying asymmetry between the joint spaces on coronal images. In young subjects in whom the prevalence of a notch is high, on any given coronal image, one side may be located within the notch while the other is not. In this scenario, an apparent asymmetry between the joint spaces will inevitably be present. When assessing for asymmetry, one should pay careful attention to the location of the medial occipital condyle notch for each joint space to prevent a false-positive result.

We hope that these normative data will be applied to patient populations with documented atlanto-occipital injury to assess

the clinical utility and establish more age-appropriate abnormal cutoff values.

## CONCLUSIONS

The null hypothesis is rejected. The average CCI increases during the first several years of life, is largest in the 2–4 year range, and then decreases through late childhood and adolescence. Average coronal measurements are larger and more variable than sagittal measurements, especially in younger patients, an age when the prevalence of the medial occipital notch is highest. These dynamic changes suggest that a single threshold value to detect atlanto-occipital dissociation may not be sensitive and specific for all age groups. Application of these normative data to documented cases of atlanto-occipital injury is needed to determine clinical utility.

## REFERENCES

1. Pang D, Nemzek WR, Zovickian J. **Atlanto-occipital dislocation, part 2: the clinical use of (occipital) condyle-C1 interval, comparison with other diagnostic methods, and the manifestation, management, and outcome of atlanto-occipital dislocation in children.** *Neurosurgery* 2007;61:995–1015; discussion 1015 CrossRef Medline
2. Pang D, Nemzek WR, Zovickian J. **Atlanto-occipital dislocation: part 1—normal occipital condyle-C1 interval in 89 children.** *Neurosurgery* 2007;61:514–21; discussion 521 CrossRef Medline
3. Bertozzi JC, Rojas CA, Martinez CR. **Evaluation of the pediatric craniocervical junction on MDCT.** *AJR Am J Roentgenol* 2009;192:26–31 CrossRef Medline
4. Vachhrajani S, Sen AN, Satyan K, et al. **Estimation of normal computed tomography measurements for the upper cervical spine in the pediatric age group.** *J Neurosurg Pediatr* 2014;14:425–33 CrossRef Medline
5. Greulich WW, Pyle SI. *Radiographic Atlas of Skeletal Development of the Hand and Wrist.* Stanford: Stanford University Press; 1959
6. Santiago RC, de Miranda Costa LF, Vitral RW, et al. **Cervical vertebral maturation as a biologic indicator of skeletal maturity.** *Angle Orthod* 2012;82:1123–31 CrossRef Medline
7. Wientroub S, Tardiman R, Green I, et al. **The development of the normal infantile hip as expressed by radiological measurements.** *Int Orthop* 1981;4:239–41 Medline
8. Kaawach W, Ecklund K, Di Canzio J, et al. **Normal ranges of scapholunate distance in children 6 to 14 years old.** *J Pediatr Orthop* 2001;21:464–67 CrossRef Medline
9. Gire JD, Roberto RF, Bobinski M, et al. **The utility and accuracy of computed tomography in the diagnosis of occipitocervical dissociation.** *Spine J* 2013;13:510–19 CrossRef Medline

# Application of Normative Occipital Condyle-C1 Interval Measurements to Detect Atlanto-Occipital Injury in Children

B. Corcoran, L.L. Linscott, J.L. Leach, and S. Vadivelu



## ABSTRACT

**BACKGROUND AND PURPOSE:** Prior studies have found that widening or asymmetry of the occipital condyle-C1 interval on CT is a sensitive and specific marker for atlanto-occipital dislocation. Previously reported abnormal occipital condyle-C1 interval values are not age-specific, possibly leading to false-positive findings in younger children, in whom this joint space is normally larger than that in adults. This study assesses the utility of applying age-specific normative occipital condyle-C1 interval ranges to documented cases of atlanto-occipital injury compared with previously reported abnormal cutoff values.

**MATERIALS AND METHODS:** Retrospective review of CT and MR imaging of 14 subjects with atlanto-occipital injury was performed, and occipital condyle-C1 interval measurements were made for each subject. Sensitivities and specificities of proposed occipital condyle-C1 interval cutoffs of 2 and 3 SDs above the mean and previously published occipital condyle-C1 interval cutoffs for atlanto-occipital injury were then calculated on the basis of occipital condyle-C1 interval measurements for each subject.

**RESULTS:** An occipital condyle-C1 interval 2 SDs above the age-specific mean has a sensitivity of 50% and specificity of 89%–100%, depending on the age group. An occipital condyle-C1 interval 3 SDs above the age-specific mean has a sensitivity of 50% and a specificity of 95%–100%. A 4.0-mm occipital condyle-C1 interval has a sensitivity of 36% and a specificity of 100% in all age groups. A 2.5-mm occipital condyle-C1 interval has a sensitivity of 93% and a specificity of 18%–100%.

**CONCLUSIONS:** Occipital condyle-C1 interval widening cutoffs used to establish atlanto-occipital injury lack both sensitivity and specificity in children and young teenagers. MR imaging is necessary to establish a diagnosis of atlanto-occipital injury in children and young teenagers when the appropriate mechanism of injury is present.

**ABBREVIATIONS:** AOD = atlanto-occipital dislocation; CCI = occipital condyle-C1 interval

This is the second part of a 2-part study assessing the occipital condyle-C1 interval (CCI) in the pediatric population. Part 1 of the study established the normative values of the CCI for 7 pediatric age groups based on 124 patients who were imaged for indications other than trauma or developmental anomaly.<sup>1</sup> Part 2 of this study aimed to determine the utility of applying age-specific abnormal CCI cutoff values to detect atlanto-occipital injury.

Prior studies have found that the CCI is a sensitive and specific marker for atlanto-occipital dislocation (AOD).<sup>2,3</sup> Pang et al<sup>2</sup> found a CCI cutoff of 4 mm to be 100% sensitive and specific for

AOD in the pediatric population. Gire et al<sup>3</sup> found a CCI cutoff of 2.5 mm for both the adult and pediatric populations to have a sensitivity of 100% and a specificity of 84% for AOD. These values assume that the CCI joint-space measurement is unchanged throughout childhood and early adolescence; this assumption is contrary to the findings in Part 1 of our study. Because we have evaluated pediatric subjects with trauma suspected of having AOD with concordant MR imaging evidence of atlanto-occipital injury, it has been our experience that the CCI joint space is not consistently widened in cases of atlanto-occipital injury. The purpose of this study was to determine the sensitivity and specificity for detection of atlanto-occipital injury by using age-specific abnormal CCI cutoff values derived from Part 1 of this study as well as the prior proposed abnormal cutoff values of 4 and 2.5 mm.

## MATERIALS AND METHODS

### Subject Selection

This is a retrospective study approved by our institutional review board and performed at a large tertiary care children's hospital.

Received September 4, 2015; accepted after revision October 31.

From the Departments of Radiology (B.C., L.L.L., J.L.L.) and Neurosurgery (S.V.), Cincinnati Children's Hospital Medical Center, University of Cincinnati School of Medicine, Cincinnati, Ohio.

Please address correspondence to Luke Linscott, MD, Cincinnati Children's Hospital Medical Center, 3333 Burnet Ave, ML 5031, Cincinnati, OH 45229; e-mail: luke.linscott@cchmc.org; @LukeLinscott

Indicates article with supplemental on-line table.

<http://dx.doi.org/10.3174/ajnr.A4641>

Patients who had received the diagnosis of atlanto-occipital injury secondary to craniocervical trauma from 2004 to 2015 were identified by using a combination of radiology and clinical data bases. The radiology data base (Illuminate Softtech; <https://www.softekinc.com/illuminate/>) was searched for the following terms: “atlanto-occipital dislocation,” “atlanto-occipital dissociation,” “craniocervical dislocation,” “tectorial membrane,” and “craniocervical fusion.” All subjects in the clinical craniocervical trauma data base were also identified. Inclusion criteria were the following: 1) CT examination of the craniocervical junction at the time of injury with coronal and sagittal reconstructions, and 2) clinical or imaging evidence of atlanto-occipital injury. Clinical evidence of AOD is defined as an appropriate mechanism of injury for AOD with neurologic symptoms referable to the brain stem and the C1–C2 level. Imaging evidence of atlanto-occipital injury is defined as tectorial membrane rupture or displacement from the dorsal clivus on MR imaging or follow-up CT demonstrating ligamentous injury (ie, calcification within the tectorial membrane not present on the initial CT examination). The mechanism of injury and subject treatment (conservative therapy versus surgical craniocervical fusion) were tabulated.

### Image Analysis

After subjects were identified, each imaging examination was reviewed by 2 investigators. The first examiner (L.L.L.) was an attending pediatric neuroradiologist with 8 years of experience interpreting MR imaging and CT in the context of craniocervical trauma. The second examiner (B.C.) was a fourth-year medical student who received instruction by the first examiner on how to appropriately make CCI measurements on a subset of cases. The same technique as in part 1 of the study was used to determine the average CCI for each joint space.<sup>1</sup> This technique is similar to that used by Pang et al,<sup>2</sup> except that sagittal localizer images were used to confidently exclude the medial occipital condyle notch, when present.<sup>1</sup> The average CCI measurements made by the 2 examiners were averaged. In Part 1 of our study, the average sagittal CCI was found to have smaller SDs and interobserver variability. Thus, we chose the average sagittal CCI in the midjoint as our standard.

For a subject examination to be considered positive, the following definitions applied: For 2 and 3 SDs above the age-specific means from Part 1 of the study, any 1 of the 2 (right or left) average sagittal CCI measurements must be  $\geq 2$  or 3 SD cutoffs. The age-specific sagittal plane cutoff values 2 and 3 SDs above the mean derived from Part 1 of this study are as follows: younger than 12 months (2.30, 2.60 mm), 12–24 months (2.81, 3.12 mm), 2–4 years (3.16, 3.54 mm), 5–8 years (2.71, 3.03 mm), 9–12 years (2.50, 2.75 mm), 13–17 years (1.59, 1.84 mm), and older than 17 years (1.20, 1.35 mm). For the standard of Pang et al,<sup>2</sup> the average CCI (defined as the average of unilateral coronal and sagittal average CCI measurements) must be  $\geq 4$  mm<sup>2</sup>. For the standard of Gire et al,<sup>3</sup> the “revised CCI” (defined as the largest single measurement on sagittal images in the midjoint) must be  $\geq 2.5$  mm<sup>3</sup>.

Initial CT images were also evaluated for qualitative findings suggesting atlanto-occipital injury, including retroclival epidural hematoma, subarachnoid hemorrhage in the perimedullary cistern, or perivertebral hemorrhage. MR images were reviewed for findings of major ligamentous injury at the craniocervical junction,

including tectorial membrane disruption or the tectorial membrane being separated from the clivus or odontoid.

### Statistical Analysis

Sensitivities with 95% CIs were calculated for each of the 4 abnormal cutoff standards by using the subjects with atlanto-occipital injury. Due to the small sample size, age-specific sensitivities could not be calculated. Age-specific specificities with 95% CIs were calculated by applying the 4 abnormal cutoff standards to each individual subject from the subjects without trauma in Part 1 of the study (124 subjects in 7 different age groups). Sensitivities and specificities, including 95% CIs, were calculated by using the Wilson procedure without a correction for continuity at VassarStats ([www.vassarstats.net](http://www.vassarstats.net)).

### RESULTS

Fourteen subjects (10 boys and 4 girls) 1–16 years of age (mean, 6.9 years) met the inclusion criteria for the study. The On-line Table summarizes the following: subject demographics, CCI measurements for the right and left OC–C1 joint spaces, interpretation of the study (positive versus negative) based on the 4 tested abnormal cutoffs, initial CT findings, follow-up MR imaging/CT results, mechanism of injury, clinical symptoms at presentation, and treatment.

With an abnormal average unilateral CCI cutoff of 4 mm proposed by Pang et al,<sup>2</sup> 5/14 subjects would have a positive result, yielding a sensitivity of 36% (95% CI, 0.16–0.61). With the revised CCI proposed by Gire et al,<sup>3</sup> 13/14 would have a positive result, generating a sensitivity of 93% (95% CI, 0.69–0.99). With a CCI cutoff of 2 and 3 SDs above the age-specific mean sagittal CCI from Part 1 of our study, 7/14 and 7/14 examinations would have positive results, yielding a sensitivity of 50% (95% CI, 0.27–0.73) and 50% (95% CI, 0.27–0.73), respectively.

Specificities for each of the 4 cutoff values by age group calculated using healthy subjects from Part 1 of our study as controls are found in the Table.

Figures 1–3 show CT and MR images from 3 select cases (cases 10, 3, and 2) among the case series. Figure 4 shows the average sagittal and coronal CCI measurements in these same 3 cases compared with age-specific normative data.

### DISCUSSION

In Part 1 of our series, concerning the normative CCIs in children and young adults, we found age-related variability in CCI measurements related to developmental dynamics of CCI morphology and increased prevalence of the medial occipital notch. Two earlier studies examined the normal CCI measurements in patients without AOD trauma and incorporated single-plane measurements, with one of the studies (Vachhrajani et al<sup>4</sup>) demonstrating a nearly 2-fold difference from that of Pang et al.<sup>5</sup> Vachhrajani et al were the first to report age-related changes in the CCI, and we further confirmed that finding with our normative study by using the largest 100% nontraumatic subject group to date.<sup>1</sup> In Part 2 of our study reported here, we examined the clinical presentation of children diagnosed with AOD after substantial trauma and symptoms referable to the brain stem and/or C1–C2 level deficits. As we began this study, it was our hope that

**Proportions of false-positive examination findings and resulting specificities with 95% CIs when applying the 4 proposed abnormal cutoffs to the 124 healthy subjects without trauma in Part 1 of the study**

Age Group	Proportion of False-Positive Examination Findings				Specificities (95% CIs)			
	Pang et al <sup>2</sup> (4 mm)		Gire et al <sup>3</sup> (2.5 mm)		Pang et al <sup>2</sup> (4 mm)		Gire et al <sup>3</sup> (2.5 mm)	
	2 SDs	3 SDs	2 SDs	3 SDs	2 SDs	3 SDs	2 SDs	3 SDs
Younger than 12 mo	0/21	1/21	1/21	1/21	1.0 (0.85–1.0)	0.95 (0.77–0.99)	0.95 (0.77–0.99)	0.95 (0.77–0.99)
12–24 mo	0/19	12/19	1/19	0/19	1.0 (0.83–1.0)	0.37 (0.19–0.59)	0.94 (0.73–0.99)	1.0 (0.83–1.0)
2–4 yr	0/17	14/17	1/17	0/17	1.0 (0.82–1.0)	0.18 (0.06–0.41)	0.94 (0.73–0.99)	1.0 (0.82–1.0)
5–8 yr	0/19	13/19	0/19	0/19	1.0 (0.83–1.0)	0.32 (0.15–0.54)	1.0 (0.83–1.0)	1.0 (0.83–1.0)
9–12 yr	0/16	3/16	0/16	0/16	1.0 (0.81–1.0)	0.81 (0.57–0.93)	1.0 (0.72–0.99)	1.0 (0.81–1.0)
13–17 yr	0/19	0/19	2/19	0/19	1.0 (0.83–1.0)	1.0 (0.83–1.0)	0.89 (0.69–0.97)	1.0 (0.83–1.0)
Older than 17 yr	0/13	0/13	1/13	0/13	1.0 (0.67–1.0)	1.0 (0.67–1.0)	0.92 (0.67–0.99)	1.0 (0.67–1.0)

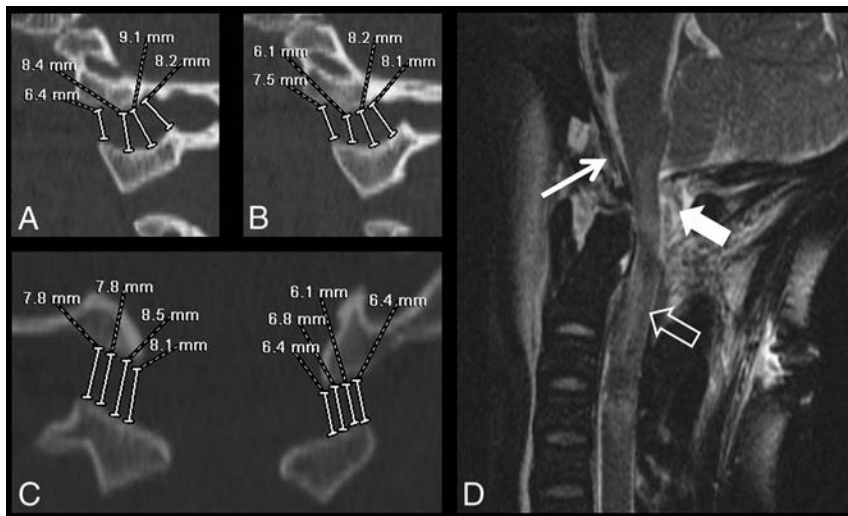


**FIG 1.** Subject 10. A 9-year-old girl involved in a motor vehicle collision. Initial sagittal (right, A; left, B) and coronal (C) CT images demonstrate substantial widening of the bilateral CCI. MR imaging examination (D) of the cervical spine performed 27 hours later demonstrates complete transection of the tectorial membrane (white arrow), complete transection of the posterior dural reflection at the craniocervical junction (black white arrow), and cord signal abnormality (open white arrow).

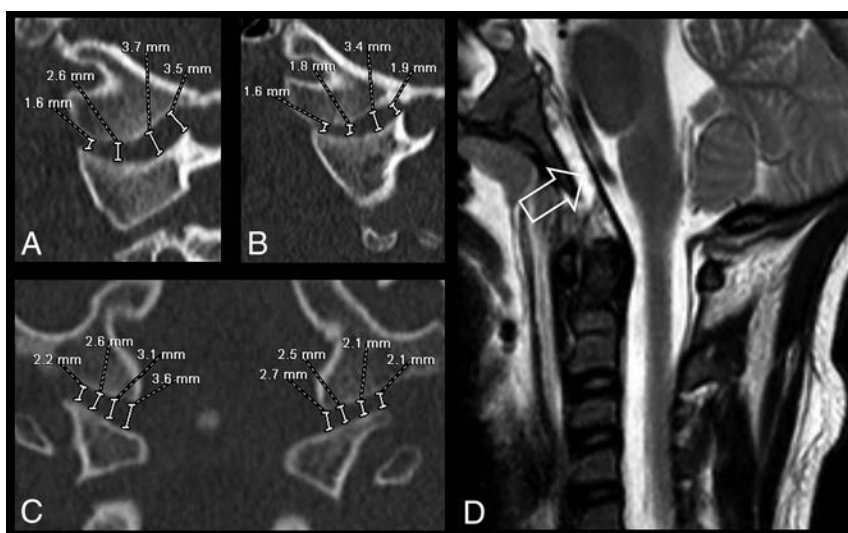


**FIG 2.** Subject 3. A 7-year-old girl involved in a motor vehicle collision. Initial sagittal (right, A; left, B) CT images demonstrate widening of the posterior CCI joint space, and coronal (C) images demonstrate mild asymmetry of the CCI joint spaces. Sagittal T2-weighted image of the cervical spine (D) performed 3 days later demonstrates lifting of the tectorial membrane off the dorsal clival cortex (open white arrow).

applying abnormal CCI cutoff values based on age-specific normative data would provide us with an optimally sensitive and specific quantitative measure to detect atlanto-occipital injury in children.

Our data suggest that the mechanisms involved in atlanto-occipital injury do not consistently result in an enlarged CCI measure, particularly in cases of mild-to-moderate severity. The age-specific CCI cutoff values of 2 and 3 SDs above the mean, respectively, were selected to ensure a high specificity. While offering quite good specificity, the age-specific standard of 2 and 3 SDs above the mean CCI cutoff resulted in an unacceptably low sensitivity (50% for both cutoff values) for atlanto-occipital injury in this case series. Our findings do not support the high sensitivities and specificities reported previously by Pang et al (4 mm)<sup>2</sup> and Gire et al (2.5 mm).<sup>3</sup> The 4-mm average CCI abnormal cutoff value proposed by Pang et al does allow excellent specificity and avoids false-positive results but has very poor sensitivity for atlanto-occipital injury. In contrast, the revised CCI method proposed by Gire et al with a single 2.5-mm measurement cutoff value has excellent sensitivity for atlanto-occipital injury but has a very low specificity in younger age groups. The revised CCI method would presumably result in a high false-positive rate and low positive predictive values in the pediatric traumatic population, given the overall low incidence of atlanto-occipital injuries among all pediatric cervical spine trauma patients.<sup>6</sup>

We were surprised by the discrepant results we found in comparison with those of Pang et al<sup>2</sup> regarding the sensitivity of their proposed 4-mm cutoff value. While these results may be at least

partly due to variability in the imaging assessment, a careful comparison of subjects in each of these studies suggests that the clinical severity of injury is the most likely explanation. Overall, subjects in the article of Pang et al were more likely to have severe

C1–C2 neurologic deficits, while many of our subjects did not. This finding suggests that a 4-mm cutoff is likely highly sensitive and specific for severe cases of AOD but not for cases presenting with mild-to-moderate severity, which also may require surgical treatment.

The revised CCI 2.5-mm abnormal cutoff proposed by Gire et al<sup>3</sup> appears to be highly sensitive as reported in their study. However, this measure would result in many false-positive findings in young children and young teenagers. For example, according to our normative data, most (82%; 59%–94%) healthy subjects between 2 and 4 years of age would have single midjoint sagittal plane measurements of >2.5 mm, and these measurements would thus be considered abnormal and suspicious for atlanto-occipital injury. The Table illustrates the low specificity of the 2.5-mm cutoff in subjects ages 1–12 years. A careful analysis of the subjects in the article of Gire et al provides a likely explanation for their reported high specificity (86%). While many of the subjects with AOD in their study were young children, none of the control subjects used to cal-

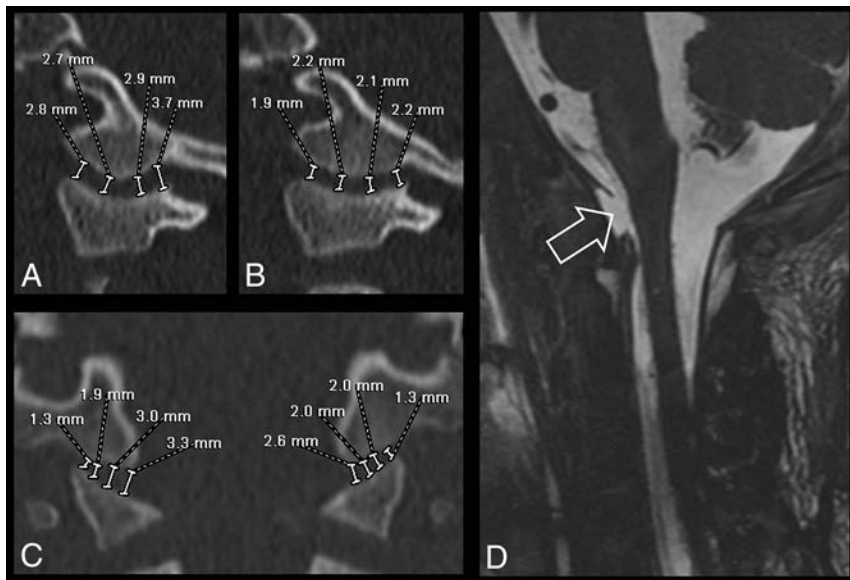


**FIG 3.** Subject 2. A 3-year-old boy hit by a car. Initial sagittal (right, A; left, B) and coronal (C) CT images demonstrate normal measurements of the bilateral CCI. MR imaging examination (D) of the cervical spine performed 34 hours later demonstrates complete transection of the tectorial membrane (open white arrow).

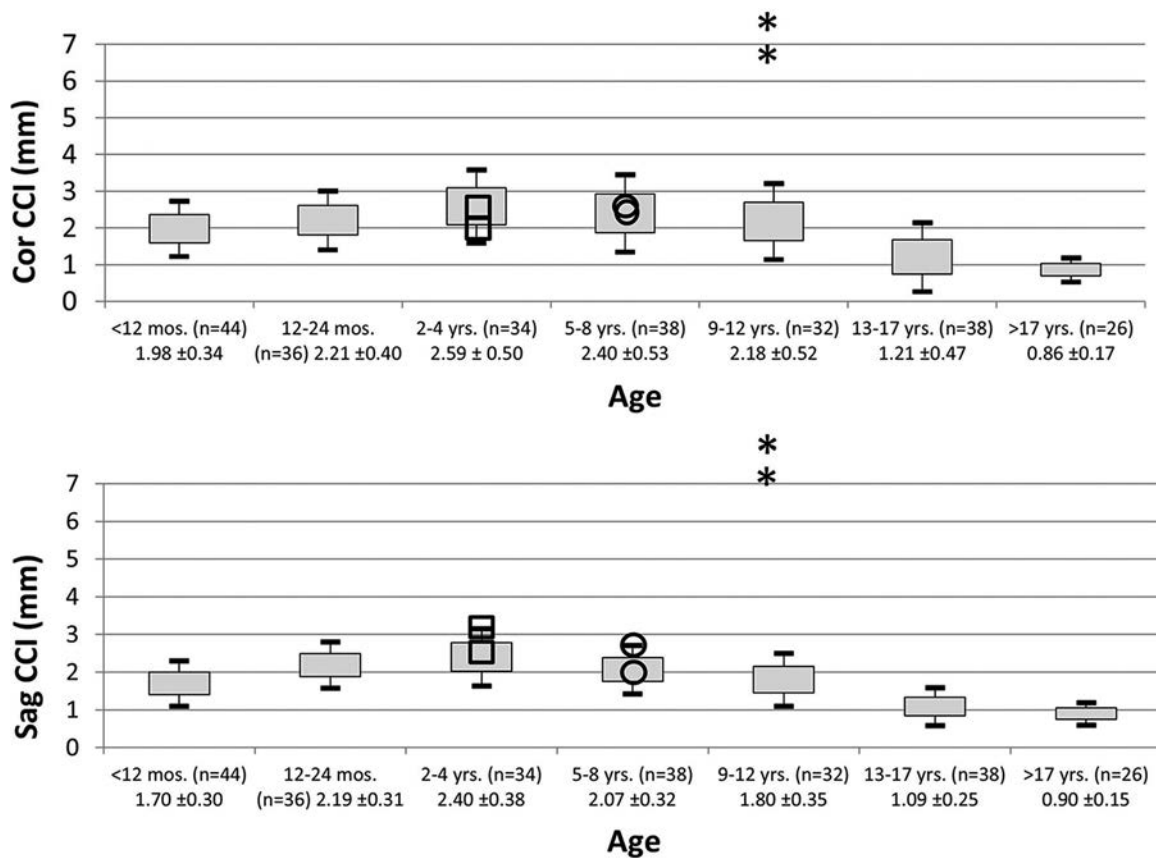


**FIG 4.** Representation of CCI measurements for subjects 10 (asterisks), 3 (circles), and 2 (squares) in relation to age-specific normative data from Part 1 of this study. Sag indicates sagittal; Cor, coronal.

culate their specificity values were younger than 18 years of age. Thus, as confirmed in our study, the revised CCI cutoff value of 2.5 mm is likely highly sensitive and specific in subjects older than 18 years of age. On the basis of the results of Gire et al and this study, we do not recommend applying this cutoff value in subjects younger than 13 years of age.

While overall our results suggest that abnormal CCI measurements are somewhat limited in establishing a diagnosis of atlanto-occipital injury, especially in mild-to-moderate cases, the CCI remains the best quantitative measure among many others (eg, Powers ratio, basion-dens interval, basion-axis interval, and so forth) for this diagnosis.<sup>2,7</sup> Also, when we took all CT imaging findings into account, CT remains an excellent initial test for detecting injury at the CCI, with only 3/14 (21%) CT examinations in our study showing no evidence of injury at the craniocervical junction. CCI measurements should not be used in isolation, but rather in the context of other imaging and clinical findings.

The utility of MR imaging in the evaluation of acute craniocervical and cervical spine injury has been extensively studied in adults and shows little-to-no benefit after normal findings on CT evaluations of the cervical spine in neurologically intact patients.<sup>8-10</sup> However, studies in children, who are much more susceptible to atlanto-occipital injury than adults,<sup>11,12</sup> suggest a more essential role of MR imaging in the correct diagnosis of otherwise occult injuries at the craniocervical junction.<sup>13,14</sup> In 1 study of subjects younger than 18 years of age, Junewick et al<sup>13</sup> showed that 30/45 subjects with normal CT findings at the craniocervical junction had abnormal findings on MR imaging. Seventeen of these patients, most younger than 8 years of age, had findings that met the criteria for “significant craniocervical junction injury,” though the need for surgical management was not investigated in this study. Another study by Meoded et al<sup>14</sup> evaluated 10 subjects with traumatic retroclival epidural hematomas on CT who underwent MR imaging evaluation. They found that MR imaging was more sensitive for the detection of tectorial membrane disruption and recommended its use for complete evaluation of suspected atlanto-occipital injury in children. Our findings support the previous work of Junewick et al and Meoded et al in clearly identifying major differences in the value of MR imaging after initial CT imaging for children compared with adults with suspected atlanto-occipital injury.

Limitations of this study include its retrospective nature and relatively small sample size of atlanto-occipital injury. Small sample size is a limitation of many prior studies of atlanto-occipital dislocation. Larger multi-institutional studies examining the optimal diagnostic approach and management of this uncommon diagnosis would be helpful in arriving at a consensus. Some may question the authors’ decision to include patients who did not undergo spinal fusion as part of the management of atlanto-occipital injury. The threshold for surgical treatment of atlanto-occipital injury varies across institutions and individual neurosurgeons. On the basis of the mechanism of injury, imaging findings, and clinical symptoms, we thought that these non-

operative subjects were appropriately classified as having atlanto-occipital injury.

## CONCLUSIONS

A substantial percentage of children with atlanto-occipital injury will have CCI measurements within the normal range for age. Age-specific abnormal CCI cutoff values and previously reported abnormal CCI cutoff values either lack sensitivity (4 mm) or specificity (2.5 mm) for less severe, but clinically significant, cases of atlanto-occipital injury. In children with clinical suspicion for atlanto-occipital injury but normal CCI measurements, MR imaging plays an important role in complete evaluation of these injuries.

## REFERENCES

1. Smith P, Linscott LL, Vadivelu S, et al. **Normal development and measurements of the occipital condyle-C1 interval in children and young adults.** *AJNR Am J Neuroradiol* 2015 Oct 29. [Epub ahead of print] CrossRef Medline
2. Pang D, Nemzek WR, Zovickian J. **Atlanto-occipital dislocation, part 2: the clinical use of (occipital) condyle-C1 interval, comparison with other diagnostic methods, and the manifestation, management, and outcome of atlanto-occipital dislocation in children.** *Neurosurgery* 2007;61:995–1015; discussion 1015 CrossRef Medline
3. Gire JD, Roberto RF, Bobinski M, et al. **The utility and accuracy of computed tomography in the diagnosis of occipitocervical dissociation.** *Spine J* 2013;13:510–19 CrossRef Medline
4. Vachhrajani S, Sen AN, Satyan K, et al. **Estimation of normal computed tomography measurements for the upper cervical spine in the pediatric age group.** *J Neurosurg Pediatr* 2014;14:425–33 CrossRef Medline
5. Pang D, Nemzek WR, Zovickian J. **Atlanto-occipital dislocation, part 1: normal occipital condyle-C1 interval in 89 children.** *Neurosurgery* 2007;61:514–21; discussion 521 CrossRef Medline
6. Patel JC, Tepas JJ 3rd, Mollitt DL, et al. **Pediatric cervical spine injuries: defining the disease.** *J Pediatr Surg* 2001;36:373–76 CrossRef Medline
7. Horn EM, Feiz-Erfan I, Lekovic GP, et al. **Survivors of occipitoatlantal dislocation injuries: imaging and clinical correlates.** *J Neurosurg Spine* 2007;6:113–20 CrossRef Medline
8. Steigelman M, Lopez P, Dent D, et al. **Screening cervical spine MRI after normal cervical spine CT scans in patients in whom cervical spine injury cannot be excluded by physical examination.** *Am J Surg* 2008;196:857–62; discussion 862–63 CrossRef Medline
9. Schuster R, Waxman K, Sanchez B, et al. **Magnetic resonance imaging is not needed to clear cervical spines in blunt trauma patients with normal computed tomographic results and no motor deficits.** *Arch Surg* 2005;140:762–66 CrossRef Medline
10. Tomycz ND, Chew BG, Chang YF, et al. **MRI is unnecessary to clear the cervical spine in obtunded/comatose trauma patients: the four-year experience of a level I trauma center.** *J Trauma* 2008;64:1258–63 CrossRef Medline
11. Junewick JJ. **Pediatric craniocervical junction injuries.** *AJR Am J Roentgenol* 2011;196:1003–10 CrossRef Medline
12. Junewick JJ. **Cervical spine injuries in pediatrics: are children small adults or not?** *Pediatr Radiol* 2010;40:493–98 CrossRef Medline
13. Junewick JJ, Meesa IR, Luttenton CR, et al. **Occult injury of the pediatric craniocervical junction.** *Emerg Radiol* 2009;16:483–88 CrossRef Medline
14. Meoded A, Singhi S, Poretti A, et al. **Tectorial membrane injury: frequently overlooked in pediatric traumatic head injury.** *AJNR Am J Neuroradiol* 2011;32:1806–11 CrossRef Medline

# Improved Lesion Detection by Using Axial T2-Weighted MRI with Full Spinal Cord Coverage in Multiple Sclerosis

S. Galler, J.-P. Stellmann, K.L. Young, D. Kutzner, C. Heesen, J. Fiehler, and S. Siemonsen



## ABSTRACT

**BACKGROUND AND PURPOSE:** Identification of lesions in specific locations gains importance in multiple sclerosis imaging diagnostic criteria. In clinical routine, axial scans are usually exclusively obtained to depict the cervical spinal cord or used to confirm suspected lesions on sagittal scans. We sought to evaluate the detection rate for MS lesions on axial T2WI scans with full spinal cord coverage in comparison with sagittal scans.

**MATERIALS AND METHODS:** One hundred fifteen patients with definite or suspected MS underwent an MR imaging examination including 3-mm sagittal and 3.5-mm axial T2-weighted images with full spinal cord coverage. T2WI lesions were identified on axial and sagittal scans independently by 2 raters. Axial diameter, craniocaudal extension, lesion intensity, and location were analyzed.

**RESULTS:** Four hundred forty-nine of 509 (88.2%) lesions were detected on axial and 337/509 (66.2%) on sagittal scans. Only 277/449 (61.7%) axial lesions were also detected on sagittal images. The number of lesions visible on sagittal and axial images was dependent on the axial lesion diameter ( $P < .001$ ).

**CONCLUSIONS:** Axial T2WI scans with full spinal cord coverage showed 22% more lesions in patients with MS in comparison with sagittal scans, especially for lesions with small axial diameters. We suggest including biplanar spinal MR imaging with full spinal cord coverage for lesion detection in MS in clinical routine and for clinical studies.

**ABBREVIATIONS:** AD = axial diameter; CCE = craniocaudal extension

Multiple sclerosis is a chronic inflammatory disease, considered the most common demyelinating process involving the central nervous system.<sup>1</sup> The diagnosis requires typical clinical findings in addition to the evidence of lesions in the CNS disseminated in time and space seen on MR imaging of the brain or spinal cord.<sup>2</sup> While the diagnostic focus of most multiple sclerosis studies is still based on MR imaging of the brain, several studies

have revealed spinal cord lesions in 75%–90% of patients with clinically diagnosed MS.<sup>3–6</sup> As many as 20% of spinal MS lesions are isolated, without coexisting brain lesions.<sup>1</sup>

Spinal cord abnormalities seen on MR imaging were incorporated into the McDonald Diagnostic Criteria for MS in 2005.<sup>7,8</sup> Since the revision of the McDonald Diagnostic Criteria for MS in 2010,<sup>9</sup> they have gained even more importance because better spinal cord lesion detection potentially impacts the recognition of the dissemination of MS lesions in space.

In 2006, a consortium of MS centers published consensus guidelines with a standardized MR imaging protocol for spinal cord imaging in MS, recommending a 3-plane scout; a pre- and post-contrast-enhanced sagittal T1; a pre-contrast-enhanced sagittal FSE proton-density/T2; and additionally, only in case of suspected lesions, a pre-contrast-enhanced axial FSE proton-density/T2 and a post-contrast-enhanced axial T1.<sup>10</sup> In the clinical routine of MS diagnostics, axial scans are typically obtained exclusively with coverage of the cervical spinal cord or are used to confirm suspected lesions on sagittal scans. This is mainly due to the long scanning time of axial scans with full spinal cord coverage.

So far in most MS studies, spinal cord lesions were evaluated

Received July 29, 2015; accepted after revision November 3.

From the Departments of Diagnostic and Interventional Neuroradiology (S.G., D.K., J.F., S.S.) and Neurology (J.-P.S., K.L.Y., C.H.), and the Institute of Neuroimmunology and Multiple Sclerosis (J.-P.S., K.L.Y., C.H., S.S.), University Medical Center Hamburg-Eppendorf, Hamburg, Germany.

This study was supported by the Federal Ministry of Education and Research (S.S., J.-P.S., C.H.; Proposal/Contract 0315610–0315620 NEU2).

Paper previously presented at: American Society of Neuroradiology Annual Meeting and the Foundation of the ASNR Symposium, April 25–30, 2015; Chicago, Illinois.

Please address correspondence to Stephanie Galler, MD, Department of Diagnostic and Interventional Neuroradiology, University Medical Center Hamburg-Eppendorf, Martinistr 52, 20246 Hamburg, Germany; e-mail: s.galler@uke.de

Indicates open access to non-subscribers at www.ajnr.org

Indicates article with supplemental on-line table.

<http://dx.doi.org/10.3174/ajnr.A4638>

and marked on the sagittal plane,<sup>11,12</sup> while some groups included axial scans covering only the cervical spine<sup>13-15</sup> and very few studies analyzed the axial and sagittal planes of the entire spinal cord.<sup>3,16</sup> Also, lesion location and size were described on sagittal scans only or on axial scans covering the cervical spinal cord exclusively.<sup>15</sup>

We hypothesized that axial T2WI scans with full spinal cord coverage would detect more T2WI lesions in comparison with sagittal scans. We sought to evaluate detection rates for T2WI lesions on axial and sagittal scans in relation to the distribution and extent of spinal cord lesions in patients with MS. To our knowledge, this is the first study focusing on the clinical application of axial 3.5-mm scans with full spinal cord coverage. We used a sequence with reasonable duration, feasible in clinical routine.

## MATERIALS AND METHODS

### Patients

One hundred fifteen patients (81 women, 16–82 years of age; mean, 38 years; 34 men, 16–71 years of age; mean, 38 years) with diagnosed or suspected MS, and clinically suspected or known spinal cord lesions were consecutively included in our study between April 2013 and February 2014. Patients were referred for MR imaging by our associated MS day hospital. The prospective study was approved by the local ethics review committee and is in accordance with the Declaration of Helsinki. Patients or their guardians provided written informed consent. All patients underwent an MR imaging examination of the spinal cord, including axial scans, with full spinal cord coverage.

### MR Imaging Protocol

All examinations were performed on a 3T MR imaging scanner (Magnetom Skyra; Siemens, Erlangen, Germany) with a neck and spine multiarray coil including, among other sequences, an axial T2WI turbo spin-echo sequence (TR, 6600 ms; TE, 94 ms; FOV, 200 mm; section thickness, 3.5 mm; 50 sections without a section gap; acquisition time, 2 minutes and 53 seconds) in 2 slabs with full spinal cord coverage (including the tip of the odontoid process and the conus medullaris) and a sagittal T2WI turbo spin-echo sequence (TR, 3650 ms; TE, 95 ms; FOV, 300 mm; section thickness, 3 mm; 17 sections without a section gap; acquisition time, 1 minute and 55 seconds). An intersection cross-talk was avoided by interleave acquisitions.

### Lesion Evaluation

**Lesion Identification.** Lesions were defined as macular signal alterations with a minimum axial diameter of 2 mm that could be clearly isolated from their surroundings and not mistaken for artifacts. Axial and sagittal T2-weighted images were analyzed by 2 experienced neuroradiologists on a medical workstation on calibrated, high-resolution monitors. In a first reading, sagittal scans were presented to both raters separately in random order and MS lesions were identified and marked by each rater. In a second reading, corresponding axial scans were presented to both raters in the same manner. There was an interval of 2 weeks between the readings. For both readings, raters were blinded to the patient name and all other clinical and imaging parameters, especially to rating results and images of corresponding axial or sagittal scans.

**Table 1:  $\kappa$  values and numbers of detected lesions on sagittal and axial images**

	R1	R2	$\kappa$ Value
Axial	463	458	0.831
Sagittal	324	301	0.804
Axial and sagittal	248	235	0.841
Total	391	401	

**Note:**—R1 indicates rater 1; R2, rater 2.

The readings were performed with the same intensity windowing to ascertain comparability between raters and scans. After completion of the blinded reading, lesions that were found only in axial or sagittal scans were reevaluated and documented to assess whether the lesion could be identified retrospectively in the corresponding axial or sagittal plane.

**Lesion Characterization.** Each lesion was characterized according to its intensity, location in the axial plane (midline or lateral), and position (cervical or thoracic) following the blinded reading. In addition, the craniocaudal extension (CCE) and axial diameter (AD) of each lesion were documented. To assess lesion extension in the axial plane, we measured the maximum lesion diameter, and lesions were stratified accordingly: AD1, 0.2–0.3 cm; AD2, 0.3–0.5 cm; AD3, > 0.5 cm.

Lesions were grouped according to their intensity (I1 = low intensity, I2 = intermediate intensity, I3 = high intensity relative to CSF).

### Statistical Analysis

The interobserver agreement for T2 lesion detection in axial and sagittal scans was evaluated with the Cohen test, and magnitude guidelines were applied according to Landis and Koch.<sup>17</sup> For further analysis, only lesions identified by both raters were included. Ordinal data were evaluated by using the  $\chi^2$  test. All statistical analyses were conducted by using R statistical computing software, Version 3.0.0 (<http://www.r-project.org/>).

## RESULTS

### Interrater Agreement

Ratings for detection of lesions on sagittal and axial scans for raters 1 and 2 are shown in Table 1. Both raters detected more lesions on axial than on sagittal scans. The Cohen  $\kappa$  value for interrater reliability was almost perfect ( $\kappa = 0.841$ ) for lesion detection in axial and sagittal scans and only slightly lower ( $\kappa = 0.804$ ) for sagittal scans (Table 1).

### Lesion Evaluation

In total, 509 lesions were detected on axial or sagittal scans by both raters. Four hundred forty-four T2WI hyperintense spinal cord lesions were identified on axial scans, and 284 lesions, on sagittal scans during the first reading (Table 2). When scans were evaluated retrospectively, the number of lesions that were missed in the first but identified in the second reading was considerably higher on sagittal in comparison with axial scans (Fig 1). Overall, 449/509 (88.2%) lesions were detected on axial scans, while 337/509 (66.2%) lesions were detected on sagittal scans. Of all lesions detected on axial scans, only 277/449 (61.7%) were also detected on sagittal scans, while 60/337 (17.8%) were detected only on sagittal scans without any cor-

relation on axial scans, even in retrospective evaluation (Fig 1 and Table 2). Sample images are shown in Figs 2 and 3. The median number of lesions identified per patient was 2 (minimum, 0; maximum, 22 lesions). In 31/115 (27%) patients, no spinal cord lesion was identified by both raters. In the 84/115 (73%) patients with at least 1 detected spinal cord T2 lesion, the median number of lesions was 6, with a minimum of 1 lesion per patient and a maximum number of 22.

### Lesion Location, Size, and Intensity

There was no significant difference in the number of lesions located in the cervical or thoracic spinal cord ( $P > .2$ ) on axial or sagittal scans. The number of lesions detected only on sagittal but not on axial scans was significantly higher within the thoracic spinal cord than in the cervical cord ( $P < .001$ ) (Fig 4). On axial scans, 185/449 (41.2%) lesions were located in the

midline of the spinal cord, 128/449 (28.5%) on the left side, and 136/449 (30.3%) on the right side. The rate of axial lesions also recognized on sagittal scans was significantly higher for lesions with an in-plane location in the midline (126/185, 68.1%) than for lesions with a lateral location (151/264, 57.2%,  $P > .001$ ).

In addition, lesion identification did not seem to be dependent on the degree of lesion intensity. Lesions with high intensity on axial scans were also identified on sagittal scans in most cases, but the percentage of lesions with low intensity (I1) identified on axial and sagittal scans was only slightly lower in comparison with those with high intensity (I3) and slightly higher than the percentage of lesions with medium intensity (I2) (On-line Table).

The percentage of lesions detected on sagittal and axial scans seemed to be dependent on the axial lesion diameter. The larger the lesions, the higher were the percentages of axial lesions also detected on sagittal scans. Forty of 43 (93.0%) of the lesions with an axial diameter  $>0.5$  cm (AD3) were also identified on sagittal scans, while only 49/106 (46.2%) lesions in group AD1 were also detected on sagittal scans (On-line Table).

When we compared the CCE of lesions, lesions that were detected on axial and sagittal scans showed significantly larger CCEs ( $P < .001$ ) than those lesions that were only identifiable on axial scans (Fig 5). Thirty-eight of 60 (63.3%) lesions only identified on sagittal scans presented with a CCE  $\leq 0.3$  cm.

**Table 2: Lesions in the cervical and thoracic spinal cord<sup>a</sup>**

	Total Including Retrospective		Spinal Cord Location: Cervical/Thoracic
	Total	Analysis	
Axial	444	449	237/212
Sagittal	284	337	158/179
Axial and sagittal	219	277	141/136
Axial, not sagittal	225	172	96/76
Sagittal, not axial	65	60	17/43
Total	509	509	254/255

<sup>a</sup> Data are the number of detected lesions in first and second readings by both raters.

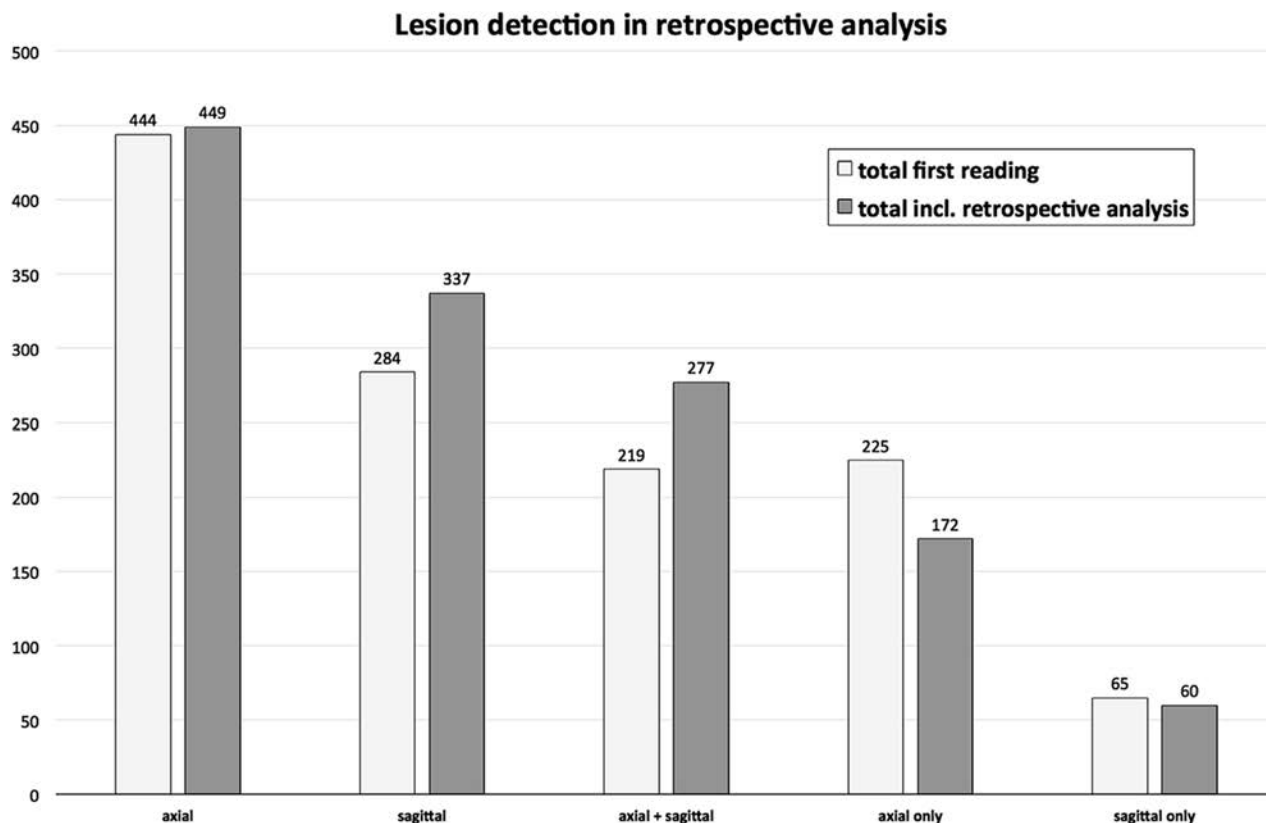


**FIG 1.** Graph displaying the total number of lesions detected on axial scans (axial), the total number of lesions detected on sagittal scans (sagittal), the number of lesions identified on both sagittal and axial scans (axial + sagittal), and the lesion number marked on axial (axial only) or sagittal (sagittal only) scans only without corresponding correlates in the other plane. Light gray bars indicate the results of the first reading, and dark gray bars correspond to lesion numbers, including the lesions that could only be identified when retrospectively analyzing the images. Incl indicates including.

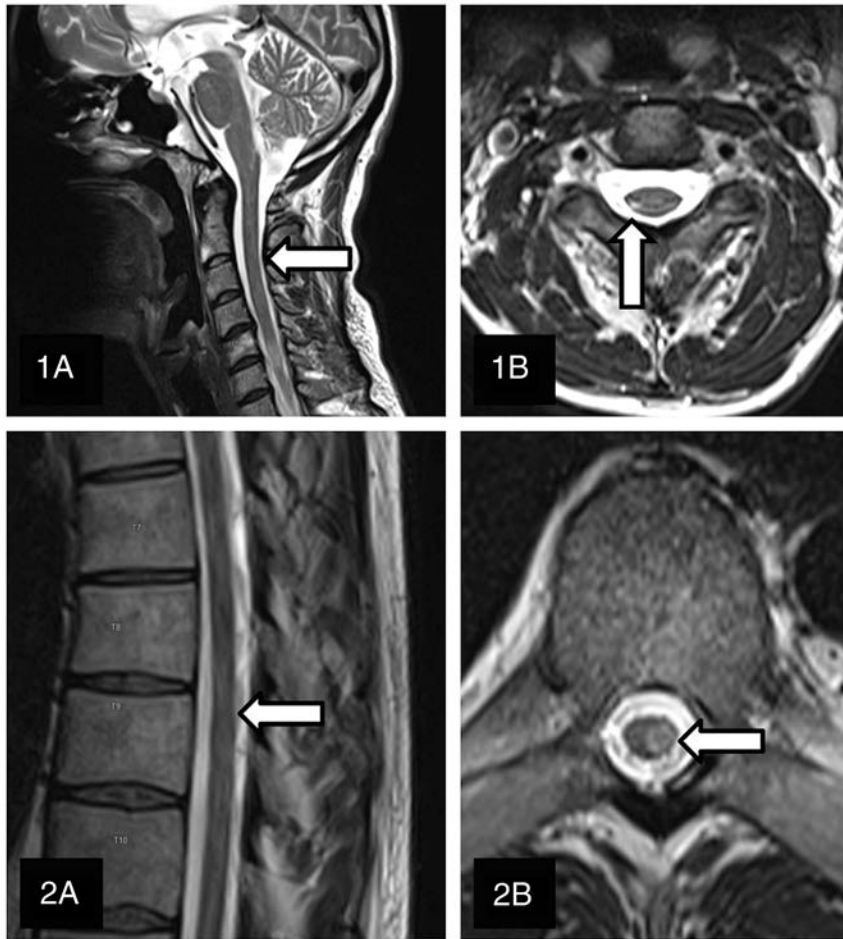


**FIG 2.** Examples of a cervical (1A and 1B) and a thoracic (2A and 2B) spinal cord lesion detected on axial scans but missed by both raters on corresponding sagittal scans.

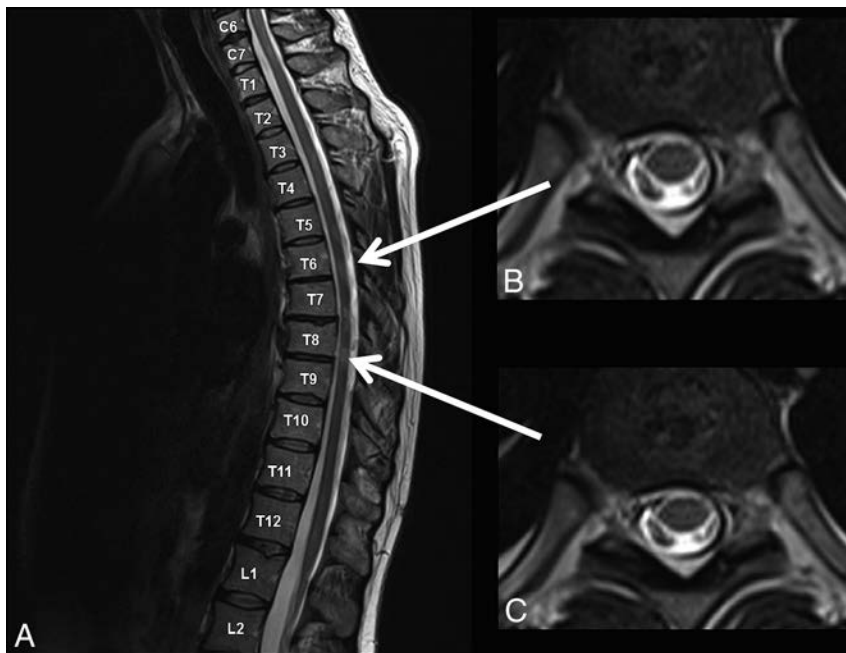


**FIG 3.** Examples of spinal cord lesions detected only on sagittal scans (A) while missed on corresponding axial scans (B and C).

## DISCUSSION

Commonly, the spinal cord is assessed on sagittal scans with additional axial sections used to ascertain focal pathologies. It seems that this scanning protocol became clinical routine because a sagittal scan could be obtained much faster than a thorough coverage of the whole spinal cord with axial sections. In the present day, parallel imaging techniques with multiarray coils provide a time-saving scanning technique with axial sections with less patient movement and artifacts.<sup>18</sup>

The present investigation is the first MR imaging study using axial T2WI sequences with full spinal cord coverage in a cohort of patients with possible inflammatory spinal cord pathology from an MS clinic, to our knowledge. We compared the lesions found in sagittal and axial scans in number, location, signal intensity, and size by using the AD and the CCE. The overall acquisition time for a combined imaging study consisting of 2 slabs of axial T2WI scans (2:53 minutes) and sagittal T2WI scans (1:55 minutes) seems reasonable even for a routine clinical setting.

In comparison with the total number of lesions detected on sagittal scans, 172/337 (51%) more lesions could only be detected on axial scans. Therefore, we focused on the analysis of all lesions depending on their size, location, and intensity, while previous studies mainly focused on the detection or exclusion of any spinal cord lesion identified on axial and sagittal scans.<sup>3,6</sup>

Previous studies gave the impression that focal spinal cord lesions in patients with MS are preferentially located in the cervical spinal cord.<sup>19-22</sup> In 2004, Bot et al<sup>4</sup> published a study with 353 spinal cord lesions in patients with MS; 56.4% of these were located in the cervical spinal cord. In line with these previous studies, 52.7% of all spinal cord lesions detected in our study were located in the cervical segment. Notably, the percentage of lesions identified in the cervical spinal cord only slightly exceeded the percentage of thoracic lesions (47.3%). Nevertheless, in both segments, cervical and thoracic, significantly more lesions were detected in the axial than on the sagittal planes.

## Lesion detection and location

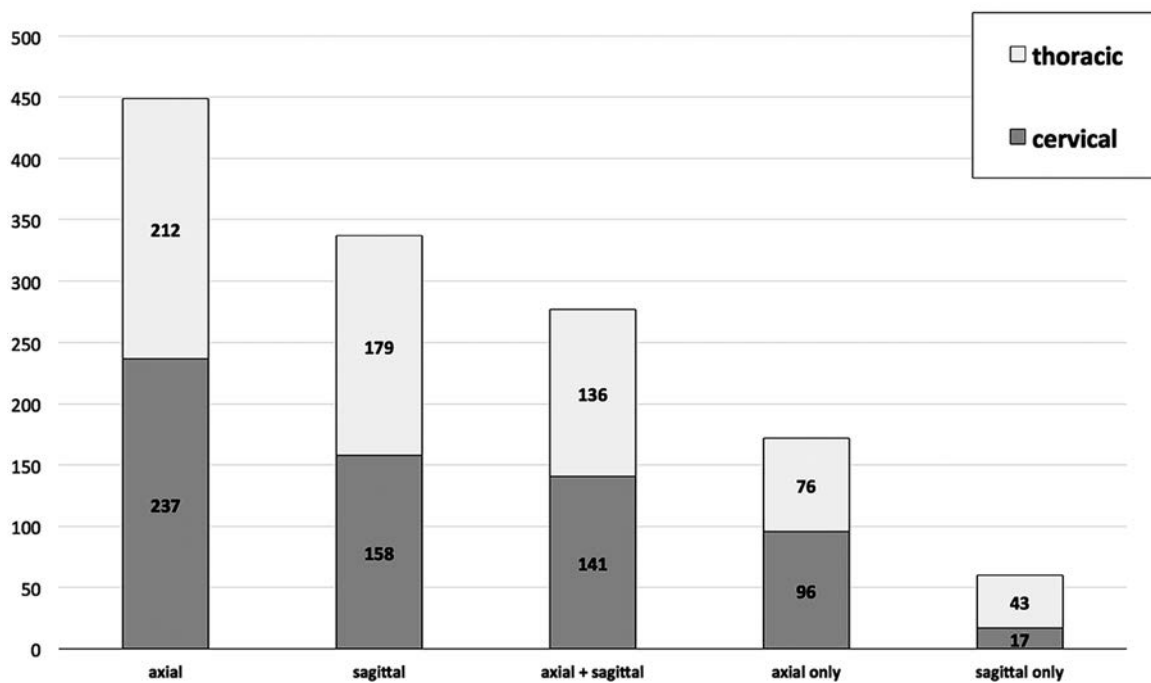


**FIG 4.** There was no significant difference in the number of lesions located in the cervical or thoracic spinal cord ( $P > .2$ ) on axial or sagittal scans. The number of lesions detected only on sagittal but not on axial scans was significantly higher in the thoracic spinal cord than in the cervical cord ( $P < .001$ ).

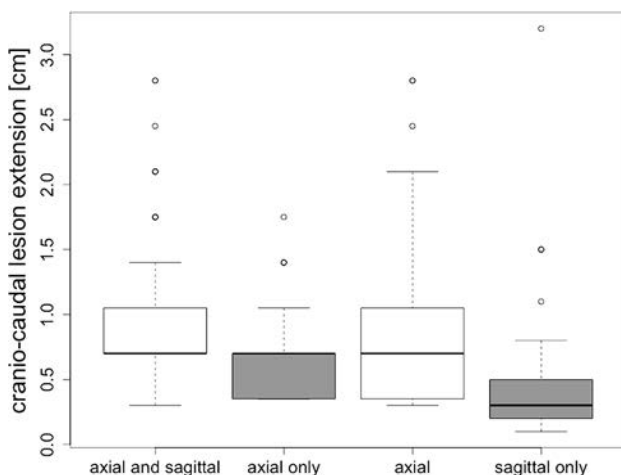


**FIG 5.** Boxplot comparing craniocaudal extension of lesions. Those lesions detected in axial and sagittal scans had a significantly larger extent ( $P < .001$ ) than those lesions that were only identifiable on axial scans (axial only).

Our findings demonstrate that the standardized MR imaging protocol for spinal cord imaging in MS, which recommends axial scans of suspicious lesions on sagittal planes only,<sup>10</sup> leaves a high percentage of lesions undetected. In addition, the common clinical procedure to cover the cervical spine with an additional axial sequence seems to disregard, specifically, thoracic lesions.

Given that spinal cord lesions have very high specificity and sensitivity to differentiate MS and other neurologic diseases, missing every third lesion in clinical practice is not acceptable. In ad-

dition, MR imaging is the only established biomarker to monitor disease activity and treatment response in MS.<sup>23</sup> Two or more new T2 lesions on MR imaging of the brain are considered predictive of relapses and disability progression (ie, poor treatment response to immunotherapy).<sup>24</sup> Currently, several treatments for MS are available. Their effectiveness is measured by their ability to decrease disease activity assessed with clinical scores and MR imaging. Therefore, detecting new lesions, also in the spinal cord, is crucial for treatment decisions.<sup>25</sup>

In line with authors of previous MR imaging and pathologic studies, we found lesions only infrequently in the anterior columns of the spinal cord.<sup>26-28</sup> In addition, most of the detected lesions on sagittal and axial planes were located in the lateral columns of the spinal cord. Lateral cord lesions were likewise detected on sagittal scans in only 57.2% of the cases. Reasons for missing lesions on sagittal scans might be the section thickness of 3 mm and partial volume effects.

Accordingly, especially, lesions with a small in-plane extension (AD) could not be identified in sagittal planes. In addition, sagittal lesions that were missed on axial scans had significantly lower CCE. This might be explained by the axial section thickness of 3.5 mm that was used in this study, which is small compared with previous trials reporting axial section thicknesses of 6<sup>3</sup> and 5 mm.<sup>16</sup>

To our knowledge, measurements of the AD of single lesions have not been reported. Previous studies mainly focused on the CCE in sagittal scans.<sup>6</sup>

The lesion signal intensity did not seem to affect the likelihood of lesion identification. However, in some cases, lesions were

more clearly identified on axial scans and only depicted as diffuse hyperintensities on the sagittal spinal cord images. This phenomenon has already been described in detail on postmortem MR imaging and histopathologic analyses.<sup>29</sup> Without knowledge of corresponding axial scans, these lesions have been mainly considered artifacts.

A major limitation of this study in line with previous studies that compared MR imaging sequences for lesion detection<sup>30</sup> was the lack of a reference standard for lesion presence. In the absence of postmortem pathologic data, which serve as the only reliable reference, we used consensus findings of 2 experienced raters in axial T2-weighted TSE images with full spinal cord coverage as a radiologic reference standard and compared these results with lesion detection on sagittal planes. In general, lesions were more clearly detectable and defined on axial than on sagittal T2WI scans. Therefore, we regarded axial scans as more reliable for lesion detection than corresponding sagittal scans. However, lesions identified only on sagittal scans might be missed because of their CCEs lying below or being equal to the section thickness of the axial sections.

The current diagnostic value of sagittal spinal MR images is limited mainly by partial volume effects, CSF pulsation artifacts, and section thickness of 3 mm, resulting in a high number of lesions missed by the reader. Nevertheless, the sagittal scan should not be abandoned because lesions with small CCEs can also be missed on axial scans with 3-mm section thicknesses. Furthermore, when we retrospectively evaluated lesions that were only seen on axial scans in the first reading, 26.5% more lesions could be identified on both scans after the second reading and might therefore be regarded as reproducible.

## CONCLUSIONS

In patients with MS, axial scans with full spinal cord coverage displayed considerably more T2WI lesions in comparison with sagittal scans in the cervical and in the thoracic spinal cord. This finding applies especially to lesions with a small axial diameter and lesions located in the lateral spinal cord. However, even large lesions can be overlooked when only assessed in the sagittal plane. Furthermore, axial scans with full spinal cord coverage allow quantification and volumetric analysis of spinal lesion load in patients with MS and might provide a new impulse for future MS studies.

We suggest biplanar spinal MR imaging with full axial spinal cord coverage as a comprehensive examination for lesion detection in MS in clinical routine and for clinical studies. The clinical implication of these additional findings needs to be confirmed and validated in future studies.

Disclosures: Stephanie Galler—RELATED: Grant: Federal Ministry of Education and Research.\* Comments: S.S., J.-P.S., C.H., Proposal/Contract 0315610–0315620 NEU2. Jan-Patrick Stellmann—UNRELATED: Grants/Grants Pending: Biogen,\* Merck Serono\*; Payment for Lectures (including service on Speakers Bureaus): Biogen\*; Travel/Accommodations/Meeting Expenses Unrelated to Activities Listed: Biogen, Novartis. Kim Lea Young—RELATED: Grant: Federal Ministry of Education and Research.\* Daniel Kutzner—UNRELATED: Grants/Grants Pending: Biogen, Novartis. Kim Lea Young—RELATED: Grant: Federal Ministry of Education and Research.\* Christoph Heesen—RELATED: Grant: German Ministry of Education and Research.\* Comments: Grant to develop MRI platform for MS as an outcome for treatment studies. Jens Fiebler—UNRELATED: Payment for Lectures (including service on Speakers Bureaus): Siemens. \*Money paid to the institution.

## REFERENCES

- Noseworthy JH, Lucchinetti C, Rodriguez M, et al. **Multiple sclerosis.** *N Engl J Med* 2000;343:938–52 CrossRef Medline
- Inglese M. **Multiple sclerosis: new insights and trends.** *AJNR Am J Neuroradiol* 2006;27:954–57 Medline
- Weier K, Mazraeh J, Naegelin Y, et al. **Biplanar MRI for the assessment of the spinal cord in multiple sclerosis.** *Mult Scler* 2012;18:1560–69 CrossRef Medline
- Bot JC, Barkhof F, Polman CH, et al. **Spinal cord abnormalities in recently diagnosed MS patients: added value of spinal MRI examination.** *Neurology* 2004;62:226–33 CrossRef Medline
- Nijeholt GJ, van Walderveen MA, Castelijns JA, et al. **Brain and spinal cord abnormalities in multiple sclerosis: correlation between MRI parameters, clinical subtypes and symptoms.** *Brain* 1998;121(pt 4):687–97 CrossRef Medline
- Qiu W, Raven S, James I, et al. **Spinal cord involvement in multiple sclerosis: a correlative MRI and high-resolution HLA-DRB1 genotyping study.** *J Neurol Sci* 2011;300:114–19 CrossRef Medline
- Korteweg T, Barkhof F, Uitdehaag BM, et al. **How to use spinal cord magnetic resonance imaging in the McDonald diagnostic criteria for multiple sclerosis.** *Ann Neurol* 2005;57:606–07 CrossRef Medline
- Polman CH, Reingold SC, Edan G, et al. **Diagnostic criteria for multiple sclerosis: 2005 revisions to the “McDonald Criteria.”** *Ann Neurol* 2005;58:840–46 CrossRef Medline
- Polman CH, Reingold SC, Banwell B, et al. **Diagnostic criteria for multiple sclerosis: 2010 revisions to the McDonald criteria.** *Ann Neurol* 2011;69:292–302 CrossRef Medline
- Simon JH, Li D, Traboulsee A, et al. **Standardized MR imaging protocol for multiple sclerosis: Consortium of MS Centers consensus guidelines.** *AJNR Am J Neuroradiol* 2006;27:455–61 Medline
- Lukas C, Sombekke MH, Bellenberg B, et al. **Relevance of spinal cord abnormalities to clinical disability in multiple sclerosis: MR imaging findings in a large cohort of patients.** *Radiology* 2013;269:542–52 CrossRef Medline
- Bot JC, Blezer EL, Kamphorst W, et al. **The spinal cord in multiple sclerosis: relationship of high-spatial-resolution quantitative MR imaging findings to histopathologic results.** *Radiology* 2004;233:531–40 CrossRef Medline
- Riederer I, Karampinos DC, Settles M, et al. **Double inversion recovery sequence of the cervical spinal cord in multiple sclerosis and related inflammatory diseases.** *AJNR Am J Neuroradiol* 2015;36:219–25 CrossRef Medline
- Raz E, Bester M, Sigmund EE, et al. **A better characterization of spinal cord damage in multiple sclerosis: a diffusional kurtosis imaging study.** *AJNR Am J Neuroradiol* 2013;34:1846–52 CrossRef Medline
- Kearney H, Altmann DR, Samson RS, et al. **Cervical cord lesion load is associated with disability independently from atrophy in MS.** *Neurology* 2015;84:367–73 CrossRef Medline
- Nair G, Absinta M, Reich DS. **Optimized T1-MPRAGE sequence for better visualization of spinal cord multiple sclerosis lesions at 3T.** *AJNR Am J Neuroradiol* 2013;34:2215–22 CrossRef Medline
- Landis JR, Koch GG. **The measurement of observer agreement for categorical data.** *Biometrics* 1977;33:159–74 CrossRef Medline
- Pruessmann KP, Weiger M, Scheidegger MB, et al. **SENSE: sensitivity encoding for fast MRI.** *Magn Reson Med* 1999;42:952–62 Medline
- Kidd D, Thorpe JW, Thompson AJ, et al. **Spinal cord MRI using multi-array coils and fast spin echo, II: findings in multiple sclerosis.** *Neurology* 1993;43:2632–37 CrossRef Medline
- Bot JC, Barkhof F, Lycklama à Nijeholt G, et al. **Differentiation of multiple sclerosis from other inflammatory disorders and cerebrovascular disease: value of spinal MR imaging.** *Radiology* 2002;223:46–56 CrossRef Medline
- Honig LS, Sheremata WA. **Magnetic resonance imaging of spinal cord lesions in multiple sclerosis.** *J Neurol Neurosurg Psychiatry* 1989;52:459–66 CrossRef Medline

22. Tartaglino LM, Friedman DP, Flanders AE, et al. **Multiple sclerosis in the spinal cord: MR appearance and correlation with clinical parameters.** *Radiology* 1995;195:725–32 CrossRef Medline
23. Dobson R, Rudick RA, Turner B, et al. **Assessing treatment response to interferon- $\beta$ : is there a role for MRI?** *Neurology* 2014;82:248–54 CrossRef Medline
24. Hauser SL, Chan JR, Oksenberg JR. **Multiple sclerosis: prospects and promise.** *Ann Neurol* 2013;74:317–27 CrossRef Medline
25. Rotstein DL, Healy BC, Malik MT, et al. **Evaluation of no evidence of disease activity in a 7-year longitudinal multiple sclerosis cohort.** *JAMA Neurol* 2015;72:152–58 CrossRef Medline
26. Gilmore CP, Geurts JJ, Evangelou N, et al. **Spinal cord grey matter lesions in multiple sclerosis detected by post-mortem high field MR imaging.** *Mult Scler* 2009;15:180–88 CrossRef Medline
27. Ikuta F, Zimmerman HM. **Distribution of plaques in seventy autopsy cases of multiple sclerosis in the United States.** *Neurology* 1976;26(6 pt 2):26–28 Medline
28. Adams RD, Kubik CS. **The morbid anatomy of the demyelinating disease.** *Am J Med* 1952;12:510–46 CrossRef Medline
29. Bergers E, Bot JC, van der Valk P, et al. **Diffuse signal abnormalities in the spinal cord in multiple sclerosis: direct postmortem in situ magnetic resonance imaging correlated with in vitro high-resolution magnetic resonance imaging and histopathology.** *Ann Neurol* 2002;51:652–56 CrossRef Medline
30. Martin N, Malfair D, Zhao Y, et al. **Comparison of MERGE and axial T2-weighted fast spin-echo sequences for detection of multiple sclerosis lesions in the cervical spinal cord.** *AJR Am J Roentgenol* 2012;199:157–62 CrossRef Medline

# Comparison of Sagittal FSE T2, STIR, and T1-Weighted Phase-Sensitive Inversion Recovery in the Detection of Spinal Cord Lesions in MS at 3T

P. Alcaide-Leon, A. Pauranik, L. Alshafai, S. Rawal, J. Oh, W. Montanera, G. Leung, and A. Bharatha

## ABSTRACT

**BACKGROUND AND PURPOSE:** Determining the diagnostic accuracy of different MR sequences is essential to design MR imaging protocols. The purpose of the study was to compare 3T sagittal FSE T2, STIR, and T1-weighted phase-sensitive inversion recovery in the detection of spinal cord lesions in patients with suspected or definite MS.

**MATERIALS AND METHODS:** We performed a retrospective analysis of 38 patients with suspected or definite MS. Involvement of the cervical and thoracic cord segments was recorded on sagittal FSE T2, STIR, and T1-weighted phase-sensitive inversion recovery sequences independently by 2 readers. A consensus criterion standard read was performed with all sequences available. Sensitivity, specificity, and interobserver agreement were calculated for each sequence.

**RESULTS:** In the cervical cord, the sensitivity of T1-weighted phase-sensitive inversion recovery (96.2%) and STIR (89.6%) was significantly higher ( $P < .05$ ) than that of FSE T2 (50.9%), but no significant difference was found between T1-weighted phase-sensitive inversion recovery and STIR. In the thoracic cord, sensitivity values were 93.8% for STIR, 71.9% for FSE T2, and 50.8% for T1-weighted phase-sensitive inversion recovery. Significant differences were found for all comparisons ( $P < .05$ ). No differences were detected in specificity. Poor image quality and lower sensitivity of thoracic T1-weighted phase-sensitive inversion recovery compared with the other 2 sequences were associated with a thicker back fat pad.

**CONCLUSIONS:** The use of an additional sagittal sequence other than FSE T2 significantly increases the detection of cervical and thoracic spinal cord lesions in patients with MS at 3T. In the cervical segment, both STIR and T1-weighted phase-sensitive inversion recovery offer high sensitivity and specificity, whereas in the thoracic spine, STIR performs better than T1-weighted phase-sensitive inversion recovery, particularly in patients with a thick dorsal fat pad.

**ABBREVIATION:** PSIR = T1-weighted phase-sensitive inversion recovery

MR imaging of the spinal cord is an important diagnostic technique in MS because the prevalence of spinal cord abnormalities in patients with clinically isolated syndrome is as high as 42%.<sup>1</sup> In clinically diagnosed MS, spinal cord involvement reaches 75%–92%, depending on the series.<sup>2–4</sup> The presence of

asymptomatic cord lesions contributes to the demonstration of dissemination in space in the McDonald 2010 criteria for MS, and imaging of the spinal cord allows an increase of 18.3% in the number of patients meeting the diagnostic criteria.<sup>5</sup> The presence of spinal cord lesions not only facilitates diagnosing MS but is also predictive of conversion to clinically definite MS, especially in patients with nonspinal clinically isolated syndrome who do not fulfill brain MR imaging criteria.<sup>6</sup> Moreover, spinal cord lesions in MS can occur in isolation in 5% of patients, particularly in primary-progressive MS.<sup>7</sup>

Spinal cord imaging is challenging because the spinal cord is a small and mobile structure.<sup>8</sup> In addition, its anatomic location

Received August 25, 2015; accepted after revision November 9.

From the Departments of Medical Imaging (P.A.-L., A.P., W.M., G.L., A.B.) and Movement Disorders (J.O.), St Michael's Hospital, Toronto, Ontario, Canada; Department of Medical Imaging (L.A.), University Health Network, Mount Sinai Hospital, Toronto, Ontario, Canada; and Department of Medical Imaging (S.R.), University Health Network, Toronto Western Hospital, Toronto, Ontario, Canada.

Author contributions: guarantors of integrity of entire study: W.M., P.A.-L., A.B.; study concepts/study design or data acquisition or data analysis/interpretation: P.A.-L., L.A., A.P., G.L.; manuscript drafting or manuscript revision for important intellectual content: all authors; approval of the final version of the manuscript: all authors; literature research: P.A.-L.; statistical analysis: P.A.-L.; manuscript editing: P.A.-L., A.B., J.O.

This study was partially funded by Novartis in the form of an educational grant to support the fellowship training position for the first author (P.A.-L.). (Money paid to the institution.)

Please address correspondence to Paula Alcaide-Leon, MD, St Michael's Hospital, Department of Medical Imaging, 30 Bond St, Toronto, ON M5B 1W8, Canada; e-mail: paulaalcaideleon@hotmail.com

Indicates article with supplemental on-line table.

<http://dx.doi.org/10.3174/ajnr.A4656>

### Acquisition parameters of MR imaging sequences

Segment	Sequence	Plane	FOV		Thickness (mm)	TR (ms)	TE (ms)	T1 (ms)	No. of Signals Acquired	Acquisition Time (min:sec)	Parallel Imaging
			(mm)	Matrix							
Cervical	PSIR	Sagittal	220	320 × 224	3	2400	9.4	400	2	4:45	GRAPPA2
Cervical	STIR	Sagittal	300	448 × 336	3	400	51	200	1	5:46	GRAPPA2
Cervical	FSE PD	Sagittal	220	320 × 288	3	2500	23		1	2:02	None
Cervical	FSE T2	Sagittal	220	384 × 307	3	3500	106		2	3:35	None
Cervical	GE T2	Transverse	180	256 × 218	3	740	17		2	4:25	GRAPPA2
Thoracic	PSIR	Sagittal	330	384 × 269	3	2400	9.5	400	2	4:45	GRAPPA2
Thoracic	STIR	Sagittal	330	448 × 336	3	4000	50	200	1	5:46	GRAPPA2
Thoracic	FSE PD	Sagittal	330	320 × 288	3	2500	21		1	4:02	None
Thoracic	FSE T2	Sagittal	330	448 × 336	3	4000	96		1	4:26	None
Thoracic	FSE T2	Transverse	180	256 × 176	5	6780	107		2	4:46	None

**Note:**—GE indicates gradient-echo; PD, proton density; GRAPPA, generalized autocalibrating partially parallel acquisition.

makes it prone to ghosting artifacts caused by the heart and great vessels as well as truncation artifacts. 3T MR imaging compared with 1.5T is more prone to artifacts caused by B<sub>1</sub> field inhomogeneity,<sup>9</sup> susceptibility, vascular pulsation, and chemical shift.<sup>10,11</sup> In addition, 3T MR imaging has a higher energy deposit within the tissue, resulting in a higher specific absorption rate than lower field scanners. These problems can be partially solved with various technical adjustments and fast (parallel) imaging.<sup>12</sup>

Traditionally, the spinal cord in patients with MS has been imaged by using sagittal and axial FSE T2/proton density sequences. Additional sequences, including STIR<sup>13,14</sup> and T1 inversion recovery,<sup>15</sup> have shown promise by increasing lesion visibility, particularly at 3T, in which conventional FSE T2 and proton density images are frequently unsatisfactory.<sup>16</sup> STIR has proved very useful as a complementary sequence in the detection of MS lesions but cannot be used in isolation due to its lower specificity.<sup>13,14</sup> Numerous studies have demonstrated the superiority of STIR over T2 at 1.5T,<sup>13,14,17-19</sup> and 1 study<sup>15</sup> also showed the advantages of STIR at 3T in the cervical cord. To our knowledge, no studies have been performed in the thoracic cord comparing sagittal FSE T2 and STIR. A recent publication showed the advantages of T1-weighted phase-sensitive inversion recovery (PSIR) for the detection of cervical spinal cord lesions in MS at 3T.<sup>16</sup> PSIR has been shown to improve lesion localization and boundary definition over STIR in the cervical spinal cord, but it has not been tested in the thoracic cord.<sup>16</sup>

The aim of our study was to compare the sensitivity and specificity of sagittal STIR, PSIR, and FSE T2 in the detection of MS spinal cord lesions at 3T, in both the cervical and thoracic segments.

## MATERIALS AND METHODS

### Subjects

Approval of the institutional review board to waive informed consent was obtained for this retrospective study. Inclusion criteria consisted of patients with definite or suspected MS who underwent MR imaging of the spinal cord at 3T, including sagittal STIR, PSIR, and FSE T2 as well as axial T2 sections in our institution from July 1 to October 31, 2013. Exclusion criteria were a final diagnosis of a disease causing spinal cord lesions different from MS and substantial motion artifacts. Spinal MR imaging of 39 consecutive patients was reviewed. One patient with a final diagnosis of Churg-Strauss syndrome was excluded. Thirty-eight patients were included in the study. In 11 patients, only the cervical

segment was imaged, and in 12 patients, only the thoracic segment was covered. In 15 patients, both segments were included. This inclusion resulted in 26 cervical and 27 thoracic spinal segments available for evaluation.

### MR Imaging Acquisition

Studies were performed on a 3T MR imaging scanner (Magnetom Skyra; Siemens, Erlangen, Germany) equipped with a 20-channel head-neck coil and a 16-channel spine-array coil. Image parameters are detailed in the Table. No contrast was administered before performing these sequences.

### Image Analysis

Images of all subjects were stripped of patient identifiers and numbered randomly to facilitate blinded analysis. Two readers (P.A.-L. and L.A., neuroradiologists with 6 years' experience in MR imaging) independently evaluated scans for the presence of spinal cord lesions on each spinal cord level on sagittal PSIR, sagittal STIR, and sagittal FSE T2 sequences. To facilitate this task and improve consistency between readers, we drew lines separating the spinal cord levels across the midpoint of the intervertebral disc, parallel to the vertebral endplates as shown in Fig 1C. These reference lines were available during all readings. The upper limit of the C1 segment was defined by the line connecting the tip of the odontoid and the upper edge of the posterior arch of C1. The lowest cord segment evaluated was T12, which was limited inferiorly by a line through the T12–L1 disc. Each sequence was evaluated independent of the other sequences so that the readers could not use them to confirm or rule out the presence of a lesion. Readings of different sequences for the same patient were separated by at least a 2-week interval to avoid memory bias. Disagreements were resolved by consensus. After the 2 independent readings were completed and the disagreements were resolved, an additional consensus reading was performed with all sequences available. This was considered the criterion standard. Combined information contained in sagittal FSE T2, proton density FSE, PSIR, and STIR and in axial gradient-echo T2 of the cervical spine and FSE T2 of the thoracic spine was taken into account to decide which spinal cord segments truly had demyelinating lesions and which were falsely identified as positive for demyelinating lesions due to the presence of artifacts. A lesion was considered a true one if visible on at least 2 sequences, regardless of the imaging plane.

In our experience, PSIR images of the thoracic spine often

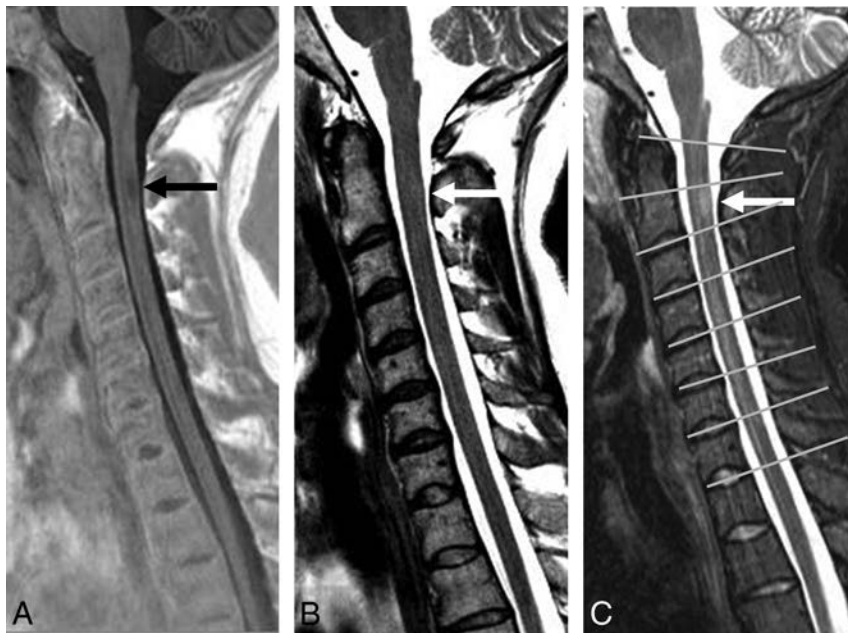


**FIG 1.** Sagittal PSIR (A), FSE T2 (B), and STIR (C) sequences in a patient with MS. A demyelinating lesion at the C2 level (arrows) is adequately visualized on PSIR (A) and STIR (C) but not on FSE T2 (B). C, An example of reference lines through the center on the disc spaces used to separate the vertebral levels (gray lines).

have very poor quality, particularly in patients with a large thoracoabdominal diameter. To confirm our hypothesis that patient size affects PSIR sequence quality in the thoracic spine, we classified images by consensus into 2 groups: good quality or poor quality on the basis of noise and CSF signal saturation. We also measured the thickness of the dorsal back fat pad on PSIR sequences of the thoracic region. This was used as a surrogate marker of the thoracoabdominal diameter, which could not be measured directly on the images. This evaluation was performed by 1 author (P.A.-L.) in the midline at the level of T1–T2, T8–T9, and L1–L2. The mean of the 3 values was calculated. Thicknesses of the back fat pad of patients with good-quality and poor-quality PSIR of the thoracic spine were compared.

### Statistical Analysis

Intrater reliability analysis by the Cohen  $\kappa$  coefficient was performed to determine segmental lesion detection consistency among raters.  $\kappa$  values were interpreted on the basis of the convention by Landis and Koch.<sup>20</sup>

Estimates of sensitivity and specificity were calculated for each sequence in the cervical and thoracic segments (On-line Table). To perform the calculation, we summated all false-positive, false-negative, true-positive, and true-negative segments of the different patients. Thus, calculated values of sensitivity and specificity do not represent directly the accuracy of the sequence in diagnosing MS but do represent the accuracy of the sequence in distinguishing an affected and nonaffected segment of the cord. Confidence intervals for sensitivity and specificity were produced with the Wilson score method.<sup>21</sup> Accuracy of the sequences was also calculated.

Mean thickness of the thoracic back fat pad of the good-quality and poor-quality groups was compared by using the

Mann-Whitney  $U$  test. The Pearson correlation coefficient was used to assess correlations between the thickness of the back fat pad and the sensitivity of the sagittal PSIR of the thoracic spine.

### RESULTS

Twenty-six female and 12 male subjects were included (mean age, 42.1 years; range, 25–68 years). Of 38 subjects included in the study, 33 had clinically definite MS ( $n = 26$ , relapsing-remitting MS;  $n = 3$ , primary-progressive MS;  $n = 3$ , secondary-progressive MS; and  $n = 1$ , progressive-relapsing MS). The mean disease duration was 9 years (range, 1–27 years). The remaining 5 subjects included 2 patients with clinically isolated syndrome, 1 patient with radiologically isolated syndrome, and 2 patients with vague sensory symptoms without a definite clinically isolated syndrome.

There were no exclusions due to motion artifacts. As per criterion standard

evaluation (consensus reading with all sequences available), spinal cord lesions were present in 84% of the cervical examinations and in 85% of the thoracic segments. In 6 patients, the upper thoracic region was not included in the FOV; thus, 8 thoracic segments could not be evaluated. One hundred eighty-two cervical and 316 thoracic spinal cord segments were evaluated. Of these, 106 cervical and 128 thoracic segments were affected by MS lesions. The number of true-positive, true-negative, false-positive, and false-negative spinal cord segments and the sensitivity, specificity, accuracy, and  $\kappa$  coefficient of each sagittal sequence are shown in the On-line Table. Comparisons among the number of true-positive, false-negative, and false-positive spinal cord segments of the 3 different sagittal sequences in the cervical and thoracic segments are shown in Fig 2. In the cervical region, the sensitivity of STIR and PSIR was significantly higher than that of FSE T2 ( $P < .05$ ) (Fig 1). No significant difference was found in sensitivity between PSIR and STIR in the cervical region. In the thoracic region, the sensitivity of STIR was significantly higher than that of FSE T2 and PSIR, and the sensitivity of FSE T2 was significantly higher than that of PSIR ( $P < .05$ ). Specificities of all cervical and thoracic sagittal sequences studied were very similar, with no significant differences identified. Interobserver agreement was higher for STIR than for FSE T2 and PSIR, in both the cervical and thoracic segments.

At visual inspection, all sequences were rated as good quality except for 10 PSIR thoracic studies that showed inhomogeneous CSF saturation and increased noise (Fig 3). The distribution of the variable “size of the back fat pad” in the good-quality and poor-quality groups is shown in Fig 3E. Back fat pad thickness in the poor-quality group was significantly higher compared with the high-quality group ( $P < .001$ ). The mean back fat pad thickness was 13 mm (95% CI, 9.9–16.1 mm) in the good-quality group

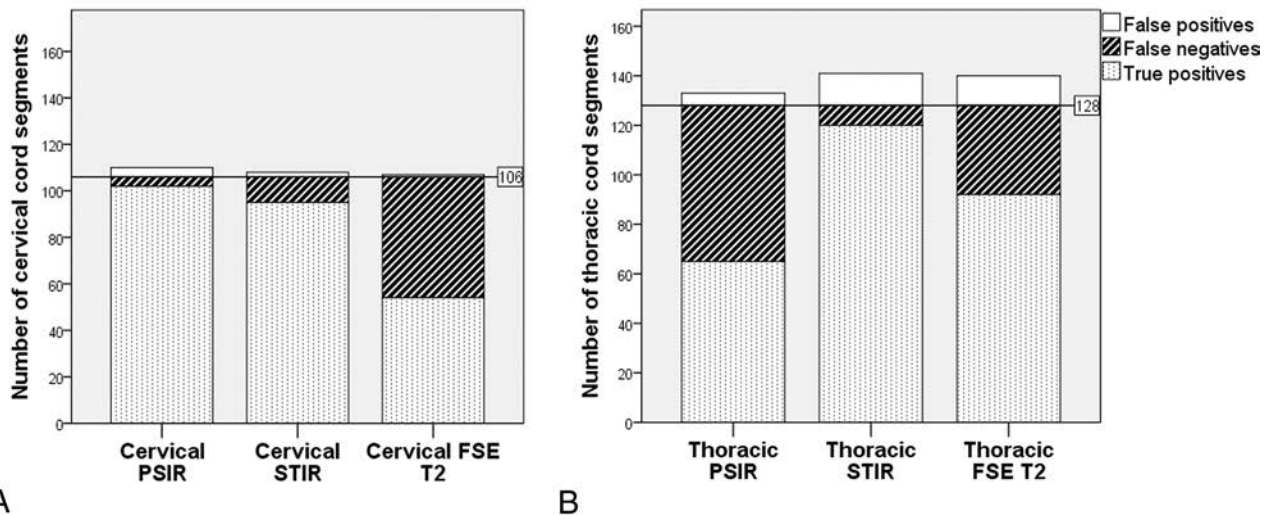


**FIG 2.** Stacked bar charts show the total number of true-positive, false-negative, and false-positive spinal cord segments in the cervical (A) and thoracic (B) regions on the 3 different sagittal sequences evaluated. The horizontal lines represent the total number of segments truly affected by lesions as per criterion standard evaluation.

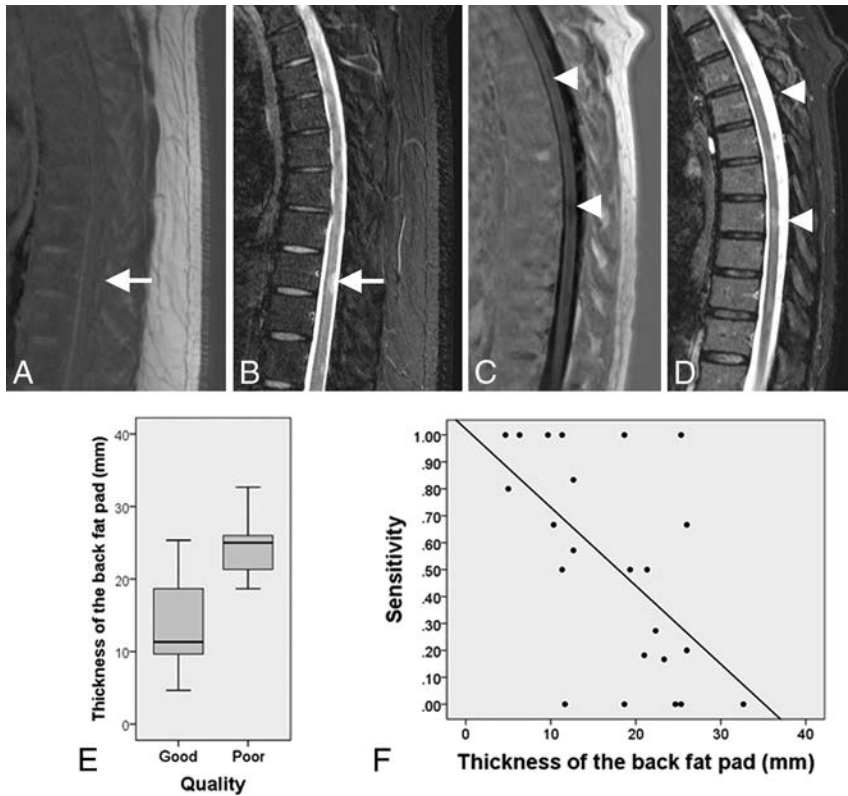


**FIG 3.** A, Thoracic sagittal PSIR image of a patient with MS with a thick back fat pad shows increased noise and failure of CSF suppression. A demyelinating lesion (white arrow) is clearly identified on STIR (B) but not seen on PSIR (A). Sagittal PSIR (C) and STIR (D) sequences of a slim patient with MS show adequate contrast between the lesions (arrow caps) and the cord and adequate CSF signal suppression on PSIR. E, The boxplot shows the distribution of the variable thickness of the back fat pad in the group of patients with good- and poor-quality thoracic PSIR images. The bottom and the top of the boxes represent the 25th and 75th percentiles, respectively; the median is represented by the horizontal line in the box; and the range corresponds to the whiskers that extend from the box. Patients with poor-quality PSIR sequences of the thoracic spine have a median back fat pad size significantly thicker than that in patients with good-quality images. F, The scatterplot shows the negative correlation between the sensitivity of the PSIR sequence of the thoracic segment and the thickness of the back fat pad ( $r = -0.53$ ).

and 24.6 mm (95% CI, 21.8–27.3 mm) in the poor-quality group. A moderate negative correlation (Fig 3F) was found between the thickness of the back fat pad and the sensitivity of the sagittal PSIR sequence of the thoracic spine ( $r = -0.58, P = .003$ ).

### DISCUSSION

This study shows that lesion detection in the cervical region is lower on sagittal FSE T2 than on PSIR and STIR. The sensitivity of sagittal PSIR in our sample was slightly higher than that of STIR; however, the differences were not significant. In the thoracic spine, lesion detection of STIR was significantly better than that of FSE T2 and PSIR and lesion detection of FSE T2 was significantly better than that of PSIR.

The poor performance of PSIR in the thoracic region appears to be related to the thickness of the back fat pad. We are unsure about the cause of this effect in large patients. One explanation may be the dielectric effect. When the abdominal diameter exceeds the radiofrequency wavelength, the 180° pulse is not homogeneous through the FOV. Therefore, some areas may be getting an inversion pulse different from 180°. This effect, however, should also be detected on STIR because both are inversion recovery sequences. Another possibility may be a problem in phase unwrapping because the generation of true phase-sensitive images requires phase images to be

unwrapped first.<sup>22</sup> The algorithm for phase unwrapping depends on a smooth variation in phase, and this constraint is sometimes not met, depending on the patient's anatomy. A similar problem was found by Riederer et al<sup>23</sup> when using a double inversion recovery sequence in the cervical cord. They excluded 10% of their sample due to artifacts presumably caused by adiposity. We did not observe this problem in the cervical examinations, but we found it in 37% of our thoracic examinations. We decided not to exclude large patients with poor image quality because our intention was to test sequences as they would be used in the routine clinical practice. Our observation is noteworthy because a sequence that provides suboptimal image quality in 37% of the patients would not be adequate for routine clinical use; thus, the utility of PSIR to detect thoracic spinal cord lesions may be limited.

Conventionally, sagittal FSE T2 is the most commonly used sequence when imaging the spinal cord in MS. Our results suggest that the use of an additional sagittal sequence can significantly increase the detection of MS lesions in the cervical and thoracic cord without a substantial decrease in specificity. Both sagittal PSIR and STIR perform well in this regard in the cervical spine, but only STIR appears to be adequate in the thoracic region. All the sequences studied have reasonable scanning times and can be implemented in routine clinical practice, but there is a small advantage for cervical PSIR because it is 1 minute shorter than STIR with our acquisition parameters.

We used a segment-based approach to quantify affected spinal cord tissue. With this method, interobserver agreement was moderate for PSIR and FSE T2 of the thoracic spine, substantial for FSE T2 and PSIR of the cervical spine and for STIR of the thoracic spine, and almost perfect for STIR of the cervical spine. Studies comparing lesion detection of different sequences in the spinal cord often had a consensus read<sup>16,24</sup> and a single read<sup>25</sup> or did not report  $\kappa$  values.<sup>14,18,19</sup> Of note, our  $\kappa$  values using a segment-based approach to quantify spinal cord lesion load are higher than those reported in prior studies<sup>13,26</sup> that used lesion count; this finding suggests that a segment-based approach may be a more reliable way to quantify lesion burden in the spinal cord in MS.

The results of our study provide useful information for the design of 3T MR imaging protocols in MS. The superiority of STIR over T2 at 1.5T has been demonstrated on prior studies.<sup>14,19</sup> Dietemann et al<sup>25</sup> reported that the use of STIR in addition to sagittal T2 in the spinal cord increases the number of MS lesions detected by 46%. Another study by Nayak et al,<sup>26</sup> which included a variety of scans performed at 1.5T and 3T, showed a 35% increase in the number of lesions detected using STIR compared with conventional sagittal T2. At 3T, Poonawalla et al<sup>16</sup> reported improved lesion detection of sagittal STIR over sagittal FSE T2; however, the sample was small ( $n = 12$ ) and no statistical analyses were performed to support the findings. In the study by Philpott and Brotchie,<sup>15</sup> sagittal STIR showed a statistically significant increase in cervical cord lesion detection compared with FSE T2 at 3T. Our findings, therefore, are in agreement with previous studies at 1.5T and 3T that have shown that sagittal T2 alone does not have adequate sensitivity to detect cervical cord lesions (Fig 1), supporting the need to incorporate alternative sequences with

higher sensitivity to accurately detect cervical cord lesions in MS. We have also demonstrated the utility of STIR sequences for improving spinal cord lesion detection in the thoracic segment at 3T, which has not been assessed in detail in prior studies.

Our findings support the use of PSIR as another alternative to improve the detection of MS lesions in the cervical spinal cord. In our study, PSIR was not superior to STIR in lesion detection in the cervical spine. Prior studies comparing these 2 sequences include the work by Poonawalla et al<sup>16</sup> (cervical STIR versus PSIR) and Philpott and Brotchie<sup>15</sup> (cervical T1 inversion recovery without phase reconstruction versus STIR); in both cases, samples were very small ( $n = 12$  and  $n = 11$ , respectively) and statistical analysis of lesion detection was not performed. Thus, the existing literature does not provide enough evidence regarding the comparison between PSIR and STIR in the cervical cord, though a trend toward PSIR superiority has been observed, as in our study.

Our results raise the question of whether sagittal T2 should be included in the cervical examinations of patients with MS at 3T, given its inferiority compared with other sequences. We have shown the advantage of substituting sagittal T2 with STIR or PSIR in terms of cervical cord lesion detection; however, we have not evaluated the impact of eliminating sagittal T2 in the characterization of nondemyelinating cord pathologies and incidental findings.

This study has a number of limitations. First, we used a segment-based lesion-quantification approach in which the only information recorded was the presence or lack of lesions in each cord segment. Although this method showed substantially better interobserver agreement than lesion count, it has the disadvantage of being insensitive to differential lesion burden within a particular segment. Second, we focused on comparing FSE T2, STIR, and PSIR, but recent studies have demonstrated that double inversion recovery<sup>23</sup> and T1 MPRAGE<sup>24</sup> can be applied in the cervical cord of patients with MS; however, their long acquisition time (>7 minutes) limits their application in routine clinical practice. Due to the retrospective nature of our study, we did not have these sequences available for analysis in our study population, but future studies comparing T1-weighted phase-sensitive inversion recovery and T1 MPRAGE with STIR and PSIR would be useful. Third, contrary to prior studies, we did not calculate the body mass index.<sup>23</sup> This parameter is easy to calculate and would allow rapid prescanning decision-making for STIR versus PSIR.

## CONCLUSIONS

Our results suggest that at 3T, an additional sequence other than sagittal FSE T2 should be incorporated to improve lesion detection in the spinal cord of patients with MS. In the cervical cord, both sagittal STIR and PSIR showed significantly better lesion detection than sagittal FSE T2. In contrast, in the thoracic spinal cord, the sensitivity of PSIR is markedly worse than that of STIR and FSE T2, particularly in large patients, and STIR is clearly superior to FSE T2. These findings should be taken into account when planning sequence protocols to optimize lesion detection in the spinal cord in MS.

## ACKNOWLEDGMENTS

We would like to thank Bart Schraa, Siemens Application Support, for his help with the technical aspects of this manuscript.

Disclosures: Paula Alcaide-Leon—RELATED: Grant: Novartis.\* Sapna Rawal—UNRELATED: Travel/Accommodations/Meeting Expenses Unrelated to Activities Listed: Association of University Radiologists—GE Radiology Research Academic Fellowship Award, Comments: I am a recipient of the Association of University Radiologists—GE Radiology Research Academic Award for 2015, and the sponsoring body paid for my travel expenses to the Association of University Radiologists meeting in April 2015. Jiwon Oh—UNRELATED: Consultancy: Biogen-Idec, Novartis, Teva, Genzyme, EMD Serono, Roche; Grants/Grants Pending: Biogen-Idec, Genzyme, Multiple Sclerosis Society of Canada\*; Payment for Lectures (including service on Speakers Bureaus): EMD Serono, Novartis, Genzyme, Teva, Biogen-Idec; Travel/Accommodations/Meeting Expenses Unrelated to Activities Listed: Genzyme, EMD Serono. General Leung—UNRELATED: Grants/Grants Pending: University of Toronto.\* Comments: Internal funding was received for a project for carotid atherosclerosis imaging; Patents (planned, pending or issued): operation of wireless devices through the Faraday Cage,\* inhibition of intraplaque hemorrhage using drug therapy\*; Other: In-kind support was received from Siemens, Synaptive Medical, VisualSonics/Fujifilm. Aditya Bharatha—RELATED: Grant: Novartis,\* Comments: educational grant to support research fellow (first author, P.A.-L.); UNRELATED: Payment for Lectures (including service on Speakers Bureaus): EMD Serono, Novartis, Biogen, Comments: honoraria for educational lectures on MS. \*Money paid to the institution.

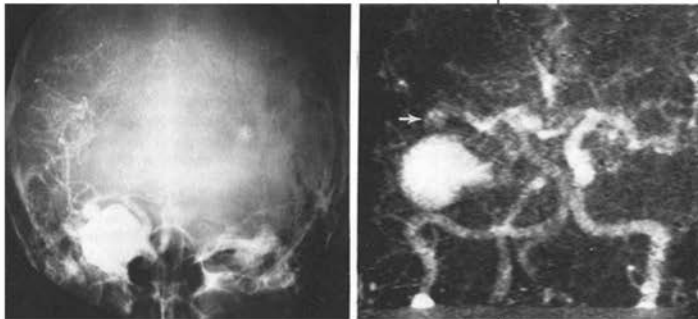
## REFERENCES

1. Brex PA, O'Riordan JI, Miszkil KA, et al. **Multisequence MRI in clinically isolated syndromes and the early development of MS.** *Neurology* 1999;53:1184–90 CrossRef Medline
2. Ikuta F, Zimmerman HM. **Distribution of plaques in seventy autopsy cases of multiple sclerosis in the United States.** *Neurology* 1976;26:26–28 CrossRef Medline
3. Nijeholt GJ, van Walderveen MA, Castelijns JA, et al. **Brain and spinal cord abnormalities in multiple sclerosis: correlation between MRI parameters, clinical subtypes and symptoms.** *Brain* 1998; 121(pt 4):687–97 CrossRef Medline
4. Bot JC, Barkhof F, Lycklama à Nijeholt G, et al. **Differentiation of multiple sclerosis from other inflammatory disorders and cerebrovascular disease: value of spinal MR imaging.** *Radiology* 2002;223: 46–56 CrossRef Medline
5. Bot JC, Barkhof F, Polman CH, et al. **Spinal cord abnormalities in recently diagnosed MS patients: added value of spinal MRI examination.** *Neurology* 2004;62:226–33 CrossRef Medline
6. Sombekke MH, Wattjes MP, Balk LJ, et al. **Spinal cord lesions in patients with clinically isolated syndrome: a powerful tool in diagnosis and prognosis.** *Neurology* 2013;80:69–75 CrossRef Medline
7. Thorpe JW, Kidd D, Moseley IF, et al. **Spinal MRI in patients with suspected multiple sclerosis and negative brain MRI.** *Brain* 1996; 119(pt 3):709–14 CrossRef Medline
8. Mikulis DJ, Wood ML, Zerdoner OA, et al. **Oscillatory motion of the normal cervical spinal cord.** *Radiology* 1994;192:117–21 CrossRef Medline
9. Yang QX, Wang J, Zhang X, et al. **Analysis of wave behavior in lossy dielectric samples at high field.** *Magn Reson Med* 2002;47:982–89 CrossRef Medline
10. Phalke VV, Gujar S, Quint DJ. **Comparison of 3.0 T versus 1.5 T MR: imaging of the spine.** *Neuroimaging Clin N Am* 2006;16:241–48, ix Medline
11. Fries P, Runge VM, Kirchin MA, et al. **Magnetic resonance imaging of the spine at 3 Tesla.** *Semin Musculoskelet Radiol* 2008;12:238–52 CrossRef Medline
12. Filippi CG, Carlson M, Johnson JM, et al. **Improvements in lumbar spine MRI at 3 T using parallel transmission.** *AJR Am J Roentgenol* 2012;199:861–67 CrossRef Medline
13. Bot JC, Barkhof F, Lycklama à Nijeholt GJ, et al. **Comparison of a conventional cardiac-triggered dual spin-echo and a fast STIR sequence in detection of spinal cord lesions in multiple sclerosis.** *Eur Radiol* 2000;10:753–58 CrossRef Medline
14. Hittmair K, Mallek R, Prayer D, et al. **Spinal cord lesions in patients with multiple sclerosis: comparison of MR pulse sequences.** *AJNR Am J Neuroradiol* 1996;17:1555–65 Medline
15. Philpott C, Brotchie P. **Comparison of MRI sequences for evaluation of multiple sclerosis of the cervical spinal cord at 3 T.** *Eur J Radiol* 2011;80:780–85 CrossRef Medline
16. Poonawalla AH, Hou P, Nelson FA, et al. **Cervical spinal cord lesions in multiple sclerosis: T1-weighted inversion-recovery MR imaging with phase-sensitive reconstruction.** *Radiology* 2008;246:258–64 CrossRef Medline
17. Rocca MA, Mastronardo G, Horsfield MA, et al. **Comparison of three MR sequences for the detection of cervical cord lesions in patients with multiple sclerosis.** *AJNR Am J Neuroradiol* 1999;20:1710–16 Medline
18. Campi A, Pontesilli S, Gerevini S, et al. **Comparison of MRI pulse sequences for investigation of lesions of the cervical spinal cord.** *Neuroradiology* 2000;42:669–75 CrossRef Medline
19. Mascalchi M, Dal Pozzo G, Bartolozzi C. **Effectiveness of the short T1 inversion recovery (STIR) sequence in MR imaging of intramedullary spinal lesions.** *Magn Reson Imaging* 1993;11:17–25 CrossRef Medline
20. Landis JR, Koch GG. **The measurement of observer agreement for categorical data.** *Biometrics* 1977;33:159–74 CrossRef Medline
21. Julious SA. **Two-sided confidence intervals for the single proportion: comparison of seven methods by Robert G. Newcombe, Statistics in Medicine 1998;17:857–872.** *Stat Med* 2005;24:3383–84 Medline
22. Moran PR, Kumar NG, Karstaedt N, et al. **Tissue contrast enhancement: image reconstruction algorithm and selection of T1 in inversion recovery MRI.** *Magn Reson Imaging* 1986;4:229–35 CrossRef Medline
23. Riederer I, Karampinos DC, Settles M, et al. **Double inversion recovery sequence of the cervical spinal cord in multiple sclerosis and related inflammatory diseases.** *AJNR Am J Neuroradiol* 2015;36: 219–25 CrossRef Medline
24. Nair G, Absinta M, Reich DS. **Optimized T1-MPRAGE sequence for better visualization of spinal cord multiple sclerosis lesions at 3T.** *AJNR Am J Neuroradiol* 2013;34:2215–22 CrossRef Medline
25. Dietemann JL, Thibaut-Menard A, Warter JM, et al. **MRI in multiple sclerosis of the spinal cord: evaluation of fast short-tau inversion-recovery and spin-echo sequences.** *Neuroradiology* 2000;42:810–13 CrossRef Medline
26. Nayak NB, Salah R, Huang JC, et al. **A comparison of sagittal short T1 inversion recovery and T2-weighted FSE sequences for detection of multiple sclerosis spinal cord lesions.** *Acta Neurol Scand* 2014; 129:198–203 CrossRef Medline

# Celebrating 35 Years of the AJNR

May 1981 edition

## Intravenous Video Arteriography of the Intracranial Vasculature: Early Experience



A computerized fluoroscopic apparatus developed by members of the University of Wisconsin Medical Physics Section was used for 12 months to perform intravenous video arteriography. In previous papers, the apparatus was described and its use was illustrated for performing time subtraction intravenous video arteriography of the extracranial carotid arteries, the arteries of the abdomen and extremities, as well as angiocardiology. In this report, the use and current limitations of this technique for evaluation of the intracranial vasculature are described and illustrated.

Until recently, it has been impossible to achieve satisfactory visualization of the intracranial vasculature following intravenous administration of contrast medium [1-3]. New digital electronic techniques permit processing of the video signal from a conventional image-intensified fluoroscopic system for isolation of the small iodine signal produced after the intravenous injection of contrast medium. Logarithmic amplification combined with subtraction can increase the ratio of the iodine signal to the signal variation of normal anatomic structures by a factor of greater than 100. This type of image processing ensures uniform visualization of the iodine as it passes from the heart to the arteries of the neck and into the cranial vault. Our experience in demonstrating the intracranial arteries with this new method is described.

### Materials and Methods

For examination of intracranial vascular structures, mask mode radiography is employed. An image is obtained before arrival of the contrast medium and is stored in one of two memories. As the iodinated contrast medium passes through the vasculature of the skull and brain, serial images are collected in a second memory, subtracted from the mask, and are then stored on a video disk and video tape. For examination of the intracranial vasculature, the exposure factors are 300 mA, 1/4 sec at 60-65 kVp. Images are generated at the rate of 1/sec. Further details of this imaging sequence have been reported previously [4-6].

Since our initial clinical reports [7, 8], our technique for intravenous injection of contrast medium has been modified. Previously, we injected 40-60 ml of contrast medium at the rate of 1.2-1.4 ml/sec through a 16-gauge, 5-cm-long Angiocath inserted into a basilic vein. While using this technique for over 300 intravenous video arteriograms, we encountered three instances of extravasation of the contrast medium at the injection site. To eliminate this potential complication and to obtain a more consistent contrast bolus, we now use a percutaneously introduced 5 French catheter with an end hole and four side holes, positioning the tip in the central venous sinus or superior vena cava.

For examination of the petrous, cavernous, and supracarotid parts of the internal carotid artery, a projection which positions the top of the petrous bones in the center of the orbit seems to provide the best results. Such a projection is also satisfactory for visualization of the distal segments of the vertebral arteries and of the major part of the basilar artery. Because our resolution is currently limited by focal spot size (over 1.1 mm during the exposure), and a large magnification factor (greater than 1.5) caused by an under-the-

Received November 17, 1980; accepted January 7, 1981.

Department of Radiology, University of Wisconsin, Clinical Science Center, 600 Highland Ave., Madison, WI 53792. Address reprint requests to C. M. Strother.

Present address: Department of Radiology, University of Utah Medical Center, Salt Lake City, UT 84143.

Department of Surgery, University of Wisconsin, Clinical Science Center, Madison, WI 53792.

Present address: Department of Surgery, Wisconsin S. Madsen Veterans Administration Hospital, Madison, WI 53792.

AJNR 3:215-216, May/June 1981  
0195-9181/81/0225-0195 \$02.00  
© American Roentgen Ray Society

## Computed Tomography in 75 Clinical Cases of Syringomyelia

M. L. Aubin<sup>1</sup>  
J. Vignaud  
C. Jardin  
D. Bar

Seventy-five patients with a clinical diagnosis of syringomyelia were examined by computed tomography after intrathecal injection of metrizamide. A cavitation was demonstrated in 67 patients. Tiltting the patient head down did not lead to cavity opacification. This evidence favors transneuronal migration of metrizamide. The spinal cord was measurably enlarged in only a minority of cases. Some of the cavities appeared to have clefts or wall defects. These results are in agreement with the etiopathogenic theories advanced by Gardner, Aboukier, and Williams.

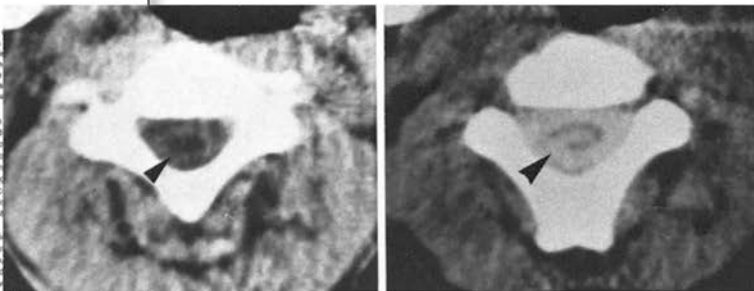
The anatomic basis for the clinical syndrome of syringomyelia is the spinal cord. This cavity may be a dilated central canal (hydromyelia) within the parenchyma (syringomyelia), or both (syringomyelocyst). Theories have been proposed to explain the phenomenon. According to Gardner et al. [1-3] (fig. 1A) failure of the foramen magnum to open at the 29th week of fetal life with continuing expansion of the fourth ventricle and the central canal allows iodine within the ventricles to be transmitted to the central canal, while at the same time, the hydrocephalus causes inferior displacement of the cord thus creating an Arnold-Chiari malformation.

In the Williams [4] theory (fig. 1B), the resulting anatomy is approximately the same, except for the often observed lack of displacement of the cord. According to this theory, efforts such as the Valsalva maneuver, increased venous pressure, which raises the cerebrospinal fluid pressure within the ventricles, which in turn is transmitted to the central canal, while efforts induce venous hypertension in the medullary veins and in the cavity.

Aboukier [5] believes that the Gardner et al. [1-3] theory is only valid for children who have hydrocephalus frequently associated with meningocoele. According to Aboukier (fig. 1C), the pathogenesis of the clinical syndrome of the syringomyelia in adults is different: a cavity develops within the parenchyma without any relation to the central canal which, in adults (according to pathologists mentioned by Aboukier [6-8]) is often collapsed, closed, or absent. The abnormality is caused by stenosis at the level of the foramen magnum due to Arnold-Chiari malformation, arachnoiditis, or tumors.

This theory is supported by canine experiments performed by Sato et al. [9] that demonstrated that 30% of cerebrospinal fluid is produced in the spinal canal. Due to the stenosis at the foramen magnum, the cerebrospinal fluid finds its way with difficulty towards the intracranial areas of resorption. The pressure of the cerebrospinal fluid within the spinal canal is higher than that of intracranial cerebrospinal fluid, resulting in edema within the cord. The last phase of this edema is a cavity. This mechanism is potentiated by increased venous pressure in the sylvian system, which may be congenital or acquired.

According to Aboukier [5], the cerebrospinal fluid filters through the parenchyma or via a pathway along the posterior roots. Ball and Dayan [10] thought



Received June 11, 1980; accepted after revision October 16, 1980.

<sup>1</sup>AR authors: Department of Radiology, Fondation A. de Rothschild, 20 Rue Mazarin, Paris 302, France. Address reprint requests to M. L. Aubin.

AJNR 3:215-216, May/June 1981  
0195-9181/81/0225-0195 \$02.00  
© American Roentgen Ray Society

## Macrocytic Gadolinium-Based Contrast Agents Do Not Cause Hyperintensity in the Dentate Nucleus

We wish to comment on the December 2015 article of Ramalho et al<sup>1</sup> entitled “Gadolinium-Based Contrast Agent Accumulation and Toxicity: An Update” in the *American Journal of Neuroradiology*.

First, the authors introduced the study of Stojanov et al,<sup>2</sup> in which gadobutrol (Gadavist; Bayer Schering Pharma, Berlin, Germany) was purported to cause hyperintensity in the dentate nucleus. However, this report lacks evidence because no hyperintensity in the dentate nucleus on T1WI could be noted in their presented figure, despite being seen in all other previous reports.<sup>3</sup> In addition, Radbruch et al<sup>4</sup> performed a replication study in which gadobutrol showed no correlation with hyperintensity in the dentate nucleus on T1WI. An animal study<sup>5</sup> also denied the association between gadobutrol and hyperintensity in the dentate nucleus on T1WI. These results demonstrated that macrocytic gadolinium-based contrast agents do not cause hyperintensity in the dentate nucleus.

Second, our group<sup>6</sup> evaluated gadolinium deposition in the dentate nucleus, internal segment of the globus pallidus, frontal cortical lobe, white matter of the frontal lobe, and cerebral white matter. McDonald et al<sup>7</sup> evaluated gadolinium deposition in the dentate nucleus, globus pallidus, thalamus, and pons. In addition, they confirmed the presence of extensive gadolinium deposits prominently clustered within the endothelial wall by using x-ray microanalysis. In the article by Ramalho et al, our work is mistaken for the great work of McDonald et al.

These 2 articles<sup>6,7</sup> were published at almost the same time. The submission of our article on November 20, 2014, was earlier than that of McDonald et al,<sup>7</sup> submitted on January 5, 2015, but the acceptance was on March 24, 2015—namely, later than the acceptance of the work of McDonald et al on February 12, 2015. Our work and the work of McDonald et al progressed independently,

and the work of McDonald et al was published a little earlier than our article.

### REFERENCES

1. Ramalho J, Semelka RC, Ramalho M, et al. **Gadolinium-based contrast agent accumulation and toxicity: an update.** *AJNR Am J Neuroradiol* 2015 Dec 10. [Epub ahead of print] CrossRef Medline
2. Stojanov DA, Aracki-Trenkic A, Vojinovic S, et al. **Increasing signal intensity within the dentate nucleus and globus pallidus on unenhanced T1W magnetic resonance images in patients with relapsing-remitting multiple sclerosis: correlation with cumulative dose of a macrocyclic gadolinium-based contrast agent, gadobutrol.** *Eur Radiol* 2016;26:807–15 CrossRef Medline
3. Kanda T, Oba H, Toyoda K, et al. **Brain gadolinium deposition after administration of gadolinium-based contrast agents.** *Jpn J Radiol* 2016;34:3–9 CrossRef Medline
4. Radbruch A, Weberling LD, Kieslich PJ, et al. **High-signal intensity in the dentate nucleus and globus pallidus on unenhanced T1-weighted images: evaluation of the macrocyclic gadolinium-based contrast agent gadobutrol.** *Invest Radiol* 2015;50:805–10 CrossRef Medline
5. Jost G, Lenhard DC, Sieber MA, et al. **Signal increase on unenhanced T1-weighted images in the rat brain after repeated, extended doses of gadolinium-based contrast agents: comparison of linear and macrocyclic agents.** *Invest Radiol* 2016;51:83–89 CrossRef Medline
6. Kanda T, Fukusato T, Matsuda M, et al. **Gadolinium-based contrast agent accumulates in the brain even in subjects without severe renal dysfunction: evaluation of autopsy brain specimens with inductively coupled plasma mass spectroscopy.** *Radiology* 2015;276:228–32 CrossRef Medline
7. McDonald RJ, McDonald JS, Kallmes DF, et al. **Intracranial gadolinium deposition after contrast-enhanced MR imaging.** *Radiology* 2015;275:772–82 CrossRef Medline

● T. Kanda  
● H. Oba  
● K. Toyoda  
● S. Furui

Department of Radiology  
Teikyo University School of Medicine  
Itabashi-ku, Japan

<http://dx.doi.org/10.3174/ajnr.A4710>

## REPLY:

We thank Dr Kanda and colleagues for their interest in our article “Gadolinium-Based Contrast Agent Accumulation and Toxicity: An Update”<sup>1</sup> and acknowledge them for their contributions to the awareness of gadolinium accumulation in the brain. Below, we will attempt to address their comments and concerns.

At the time our article was written, the study by Stojanov et al<sup>2</sup> reported that gadobutrol (Gadavist; Bayer Schering Pharma, Berlin, Germany) caused T1 hyperintensity in the dentate nucleus. Their findings were unexpected and highlighted the need for evaluation of each gadolinium-based contrast agent (GBCA). In fact, after our article was submitted to the *American Journal of Neuro-radiology*, Radbruch et al<sup>3</sup> put forward new information regarding gadobutrol deposition in the dentate nucleus. By replicating the work of Stojanov et al, they concluded that no signal-intensity increase was seen with this agent, explaining the lack of it in the image provided by Stojanov et al. More recently, Cao et al<sup>4</sup> found that unenhanced high T1 signal hyperintensity was observed in the dentate nucleus after multiple administrations of gadopentetate dimeglumine (Magnevist; Bayer HealthCare Pharmaceuticals, Wayne, New Jersey) but not after multiple administrations of gadobutrol, corroborating the findings of Radbruch et al. As stated in our article, the more stable macrocyclic GBCAs such as gadoteridol (ProHance; Bracco Diagnostics, Princeton, New Jersey) and gadoterate meglumine (Dotarem; Guerbet, Aulnay-sous-Bois, France) are not associated with substantial MR imaging changes, supporting the idea that gadolinium accumulation differs according to the stability of the agent used.<sup>5,6</sup>

Although the animal study by Jost et al<sup>7</sup> demonstrated a lack of association between gadobutrol (Gadavist) and T1 dentate nucleus hyperintensity, we recommend caution with extrapolating data from animal studies to humans. In that study, gadopentetate dimeglumine injection led to a moderately elevated dentate nucleus-to-pons signal-intensity ratio, not statistically significant, which differs from findings in human studies.<sup>4-6</sup> Moreover, a more recent animal study performed by Robert et al<sup>8</sup> showed that repeated administrations of that agent were associated with progressive and significant T1 hyperintensity in the dentate nucleus.

We remind our readers that no brain MR imaging changes have been noted in human studies after repeated administrations of the more stable GBCAs gadoteridol, gadoterate meglumine, and gadobutrol. Despite the work of Robert et al,<sup>8,9</sup> more human studies are needed to definitively exclude deposition of these agents in humans.

Although Dr Kanda claims that his article<sup>10</sup> was submitted before the one by McDonald et al,<sup>11</sup> the latter was accepted and published first. Like most investigators, we do not have access to articles not yet published. Nevertheless, our article correctly quotes the number of patients studied, the GBCAs given, and the neural structures evaluated in both articles.

Last, we apologize for misciting the statement related to gadolinium deposits in the endothelial wall. As pointed out by Dr. Kanda and colleagues, this sentence is found in the article by McDonald et al<sup>11</sup> and not the article by Kanda et al.<sup>10</sup>

<http://dx.doi.org/10.3174/ajnr.A4744>

## REFERENCES

1. Ramalho J, Semelka RC, Ramalho M, et al. **Gadolinium-based contrast agent accumulation and toxicity: an update.** *AJNR Am J Neuroradiol* 2015 Dec 10. [Epub ahead of print] CrossRef Medline
2. Stojanov DA, Aracki-Trenkic A, Vojinovic S, et al. **Increasing signal intensity within the dentate nucleus and globus pallidus on unenhanced T1W magnetic resonance images in patients with relapsing-remitting multiple sclerosis: correlation with cumulative dose of a macrocyclic gadolinium-based contrast agent, gadobutrol.** *Eur Radiol* 2016;26:807–15 CrossRef Medline
3. Radbruch A, Weberling LD, Kieslich PJ, et al. **High-signal intensity in the dentate nucleus and globus pallidus on unenhanced T1-weighted images: evaluation of the macrocyclic gadolinium-based contrast agent gadobutrol.** *Invest Radiol* 2015;50:805–10 CrossRef Medline
4. Cao Y, Huang DQ, Shih G, et al. **Signal change in the dentate nucleus on T1-weighted MR images after multiple administrations of gadopentetate dimeglumine versus gadobutrol.** *AJR Am J Roentgenol* 2016;206:414–19 CrossRef Medline
5. Kanda T, Osawa M, Oba H, et al. **High signal intensity in dentate nucleus on unenhanced T1-weighted MR images: association with linear versus macrocyclic gadolinium chelate administration.** *Radiology* 2015;275:803–09 CrossRef Medline
6. Radbruch A, Weberling LD, Kieslich PJ, et al. **Gadolinium retention in the dentate nucleus and globus pallidus is dependent on the class of contrast agent.** *Radiology* 2015;275:783–91 CrossRef Medline
7. Jost G, Lenhard DC, Sieber MA, et al. **Signal increase on unenhanced T1-weighted images in the rat brain after repeated, extended doses of gadolinium-based contrast agents.** *Invest Radiol* 2016;51:83–89 CrossRef Medline
8. Robert P, Violas X, Grand S, et al. **Linear gadolinium-based contrast agents are associated with brain gadolinium retention in healthy rats.** *Invest Radiol* 2016;51:73–82 CrossRef Medline
9. Robert P, Lehericy S, Grand S, et al. **T1-weighted hypersignal in the deep cerebellar nuclei after repeated administrations of gadolinium-based contrast agents in healthy rats: difference between linear and macrocyclic agents.** *Invest Radiol* 2015;50:473–80 CrossRef Medline
10. Kanda T, Fukusato T, Matsuda M, et al. **Gadolinium-based contrast agent accumulates in the brain even in subjects without severe renal dysfunction: evaluation of autopsy brain specimens with inductively coupled plasma mass spectroscopy.** *Radiology* 2015;276:228–32 CrossRef Medline
11. McDonald RJ, McDonald JS, Kallmes DF, et al. **Intracranial gadolinium deposition after contrast-enhanced MR imaging.** *Radiology* 2015;275:772–82 CrossRef Medline

**J. Ramalho**

University of North Carolina Hospital  
Chapel Hill, North Carolina  
Centro Hospitalar de Lisboa Central  
Lisbon, Portugal

**R.C. Semelka**

University of North Carolina Hospital  
Chapel Hill, North Carolina

**M. Ramalho**

University of North Carolina Hospital  
Chapel Hill, North Carolina  
Hospital Garcia de Orta  
Almada, Portugal

**R.H. Nunes**

University of North Carolina Hospital  
Chapel Hill, North Carolina  
Santa Casa de Misericórdia de São Paulo  
São Paulo, Brazil

**M. AlObaidy**

University of North Carolina Hospital  
Chapel Hill, North Carolina  
King Faisal Specialist Hospital and Research Center  
Riyadh, Saudi Arabia

**M. Castillo**

University of North Carolina Hospital  
Chapel Hill, North Carolina

## Cortical Superficial Siderosis Presumed due to Cerebral Amyloid Angiopathy: Minimum Standards for Rating and Reporting

With great interest, I read the recent article by Inoue et al<sup>1</sup> on the diagnostic significance of cortical superficial siderosis (cSS) for Alzheimer disease in a memory clinic setting. In line with other recent studies on the topic, the authors found cSS in 12 of 347 (3.5%) patients in the memory clinic, a prevalence much lower compared with pathologically proved cerebral amyloid angiopathy (CAA) (approximately 50%), but still higher than the 1% prevalence seen in population-based studies. Not surprisingly, in the current study, cSS was found to be associated with strictly lobar microbleeds,<sup>1</sup> a putative marker of CAA.

In a letter to the editor about this study, Bai et al<sup>2</sup> raised a number of important points on cSS definition and detection and opined that the pathogenesis of cSS in the context of CAA is still an unproven hypothesis. They suggested that an, as yet, unidentified bleeding source may account for cSS in the studied cohort instead of CAA.<sup>2</sup> Some of these issues deserve further attention. First, ample evidence suggests that cSS detected in older patients (generally older than 50 years of age) in the context of small-vessel disease (including CAA) is quite distinct from the “classic” superficial siderosis of the central nervous system with regard to underlying pathology, pattern, and clinical presentation.<sup>3</sup> The classic superficial siderosis of the central nervous system (to which Bai et al are referring), affects mainly the infratentorial regions (brain stem and posterior fossa) and spinal cord and typically presents with progressive sensorineural hearing loss, cerebellar ataxia, and corticospinal tract signs.<sup>3</sup> By contrast, published CAA cases with cSS lack these typical clinical manifestations, and cSS is limited to the supratentorial compartment over the convexities of the cerebral hemispheres (almost always sparing the brain stem, cerebellum, and spinal cord).<sup>4,5</sup> It is possible the use of the term “siderosis” for both entities is contributing to this confusion.

While I completely agree with Bai et al<sup>2</sup> that cSS has a wide variety of potential causes, in older individuals, it is emerging as a key neuroimaging signature of CAA. In fact, revised diagnostic criteria for CAA include cSS as an additional hemorrhagic manifestation of the disease, equivalent to lobar cerebral microbleeds and intracerebral hemorrhage.<sup>4</sup> The exact pathophysiologic

mechanisms of the association between cSS and CAA remain an active field of research. However, the role of CAA-related microangiopathic disease as an important cause of cSS in the elderly needs to be emphasized; the most biologically plausible hypotheses based on available evidence are extensively discussed in a recent expert review.<sup>5</sup>

Some technical issues on cSS detection and evaluation are also mentioned by Bai et al<sup>2</sup> in their letter. Most important, differentiating cSS from cortical microbleeds is not difficult if operational criteria are applied because the 2 lesions have different size ranges

### Updated minimum criteria for identification of cortical superficial siderosis and acute convexity subarachnoid hemorrhage in the context of CAA and small-vessel disease<sup>5</sup>

#### Criteria

- Well-defined, homogeneous hypointense curvilinear signal intensity (black) on T2\*-GRE or SWI MRI in the superficial layers of the cerebral cortex, within the subarachnoid space, or in both
- Blooming effect on T2\*-GRE and SWI compared with T1- or T2-weighted sequences
- Differentiation from multiple very superficial cortical cerebral microbleeds (small, generally 2–5 mm, well-defined, homogeneous, and either round or oval lesions, at least half surrounded by brain parenchyma)
- If there is corresponding signal hyperintensity in the subarachnoid space on proton density-weighted or FLAIR sequences (or hyperdensity on CT, if available), the term “acute cSAH” should be used
- Axial T1-weighted or FLAIR images should be used for anatomic confirmation of the gyral location of the signal hypointensities identified on T2\*-GRE or SWI sequences
- Absence of infratentorial (brain stem, cerebellum, spinal cord) siderosis
- Ensure exclusion of potential hemorrhagic and nonhemorrhagic cSS mimics (eg, vessel flow voids, thrombosed vessels, petechial hemorrhagic transformation of infarcts, calcium deposits)
- Consider all potential non-CAA secondary etiologies of cSS and acute cSAH
- cSS should be categorized as focal or disseminated (eg, in line with the modified Boston criteria)
- In each patient, the location (cerebral lobes and so forth) of cSS and the number of cerebral sulci affected can be recorded
- Other relevant vascular neuroimaging lesions both remote from and in close proximity (eg, up to 1 cm) to cSS should be evaluated, using established standards (eg, cerebral microbleeds, acute small DWI lesions, and so forth)

**Note:**—GRE indicates gradient recalled-echo; cSAH, convexity SAH.

and shapes on T2\*-weighted gradient-echo or susceptibility-weighted imaging sequences. cSS shows curvilinear signal intensity in the superficial layers of the cerebral cortex, within the subarachnoid space, or in both, whereas microbleeds are small (generally 2–5 mm), well-defined, homogeneous, and either round or oval lesions.<sup>6</sup> In addition, at least half of the microbleed lesion should be surrounded by brain parenchyma—unlike cSS. The differentiation of microbleeds and cSS becomes more challenging when (rarely) multiple microbleeds are located very near the cortical surface, creating “microbleeds pearls.” In this scenario, the systematic application of operational criteria is essential. Hence, Bai et al touch on a key methodologic aspect in small-vessel disease imaging marker research, namely the use of consistent imaging criteria and standards for evaluating and reporting cSS in relevant studies in the field. To facilitate this, we have recently suggested definitions and minimum imaging standards for cSS evaluation<sup>5</sup>—a slightly modified version of these is provided in the Table. Further studies on the sensitivity and specificity of cSS as a diagnostic MR imaging marker of CAA are necessary.

## REFERENCES

1. Inoue Y, Nakajima M, Uetani H, et al. **Diagnostic significance of cortical superficial siderosis for Alzheimer disease in patients with cognitive impairment.** *AJNR Am J Neuroradiol* 2015 Oct 8. [Epub ahead of print] CrossRef Medline
2. Bai HX, Zhou H, Tan X, et al. **Cerebral amyloid angiopathy as an etiology for cortical superficial siderosis: an unproven hypothesis.** *AJNR Am J Neuroradiol* 2015 Dec 31. [Epub ahead of print] CrossRef Medline
3. Linn J, Brückmann H. **Superficial siderosis in cerebral amyloid angiopathy.** *AJNR Am J Neuroradiol* 2010;31:E29 CrossRef Medline
4. Linn J, Halpin A, Demaerel P, et al. **Prevalence of superficial siderosis in patients with cerebral amyloid angiopathy.** *Neurology* 2010;74:1346–50 CrossRef Medline
5. Charidimou A, Linn J, Vernooij MW, et al. **Cortical superficial siderosis: detection and clinical significance in cerebral amyloid angiopathy and related conditions.** *Brain* 2015;138:2126–39 CrossRef Medline
6. Greenberg SM, Vernooij MW, Cordonnier C, et al; Microbleed Study Group. **Cerebral microbleeds: a guide to detection and interpretation.** *Lancet Neurol* 2009;8:165–74 CrossRef Medline

● **A. Charidimou**

J. Philip Kistler Stroke Research Center  
Department of Neurology  
Massachusetts General Hospital Stroke Research Center  
Harvard Medical School  
Boston, Massachusetts

## Cooling Catheters for Selective Brain Hypothermia

We read with interest “Endovascular Cooling Catheter for Selective Brain Hypothermia: An Animal Feasibility Study of Cooling Performance” by Cattaneo et al.<sup>1</sup> The authors achieved mild brain hypothermia by using a novel indwelling cooling catheter. We appreciate the authors’ acknowledgment of our work in selective brain cooling.<sup>2</sup> However they may have misunderstood the TwinFlo catheter evaluated in our study (ThermoPeutiX, San Diego, California). The TwinFlo inner coaxial balloon catheter is 9.5F, with an inner diameter of 2.0 mm (0.080 inches). This is well within the lumen size needed to perform simultaneous mechanical stent-retriever thrombectomy during selective brain cooling.

Reduction in brain metabolic demand is related to the depth of hypothermia.<sup>3</sup> Brain cooling using the authors’ device was only mild (−4.2°C to −4.5°C) and took >2 hours to achieve. On the other hand, endovascular cold blood perfusion seems better able to achieve the very low temperatures (25°C–26°C) necessary to avert ischemic stroke and can do so very rapidly (<30°C in a median of 15 minutes). We demonstrated a substantial reduction in stroke volume in our large-animal model, despite starting cooling well into the reperfusion phase and after 3 hours of focal ischemia.

<http://dx.doi.org/10.3174/ajnr.A4749>

Disclosures: Thomas K. Mattingly—RELATED: Grant: Heart and Stroke Foundation,\* ThermoPeutiX.\* Comments: HSF GIA 7273; ThermoPeutiX provided the TwinFlo catheters and assisted in data collection on catheter performance. Stephen P. Lownie—Travel/Accommodations/Meeting Expenses Unrelated to Activities Listed: Vice-President, Canadian Neurosurgery Society. \*Money paid to the institution.

### REFERENCES

1. Cattaneo G, Schumacher M, Maurer C, et al. **Endovascular cooling catheter for selective brain hypothermia: an animal feasibility study of cooling performance.** *AJNR Am J Neuroradiol* 2015 Dec 24. [Epub ahead of print] CrossRef Medline
2. Mattingly TK, Denning LM, Siroen KL, et al. **Catheter based selective hypothermia reduces stroke volume during focal cerebral ischemia in swine.** *J Neurointerv Surg* 2015 Feb 12. [Epub ahead of print] CrossRef Medline
3. Lougheed WM, Kahn DS. **Circumvention of anoxia during arrest of cerebral circulation for intracranial surgery.** *J Neurosurg* 1955;12: 226–39 CrossRef Medline

✉ T.K. Mattingly

Neurosurgical Associates  
Richmond, Virginia

✉ D.M. Pelz

✉ S.P. Lownie

London Health Sciences Centre  
London, Ontario, Canada

## REPLY:

We would like to comment on the letter by our colleagues Mattingly et al regarding our article “Endovascular Cooling Catheter for Selective Brain Hypothermia: An Animal Feasibility Study of Cooling Performance.”<sup>1</sup> We appreciate the innovative research by Mattingly et al,<sup>2</sup> who have studied a novel catheter system dedicated to selective brain hypothermia in their recently published work. In our above-referenced article, we have underlined the cooling performance of the extracorporeal blood cooling system described in Mattingly et al<sup>2</sup> with regard to the depth and velocity of the provided brain hypothermia.

Our endovascular approach for selective brain cooling is different in many respects from the technique presented by Mattingly et al. We aimed for a combination of selective brain cooling with mechanical thrombectomy for treatment of acute stroke related to large cerebral artery occlusion. Therefore, the inner coolant circuit of our catheter system provides for blood cooling independent of the larger central working lumen. The latter is dedicated to mechanical thrombectomy only and permanently allows stent-retriever placement and clot retrieval under aspiration without interfering with the cooling performance. Thus, our system can provide a very early selective brain hypothermia initiated before recanalization and extended during and after the critical phase of reperfusion; this system represents, in our view, a paradigm shift compared with recently favored postreperfusion cooling approaches. This “cold reperfusion” approach may allow early neuroprotection by addressing specific inflammatory pathways of ischemia and reperfusion insult as depicted by Pan et al,<sup>3</sup> presumably increasing the therapeutic window for recanalization techniques in the future.

The TwinFlo catheter (ThermopeutiX, San Diego, California) system as described by Mattingly et al consists of a 14F outer catheter placed into the descending aorta and a 9.5F inner catheter with a balloon at the tip, placed into the common carotid artery, which supplies the ischemic hemisphere. In our understanding of the presented work, the inner lumen of 2-mm diameter is not free for use in mechanical thrombectomy and aspiration during cooling because it is needed for the inflow of cooled blood from the extracorporeal cooling circuit. We agree that the size of the inner catheter lumen is suitable for standard access to the intracranial vessels in a mechanical thrombectomy procedure. However, interruption of this extracorporeal blood circuit during the procedure may impose a high risk of catheter thromboembolism or generation of thrombus within the blood pump components, even with short periods of blood stasis. Thus, extracorporeal blood cooling may only be initiated after successful recanalization of the occluded cerebral artery in the postreperfusion phase as it was presented in the study of a swine model with focal ischemia due to transient MCA branch occlusion.<sup>2</sup>

With regard to the optimal target temperature for brain hypothermia in acute stroke treatment, Mattingly et al referred to an older study published in 1955 that described the reduction of metabolic demand in the hypoperfused brain, which decreased almost “linearly” with the reduction in temperature.<sup>4</sup> However,

this finding represents only one of the multiple proposed neuroprotective effects of therapeutic hypothermia in cerebral ischemia, including a reduction of detrimental neuroinflammatory responses, suppression of neurotransmitter release, attenuation of neuronal apoptosis, and dampening of free radical generation.<sup>5</sup> Recent in vivo studies with ischemic models, clinical studies, and guidelines for patients with cardiac arrest put more emphasis on mild therapeutic hypothermia with target temperatures between 33°C and 35°C, which aim at a balance between the neuroprotective effects and the control of adverse events, for implementation in clinical practice.<sup>6,7</sup> In our experimental study, we demonstrated that systemic temperatures followed local brain temperatures in selective intracarotid blood cooling with a relatively stable temperature gradient. The lower brain temperatures of <30° achieved within 15 minutes by extracorporeal blood cooling, which were described in the work of Mattingly et al, involve important issues in the management of patients with stroke, such as infection, shivering, and coagulation impairment<sup>8</sup> due to high-dose heparinization. These issues have to be weighed against the potential benefits of an assumed stronger neuroprotection related to a lower metabolic demand.

We esteem the work of Mattingly et al, who have shown an exciting approach for selective brain hypothermia in acute stroke treatment. Applying 3 hours of early postreperfusion cooling, they could demonstrate, in a swine model, a marked reduction of infarct volume by 42% of transient MCA branch occlusion. Our approach aims at simultaneous neuroprotection in patients with acute large-artery occlusions (MCA M1 or terminal ICA) that undergo endovascular mechanical thrombectomy as a standard treatment. Thus, it should not interfere or delay the standard endovascular procedure and at the same time provide selective brain hypothermia with limited systemic effects and minimized influence on management of patients with stroke. Currently, both approaches may coexist until further validation in a clinical context in patients with acute stroke has been performed.

## REFERENCES

1. Cattaneo G, Schumacher M, Maurer C, et al. **Endovascular cooling catheter for selective brain hypothermia: an animal feasibility study of cooling performance.** *AJNR Am J Neuroradiol* 2015 Dec 24. [Epub ahead of print] CrossRef Medline
2. Mattingly TK, Denning LM, Siroen KL, et al. **Catheter based selective hypothermia reduces stroke volume during focal cerebral ischemia in swine.** *J Neurointerv Surg* 2015 Feb 12. [Epub ahead of print] CrossRef Medline
3. Pan J, Konstas AA, Bateman B, et al. **Reperfusion injury following cerebral ischemia: pathophysiology, MR imaging, and potential therapies.** *Neuroradiology* 2007;49:93–102 CrossRef Medline
4. Loughheed WM, Kahn DS. **Circumvention of anoxia during arrest of cerebral circulation for intracranial surgery.** *J Neurosurg* 1955;12: 226–39 CrossRef Medline
5. Wu TC, Grotta JC. **Hypothermia for acute ischaemic stroke.** *Lancet Neurol* 2013;12:275–84 CrossRef Medline
6. van der Worp HB, Macleod MR, Kollmar R, et al; European Stroke Research Network for Hypothermia (EuroHYP). **Therapeutic hypothermia for acute ischemic stroke: ready to start large randomized trials?** *J Cereb Blood Flow Metab* 2010;30:1079–93 CrossRef Medline
7. Ding Y, Li J, Luan X, et al. **Local saline infusion into ischemic territory induces regional brain cooling and neuroprotection in rats with transient middle cerebral artery occlusion.** *Neurosurgery* 2004; 54:956–64; discussion 964–65 CrossRef Medline

8. Foerster K, D'Inka M, Beyersdorf F, et al. **Prolonged cardiac arrest and resuscitation by extracorporeal life support: favourable outcome without preceding anticoagulation in an experimental setting.** *Perfusion* 2013;28:520–28 CrossRef Medline

**G. Cattaneo**

Acandis GmbH and Co. KG  
Pforzheim, Germany

**M. Schumacher**

Department of Neuroradiology

**G. Trummer**

University Heart Center

**H. Urbach**

**S. Meckel**

Department of Neuroradiology

University Hospital Freiburg,

Freiburg, Germany

## Hypothalamic Adhesions: Asymptomatic, Incidental, or Not?

The term “hypothalamic adhesion” was first described in 2008 as a common associated finding (48%) in Chiari II malformation by the neuroradiology group at the Hospital for Sick Children in Toronto.<sup>1</sup> It has been subsequently presented outside the context of Chiari II in a number of radiologic meetings by us and other groups since 2010 and has been variously referred to as hypothalamic adhesions, hypothalamic fusion bands, interhypothalamic adhesions, intrahypothalamic adhesions, transhypothalamic connections, and even asymptomatic hypothalamic hamartomas. We do not prefer the term “interhypothalamic” because anatomically, there is only 1 hypothalamus that extends to both sides via the tuber cinereum and floor of the third ventricle. Routine use of high-resolution imaging facilitates the detection of this imaging finding, and it is expected that more reports of this finding and its potential association will follow.

In 2014, the presence of this finding was reported in the *American Journal of Neuroradiology (AJNR)* to be highly associated with other malformations and abnormalities in most instances, in a small case series of 13 patients.<sup>2</sup> The authors proposed that it may be a form fruste of holoprosencephaly, given the prevalence of midline abnormalities. Ahmed et al<sup>3</sup> recently reported in the *AJNR* that most patients with this finding are asymptomatic and that these are often incidental findings. So what is the practitioner to do with these seemingly conflicting results? How would the neuroradiologist explain the significance of this finding to referring physicians and patients, given that it is so sparsely reported in the literature? Every time we describe this finding in our clinical radiology reports, we receive these inevitable enquiries from our colleagues. These questions could only be explained with further

cumulative experience in the field, a larger number of patients, and perhaps genomic testing.

In our experience with 3 dozen of these cases in the past 6 years, most were not associated with clinical symptomatology referable to the hypothalamic-pituitary axis and most did not have other anatomic abnormalities. Even when some patients underwent endocrine work-up, no abnormality was found. Nevertheless, we had 1 patient with central precocious puberty and 4 presenting with seizures, though the seizure characteristics were not typical of those with hypothalamic hamartomas. Even though 2 had callosal abnormalities and 3 had nodular heterotopias in our cohort, most have not been associated with discernible midline or nonmidline abnormalities on MR imaging, in our experience. While it is certainly prudent to carefully look for subtle midline and other anatomic abnormalities, we agree with the main tenet of the article by Ahmed et al<sup>3</sup> that neuroradiologists and other care team members perhaps should not be unnecessarily alarmed because these findings can be incidental in many patients.

### REFERENCES

1. Miller E, Widjaja E, Blaser S, et al. **The old and the new: supratentorial MR findings in Chiari II malformation.** *Childs Nerv Syst* 2008;24: 563–75 CrossRef Medline
2. Whitehead MT, Vezina G. **Interhypothalamic adhesion: a series of 13 cases.** *AJNR Am J Neuroradiol* 2014;35:2002–06 CrossRef Medline
3. Ahmed FN, Stence NV, Mirsky DM. **Asymptomatic interhypothalamic adhesions in children.** *AJNR Am J Neuroradiol* 2015 Dec 3. [Epub ahead of print] CrossRef Medline

● A. Vossough

● S.A. Nabavizadeh

University of Pennsylvania  
Children's Hospital of Philadelphia  
Philadelphia, Pennsylvania

<http://dx.doi.org/10.3174/ajnr.A4743>